Supramolecular Assemblies Based on Pyridylhydrazone and Imidazolylimine Schiff Base Ligands

A Thesis Submitted in Partial Fulfilment of the Requirements for the Degree of Doctor of Philosophy in Chemistry

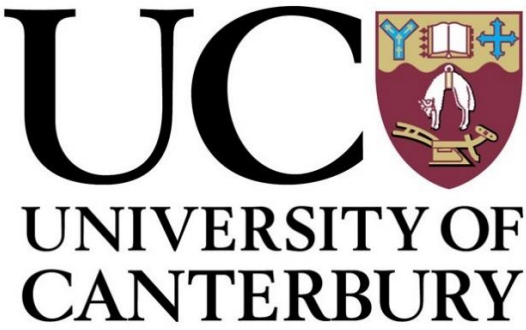

Benjamin Henry Cropp Wilson

Department of Chemistry University of Canterbury

In collaboration with

Centre De Recherche Paul Pascal, University of Bordeaux

Table of Contents

Acknowledgements

Firstly, I would like to acknowledge my supervisor Prof. Paul Kruger for his patience, enthusiasm and support during my time at the University of Canterbury. I was lucky to be part of such a supportive research group during my PhD. I would like to thank all past and present Kruger group members, in particular Dr Dave Young and Dr Rob Staniland for helping me immensely with crystallography, Dr Hayley Scott for taking the time to proof-read much of my work and Dr Dan Preston for showing me the basics in POV-Ray. Furthermore, I would like to thank the Fitchett group for their advice on organic chemistry, the borrowing of chemicals and sharing their lab space with me in the last few months of my PhD.

I was privileged to spend a significant amount of time working at the Centre de Recherche Paul Pascal, University of Bordeaux under the supervision of Dr Rodolphe Clérac and in collaboration with Prof. Corine Mathonière at Institut de Chimie de la Matière Condensée, University of Bordeaux. The work undertaken during my time in Bordeaux would not have been possible without the help of Mathieu Rouzières, Dr Daniel Rosario, Dr Pierre Dechambenoit, Dr Elizabeth Hillard and Dr Ahmed Bentaleb. I would like to thank members of the M3 research team for being warm and welcoming during my stay in Bordeaux. This travel would not have been possible without the financial support of the New Zealand-France Friendship Fund. I would like to thank Prof. Shane Telfer and Omid Qazvini at Massey University for the gas sorption measurements in chapter three along with Prof. Keith Gordon and Josh Sutton at Otago University for the Raman measurements in chapter five.

I am grateful to the staff of the chemistry department for providing a productive and stimulating environment. In particular I would like to thank Dr Marie Squire, Dr Amelia Albret and Dr Amanda Ingles for their expertise in NMR and mass-spectrometry, Dr Matt Polson for practical advice on crystallography, organic chemistry and much more. Finally, I would like to acknowledge Wayne Mackay and Nick Oliver for their dedication in getting the labs in new RRSIC building up and running.

I would like to thank NZIC for travel funding and Universities New Zealand for a Claude McCathy Fellowship to attend ICCC2018 in Sendai, Japan and the School of Physical and Chemical

Sciences for the Jim Coxon Prize to attend MOF2018. I gratefully thank the University of Canterbury for providing a PhD scholarship and Universities New Zealand for the award of a Shirtcliffe Fellowship.

Finally, I would like to thank my family and friends and Bordeaux wine.

Abstract

Functional materials, in particular those that display spin crossover (SCO), single molecule magnetism (SMM) and porosity are of increasing interest due to their potential application in spintronic devices and gas storage and separation materials. To further investigate these classes of materials, a variety of Fe(II), Fe(III) and Co(II) complexes have been synthesised featuring pyridylhydrazone and imidazolylimine ditopic ligands. These two families of ligands were selected due to their applicability to Fe(II) and Fe(III) SCO. However, during the course of this work it was uncovered that they were also suitable for the synthesis of molecular porous materials (MPMs) and Co(II) SMMs. Structural characterisation of all complexes was carried out by single crystal X-ray diffraction, accompanied by NMR, ESI-MS, IR, TGA and elemental analysis where appropriate. The SCO properties were analysed in the solid state via variable temperature magnetic susceptibility and absolute reflectivity measurements. Preliminary photomagnetic measurements were conducted on one complex to investigate the presence of Light Induced Excited Spin-State Trapping (LIESST) behaviour. Magnetic anisotropy of Co(II) complexes was indicated via DC magnetic susceptibility measurements and therefore AC magnetic susceptibility measurements were conducted to investigate the slow relaxation of the magnetic moment. The stability of potentially porous materials was first assessed by powder X-ray diffractions while the porosity was verified by gas sorption measurements.

The first part of the work detailed in this thesis focuses on the dinuclear helicates, mesocates and tetranuclear grid complexes formed with Fe(II), Fe(III) and Co(II) with ditopic pyridylhydrazone ligands. Particular attention was paid to their intramolecular interactions and crystal packing. Where appropriate, the SCO and porosity were investigated using the techniques outlined above. The second part of this work focuses on the use of ditopic imidazolylimine ligands for the synthesis of Fe(II) SCO helicates. The variation of the peripheral imidazole functionality, the anion and crystallisation conditions had a significant impact on the crystal packing and therefore the SCO properties. Preliminary investigation were carried out using Co(II) in the place of Fe(II) for the synthesis of SMM helicates and synthesising Fe(II) SCO helicates featuring mesogenic substituents. The latter was analysed via DSC and SAXS to investigate the occurrence of a phase change associated with the formation with a mesogenic phase.

UNIVERSITY OF CANTERBURY
Te Whare Wānanga o Waitaha
CHRISTCHURCH NEW ZEALAND

Deputy Vice-Chancellor's Office
Postgraduate Office

Co-Authorship Form

This form is to accompany the submission of any thesis that contains research reported in co-authored work that has been published, accepted for publication, or submitted for publication. A copy of this form should be included for each co-authored work that is included in the thesis. Completed forms should be included at the front (after the thesis abstract) of each copy of the thesis submitted for examination and library deposit.

Please indicate the chapter/section/pages of this thesis that are extracted from co-authored work and provide details of the publication or submission from the extract comes:

Sections 2.3.9 and 2.5 from chapter two of this thesis are extracted from: Wilson, B.H.; Scott H.S.; Qazvini, O. T.; Telfer S. G.; Mathonière, C.; Clérac, R.; Kruger, P. E. "A supramolecular porous material comprising Fe(II) mesocates" Chem. Commun. **2018**, *54*, 13391-13394

Please detail the nature and extent (%) of contribution by the candidate:

50% - compound synthesis and structural characterisation, draft manuscript preparation.

Certification by Co-authors:

If there is more than one co-author then a single co-author can sign on behalf of all

The undersigned certifys that:

- The above statement correctly reflects the nature and extent of the PhD candidate's contribution to this co-authored work
- In cases where the candidate was the lead author of the co-authored work he or she wrote the text

Name: Prof. Paul E. Kruger  Signature: Date: 28/1/19

Abbreviations

SCO	Spin crossover
HS	High spin
LS	Low spin
LIESST	Light induced excited spin state trapping
UV-Vis	Ultraviolet-visible
ESI-MS	electrospray ionisation mass spectrometry
TOF	Time of flight
NIR	Near infrared
SMM	Single molecule magnet
SQUID	Super conducting quantum interference device
PPMS	Physical property measurement system
QTM	Quantum tunnelling of magnetization
ZFS	Zero field splitting
MOF	Metal organic framework
COF	Covalent organic framework
MPM	Molecular porous material
TGA	Thermal gravimetric analysis
NBS	N-bromo succinimide
DMF	Dimethyl formamide
DCM	Dichloromethane

Triflate	Trifluoromethanesulfonate
DSC	Differential scanning calorimetry
SC-XRD	Single crystal X-ray diffraction
MIM	Mechanically interlocked molecule
HOF	Hydrogen bonded organic framework
SMOF	Supramolecular metal organic framework
MOS	Metal organic squares
MOP	Metal organic polyhedral
BET	Brunauer–Emmett–Teller

Atom colour scheme

Black: Carbon

Red: Oxygen

Blue: Nitrogen

Orange: Iron

Purple: Iodide, Cobalt

Yellow: Sulfur

Green: Chlorine

Pale green: Fluorine

Pale Orange: Phosphorus

Pale pink: Boron

Chapter One

Introduction

1.1 Preamble and scope

The research detailed in this thesis covers a wide range of areas in both synthetic and physical chemistry. The three key areas covered in this introduction are supramolecular chemistry, porous materials and molecular magnetism. Supramolecular chemistry is a particularly broad topic and therefore only a brief overview will be given to highlight the significant discoveries and core concepts. Where relevant to the work reported in later chapters, a more detailed description is given. All of the work detailed in this thesis focuses on discrete metallo-supramolecular assemblies. Therefore, the bulk of the introduction does not cover infinite metallo-supramolecular assemblies, although they are a significant part of supramolecular chemistry, particularly in the context of porous materials. The introduction to molecular magnetism is divided into two sections: spin crossover (SCO) and single molecule magnetism (SMM). A brief history of each phenomenon, along with a basic explanation of the underlying theory is given. Particular detail is paid to the various techniques used to study these two phenomena, with the use of relevant examples where appropriate. The bulk of the study focuses on Fe(II) SCO, which is reflected in the introduction. There are some preliminary investigations made in the field of Fe(III) SCO and therefore the relevant details for Fe(III) are briefly presented. The metal ion of interest for SMM is Co(II) and hence, a detailed discussion is provided for 3d single molecule magnets with a particular focus on Co(II). Cluster based SMMs and lanthanide based systems are not covered, despite their prominence in the field.

1.2 Supramolecular chemistry: An overview

1.2.1 A brief history and notable landmarks in supramolecular chemistry

The earliest concepts in supramolecular chemistry arose through the study of biological molecules such as enzymes. In 1894, Emil Fischer proposed the ‘lock and key’ analogy for an enzyme interacting with a specific substrate.[1-4] This theory laid the ground work for modern biochemistry and highlighted the importance of weak intermolecular interactions in nature. Approximately half a century later, Watson and Crick deduced the structure of DNA from the diffraction experiments carried out by Franklin.[5] The complementary hydrogen bonded base pairs of DNA highlighted how weak intermolecular interactions were used by nature to assemble large architectures from

smaller constituent molecules (*Figure 1.2.1.i*). Since these discoveries, the field of synthetic supramolecular chemistry began to grow as chemists developed methodologies for using these interactions to craft large supramolecular assemblies. Lehn later defined supramolecular chemistry as "*chemistry beyond the molecule*".[6-8] In 1987 the Nobel prize in chemistry was awarded to Lehn,[9-10] Pedersen[11] and Cram[12] for their advances in the synthesis of organic cryptand and crown ether molecules and the binding of metal ions within them (*Figure 1.2.1.i*). The field of supramolecular chemistry has since evolved with the use of metal ions as nodes and organic ligands as linkers to form evermore complex structures.[13-14] A later Nobel prize in this field was awarded to Stoddart,[15-19] Feringa[20-24] and Sauvage[25-33] in 2016 for their breakthrough work on molecular machines. The work by Stoddard and Sauvage was particularly important to the field of supramolecular chemistry. Their methodologies allowed for the synthesis of highly complex, mechanically interlinked supramolecular assemblies such as catenanes and rotaxanes (*Figure 1.2.1.i*). Leigh and co-workers have since shown mechanically interlinked assemblies can be used to carry out work on a molecular scale, such as the assembly of peptides in a specific sequence, much like the enzymes studied by Fischer over 100 years previously.[34]

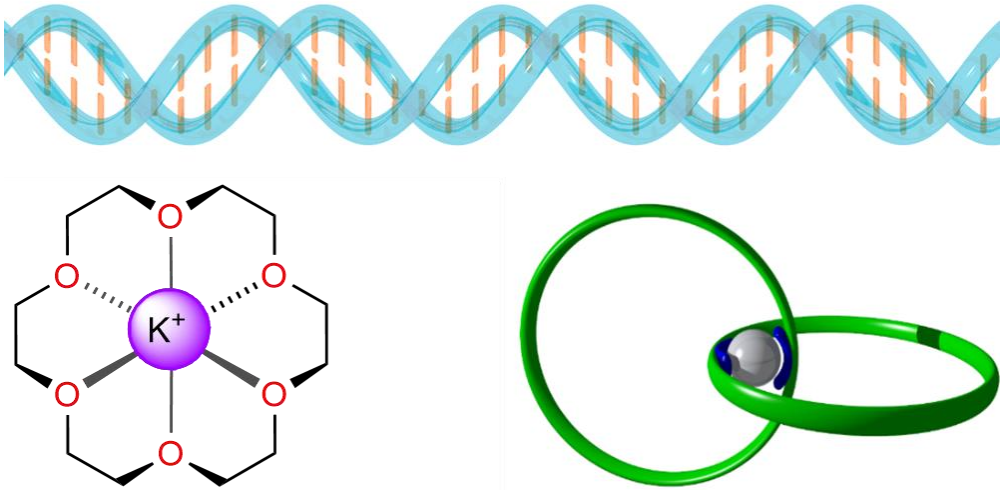

Figure 1.2.1.i: (top) Model of a section of DNA double helix with the phosphate-ribose backbone shown in blue and the hydrogen bond base pairs shown in orange. Figure adapted from POV-Ray source code by Milev and Dominik.[35] (bottom left) Binding of a potassium cation in a crown ether molecule, 18-Crown-6. (bottom right) Model of a metal templated [2]-catenane of the type reported by Sauvage and co-workers.[36] The organic ring components are shown in green, each with a coordination site shown in blue binding to the templating metal ion in grey.

1.2.2 Self-assembly and synthons in supramolecular chemistry

The foundation of supramolecular chemistry is built on the concept of molecular self-assembly. Molecules self-organise to give the supramolecular assembly of the lowest energy when the system is under thermodynamic control.[37-39] A crucial requirement for thermodynamic control is that the interactions between the molecules must be relatively weak and therefore reversible. This reversibility allows two or more molecules to separate and then re-orientate such that reassembly results in the lowest energy architecture (*Figure 1.2.2.i*). These weak interactions take the form of weak intermolecular interactions such as hydrogen bonds,[40-41] π-π stacking interactions[41-44] and halogen bonds[45-46] amongst others. These interactions, particularly hydrogen bonds, are highly directional.[47] Therefore, when a molecule contains a functionality capable of forming one or more of these interactions, there is a degree of structural information encoded into the molecule. An understanding of the directionality of these interactions allows molecules to be synthesised with these functionalities arranged in a specific manner. This allows control over the resultant topology of the supramolecular architecture, post self-assembly. When intermolecular interactions are chosen for the purpose of assembling a specific supramolecular architecture, they are known as 'synthons'.[48] This concept was concisely summarised by Corey as "*structural units within molecules which can be formed and/or assembled by known or conceivable synthetic operations*" and highlights how these molecular functionalities can be used to form predictable supramolecular motifs.[49] A summary of some of the commonly encountered supramolecular synthons will be given with focus given to hydrogen bonds, π-π stacking and halogen bonds. Metal-ligand coordinate bonds are fundamental to the work reported in this thesis and therefore *section 1.3* is dedicated to this topic.

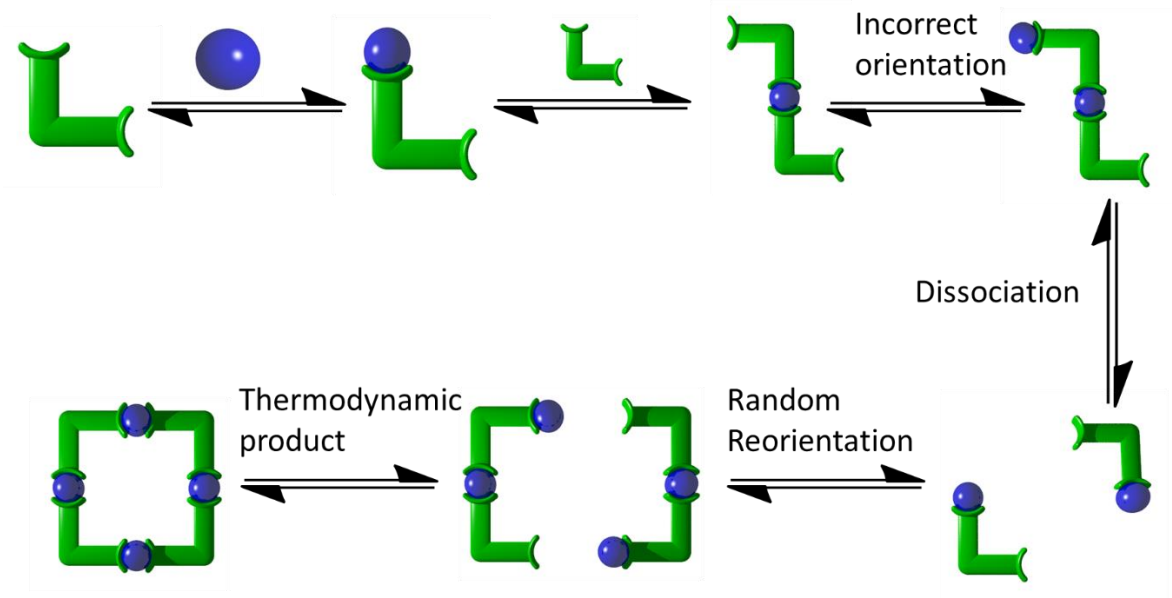

Figure 1.2.2.i: Schematic representation of the reversibility of supramolecular interactions that allows for the thermodynamically most stable product to form. Figure adapted from reference.[38]

1.2.2.i Hydrogen bonds

Hydrogen bond interactions are a cornerstone of supramolecular chemistry and are particularly important to molecular organisation in biological systems. As defined by IUPAC, a hydrogen bond is *"A form of association between an electronegative atom and a hydrogen atom attached to a second, relatively electronegative atom".*[50] A hydrogen bond is composed of two constituent parts: the hydrogen bond donor, D-H, and; acceptor, A. The hydrogen bond donor is the moiety containing the hydrogen atom bonded to an electronegative atom which induces a strong δ+ dipole in the hydrogen atom. The hydrogen bond acceptor is an electronegative atom with a free lone pair of electrons possessing a significant δ- dipole.[40] A conventional hydrogen bond occurs when both the **D** and **A** components are highly electronegative atoms such as nitrogen, oxygen or fluorine. The bond enthalpy of these more commonly encountered hydrogen bonds ranges from 16 to 60 kJ mol^{-1}.[41]

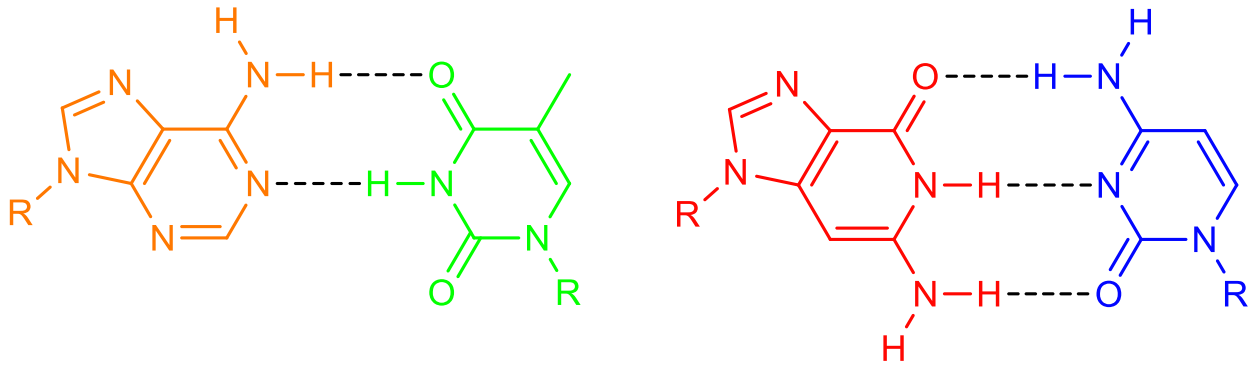

Figure 1.2.2.ii: The complementary hydrogen bond interactions between nucleobases Adenine (orange) and Thymine (green) and Guanine (red) and Cytosine (blue).

Weaker hydrogen bond interactions (<16 kJ mol^{-1}), known as non-conventional hydrogen bonds can occur where an electron deficient C-H moiety acts as a hydrogen bond donor.[41, 51-53] These interactions commonly occur when the carbon atom is part of an aromatic ring, particularly if the aromatic system has electron withdrawing substituents or is electron deficient such as the pyridine aromatic system. These types of interactions are particularly important in the field of synthetic supramolecular chemistry where a large proportion of the organic molecules and ligands contain aromatic rings.

Directionality is a particularly important concept for hydrogen bonds.[47] Due to the nature of the hydrogen bond, there is a predisposition for a D-H···A angle close to 180°. When molecules contain multiple hydrogen bond donors and acceptors, this directionality is important as it results in there being a preferred orientation of the molecules when they interacted to form hydrogen bonds. An extreme case of this is observed for the base pairing of DNA (*Figure 1.2.2.ii*). Due to the arrangement of complementary hydrogen bond donors and acceptors, Adenine only bonds to Thymine and Guanine only bonds to Cytosine a majority of the time. This phenomenon has been exploited synthetically in the form of hydrogen bonded rosettes made up of complementary hydrogen bond donor and acceptor components melamine and cyanuric acid.[54]

1.2.2.ii π-π Interactions

The interaction between aromatic rings is commonly observed in the solid state, indicative of a stabilising interaction. Although implied by the name, direct face-to-face π···π stacking of aromatic rings is generally unfavourable.[41] This is due to the quadrupole moment that arises in

aromatic systems in the model proposed by Hunter and Saunders.[42] This quadrupole moment results in a partial negative charge above and below the aromatic faces and a partial positive charge around the periphery of the aromatic rings. This results in offset stacking of aromatic rings being favourable along with edge-to-face interactions, also known as C-H···π interactions (*Figure 1.2.2.iii*). An off-set π···π stacking interaction typically occurs with a separation of *ca.* 3.5 Å and a bond enthalpy of 2 to 8 kJ mol^{-1}.[41, 44] Direct face-to-face stacking of significantly polarised aromatic systems can lead to stabilising interactions. Alternating stacking of electron rich and electron poor aromatic rings results in an overall attractive intermolecular interaction. This occurs as the quadrupole moment in electron deficient aromatic rings is different to electron rich aromatic rings. The centre of an electron deficient aromatic system now possesses the partial positive charge (*Figure 1.2.2.iii*). This special case of π···π stacking is often referred to as an *"aromatic donor-acceptor interaction"*.[43]

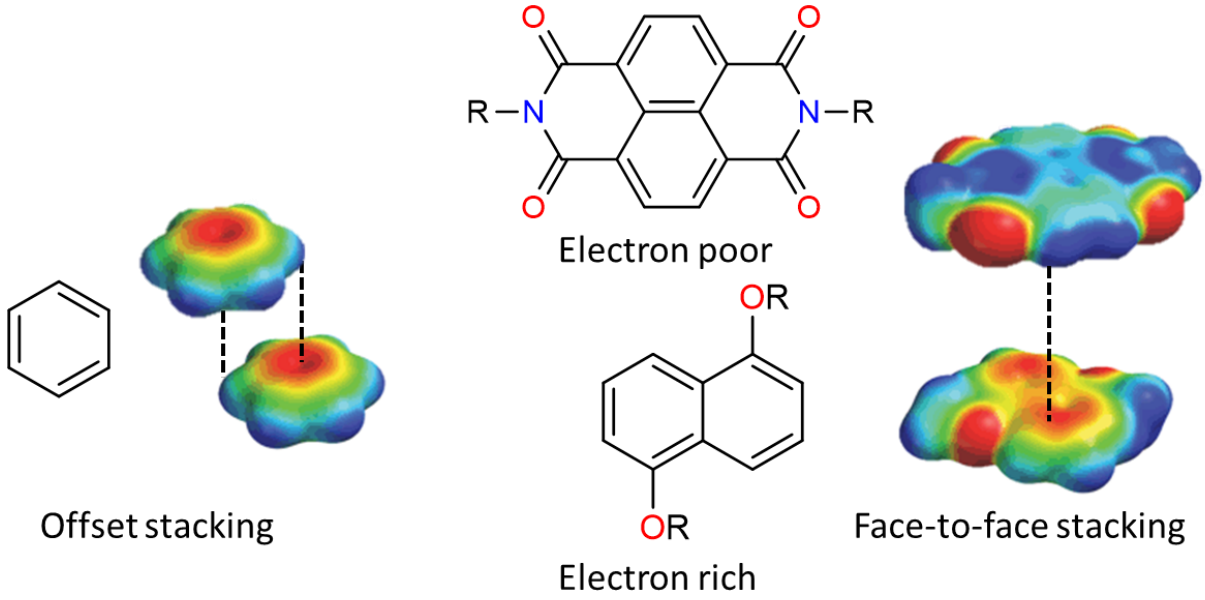

Figure 1.2.2.iii: (left) The offset π···π stacking mode adopted by benzene showing the regions of partial negative charge in red and the regions of partial positive charge in blue. (right) The aromatic donor-acceptor form of π···π stacking between electron poor and electron rich molecules such as the naphthaldiimide and 1,5-dialkoxynaphthalene derivatives as pictured. Electron density maps adapted from reference.[43]

1.2.2.iii Halogen bonds

Compounds containing halogen bonds were synthesised as early as 1814, however, the use of such interactions in crystal engineering was not until recently.[46] A halogen bond occurs between a polarised halogen substituent which is electrophilic and a nucleophilic region on another molecule, which may also be another halogen.[45] These interactions are typically represented as R-X···Y-Z, where X is the halogen, and Y-Z is the nucleophilic region with Y being the atom that the halogen interacts with directly. When halogen atoms are in strongly polarised environments a region of positive charge develops known as a σ-hole. The interaction of the σ-hole with the nucleophilic region is the basis of the halogen bond.[55] A form of halogen bonds is the R-X···X-Z type, where the halogen bond is formed between two halogens. These can be divided into two classes: type I and type II. These are differentiated by the angles of the R-X···X (θ_1) and X···X-Z bonds (θ_2).[56] Type I halogen bonds are symmetrical with $\theta_1 \approx \theta_2$ with values of $90° < \theta < 180°$. These interactions, while formally referred to as halogen bonds, are in fact simply a dispersive interaction as they do not feature the interaction of the σ-hole with a nucleophilic region. Type II halogen bonds are asymmetric with $\theta_1 \approx 90°$ and $\theta_2 \approx 180°$. The 90° angle of θ_1 results in the σ-hole of a polarised halogen interacting with the electron rich equatorial belt of the other halogen (*Figure 1.2.2.iv*). Halogen bonds have also been detected in solution and have shown promise for anion binding.[57]

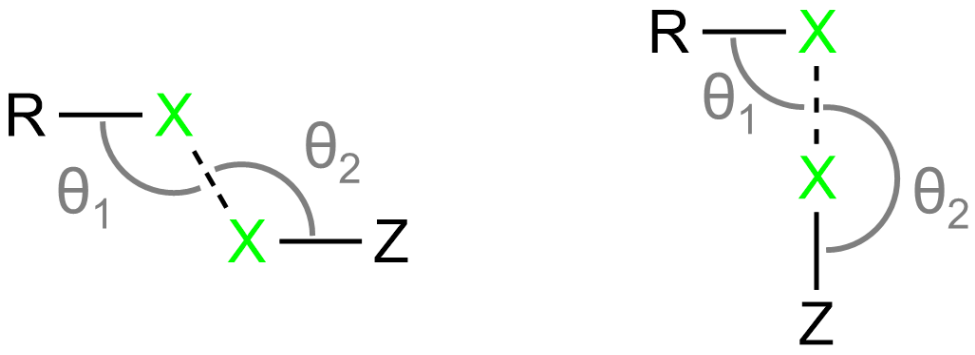

Figure 1.2.2.iv: Type I (left) and type II (right) halogen bonding interactions between R-X and X-Z moieties containing the halogen X. θ_1 and θ_2 are shown in grey highlighting the asymmetric nature of type I interactions and type II interactions.

1.2.2.iv Other supramolecular interactions

There are myriad other supramolecular interactions such as cation$\cdots\pi$,[58-59] anion$\cdots\pi$,[60-61] argentophilic[62-65] and aurophilic interactions.[66-67] These are less commonly encountered than those discussed above. They are much weaker and are typically only encountered in the solid state. These interactions are not directly relevant to the work conducted in this thesis and therefore will not be discussed further.

1.3 Metallo-supramolecular chemistry

1.3.1 Overview and the coordinate bond

Coordination chemistry has become a prominent part of supramolecular chemistry and has generated its own sub-discipline known as metallo-supramolecular chemistry. In this field, the foremost supramolecular interaction is between metal ions and ligands to form coordinate bonds. Our basic understanding of coordination compounds stems from the work by Werner in the late 1800s. He was the first to propose the octahedral geometry of some transition metal complexes and identify the occurrence of isomers in Co(III) chloride ethylenediamine complexes, for which he was awarded the Nobel prize in 1913.[68-71] This seminal work highlighted the importance of the geometry of the ligands about a metal centre. Later work by Griffith and Orgel formed the basis of ligand field theory and more accurately described the exact nature of the coordinate bond.[72-73]

The identity of the metal ion determines both the coordination number and geometry of the ligands, often in a highly predictable manner (*Figure 1.3.1.i*). This means that metal ions are a useful synthon for the synthesis of supramolecular assemblies via the formation of coordinate bonds. The relatively labile nature of metal-ligand coordinate bonds fulfils the reversibility requirement for molecular self-assembly. When polytopic ligands containing multiple metal coordination sites are employed, multinuclear metallo-supramolecular assemblies are formed. Both the ligand and metal ions have strict geometric requirements which allows a specific structure to be assembled by judicious selection of the interacting components.[38, 74]

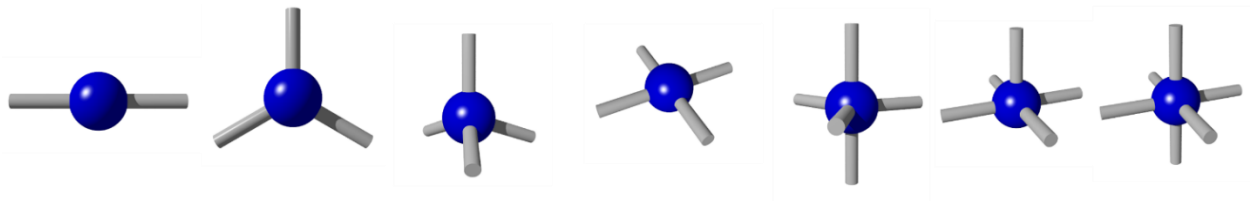

Figure 1.3.1.i: Schematic representation of the various types of metal coordination geometries ranging from linear two coordinate to six coordinate octahedral.

1.3.2 Discrete supramolecular assemblies

As mentioned in the previous section, the use of polytopic ligands, with multiple metal coordination sites, allows for the synthesis of metallo-supramolecular assemblies containing two or more metal ions. Many structures can be designed simply by selecting a metal ion of a given coordination geometry and combining it with a ligand of a specific geometry. Therefore, it is envisioned that a huge range of structures could be synthesised from a relatively small set of starting components. Stoddart coined an apt analogy for this process, by referring to it as '*molecular lego'*.[75] This process has allowed complex structures to be synthesised in relatively high yield making it both a versatile and efficient. When convergent ligands or metal centres are employed in the synthesis, a discrete structure is formed. However, when divergent ligands and metal ions are used, an infinite metallo-supramolecular framework results. The scope of this field is vast and thus the following section will provide simply an overview of some discrete metallo-supramolecular structures. While infinite framework materials compose a vital and ever-growing component of metallo-supramolecular chemistry, a more in-depth discussion is not relevant to the work of this thesis. However, the reader is directed to the following comprehensive reviews.[76-79]

1.3.2.i Polygons and cages

Simple shapes such as squares, triangles, rectangles and hexagons can be readily synthesised from an appropriate diatopic ligand and a square planar metal ion. Stang and co-workers in particular have made an immense contribution to this field, with complexes based on Pd(II) and Pt(II) square planar metal centres.[80-81] Two of the coordination sites were capped with either monodentate or bidentate ligands to give linear or 90° angle nodes, respectively. Metal centres as 90° nodes are particularly useful as there are very few organic molecules that contain a 90° angle. The use of a tritopic ligand can result in the formation of three-dimensional structures which possess an internal cavity. Notable examples such as octahedral and trigonal prism type cages have been reported by

Fujita,[82-84] along with other significantly larger and more complex cages.[85] *Figure 1.3.2.i* summarises how the various combination of metal nodes and ligand linkers result in a variety of supramolecular two-dimensional polygons and three-dimensional cages.

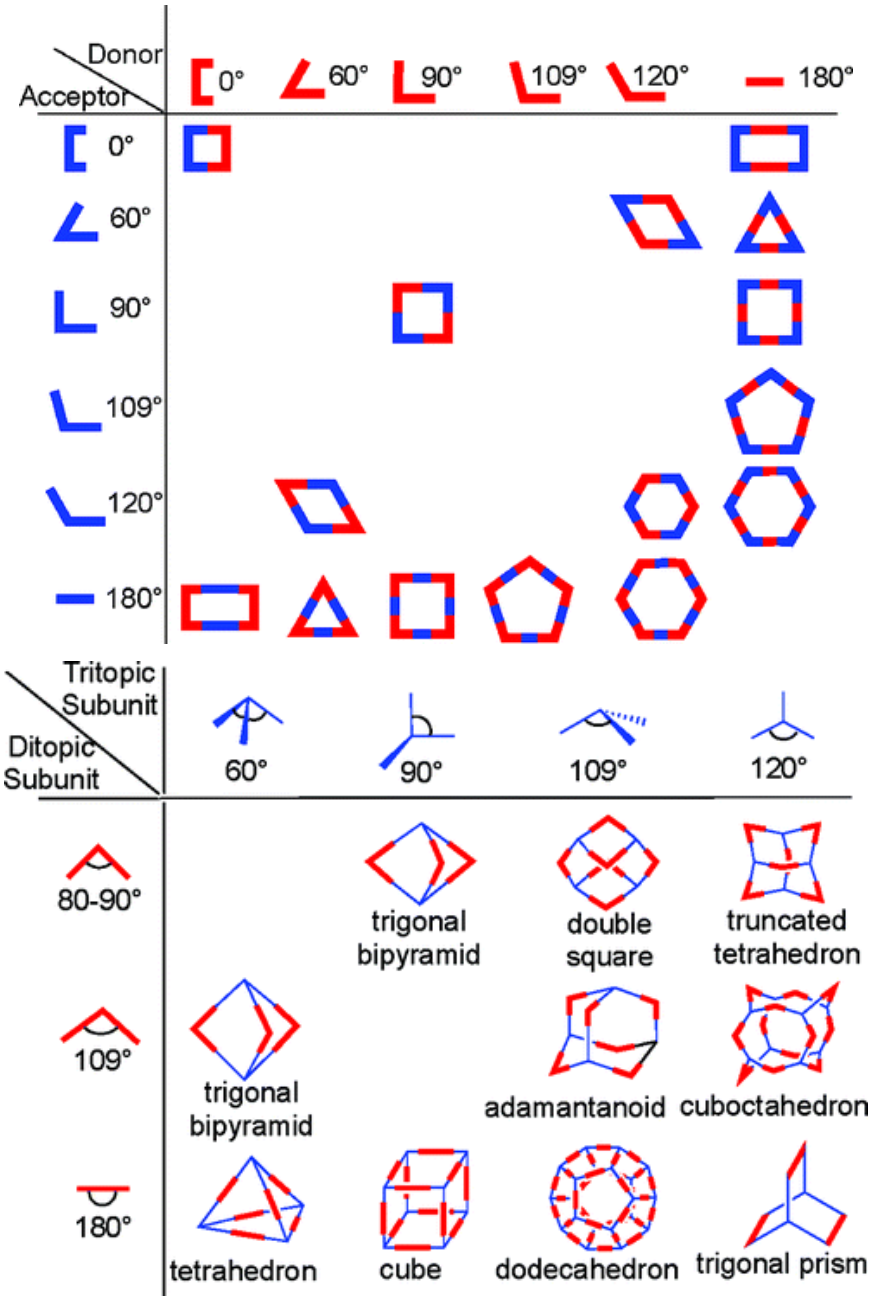

Figure 1.3.2.i: (top) Table illustrating how diatopic donor and acceptor molecules can be combined to form a variety of two-dimensional shapes. (bottom) Table illustrating how tritopic and diatopic subunits can be combined to make three-dimensional polygons. Figures adapted from reference.[38]

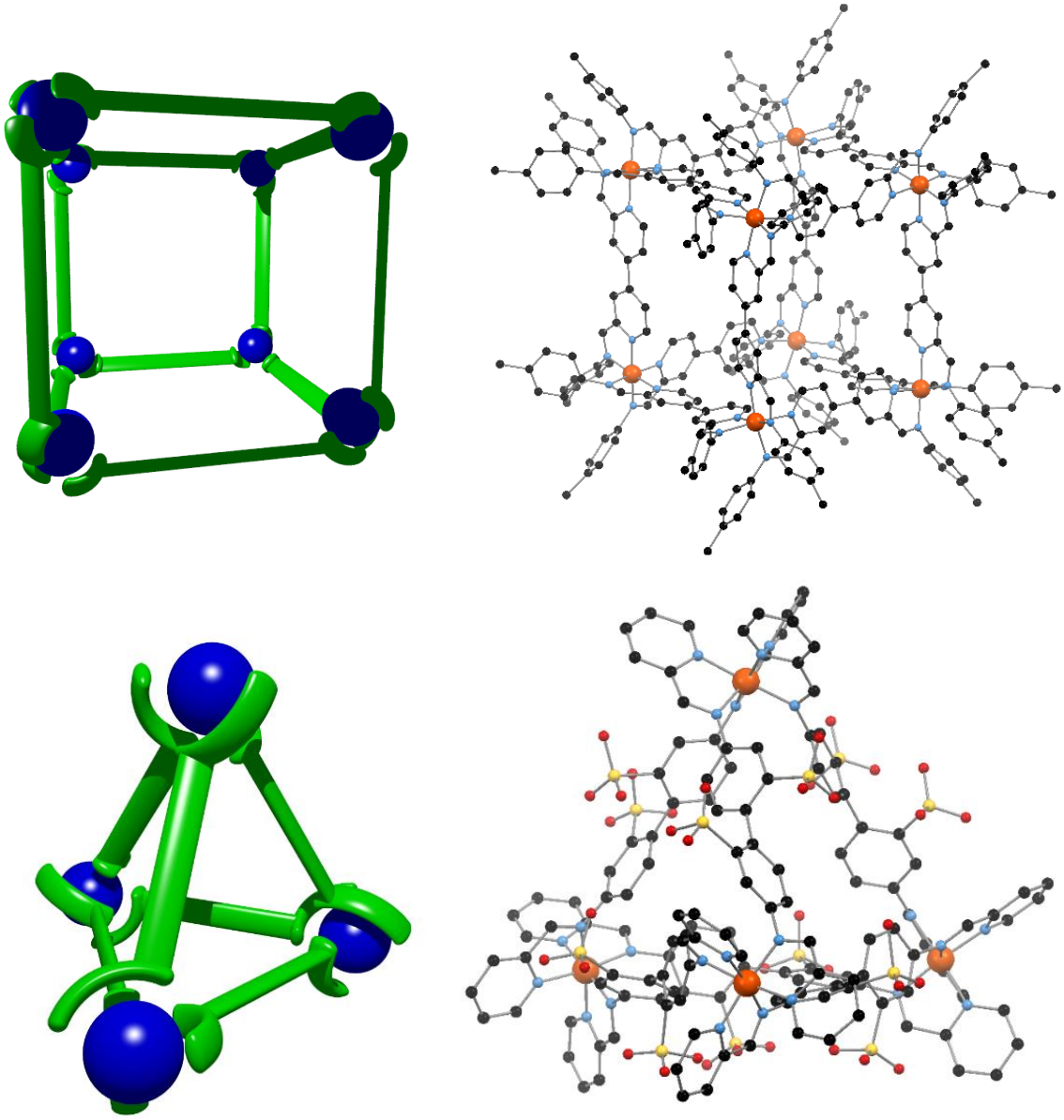

Figure 1.3.2.ii: (top) Schematic representation of an edge bridged cube and crystal structure of an edge bridged cube reported by Nitschke and co-workers.[86] (bottom) Schematic representation of an edge-bridged tetrahedron and crystal structure of an edge-bridged tetrahedron reported by Nitschke and co-workers.[87]

First row transition metal ions have also been used to form a wide range of metallo-supramolecular cage assemblies. Octahedral metal ions in combination with polytopic bidentate ligands have been of particular interest. The work of Nitschke,[88-90] Ward,[91-95] Raymond[96-99] and Kruger[100-101] has demonstrated how ditopic and tritopic ligands can form edge-bridged or face-capped tetrahedral

cages respectively (*Figure 1.3.2.ii*). A key feature of these tetrahedral cage compounds is the capability for a guest molecule to be encapsulated inside the internal cavity. This has formed the basis of a number of *Host-Guest* studies which will be briefly covered in a following section. Octanuclear assemblies can be synthesised from eight octahedral metal ions and an appropriate number of bis-bidentate[86, 102-104] or tetrakis-bidentate[86, 105-106] to form edge-bridged or face-capped cubes respectively (*Figure 1.3.2.ii*). Work by the Nitschke group has pioneered the synthesis of metal-organic polyhedra by a technique known as sub-component self-assembly.[107] A vast majority of their metallo-supramolecular assemblies feature pyridylimine coordinating motifs which are formed *in situ* by reacting the poly-amine precursor with 2-pyridinecarboxaldehyde in the presence of a metal ion. They have since extended this methodology to include post-synthetic modification of the assembly in the solution by displacing either the pyridine or the amine component with an appropriate alternative. This has been utilised to achieve spin switching[108] and cage breakdown/reformation in solution.[109]

1.3.2.ii Metallo-helicates and mesocates

A commonly encountered type of metallo-supramolecular assembly is a metallo-helicate. These assemblies contain two or more metal cations bridged by two or more ligands with an angular and/or flexible linker unit. The helical twist adopted by the ligand, particularly prominent with flexible ligands, results in the complex exhibiting helical chirality, designated *P* (right-handed helical twist) or *M* (left-handed helical twist).[110-112] A requirement for the helicate to exhibit this helical chirality is that the handedness at each of the metal centres (Δ or Λ) must be the same (*Figure 1.3.2.iii*). A related family of structures, often grouped under the umbrella of metallo-helicates, are metallo-mesocates.[113-114] As the name suggests, these types of metallo-supramolecular assemblies possess an internal mirror plane and are therefore achiral (*Figure 1.3.2.iii*). The handedness of the metal centres at either end are different such that if the coordination about one metal ion is Δ then the coordination about the other metal ion is Λ.

There is a large amount of nomenclature associated with these types of metallo-supramolecular assemblies and a brief overview of the relevant terms will be outlined in this section. A dinuclear double helicate refers to a helicate assembly containing two metal centres bridged by two ligands. If the metal ion adopts a tetrahedral coordination geometry, the coordination motif of the ligand is bidentate. Alternatively, if the ligand adopts an octahedral coordination geometry, the coordination

motif of the ligand is tridentate. Both these cases assume the helicate is saturated and there are no solvent molecules or anions coordinating to the metal centre along with the ligands.

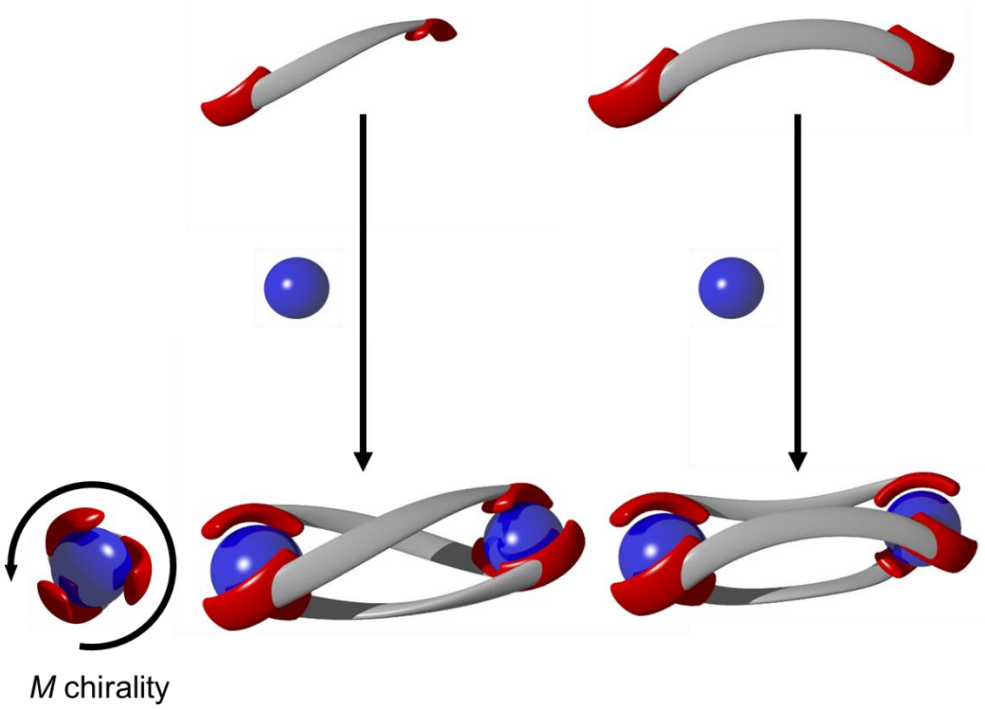

Figure 1.3.2.iii: Schematic representation of the formation of a homotopic dinuclear triple helicate exhibiting M chirality (left) and a homotopic dinuclear triple mesocate (right). The coordinating moieties are shown in red, metal centres in blue and the bridging ligands component in grey.

If the ligand is symmetrical, this results homotopic helicates and mesocates for which both the metal centres exists in chemically identical coordination environments (*Figure 1.3.2.iii*). If the ligand is asymmetric, this results in the formation of heterotopic helicates and/or mesocates. The heterotopic ligands can coordinate in two ways; head-to-head where the two different binding domains each bind to a different metal. Alternatively, they can bind head-to-tail where the binding of each domain occurs at both metal ions. Self-sorting occurs when a mix of ligands with differing numbers of binding domains are present in solution.[115] This phenomenon has been widely studied by Lehn and revealed that when a mix of four ligands containing a differing number of

coordination sites were present in solution, a family of four helicates of defined lengths were formed and no mixed ligand complexes were detected.[116] The inherent chirality of helicate complexes has made them attractive candidates for biochemical applications.[117] In particular, DNA binding of helicates is of great interest as the helical twist of DNA is complemented by the helical nature of the complex. This can result in the metal complex binding to defined areas of the DNA along with certain RNA species.[118-121] Work by Hannon and co-workers has highlighted the potential of dinuclear triple helicates in this field by showing the specific binding of Ru(II) and Fe(II) helicates to DNA and RNA respectively. The binding of the Ru(II) helicate to DNA resulted in cytotoxicity to breast cancer cells,[120] while the binding of the Fe(II) helicate to RNA resulted in the inhibition of the HIV-1 replication cycle.[118] The relationship between the linker unit and the preference for helicate or mesocate formation has been explored by Albrecht and co-workers.[113] For this study the coordinating motifs were linked with flexible alkyl linker moieties. A linker unit containing an even number of carbon atoms adopted a conformation resulting in the formation of a helicate while an odd number of carbon atoms led to the formation of a mesocate. This has since been generalised to other families of helicate/mesocates.[122] The examples of helicates and mesocates discussed above can all be termed 'linear helicates' as all of the metals are aligned along a single axis. Helical twists can be imbued into other types of metal complexes such as the circular helicates by Lehn and co-workers.[123-124] In this example, while the metal centres are arranged in a macrocyclic and not linear manner, the coordination mode of the ligands results in the complex featuring an intrinsic helical twist.

1.3.2.iii Metallo-grids

Metallo-supramolecular grid complexes are a class of metallo-supramolecular assembly in which rigid ligands coordinate to metal ions resulting in a grid architecture of parallel and orthogonal ligands.[125-126] The most simple of these assemblies feature ditopic ligands and are referred to as 2 x 2 grids with four linkers bridging four metal ions in a square fashion.[127-128] When the metal ion favours a tetrahedral coordination geometry, a rigid ligand containing two or more bidentate coordination sites is required. However, if the metal favours an octahedral coordination geometry a rigid ligand containing two or more tridentate coordination sites is required.[128-131] In supramolecular grid assemblies the ligands adopt one of two types of conformation. The first is where the two binding domains are orientated in the same direction and will be referred to

henceforth as the *syn* conformation. When all the ligands adopt the *syn* conformation, the resultant grid is referred to as *syn* (*Figure 1.3.2.iv*) and is the most common conformation in the literature.[126] If the binding motifs are orientated in opposing directions, the conformation of the ligand is referred to as *trans*. When all the ligands adopt the *trans* conformation, the resultant grid is referred to as *trans*. While this type of conformation is less common, there are several reports of grid architectures adopting this conformation.[132-133] There is a third, much less common grid architecture which contains a mix of the two ligand conformations. In the case of a 2 x 2 type grid, two parallel ligands adopt the *syn* conformation while the remaining two adopt the *trans* conformation. There has been several reports of grids adopting this type of structure which will be referred to a s*yn-trans*.[134] Much like the helicate type structures discussed in the previous section, the self-sorting of metallo-supramolecular grids based on ligand with differing number of coordination sites was investigated by Lehn. However, for the case of supramolecular grids, ligands containing differing numbers of coordination sites were incorporated in the same structure.[135-136] In one example this resulted in a 2 x 3 grid containing six Ag(I) ions, three bis-bidentate ligands and two tris-bidentate ligands.[136]

Figure 1.3.2.iv: The three forms of metallo-supramolecular grids; syn (left), trans (middle) and syn-trans (right). Ligands adopting the syn conformation shown in green while ligands adopting the trans conformation are shown in blue. Metal ions are represented by the grey spheres.

1.3.2.iv Mechanically interlocked molecules and molecular knots

The two previously discussed types of supramolecular architectures, helicates and grids, can be used as building blocks for the synthesis of mechanically interlocked molecules (MIMs) and knots. MIMs consist of two or more molecules which are not covalently linked but encircle on another such that they cannot be separated.[15, 17, 29, 33] Two key classes of MIMs are rotaxanes and catenanes.

The seminal work of Sauvage demonstrated the importance of coordination chemistry by using the coordination of the organic precursors to a metal ion in order to arrange them in a suitable conformation before the ring closing step formed the catenane.[28, 30-31] A similar procedure has been employed to synthesise rotaxanes with a macrocycle encircling an organic thread with bulky capping groups at either end. Later work by Fujita revolutionised the synthesis of catenanes by using metal-ligand supramolecular self-assembly and exploiting the reversibility of the metal-ligand coordinate bond.[137-138] Simply by increasing the ionic strength of a solution of Pd(II) rings, the formation of π-π interactions between the hydrophobic aromatic rings of the ligand resulted in the formation of metallo-supramolecular catenanes. This metallo-supramolecular approach has been since used to form several catenanes based on 2x2 grids (*Figure 1.3.2.v*).[134, 139] Molecular knots are a single molecule that is entwined through itself and cannot be untangled without the breaking of covalent bonds.[140-141] The circular helicate discussed in *section 1.3.2.ii* was used as the basis for the first such molecule. The reaction of the ends of each ligand with a suitable capping molecule resulted the first pentafoil knot (*Figure 1.3.2.v*).[142]

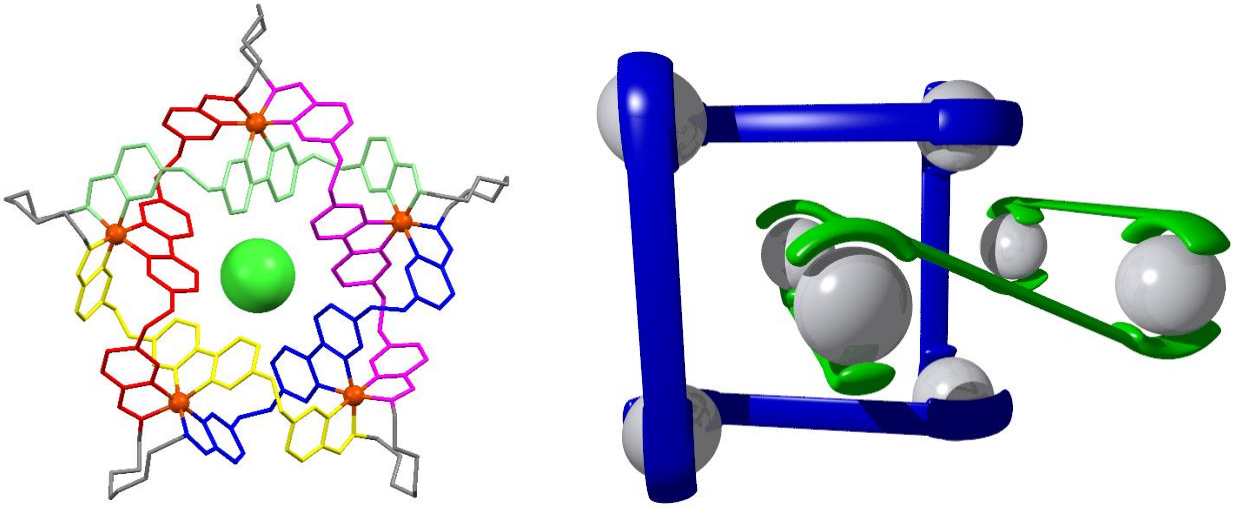

Figure 1.3.2.v: (left) the pentafoil knot reported by Leigh and co-workers containing the templating chloride anion in the central cavity.[142] A schematic representation of the metallo-catenane reported by Thompson and co-workers,[134] made up of two tetranuclear grid complexes; one in blue and one in green and metal ions represented by grey spheres.

1.4 Applications of supramolecular chemistry

There are many potential applications for synthetic supramolecular assemblies, most of which involve the interaction of the assembly with an analyte or guest molecule. Molecules containing potent hydrogen bond donor groups such as urea and squaramide moieties can be used as anion sensors. These are particularly effective when the anion binding group is conjugated to a photoactive functionality, allowing for colorimetric sensing by the naked eye.[143-145] These hydrogen bond motifs have been incorporated into metallo-supramolecular cages which have shown to selectively bind high charge density oxo-anions such as sulfate (*Figure 1.4.1*).[146-147] This capture of a molecular guest inside a supramolecular cage, referred to as *Host-Guest* chemistry contributes to a number of other potential applications. The confinement of the guest molecule inside the cage results in it experiencing a different micro-environment compared to in solution. This is particularly important for catalysis as the confinement of molecules in the cage increase the effective concentration.[148-149] In the case of flexible molecules, a different conformation may be adopted.

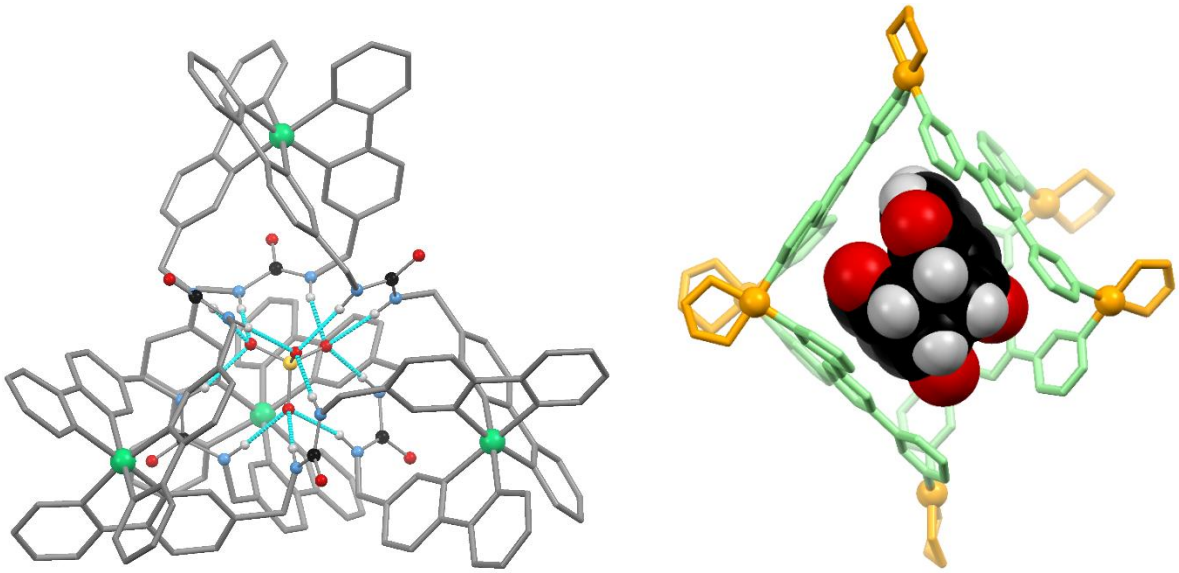

Figure 1.4.1: (left) The metallo-supramolecular cage reported by Hay and co-workers encapsulating a sulfate anion via 12 hydrogen bonds from the urea moieties.[146] (right) The octahedral metallo-supramolecular cage reported by Fujita and co-workers encapsulating two naphthoquinone molecules that have undergone photo-dimerization in the cavity.[150]

Alternatively, two molecules are made to approach one another in a different manner due to confinement in the cavity of the cage, resulting the stabilisation of a different transition state. This allows for different stereo- or regio-chemical out comes compared to the analogous reaction carried out by conventional means. A Pd(II) octahedral cage reported by Fujita and co-workers has been used to catalyse a number of photo-dimerization reactions (*Figure 1.4.1*).[150-151] In one such example, at low concentrations the photo-dimerization of acenaphthylene did not occur and at elevated concentrations occurred with a poor stereo- and regio-selectivity. However, when the Pd(II) octahedral cage was employed as a catalyst, the reaction occurred with a quantitative yield at low concentration with exceptionally high stereo- and regio-selectivity. Such metallo-supramolecular cages are very versatile catalysts. An anionic tetrahedral cage reported by Raymond and co-workers has been reported to stereo and regio-chemically mediate C-H activation reactions and catalyse Aza-Cope and orthoformate hydrolysis reactions.[152-156] While supramolecular host complexes have been investigated for catalytic applications, they have also been utilised to do the opposite; protect reactive molecules. A water-soluble tetrahedral cage reported by Nitschke and co-workers allowed for solubilisation of highly reactive P_4 in aqueous solution due to its encapsulation.[87] In a similar manner, the previously discussed tetrahedral cage by Raymond and co-workers stabilised reactive diazonium ions, the tropylium cation, iminium cations and phosphonium adducts.[157-159]

MIMs such as catenanes and rotaxanes have found application in the form of chemical sensors and molecular machines. Hydrogen bond and halogen bond interactions of the macrocycles of catenanes and rotaxanes allows for them to selectively bind analytes.[160] The use of chiral macrocycles in the synthesis of rotaxanes allows for the assembly to selectively bind one enantiomer over another.[161] A molecular machine can be thought of as a molecule that carries out some form of mechanical work on the molecular scale.[33, 162-165] Rotaxane assemblies have been synthesised in such a way that they can expand and contract by the thread moving through the macrocycle upon the application of an external stimuli. This allows them to mimic the behaviour of muscle fibres.[27, 166] Rotaxanes have also been used as assembly lines for the synthesis of oligo-peptides. Leigh and co-workers synthesised a rotaxane with three amino acid residues covalently linked at various points on the thread of the rotaxane (*Figure 1.4.2*).[34] As the macrocycle moves down the thread, the amino acid residues are added sequentially to the growing peptide anchored on the macrocycle. This results in the controlled synthesis of the oligo-peptide.

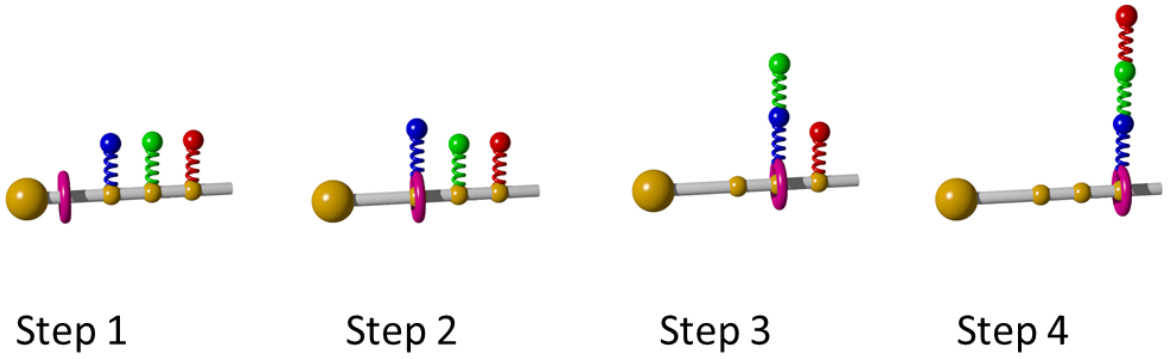

Figure 1.4.2: A schematic representation of the pseudo rotaxane employed by Leigh and co-workers for the stepwise synthesis of an oligo-peptide.[34] The amino acid residues (blue, green and red) are added sequentially as the macrocycle (pink) moves down the tread of the rotaxane.

1.5 Molecular porous materials

Porous materials are a significant area of current research endeavour. The synthesis of porous materials capable of separating greenhouse gases and/or catalytically converting them into synthetically useful molecules or fuels has resulted in interest this field growing significantly.[167] Porous materials are not just applicable to gas storage but can be utilised for separation and sensing of other molecules. A key industrial process applicable to porous materials is the separation of CO_2 from environmentally benign N_2 in flue gas from coal burning power stations for electricity generation.[168-172] In order for this process to be efficient, the porous material must be selective for CO_2 over N_2, meaning that CO_2 is trapped while N_2 gas passes through relatively unencumbered. While both CO_2 and N_2 are non-polar, CO_2 possesses a strong quadrupole moment. This quadrupole moment has been exploited by synthesising materials with polar pore functionalities that interact with CO_2 more strongly than N_2.[173-176] At present, the class of porous materials most commonly associated with supramolecular chemistry are Metal-Organic Frameworks (MOFs). MOFs are infinite framework materials made up of a node containing one or more metal ions and divergent organic linker ligands. The extension of these nodes and linkers in three-dimensions results in a porous framework material. These materials are synthesised following the principals of supramolecular self-assembly, with the target framework being the thermodynamic product under the conditions present. MOFs are such a large field of research in porous materials as metal

ions are particularly apt for the synthesis of regular framework type materials for a number of reasons:

1) The lability of the metal-ligand coordinate bond permits a degree of reversibility during supramolecular self-assembly and results in the formation of crystalline materials.

2) The directionality of metal-ligand coordinate bond and the arrangement of coordination sites about a metal ion or cluster are predisposed for the formation of three-dimensional polymeric materials.

3) The metal-ligand coordinate bond is more inherently stable than other types of weak supramolecular interactions such as those describe in *section 1.2.2*.

However, MOFs are not the sole category of porous materials containing organic linkers. More recently wholly organic frameworks known as Covalent-Organic Frameworks (COFs) have been synthesised using organic functional groups that react with one another to form covalent bonds that also have a degree of reversibility.[177] Common functional groups include the formation of boric anhydrides, borate esters and imines. A key advantage of COFs is that the gas uptake weight percentage is higher as the lack of metal ions results in a compound of lower density. However, the strength of the covalent bond typically limits the reversibility, so highly crystalline materials are far more difficult to obtain. A limitation of both MOFs and COFs is their solution processability, which restricts their mass production for industrial application. An emerging class of porous materials are molecular porous materials (MPMs). These are molecular entities that contain micro-pores however, they are not infinite framework materials. The building units are not linked by covalent or coordinate bonds but by intermolecular interactions, most typically hydrogen bonds. MPMs can be divided into two main classes; organic materials such as hydrogen-bonded organic frameworks (HOFs)[178-181] and organic cages[182-183] or metal-organic molecular materials such as supramolecular metal-organic frameworks (SMOFs),[184-188] metal-organic polyhedral (MOPs)[189-194] and metal-organic squares (MOSs).[195-197] These types of materials are less common for two key reasons:[198]

1) The packing density of molecular compounds is typically high and therefore compounds containing micropores are comparatively rare.

2) As hydrogen bonds are weaker than both coordinate and covalent bonds, the framework integrity is often lost when the solvent molecules of crystallisation are removed from the pores leading to framework collapse.

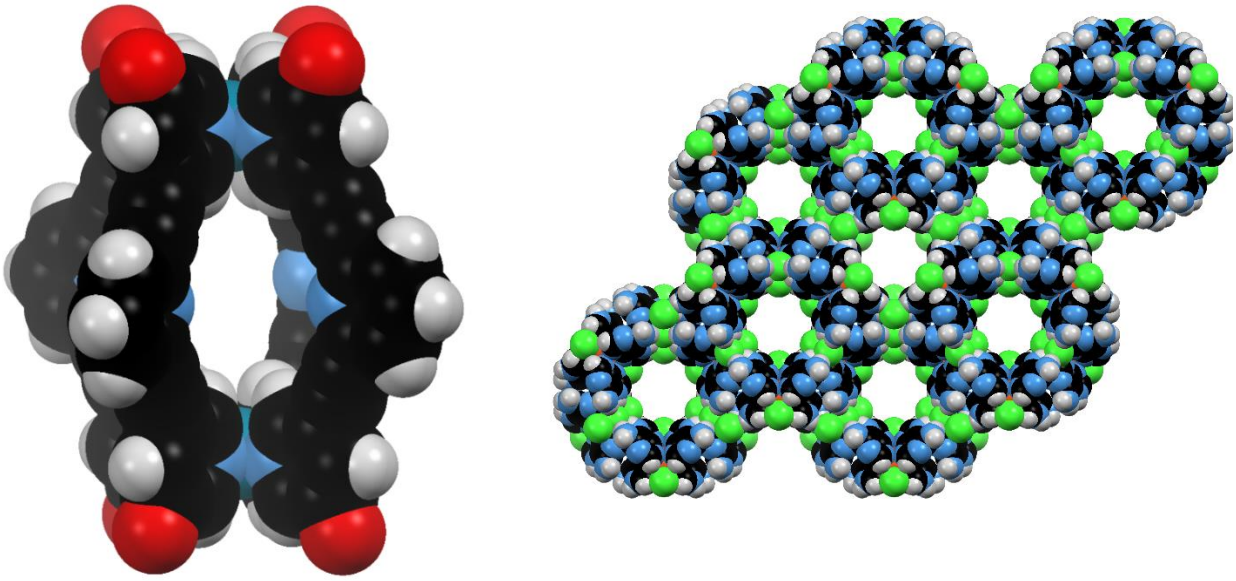

Figure 1.5.1: (left) $[Pd_2(L)_4]^{4+}$ cage reported by Crowley and co-workers exhibiting intrinsic porosity by virtue of the internal cavity.[189] The PEG substituents are omitted for clarity. (right) MPM-1-Cl as originally reported by Roman and co-workers[199] and later investigated by Zaworotko and co-workers.[184] The packing of the Cu(II) paddlewheel complexes result in hexagonal channels and thus the material exhibits extrinsic porosity.

When discussing MPMs, there are two ways in which to describe the nature of the porosity of the compound. If the molecular compound contains an internal void capable of gas uptake such as MOPs, then the porosity is referred to as *intrinsic porosity* (*Figure 1.5.1*). However, if the complex packs in the crystalline lattice in such a manner that there are voids formed between the molecular building units, the porosity is referred to as *extrinsic porosity* (*Figure 1.5.2*). The latter is rare due to the often high packing density of molecular compounds. The incorporation of directional hydrogen bond donors and acceptors can circumnavigate the high packing density by the formation of hydrogen bond networks to interrupt the close packing arrangement.

The incorporation of fluoride containing moieties into MPMs based on metal complexes possessing both intrinsic and extrinsic porosity has been demonstrated to improve the CO_2/N_2 selectivity.[185, 200] MPM-1-Cl is an MPM based on a Cu(II) adenine paddle wheel complex that forms a hydrogen bond network with chloride anions featuring hexagonal microporous channels.[186, 200] A near isostructural framework can be synthesised using TiF_6^{2-} anions, resulting in the hexagonal pore being lined with fluoride moieties.[200] This significantly improves the CO_2/N_2 selectivity. Subsequent theoretical calculations demonstrated that the CO_2 interaction with the fluoride moieties of the TiF_6^{2-} anions was responsible for the remarkably higher enthalpy of adsorption.

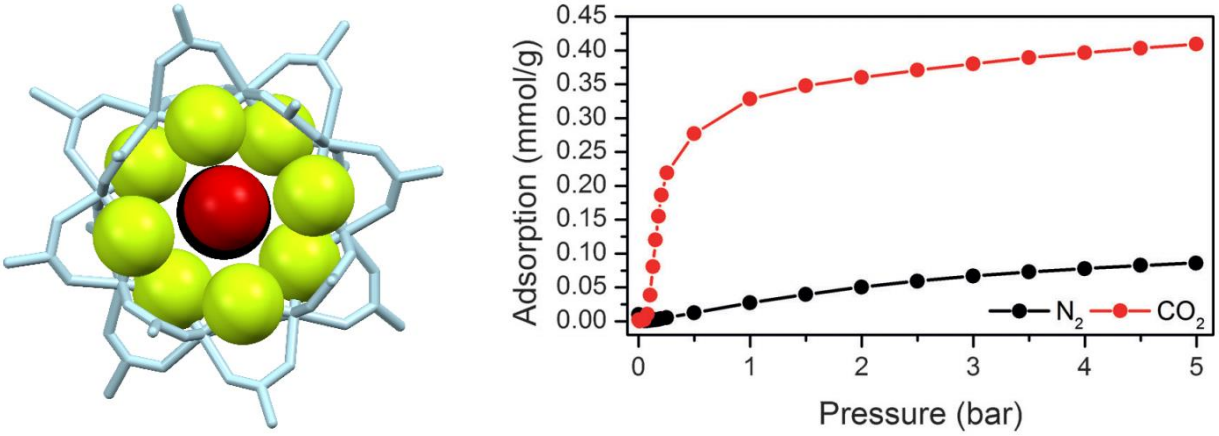

Figure 1.5.2: (left) the Cr(III) macrocycle reported by Winpenny and co-workers containing bridging fluoride anions interacting with the carbon dioxide molecule in the central cavity. (right) The gas sorption isotherms of the Cr(III) macrocycle showing a distinct selectivity for CO_2 over N_2. Figures adapted from reference.[201]

A similar effect has been shown crystallographically by Winpenny and co-workers for a Cr(III) fluoride macrocycle.[201] While the crystal is non-porous, the macrocycle contains a vacant internal void. Upon application of high-pressure CO_2, single crystal X-ray diffraction revealed the binding of CO_2 at two distinct sites. The site of major occupancy was the centre of the macrocycle surrounded by the coordinated fluoride anions (*Figure 1.5.2*). It was postulated that the close contact of the electron rich fluoride anions to the electron poor carbon of the CO_2 molecule resulted in a significant electrostatic attraction that was unable to occur for N_2 (*Figure 1.5.2*).

1.6 Spin crossover (SCO)

1.6.1 Introduction and overview

Octahedral transition metal ions with a d^4 to d^7 electron configuration can exist in either a high spin (HS) or low spin (LS) state and therefore may exhibit a phenomenon known as spin crossover (SCO).[202-204] Primarily this behaviour is observed in octahedral metal ions of which the following overview will exclusively cover. Although strikingly similar, electron transfer[205-207] and valence tautomerism systems will not be discussed.[208-209] In an idealised octahedral crystal field, the d orbitals are split to give the lower energy t_{2g} and the higher energy e_g orbitals. The e_g orbitals can be regarded as non-bonding or antibonding depending on the covalency of the metal to ligand bonds. The energy split of the orbitals is quantified by the parameter Δ_o. When the splitting of the t_{2g} and e_g orbitals is small, the energy cost required to spin pair two electrons (P) in the same orbital is greater than the energy cost associated with occupying the higher energy e_g orbitals and thus $\Delta_o < P$. This is the case when a weak field ligand is present and results in an HS electron configuration with the greatest number of parallel spins. Alternatively, when the splitting of these orbitals is large, the pairing energy is lower than the energy of occupying the e_g orbitals, resulting in a LS electron configuration as $\Delta_o > P$.

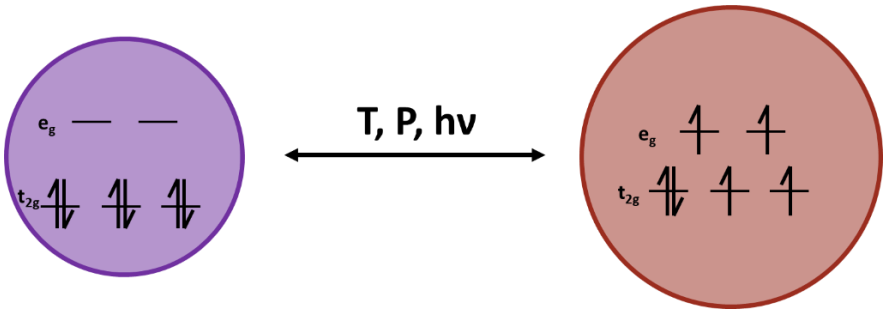

Figure 1.6.1.i: Diagram illustrating the key differences between the diamagnetic LS (left) and the paramagnetic HS (right) states and the external perturbations that can induce SCO: a change in temperature (T), a change in pressure (P) or light irradiation (hv).

When the energy split of the t_{2g} and the e_g orbitals is moderate, Δ_o and P are of similar magnitudes and an external stimuli can induce a change in the free relative free energies of the HS and LS states which can result in a spintransion from the LS to HS state and *vice versa* (*Figure 1.6.1.i*). External stimuli are commonly temperature, pressure or light irradiation. The change in the

electronic state results in dramatic changes to the magnetic, electrical, structural and optical properties which has promoted much of the work in this field.[210-213] While in theory there is a wide variety of metal ions capable of exhibiting SCO, in practise most work is restricted to Fe(II),[212, 214-216] Fe(III)[217] and Co(II),[218] for which a range of different coordinating motifs are known to allow for SCO. For other metal ions such as Co(III)[219] and Mn(III),[220-221] SCO is known but decidedly rare. The phenomenon of SCO was first observed in Fe(III) dithiocarbamate complexes in 1931.[222] Since that time, while the field of Fe(III) SCO has developed, Fe(II) SCO has been at the forefront of research in recent years. This is due to Fe(II) SCO exhibiting several key advantages over Fe(III) and Co(II) SCO. The HS and LS states for Fe(II) give complexes of significantly different colours, most notably when all the ligand donor atoms are nitrogen. The HS state is often a pale yellow or orange colour while the LS state is typically dark purple due to an MLCT electronic transition. Therefore, Fe(II) complexes exhibit significant thermochromic properties which make them attractive candidates for optical sensors. The LS state of Fe(II) is an $S = 0$, $^1A_{1g}$ state in which all the electrons are paired and is therefore diamagnetic. On the other hand, the HS state of Fe(II) is an $S = 2$, $^5T_{2g}$ state in which there are four unpaired electrons resulting in a paramagnetic complex. Therefore, Fe(II) SCO complexes can effectively operate as magnetic switches. The population of the antibonding e_g orbitals weakens the metal-ligand coordinate bonds. This results in the Fe(II)-ligand bonds increasing form 1.9 to 2.0 Å in the LS state to approximately 2.2 Å in the HS state and consequently a mechanical expansion of the material occurs. For Fe(III) the SCO occurs between a $S = 1/2$, $^2T_2$ LS state to a $S = 5/2$, $^6A_1$ HS state. The change in the Fe(III)-ligand bond lengths upon SCO from the LS to HS states is noticeably smaller than Fe(II) with an increase between 0.10 to 0.13 Å.[217, 223]

1.6.2 Influence of supramolecular interactions upon spin crossover

In solution, the interactions of neighbouring molecules are removed, and the SCO at each metal centre is isolated. Therefore, the SCO can be regarded as a thermal equilibrium with a Boltzmann distribution over all vibronic levels of both the HS and LS states and is thus gradual.[202] The ideal solution model describes this behaviour in terms of the Gibbs' energy of the SCO (equation **1**). The equation is derived from terms accounting for the enthalpy and entropy change between the HS and LS states and the entropy linked to the random distribution of *n* proportion of HS molecules and *1-n* proportion of LS molecules.[224]

$$X = \frac{1}{1+exp\left(\frac{\Delta H}{R}\left(\frac{1}{T}-\frac{1}{T_{1/2}}\right)\right)} \qquad \textit{Eqn. 1}$$

Equation 1: the ideal solution model where X = fraction HS, ΔH = enthalpy of SCO, R = ideal gas constant, T = temperature and $T_{1/2}$ = the critical temperature at which there are even populations of HS and LS states.

In the solid state, supramolecular interactions contribute greatly to the SCO behaviour. This may occur due to weak intermolecular interactions such as hydrogen bonding and π-π stacking, or stronger intramolecular interactions like those present in coordination polymers. This introduces the concept of cooperativity which results in SCO that may be more abrupt than predicated from a simple Boltzman distribution. Slichter and Drickamer proposed the introduction of an interaction parameter, Γ, to account for these interactions and provide a degree of quantification of their importance (equation **2**).[225]

$$ln\left(\frac{1-x}{x}\right) = \frac{\Delta H + \Gamma(1-2x)}{RT} - \frac{\Delta S}{R} \qquad \textit{Eqn. 2}$$

Equation 2: Slichter and Drickamer model containing the Γ parameter to account for intermolecular cooperativity and x represents the fraction HS.

Thermal hysteresis may be observed for complexes exhibiting a high degree of cooperativity. This 'memory effect' results in the complex exhibiting bi-stability. This means it can exist in either the HS or LS state over the width of the hysteresis loop, depending on if the system is being heated or cooled.[226] These hysteresis loops can be exceptionally wide;[227-229] the largest currently being 88 K.[229] Recent work by Harding and co-workers has shown crystallographically that for a mononuclear Fe(III) complex; $[Fe(qsal\text{-}I)_2]NTf$ (NTf^- = bis(trifluoromethane)sulfonimide), the reorientation of the CF_3 'arms' of the bis(trifluoromethane)sulfonimide anion was intrinsically linked to the occurrence of a wide hysteresis loop.[230] In some cases, the SCO does not occur in one smooth step but instead in several smaller steps separated by plateaus. These are most commonly observed in complexes which exhibit crystallographic symmetry breaking processes[231-236] and/or in Hoffman type cyanometallate frameworks.[237-239] In both cases, minor changes to the coordination environments result in seemingly similar Fe(II) centres existing in slightly different chemical environments so they do not undergo SCO simultaneously (*Figure 1.6.2.i*).

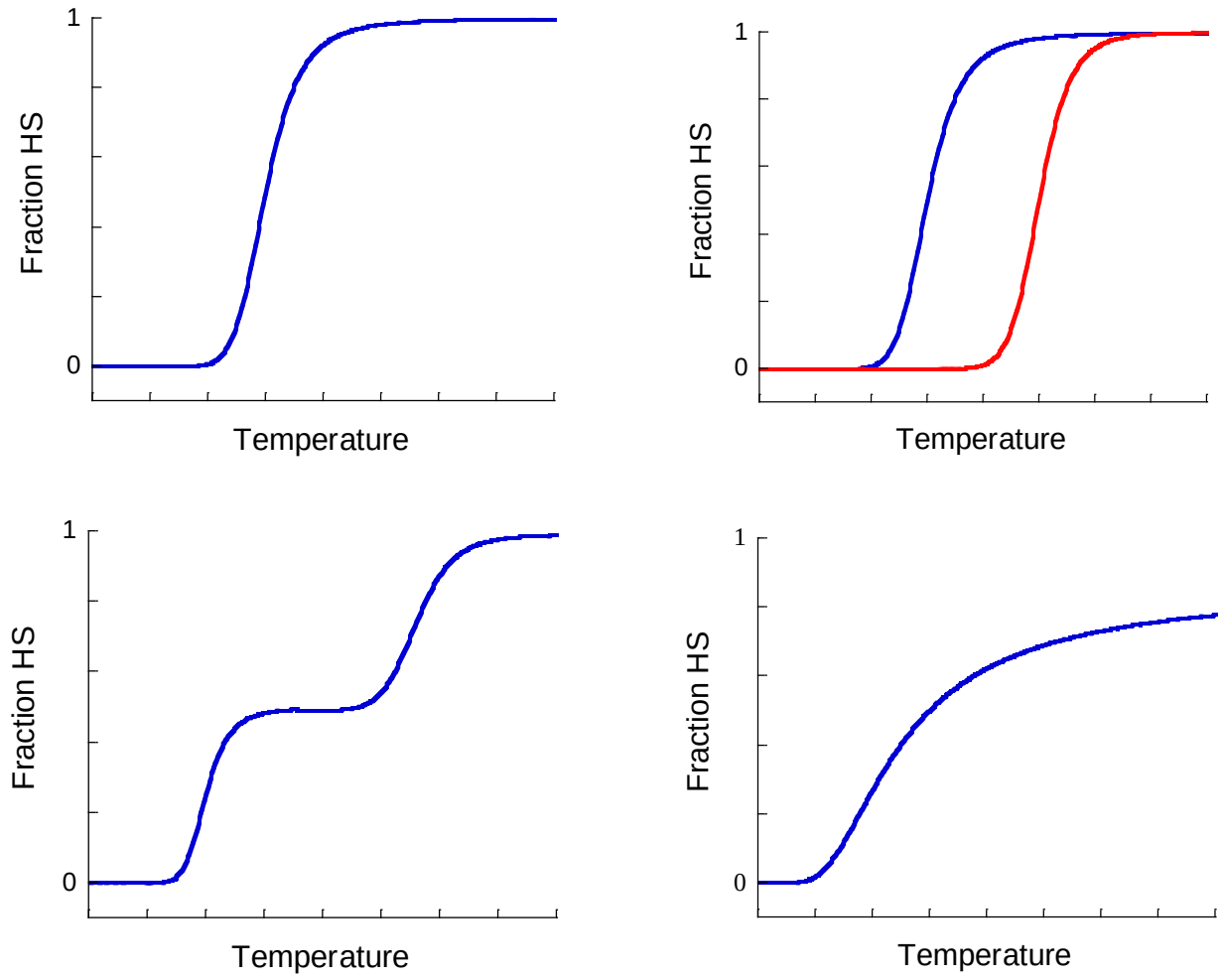

Figure 1.6.2.i: The various profiles that the SCO process can adopt: abrupt (top left), with hysteresis (top right), multi-stepped (bottom right) and broad and incomplete (bottom left). Profiles were simulated using the ideal solution model.

1.6.3 Light Induced Excited Spin State Trapping (LIESST)

While SCO was first discovered by studying the temperature dependence of the various physical properties, it has since been shown that a similar effect can be achieved with light irradiation. This effect was first detected for complexes in solution upon irradiation with a pulsed laser and later revealed to also occur in the solid state.[240-241] It was the study by Decurtins on $[Fe(ptz)_6](BF_4)_2$ (ptz = 1-propyltetrazole) from which the term Light Induced Excited Spin State Trapping (LIESST) originates.[242-243] Irradiation of the complex at low temperatures results in photo-excitation from the LS to HS state, which is stable at low temperatures. Upon heating, this photoexcited HS state undergoes rapid thermal relaxation to the LS state and generally the LIESST

effect is only observed below 60 K (*Figure 1.6.3.i*). Further studies into the effects of light irradiation revealed that while specific wavelengths of light result in LIESST, such as green for $[Fe(ptz)_6](BF_4)_2$, other wavelengths can result in a de-excitation. This is known as reverse-LIESST featuring an HS to LS transition. For $[Fe(ptz)_6](BF_4)_2$, red light was shown to be the most efficient for this reverse-LIESST effect.[244] These photo-excitation effects have been used more recently to probe the excited states of LS complexes such as $[Fe(2,2\text{-bpy})_3]^{2+}$ (2,2-bpy = 2,2-bipyridine) using pump-probe transient absorption spectroscopy.[245]

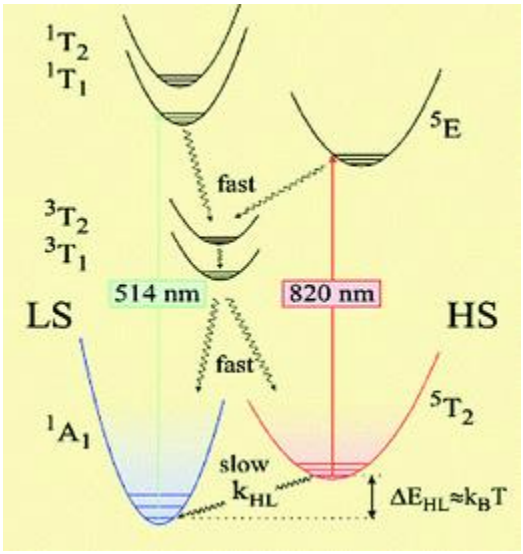

Figure 1.6.3.i: A Jablonski diagram representing the excitations and subsequent non-radiative decay and intersystem crossing processes occurring during LIESST and reverse-LIESST. Figure adapted from reference.[213]

The ability to switch between the HS and LS states simply with light irradiation makes SCO complexes promising candidates for molecular scale devices.[246] However, as the LIESST effect is confined to low temperatures, application of this behaviour in potential devices is not possible in a practical sense at this time. Efforts are on-going to raise the temperature at which the LIESST effect can be observed. Photoexcited states stable to 130 K have been reported for $[Fe(DTP)(CN)_2]$ (DTP = 2,13-dimethyl-6,9-dioxa-3,12,18-triazabicyclo[12.3.1]octadeca-1(18),2,12,14,16-pentaene).[247-251] The cause for this remarkably stable photoexcited HS state is due to the formation of a 7-coordinate Fe(II) centre in the HS state which is observed crystallographically. A similar bond forming behaviour upon photo-excitation has recently be observed for the related complex $[Fe(DPP)(CN)_2]$ (DTP = 2,13-dimethyl-3,6,9,12,18-pentaazabicyblo[12.3.1]octadeca-

1(18),2,12,14,16-pentaene), however, this complex does not exhibit the LIESST effect at unusually high temperatures.[252] Letard formulated an empirical equation to rationalise LIESST (equation **3**). It consists of the $T_{1/2}$ value, the temperature at which there are equal proportions of the HS and LS states, and T(LIESST), the temperature at which complete thermal relaxation of the photo induced HS state has occurred and T_0, the theoretical value of T(LIESST) when $T_{1/2}$ = 0 K.

$$T(LIESST) = T_0 - 0.3T_{1/2} \qquad Eqn.\ \boldsymbol{3}$$

Equation 3: T(LIESST) = temperature at which complete thermal relaxation of photoinduced HS state is achieved, T_0 = theoretical value of T(LIESST) when $T_{1/2}$ = 0 K and $T_{1/2}$ = temperature at which there are equal proportions of the HS and LS states

This equation indicates the common experimental observation that a lower $T_{1/2}$ value will result in a higher T(LIESST) and therefore a photoinduced HS state which is stable at higher temperatures. The most obvious factor that influences the $T_{1/2}$, is the field strength of the ligand. Hence, a commonly observed trend for SCO complexes is that weaker field ligands display the LIESST photo-induced HS states at higher temperatures. When T(LIESST) is plotted against $T_{1/2}$ for the wide variety of complexes surveyed in this study, distinct patterns emerged.[253-254] Complexes with the same basic ligand type and coordination sphere were all located around the same T_0 line (*Figure 1.6.3.ii*). Complexes of the form $[FeL_6]^{2+}$ where **L** was a monodentate nitrogen heterocycle ligand were clustered about the T_0 = 100 K line. $[FeL_3]^{2+}$ type complexes where **L** was a bidentate ligand were clustered about the T_0 = 120 line while for $[FeL_2]^{2+}$ complexes where **L** is a tridentate ligand were clustered about 150 K. Therefore, as the denticity of the ligand increased, so too did the T_0 value. Another type of photo-induced SCO, not to be confused with LIESST is Ligand Driven Light Induced SCO (LD-LISC). For this process, the light does not directly excite the metal ion to the HS state. Instead, it induces a moiety of the ligand to photo-isomerise which results in the change of the ligand field strength or the coordination of a vacant donor atom. Common functionalities include the stilbene,[255-256] azobenzene,[257-258] and diarylethene moieties.[259] One distinct advantage of LD-LISC over the LIESST effect is that it is not restricted to low temperatures as the *cis* and *trans* states for azobenzene and stilbene functionalities and the open and closed forms for diarylethene functionalities are both stable at room temperature.

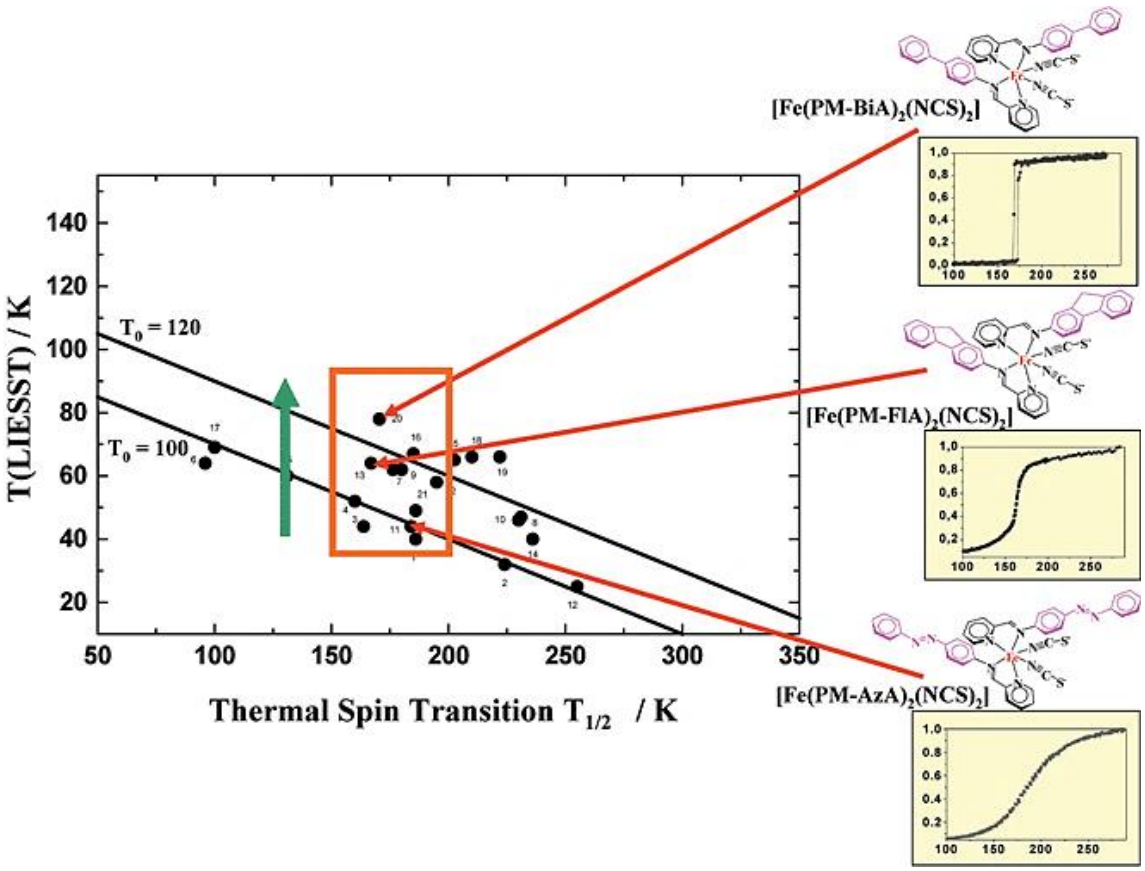

Figure 1.6.3.ii: The plot of T(LIESST) vs. $T_{1/2}$ for a family $[Fe(L)_2(NCS)_2]$ compounds showing the clustering of the complexes about two T_0 lines, one at 100 k and the other at 120K. Figure adapted from reference.[253]

1.6.4 Effect of ligand field

The synthesis of SCO complexes requires a thorough understanding of the factors the influence the ligand field, both steric and electronic. This following section will focus predominately on $[Fe(II)N_6]^{2+}$ type coordination spheres and will briefly outline some relevant examples of $[Fe(II)N_4O_2]$ and $[Fe(III)N_4O_2]^+$ coordination spheres. Bidentate di-imine ligands are an important class of SCO ligands and are central to the work discussed herein. Tridentate tri-imine ligands, while also a key class of SCO ligands, are not relevant to this work and the reader is directed to the following comprehensive reviews.[202-204, 212] The ligands 2,2-bipyridine and 1,10-phenanthroline are two prototypical di-imine ligands and both form LS complexes with Fe(II). When one bidentate ligand is replaced by two monodentate coordinating anions of the type NCX where X is S, Se or BH_3, the ligand field is reduced sufficiently to give complexes of the type

$[Fe(\mathbf{1})_2(NCX)_2]$[260-262] and $[Fe(\mathbf{2})_2(NCX)_2]$[254, 263-267] which can display SCO behaviour. Modifications of 2,2-bipyridine, *para* to the nitrogen donor atoms has little effect on the field strength. The methoxy substituted bipyridine, **3** (*Figure 1.6.4.i*) formed only LS complexes with Fe(II).[268] However, when modifications were made closer to the coordination site, significant changes to the field strength occurred. In the case of 3-methyl-2,2-bipyridine, the methyl group *ortho* to the nitrogen donor atom results in a distortion upon coordination to Fe(II). This steric effect weakens both the σ-donor and π-acceptor capabilities of the ligand, reducing the ligand field such that for $[Fe(\mathbf{4})_3]^{2+}$ type complexes, partial SCO behaviour is observed.[269] Upon the addition of a second methyl group to give 3,3-dimethyl-2,2-bipyridine, **5**, the steric crowding is so great that coordination to Fe(II) was not detected.[270]

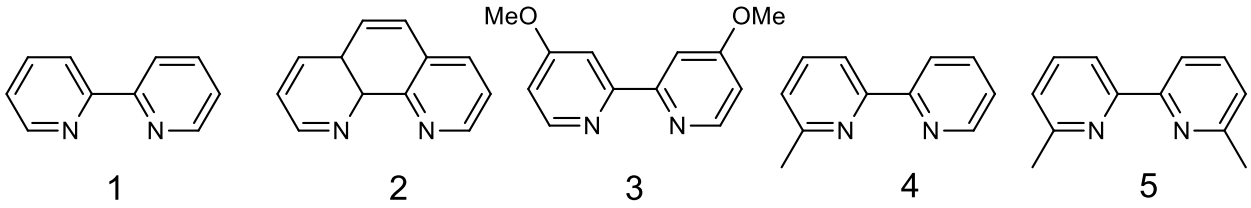

Figure 1.6.4.i: Family of bidentate ligands with nitrogen donor atoms. [For $Fe(\mathbf{L})_6]^{2+}$ type complexes: 1, 2, and 3 form LS complexes, 4 forms SCO complexes and 5 forms HS complexes.

If the methyl groups are instead placed in the 3-positions of the pyridine rings, the steric crowding of the coordination site is removed and the ligand forms $[Fe(\mathbf{6})_3]^{2+}$ type complexes (*Figure 1.6.4.ii*).[271] However, the steric clash of the methyl groups on the back part of the ligand causes the pyridine rings to twist relative to one another which reduces the conjugation of the π system and therefore the π-acceptor capability. This results in the complexes exhibiting SCO below room temperature.

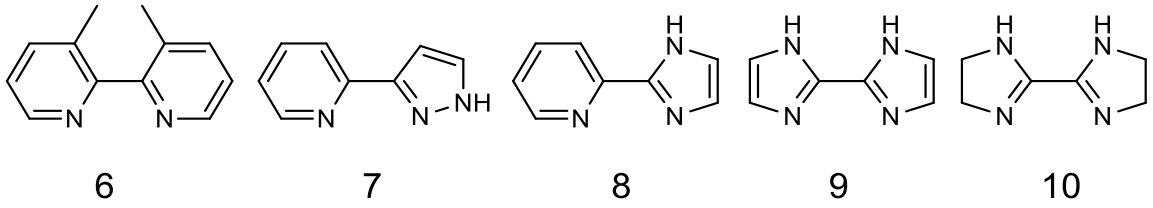

Figure 1.6.4.ii: Family of bidentate ligands with nitrogen donor atoms. [For $Fe(\mathbf{L})_6]^{2+}$ type complexes: 6, 7, 8 and 10 form SCO complexes while 9 forms HS complexes.

The replacement of one or both of the pyridine rings with a 5-membered nitrogen heterocycle also reduces the ligand field. 5-Membered nitrogen heterocycles such as imidazole and pyrazole are more electron rich than pyridine and are therefore weaker π-acceptors (*Figure 1.6.4.ii*). The ligands **7** and **8** form complexes of the type $[Fe(\mathbf{7})_3]^{2+}$ and $[Fe(\mathbf{8})_3]^{2+}$ which exhibit SCO.[272-273] When both pyridine rings are replaced with imidazole rings to give **9**, the ligand field is reduced to an extent that $[Fe(\mathbf{9})_3]^{2+}$ type complexes exist only in the HS state.[274] It is particularly interesting that when the aromaticity of **9** is removed to give the ligand 2,2-biimidazoline, **10**, the complex $[Fe(\mathbf{10})_3](ClO_4)_2$ exhibits abrupt SCO. The loss of aromaticity results in the electron density of the π system being localised on the diamine chelate resulting in a stronger π-acceptor and thus a stronger field ligand.[275] This brief survey of ligands has revealed two key methodologies for the modulation of the field strength. The first is that the addition of groups close to the metal binding site result in steric hindrance that reduces the field strength of the ligand. Alternatively, the bulky groups may be distal to the binding site but induce a similar effect if they cause the binding site to be distorted. Secondly, for di-imine ligands, the replacement of the pyridine rings with more electron rich 5-membered nitrogen heterocycles results in a reduction of the field strength. These methodologies are merely starting points for the synthesis of a ligand capable of forming a SCO complex.

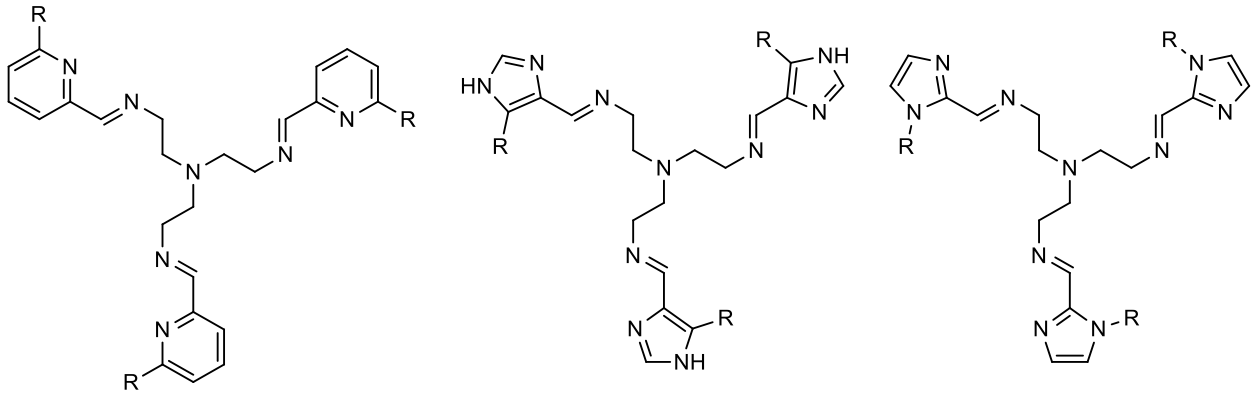

11: R = H
12: R = Me

13: R = H
14: R = Me

15: R = H
16: R = Me

*Figure 1.6.4.iii: Family of tripodal hexadentate ligands with nitrogen donor atoms. For Fe(**L**)]$^{2+}$ type complexes: **11** forms LS complexes while **12**, **13**, **14**, **15** and **16** form SCO complexes.*

Some attempts have been made in predicting whether a ligand will exhibit SCO. Shatruk and co-workers proposed an empirical rule by analysing the N-N separations of the donor nitrogen atoms of a variety of ligands.[276]

"The spin state of Fe(II) complexes that bear a set of three bidentate diimines is determined by the chelating N– N distance in the non-coordinated ligand. Complexes with d(N–N) < 2.78 Å and d(N–N) > 2.93 Å adopt the LS and HS states, respectively, while complexes with 2.78 Å < d(N–N) < 2.93 Å exhibit SCO."

The field strength of a coordinating imine such as in ligands **11** – **16** can be regarded to be similar to a pyridine ring (*Figure 1.6.4.iii*). These coordinating motifs are typically found in tris-bidentate tripodal ligands formed by reacting three equivalents of the appropriate N-heterocyclic aldehyde with a triamine molecule such as tren (tren = tris(2-aminoethyl)amine). These hexadentate ligands coordinate to Fe(II) to give the *fac* isomer of [Fe(**L**)]X_2 type complexes where **L** is a tris-bidentate ligand **12** to **15** and X is any one of the typically encountered anions in coordination chemistry. As anticipated, pyridylimine ligands such as **11** form LS complexes with Fe(II).[277] However, the addition of the methyl groups *ortho* to the coordinating nitrogen atoms results in a steric clash which reduced the ligand field strength sufficiently for SCO to occur.[278-280] Much like the pyridylimidazole ligand discussed above, **8**, imidazolylimine ligands of the type **13** to **16** form SCO complexes with Fe(II). Ligands **13** and **14** contain a 4-imidazole ring[281-287] while ligands **15** and **16** contain a 2-imidazole ring.[288-291] Masumoto and co-workers have shown through a series of studies that for these [Fe(**L**)]X_2 complexes the trend in the ligand field strength is **10** > **15** ≈ **14** > **12** >**13**. The N-H moiety was revealed to play a crucial role in the crystal packing via the formation of hydrogen bond networks which were particularly prominent with halide anions such as chloride.[283-284, 286-287] Furthermore, work by both Brewer[288, 292] and Masumoto[282, 287, 293] on these [Fe(**L**)]X_2 complexes has investigated the effect of deprotonation of the imidazole N-H moiety under both aerobic and anaerobic conditions. In the case of the former, oxidation to Fe(III) is commonly observed, resulting in a neutral complex. Co-crystallisation of the cationic Fe(II) and neutral Fe(III) complexes was possible under certain conditions resulting in novel hydrogen bond networks between the N-H moiety of the Fe(II) complexes and the deprotonated nitrogen atoms of the Fe(III) complexes.[294] Work by Real and co-workers has examined the use of these types of complexes to make multifunctional materials by in incorporating them into ferromagnetically

coupled oxalate based framework materials.[295] Kruger and co-workers have reported a mononuclear complex of the type $[Fe(\mathbf{17})_3](ClO_4)_2$ with the bidentate ligand **17** featuring the 2-imidazole moiety and a *para*-methoxy group on the aromatic ring (*Figure 1.6.4.iv*).[296] This complex displayed both thermally induced SCO and LIESST behaviour with complete conversion to the photo-excited state. Imidazolylimine coordination motifs have been established to be versatile ligands for the synthesis of SCO complexes and can be incorporated into a range of multinuclear SCO assemblies and is a subject of the current work. For a thorough summary of imidazolylimine SCO complexes, the reader is directed to the review by Kruger and co-workers.[297]

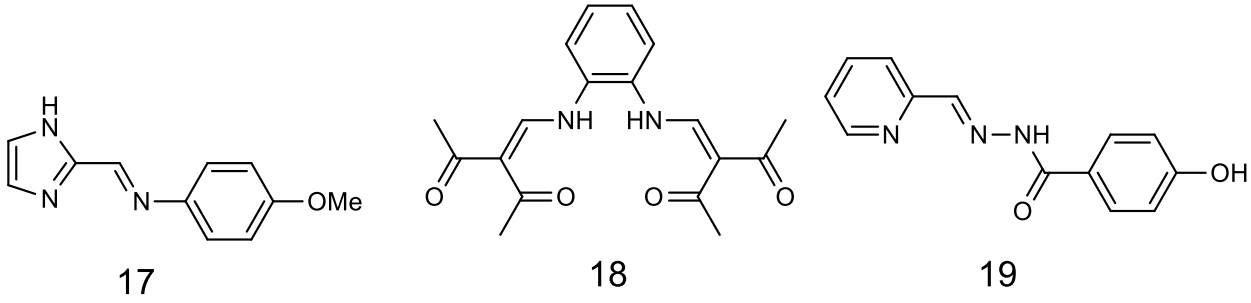

17 18 19

Figure 1.6.4.iv: the bidentate ligand 16 forms charged Fe(II) complexes exhibiting SCO while the macrocyclic ligand 17 and the tridentate ligand 18 deprotonate to form neutral Fe(II) SCO complexes.

While the $[FeN_6]^{2+}$ coordination sphere is the most prominent in Fe(II) SCO chemistry, in recent years the $[FeN_4O_2]$ coordination sphere has gained increasing attention.[298-306] In contrast, the $[FeN_4O_2]^+$ coordination sphere composes a large proportion of known Fe(III) SCO complexes. Weber and co-workers have reported various complexes containing macrocyclic ligands based on **18**,[301, 307-309] in which the ligand coordinates to Fe(II) in the equatorial positions while ligands containing nitrogen donor atoms coordinate in the axial positions (*Figure 1.6.4.iv*). By using divergent, ditopic ligands in the axial positions such as 4,4'-bipyridine, these mononuclear complexes can be linked together to form dimers and coordination polymers. Gao and co-workers have reported a number of neutral Fe(II) complexes based on the tridentate pyridylhydrazone ligand **19** and other structurally similar ligands (*Figure 1.6.4.iv*).[304-306] A consistent feature of this family of complexes is the presence of electron donating methoxy or hydroxy substituents on the aromatic ring. It is interesting to note that these types of pyridylhydrazone ligands also form SCO

complexes with Fe(III), a rare example of a ligand class which is SCO active with both Fe(II) and Fe(III).[302]

1.6.5 Multinuclear spin crossover complexes

The concept of using polytopic ligands to synthesise multinuclear supramolecular assemblies has been discussed in *section 1.3.2*. The incorporation of SCO centres into such assemblies is a particularly interesting avenue of research due to the potential for communication between the metal centres via the ligand framework (*Figure 1.6.5.i*).[310] A variety of dinuclear Fe(II) SCO helicates have been reported in the literature. These can be divided into two classes; dinuclear triple helicates synthesised from bis-bidentate ligands[310-321] and dinuclear double helicates synthesised from bis-tridentate ligands.[322] A majority of SCO dinuclear triple helicates contain ligands featuring an imidazolylimine coordinating motif.[311, 314, 316, 319-322] The groups of Kruger,[316, 320] Li,[311] and Hanon[319] have all contributed to a family of helicates based on oxo, methylene, or sulfide bridged dianiline type ligands which will be discussed in more detail in *section 5.1* chapter five. Masumoto and co-workers have reported more compact helicates with ligands based on a short hydrazone linker.[314, 317] Tetranuclear SCO assemblies have been reported in the form of tetrahedral cages and grids. Kruger and co-workers reported the first SCO face capped tetrahedral cage based on a tris-bidentate imidazolylimine ligand.[100] Later work by Brooker and Lindoy focused on similar tris-bidentate imidazolylimine ligands.

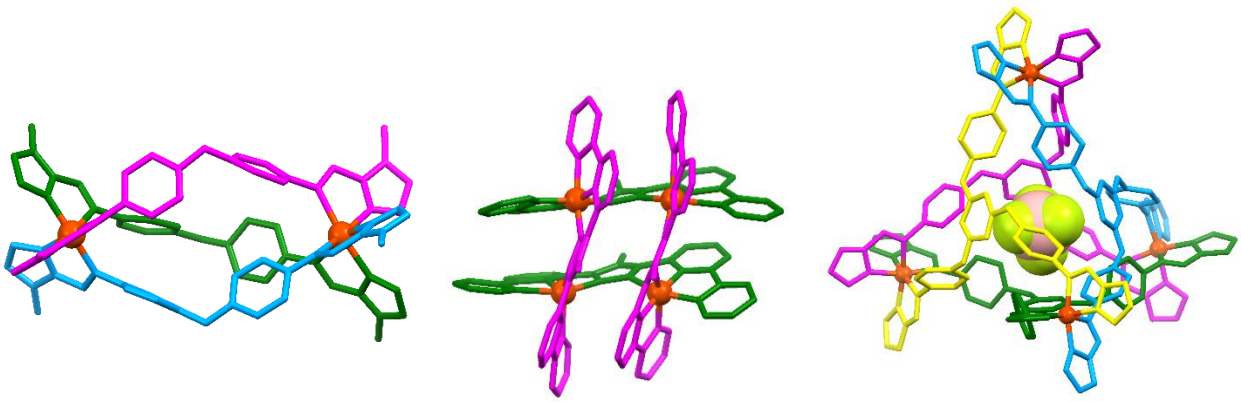

Figure 1.6.5.i: Examples of some multinuclear SCO assemblies: a $[M_2L_3]^{4+}$ dinuclear triple helicate (left), a $[M_4L_4]^{8+}$ tetranuclear grid (middle) and a $[M_4L_4]^{8+}$ face-capped tetrahedral cage (right).

These featured a significantly more rigid pseudo C_3-symmetric core.[323-324] Edge bridged tetrahedral cages have been reported more recently containing exceptionally flexible bis-bidentate imidazolylimine ligands.[325-326] Rigid, bis-tridentate ligands have been used to form tetranuclear SCO grids.[327-331] Meyer and co-workers constructed a grid based on a ligand containing a central bridging pyrazolate ring[329] while Sato and co-workers utilised a bridging imidazolate ring.[328] A more expanded grid type complex by Ruben and co-workers features a ligand capable of adopting two different conformations which had a significant impact on the SCO properties.[133] A hexanuclear 'nano-ball' has been reported by Batten and co-workers, containing the Fe(II) centres on the six faces of a cube like structure.[332-333] The assembly is composed of Cu(I) containing metallo-ligands with three pendant pyridine rings that coordinate to Fe(II) in the equatorial positions with acetonitrile or thiocyanate anions coordinating in the axial positions. This complex demonstrated both thermally induced SCO, LIESST and reverse-LIESST behaviour. To date, the discrete supramolecular structure containing the largest number of SCO Fe(II) centres is an octanuclear cube reported by Nitschke and co-workers. This large cube structure contained an internal void capable of hosting fullerene molecules and exhibited SCO in solution. No SCO behaviour was reported for the complex in the solid state.[334]

1.6.6 Multifunctional spin crossover complexes and potential applications

The magnetic and optical bistability of SCO complexes has made them attractive options for the synthesis of nano-scale devices.[335-336] Multifunctional SCO materials combine SCO with one or more useful properties such as porosity,[337] conductivity,[338] fluorescence[339] or ferroelectric behaviour.[340-341] These secondary properties can be modulated by the spin state of the complex, where the SCO component acts as the switch. Work by Coronado and co-workers has focused on the deposition of SCO active complexes onto a variety of surfaces and nanoparticles, an important step in the synthesis of devices containing SCO components.[342-344] Recent work by Clérac and co-workers featured microelectromechanical sensors functionalised with SCO complexes (*Figure 1.6.6.i*).[345] The expansion of the crystal upon generation of the HS state resulted in a significant change in the resonant frequency of the piezoelectric material. This change was achieved both thermally and via light irradiation. Alternatively, the secondary property can modulate the spin state and the SCO component acts as a sensor. There are several examples of MOFs for which SCO is triggered by the presence or absence of gas molecules. This occurs either binding of the

gas to the Fe(II) sites[346] or gas molecules interacting with the ligands in such a way that that the SCO behaviour is significantly altered upon adsorption.[337]

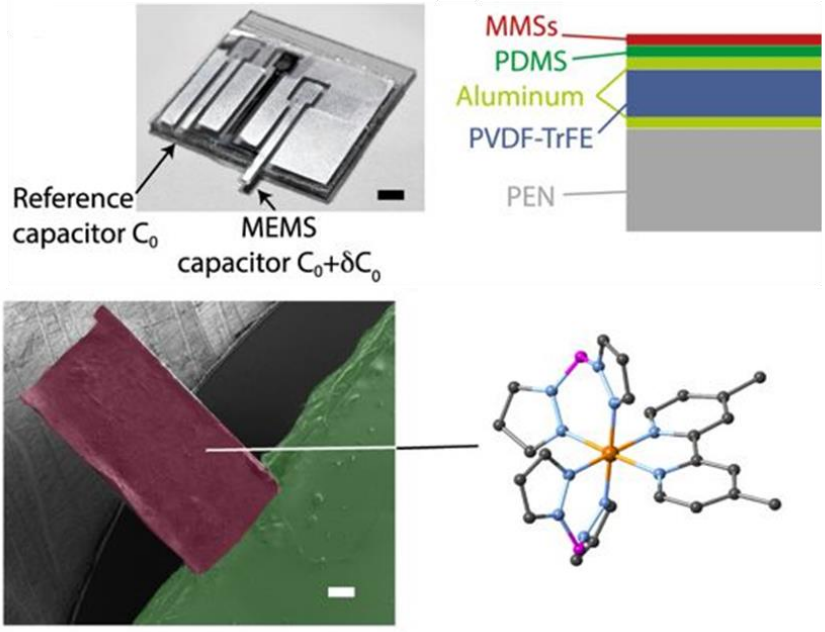

Figure 1.6.6.i: (top left) Picture of a microelectromechanical sensor (MEMS) incorporating a SCO complex. (top right) Schematic of the layered design of the MEMS where the SCO complex layer/magnetic molecular switches (MMSs) is shown in red, the polydimethylsiloxane (PDMS) protective layer shown in green, aluminium layers shown in yellow, the poly(vinylidene fluoride-trifluoroethylene) (PVDF-TrFE) piezoelectric block co-poylmer layer shown in blue and the polyethylene naphtalate substrate shown in grey. (bottom left) SEM micrograph of MMSs layer. (bottom right) crystal stucture of the [Fe(dmbpy)($H_2B(pz)_2)_2$] SCO complexes used for the MMSs. Figure adapted from reference.[345]

When considering the fabrication of a device containing SCO material, there are a number of practical considerations. Much of the synthesis and characterisation of SCO complexes in the literature focuses on crystalline materials as the structure can be easily elucidated via X-ray diffraction techniques. However, soft materials such as liquid crystals and gels, thin films or nanoparticles may be more appropriate for a future device. Hence, a rapidly expanding field in SCO chemistry is the synthesis SCO soft materials and SCO nanoparticles. The synthesis of thin films has been carried out using Langmuir-Blodgett techniques. This typically requires the SCO complexes be functionalised with large non-polar alkyl substituents in order for them to be

solubilised in non-polar organic solvents.[347-348] SCO complexes can be directly incorporated into polymer matrices, which does not require further functionalisation of the complex. However, dispersion in a non-SCO matrix often alters the SCO properties.[349] An alternative technique is to directly anchor the SCO complex to a surface. SCO active Hoffman frameworks of the type $[Fe(Pz)_2(M(CN)_4)_2]$ (Pz = pyrazine, M = Ni(II), Pd(II) or Pt(II)) can be grown directly onto a surface via a layer by layer assembly.[350] Alternatively, discrete SCO active complexes have been functionalised with pyrene moieties that promote the adsorption of the complex to an exfoliated graphene surface.[351] SCO complexes that exist as liquid crystalline phases have been proposed as candidates in optical displays. In order for the SCO complex to form a liquid crystalline phase, it must first be functionalised with mesogenic substituents. SCO active mesogens have been reported for both neutral and charged Fe(II) complexes in the work of Real and co-workers (*Figure 1.6.6.ii*).[300, 352-353] In a similar fashion the archetypal SCO Fe(II) triazole has been functionalised with long alkyl substituent in work by Clérac and co-workers. These complexes formed both liquid crystalline phases upon heating and gels upon dispersion in decane which exhibited SCO (*Figure 1.6.6.ii*).[354-356]

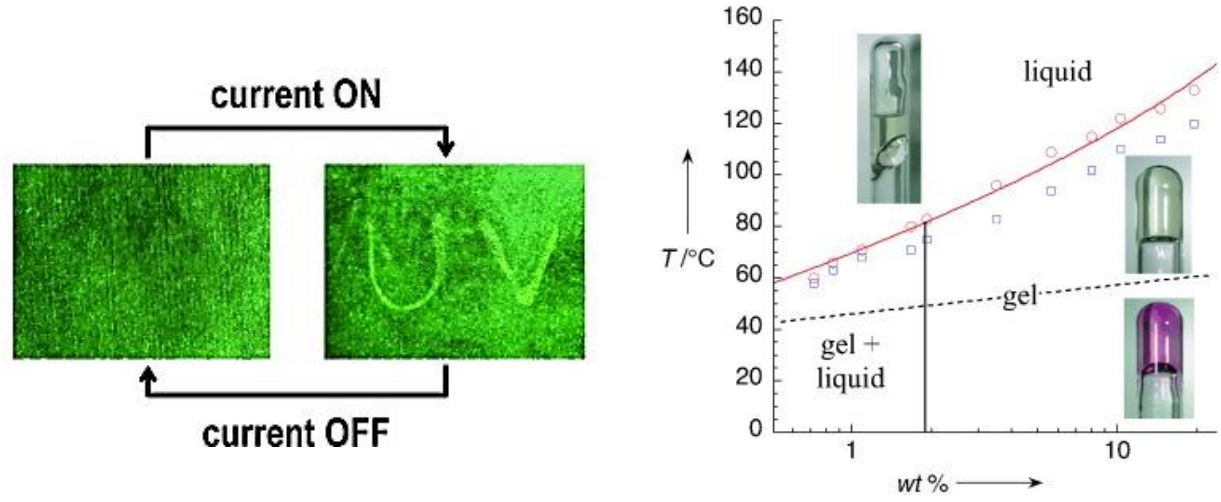

Figure 1.6.6.ii: (left) The reversible writing of the letters UV using SCO induced by the melting of mesogenic functionalized complexes.[300] (right) A phase diagram (temperature vs. weight percentage of complex in decane) for a Fe(II) 1,2,4-trizole gel showing both the HS and LS states are accessible in the gel phase.[356] The blackline separates the gel and biphasic regions while the red circles and black squares represent the $T_{1/2}$ for heating and cooling processes respectively. The red line is the fitting of the heating data to the ideal solution model.

The coordination polymer comprised of Fe(II) and 1,2,4-triazole derivatives is one of the most promising candidates for practical applications. It exhibits significant thermochromic effects with the LS state being a purple colour while the HS state is white. The SCO is typically abrupt and centred around room temperature. These types of complexes also often exhibit hysteresis and hence they have been proposed as potential components in solid state memory devices.[357]

1.6.7 Methods and techniques characterisation of spin crossover

A large number of techniques have been used to study SCO. They can be grouped based on which physical property they measure: optical, structural, magnetic or enthalpic. A brief summary of relevant techniques to this work will be given, with a particular focus on nomenclature and terminology. The significant colour change associated with SCO can be measured in both solution via UV-Visible spectroscopy or in the solid state via absolute reflectivity measurements. LS Fe(II) complexes are typically dark red/purple due to an MLCT that can be ascribed to a $^1T_1 \leftarrow\!\!- {}^1A_1$ electronic transition. The equivalent transition in HS Fe(II) complexes can be ascribed to a $^5E \leftarrow\!\!- {}^5T_2$ occuring in the NIR region which is considerably weaker. UV-Visible spectroscopic measurements carried out on samples in solution typically measure the increase in the MLCT band as the solution is cooled. However, UV-Visible spectroscopic measurements are often limited by the solubility of the complex in an appropriate solvent. The accessible temperature regime is also limited by the melting and boiling points of the solvent and therefore, this technique is only suitable for complexes that exhibit SCO at close to room temperature. The plot of the absorption maxima or absorption coefficient as a function of the temperature can be fitted to the ideal solution model to extract the $T_{1/2}$, ΔH and ΔS values. The limited temperature window due to the solvent often results in only partial observance of the SCO process which makes accurate fitting of the data to the ideal solution model problematic. Absolute reflectivity measurements, as the name suggests measure reflected light and not absorption. Therefore, as the sample is cooled there is typically an increase in the NIR region (*ca.* 900 nm) due to an HS to LS transition. As absolute reflectivity measurements are performed on samples in the solid state, the temperature regime is not solvent dependent and temperatures as low as 10 K are easily accessible. Significant structural changes between the HS and LS states occur due to the change in the metal-ligand bond lengths. In LS Fe(II) complexes the Fe-L bond lengths are 1.9 to 2.0 Å. Upon SCO to HS Fe(II) these bond lengths increase to approximately 2.2 Å. This increase in the Fe-L bond lengths are typically

elucidated from single crystal X-ray diffraction experiments carried out at temperatures for which the Fe(II) centre is in the HS or LS state. In some cases, single crystal X-ray structures are unable to be obtained and therefore spectroscopic techniques are employed. Raman spectroscopy is particularly useful as the vibrational modes for the LS Fe-L and HS Fe-L coordinate bonds are noticeably different. This spectroscopic technique is particularly for complexes for which single crystal structures cannot be obtained. The increase in the metal-ligand coordinate bond lengths is acompanied by an increase in the distortion of the coordination sphere from idealised octahedral symmetry. This increase in distortion can be quantified by the octahedral distortion parameter Σ. The Σ value is defined as the sum of the deviations of the 12 bond angles of the $[FeL_6]^{2+}$ coordination sphere from 90° (*Figure 1.6.7.i*). While there is no definitive range of values for Σ corresponding to HS and LS Fe(II), the Σ value corresponding to HS Fe(II) is noticeably larger than that of LS Fe(II).[358]

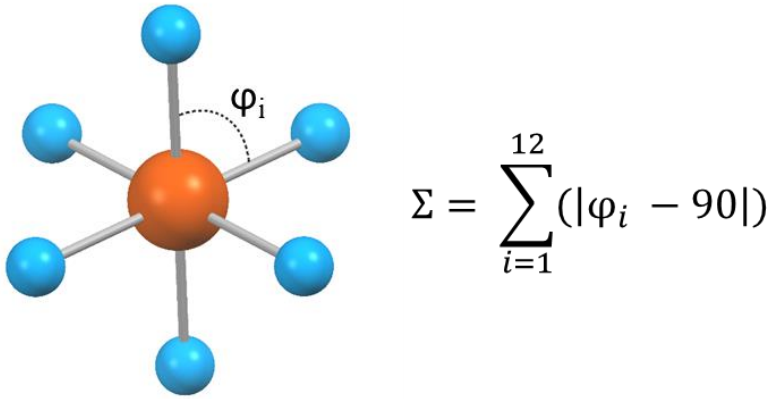

Figure 1.6.7.i: Schematic representation of the calculation of the octahedral distortion parameter (Σ) from the 12 cis bond angles (φ).

The LS electronic configuration of Fe(II) is $^1A_1$ with $S = 0$ and therefore diamagnetic. However, the HS state of Fe(II) has four unpaired electrons with an electronic configuration of $^5T_2$ and is therefore paramagnetic. By measuring the magnetic moment as a function of temperature in a magnetometer, the increase in the magnetic moment shows the evolution of the HS state. These measurements are typically carried out in a SQUID (Superconducting Quantum Interference Device) magnetometer over a temperature range of 1.85 to 400 K for compounds in the solid state. This data is often presented in terms of the magnetic susceptibility χ in the form of a χT *vs.* T plot.

For samples showing no spin orbit coupling, the χT value for an HS Fe(II) centre with g = 2 can be estimated as 3 cm^3 K mol^{-1} using equations **5** and **6**. It is common for HS Fe(II) centres to exhibit some degree of magnetic anisotropy resulting in a g-factor higher than 2, giving χT values larger than 3 cm^3 K mol^{-1}. Fitting of this data to the ideal solution model allows the $T_{1/2}$, ΔH and ΔS values to be extracted.

$$\chi T = \frac{N_A \mu_B^2}{3k_B} g^2 S(S+1) \qquad \textit{Eqn. } \boldsymbol{5}$$

$$\chi T \approx \frac{1}{8} g^2 S(S+1) \qquad \textit{Eqn. } \boldsymbol{6}$$

Equations 5 and 6: N_A = Avogadro's number, μ_B = Bohr magneton, k_B = Boltzmann constant, g = g-factor, S = spin state.

Magnetic measurements of compounds in solution are most commonly carried out using the Evan's method with an NMR spectrometer.[359] The difference in the chemical shift of the solvent in a diamagnetic and paramagnetic environment can be used to calculate the magnetic susceptibility using the equation **7**.

$$\chi_m = \frac{447 \Delta f}{2fc} \qquad \textit{Eqn. } \boldsymbol{7}$$

Equation 7: χ_m = molar susceptibility, f = frequency and c = concentration.

The LS to HS transition is an endothermic process while the reverse HS to LS transition is exothermic and therefore can be tracked using DSC (Differential Scanning Calorimetry). Thermodynamic parameters such as the enthalpy of the phase transition can be extracted and compared to those obtained from heat capacity measurements carried out in a PPMS (Physical Property Measurement System) instrument. SCO processes often occur in conjunction with phase changes and therefore DSC can be used to reveal these phase transitions. Complexes functionalised with mesogenic substituents often exhibit phase transitions between crystalline and liquid crystalline states which have dramatic consequences for the SCO behaviour, and these can be tracked by DSC.

1.7 Single molecule magnetism (SMM)

1.7.1 Introduction and history

A macroscopic magnet retains magnetisation upon the removal of a magnetic field due to the alignment of many domains in the structure via ferro or ferrimagnetic interactions. This magnetic property is not intrinsic to the atoms or molecules that make up the domain itself. Alternatively, single molecule magnets (SMMs) are molecules that exhibit the same retention of magnetisation as macroscopic magnets. However, this magnetic behaviour is intrinsic to the individual molecule and not due to magnetic interactions of a collection of molecules in a bulk material. Therefore, the definition of a SMM is a molecule that retains its induced magnetic moment upon removal or reversal of the magnetic field.[360-361] As thermal energy allows the relaxation of the magnetised state, materials exhibit this behaviour below a specific temperature, known as the blocking temperature (B_T). Hysteric magnetic behaviour is revealed in variable field magnetisation experiments when $T < B_T$ for complexes with a ground state of $S > 0$. Typically, the blocking temperature for these molecular compounds is very low and can only be achieved using liquid helium. Current efforts in this field have focused on the use of new ligands and coordination modes to increase the blocking temperature to more useful and accessible temperatures required for the potential applications in spintronics and data storage.[362]

For molecules with $S > 0$, the spin projection number (m_s) can exist as $\pm S$ with $-S$ referring to the 'spin up' and $+S$ as 'spin down' configuration. Prior to application of a magnetic field at a temperature above B_T, these states are in thermal equilibrium. However, applying a magnetic field results in one state being stabilised over the other. For the purpose of this explanation, the stabilised state will be denoted $m_s = -S$. Population of the $m_s = -S$ state results in an induced magnetic moment which must pass over an energy barrier for relaxation to occur as described in equation **8**. When represented in the form of equation **8**, the energy barrier (U_{eff}) is dependent on the spin of the system (S) and the axial zero field splitting parameter (D) for metal ions featuring axial anisotropy.[362] The zero-field splitting (ZFS) responsible for the anisotropy is due to the spin orbit coupling to excited states which is discussed in due course.

$$U_{eff} = |D|S^2 \qquad Eqn.\ \boldsymbol{8}$$

Equation 8: U_{eff} = the energy barrier to magnetisation relaxation, D = the axial ZFS parameter, S = the spin state.

Below B_T there is insufficient thermal energy for this relaxation to occur and therefore the induced magnetisation is retained after removal of the external magnetic field. As the magnetisation can occur in one of two possible directions, SMM is commonly referred to as a form of magnetic bistability like SCO. The magnetisation process and relaxation barrier are commonly presented schematically using a double well potential like that shown in *Figure 1.7.1.i.*

$[Mn_{12}O_{12}(OAc)_{16}(H_2O)_4]$, more commonly referred to as Mn_{12}, was the first reported single molecule magnet.[363-364] The Mn_{12} core contains four Mn(IV) S = 3/2 centres and eight Mn(III) S = 2 centres coupled antiferromagnetically through the bridging oxygen atoms to give a total spin of S = 10 (*Figure 1.7.1.ii*). The axial ZFS parameter for Mn_{12} is -0.5 cm^{-1} and therefore the energy barrier for magnetisation reversal can be calculated to be 50 cm^{-1} using equation **8**. The stability of the magnetisation of Mn_{12} was sufficiently high that if magnetised at 2 K, upon removal of the magnetic field, the magnetisation reversal is so slow that even after two months *ca.* 40% of the initial magnetisation at saturation is retained.

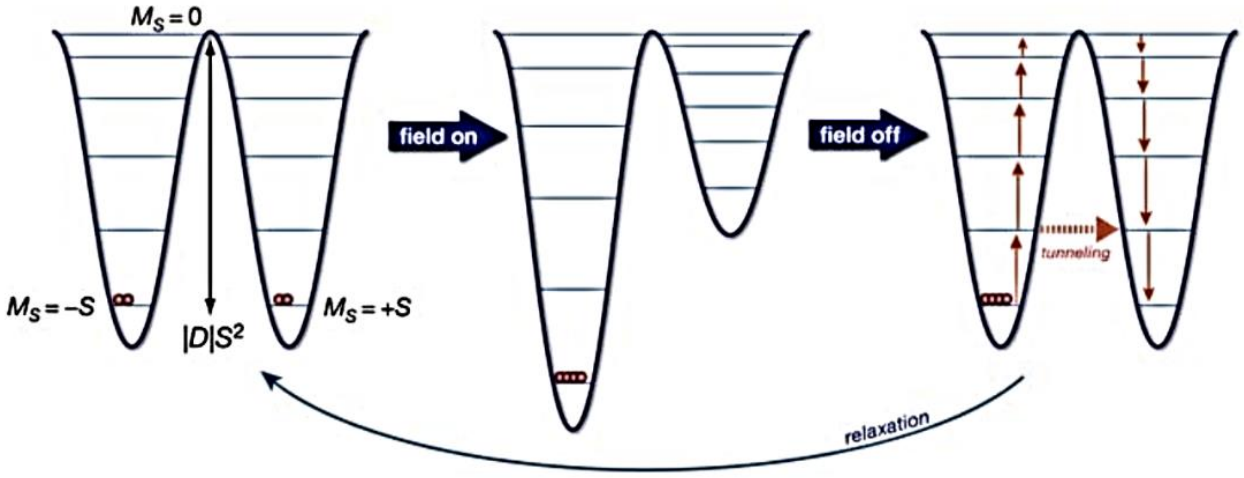

Figure 1.7.1.i: The double well potential representation of the barrier to relaxation of the magnetic moment where -S and +S represent the 'spin up' and 'spin down' states, respectively, while $|D|S^2$ represents the energy barrier U_{eff}.[365]

Variable field magnetisation measurements on Mn_{12} at 2.1 K show the presence of magnetic hysteresis loops that are open until *ca.* 4 K (*Figure 1.7.1.ii*). The loops are not perfectly sigmoidal

in shape and feature steps. These steps are due to a process known as quantum tunnelling (QTM) which occurs when the $-m_s$ and $+m_s$ wavefunctions are degenerate and overlap allows tunnelling through the energy barrier to occur. Other relaxation modes are also possible which will be discussed in due course.[366]

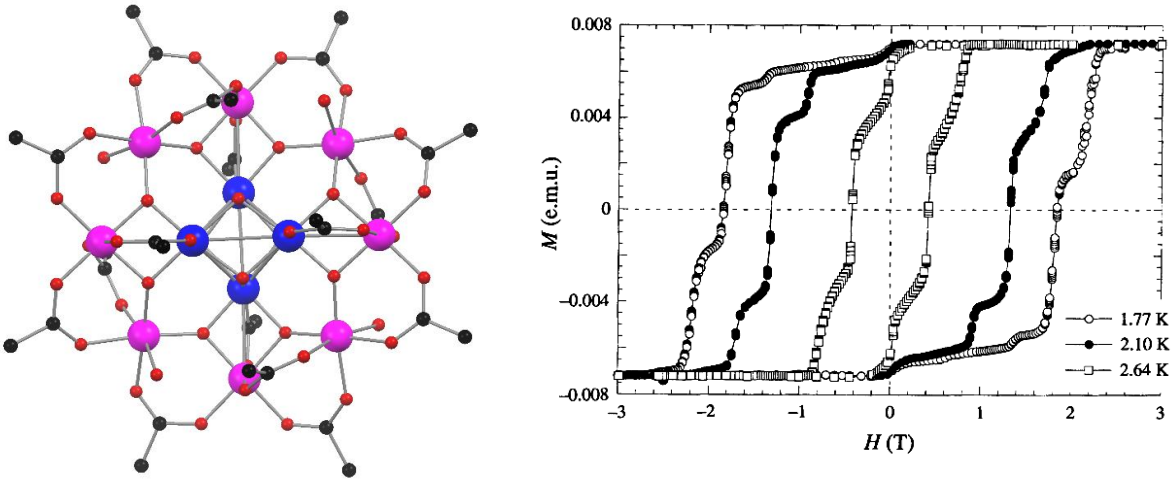

Figure 1.7.1.ii: (left) The crystal structure of Mn_{12} (hydrogen atoms omitted for clarity) with the Mn(III) centres shown in purple and the Mn(IV) centres shown in blue. (right) The hysteresis loops of Mn_{12} at 1.77, 2.10 and 2.64 K with steps indicative of QTM effects. Figure adapted from reference.[366]

Following the discovery of Mn_{12}, a number of first row transition metal cluster SMMs were reported.[367-368] As U_{eff} was proposed to be proportional to S^2, it was envisioned that increasing spin systems would result in larger U_{eff} values and therefore larger B_T values. The current record for the highest spin system is an S = 83/2 Mn_{19} cluster.[369] However, while these clusters possessed larger values of S, the values of D remained relatively low. This is due to two key factors, the first and most important is that the simple representation of equation **8** is misleading as U_{eff} is in fact not proportional to S^2. This can be rationalised by taking into account the equations that describe the spin orbit coupling (SOC) contribution to D. These show that $D \propto \frac{1}{S^2}$ and therefore U_{eff} is solely proportional to D. The second factor is that the magnetic anisotropy of the system is strongly dependent on the alignment of the anisotropy axis, especially Jahn-Teller axis. If the axes are misaligned, the anisotropy of the system is reduced, and this becomes very significant as the nuclearity and therefore number of potentially misaligned axes increases.[365]

The use of single lanthanide ions has since become a popular alternative due to the high spin ground state and more importantly large single ion anisotropies. Recently, a dysprosocenium complex has been reported by the groups of both Layfield and Mills with the highest U_{eff} to date of 1223 cm^{-1}. Furthermore it demonstrates open hysteresis loops at 60 K, the highest temperature currently reported.[370-371] While lanthanide complexes, in particular organometallic type complexes, are a crucial part of the SMM field of research, they are not relevant to the work of this thesis. The reader is directed to the following reviews for further information.[372-374] A key disadvantage of lanthanide based SMMs is the inherent cost of lanthanides compared to more affordable first row transition metals. This had led to a resurgence of SMMs containing first row transition metals, however, unlike the Mn_{12} and its analogues they are based on single ions.[375-376] It is these compounds that are of relevance to this work and will be discussed in detail in the following section

1.7.2 First row transition metal single ion magnets (SIMs)

As alluded to in the previous section, there is growing interest in single ion magnets (SIMs) containing 3d metal ions. When $S > 1/2$ and the symmetry about the metal ion is lower than cubic, ZFS may occur when the ground state couples to the excited states via SOC.[375-377] ZFS is the separation of otherwise degenerate electronic states and can be split into axial (D) and rhombic (E) contributions. However, in the case of 3d SIMs, the axial contribution is much more significant. The 3d orbitals are more diffuse than the relatively contracted 4f orbitals of lanthanide ions. Therefore, the interaction of the 3d orbitals with the molecular orbitals of the ligands is far more prominent and results in the quenching of the first order angular momentum. However, second order SOC can give rise to axial ZFS resulting in axial anisotropy. One method that has been studied to increase U_{eff} is to synthesise low coordination number and unusual coordination geometry complexes. This approach minimises the quenching of the first order angular momentum similar to lanthanide anions which have a large first order angular momentum. A disadvantage of 3d transition metal SIMs is that QTM processes are often very efficient and often require the application of an external DC magnetic field in order for them to be supressed. For example, the first reported 3d transition metal SIM, $Na[Fe(tpa^{Mes})]$ (H_3tpa^{Mes} = tris-mesityltris(pyrrolylmethyl)amine) required an external field of 1500 Oe to be applied.[378] Therefore, these species are sometimes referred to as *field induced* SIMs. This complex featured

the Fe(II) centre in an unusual three coordinate trigonal planar coordination geometry. As alluded to earlier, unusually low coordination numbers minimise the quenching of the first order angular momentum and in the case of Fe(I)/(II), coordination numbers of two to four are almost always essential for them to exhibit SIM behaviour.[378-380] At the time of writing there is only one six coordinate Fe(II) complex which behaves as a SIM.[381] The complex features the Fe(II) centre in a D_{3d} local symmetry and a strongly axial ligand field. More recently a family of 8-coordinate Fe(II) complexes with distorted triangulardodecahedral coordination spheres have been reported to exhibit SMM.[382] While exotic coordination numbers and geometries are required for some metal ions such as the aforementioned Fe(II) along with Fe(I) and Ni(I), both Co(II) and Mn(III) ions can act as SIMs in more conventional coordination geometries.[376] In the case of six coordinate Mn(III) complexes, Jahn-Teller distortion results in distortion from O_h to D_{4h} local symmetry. This causes the ^5E electronic state to split resulting in a $^5B_1$ ground state that upon mixing with excited states results in ZFS with $D < 0$. The case of Co(II) will be covered in more detail with relevant examples in the following section.

1.7.2.i Co(II) SIMs – Background

Co(II) is a d^7 ion with $S = 3/2$ in the HS state corresponding to a $^4T_{1g}$ ground state when in six coordinate complexes with idealised octahedral symmetry. However, distortion from idealised octahedral geometry is commonly enforced by the ligand. This often results in tetragonal distortion which lowers the local symmetry about the Co(II) ion. This results in the $^4T_{1g}$ ground state splitting into a $^4A_{2g}$ ground state and a ^4E_g excited state (*Figure 1.7.2.i*). SOC results in mixing of the $^4A_{2g}$ state with excited states causing it to split into two Kramers doublets with an energy difference of $2D$. When D is negative the lower energy Kramers doublet is $m_s = \pm 3/2$ while the higher energy Kramers doublet is $m_s = \pm 1/2$. The splitting of these Kramers doublets is an example of ZFS and is responsible for single ion anisotropy. A similar effect occurs for the ^4E_g excited state resulting in splitting into four Kramers doublets. However, assuming the energy separation between the $^4A_{2g}$ and ^4E_g states is large, only the two Kramers doublets arising from the $^4A_{2g}$ state are occupied.[377] For Co(II) a majority of the complexes studied display negative D parameters, although, some complexes with positive D parameters have been reported. When the D parameter is positive the energy ordering of the Kramers doublets is reversed.[375-376]

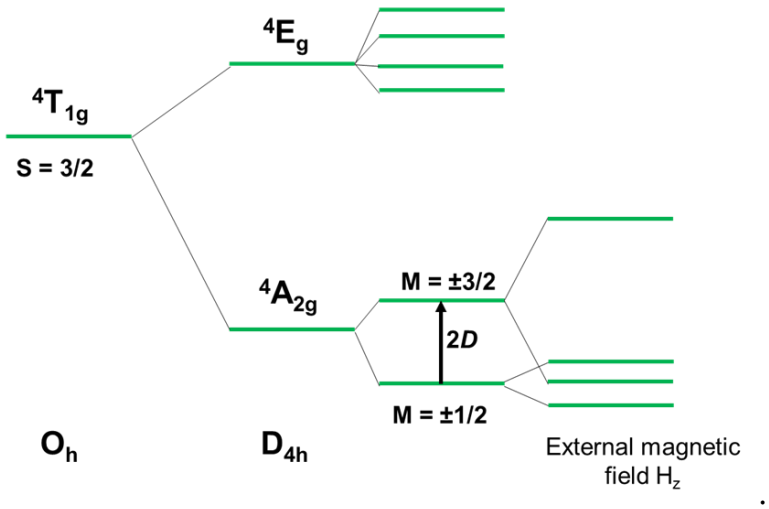

Figure 1.7.2.i: The splitting of the $^4T_{1g}$ ground state for HS Co(II) (S = 3/2) due to axial distortion to D_{4h} symmetry and zero field splitting with a positive D parameter.

As with most other 3d SIMS, slow relaxation of the magnetisation in the absence of an applied DC field is rare for Co(II) SIMs due to QTM. The QTM effects for Co(II) are less significant compared to other 3d metal ions due to $S = 3/2$. Despite QTM being formally forbidden between $\pm n m_s$ states due to parity effects, it occurs rapidly in Co(II) ions at zero field due to rhombicity of the anisotropy.[383-384] The application of an external DC field offsets the lowest $\pm n m_s$ states such that the two states are not degenerate in energy and therefore minimal overlap of the wave functions can occur.

1.6.3.ii Co(II) SIMs – selected examples

The effect of the local symmetry about the Co(II) centre and the importance of distortion is demonstrated by two $[Co(Imidazole)_6]X_2$ complexes.[385] When $X^- = BPh_4^-$ the local symmetry of the Co(II) is C_i however when $X = NO_3^-$ the local symmetry is less distorted D_{3d}. While both complexes display field induced SMM behaviour, the complex with D_{3h} local symmetry had a noticeably lower U_{eff} value. The use of ligands that result in more distorted coordination spheres maybe be a route to higher U_{eff} values for octahedral Co(II) SIMs. An even more dramatic difference was observed for two polymorphic $[Co(neo)(PhCOO)_2]$ complexes (neo = neocuproine).[386] One complex showed a significantly larger trigonal distortion than the other and displayed easy plane anisotropy ($D > 0$) while the less distorted polymorph displayed the more common axial anisotropy ($D < 0$). Trigonally distorted complexes are particularly interesting in

the field of Co(II) SIMs. Due to rapid QTM, zero field Co(II) SIMs are rare, however six coordinate Co(II) complexes can exhibit SMM behaviour in the absence of a DC field if they feature sufficient trigonal distortion (*Figure 1.7.2.ii*). This results in an orbitally degenerate ^4E ground state and therefore unquenched orbital angular momentum which results in a highly anisotropic Co(II) ion.[387-389]

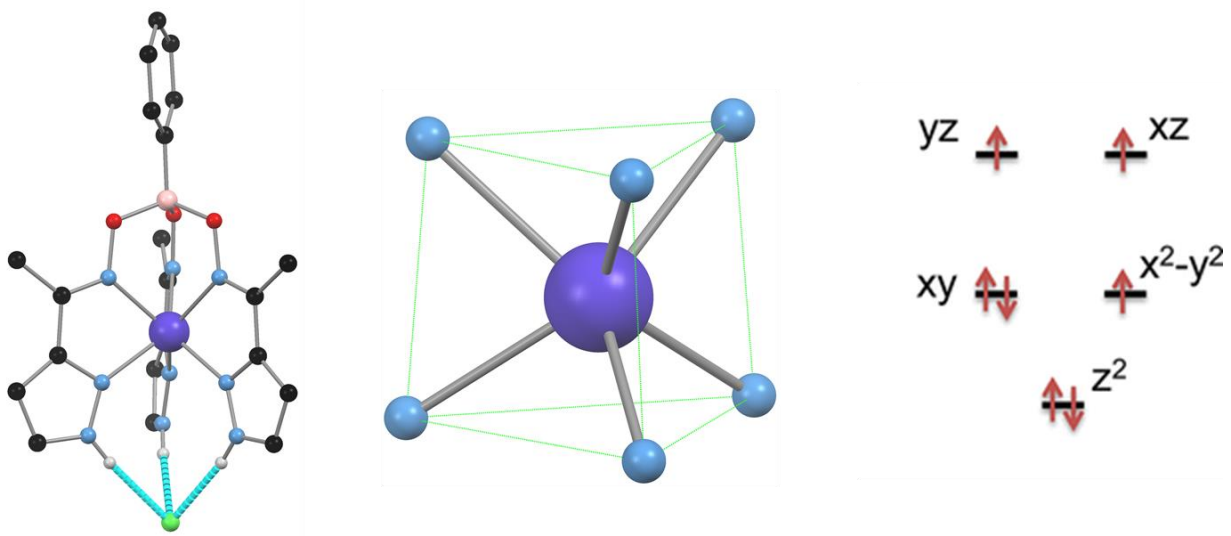

Figure 1.7.2.ii: (left) A Co(II) pseudoclatherochelate complex reported by Voloshin and co-workers.[387] (middle) The strongly trigonally distorted coordination sphere of the HS Co(II) ion in the pseudoclatherochelate complex shown. (right) The orbital splitting for a d^7 S = 3/2 metal ion is in a tetragonal crystal field. Figure adapted from reference.[390]

Another emerging class of Co(II) SIMs are those based on tetrahedral Co(II) centres. While not directly applicable to the work of this thesis, a brief overview will be given. Unlike other low coordinate first row transition metal ions of interest for SIMs, tetrahedral Co(II) complexes are readily synthesised. Tetrahedral Co(II) SIMs are particularly important as they can exhibit slow magnetic relaxation in the absence of an applied field, unlike the vast majority of six coordinated Co(II) SIMs. In fact the first Co(II) SIM was a tetrahedral complex reported by Zadrozny and Long in 2011.[391] Since this discovery a variety of tetrahedral Co(II) SIMs have been reported using monodentate sulfur containing ligands along with other chalcogenides and soft donor atoms such as phosphorous.[392-393] Another emerging class of ligands are bidentate ligands where one donor atom is nitrogen while the other is a phenolic oxygen atom. Two ligands coordinate to the Co(II) centre resulting in a distorted tetrahedral coordination geometry with an N_2O_2 coordination sphere.

The first such complex was reported in 2012 containing an imidazolylphenol based ligand.[394] More recently ligands on the related salicylidenimine coordinating motif have been used to synthesise both mononuclear Co(II) SIMs[395] and Co(II) dinuclear double helicates showing SIM behaviour.[396]

1.7.3 Methods and techniques of characterisation of SMM

DC magnetic measurements with a static magnetic field are the first measurements carried out on any species with magnetic properties of interest. The slow relaxation of magnetisation of SMMs manifests itself as a roughly sigmoidal hysteresis loop in *M vs. H* magnetisation measurements. *M* is the magnetisation, typically in μ_B and *H* is the applied field given in either tesla (T) or Oersted (Oe). Steps in these hysteresis loops indicate the presence of QTM effects. The hysteresis loops are open until B_T after which they are closed and the hysteretic magnetic behaviour is lost. When the B_T is lower than the temperature that a conventional SQUID magnetometer can reach (1.85 K) and specialist set ups using Helium-3 are required to observe hysteresis loops.

Magnetisation as a function of the field can reveal the presence of anisotropy when conducted at multiple low temperatures. In these experiments the field is increased from 0 to 7 T at which point the metal ion(s) have usually reached magnetic saturation. As the measurement temperature increases, the curvature of the magnetisation isotherm decrease until linearity is reached at high temperature (*Figure 1.7.3.i*). When plotted as M *vs.* $H\,T^{-1}$ the isotherms may be superimposed or adopted a 'nested' like appearance. The latter is when the curves are superimposed at low values of $H\,T^{-1}$ but not at higher values and is indicative of the system possessing anisotropy. Simultaneous fitting of the magnetic susceptibility (χT *vs. T*) and the magnetisation isotherms (*M vs. H*) to an appropriate Hamiltonian can be used to extract the value of the *D* parameter. High field EPR is a more accurate method of determining the magnitude and sign of the *D* parameter, however the large *D* values often encountered prevent the use of this technique.[397]

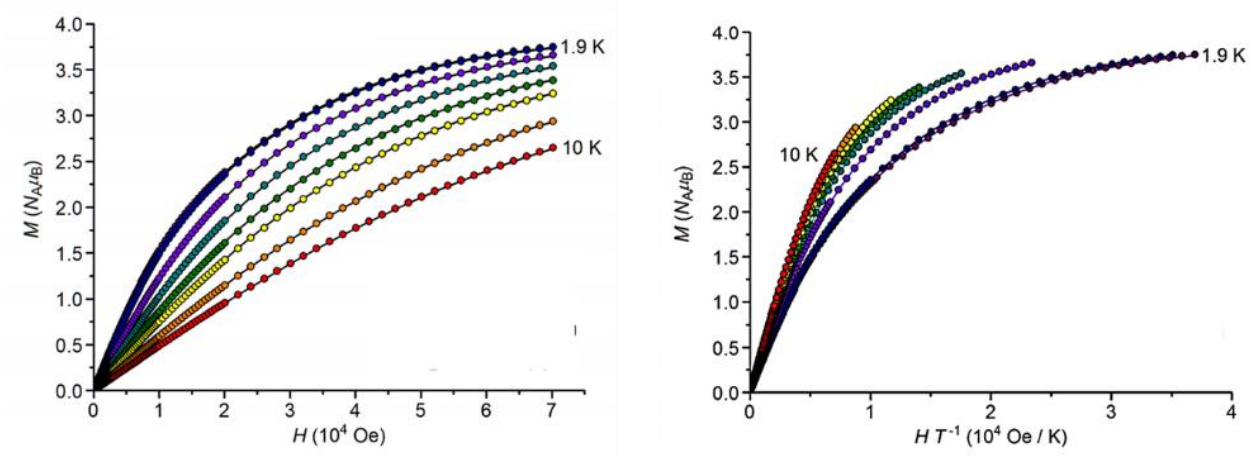

Figure 1.7.3.i: Examples of M vs. H (left) and M vs. H T^{-1} (right) for a complex reported by Cornia and co-workers exhibiting SMM. Figure adapted from reference.[398]

Due to the aforementioned difficulty of measuring hysteresis loops of many transition metal ion complexes, AC magnetic susceptibly measurements are used instead to show SMM behaviour. A weak AC magnetic field (1 to 5 Oe) of frequency ν is superimposed on a significantly stronger DC field (200 to 7000 Oe). The alternating component of the magnetic field experienced by the sample results in a time dependant magnetic moment (*Figure 1.7.3.ii*).

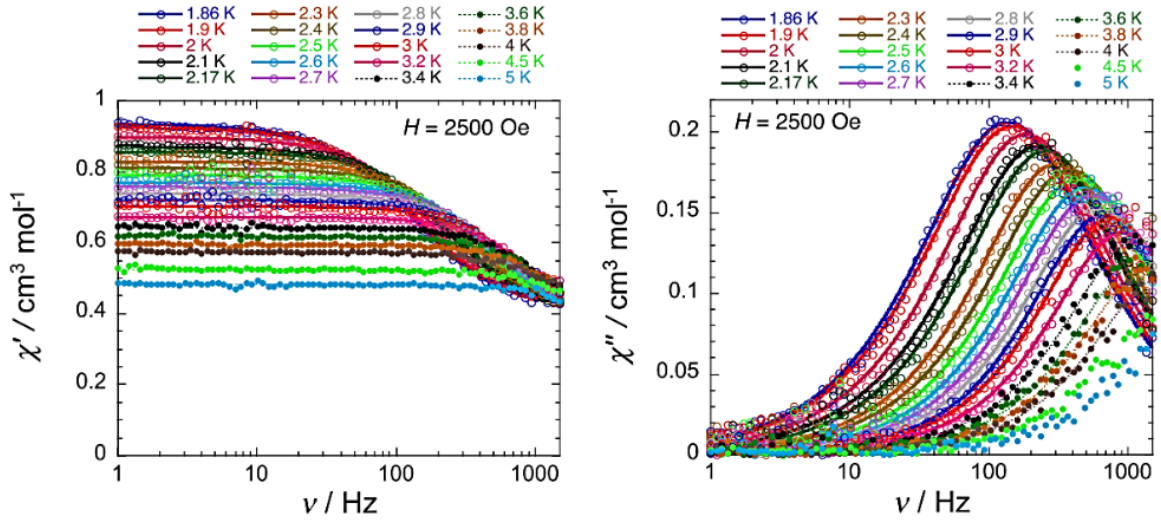

Figure 1.7.3.ii: The plots of the in-phase (χ′) and out-of-phase (χ″) verses the frequency at a variety of temperatures for a single molecule magnet reported by Cornia and co-workers. Note the external DC field of 2500 Oe, applied to supress QTM processes. Figure adapted from reference.[398]

This measurement is carried out in a PPMS instrument which is particularly sensitive to the small changes in the magnetic moment due to the alternating magnetic field. For complexes exhibiting very rapid relaxation of magnetisation (*i.e.* not SMMs), the magnetic moment is always in phase with the AC magnetic field. However, when the metal complex displays slow relaxation of magnetisation, the magnetic susceptibility 'lags' behind the AC magnetic field. Therefore, the magnetic susceptibly can be split into in-phase (χ') and out-of-phase components (χ'') related by the phase shift (φ) relative to the applied frequency. As the frequency of the AC field increases the 'lag' of the magnetic susceptibility becomes more prominent and therefore the out-of-phase component increases (χ'') (equations **9** and **10**).

$$\chi = \sqrt{\chi'^2 + \chi''^2} \qquad \textit{Eqn. } \boldsymbol{9}$$

$$\chi' = \chi'' cos\varphi \text{ and } \chi'' = \chi' sin\varphi \qquad \textit{Eqn. } \boldsymbol{10}$$

Equations 9 and 10: The χ represents the magnetic susceptibility while the ' and '' indicate the inphase and out-of-phase components and φ is the phase shift.

When the AC measurements are performed as a function of the frequency ν at different temperatures, the χ' and χ'' data can be fitted to the generalised Debye model. The Debye model was first proposed to model the frequency dependence of dielectric measurements and has since been generalised to model the frequency dependence of the magnetic susceptibility.[399-400] By fitting the data to the generalised Debye model, the relaxation time (τ) can be obtained for each temperature (*T*). The plotting of T^{-1} *vs.* ln(τ) provides insight into the nature of the relaxation process occurring. At higher temperature the plot is linear and fitting to the Arhenius equation gives the pre-exponential factor τ_0 and the energy barrier to relaxation U_{eff} (equation **11**).

$$\tau = \tau_0 exp \frac{U_{eff}}{k_B T} \qquad \textit{Eqn. } \boldsymbol{11}$$

Equation 11: τ = relaxation time, τ_0 = pre-exponential constant, U_{eff} = energy barrier to magnetisation relaxation, k_B = Boltzmann constant and T = temperature.

The linear region of the T^{-1} *vs.* ln(τ) plot corresponds to the thermally induced Orbach relaxion process (*Figure 1.7.3.iii*). At lower temperature where there is significantly less available thermal energy, other relaxation modes are more prominent. A linear line with a gradient of zero can be indicative of QTM relaxation process.

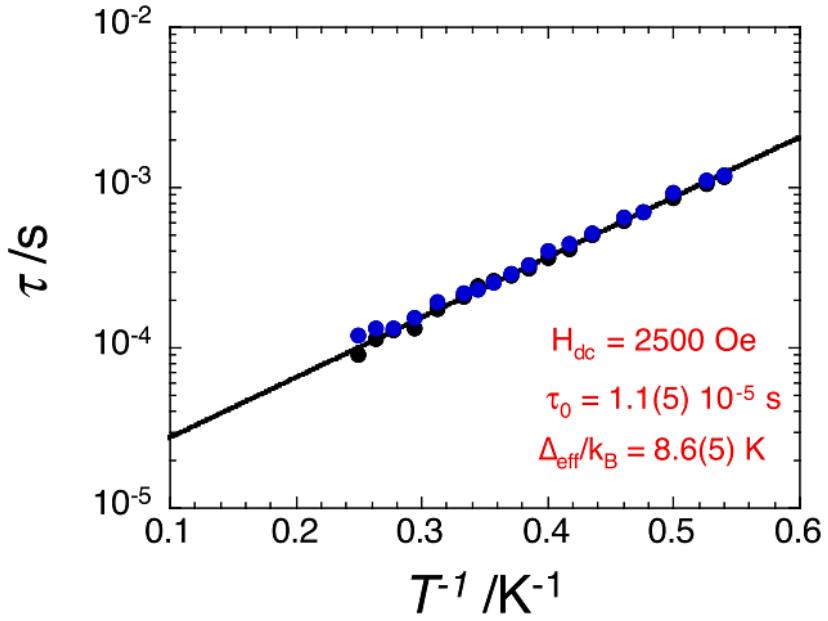

Figure 1.7.3.iii: τ vs. T^{-1} plot showing the linear relationship between the relaxation time (τ) and the inverse of the temperature. T is obtained from fitting the χ' (blue) and the χ'' (black) to the generalised Debye model. Figure adapted from reference.[398]

Two further relaxation modes are Raman and Direct relaxation processes both of which are related to lattice-phonon coupling. The Raman relaxation is a two-phonon process that goes via a virtual Raman state. The Direct relaxation is a single phonon process occurring via a direct transition from one microstate to another. Further details on these relaxation processes are beyond the scope of this thesis and the reader is directed to the following reference.[401]

1.8 Present study

The overarching aim of this work is to investigate the influence of supramolecular interactions between multinuclear assemblies on various physical properties. The coordination of ligands to a metal centre results in them adopting defined geometries relative to one another. This has a profound effect on the types of supramolecular interactions occurring between discrete assemblies. Complexes containing multiple metal centres allow the relative orientations of the ligands at each metal centre to be pre-defined due to them being linked by the bridging ligand backbone. The modulation of the peripheral ligand functionality, solvents of crystallisation and counter anion all allow for the exact type of the supramolecular interactions, occurring for a specific type of

supramolecular assembly, to be varied in a systematic manner. The effect of changing each of these variables is elucidated via structural characterisation techniques, predominantly single crystal X-ray diffraction. The work detailed in this thesis concerns metallo-supramolecular assemblies consisting of dinuclear helicates and mesocates along with tetranuclear grid complexes. Two key ligand types were used in this study: pyridylhydrazone and imidazolylimine and as such the thesis naturally divides into two sections. Chapters two and three concern the assemblies made with pyridylhydrazone ligands while chapters four and five concern the assemblies made with imidazole-imine ligands.

The predominant physical property of interest is the magnetic susceptibility in the form of SCO behaviour for Fe(II) and Fe(III) centres and SMM behaviour for Co(II) centres. Both of these behaviours are investigated by variable temperature DC magnetic susceptibility measurements along with absolute reflectivity and AC susceptibility measurements for SCO and SMM respectively. Gas sorption measurements were performed on one complex for which the crystal structure indicated the presence of permanent porosity. Where possible, the difference in the physical properties for related complexes was correlated to the difference in the solid-state structures due to the occurrence of different supramolecular interactions.

Chapter two investigates the use of the pyridylhydrazone coordinating motif incorporated into rigid ligands. Tetranuclear grid structures are formed upon coordination to Fe(II), Fe(III) and Co(III) in the tridentate anionic imino-enolate form. When the ligand coordinates to Fe(II) in the neutral imino-keto form it adopts an unusual bidentate coordination mode resulting in duncelar triple mesocates. The SCO behaviour of the Fe(II) and Fe(III) grid complexes was investigated and displayed significantly different behaviour upon modulation of the peripheral ligand functionality. The replacement of the pyridine ring with a pyrazine ring results in one of the dinuclear mesocates exhibiting permanent porosity.

Chapter three continues the theme of pyridylhydrazone ligands and introduces the related quinolinylhydrazone coordinating motif. These coordinating moieties are incorporated into flexible ligands to synthesise dinuclear double helicates with Co(II). Chapter two highlighted the importance of the pyridylhydrazone N-H moiety towards the crystal packing. Therefore, particular interest is paid to the different hydrogen bond modes of the N-H moiety and the differing propensities of pyridine and quinoline rings towards π-π interactions.

Chapter four moves onto the second part of the investigation, utilising imidazolylimine based ligands to synthesise dinuclear triple helicates via sub-component self-assembly. This work looks to expand on a family of Fe(II) helicates complexes previously reported by the Kruger group which displayed thermal and photo induced SCO. The use of Co(II) in the place of Fe(II) was investigated with the goal of synthesising SMM materials.

Chapter five details some preliminary work on the functionalisation of helicates with mesogenic substituents. A family of helicates previously reported by the Kruger group, different to those in chapter four was selected for functionalisation. Both the possible phase change behaviour and SCO properties for two such Fe(II) dinuclear triple helicates were investigated.

Chapter six serves as a summary of the work conducted in the previous four chapters. Some final thoughts on the successes and difficulties encountered during this work are included. Finally, some possible avenues for future work, based on the findings of this thesis are included.

Chapter Two

Supramolecular Grids and Mesocates Based on Rigid Pyridylhydrazone and Related Ligands

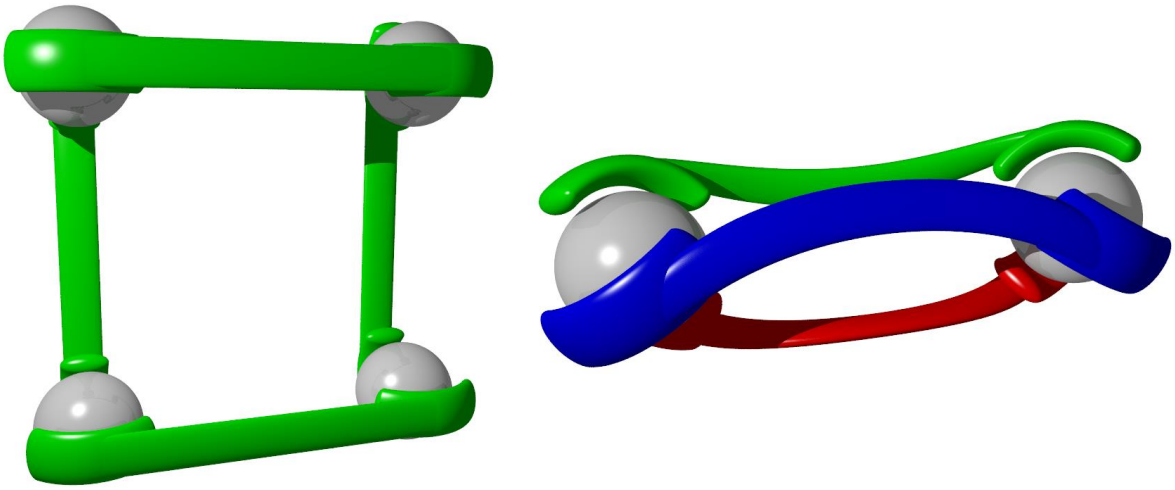

2.1 Introduction

2.1.1 Rigid ditopic pyridylhydrazone ligands

Ditopic ligands with pyridylhydrazone and the related pyridylacylamidrazone coordinating motifs, separated by a rigid linker, are prevalent in the literature. The coordinating moieties can be directly fused together or separated by one or multiple phenyl rings.[139, 402-406] While pyridylhydrazone and pyridylacylamidrazone moieties are commonly employed as a tridentate ligands, they can also coordinate in a bidentate fashion via the two nitrogen atoms. The pyridylhydrazone moiety can coordinate in a neutral imino-keto or an anionic imino-enolate form following tautomerism and subsequent deprotonation. Pyridylhydrazone ligands have been reported to form metal complexes ranging in nuclearity from two to six. Dinuclear complexes take the form of helicates or mesocates depending on whether they exhibit helical chirality.[407-410] Trinuclear triangle complexes of the type $[M_3L_3]^{6+}$ have been reported by Duan and co-workers.[411-412] Tetranuclear structures can either exist as $[M_4L_4]^{8+}$ grids[402, 413] or $[M_4L_6]^{8+}$ tetrahedral cages,[414] depending on whether the ligand coordinates in a tridentate or bidentate fashion. Hexanuclear structures have been synthesised using ligands incorporating three coordinating moieties which form faced capped octahedral cages of the type $[M_6L_4]^{n+}$.[403-404] Of particular relevance to the current study are ligands in which the coordinating moieties are separated by a single phenyl spacer.

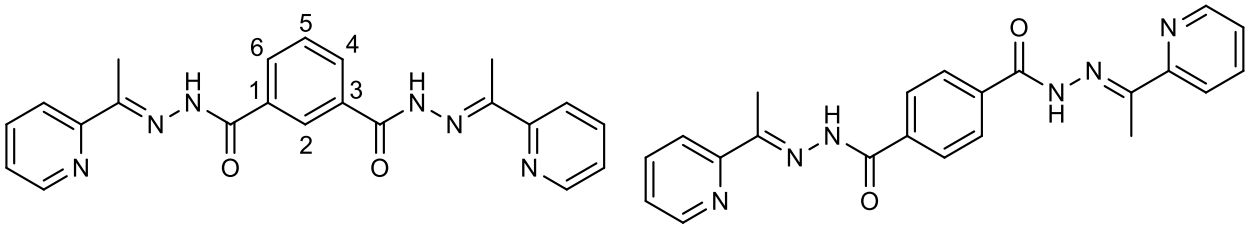

Figure 2.1.1.i: (left) Ditopic pyridylhydrazone ligand with an isophthaloyl bridging group showing the numbering scheme of the central aromatic ring. (right) Ditopic pyridylhydrazone ligand with a terephthaloyl bridging group. Both ligands are examples that form tetranuclear grid complexes with Zn(II).[402]

These ligands are readily prepared from the appropriate phthalic acid isomer with either *meta* (isophthalic acid) or *para* (terephthalic acid) substitution. Both ligand isomers (*meta* and *para*) have been reported to form tetranuclear grid type structures with Zn(II) when coordinating in the

neutral imino-keto form (*Figure 2.1.1.i*).[402] The *meta* isomer was investigated in the current study as the 5-position of the isophthalate spacer can be readily functionalized.

2.1.2 Spin crossover in pyridylhydrazone complexes

As previously discussed, the pyridyl hydrazone moiety can coordinate in either the imino-keto or imino-enolate form. The former produces only HS Fe(II) complexes while the latter has been reported to form SCO complexes with both Fe(II)[300, 304-306, 415] and Fe(III).[302] The examples in the literature are limited to mononuclear complexes, of which the majority are Fe(II). A common feature of pyridylhydrazone based ligands bound to Fe(II) SCO centres is the presence of hydroxy or methoxy substituents on the aromatic ring conjugated to the hydrazone moiety (*Figure 2.1.2.i*).

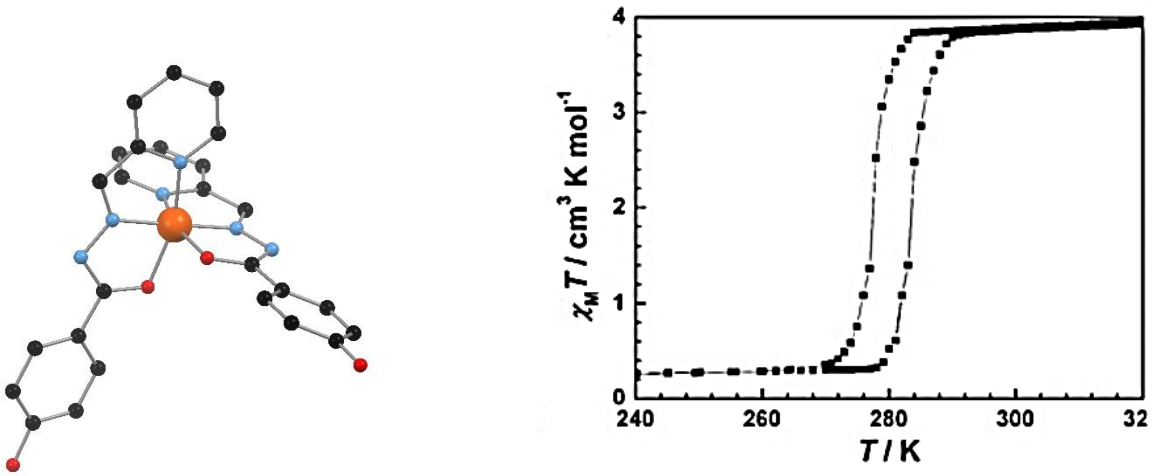

Figure 2.1.2.i: (left) An Fe(II) complex coordinated to two pyridylhydrazone ligands in the imino-enolate form with hydroxy substituents in the para position of the aromatic rings. Hydrogen atoms are omitted for clarity. (right) χT vs. T plot for the Fe(II) complex showing complete SCO with hysteresis ($T_{1/2}$ heating = 285 K and $T_{1/2}$ cooling = 278 K). Figure reproduced from reference.[306]

The Fe(II) complexes are of particular interest as they are neutral. Therefore, upon functionalisation with mesogenic substituents, they are predisposed to forming liquid crystals that exhibit SCO. At the time of writing, there were only two examples for which Fe(II) complexes with this type of ligand are functionalised with mesogenic substituents.[300, 415] In both cases, while a liquid crystalline phase was not formed, melting of the crystals resulted in a reversible SCO.

2.1.3 Scope of research

The aim of this work was to synthesise $[M_4L_4]^{n+}$ grids from Fe(II), Fe(III) and Co(III) with rigid ditopic ligands based on a isophthalate linker (*Figure 2.2.1*). It was envisioned that functionalisation of the 5-positon would allow for tuning of the electronic nature of the aromatic ring which would in turn adjust the field strength of the ligand. These types of ligands feature additional sites for modification, such as the pyridine ring, that were investigated in a preliminary manner. Synthesis of complexes featuring the ligand in both the imino-keto and imino-enolate form were carried out. As discussed in due course, the synthesis and characterisation of $[M_4L_4]^{n+}$ complexes in which the ligand coordinates in the imino-enolate form presented a wide range of unforeseen difficulties. Therefore, only preliminary work was conducted in this area. However, the synthesis of complexes with the ligand coordinating in the imino-keto form resulted in the unexpected formation of $[M_2L_3]^{4+}$ mesocate complexes. A comprehensive investigation of these, including their amenability towards the synthesis of molecular porous materials (MPMs) was carried out. This study was extended by replacing the pyridine rings with pyrazine rings and investigating the potential of the non-coordinated nitrogen atom of the pyrazine ring to act as a hydrogen bond acceptor.

2.2 Ligand synthesis

The family of ligands discussed in this chapter were prepared following literature or adapted literature preparations and a general synthesis scheme is shown below (*Figure 2.2.1*). The hydrazide is synthesised either directly from the diester or in a two-step reaction from the diacid via the diester, depending on which commercially available precursor is used. The ester is then converted to the hydrazide with hydrazine monohydrate in ethanol. The hydrazide is then reacted with either 2-pyridine carboxaldehyde, 2-acetylpyridine or 2-acetylpyrazine to form the appropriate ligand. For the 5-bromo functionalised ligands, the precursor diacid was prepared via a bromination reaction of isophthalic acid with NBS in sulfuric acid. For the 5-iodo functionalised ligand, the precursor diester was prepared from dimethyl 5-aminoisophthalate via the diazonium salt using a Sandmeyer reaction. The 5-methoxy functionalised ligand was prepared from the commercially available 5-hydroxyisophthalate via a simultaneous esterification and alkylation using dimethyl sulfate. This range of functional groups was selected based on their electronic

effects which influence the ligand field e.g. the electron donating properties of the methoxy and amino functional groups. The halogen containing ligands were synthesised to investigate the effect moieties capable of forming halogen bonds would have on the crystal packing.

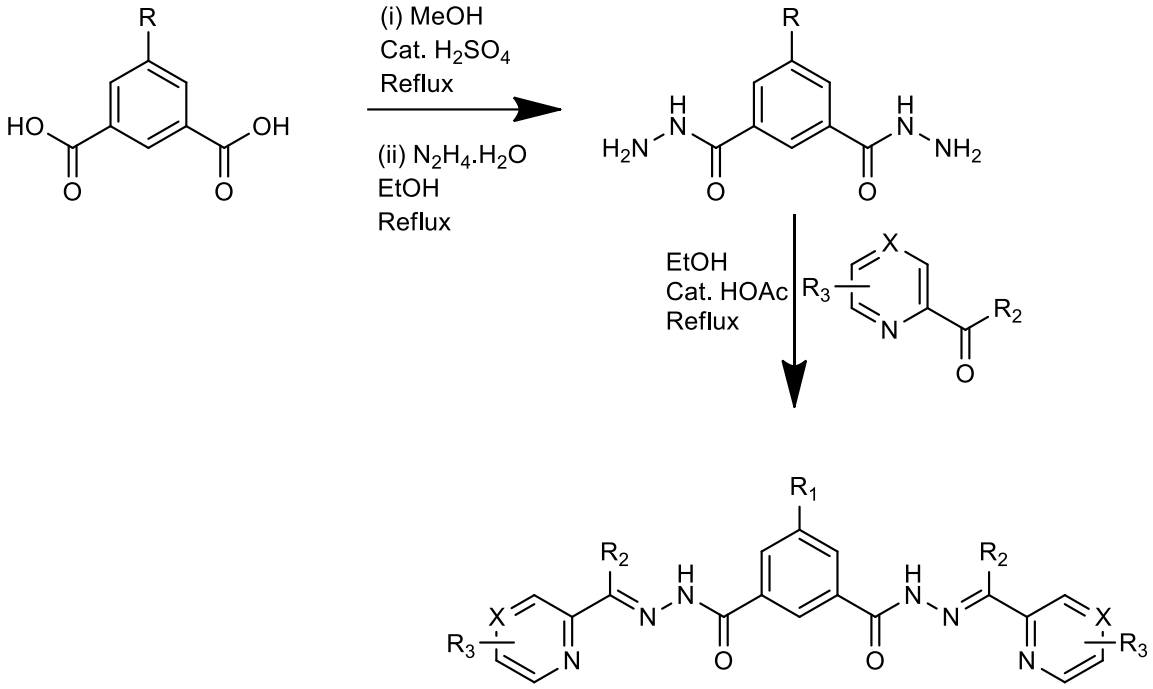

Figure 2.2.1: The synthesis scheme used to form the pyridylhydrazone and pyrazinylhydrazone ligands. R_1 = H, Br, I, NH_2, OH or OMe. R_2 = H or Me. R_3 = H, 4-Cl or 6-Cl. X = CH or N.

All of these pyridylhydrazone or pyrazinylhydrazone ligands were insoluble in common deuterated solvents which precluded their analysis by NMR spectroscopy. However, in most cases the ligand could be solubilised in methanol using formic acid and analysed by mass spectrometry. Ligands featuring 4-chloro or 6-chloro pyridine rings, H_2**L2.3** and H_2**L2.4**, were not isolated as the complete ligand and instead were synthesised via a sub-component self-assembly reaction from the aldehyde precursor and the appropriate hydrazide and Fe(II) salt.

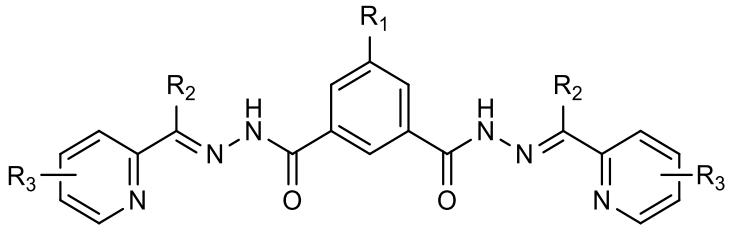

*Figure 2.2.2: The naming scheme for the pyridylhydrazone ligands discussed in this chapter. H_2**L2.1**: R_1=H, R_2=Me, R_3=H. H_2**L2.2**: R_1=Br, R_2=H, R_3=H. H_2**L2.3**: R_1=H, R_2=H, R_3=4-Cl. H_2**L2.4**: R_1=H, R_2=H, R_3=6-Cl.*

This was due to the high cost of the precursor aldehydes and thus low scale used when working with these ligands. The various points of ligand functionalisation are shown above for the pyridylhydrazone (*Figure 2.2.2*) and below for the pyrazinylhydrazone ligands (*Figure 2.2.3*).

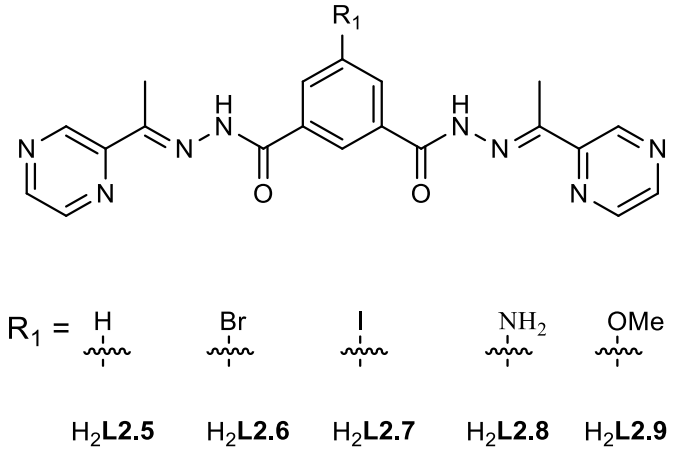

Figure 2.2.3: The naming scheme for the pyrazinylhydrazone based ligands.

Vapor diffusion of petroleum ether into a 10:1 DCM/methanol solution of H_2**L2.2** gave colourless plate crystals suitable for single crystal X-ray diffraction. H_2**L2.2** crystallised in the triclinic space group *P*-1 (R = 4.08%) with two H_2**L2.2** molecules and one DCM molecule in the asymmetric unit (*Figure 2.2.4*). The C=O carbonyl bond lengths range from 1.227(4) to 1.236(4) Å while the C-N hydrazide bond lengths range from 1.349(5) to 1.361(5) Å, indicating that all of the hydrazone moieties exist as the imino-keto tautomer. The two H_2**L2.2** molecules exist as closely packed dimers, due to two sets of hydrogen bond interactions between the hydrazide moieties of neighbouring molecules. The first hydrogen bond interaction occurs between a hydrazide N-H moiety and a carbonyl oxygen atom with an H···O separation of 2.088(2) Å. The second hydrogen

bond interaction occurs with the N-H hydrazide moieties acting as hydrogen bond donors while the C=N and carbonyl oxygen moieties act as hydrogen bond acceptors. The H···O and H···N separations are 2.198(2) and 2.439(3) Å, respectively and this interaction can be described as $R_1^2(5)$ using graph set notation.[416-417]. This results in the formation of a hydrogen bonded chain running approximately parallel to the crystallographic *c*-axis. Neighbouring chains are held together via C-H···Br interactions with an H···Br separation of 2.9315(3) Å and C-H···Br angle of 106.3(1)°. The dichloromethane solvent molecule interacts with the bromine substituent via a type II halogen bond with a Cl···Br separation of 3.525(1) Å and a C-Cl···Br angle of 104.5(2)°.[45-46, 56]

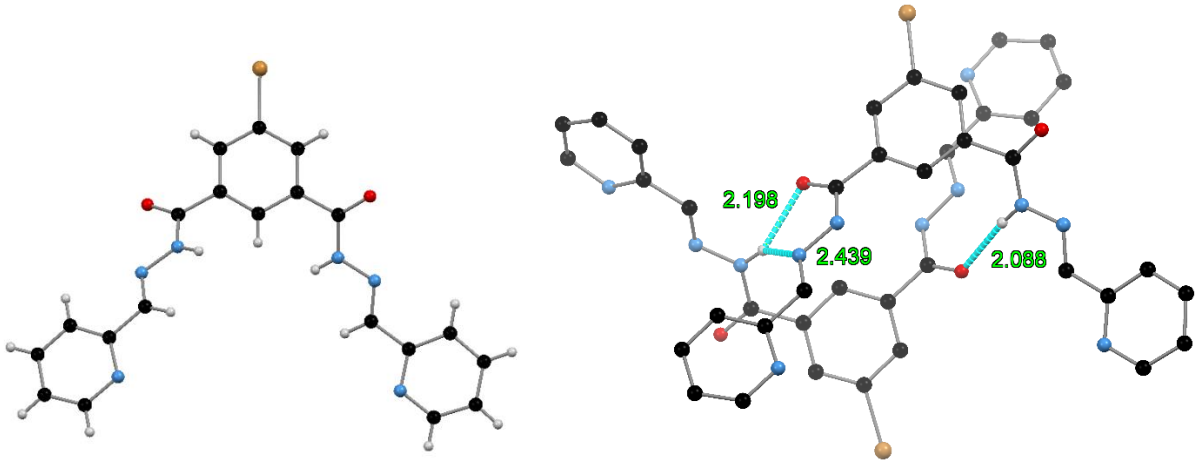

*Figure 2.2.4: (left) Ligand H_2**L2.2** with both pyridylhydrazone moieties in the trans conformation. (right) The reciprocal hydrogen bond interactions occurring between the two crystallographically unique H_2**L2.2** ligands in the asymmetric unit. Hydrogen atoms not participating in the illustrated interactions omitted for clarity. Hydrogen bonds shown in light blue.*

The ligand adopts a conformation in which both of the hydrazone moieties are orientated in the opposite directions while the nitrogen atoms of the pyridine rings are orientated towards one another. This conformation is different to how the ligands are typically depicted in the literature and in this thesis.[402]

2.3 Complex synthesis and characterization

A number of difficulties were encountered when synthesising Fe(II) complexes using the pyridylhydrazone ligands in the anionic imino-enolate form. The first was that the Fe(II)

complexes were very sensitive to oxidation while in solution and were therefore synthesised under an argon atmosphere in a glove box. The second was, upon crystallisation all $[M_4L_4]^{n+}$ complexes exhibited very poor crystallinity and only low-resolution single crystal X-ray diffraction data could be obtained. In some cases, synchrotron radiation was used, however, this only resulted in minor improvements. The third, major difficulty was the neutral Fe(II) complexes were extremely insoluble. Crystals were obtained either from dilute solutions of DMF or very dilute solutions of DCM in low yields. Despite these challenges a number of crystal structures were obtained, and enough sample synthesised to carry out magnetic susceptibility experiments in some cases. However, due to the quality of the diffraction data and in most cases absence of SCO behaviour, the complexes were not fully characterised (elemental and TGA) with the exception of complex **2.13**. The complexes formed from the ligands in the imino-keto form did not present the challenges describe above or did so to a lesser extent and were therefore fully characterised.

2.3.1 $[Fe_4(L2.1)_4]$, 2.12

This complex was synthesised in an argon filled glovebox due to the propensity toward oxidation of Fe(II) for this ligand system. The ligand H_2**L2.1** was stirred in methanol and a 4-fold excess of triethyl amine. A solution of Fe(II) perchlorate was added and the complex was isolated as a green solid. Crystals suitable for single crystal X-ray diffraction were generated via slow evaporation of a very dilute dichloromethane solution of the complex and vapor diffusion of methanol which resulted in green plate crystals. The data were collected at 120 K and solved and refined in the tetragonal space group *I*4/*m* (R = 14.67%). The crystals were weakly diffracting due to their thin nature, resulting in poor quality data. However, the data collection was sufficient to obtain the connectivity of the structure. The asymmetric unit contains one ligand, one Fe(II) centre and a partial occupancy triethyl amine molecule situated on a symmetry element, modelled with 75% occupancy (*Figure 2.3.1.i*). The action of a 4-fold rotoinversion generates a tetranuclear $[Fe_4($**L2.1**$)_4]$ grid from the asymmetric unit.

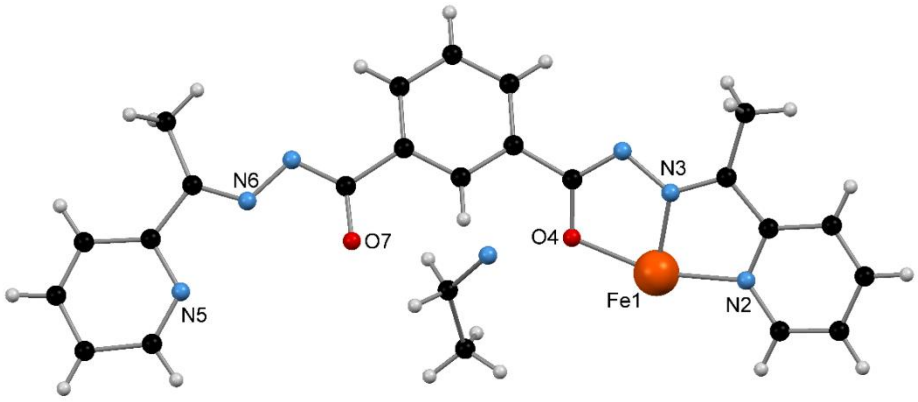

Figure 2.3.1.i: Asymmetric unit of ***2.12*** *comprised of one* ***L2.1***$^{2-}$ *ligand, one Fe(II) centre and 1/4 of the disordered triethyl amine guest molecule. The atoms of* ***L2.1***$^{2-}$ *coordinating to the Fe(II) centre are labeled and only one orientation of the disordered central phenyl ring is shown for clarity.*

The anionic pyridylhydrazone moiety coordinates to the Fe(II) centres in a tridentate fashion such that the Fe(II) centres exist in an N_4O_2 coordination sphere. The deprotonation of the ligand and the oxidation state of the Fe(II) centre is verified by the lack of anions in the crystal structure. The Fe-N and Fe-O bond lengths are indicative of Fe(II) in the LS state at 120 K (*Appendix Table 2.8.5.i*). The low octahedral distortion parameter (Σ) of 99°, compared to that of 154° for a mononuclear analogue in the HS state reported by Clérac and co-workers,[415] is further evidence for the Fe(II) centres existing in the LS state. The central aromatic ring features disorder which is modelled equally over two positions. There is a twist in the backbone of the coordinating ligand resulting in both positions of the disordered phenyl ring being twisted out of the plane of one of the coordinating oxygen atoms. This can be quantified by the $C_{aromatic}$-$C_{aromatic}$-$C_{hydrazone}$-$O_{hydrazone}$ torsion angles which are 28(2)° and 20(2)° for the two phenyl ring orientations. The grid is relatively distorted as the Fe(II) centres do not lie in the same plane however, by virtue of symmetry, all Fe1⋯Fe1' distances are 8.433(3) Å (the prime symbol ' denotes symmetry generated atom). The grid adopts a twisted shape where one Fe(II) centre is out of the plane relative to the other three *(Figure 2.3.1.ii*).

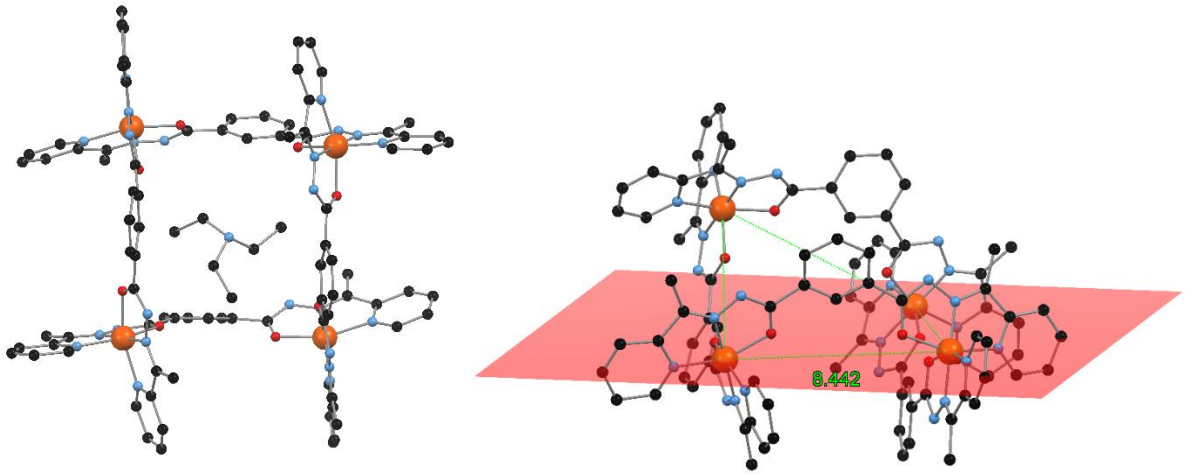

Figure 2.3.1.ii: (left) The complete tetranuclear grid structure generated by the 4-fold rotoinversion. Only one orientation of the triethyl amine is shown and hydrogen atoms are omitted for clarity. (right) Representation of the out of plane twist of one Fe(II) centre relative to the other three with the Fe···Fe separation shown in green. Hydrogen atoms omitted for clarity.

The grid structures pack closely together in the [001] crystallographic plane. The pyridine rings at the corners of the grids interact via π-π and C-H···π interactions (*Figure 2.3.1.iii*). There is a weak offset π-π stacking interaction between non-symmetry equivalent pyridine rings on neighbouring grids with a π(centroid)···π(centroid) separation of 4.064(9) Å. There are two types of C-H···π interactions present. The first occurs between the hydrogen atom on the methyl substituent of one grid and the centre of a pyridine ring of a neighbouring grid with an H···π(centroid) separation of 3.384(6) Å. The second, stronger C-H···π interaction occurs between the hydrogen atom at the 4-position of the pyridine ring and the π-face of a symmetry equivalent pyridine ring on a neighbouring grid. For this interaction, the H···π(centroid) separation is 2.667(6) Å (*Figure 2.3.1.iii*). Along the crystallographic *c*-axis the grid complexes do not pack closely. There are no significant interactions between the grid complexes in the back-to-back stacked two-dimensional sheets (*Figure 2.3.1.iv*). This may influence the very thin plate morphology of the crystals, resulting in the poor crystallinity. The poor quality of the diffraction data resulted in a large amount of electron density that was unable to be modelled. Therefore, the SQUEEZE[418] function of PLATON[419] (1.2 Å probe) was employed to remove the contribution of this diffuse electron density.

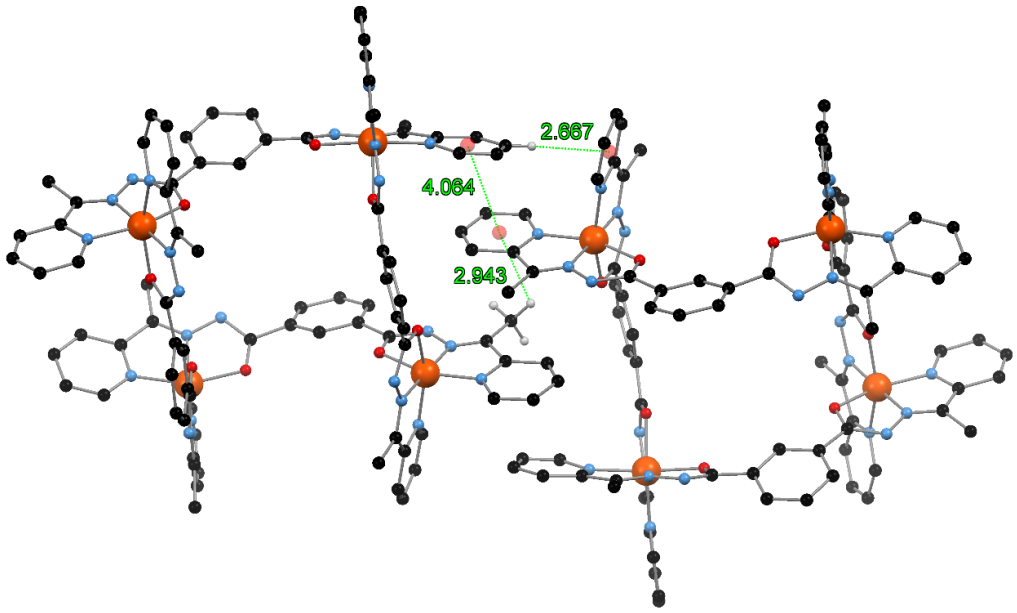

Figure 2.3.1.iii: The π-π and C-H···π interactions occurring between the coordinated pyridine rings and the methyl C-H and 4-pyridyl C-H moieties. The π(centroid) are represented by red spheres and π(centroid)···π(centroid) separations are shown in green. Hydrogen atoms not participating in the illustrated interactions are omitted for clarity.

The improvement to the structure was minor and thus the solvent mask function of OLEX2[420] (1.2 Å probe) was used instead which resulted in a more satisfactory improvement. The solvent mask function of OLEX2[420] found two crystallographically identical solvent accessible voids in the unit cell with a volume of 2344.5 $Å^3$, calculated to contain approximately 528 electrons. This corresponds to 132 electrons per grid complex and therefore the solvent content can be approximated as two DCM and 2.5 methanol molecules (129 electrons). Complex **3.12** was crystallised from a very dilute solution of DCM and therefore obtained in a very low yield. Hence, synthesis of a bulk quantity of **2.12** posed a significant challenge. While enough sample was prepared for magnetic susceptibility measurements and IR spectroscopy, elemental analysis and TGA were not carried out.

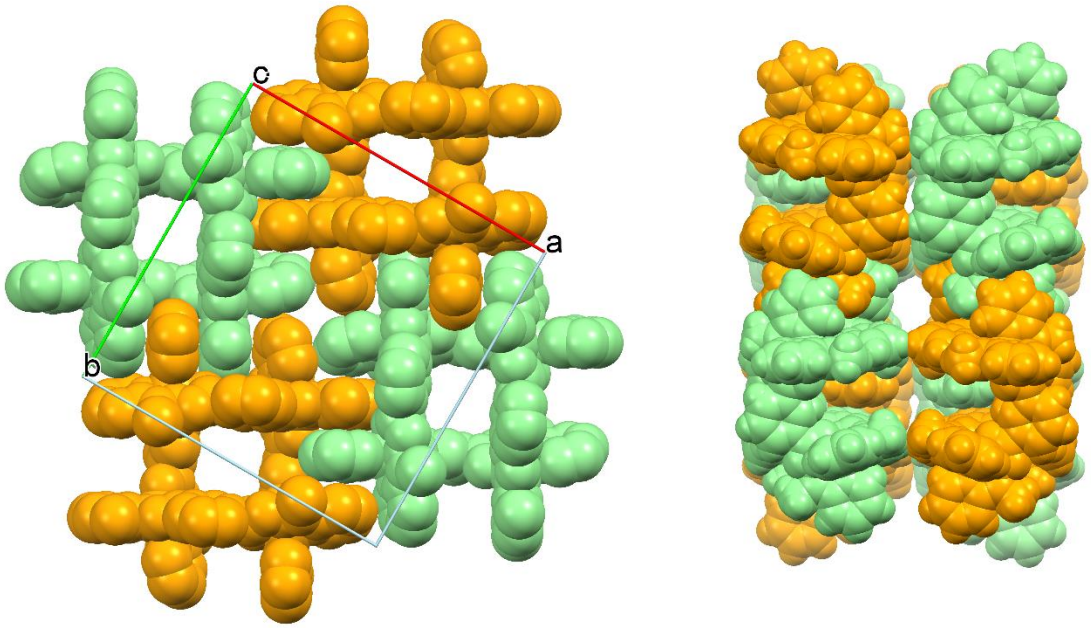

*Figure 2.3.1.iv: (left) Crystal packing of **2.12** viewed down the crystallographic c-axis with superimposed cell axes. Complexes are shown in space filling representation in green and orange to highlight the π-π stacking interaction. (right) Crystal packing of (left) rotated 90° to show the back to back arrangement of the grids along the crystallographic c-axis.*

Due to the poor resolution of the crystal structure, IR spectroscopy was used to confirm that the ligand existed in the anionic enolate form. The C=N and C-O stretches at 1667 and 1385 cm^{-1}, respectively show that the hydrazone indeed exists in its anionic imino-enolate form as these values are comparable to those obtained for related mononuclear complexes reported in the literature.[302]

2.3.2 $[Fe_4(L2.2)_4]$, 2.13

The complex was isolated as a green powder following a similar synthetic procedure to **2.12**, carried out in an argon filled glovebox. Crystals suitable for single crystal X-ray diffraction were formed by layering a DMF solution of the complex with a buffer layer of DMF followed by methanol. The data were collected at 120 K and solved and refined in the monoclinic space group *C*2/*m* (R = 6.52%). The asymmetric unit contains two half grid structures each comprised of two Fe(II) centres, one complete ligand and two half ligands. Crystallographically there are four unique Fe(II) centres comprising the two grid complexes (*Figure 2.3.2.i*). The ligand coordinates in the

expected tridentate meridional fashion such that the Fe(II) centres exist in an N_4O_2 coordination sphere. Although the resolution of the crystal structure is poor, the Fe-N and Fe-O bond lengths are indicative of the Fe(II) centres existing in a LS state (*Appendix Table 2.8.5.ii*).

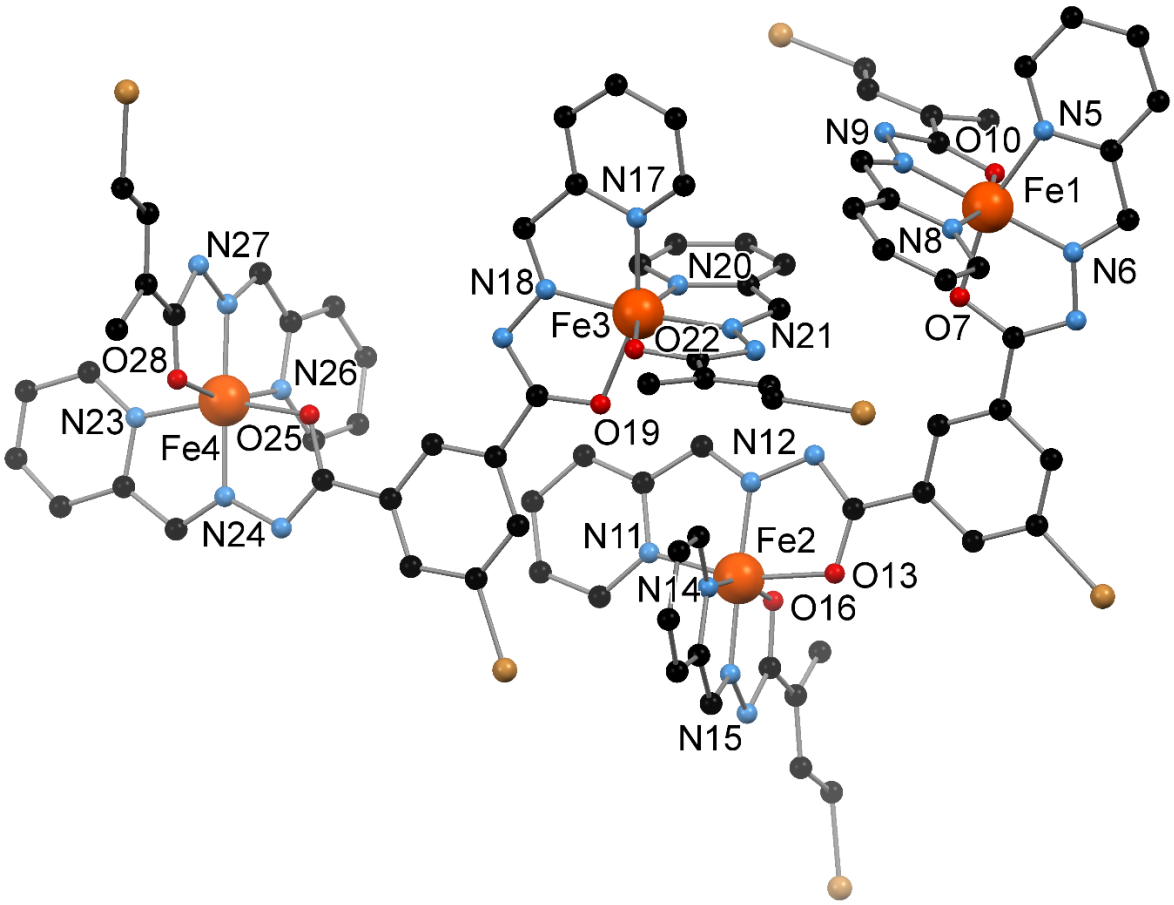

*Figure 2.3.2.i: The asymmetric unit of **2.13** with the four crystallographically unique Fe(II) centres labeled along with the coordinating nitrogen and oxygen atoms. Hydrogen atoms omitted for clarity.*

The octahedral distortion parameters (Σ) are further evidence for all four Fe(II) centres in the LS state. The Σ values are 78°, 79°, 94° and 83° for Fe1, Fe2, Fe3 and Fe4, respectively, which are all relatively low compared to that of 154° for a mononuclear analogue in the HS state reported by Clérac and co-workers.[415] The C=N bonds range from 1.30(3) to 1.37(2) Å while the C-O bonds range from 1.26(2) to 1.31(2) Å. While these hydrazone bond lengths are inconclusive for the pyridylhydrazone moieties coordinating in the anionic imino-enolate form, the lack of anions is confirmation.

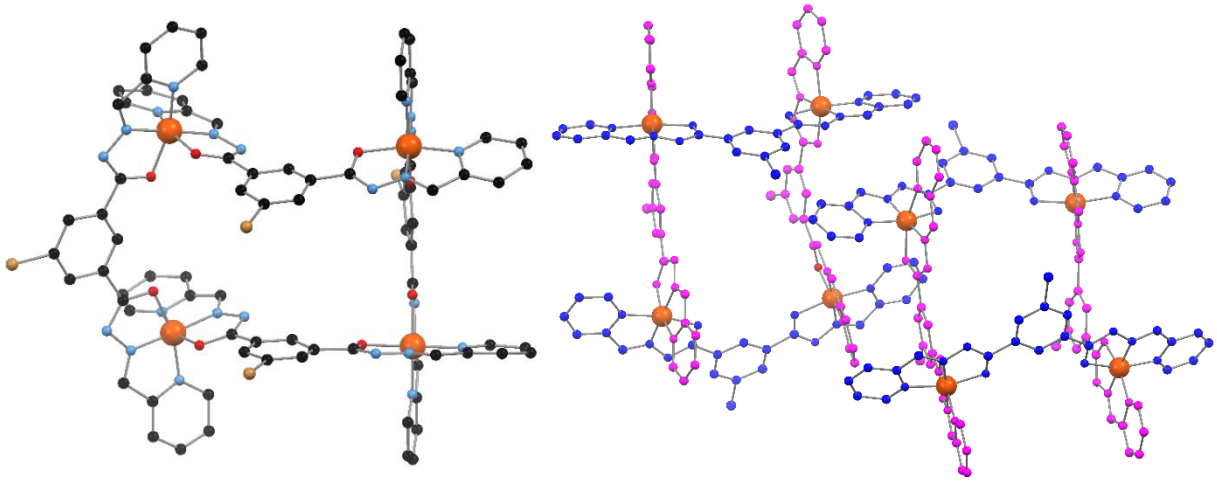

Figure 2.3.2.ii: (left) The complete tetranuclear structure generated by the action of a mirror plane. (right) The two complete tetranuclear grid structures generated from the two crystallographically unique halves in the asymmetric unit. The ligands adopting the syn conformation are shown in blue while the ligands adopting the trans conformation are shown in purple. Hydrogen atoms omitted for clarity.

There are two ligand conformations present, unlike **2.12**. In one conformation, the tridentate sites point in the same direction (*syn*) while in the other they point in the opposite direction (*trans*). Therefore, this grid can be classified as *syn-trans* using the terminology outlined previously (*Figure 2.3.2.ii*). Due to the *syn-trans* conformation of the ligands, three of the bromine substituents are orientated in one direction while the fourth is orientated in the opposite direction. The tetranuclear complex adopts a more distorted form than the previously described *syn* grid **2.12**. There are two crystallographically unique Fe··Fe distances per grid structure which range from 8.332(5) to 9.312(5) Å, while the Fe···Fe···Fe angles range from 89.37(3)° to 90.63(3)°. Therefore, with regard to the arrangement of Fe(II) centres, the grid complexes are only slightly distorted from an idealised square geometry. There are three key interactions between neighbouring complexes which influence the crystal packing. The first is the off-set π-π stacking interaction between the central aromatic ring and a coordinating pyridine ring on a neighbouring complex. This interaction can be regarded as intermediate in strength with a π(centroid)···π(centroid) separation of 3.68(2) Å. On the same central aromatic ring, a C-H···π interaction with a pyridine ring coordinated to the same Fe(II) centre as the previous interaction also occurs. This C-H···π interaction is relatively short with an H···π(centroid) separation of

2.97(1) Å. Lastly, there is a weak non-conventional hydrogen bond interaction between the imine hydrogen atom of one grid and the coordinating oxygen atom of a neighbouring grid with a C-H···O separation of 2.63(2) Å (*Figure 2.3.2.iii*). This complex adopts both a different ligand conformation and crystal packing to that of **2.12**. The differences in the ligand are the bromine substituent at the 5-position of the central aromatic ring and the imine substituent is a hydrogen atom and not a methyl group. The latter may promote the *trans* conformation of two of the four ligands in the complex as it is on the *trans* ligands that the imine hydrogen atom forms the weak non-conventional hydrogen bond with the oxygen atom of the neighbouring complex.

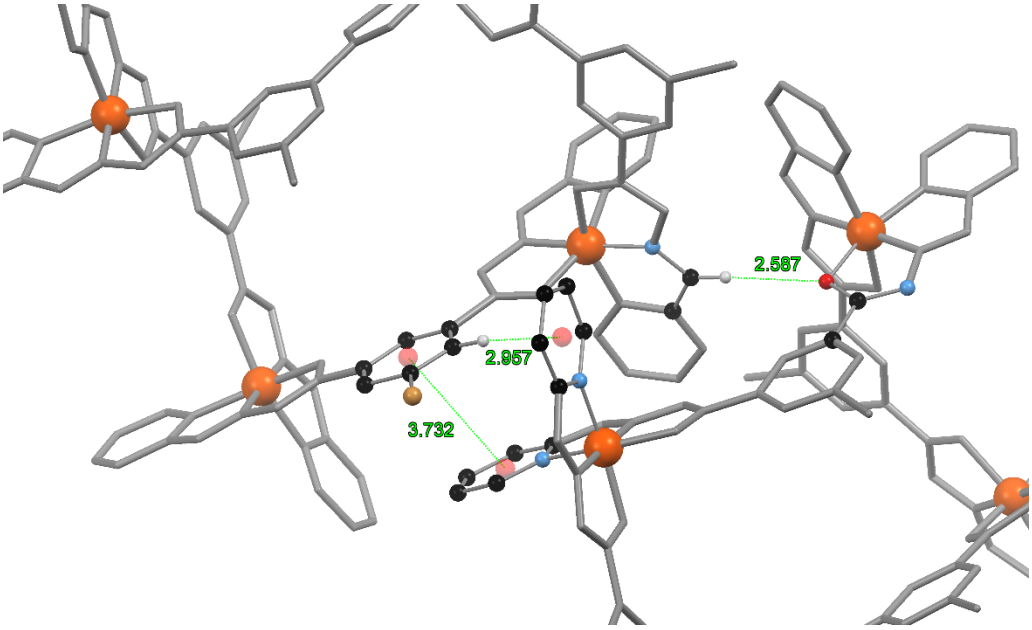

Figure 2.3.2.iii: The π-π stacking interaction between the central phenyl spacer and the coordinating pyridine ring. The C-H···π, π-π and C-H···N interactions are shown in green. The π(centroid) are represented by red spheres. Hydrogen atoms not participating in the illustrated interactions are omitted for clarity.

It was hypothesised that the inclusion of the bromine substituent at the 5-position would have a minor effect on the crystal packing, based on the crystal structure of **2.12**. This is because the 5-postion of the central aromatic ring is remote to the pyridine rings which undergo π-π stacking interactions to form a supramolecular two-dimensional sheet. However, the presence of the bromo substituent results in the formation of halogen bonds and halogen-π interactions (*Figure 2.3.2.iv*). When two of the ligands adopt the *syn* conformation and the remaining two adopt the *trans* conformation two crystallographically identical halogen bonds and one halogen···π interaction

occur between two neighbouring grid complexes. The *syn-trans* conformation is required as it orientates three bromine substituents of each grid in the same direction while the *syn* conformation observed for **2.12** would orientate only two in the same direction. The Br···Br interactions occur with a separation of 3.424 Å and can be formally classed as a type I halogen bond due to the large C-Br···Br angle of 129.3(6)°.[45-46] This type of interaction, while commonly referred to as a halogen bond is in fact generally considered a dispersive interaction as previously discussed. This type I halogen bond interaction occurs between bromo substituents on ligands adopting the trans conformation. There are two crystallographically unique Br···π interactions.[421] The stronger of the two interactions occurs between a bromo substituent on a ligand adopting the *syn* conformation in the grid containing Fe1 and Fe2 and the π-system of the central phenyl space on a neighbouring complex containing Fe3 and Fe4. This interaction occurs with a Br···π(centroid) separation of 3.206(8) Å. The second, weaker Br···π interaction occurs between a bromo substituent on a grid containing Fe3 and Fe4 and the neighbouring central phenyl spacer on a crystallographically identical grid complex. This interaction occurs with a Br···π(centroid) separation of 3.574(8) Å. These types of interactions can either be classed as lone pair-π or σ-hole-π interactions depending on the π-acidity of the aromatic system and whether the halogen is acting as σ-donor or possesses a σ-hole. Quantum chemical calculations would be required to confirm the exact nature of this interaction.[55]

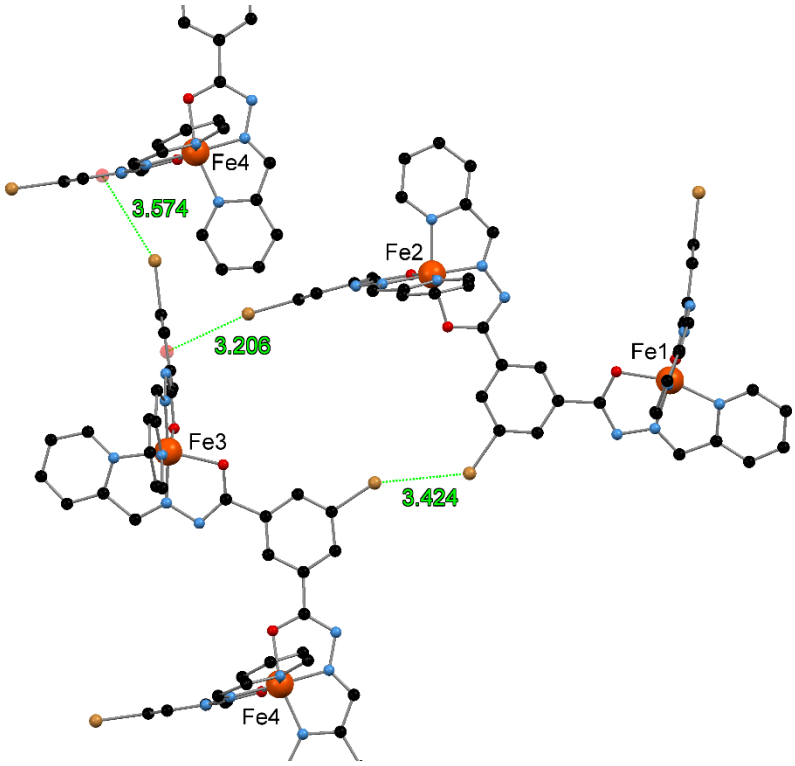

Figure 2.3.2.iv: The Br···Br interaction of which there are two crystallographically unique interactions occurring between two neighbouring complexes. The stronger Br···π interaction occurs between the two crystallographically unique complexes for which the Br···Br interactions occur. The weaker Br···π interaction occurs between two crystallographically identical complexes. Hydrogen atoms omitted for clarity.

The π-π, C-H···π and C-H···O interactions and the weak Br···π interactions result in the formation of a two-dimensional supramolecular sheet. Unlike the close packing observed to **2.12**, the packing of the complexes to give the two-dimensional sheet in **2.13** is more 'loose'and less symmetrical. This two-dimensional sheet occurs approximately perpendicular to the crystallographic *a*-axis. The Br···Br and strong Br···π interactions occur above and below the plane of this two-dimensional sheet, linking them together in the third dimension (*Figure 2.3.2.v*). The structure contains a large solvent accessible void, the contents of which was highly disordered and therefore its contribution to the structural data were removed using the SQUEEZE[418] function of PLATON (1.2 Å probe).[419] This revealed a solvent accessible void of 8713 Å^3. Calculated to contain approximately 2538 electrons and corresponds to 317 electrons per grid complex. This can be approximated as six DMF and four methanol molecules (156 electrons). The elemental analysis

shows the presence of one DMF, one methanol and 8.5 water molecules. With large supramolecular structures, it is common for the solvent molecules to be lost and replaced with water molecules from the atmosphere when removed from the mother liquor. TGA analysis verified the rapid loss of solvents of crystallisation. Between room temperature and 51 °C there is a mass loss due both surface adsorbed solvent and solvent of crystallisation. Between 51 °C and 302 °C there is a gradual mass loss of 5.3%. This can be attributed to the loss of 1.5 DMF molecules from **2.13**·1.5DMF which constitutes a mass loss of 5.1%. Above 302 °C decomposition of the occurs. Due to the high degree of solvation and the facile loss of solvent molecules under ambient conditions, elemental analysis and TGA do not provide an accurate approximation of the solvated complex which is why they differ from the solvent content approximated by the SQUEEZE function in PLATON. Due to the poor resolution of the crystal structure, IR spectroscopy was used to confirm that the ligand exists in the anionic imino-enolate form. The C=N and C-O-Fe stretches at 1656 and 1329 cm^{-1} respectively show that the hydrazone indeed exists in its anionic form as these values are comparable to those obtained for related complexes in the literature.[302]

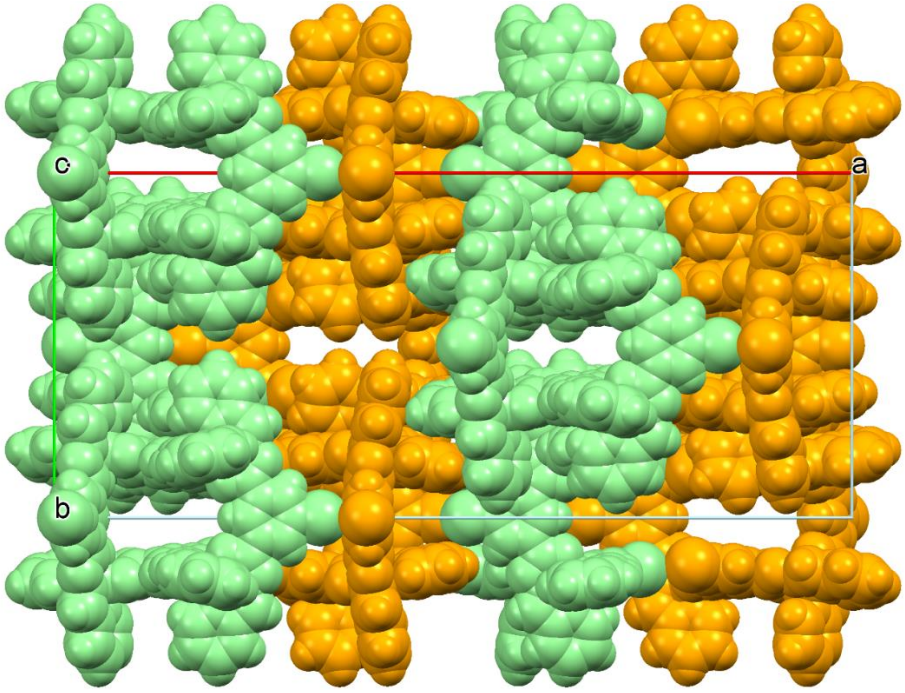

*Figure 2.3.2.v: Space filling representation of the three-dimensional packing of **2.13** as viewed down the crystallographic c-axis with the cell axes superimposed. Complexes of the same color (green or orange) interact via the π-π, C-H···π, C-H···O and weak Br···π interactions. The green*

and orange complexes interact via the Br···Br type I halogen bonds and the strong Br···π interactions.

2.3.3 [Fe$_4$(L2.4)$_4$], 2.14

This complex was synthesised via sub-component self-assembly in an argon filled glovebox; 4-chloro-2-pyridinecarboxaldehyde and isophthaloyl hydrazide were stirred in a mixture of methanol and DCM in a 2:1 stoichiometry with an excess of triethyl amine. A methanol solution of Fe(II) perchlorate was added, resulting in a green suspension that was stirred overnight at room temperature and the complex was isolated as a green powder. Green plate crystals suitable for single crystal X-ray diffraction were formed by vapor diffusion of water into a DMF solution of **2.14**. The data were collected at 120 K and solved and refined in the tetragonal space group $I4_1/a$ (R = 9.36%). Much like **2.12**, the asymmetric unit contained one complete ligand and one Fe(II) centre along with several DMF and water solvent molecules. The ligand coordinates in the expected tridentate meridional manner as observed in the previously discussed complexes. The bond lengths in the crystal structure of complex **2.14** at 120 K reveal that the single crystallographically unique Fe(II) centre is in the LS state (*Appendix Table 2.8.5.iii*). The octahedral distortion parameter (Σ) for Fe1 is 72° which is further evidence of LS Fe(II) compared to that of 154° for a mononuclear analogue in the HS state reported by Clérac and co-workers.[415] The two crystallographically unique C-O bonds are 1.287(9) and 1.286(9) Å while the C-N bond lengths of the hydrazone are 1.326(9) and 1.343(9) Å. These bond lengths are not conclusive evidence for the ligand coordinating in the anionic imino-enolate form, however the lack of anions in the crystal structure confirms this is the case. The complete **2.14** grid structure is generated via the action of a 4-fold rotoinversion axis. The conformation of the ligands in the grid structure can be described as *syn*, the most common conformation adopted in this series of complexes (*Figure 2.3.3.i*). The single crystallographically unique Fe···Fe separation is 8.320(1) Å while the Fe···Fe···Fe angle is 89.75(1) Å and this **2.14** can be regarded as approximately square.

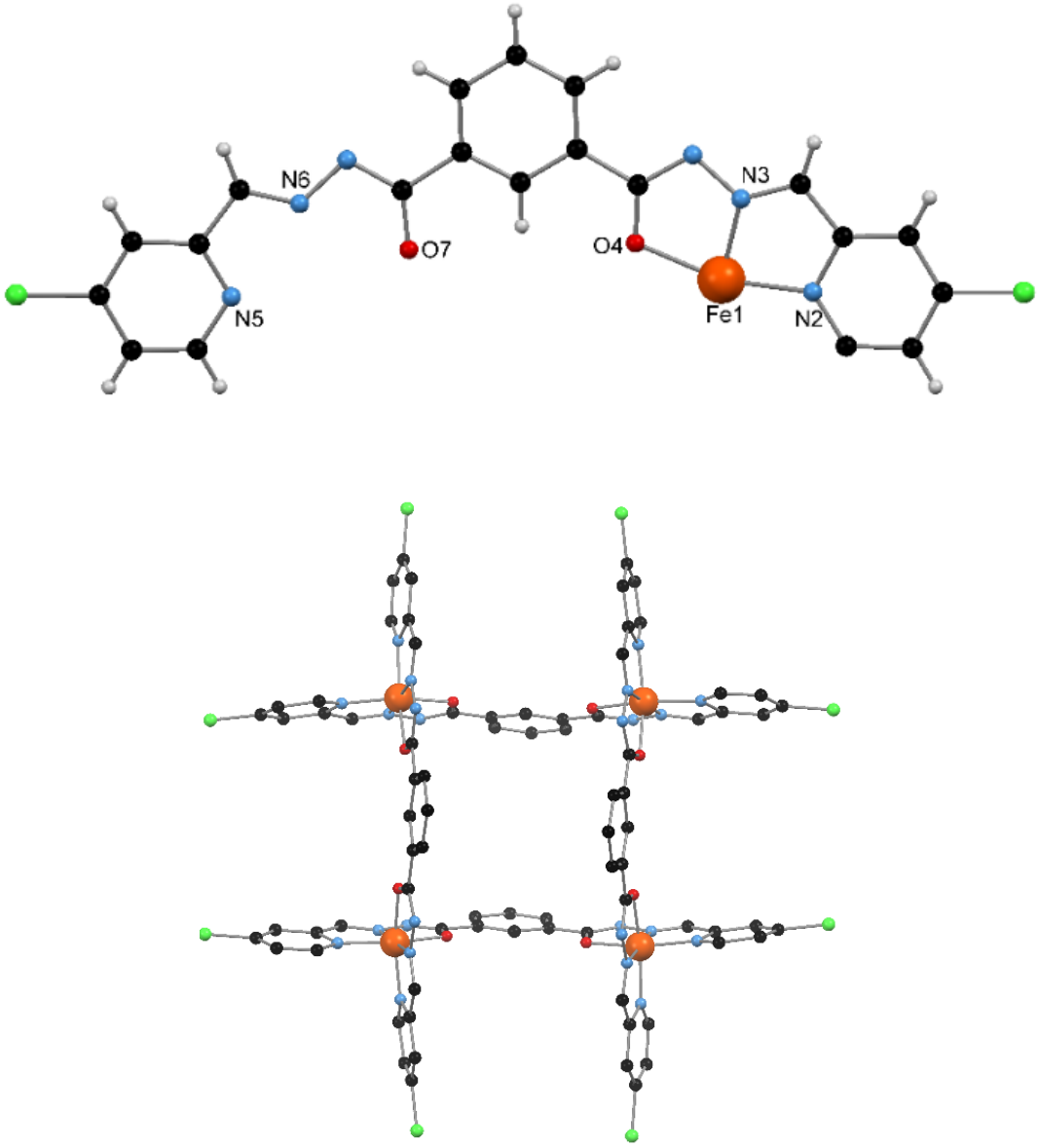

*Figure 2.3.3.i: (left) The asymmetric unit of **2.14** with the Fe(II) centre with coordinating nitrogen and oxygen atoms labeled. (right) The complete tetranuclear structure of **2.14** generated by the action of the 4-fold rotoinversion axis. Hydrogen atoms omitted for clarity.*

Similar crystal packing to **2.12** is observed, however, the presence of the chloro substituent in the 4-position prevents the close approach of the coordinated pyridine ring to the central aromatic ring. This results in π-π stacking of the pyridine rings on neighbouring complexes being significantly off-set with large π(centroid)···π(centroid) separations of 4.646(5) Å. Therefore, the π-π interactions can be regarded as having a reduced contribution to the overall crystal packing

compared to the previous complexes. The predominate supramolecular interaction resulting in the formation of two-dimensional supramolecular sheets is a Cl···π interaction. This halogen-π interaction is similar to the Br···π interaction discussed for **2.13**.[421] It occurs between the 4-chloro substituent and the π-face of a pyridine ring on a neighbouring complex with a Cl···π(centroid) separation of 3.403(4) Å. This interaction effectively replaces the C-H···π interactions observed for **2.13**. A tetramer of crystallographically identical interactions occurs linking four neighbouring complexes. Four of these interactions occurs per complex, resulting in the propagation of a two-dimensional sheet *(Figure 2.3.3.ii*).

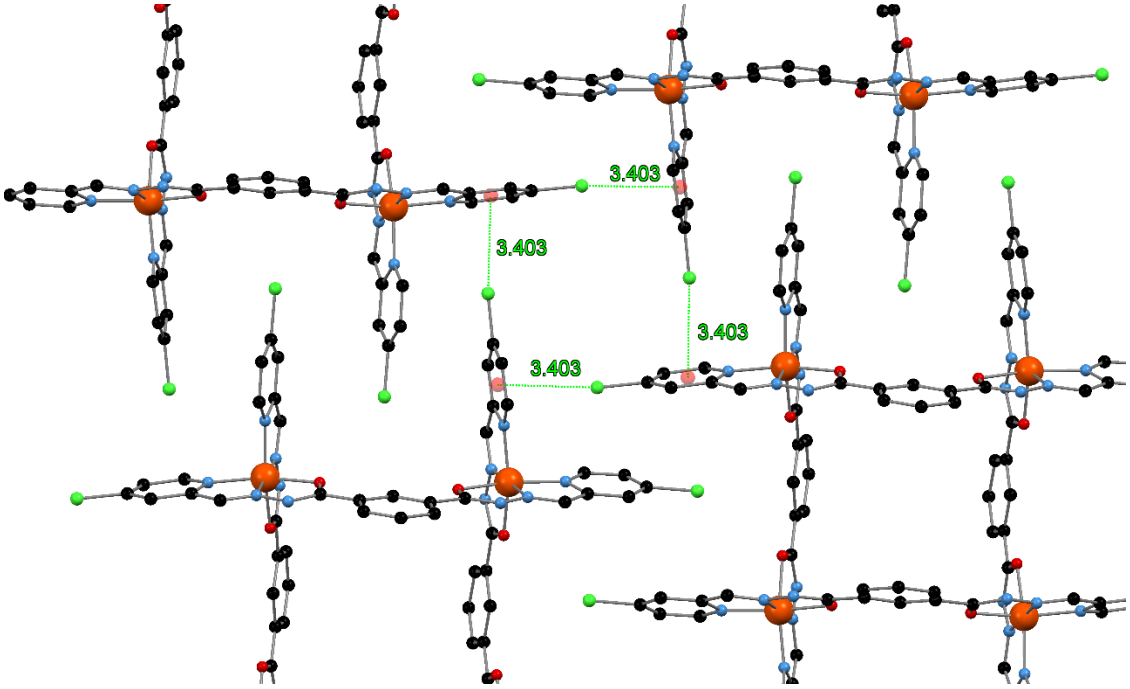

Figure 2.3.3.ii: The tetrameric structure of the four crystallographically identical Cl···π interactions linking four neighbouring complexes together resulting in the propagation of a supramolecular two-dimensional sheet. The π(centroid) are represented by red spheres while the Cl···π(centroid) interactions shown in green. Hydrogen atoms omitted for clarity.

The two-dimensional sheets pack in offset layers relative to the sheets above and below in an ABAB type manner. The sheets pack in an alternating back-to-back and front-to-front arrangement. This is mediated by a water molecule hydrogen bond to the nitrogen atoms of the hydrazone functionality of two back-to-back grids. The H···N separations for this interaction measure 1.931(6) and 1.891(6) Å (*Figure 2.3.3.iii*). The complex **2.14** crystallizes with a number

of solvent molecules. There is one full occupancy DMF molecule modeled as disordered over two positions with occupancies ratio of 70% and 30%. There is a further partial occupancy (45%) DMF molecule modeled as disordered over two positions with occupancies of 25% and 20%. There are two water molecules, one modeled with full occupancy and the second with 50% occupancy. As this complex could only be isolated in very low yields, further analysis of the complex was not carried out.

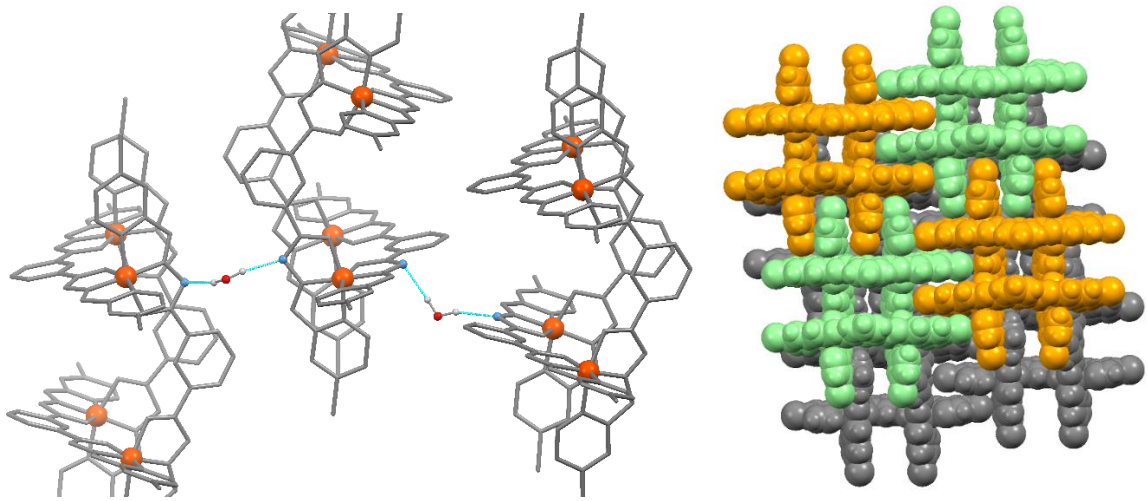

*Figure 2.3.3.iii: (left) The hydrogen bond interactions between the water molecules and non-coordinated nitrogen atom of the hydrazone moiety. Hydrogen atoms not participating in the illustrated interactions omitted for clarity. Hydrogen bond interactions shown in light blue. (right) The offset packing of **2.14** viewed down the crystallographic c-axis. The top sheet is shown in orange and green while the bottom offset sheet is shown in grey for clarity.*

2.3.4 $[Fe_4(L2.5)_4]$, 2.15

This complex was synthesised via sub-component self-assembly much like **2.14**; 6-chloro-2-pyridinecarboxaldehyde and isophthaloyl hydrazide were stirred in a 2:1 stoichiometry in a mixture of methanol and dichloromethane with an excess of triethyl amine. A solution of Fe(II) perchlorate in methanol was added resulting in a green suspension that was stirred overnight at room temperature. After filtering off a small amount of pale green solid and washing with methanol, thin green plate crystals suitable for single crystal X-ray diffraction formed in the filtrate overnight. The crystals were very weakly diffracting resulting in poor data quality, however the connectivity of the structure could be obtained. The data were collected at 120 K and solved and refined in the triclinic space group *P*-1 (R = 21.05%). The asymmetric unit contained two complete

tetranuclear grid structures and therefore eight crystallographically unique Fe(II) centres (*Figure 2.3.4.i*).

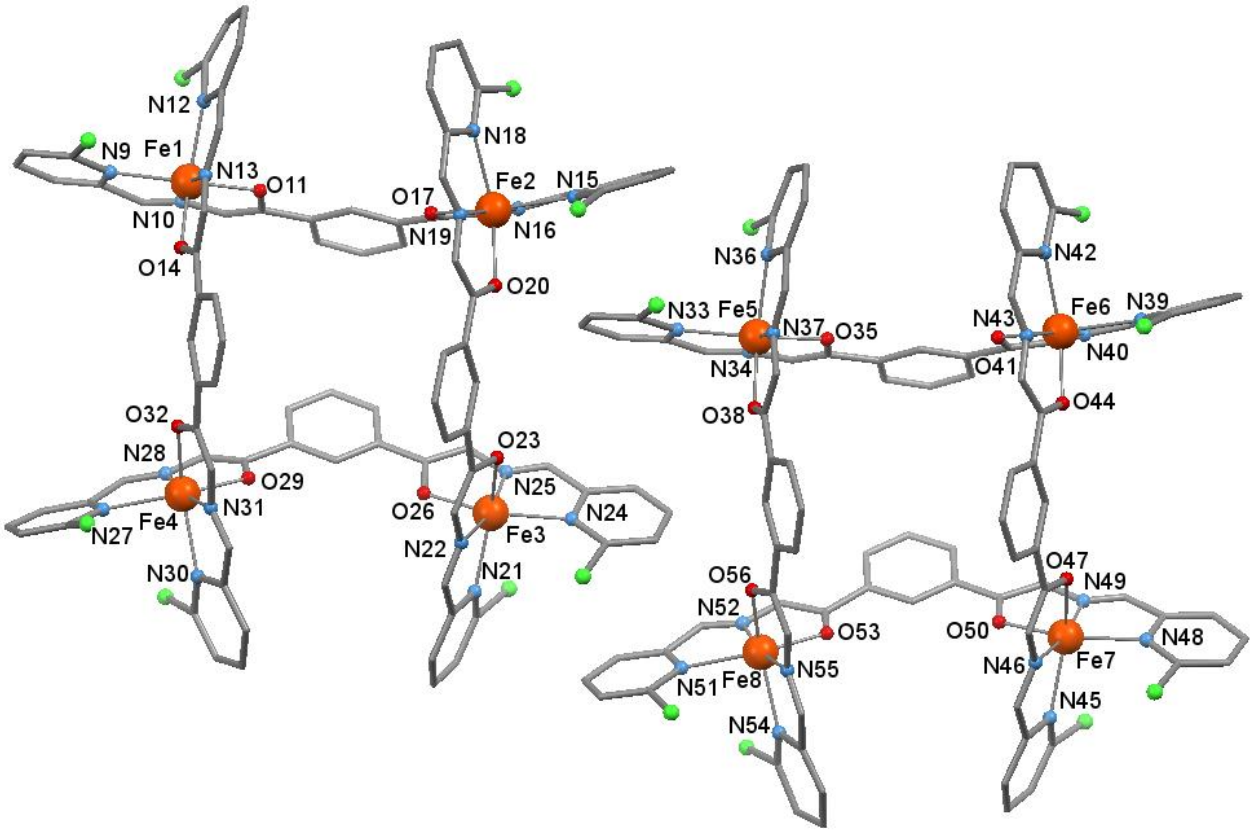

Figure 2.3.4.i: The two crystallographically unique tetranuclear grid complexes in the asymmetric unit with the eight unique Fe(II) centres and coordinating atoms labeled. Hydrogen atoms omitted for clarity.

The ligand coordinates in the expected tridentate meridional manner as observed in the previous complexes with each Fe(II) centre existing in an N_4O_2 coordination environment. The two binding domains on each ligand are orientated in the same direction and therefore the grid structure can be regarded as *syn*. While the data obtained for the crystal structure is low resolution, the Fe-N and Fe-O oxygen bond lengths indicate that the Fe(II) centres are HS at 120 K (*Appendix Tables 2.8.5.iv-v*). The large octahedral distortion parameters (Σ) are further evidence of all the Fe(II) centres existing in the HS state. The Σ values range from 144° to 155° and are summarised in *Appendix Table 2.8.5.vi*. These Σ values are similar to that of 154° for a mononuclear analogue in the HS state reported by Clérac and co-workers,[415] indicative that all Fe(II) centres are in the HS state. The C-O bond lengths range from 1.23(3) to 1.37(3) Å, while the C-N bond lengths range

from 1.26(4) and 1.42(3) Å. These bond lengths are not conclusive evidence for the ligand coordinating in the anionic imino-enolate form, however the lack of anions in the crystal structure confirms this. Much like **2.12**, there appears to be a disordered triethyl amine molecule in the middle of at least one of the grids. However, the poor quality of the data meant that it was unable to be modelled so it was removed using the SQUEEZE[418] function of PLATON[419] (1.2 Å probe). This revealed a solvent accessible void of 4028.2 $Å^3$, calculated to contain approximately 1246 electrons, corresponding to 334 electrons per grid complex. Assuming there is a triethyl amine molecule in the cavity of both crystallographically unique grids, the solvent content can be approximated as one triethylamine, four dichloromethane and six methanol molecules (333 electrons) per complex. Even after removal of electron density using a 2.1 Å probe, there was still a large amount of residual electron density, the greatest of which is 3.53 $e^- Å^{-3}$. The poor crystallinity of the plate like crystals may mean that the crystal the X-ray diffraction experiment was performed on was in fact made up of multiple slightly offset plate crystals. Refining the crystal as a twin did not improve the quality of the structure. The crystal used for the diffraction experiment was the best of the numerous crystals screened initially. The Fe···Fe separations range from 8.417(7) to 8.689(5) Å with Fe···Fe···Fe angles ranging from 85.89(6)° to 92.34(6)° and therefore both crystallographically unique grids are noticeably distorted from an idealised square. There are numerous non-conventional aromatic C-H···O and C-H···N hydrogen bond interactions between the neighbouring grid structures. Four of these feature participation of the hydrogen atom in the 5-position of the coordinated pyridine ring and the oxygen atom of the coordinated hydrazone moiety. The H···O separations range from 2.26(2) to 2.39(2) Å and are summarised in *Appendix Table 2.8.5.vii*. The 5-position of the pyridine ring is orientated in the direction that is the most amenable to forming supramolecular interactions with neighbouring complexes in the same plane due to the manner with which the grid complexes pack (*Figure 2.3.4.ii*). This results in two C-H···N interactions occurring between the C-H moiety in the 5-position of a coordinated pyridine ring and the non-coordinate nitrogen atom of the hydrazone moiety of a neighbouring grid in the plane below. The H···N separations are 2.62(2) and 2.72(2) Å respectively.

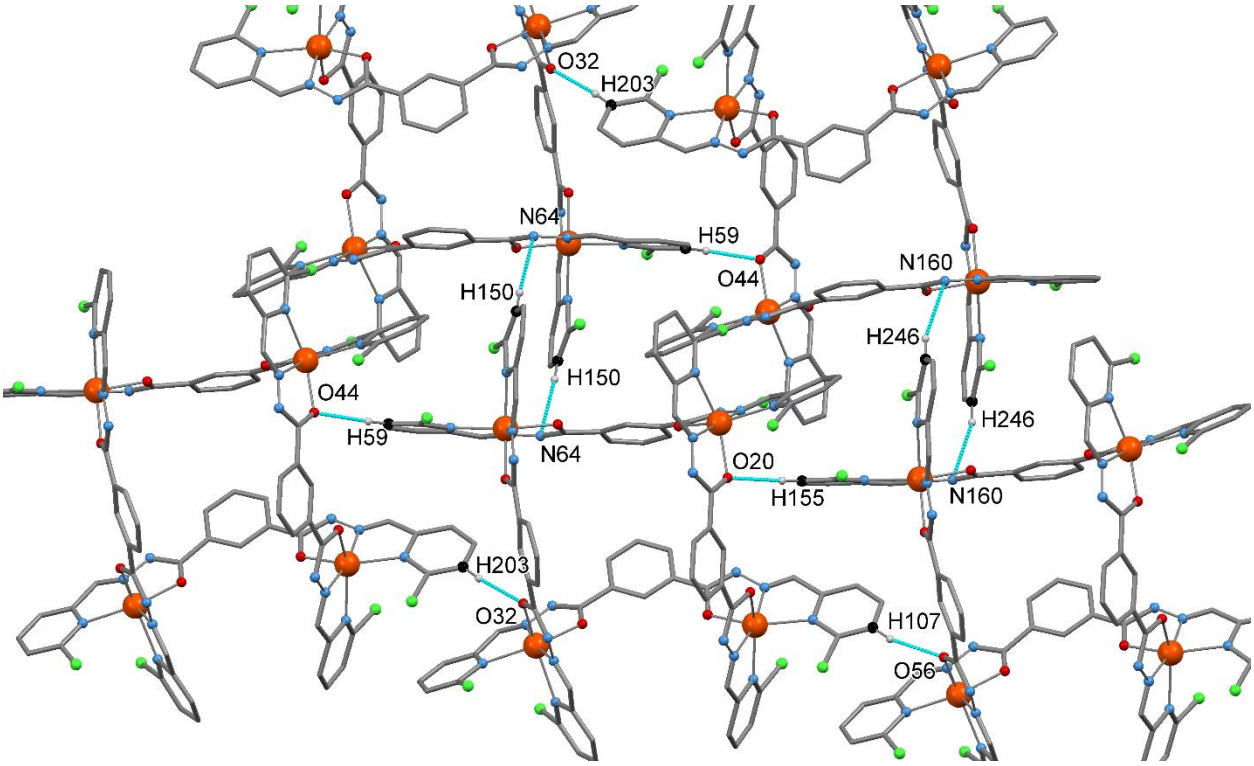

Figure 2.3.4.ii: The C-H···O and C-H···N non-conventional hydrogen bond interactions of the two crystallographically unique grids. The H···X (X = N or O) interactions are shown in blue and summarized in Appendix Table 2.8.5.vii. Hydrogen atoms not participating in the illustrated interactions omitted for clarity.

The packing of the tetranuclear grid structures differs from that of the previous complexes. This can be attributed to the presence of the chlorine substituent on the 6-position of the pyridine ring and the imine substituent being a hydrogen atom and not a methyl group. The strong π-π stacking and C-H···π interactions observed for **2.12** do not occur. The large distortion about the Fe(II) centres imposed by the chloro substituent has resulted in a significant 'bowing' of the ligand such that the central phenyl spacers on parallel side of the grid are significantly closer and concomitantly the pyridine rings on parallel ligands are further apart. This more expanded and distorted arrangement of the pyridine rings and the presence of the chloro substituent therefore disrupt the envisioned π···π stacking interactions. The chloro substituent on one grid complex is noticeably closer to π-face of a coordinating pyridine ring on a neighbouring complex than the π-system of the substituent itself. This is indicative of a halogen···π interaction occurring in preference to a π···π interaction. The lack of any significant π-π stacking interactions results in relatively 'loose'

packing of the grid complex, contributing to the large solvent accessible void. The crystal packing is therefore predominantly mediated via the C-H···O and C-H···N interactions described above.

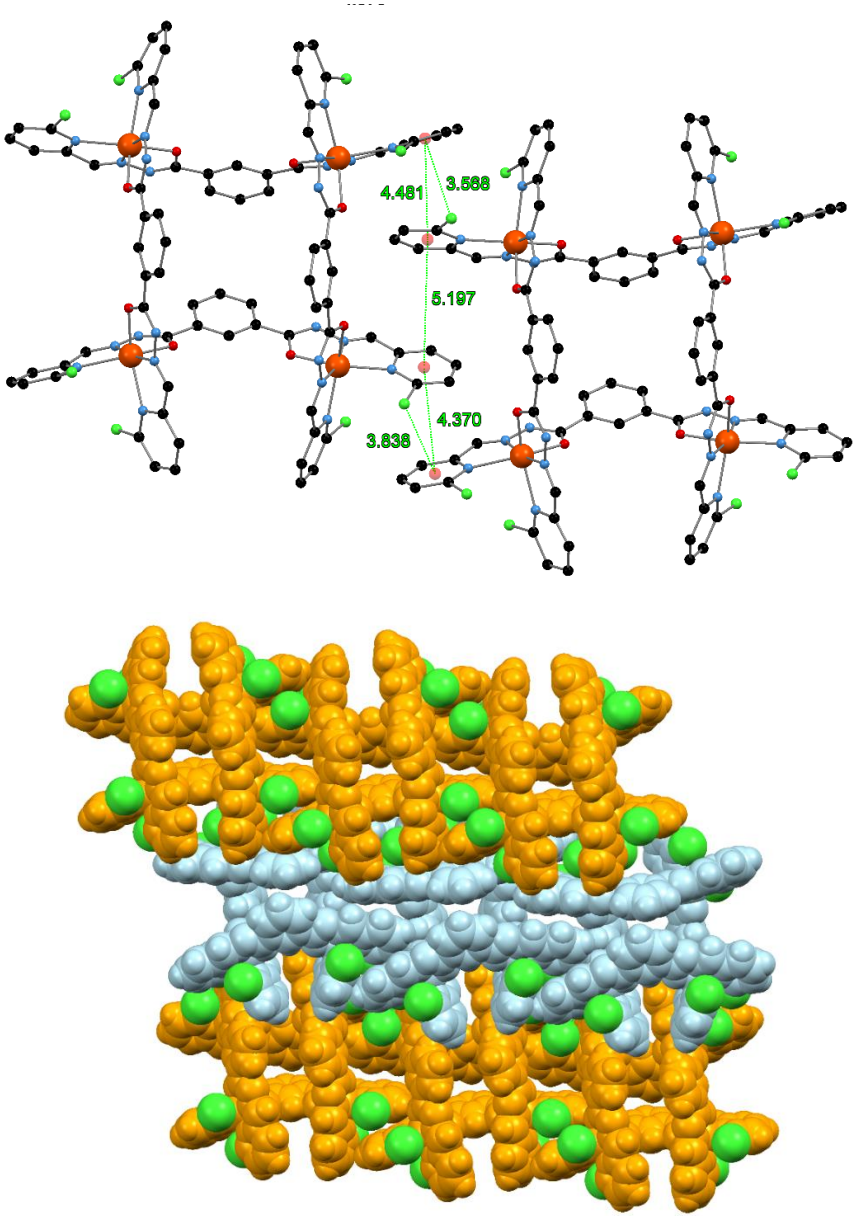

Figure 2.3.4.iii: (top) The π···π and Cl···π separation are shown in green. The stronger Cl···π interaction predominates over any π···π interaction. Hydrogen atoms omitted for clarity. (bottom) The crystal packing of ***2.15*** *viewed at an arbitrary angle shown in space filling representation. The supramolecular chains are shown alternating in orange and light blue with the chloro substituents shown in green.*

The propagation of these interactions results in the formation of a one-dimensional supramolecular chain. These supramolecular chains pack in an off-set manner in two dimensions to give the three-dimensional crystal packing (*Figure 2.3.4.iii*).

2.3.5 $[Fe_4(L2.1)_4](PF_6)_4$, 2.16

As discussed in the introduction, the pyridylhydrazone moiety coordinating in the anionic imino-enolate form can also results in Fe(III) SCO complexes. Therefore, the Fe(III) equivalent of **2.12** was synthesised. Equimolar amounts of H_2**L2.1** and Fe(III) nitrate were stirred in methanol at room temperature. The complex was isolated as the hexafluorophosphate salt as an olive-green powder by the addition of potassium hexafluorophosphate. Vapor diffusion of diisopropyl ether into an acetonitrile solution of **2.16** gave brown plate crystals suitable for single crystal X-ray diffraction with synchrotron radiation. These thin plate crystals were very weakly diffracting and despite using synchrotron radiation, only a low-resolution structure was able to be obtained. However, the structure was sufficient for the connectivity of the complex to be obtained and to confirm that a tetranuclear grid structure was formed as expected.

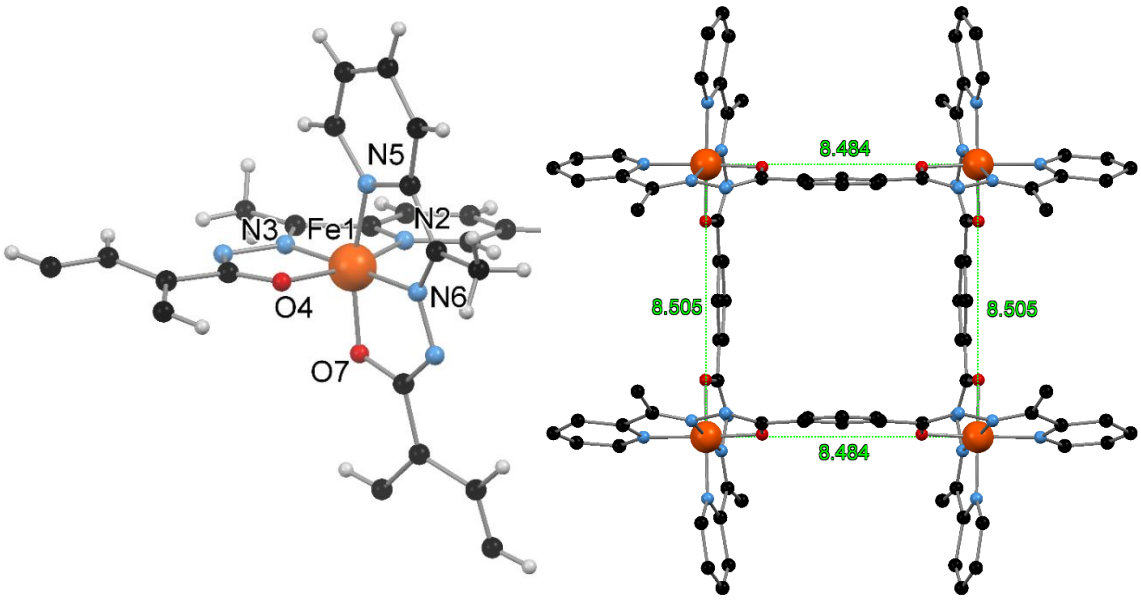

*Figure 2.3.5.i: (left) The asymmetric unit of **2.16** with the Fe(III) centre and coordinating nitrogen and oxygen donor atoms labeled. The hexafluorophosphate anion has been omitted for clarity. (right) The complete tetranuclear structure generated by the action of the action of two orthogonal mirror plane showing the two crystallographically unique Fe···Fe separations shown in green.*

The data were collected at 100 K and solved and refined in the orthorhombic space group *Pmmn* (R = 12.22%). The asymmetric unit contains 1/4 of a the complete tetranuclear complex (*Figure 2.3.5.i*). There are two half ligands in the imino-enolate form coordinated to one Fe(III) centre. The charge is balanced by a single hexafluorophosphate anion. It is interesting to note that the ligand spontaneously deprotonates upon coordination to the Fe(III) centre without the need for additional base during the synthesis. The pyridylhydrazone moiety coordinates in a meridional fashion via the pyridyl nitrogen atom and the nitrogen and oxygen atoms of the hydrazone such that the Fe(III) centres exist in an N_4O_2 coordination sphere. Although the resolution of the crystal structure is poor, approximate Fe-N and Fe-O bond lengths can be obtained (*Appendix Table 2.8.5.viii*). These indicate that all Fe(III) centres exist in the LS state at 100 K. Further evidence for this is the relatively low octahedral distortion parameter (Σ) of 75°. The C-O bond lengths are 1.28(2) and 1.32(2) Å and the C=N bond lengths are 1.33(2) and 1.35(2) Å, similar to those in the literature for related complexes.[302] However, the poor resolution of the structure reduces the accuracy of the bond lengths. The lack of additional anions to those modeled confirms that the ligand is indeed in the anionic form with a formally single C-O bond and a formally double C=N bond. Strong bands in the ranges 1350 to 1490 cm^{-1} and 1520 to 1600 cm^{-1} are expected for the imino-enolate backbone of the ligand in the anionic form.[302] There are peaks at 1374 and 1600 cm^{-1} which can be attributed to these bands, indicative that the ligand is indeed in the anionic imino-enolate form. The grid is not a perfect square as there are two crystallographically unique Fe···Fe distances of 8.484(4) and 8.505(4) Å while the Fe···Fe···Fe angle is 90.0(2)°. The two crystallographically unique central aromatic rings are not perfectly planar with the coordinating pyridylhydrazone moieties with $C_{aromatic}$-$C_{aromatic}$-$C_{hydrazone}$-$C_{hyrazone}$ torsion angles of 14(2)° and 11(1)°. The crystallographically identical pyridine rings of neighbouring grids interact via off set π-π stacking interactions of 3.79(1) Å (*Figure 3.3.5.ii*). This occurs at each vertex resulting in a supramolecular two-dimensional 4,4-grid. This vertex-based interaction is reinforced by C-H···π interactions from the 4-position of a coordinated pyridine ring to the centre of a coordinated pyridine ring of a neighbouring grid complex not participating in a π-π stacking interaction. The H···π(centroid) separation of this interaction is 3.080(7) Å and two complementary interactions occur per vertex of each grid and are reciprocal in nature.

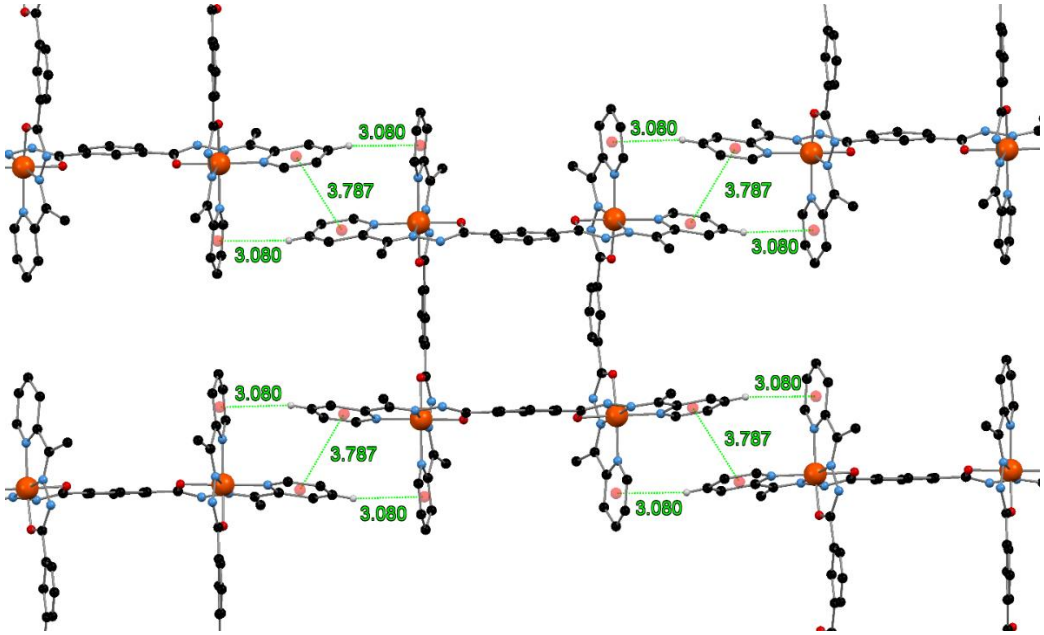

Figure 2.3.5.ii: The π-π stacking and C-H···π interaction occurring at each of the four corners of the grid structures are shown in green and the π(centroid) are represented by red spheres. Hydrogen atoms not participating in the illustrated interactions and hexafluorophosphate anions omitted for clarity.

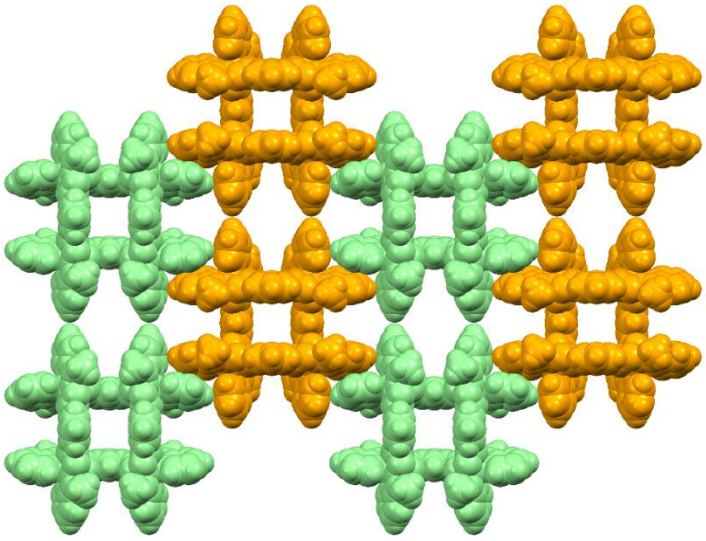

Figure 2.3.5.iii: The two-dimensional supramolecular sheet viewed down the crystallographic c-axis. The complexes in green have the vertical ligands of the grid orientated out of the plane of the page while the complexes in orange have the horizontal ligands orientated out of the plane of the page. Hexafluorophosphate anions omitted for clarity.

This results in one grid of **2.17** being surrounded by four crystallographically identical complexes leading to the formation of a two-dimensional supramolecular sheet extending along the crystallographic *a*- and *b*-axes (*Figure 2.3.5iii*). These two-dimensional supramolecular sheets then pack directly on top of one another with an AAAA type packing arrangement. This is promoted by the formation of non-conventional C-H···N hydrogen bonds. These occur between the C-H moieties in the 4- and 6-positions of the central aromatic ring and the non-bonding nitrogen atoms of the hydrazone moiety.

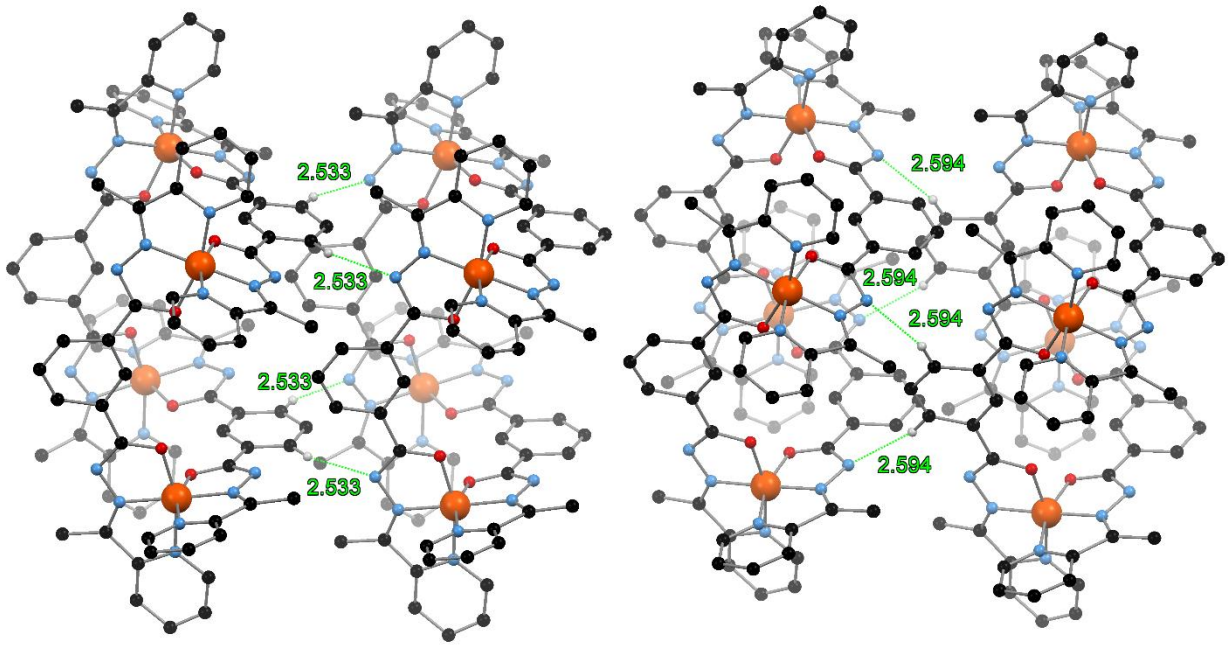

Figure 2.3.5.iv: The two types of C-H···N non-conventional hydrogen bonds occurring between grid complexes in different two-dimensional layers shown in green. Hydrogen atoms not participating in the illustrated interactions and hexafluorophosphate anions are omitted for clarity.

There are two crystallographically distinct C-H···N interactions with H···N separations of 2.53(1) and 2.59(1) Å *(Figure 2.3.5.iv*). The hexafluorophosphate anions interact weakly with the periphery of the grids via C-H···F interactions. For the fragment of the grid complex present in the asymmetric unit there are two methyl C-H···F interactions with H···F separations of 2.84(2) and 1.97(2) Å. There is also an aromatic C-H···F interaction with an H···F separation of 2.22(2) Å (*Figure 2.3.5.v*). The hexafluorophosphate anions are located in cavities situated around the

corners of the grid complexes in the space between the two-dimensional supramolecular sheets. No hexafluorophosphate anions are located within the square cavity in the centre of the grid. The electron density within this central cavity was attributed to the presence of solvent molecules. The large amount of disordered solvent and the high symmetry means that a suitable disorder model for the solvent could not be found. Therefore, the SQUEEZE[418] function of PLATON[419] was applied (1.2 Å probe). Two crystallographically identical solvent accessible voids of 1484 $Å^3$ and 1475 $Å^3$ were located and calculated to contain approximately 322 and 323 electrons respectively. This corresponds to 323 electrons per grid complex, therefore, the solvent content can be approximated as 12 acetonitrile and one diisopropyl ether molecule (322 electrons). ESI-MS of a solution of **2.16** revealed two major peaks, one at 454.0802 (4+) and the other at 201.0896 (2+). The peak at 454.0842 (4+) corresponds to $[Fe_4(\mathbf{L2.1})_4]^{4+}$ with a calculated *m/z* of 454.0853 (4+). The peak at 201.0896 (2+) does not correspond to the complex but the ligand $[H_2\mathbf{L2.1}+2H]^{2+}$ in the di-protonated form with a calculated *m/z* of 201.0897 (2+) (*Figure 2.3.5.vi*). A complete summary of the mass spectrometry analysis is provided in *Appendix 2.8.1.i.*

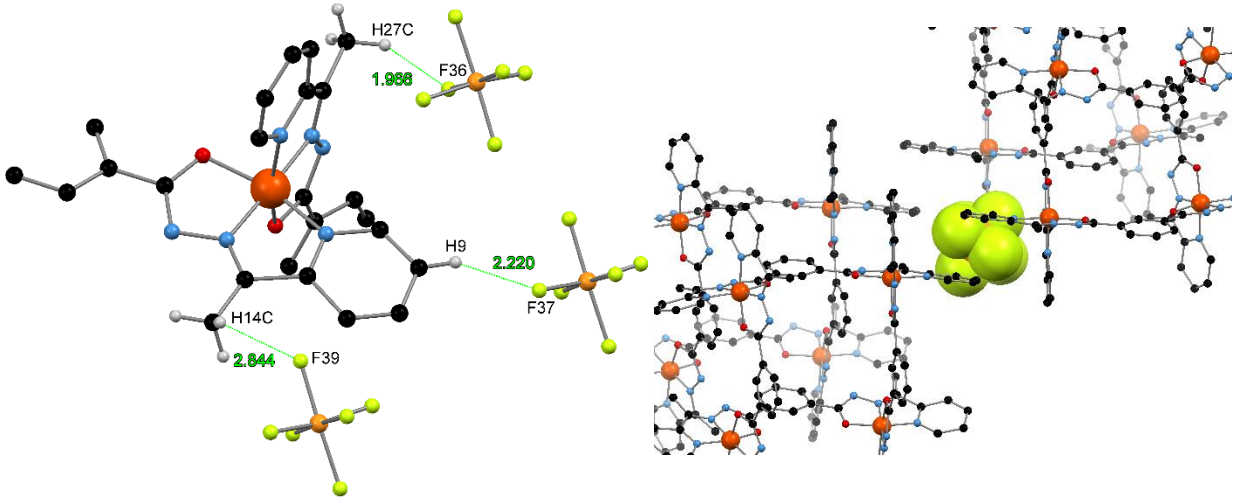

Figure 2.3.5.v: (left) The three types of C-H···F interactions occurring at each corner of the grid ***2.16****. Hydrogen atoms not participating in the illustrated reactions omitted for clarity. (right) The location of the hexafluorophosphate anions in the cavity located between the corners of four grid complexes. Hydrogen atoms omitted for clarity.*

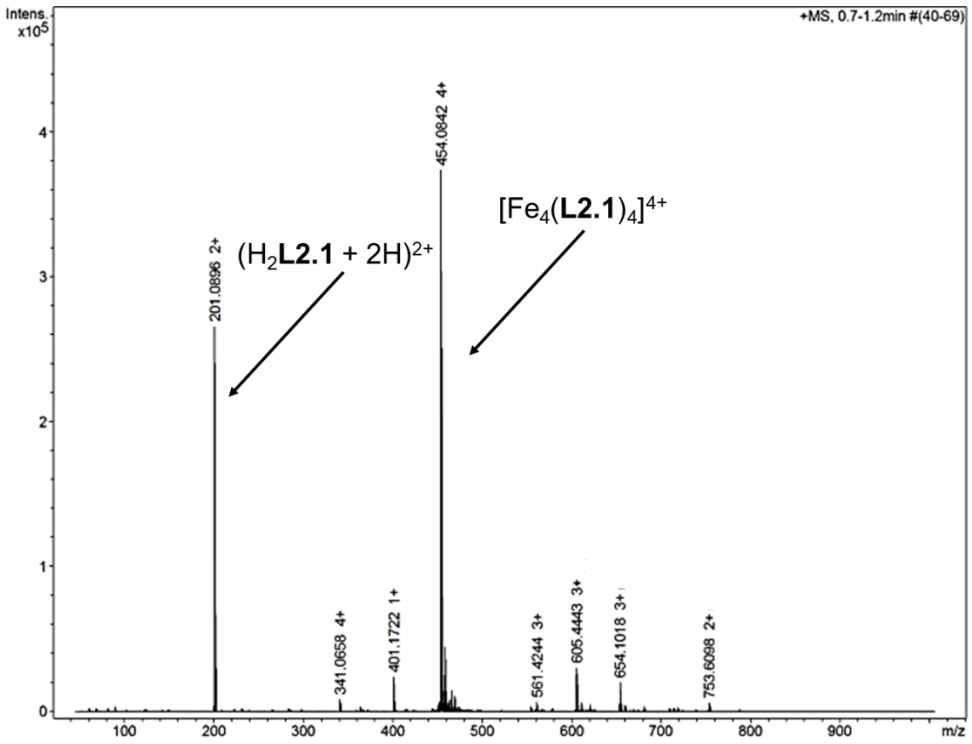

*Figure 2.3.5.vi: Mass spectrum for **2.16** showing with the two major peaks labeled corresponding to the di-protonated ligand and [Fe4(**L2.1**)4]4+.*

2.3.6 [Co4(L2.1)4](PF6)4, 2.17

Initially, it was intended to synthesise the Co(III) analogue of **2.16** by first synthesizing the Co(II) complex followed by oxidation to Co(III) so an analogous procedure to **2.16** was performed. Equimolar amounts of ligand H_2**L2.1** and Co (II) nitrate were stirred in methanol at room temperature. The complex was isolated as the hexafluorophosphate salt as a yellow powder by the addition of potassium hexafluorophosphate. ^{1}H NMR spectrum in deuterated acetonitrile indicated that only one major product and /or stereoisomer was present and the complex was diamagnetic. This indicates that *in situ* oxidation to Co(III) has I during the synthesis. As described previously for the Fe(II) complexes, the pyridylhydrazone motif promotes oxidation to Fe(III) when coordinating in the anionic form under aerobic conditions. In a similar fashion it appears that when anionic, the ligand also promotes oxidation of Co(II) to Co(III). While no base was added to the reaction, the hydrazide proton becomes sufficiently acidic when the ligand is coordinated to the Co(II), that another species in solution such as some unreacted ligand may act as a base. This establishes an equilibrium between the protonated and deprotonated forms of the ligand. As the anionic form of the ligand promotes oxidation of Co(II) to Co(III), thus forming a particularly

stable complex. Therefore, the anionic form of the ligand is removed from the equilibrium driving the oxidation of Co(II) to Co(III) to completion. The ^{1}H NMR spectrum shows seven peaks are observed in the aromatic region, corresponding to the seven unique proton environments when the ligand is symmetrical. The peak corresponding to the methyl substituent of the hydrazone occurs at 3.30 ppm and is split into a doublet, potentially due to a long-range coupling interaction. Assignment of the ^{1}H NMR spectra was achieved with the aid of a COSY spectra. No comparison with the free ligand is possible due to the insolubility of the ligand in acetonitrile. The symmetrical nature of the ligand is confirmed by the 12 signals observed in the ^{13}C NMR. The NMR spectra are summarized in *Appendix 2.8.2.i*.

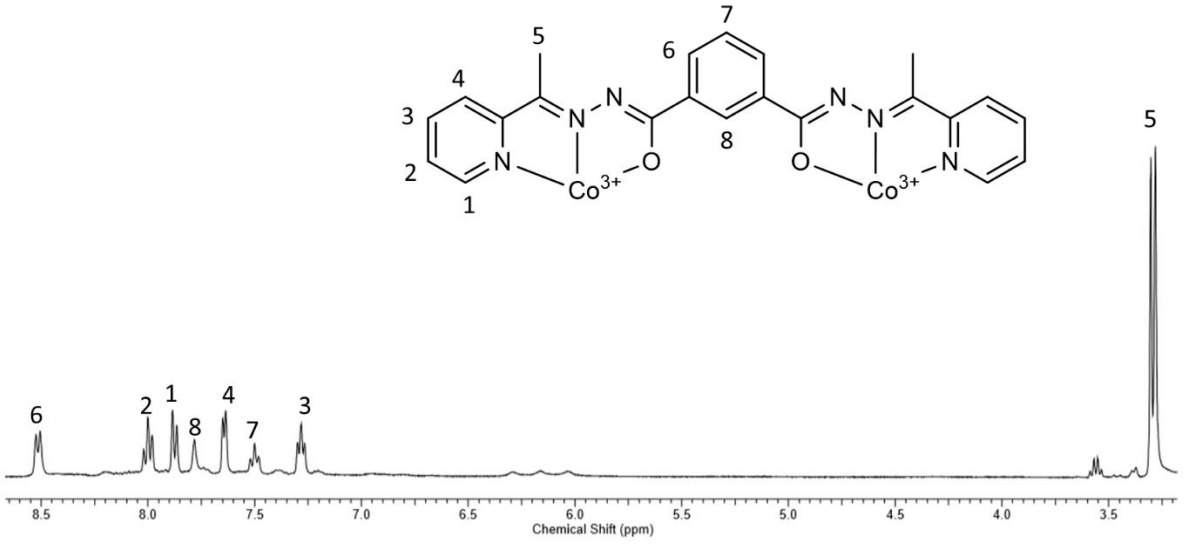

*Figure 2.3.6.i: ^{1}H-NMR spectra of **2.17** in deuterated acetonitrile at 25 °C.*

ESI-MS of an acetonitrile solution of **2.17** revealed a number of peaks corresponding to **2.17** with various protonation states of the ligand and oxidation states of the cobalt centres. The major peak at 457.0836 (+4) corresponds to $[Co_4(\mathbf{L2.1})_4]^{4+}$ with all cobalt centres in in the +3 oxidation state with a calculated *m/z* of 457.0818. This peak is superimposed with a +3 peak of a similar molecular weight which may be attributed to a fragmentation product of the complex. The peak at 366.0688 (+5) can be attributed to $([Co_4(\mathbf{L2.1})_4] + 2H)^{5+}$ with three Co(III) centres and one Co(II) centre with a calculated *m/z* of 366.0684 (*Figure 2.3.6.ii*). There are various other peaks that cannot be fitted to the complex in any possible protonation state of the complex or oxidation state of the cobalt centres. Fragmentation of the complex under the mass spectrometry conditions is the most

likely cause of these minor peaks in the mass spectrum. A complete summary of the mass spectrometry experiment is given in *Appendix 2.8.1.ii*.

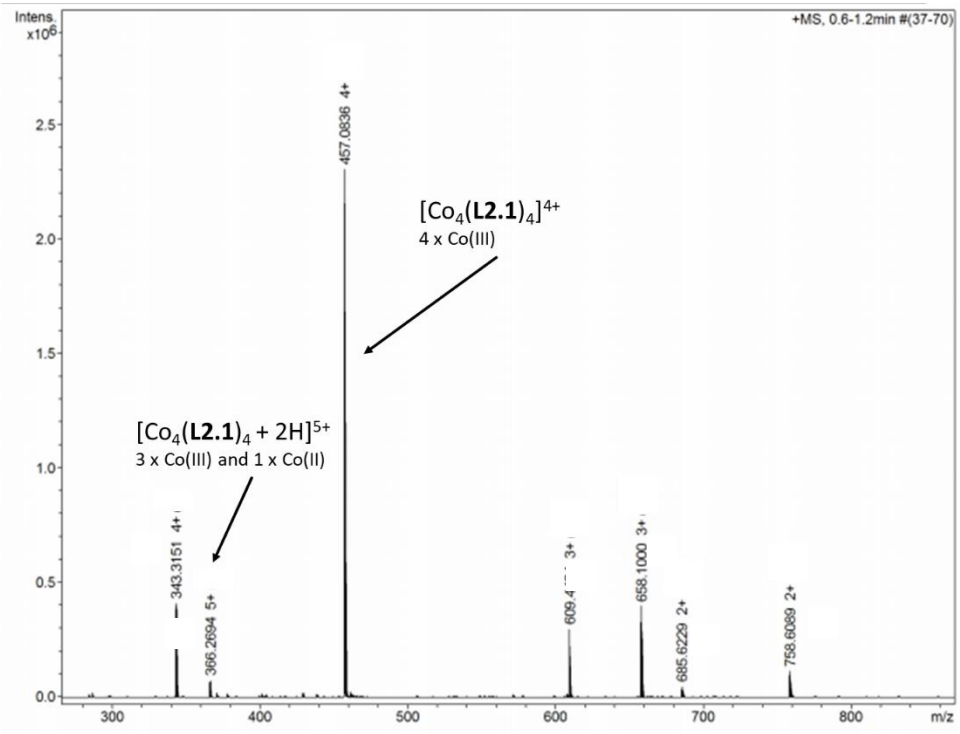

*Figure 2.3.6.ii: Mass spectrum for **2.17** showing with the two major peaks labeled corresponding to $[Co_4(\mathbf{L2.1})_4 + 2H]^{5+}$ and $[Co_4(\mathbf{L2.1})_4]^{4+}$.*

Vapor diffusion of diisopropyl ether into an acetonitrile solution of **2.17** gave orange block crystals suitable for single crystal X-ray diffraction with synchrotron radiation. The data were collected at 100 K and solved and refined in the orthorhombic space group *Pmmn* (R = 7.69%). The asymmetric unit contains 1/4 of the $[Co_4(\mathbf{L2.1})_4]^{4+}$ grid complex much like **2.18**. There is one hexafluorophosphate anion, disordered over two positions which requires the ligand to be doubly deprotonated for the charge to balance (*Figure 2.3.6.iii*). Analysis of the Co-N and Co-O bond lengths verify that crystallographically, the oxidation state of the cobalt is +3 (*Appendix Table 2.8.5.ix*). The low value of the octahedral distortion parameter (Σ), 67°, is further evidence for the presence of Co(III). The C-O bond lengths are 1.296(5) and 1.302(5) and the C-N bond lengths are 1.330(5) and 1.333(5) which confirms that the ligand is deprotonated and coordinating in its imino-enolate form as they are similar to those in the literature for related complexes.[302]

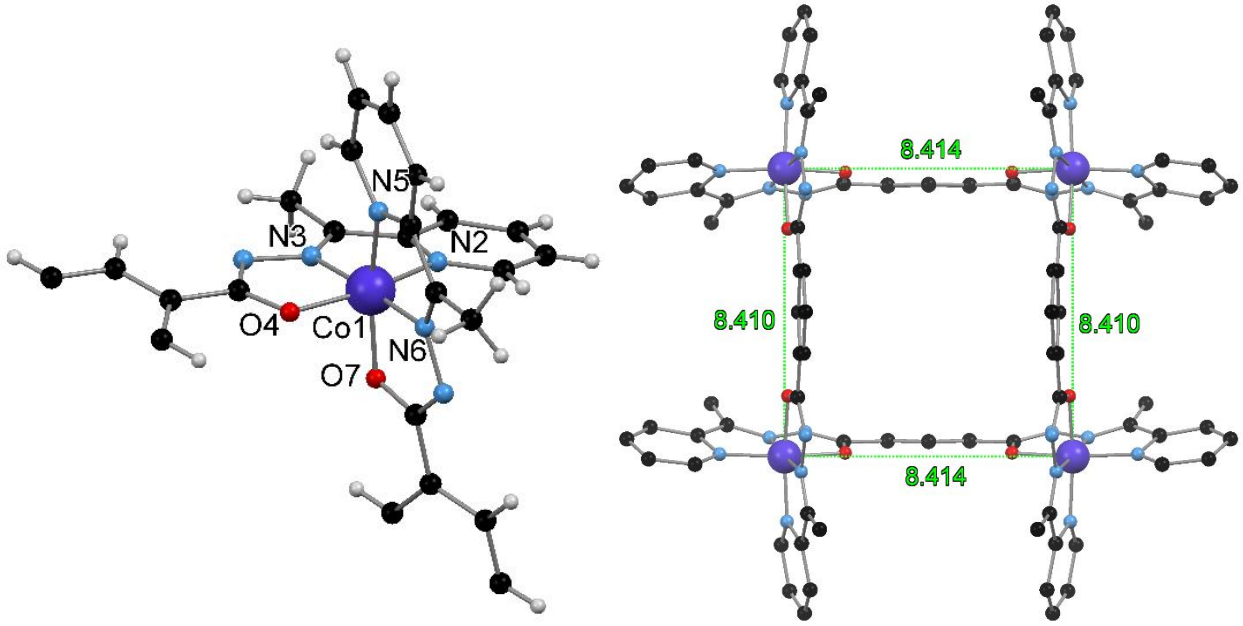

*Figure 2.3.6.iii: (left) The asymmetric unit of **2.17** with the Co(III) centre and coordinating nitrogen and oxygen atoms labeled. The hexafluorophosphate anion has been omitted for clarity. (right) The complete tetranuclear structure generated by the action of two orthogonal mirror planes showing the two crystallographically unique Co···Co separations in green.*

The grid is not a perfect square as there are two crystallographically unique Co1···Co1' distances of 8.484(2) and 8.505(2) Å (prime symbol ' denotes symmetry generated atom), while the Co···Co···Co angles are all 90.00(1)° (*Figure 2.3.6.iii*). The ligand is not entirely flat as the coordinating pyridine ring is twisted out of the plane of the central aromatic ring by 14.3(3) °. This occurs for both crystallographically distinct ligand fragments, as measured by the $C_{aromatic}$-$C_{aromatic}$-$C_{hydrazone}$-$C_{hyrazone}$ torsion angle. The crystallographically identical pyridine rings of neighbouring grids interact via off set π-π stacking interactions of 3.862(4) Å, slightly longer than those of **2.16**. This occurs at each vertex resulting in a supramolecular two-dimensional 4,4-grid, in an analogous manner to **2.16**. This interaction is reinforced by C-H···π interactions from the 4-position of a coordinated pyridine ring to the π-face of a coordinated pyridine ring of a neighbouring grid complex not participating in a π-π stacking interaction. These reciprocal interactions occur with an H···π(centroid) separation of 3.452(4) Å (*Figure 2.3.6.iv*). This results in one grid complex of **2.17** being surrounded by four crystallographically identical complexes, leading to the formation of a two-dimensional supramolecular sheet extending along the crystallographic *a*- and *b*-axes.

Neighbouring complexes interacting via π-π interaction pack in an end-on-end fashion such that the C-H moieties in the 4-position of the pyridine rings are orientated towards one another. These two-dimensional supramolecular sheets then pack directly on top of one another with an AAAA type packing arrangement in the same manner as **2.16**. This is promoted by the formation of non-conventional C-H···N hydrogen bonds between the C-H moieties in the 4- and 6-positions of the central aromatic ring and the non-bonding nitrogen atoms of the hydrazone moiety. There are two crystallographically distinct interactions with H···N separations of 2.508(4) and 2.551(3) Å (*Figure 2.3.6.v*).

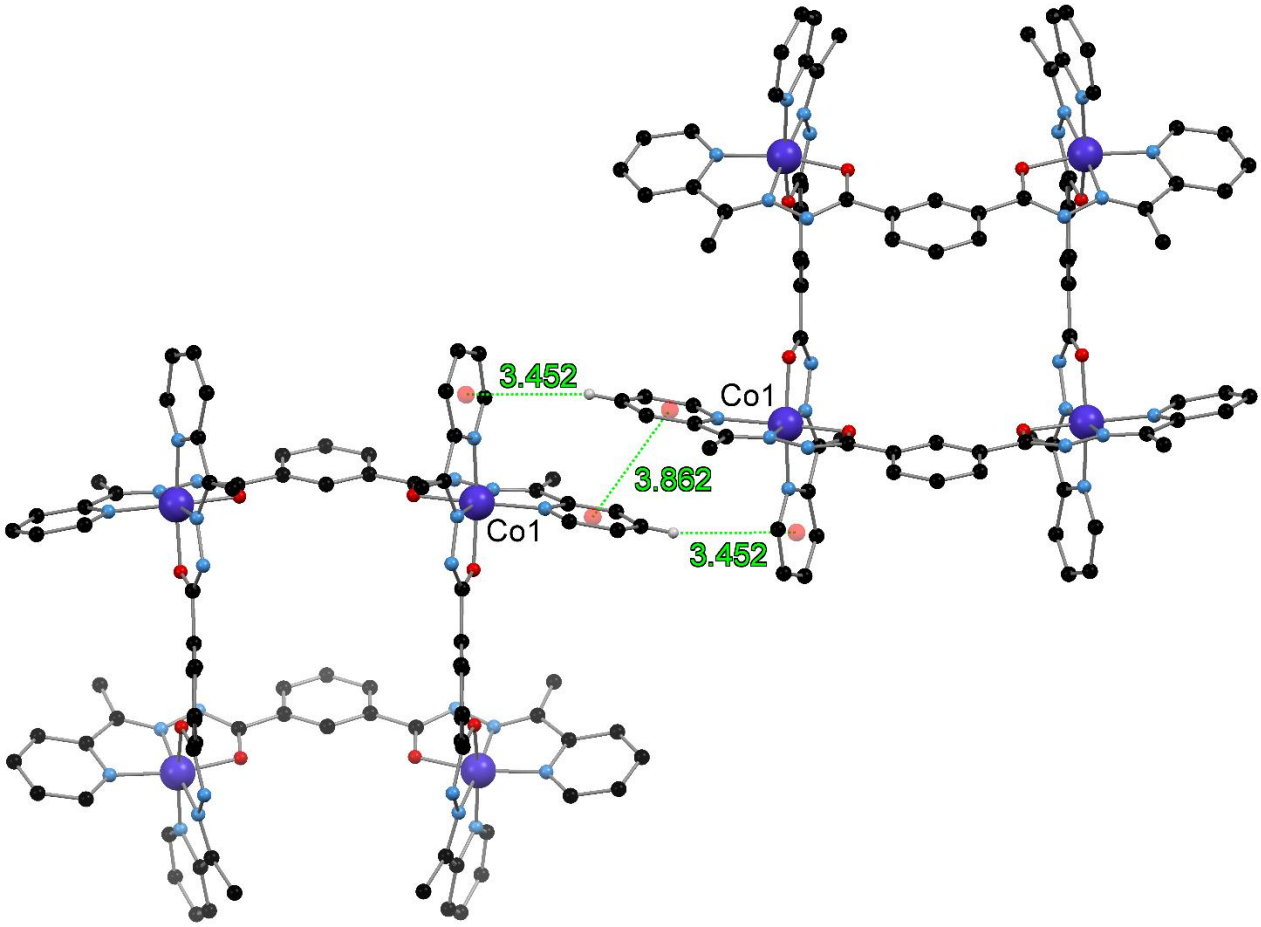

*Figure 2.3.6.iv: The reciprocal C-H···π and π-π stacking interactions between two neighbouring grid complexes of **2.17** shown in green while the centroids are shown in red. Hydrogen atoms not participating in the illustrated interaction and hexafluorophosphate anions are omitted for clarity.*

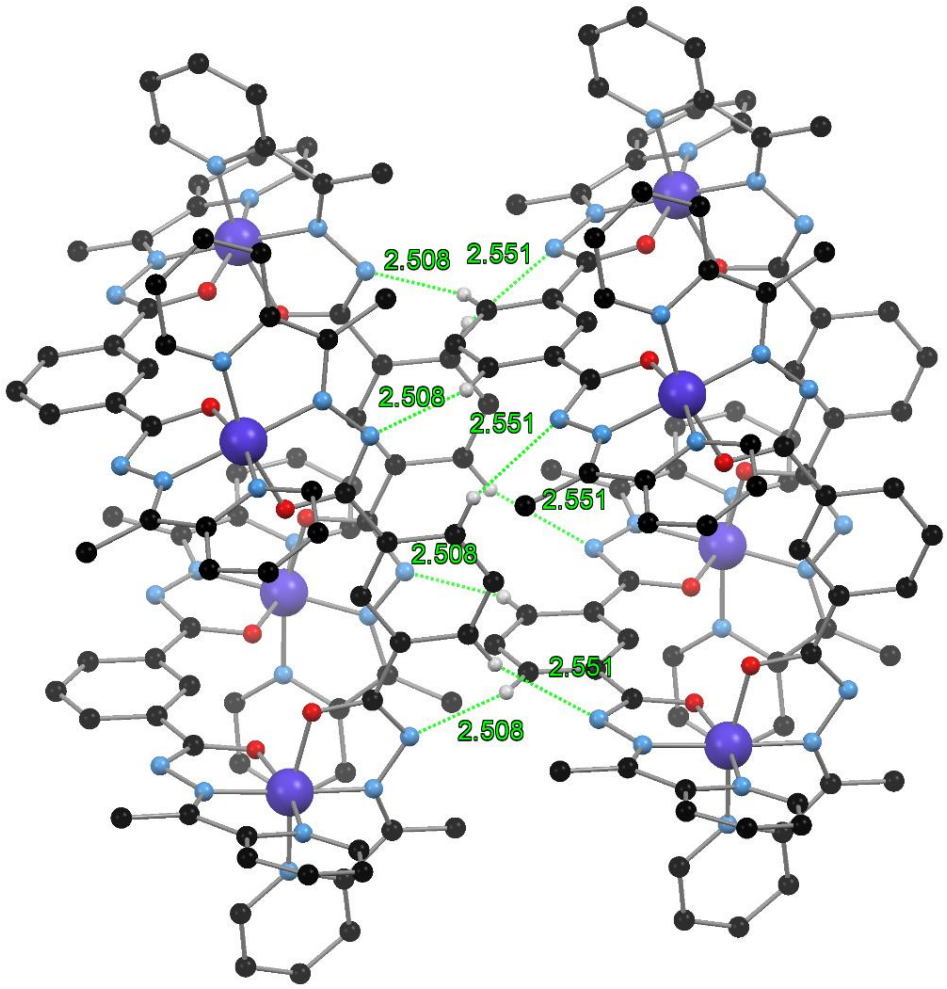

Figure 2.3.6.v: The two crystallographically unique non-conventional C-H···N non-conventional hydrogen bonds between the aromatic C-H moieties and the non-coordinating nitrogen atoms of the hydrazone moieties on a neighbouring grid complex shown in green for ***2.17****. Hydrogen atoms not participating in the illustrated interaction and hexafluorophosphate anions are omitted for clarity.*

The hexafluorophosphate anions interact weakly with the periphery of the grids via C-H···F non-conventional hydrogen bonds. For the complex fragment in the asymmetric unit there are two methyl C-H···F interactions with H···F separations of 2.538(4) and 2.603(4) Å. These are reinforced by an aromatic C-H···F interaction with an H···F separation of 2.324(4) Å (*Figure 2.3.6.vi*). The hexafluorophosphate anions are located in cavities situated around the corners of the grid complexes, between the two-dimensional supramolecular sheets. Hexafluorophosphate anions do not occupy within the square cavity in the centre of the grid.

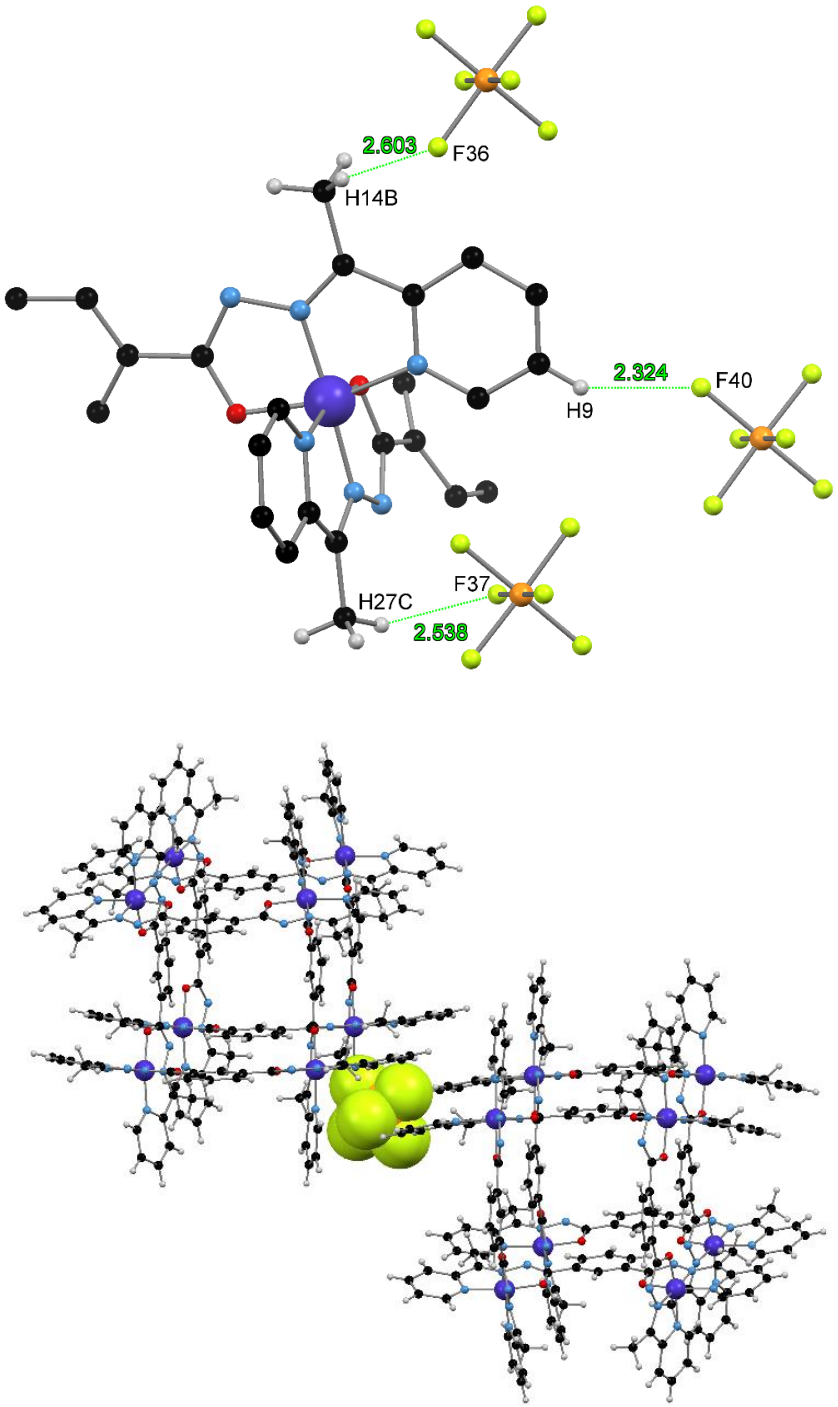

Figure 2.3.6.vi: (top) Three types of C-H···F interactions occur at each corner of the grid complex ***2.17****. Hydrogen atoms not participating in the illustrated interactions omitted for clarity. (bottom) The location of the hexafluorophosphate anions, shown in space filling representation, in the cavity located between the corners of four grid complexes.*

The large amount of disordered solvent and the high symmetry of the complex means that a suitable disorder model for the solvent could not be found so the SQUEEZE[418] function of PLATON[419] was applied (1.2 Å probe). Two crystallographically unique solvent accessible voids were located in the unit cell; two of 1014 $Å^3$ and two of 237 $Å^3$ calculated to contain 366 electrons in total. This corresponds to approximately 183 electrons per grid complex. Therefore, the solvent content can be approximated as six acetonitrile molecules and one diisopropyl ether molecule (190 electrons).

2.3.7 $[Fe_2(H_2L2.1)_3](PF_6)_4$, 2.18

Following the results obtained for **2.16**, the nature of the complex synthesised when Fe(II) chloride was used in the place of Co(II) nitrate was investigated. Based on the spontaneous oxidation of Co(II) to Co(III), it was expected that under the same conditions, Fe(II) would also be oxidized to Fe(III). Equimolar amounts of ligand H_2**L2.1** and Fe(II) chloride were stirred in methanol at room temperature for one hour. The complex was isolated as the hexafluorophosphate salt as a dark red/purple solid by the addition of potassium hexafluorophosphate. The color of the solid obtained is different to that of the Fe(III) complex **2.16** which is an olive green color. ^{1}H NMR in deuterated acetonitrile indicated that only one product was present and that at 25 °C, the complex was diamagnetic. This is indicative of LS Fe(II) as opposed to HS or LS Fe(III), both of which are paramagnetic. The tridentate coordinating motif is known to generate paramagnetic HS Fe(II) complexes when in the neutral imino-keto form. Therefore, if the ligand was coordinating in the expected tridentate fashion in this complex, it would be expected to show paramagnetic shifting of the peaks in the ^{1}H NMR spectrum. There are nine peaks corresponding to the complex in the ^{1}H NMR spectrum indicating that the ligand remains in a symmetrical environment and therefore, the two coordinating motifs exist in the same chemical environment. Seven signals are observed in the aromatic region corresponding to the seven aromatic protons for the ligand containing an internal mirror plane, *i.e.* each arm of the ligand are chemically identical on the NMR time scale *(Figure 2.3.7.i*). The symmetrical nature of the ligand is confirmed by the 12 signals observed in the ^{13}C NMR. The peak at approximately 9.8 ppm can be assigned to the N-H hydrazide proton, further evidence for the ligand existing in the protonated form. The peak at approximately 2.6 ppm can be attributed to the methyl substituent of the hydrazone moiety. Assignment of the ^{1}H NMR spectra was achieved with the aid of a COSY spectra however, no comparison with the free ligand

is possible due to the insolubility of the ligand in acetonitrile. The NMR spectra are summarized in *Appendix 2.8.2.ii*.

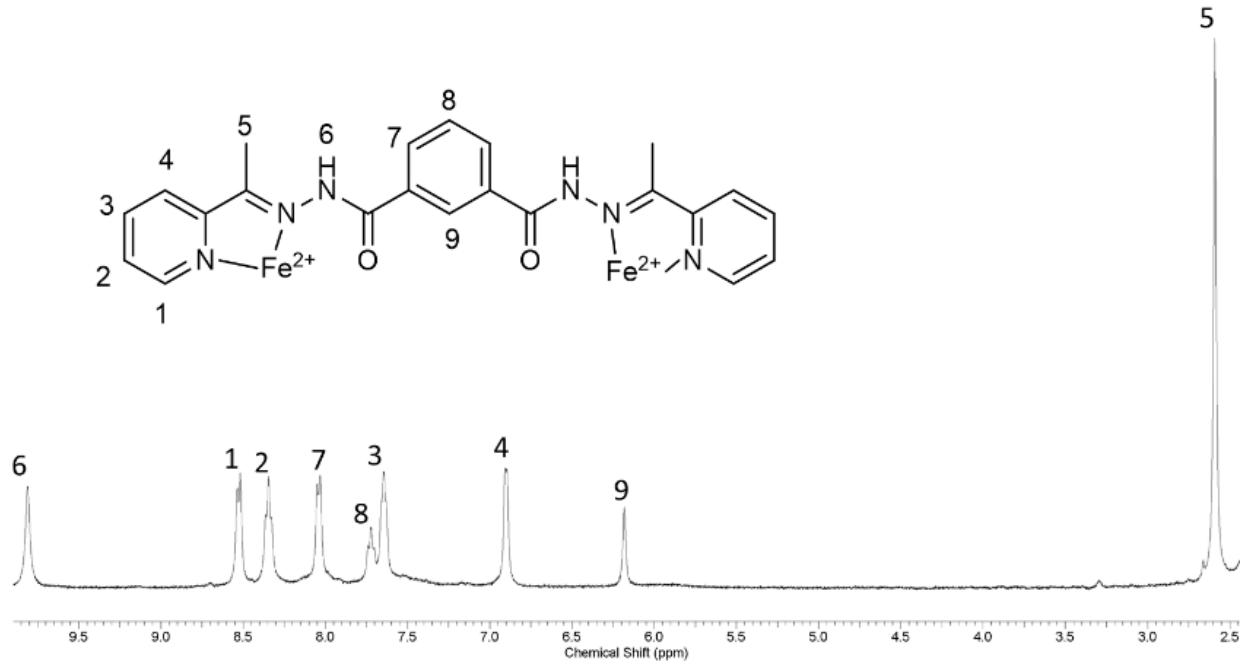

*Figure 2.3.7.i: ^{1}H NMR spectra for **2.18** in deuterated acetonitrile at 25 °C.*

The purple color of the solution used in the NMR experiment indicates the pyridylhydrazone moiety is in the neutral imino-keto form as the anionic form of the ligand results in Fe(II) complexes which are typically dark green. This is reinforced by ^{19}F NMR that shows a single peak due to the hexafluorophosphate anion. If the ligand was deprotonated, the complex would be neutral and therefore no hexafluorophosphate anions would be present. Together, these results indicate that the ligand is not coordinating in the expected tridentate manner. Vapor diffusion of toluene into a nitromethane solution of complex **2.18** resulted in dark red/purple hexagon shaped crystals suitable for single crystal X-ray diffraction with synchrotron radiation. The data were collected at 100 K and solved and refined in the hexagonal space group $P6_3/m$ (R = 5.87%). The asymmetric unit contains 1/6 of a Fe(II) dinuclear triple mesocate comprised of one half ligand and one third of an Fe(II) centre. Two partial occupancy hexafluorophosphate anions balance the charge along with a nitromethane molecule which are all situated on symmetry elements. The presence of two hexafluorophosphate anions per Fe(II) centre confirms that the ligand is the neutral imino-keto form (*Figure 2.3.7.ii*). One hexafluorophosphate anion is ordered while the second is

disordered about a 6-fold rotoinversion axis, as is the nitromethane solvent molecule. This results in the formula unit of the crystal structure being **2.18**·6$MeNO_2$. The presence of one half of the full ligand is in agreement with the symmetrical conformation observed in the NMR experiments.

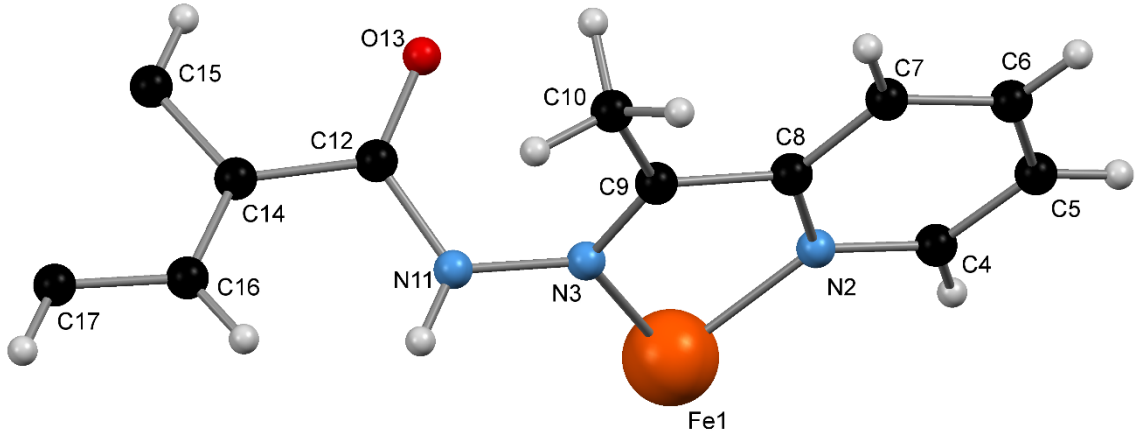

*Figure 2.3.7.ii: The asymmetric unit of **2.18** with the non-hydrogen atoms labeled. The hexafluorophosphate anions and the disordered nitromethane molecules are omitted for clarity.*

The complete mesocate structure is generated by the action of a 3-fold rotation axis along the pitch of the mesocate and a reflection about a mirror plane. Unlike the expected tridentate coordination mode, the pyridylhydrazone functionality acts as a bidentate coordinating motif. Therefore, the Fe(II) centres exist in an N_6 coordination sphere and not the expected N_4O_2 coordination sphere. The coordination of only the nitrogen atoms of a similar pyridylhydrazone ligand has been previously reported for a tetrahedral Ag(I) centre and an octahedral Fe(II) centre with a related pyridylacylamidrazone ligand.[422-423] The Fe-N bond lengths are indicative of LS Fe(II) at 100 K and are summarized below (*Table 2.3.7.i*). However, the octahedral distortion parameter (Σ) of 80° is relatively high for LS Fe(II).

Bond	**Distance (Å)**	**Atoms**	**Angle (°)**	**Atoms**	**Angle (°)**
Fe1-N2	1.948(4)	N2-Fe1-N2'	93.4(1)	N3-Fe1-N3'	96.8(1)
Fe1-N3	1.957(3)	N2'-Fe1-N3	89.9(1)	N3-Fe1-N2	80.3(1)

*Table 2.3.7.i: Table of crystallographically unique Fe-N bond lengths and N-Fe-N bond angles for **2.18** from single crystal X-ray crystallographic data collected at 100 K. The prime symbol (') indicates a symmetry generated atom.*

The ligand H_2**L2.1** was initially perceived to be rigid and was expected to form $[Fe_4(H_2\mathbf{L2.1})_4]^{8+}$ grid complexes. However, the crystal structure reveals that a dinuclear triple mesocate with a different metal to ligand stoichiometry to that present during the synthesis was formed; $[Fe_2(H_2\mathbf{L2.1})_3]^{4+}$, **2.18** (*Figure 2.3.7.iii*). Entropically, it is more thermodynamically favorable for a ligand to assemble the smallest possible structure with the metal ions present as this results in a greater number of individual species present in solution. When the results obtained from the reaction of the ligand with Co(II) under the same conditions are taken into account, the entropy explanation is not sufficient, as the reaction does not proceed in the same manner. A more likely explanation is that Fe(II) has a strong preference for the N_6 coordination sphere afforded by three ligands coordinating in a bidentate fashion, which is then stabilized by the internal C-H···π interactions and N-H···O hydrogen bonds. The twist of the hydrazone moiety, measured as the C9-N3-N11-C12 torsion is 64.9(4)°. The carbonyl functionality is likewise twisted out of the plane of the central aromatic ring with an out of plane twist of 20.4(5)° (measured as the O13-C12-C14-C15 torsion). This results in the formation of intramolecular hydrogen bond interactions between the carbonyl oxygen atom and a hydrazide group on an adjacent (inter-strand) ligand with an H···O separation of 2.485(2) Å and an angle of 116.5(2)°. By virtue of symmetry, six crystallographically identical hydrogen bonds occur per mesocate. These hydrogen bond interactions are reinforced by three crystallographically identical reciprocal edge-to-face C-H···π interactions with an H···π(centroid) separation of 2.910(3) Å and an angle of 23.0(3)°. Six interactions per mesocate complex occur and may contribute to the stability of this unexpected coordination mode of the ligand. Therefore, the dinuclear triple mesocate formed by the ditopic ligands is more enthalpically favorable than the tetranuclear grid under the same conditions. The Fe1···Fe1' separation measures 11.548(3) Å and is congruent with the crystallographic *c*-axis (prime symbol ' denotes symmetry generated atom). The Fe(II) centre in the asymmetric unit possesses Λ stereochemistry while the Fe(II) centre generated via symmetry exhibits Δ stereochemistry resulting in the dinuclear complex being achiral and therefore a mesocate.

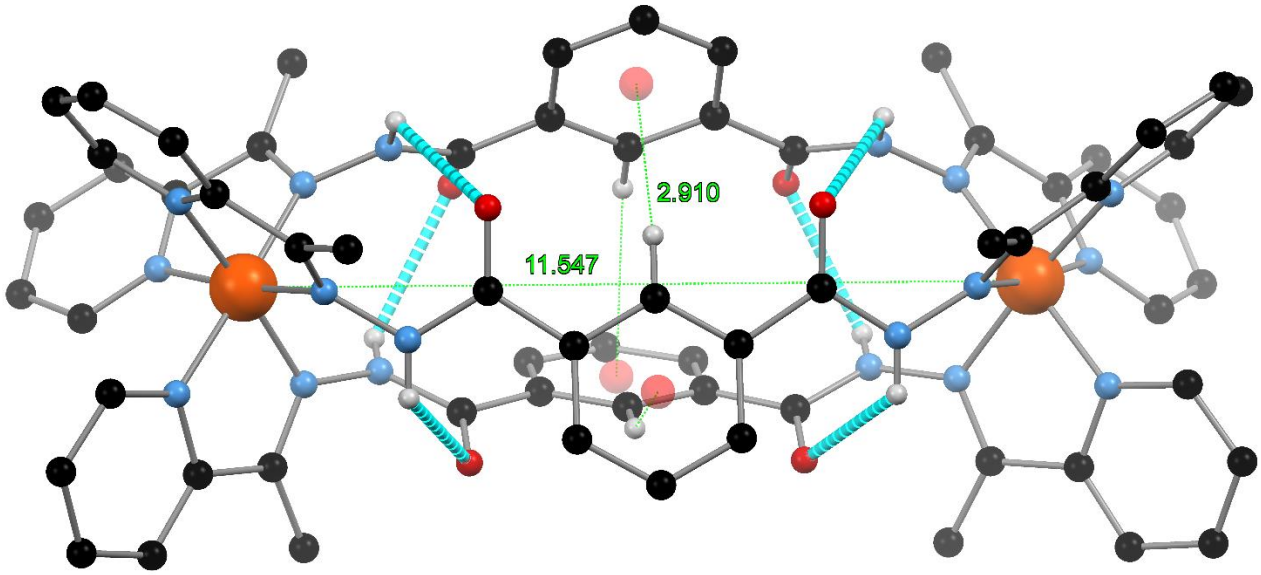

*Figure 2.3.7.iii: The complete structure of the dinuclear triple mesocate **2.18** generated by the action of a mirror plane and a 6-fold rotation axis. The Fe1···Fe1' separation and the three C-H···π interactions are shown in green while the π(centroid) are represented as red spheres. Hydrogen atoms, hexafluorophosphate anions and nitromethane solvent molecules are omitted for clarity.*

The mesocate structures are not interacting via any other weaker interactions such as π-π stacking. They pack in one-dimensional chains along the crystallographic *b*- and *c*-axes (*Figure 2.3.7.iv*). The mesocates pack side-by-side down the crystallographic *b*-axis and end-on-end down the crystallographic *c*-axis. These chains then pack in an offset arrangement with the hexafluorophosphate and nitromethane solvent molecules occupying the spaces between them. The elemental analysis indicates the presence of two nitromethane molecules and 10 water molecules in the form **2.18**·2$MeNO_2$·10H_2O. The loss of volatile solvent molecules upon removal of the crystals from the mother liquor and hydration of the sample with water from the atmosphere is commonly observed for supramolecular metal complexes. TGA shows a mass loss of 6.1% between 24 and 215 °C which corresponds to the loss of two nitromethane molecules (5.9 %) from **2.18**·3$MeNO_2$ followed by decomposition after 215 °C.

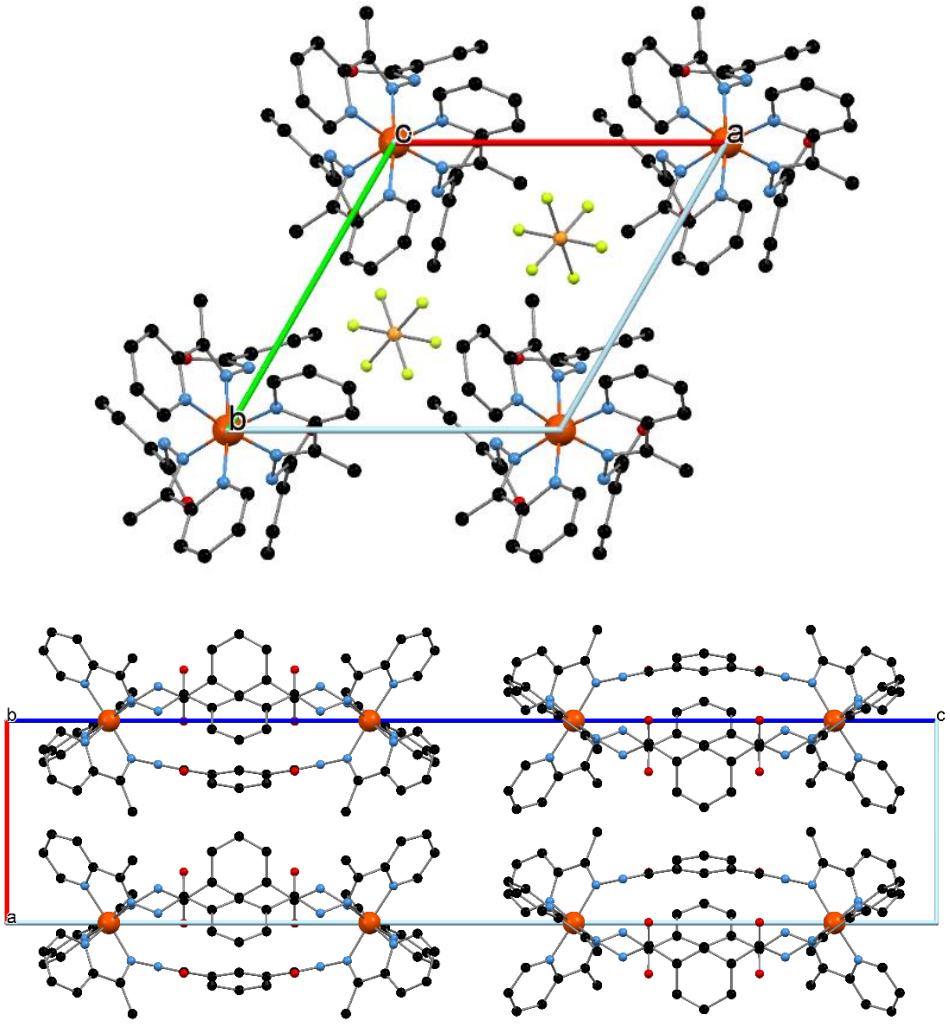

*Figure 2.3.7.iv: (top) View down the crystallographic c-axis of the crystal packing of **2.18** showing the position of the ordered hexafluorophosphate anion. Hydrogen atoms, disordered hexafluorophosphate anions and nitromethane solvent molecules omitted for clarity. (bottom): View down the crystallographic b-axis of **2.18** showing the alignment of the mesocate structures relative to the one in front. Hydrogen atoms, hexafluorophosphate anions and nitromethane solvent molecules omitted for clarity.*

2.3.8 $[Fe_2(H_2L2.5)_3](BF_4)_4$, 2.19

The ligand H_2**L2.5** was synthesised as an analogue of ligand H_2**L2.1**. The use of pyrazine rings in the place of pyridine rings adds a nitrogen atom distal to the coordination site which can act as hydrogen bond acceptor. The N-H moiety of the pyridylhydrazone functionality can act as a potent

hydrogen bond donor when a suitable acceptor is present, which is the focus of chapter three. In the case of H_2**L2.6**, this hydrogen bond acceptor is incorporated into the ligand. H_2**L2.6** and Fe(II) tetrafluoroborate were stirred in nitromethane overnight to give a purple red solution. Vapor diffusion of toluene gave red prismatic crystals suitable for single crystal X-ray diffraction.[424] The data were collected at 120 K and solved and refined in the same hexagonal space group as **2.18**; $P6_3/m$ (R = 9.27%), however, the unit cell parameters were significantly different to those of **2.18**. The asymmetric unit contains 1/6 of the Fe(II) dinuclear triple mesocate and therefore there is one crystallographically unique Fe(II) centre much like **2.18** (*Figure 2.3.8.i*). The Fe-N bond lengths are indicative of LS Fe(II) at 120 K and are summarized below (*Table 2.3.8.i*). The low octahedral distortion parameter (Σ) of 59° is further evidence of this.

Bond	Distance (Å)	Atoms	Angle (°)	Atoms	Angle (°)
Fe1-N2	1.956(4)	N2-Fe1-N2'	93.4(2)	N3-Fe1-N3'	95.2(2)
Fe1-N3	1.960(5)	N2'-Fe1-N3	91.3(2)	N3-Fe1-N2	80.5(2)

*Table 3.3.8.i: Table of crystallographically unique Fe-N bond lengths and N-Fe-N bond angles for **2.19** from single crystal X-ray crystallographic data collected at 120 K. The prime symbol (') indicates a symmetry generated atom.*

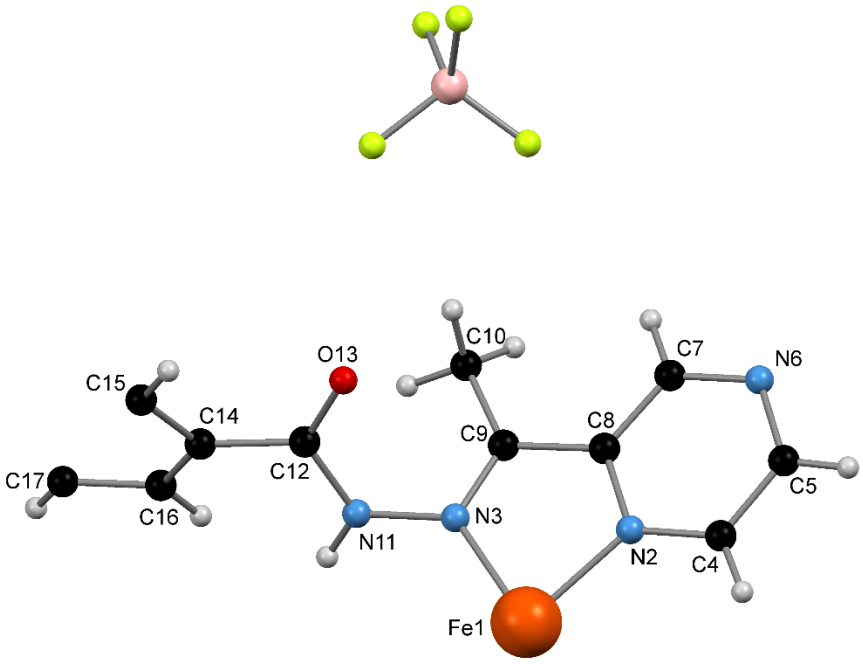

*Figure 2.3.8.i: The asymmetric unit of **2.19** with the non-hydrogen atoms of the complex labeled. Only one orientation of the disordered tetrafluoroborate anion is shown for clarity.*

The Fe1···Fe1' separation (prime symbol ' denotes symmetry generated atom), located on a 3-fold rotation axis, runs parallel to the crystallographic *c*-axis and measures 11.622(2) Å (*Figure 2.3.8.ii*). The twist of the hydrazone moiety, measured as the C9-N3-N11-C12 torsion, is 61.8(6)°. The carbonyl functionality is not coplanar with the central isophthalate ring, with an out of plane twist of 24.7(8)° as measured by the O13-C12-C14-C15 torsion. This results in the formation of intramolecular hydrogen bond interactions between the carbonyl oxygen atom and a hydrazide group on an adjacent (inter-strand) ligand with an H···O separation of 2.355(3) Å and an angle of 111.0(3)°. By virtue of symmetry, six of these interactions occur per complex. These hydrogen bond interactions are reinforced by three crystallographically identical reciprocal edge-to-face C-H···π interactions with an H···π(centroid) separation of 2.903(3) Å and an angle of 23.0(5)°.

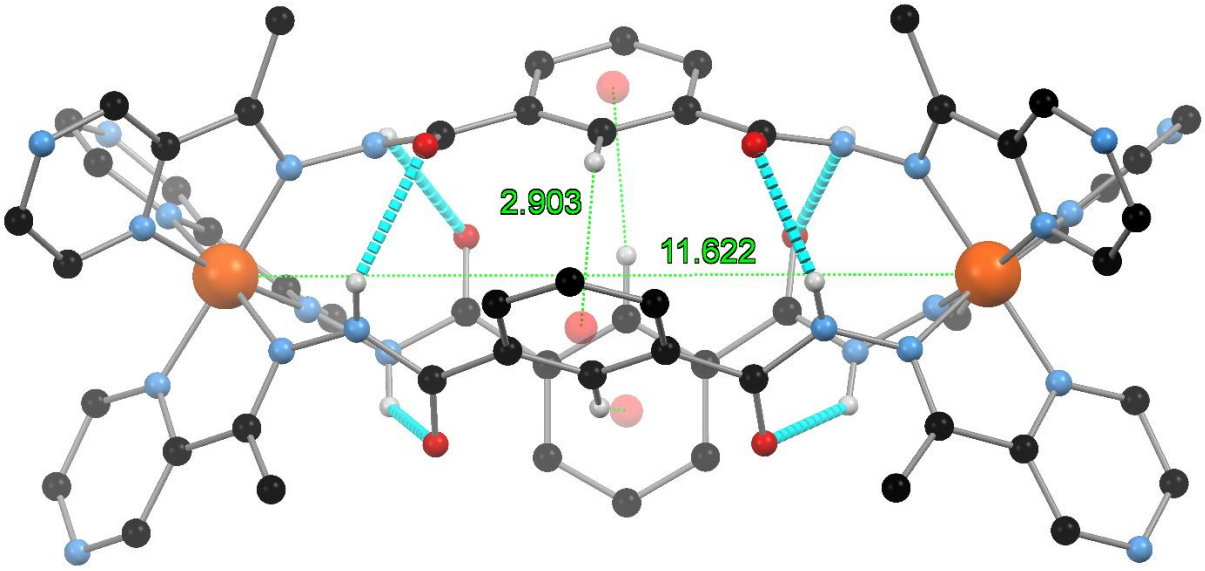

*Figure 2.3.8.ii: The complete structure of the dinuclear triple mesocate **2.19** generated by the action of a mirror plane and a 3-fold rotation axis. The Fe1···Fe1' separation and the three C-H···π interactions are shown in green while the π(centroid) are represented as red spheres. Hydrogen atoms, tetrafluoroborate anions and nitromethane solvent molecules are omitted for clarity.*

The introduction of the pyrazine ring has a pronounced effect on the crystal packing when compared to the pyridine analogue, **2.18**. The mesocates pack throughout the crystal lattice via extensive supramolecular interactions, the most salient of which is the hydrogen bond between pyrazine and hydrazide groups of adjacent mesocates with an H···N separation of 3.009(8) Å

(*Figure 2.3.8.iii*). There are six reciprocal intermolecular hydrogen bonds between adjacent pyrazine and hydrazide moieties with offset face-to-face π-π interactions involving each pyrazine ring of neighbouring mesocates with π(centroid)···π(centroid) separations of 3.687(3) Å. These extend down the crystallographic *c*-axis, to propagate a three-dimensional network containing one-dimensional hexagonal channels parallel to the *c*-axis (*Figure 2.3.8.v*). The channel diameter at closest contact is *ca.* 5.77 Å. The tetrafluoroborate anions line the one-dimensional channels and are disordered over two positions.

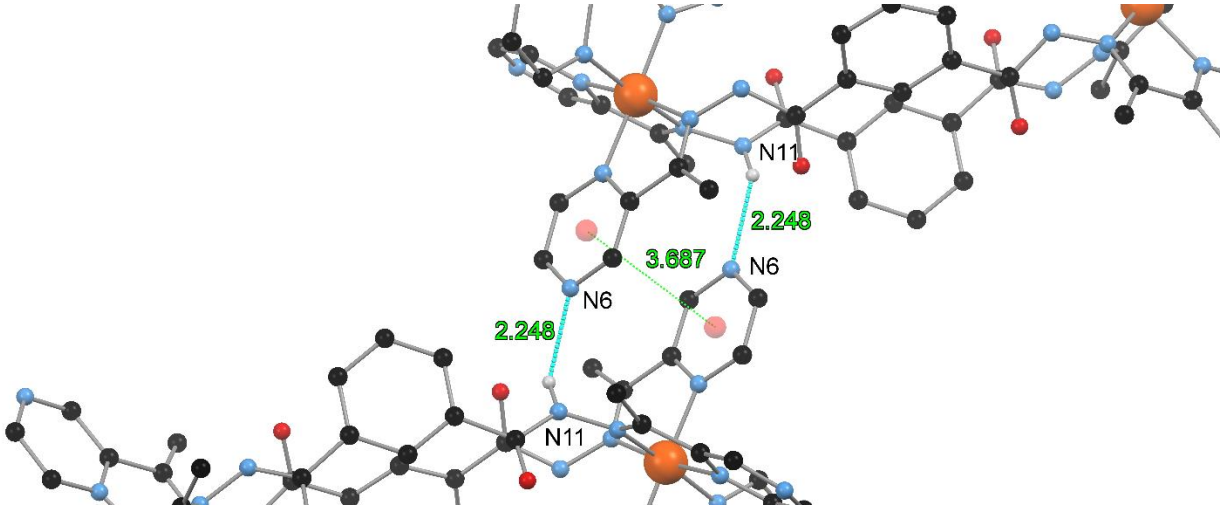

Figure 2.3.8.iii: The pyrazine π-π stacking interactions occurring between two neighbouring complexes with the π(centroid) represented as red spheres and the π(centroid)-π(centroid) separation is shown in green. The π-π interaction is reinforced by two N-H···N hydrogen bond interactions, shown in blue. Hydrogen atoms not participating in the illustrated interactions and the tetrafluoroborate anions are omitted for clarity.

The high symmetry of the space group and the disordered nature of the solvent means it was unable to be modelled satisfactorily and therefore the SQUEEZE[418] function of PLATON[419] was applied (1.2 Å probe). This equates to a solvent accessible void volume of 1164 $Å^3$ calculated to contain 369 electrons (185 per mesocate complex). The onset of mass loss from freshly isolated crystals of **2.19** was evident from TGA. A mass loss of 12% occurs immediately up to 60 °C with a further mass loss of 4% between 60 and 200 °C after which decomposition occurs. Elemental analysis suggested a molecular formula of **2.19**·7.5H_2O·$MeNO_2$ with the solvent accounting for 13-15% molecular mass per mesocate unit, matching the volatile contents suggested by TGA.

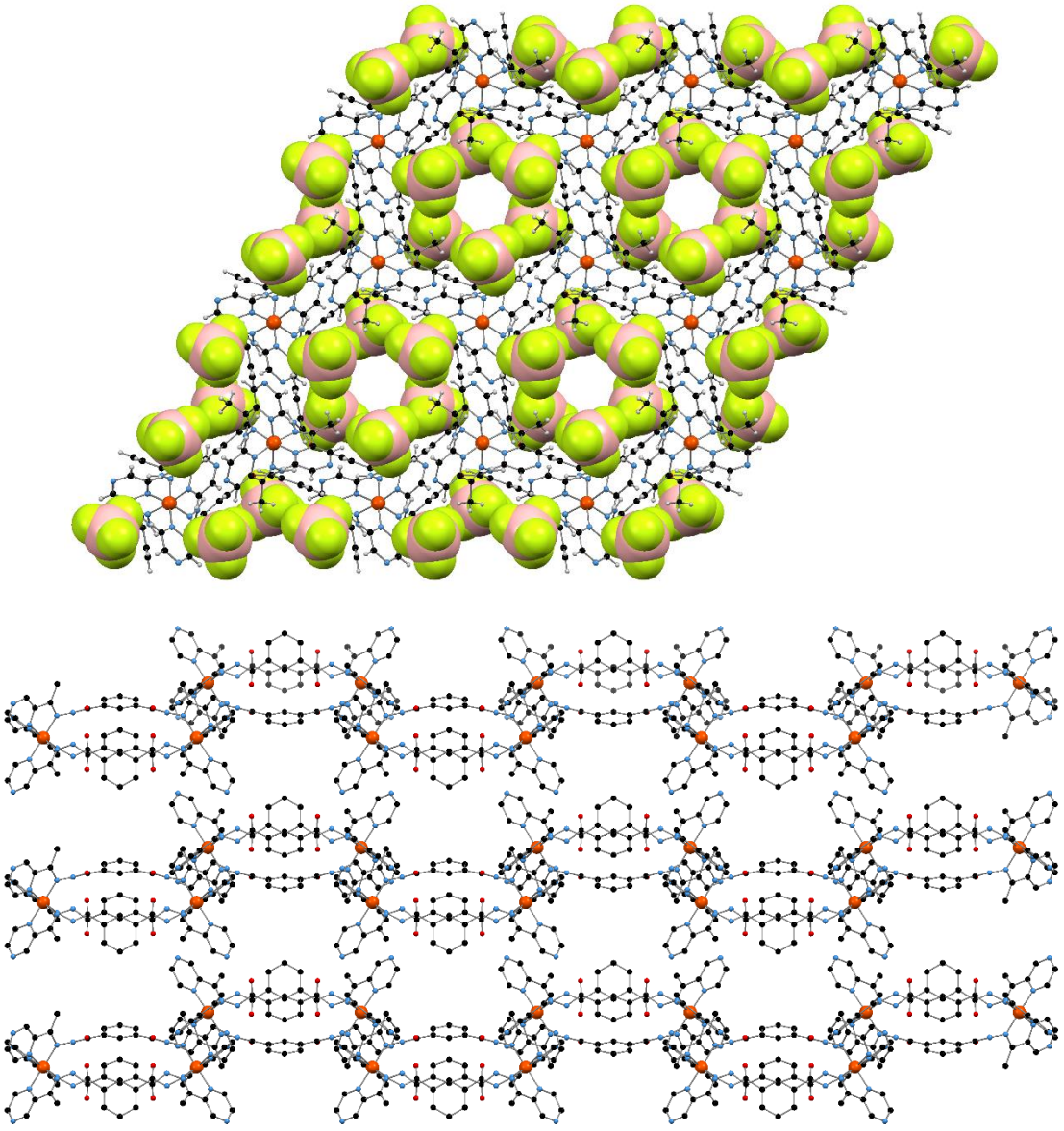

Figure 2.3.8.iv: (top) View down the crystallographic c-axis of ***2.19****. The tetrafluoroborate anions are shown in space filling representation to emphasize the polar nature of the hexagonal channel. (bottom) View down the crystallographic b-axis showing the offset packing of the mesocate structures relative to the crystallographic c-axis (plane of the page) due to the π-π and N-H···N hydrogen bond interactions. Hydrogen atoms and tetrafluoroborate anions omitted for clarity.*

The occurrence of six π-π interactions and 12 hydrogen bond interactions per mesocate complex results in a highly stable hydrogen bonded framework. The crystallinity of the complex was

maintained upon removal from solution, resulting in the crystals exhibiting remarkable stability. Due to the one-dimensional channels in the structure, the removal of the solvent from the pores was attempted in order to investigate the possibility of measuring the gas sorption properties. Solvent exchange was carried out by soaking crystals of **2.19** in DCM and exchanging the solvent three times over the course of three days followed by drying under high vacuum for three hours. The PXRD pattern for the activated sample matches that of the freshly isolated sample, indicating that the integrity of the framework is retained upon the removal of the solvent from the pores of the structure (*Figure 2.3.8.vi*).

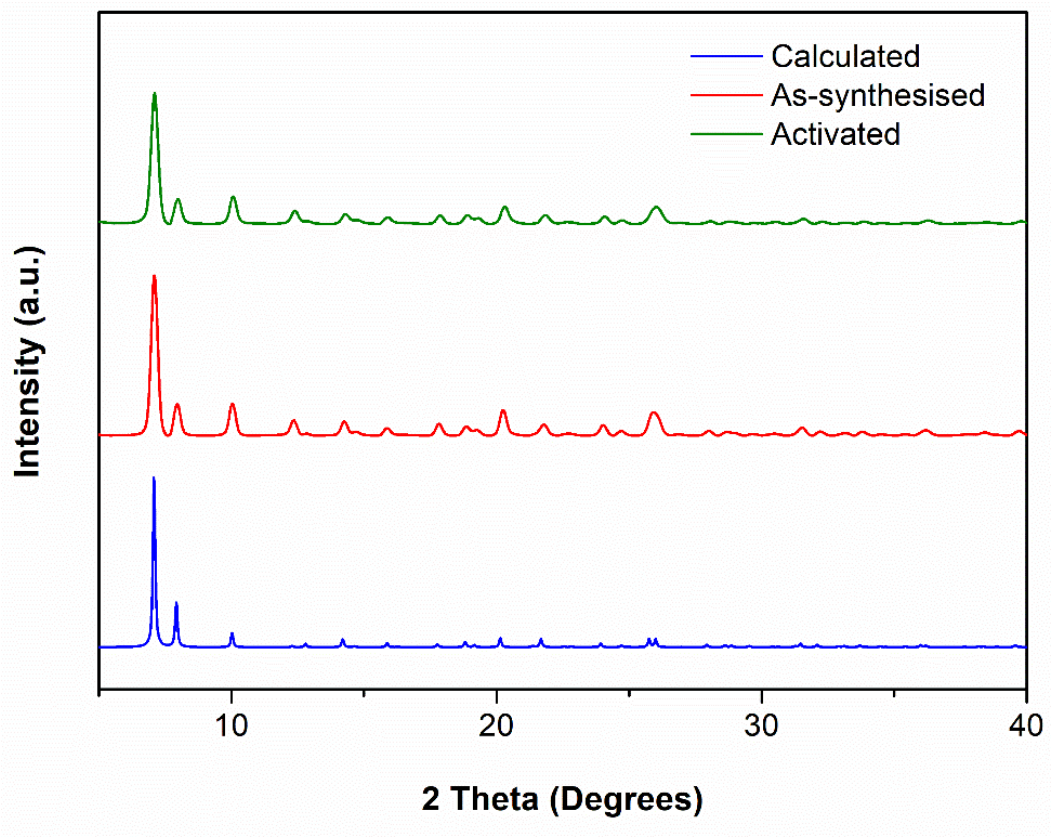

*Figure 2.3.8.vi: The PXRD patterns for **2.19**. The PXRD pattern calculated from the crystal structure is shown in red, the experimental from a freshly isolated sample of crystals in blue and the activated sample of the crystals in green.*

2.3.9 $[Fe_2(H_2L2.6)_3](BF_4)_4$, 2.20

Synthesis of this complex was attempted in nitromethane; however, this was unsuccessful due to the insolubility of the ligand under these conditions. Therefore, H_2**L2.6** and Fe(II) tetrafluoroborate

were stirred in acetonitrile to give a purple red solution, the solvent was removed under reduced pressure and the purple red residue was re-dissolved in nitromethane. Vapor diffusion of diisopropyl ether into the nitromethane solution of **2.20** gave red rod-shaped crystals suitable for single crystal X-ray diffraction. The data were collected at 120 K and solved and refined in the same hexagonal space group as **2.19**, $P6_3/m$ (R = 13.24%), however with noticeably different unit cell parameters. The asymmetric unit contained 1/6 of a Fe(II) dinuclear triple mesocate comprised of one half of a ligand and one third of an Fe(II) centre (*Figure 2.3.9.i*). The Fe-N bond lengths are indicative of LS Fe(II) at 120 K and are summarized below (*Table 2.3.9.i*). The low octahedral distortion parameter (Σ) of 62° is further evidence of this.

Bond	Distance (Å)	Atoms	Angle (°)	Atoms	Angle (°)
Fe1-N2	1.95(1)	N2-Fe1-N2'	95.3(5)	N3-Fe1-N3'	95.3(5)
Fe1-N3	1.953(9)	N2'-Fe1-N3	91.7(5)	N3-Fe1-N2	80.0(5)

*Table 2.3.9.i: Table of crystallographically unique Fe-N bond lengths and N-Fe-N bond angles for **2.20** from single crystal X-ray crystallographic data collected at 120 K. The prime symbol (') indicates a symmetry generated atom.*

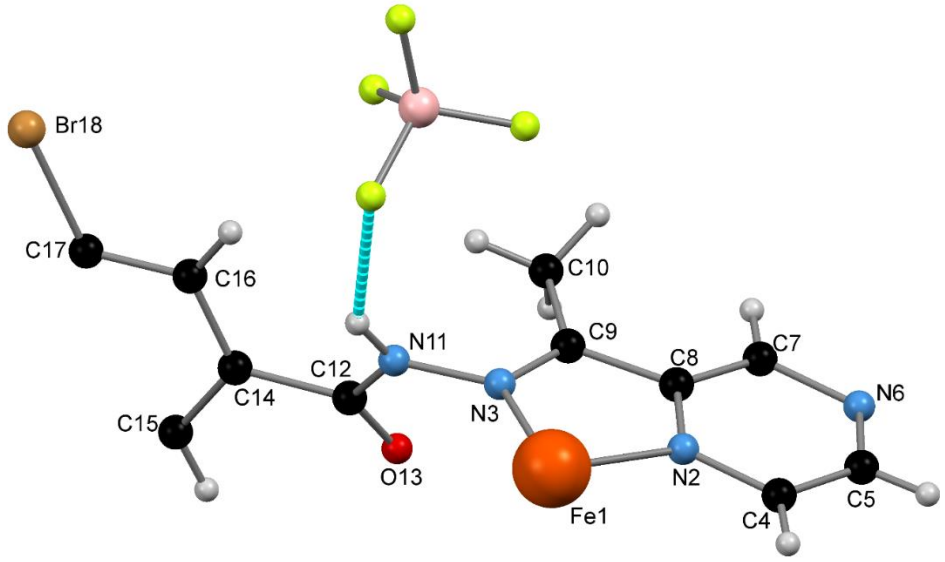

*Figure 2.3.9.i: The asymmetric unit of **2.20** with the non-hydrogen atoms of the complex labeled and the hydrogen bond interaction between the hydrazide moiety and the tetrafluoroborate anion shown in light blue. Only one orientation of the disordered tetrafluoroborate anion is shown for clarity.*

Like the previous complex, the Fe1···Fe1' separation runs parallel to the crystallographic *c*-axis and measures 11.599(5) Å (prime symbol ' denotes symmetry generated atom). The action of the symmetry elements discussed for **2.19** complete dinuclear triple mesocate structure (*Figure 2.3.9.ii*). A similar twist of the hydrazone moiety to **2.19** occurs with a torsion angle of 62(1)°, while the carbonyl functionality features an out of plane twist of 23(2)°. In a similar manner to **2.19** intramolecular hydrogen bond interactions between the carbonyl oxygen atom and a hydrazide moieties with an H···O separation of 2.370(8) Å and an angle of 123.4(7)°. These hydrogen bond interactions are reinforced by the same edge-to-face C-H ···π interactions as **2.19**. These interactions occur with an H···π(centroid) separation of 2.882(7) Å and an angle of 148.8(1)°. The pyrazine rings π-π stack upon one another with a noticeably larger centroid separation of 4.16(1) Å. This is due to the stacking interaction occurring between the opposite faces of the pyrazine rings in comparison to **2.19**.

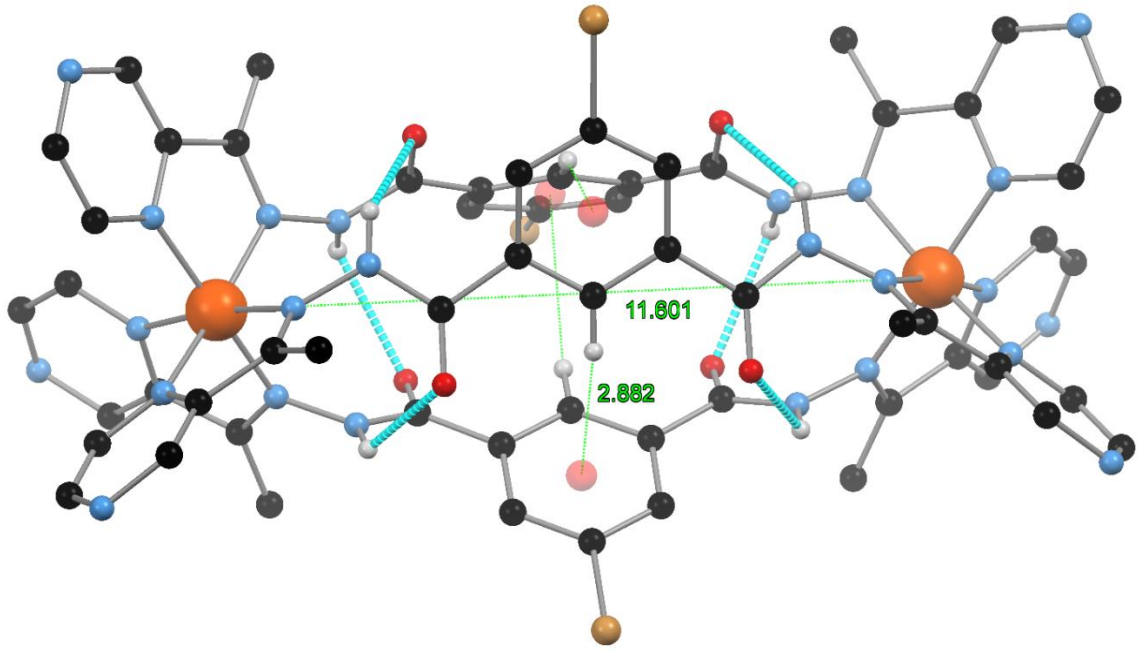

*Figure 2.3.9.ii: The complete structure of the dinuclear triple mesocate **2.20** generated by the action of a mirror plane and a 3-fold rotation axis. The Fe1···Fe1' separation and the three C-H···π interactions are shown in green. Hydrogen bonds are shown in light blue. Hydrogen atoms and tetrafluoroborate anions molecules are omitted for clarity. The six crystallographically identical hydrogen bond interactions are shown in light blue and π(centroid) represented as red spheres.*

A direct consequence of this change in π-π stacking is that the pyrazine···hydrazide hydrogen bond, observed in **2.19**, does not form. Instead a weak C-H···N interaction between C4 and N6 of neighbouring pyrazine rings occurs with an H···N separation of 2.50(2) Å (*Figure 2.3.9.iii*). The now vacant hydrazone hydrogen bond donor forms an interaction with a tetrafluoroborate anion of 2.13(2) Å. The Fe1···Fe1' spacing of the Fe(II) centres coordinated to these pyrazine rings also increases to 9.410(3) Å. Because this π-π stacking interaction results in the mesocates being positioned relative to one another in a broadly similar manner to **2.19**, the same hexagonal channels are formed. Therefore, when the packing is viewed down the crystallographic *c*-axis, it is similar to that of **2.19**. The change in packing along the crystallographic *c*-axis can be attributed to the incorporation of the bromine functionality on C17. These bromine atoms are orientated into the hexagonal channel towards one another with a Br18···Br18 separation of 3.837(4) Å, 144.1(7) ° resulting in the formation of a trimeric type II halogen bond between three complexes in the same plane.[56]

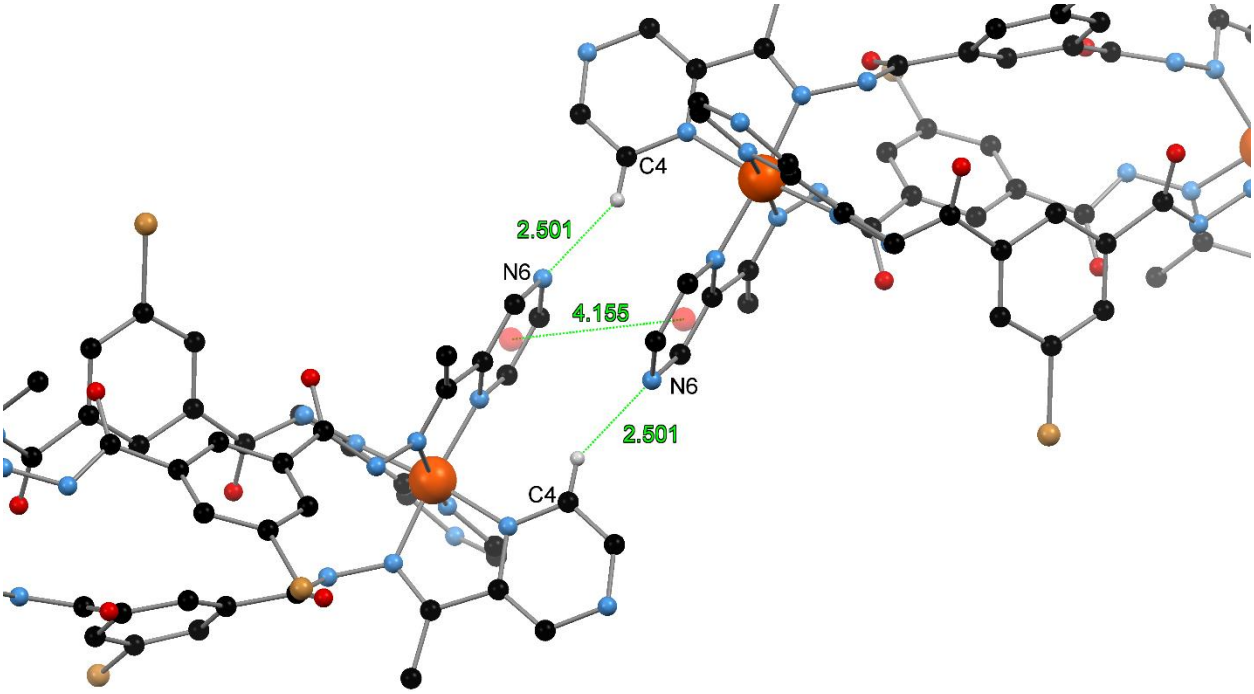

Figure 2.3.9.iii: The pyrazine π-π stacking interactions occurring between two neighbouring complexes with the π(centroid) represented as red spheres and the π(centroid)···π(centroid) separation shown in green. The π-π interaction is reinforced by two C-H···N interactions also shown in green. Hydrogen atoms not participating in the illustrated interactions, and tetrafluoroborate anions omitted for clarity.

This more expanded packing of the mesocates propagates along the *c*-axis resulting in a significantly longer *c*-axis dimension for **2.20** (34.658(6) Å) in comparison to **2.19** (24.9442(4) Å) (*Figure 2.3.9.iv*). There is also a small decrease in the crystallographic *a*- and *b*-axes from 14.340(1) Å for **2.19** to 12.928(3) Å for **2.20**. The compression in the crystallographic *a*- and *b*-axes manifests itself as a more compact one-dimensional channel with a diameter at the closest contact of *ca.* 4.77 Å. The tetrafluoroborate anions line the sides of the noticeably thinner channel much like **2.19**. There is a significant number of solvent molecules occupying the one-dimensional channel. However, the high symmetry of the space group and the disordered nature of the solvent means it is unable to be modelled satisfactorily and therefore the SQUEEZE[418] function of PLATON[419] was applied (1.2 Å probe). The solvent accessible void was found to be 1157 $Å^3$ and calculated to contain 362 electrons. This corresponds to 181 per mesocate complex which can be approximated as four nitromethane and one diisopropyl ether molecules (186 electrons).

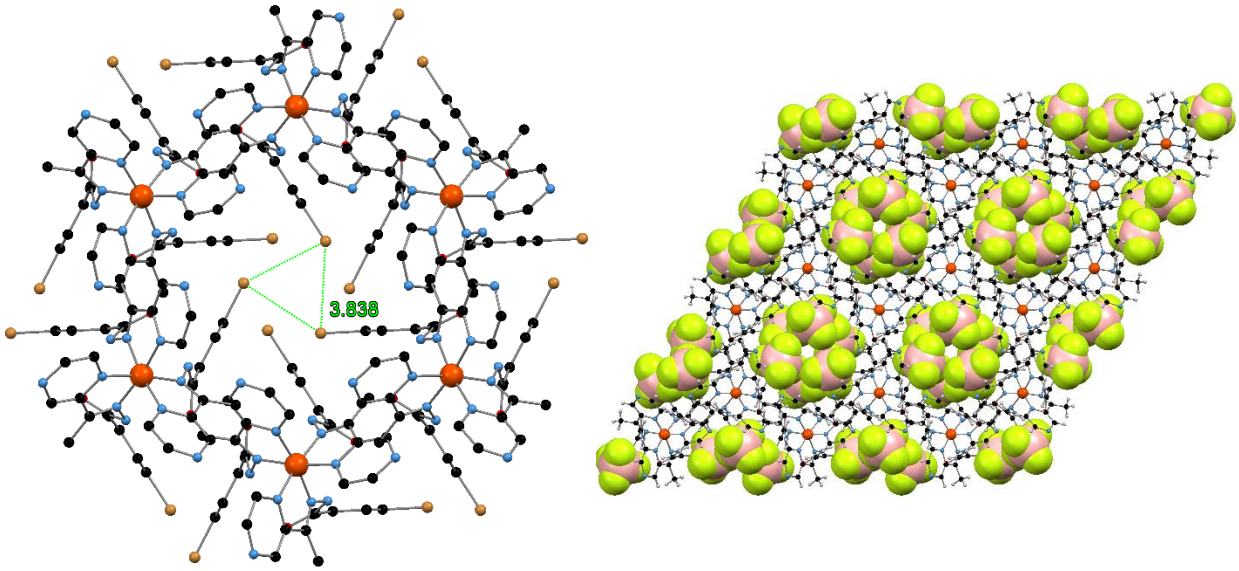

Figure 2.3.9.iv: (left) View down the crystallographic c-axis of the hexagonal channel. The Br···Br separations of the three bromo substituents in the same plane forming a trimeric halogen bonding motif are shown in green. Hydrogen atoms and tetrafluoroborate anions omitted for clarity. (right) View down the crystallographic c-axis showing the tetrafluoroborate anions occupying the hexagonal channel in space filling representation.

TGA reveals a mass loss of 5.9% between 26 and 133 °C which corresponds to the loss of one diisopropyl ether molecule. This constitutes 5.1% of the mass of **2.20**·$C_6H_{14}O$ and is also observed

in the elemental analysis. The complex is stable until 200 °C after which there is a rapid mass loss due to decomposition.

2.3.10 $[Fe_2(H_2L2.7)_3](BF_4)_4$, 2.21

Similar issues as H_2**L2.6** with ligand solubility were encountered with H_2**L2.7**. Therefore, an analogous synthesis procedure to **2.20** was carried out. Vapor diffusion of diisopropyl ether into a nitromethane solution of **2.21** gave red prismatic crystals suitable for single crystal X-ray diffraction. The data were collected at 120 K and solved and refined in the hexagonal space group $P6_3/m$ (R = 9.21%). The asymmetric unit contained 1/6 of the Fe(II) dinuclear triple mesocate comprised of one half ligand and one third of an Fe(II) centre (*Figure 2.3.10.i*).

Bond	Distance (Å)	Atoms	Angle (°)	Atoms	Angle (°)
Fe1-N2	1.958(6)	N2-Fe1-N2'	93.6(3)	N3-Fe1-N3'	95.5(3)
Fe1-N3	1.955(8)	N2'-Fe1-N3	91.2(3)	N3-Fe1-N2	80.2(3)

*Table 2.3.10.i: Table of crystallographically unique Fe-N bond lengths and N-Fe-N bond angles for **2.21** from single crystal X-ray crystallographic data collected at 120 K. The prime symbol (') indicates a symmetry generated atom.*

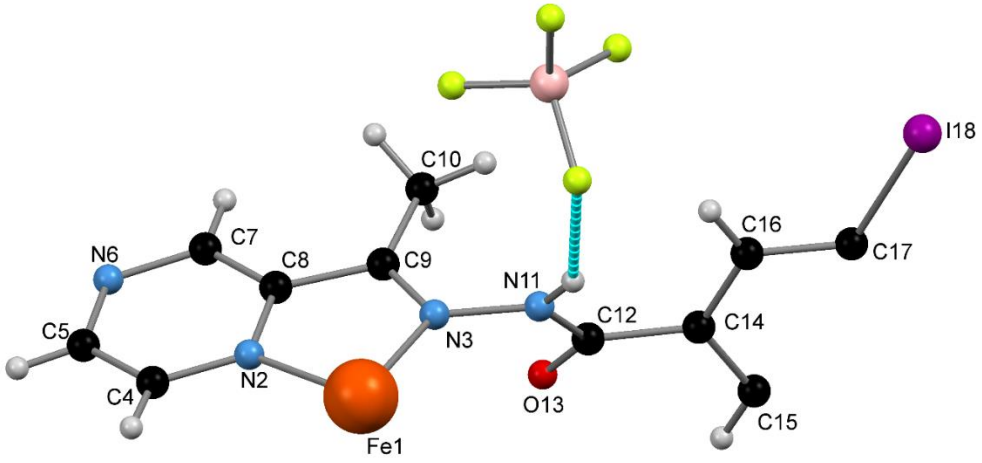

*Figure 2.3.10.i: The asymmetric unit of **2.21** with the non-hydrogen atoms of the complex labeled and the hydrogen bond interaction between the hydrazone moiety and the tetrafluoroborate anion shown in blue. Only one orientation of the disordered tetrafluoroborate anion is shown for clarity.*

The iodine substituent is modelled as disordered over two positions with occupancies of 90% and 10%. The Fe-N bond lengths are indicative of LS Fe(II) at 120 K and are summarized below *(Table 2.3.10.i*). The low octahedral distortion parameter (Σ) of 60° is further evidence of this. The Fe1···Fe1' separation of the mesocate runs parallel to the crystallographic *c*-axis and measures 11.622(4) Å (prime symbol ' denotes symmetry generated atom). The structure of **2.21** is isomorphous with **2.20** (*Figure 2.3.10.ii*) and therefore, only the salient details will be given. The twist of the hydrazone moiety and carbonyl functionality are comparable to **2.19** and **2.20** at 61.9(9)° and 22.9(9)°, respectively. The twisted ligand conformation results in analogous intramolecular hydrogen bond interaction to **2.19** and **2.20** with an H···O separation of 2.942(9) Å and an angle of 125.0(6)°. Like wise, these hydrogen bond interactions are reinforced by analogous edge-to-face C-H···π interactions to **2.19** and **2.20** with an H···π(centroid) separation of 2.850(5) Å and an angle 147.3(7) °.

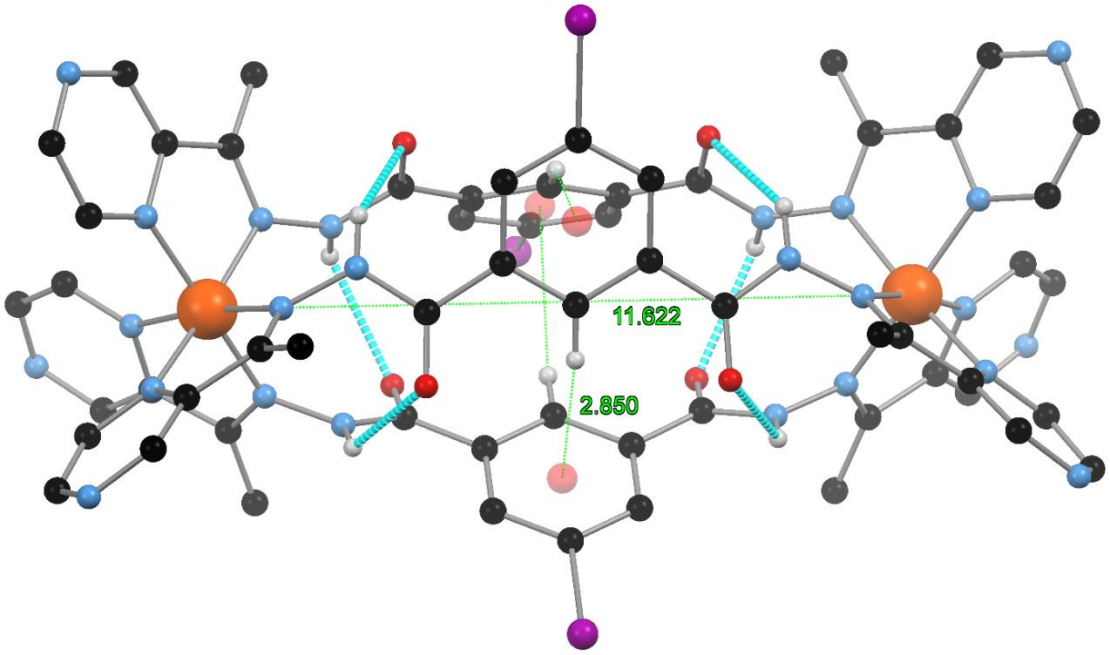

*Figure 2.3.10.ii: The complete structure of the dinuclear triple mesocate **2.21** generated by the action of a mirror plane and a 3-fold rotation axis. The Fe1···Fe1' separation and the three C-H···π interactions are shown in green. Hydrogen atoms tetrafluoroborate anions molecules are omitted for clarity. The six crystallographically identical hydrogen bond interactions are shown in light blue and π(centroid) are represented as red spheres.*

The pyrazine rings π-π stack upon one another with a centroid separation of 4.182(7) Å, noticeably longer than that of **2.19** and similar to that of **2.20**. Much like **2.20**, the opposite faces of the pyrazine rings are involved in this stacking interaction in comparison to **2.20**. This results in the absence of the pyrazine···hydrazide hydrogen bond interaction. Instead a weak C-H···N interaction between C4 and N6 of neighbouring pyrazine rings occurs (*Figure 2.3.10.iii*). The Fe1···Fe1' spacing of the Fe(II) centres coordinated to these pyrazine rings also increases to 9.424(2) Å similar to that of **2.20**. This Fe···Fe separation expansion can be attributed to the incorporation of the iodine functionality on C17. These iodine atoms are orientated into the hexagonal channel towards one another with an I18···I18 separation of 3.985(2) Å resulting in a trimeric type II halogen bond analogous to **2.20**.[56]

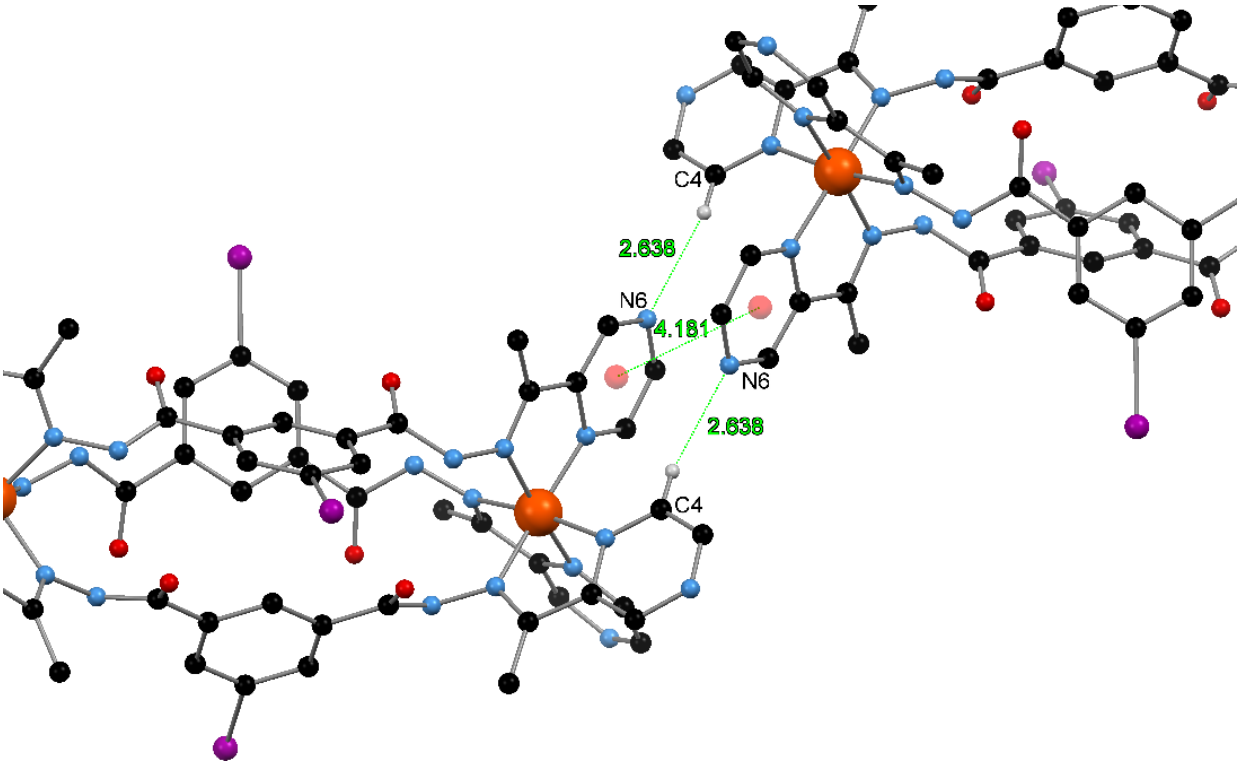

Figure 2.3.10.iii: The pyrazine π-π stacking interactions occurring between two neighbouring complexes with the centroid···centroid separation shown in green. The π-π interaction is reinforced by two C-H···N interactions also shown in green and π(centroid) represented as red spheres. Hydrogen atoms not participating in the illustrated interactions, and tetrafluoroborate anions omitted for clarity.

The hydrazide hydrogen bond donor forms an interaction with a tetrafluoroborate anion with an H···F separation of 2.13(2) Å. This more expanded packing of the mesocates propagates along the *c*-axis resulting in a significantly longer *c*-axis dimension of 34.554(2) Å in comparison to **2.20** (24.9442(4) Å). This expansion is similar to that observed for **2.20** and can similarly be attributed to the formation of a trimeric halogen bonds in the hexagonal channel (*Figure 2.3.10.iv*). There is also a small decrease in the crystallographic *a*- and *b*-axes from 14.340(1) Å for **2.19** to 12.928(3) Å for **2.21**. The compression in the crystallographic *a*- and *b*-axes manifests itself as a more compact one-dimensional channel with a diameter at the closest contact of *ca.* 3.99 Å lined by the tetrafluoroborate anions.

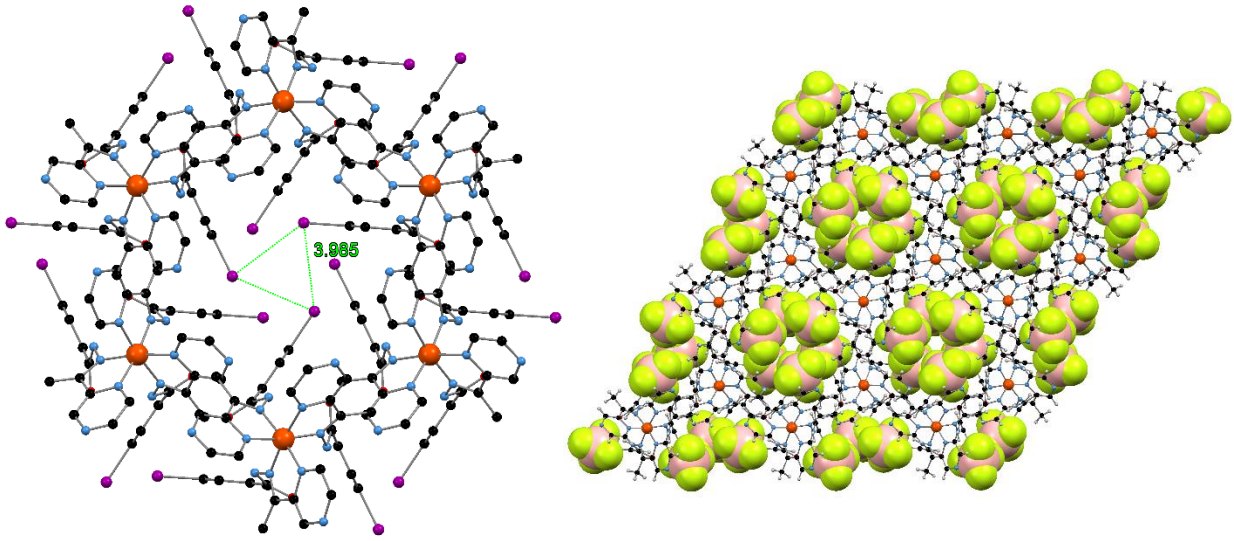

Figure 2.3.10.iv: View down the crystallographic c-axis of the one-dimensional hexagonal channel. The I···I separations of the three iodo substituents in the same plane, forming the trimeric halogen bonding motif are labelled in green. Hydrogen atoms and tetrafluoroborate anions omitted for clarity. (right) View down the crystallographic c-axis showing the tetrafluoroborate anions occupying the hexagonal channel in space filling representation.

There is a significant number of solvent molecules occupying the one-dimensional channel. However, the high symmetry of the space group and the disordered nature of the solvent means it is unable to be modelled satisfactorily and therefore the SQUEEZE[418] function of PLATON[419] was applied (1.2 Å probe). The solvent accessible void was calculated to be 1129 Å^3 and contained 312 electrons. This corresponds to 159 electrons per mesocate complex which can be approximated as one water molecule, one nitromethane and two diisopropyl ether molecules (158 electrons). The

solvent accessible void is only slightly smaller than that of **2.19** because, while the iodine substituents occupy space in the channel, they also cause an expansion down the crystallographic *c*-axis, compensating the decrease in the channel diameter. TGA reveals a mass loss of 4.81% between 41 and 177 °C which corresponds to the loss of one diisopropyl ether molecule which constitutes 4.8% of the mass of **2.21**·$C_6H_{14}O$ and is also observed in the elemental analysis. TGA also reveals that the complex is stable until 200 °C after which there is a rapid decrease in the mass due to decomposition.

2.3.11 $[Fe_2(H_2L2.8)_3](BF_4)_2$, 2.22

H_2**L3.8** and Fe(II) tetrafluoroborate were stirred in nitromethane overnight to give a purple red solution. Vapor diffusion of toluene into the nitromethane solution of **2.22** gave red rod-shaped crystals suitable for single crystal X-ray diffraction. The data were collected at 120 K and solved and refined in the hexagonal space group $P6_3/m$ (R = 7.07%). The asymmetric unit contained 1/6 of an Fe(II) dinuclear triple mesocate comprised of one half of a ligand and one third of an Fe(II) centre (*Figure 2.3.11.i*). The Fe-N bond lengths are indicative of LS Fe(II) at 120 K and are summarized below (*Table 2.3.11.i*). The low octahedral distortion parameter (Σ) of 61° is further evidence of this.

Bond	Distance (Å)	Atoms	Angle (°)	Atoms	Angle (°)
Fe1-N2	1.946(4)	N2-Fe1-N2'	93.8(2)	N3-Fe1-N3'	95.2(1)
Fe1-N3	1.962(4)	N2'-Fe1-N3	91.4(2)	N3-Fe1-N2	80.0(2)

*Table 2.3.11.i: Table of crystallographically unique Fe-N bond lengths and N-Fe-N bond angles for **2.22** from single crystal X-ray crystallographic data collected at 120 K. The prime symbol (') indicates a symmetry generated atom.*

The Fe1···Fe1' separation runs parallel to the crystallographic *c*-axis and measures 11.625(2) Å (prime symbol ' denotes symmetry generated atom). The structure of **2.21** is isomorphous with **2.20** (*Figure 2.3.11.ii*) and therefore, only the salient details will be given. The twist of the hydrazone moiety and carbonyl functionality are comparable to **2.19** and **2.20** at 60.9(6)° and 26.4(7)°, respectively. The twisted ligand conformation results in analogous intramolecular hydrogen bond interaction to complexes **2.19** to **2.21** with an H···O separation of 2.328(3) Å and a angle of 127.7(3)°. Like wise, these hydrogen bond interactions are reinforced by analogous

edge-to-face C-H ···π interactions to complexes **2.19** to **2.21** with an H···π(centroid) separation of 2.928(4) Å and angle 152.7(5)°.

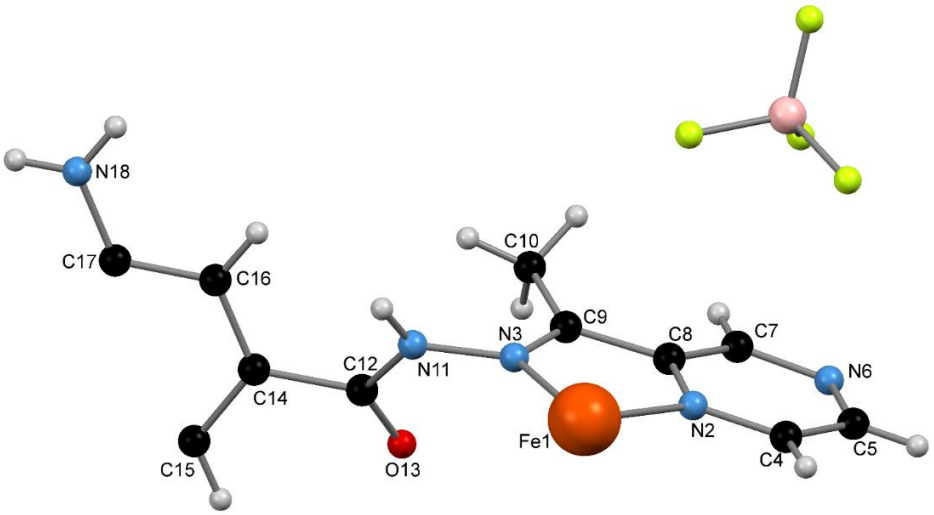

*Figure 2.3.11.i: The asymmetric unit of **2.22** with the non-hydrogen atoms of the complex labeled. Only one orientation of the disordered tetrafluoroborate anion is shown for clarity.*

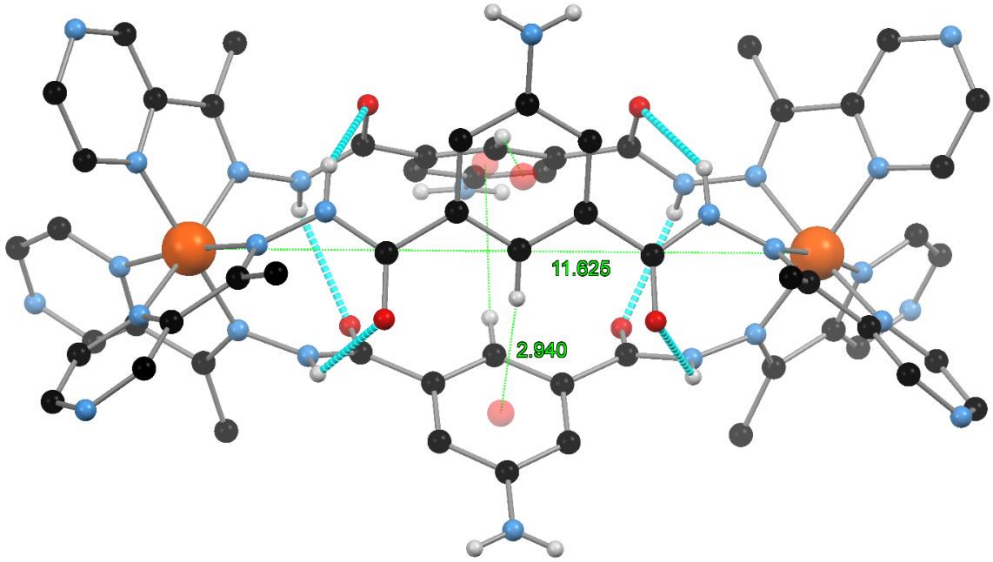

*Figure 2.3.11.ii: The complete structure of the dinuclear triple mesocate **2.22** generated by the action of a mirror plane and a 3-fold rotation axis. The Fe1···Fe1' separation and the three C-H···π interactions are shown in green. Hydrogen atoms not participating in the illustrated interactions and tetrafluoroborate anions are omitted for clarity. The six crystallographically identical hydrogen bond interactions are shown in light blue and π(centroid) represented as red spheres.*

A hydrogen bond interaction occurs between the N6 atom of the pyridine ring and the hydrazide hydrogen atom, H11, on a neighbouring mesocate with an H···N separation of 2.240(5) Å (*Figure 2.3.11.iii*). An off-set π-π stacking interaction between the pyrazine rings of neighbouring mesocates is also evident with a π(centroid)···π(centroid) separation of 3.719(4) Å. This results in off-set packing down the crystallographic *c*-axis. This gives rise to the formation of large hexagonal channels parallel to the crystallographic *c*-axis in a manner analogous to **2.19**.

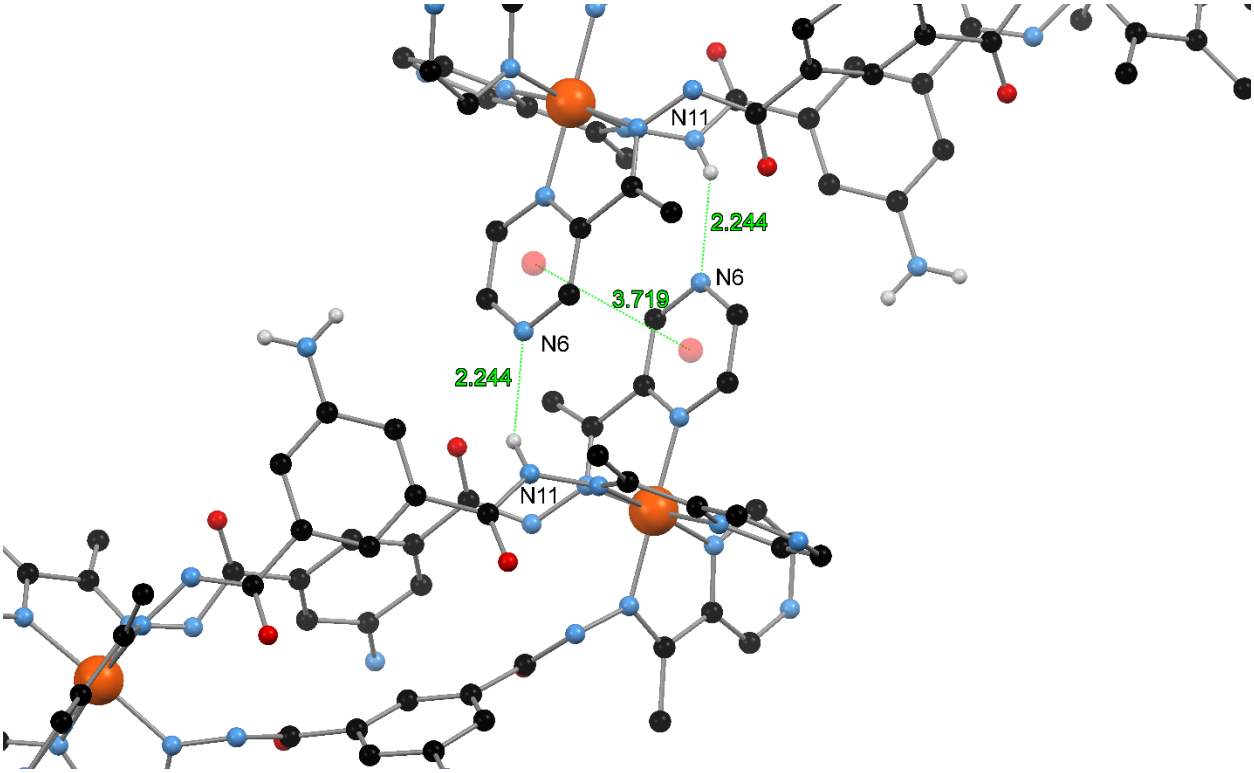

Figure 2.3.11.iii: The pyrazine π-π stacking interactions occurring between two neighbouring complexes with the π(centroid)···π(centroid) separation shown in green while the π(centroid) are represented by red spheres. The π-π interaction is reinforced by two N-H···N hydrogen bond interactions, shown in blue. Hydrogen atoms not participating in the illustrated interactions and the tetrafluoroborate anions are omitted for clarity.

The Fe1···Fe1 spacing of adjacent mesocates is 8.3172(6) Å while the Fe1···Fe1 spacing of mesocates opposite to one another in the channel is 16.579(2) Å. The tetrafluoroborate anions line the sides of the channel while disordered solvent molecules occupy the middle of the channel (*Figure 2.3.11.v*). The high symmetry of the space group and the disordered nature of the solvent means it is unable to be modelled satisfactorily and therefore the SQUEEZE[418] function of

PLATON[419] was applied (1.2 Å probe). The solvent accessible void was calculated to be 1031 Å^3 and contained 330 electrons corresponding to 145 electrons per mesocate. Therefore, the contents of the channel can be approximated as three toluene molecules (150 electrons). TGA showed a 4.97% mass loss between 20 and 152 °C, which approximates one molecule of toluene constituting 5.1% of the mass of **2.22**·C_6H_7, in agreement with the elemental analysis. TGA also revealed that **2.22** is stable until 200 °C after which there is a rapid mass loss due to decomposition.

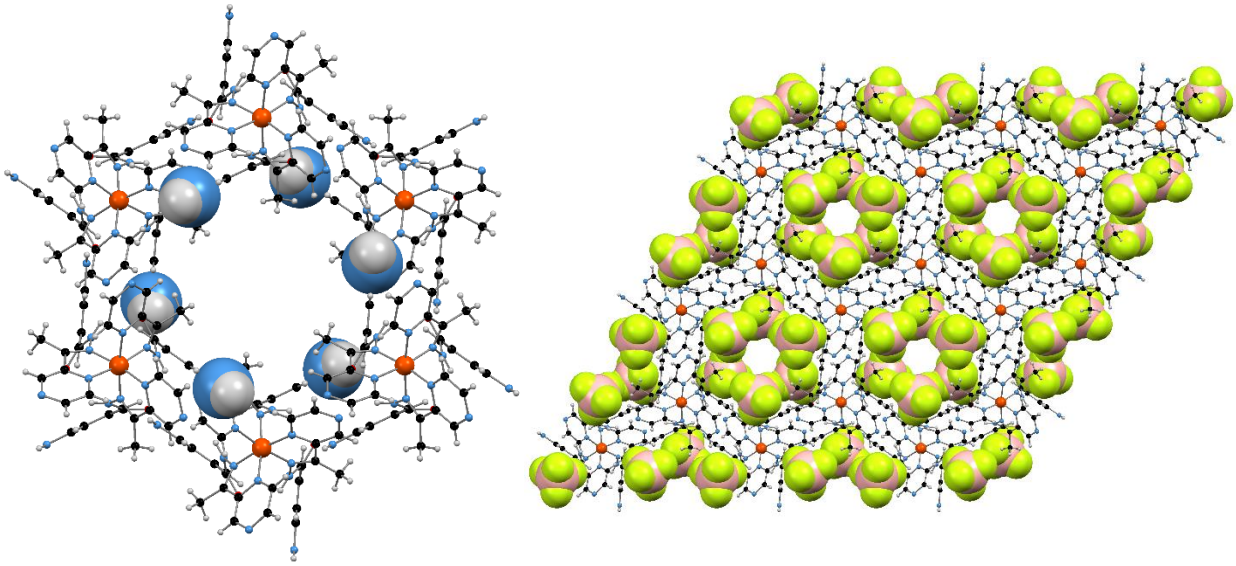

Figure 2.3.11.iv: (right) View down the crystallographic c-axis with the amino substituents shown in space filling representation while the tetrafluoroborate anions are omitted for clarity. (right) View down the crystallographic c-axis with the tetrafluoroborate anions shown in space filling representation to emphasize the polar nature of the hexagonal channel.

2.3.12 $[Fe_2(H_2L2.9)_3](BF_4)_2$, 2.23

Similar ligand solubility issues as for H_2**L2.8** and H_2**L2.7** were encountered with H_2**L2.9**. Therefore, an analogous synthesis procedure to **2.20** and **2.21** was carried out. Vapor diffusion of diisopropyl ether into a nitromethane solution of the complex gave red plate crystals suitable for single crystal X-ray diffraction. The data were collected at 120 K and solved and refined in the triclinic space group *P*-1 (R = 7.04%). The asymmetric unit contains one complete **2.23** mesocate complex and therefore there are two crystallographically unique Fe(II) centres (*Figure 2.3.12.i*). The bond lengths are summarised in *Appendix Table 2.8.5.x*. The Fe-N bonds indicate that both Fe(II) centres exist in the LS state. The low octahedral distortion parameters (Σ) of 58° and 60° for

Fe1 and Fe2, respectively, are further evidence of this. Complex **2.23** crystallised with a number of partial occupancy nitromethane solvent molecules, two of which are modelled as disordered over two positions. The solvent content modelled in the structure can therefore be approximated as **2.23**·1.1$MeNO_2$. Two of the tetrafluoroborate anions also exhibit disorder; one of which is over two positions. The second features significant disorder which is modelled over four positions. One of the methoxy groups is also modelled as disordered, equally over two positions.

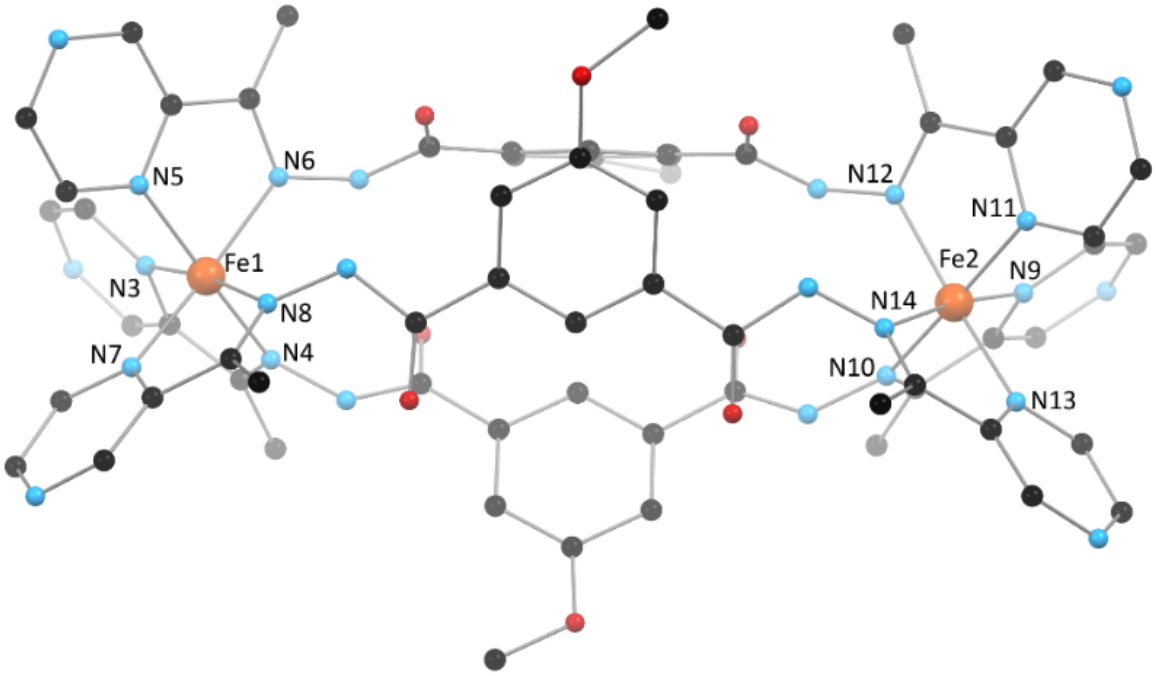

*Figure 2.3.12.i: The asymmetric unit of **2.23** containing one complete complex with two crystallographically unique Fe(II) centres. The disorder of the methoxy group, hydrogen atoms, tetrafluoroborate anions and solvent molecules omitted for clarity.*

The packing of this complex is entirely different to the previously discussed complexes as evidenced by the different space group. The Fe1···Fe2 separation of the mesocate measures 11.624(1) Å and the helical axis is no longer coincident with the crystallographic *c*-axis (*Figure 2.3.12.ii*). There is a range of values for the twist of the hydrazone moieties from 59.7(5) to 64.8(4)° (*Appendix Table 2.8.5.xi*). Like the previous complexes, the carbonyl functionality is not coplanar with the central aromatic rings of the ligands and with an out of plane twist ranging from 19.5(5) to 23.0(6)°. As the previously discussed complexes, intramolecular hydrogen bond interactions occur between the carbonyl oxygen atom and a hydrazide group on an adjacent (inter-

strand) ligand with H···O separations ranging from 2.856(5) to 3.098(4) Å. These hydrogen bond interactions are reinforced by three crystallographically unique reciprocal edge-to-face C-H···π interactions with π(centroid)···π(centroid) separations ranging from 2.834(2) Å to 2.900(2) Å.

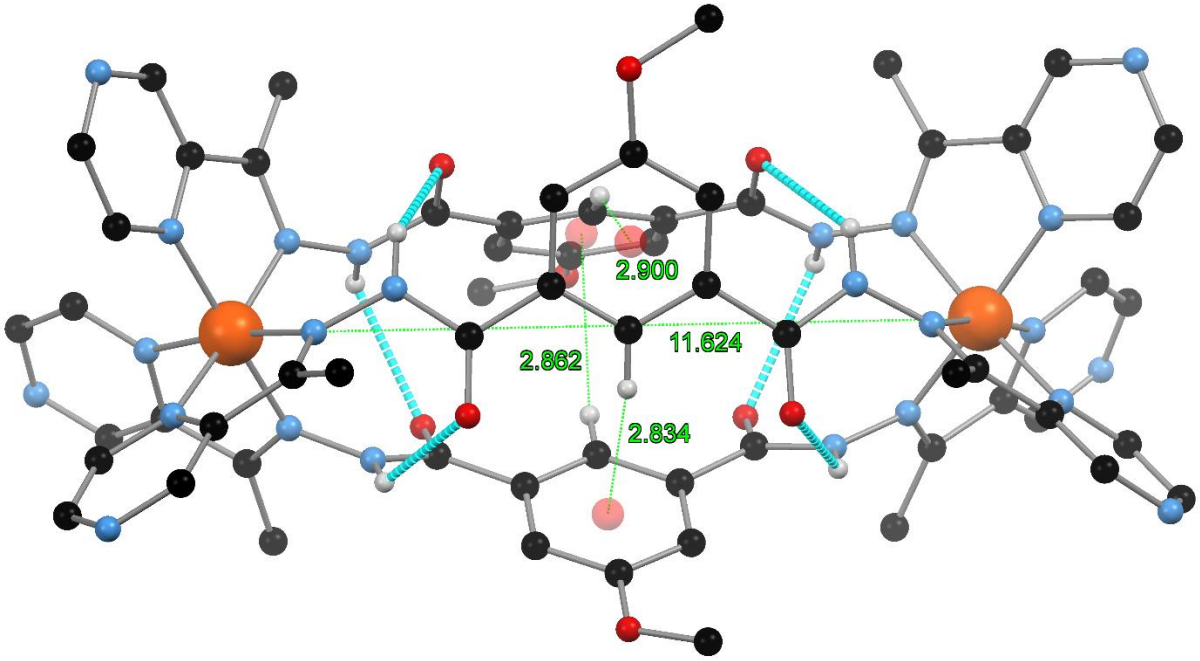

*Figure 2.3.12.ii: The complete structure of the dinuclear triple mesocate **2.23** in the asymmetric unit. The Fe1···Fe2 separation and the three C-H···π interactions are shown in green while the π(centroids) are represented by red spheres. The disorder in the methoxy groups, hydrogen atoms not participating in the illustrated interaction, tetrafluoroborate anions and nitromethane molecules are omitted for clarity. Hydrogen bond interactions shown in light blue.*

The inclusion of the methoxy functionality results in a significantly more sterically encumbered complex. Therefore, the packing observed for **2.19**, **2.20**, **2.21** and **2.22** cannot occur. Instead the hydrazide moieties participate in hydrogen bond interactions with the tetrafluoroborate anions and a nitromethane molecule. Only weak interactions between neighbouring mesocates such as non-conventional hydrogen bonds occur. There are two types of C-H···O non-conventional hydrogen bonds involving the methyl substituent of the hydrazone (*Figure 2.3.12.iii*). These occur between the methyl C-H moiety on one mesocate and the carbonyl oxygen and the methoxy oxygen atoms on a neighbouring mesocate. These interactions result in dimers which pack end-on-end down the crystallographic *c*-axis. Four of the hydrazide N-H moieties form hydrogen bond interactions with the fluorine atoms of the tetrafluoroborate anions. A fifth N-H moiety forms a weak hydrogen

bond interaction with the oxygen atom of a nitromethane solvent molecule. One tetrafluoroborate anion interacts with two ligands of the complex via two non-conventional C-H···F hydrogen bond interactions. One occurs between a C-H moiety of the methyl substituent on the hydrazone moiety and the fluorine atom of the anion. The second occurs between a C-H moiety of the methoxy group and a different fluorine atom on the same anion. These interactions are summarized in *Appendix Table 2.8.5.xii*. The N-H···F interactions range from 2.152(5) to 2.470(5) Å while the non-conventional C-H···F interactions range from 2.293(3) to 2.576(3) Å. These interactions result in the complexes packing in a non-porous manner (*Figure 2.3.12.iv*). While some of the nitromethane solvent molecules were modelled in the crystal structure, there remained a large amount of disordered electron density and therefore the SQUEEZE[418] function of PLATON[419] was applied (1.2 Å probe). The solvent accessible void was calculated to be 1126 Å^3 and contained 345 electrons. This corresponds to 173 electrons per mesocate which can be approximated as two diisopropyl ether and two nitromethane molecules (180 electrons).

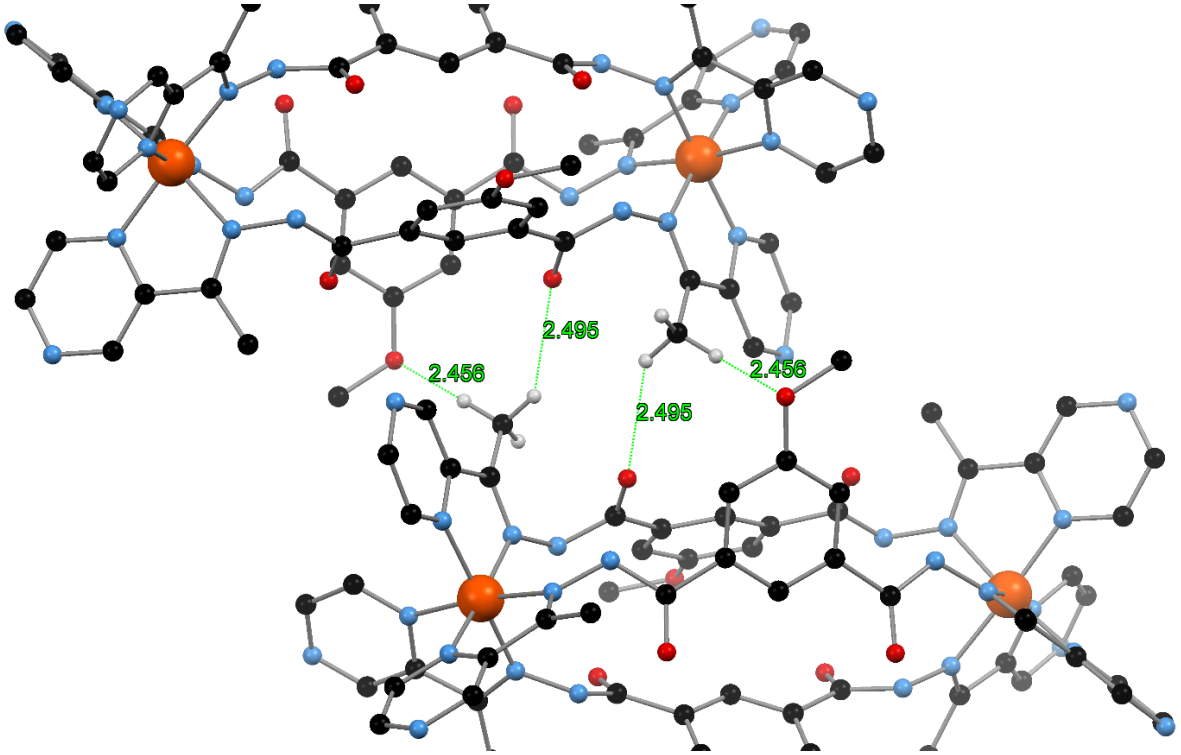

Figure 2.3.12.i: Two complexes interacting via non-conventional C-H···O interactions centred about an inversion centre. H···O separations are shown in green Hydrogen atoms not participating in the illustrated interactions, solvent molecules and tetrafluoroborate anions omitted for clarity.

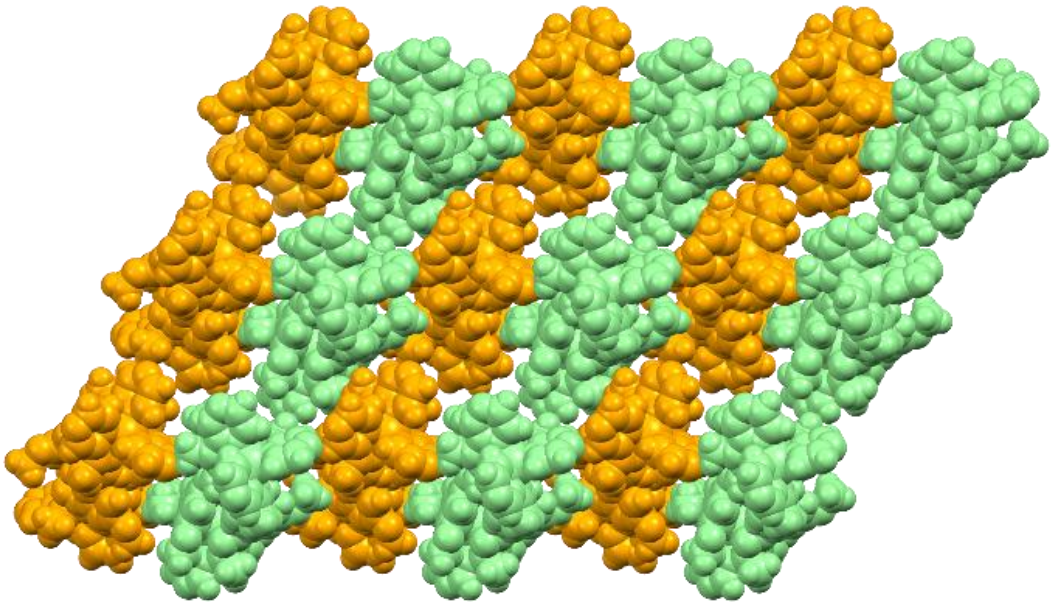

Figure 2.3.12.iv: Space-filling representation highlighting the close packing and the lack of porosity as viewed down the crystallographic c-axis. The complexes shown in orange are related to the complexes shown in green by the action of an inversion centre.

TGA reveals a mass loss of 6.12% between 41 and 177 °C which corresponds to the loss of one diisopropyl ether and one water molecule. These constitute 6.4% of the mass of **2.23**·$C_6H_{14}O$·H_2O and are also observed in the elemental analysis. TGA also reveals that the complex is stable until 200 °C after which there is a rapid mass loss due to decomposition.

2.4 Magnetic susceptibility measurements

2.4.1 $[Fe_4(L2.1)_4]$, 2.12

DC magnetic measurements were carried out on a freshly filtered crystalline sample of **2.12**. The measurements were carried out using a SQUID magnetometer with applied fields of 1000 and 10000 Oe between 1.85 and 400 K with a scan rate of 0.4 K min^{-1}. Across this temperature window, the complex remained diamagnetic and therefore in the LS state (S = 0) (*Figure 2.4.1.i*). This is in agreement with the crystal structure which shows all Fe(II) centres exist in the LS state at 120 K.

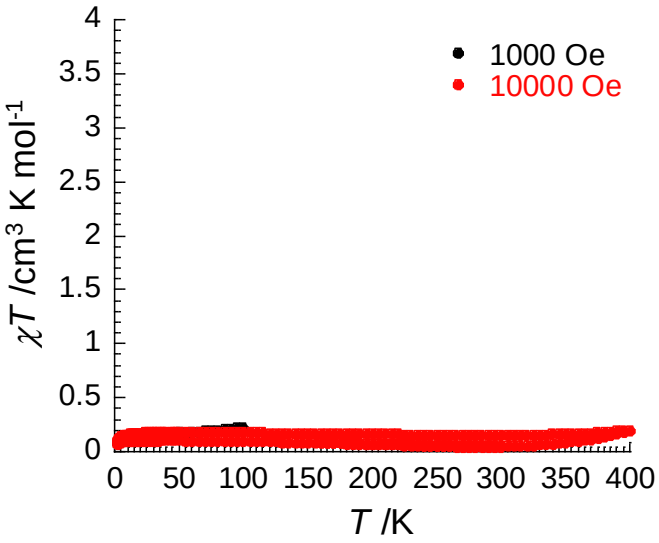

*Figure 2.4.1.i: The χT vs. T plot for **2.12** between 1.85 and 400 K with an applied field of 1000 Oe (black) and 10000 Oe (red) and a scan rate of 0.4 K min^{-1}.*

2.4.2 [Fe$_4$(L2.2)$_4$], 2.13

DC magnetic measurements were carried out on a freshly filtered crystalline sample of **2.13**. The measurements were carried out using a SQUID magnetometer with an applied field of 10000 Oe between 1.85 and 400 K at a scan rate of 0.4 K min^{-1} (*Figure 2.4.2.i*). The sample is diamagnetic until approximately 275 K, in agreement with the crystal structure which shows all Fe(II) centres are in the LS state at 120 K. Between 275 and 340 K the χT value increases to 0.6 cm^3 K mol^{-1} which can be attributed to a partial SCO process. Cooling from 300 to 250 K and the subsequent re-heating cycle approximately follows the original heating trace, indicating the that increase in the χT value can be attributed to thermally induced SCO and not de-solvation induced SCO. Similar behaviour is observed when cooling from 320 to 270 K and the subsequent re heating cycle. Above 340 K the χT value continues to increase to approximately 5.5 cm^3 K mol^{-1} at 400 K. This corresponds to *ca.* 46% of the Fe(II) centres in the HS state (g = 2). While this increase can be regarded as SCO, it is important to note that it is driven by de-solvation. When cooling from 360 to 310 K, a different trace to the original heating cycle is followed, strongly indicative of de-solvation occurring. Similar behaviour was observed when cooling from 380 to 330 K. Upon cooling from 400 K to 1.85 K the χT value follows a more gradual trace, due to de-solvation of the sample. This gradual SCO during the cooling cycle stops at 100 K with a residual χT value of approximately 1.4 cm^3 K mol^{-1} indicating that *ca.* 12% of the Fe(II) centres are remain in the HS

state. The decrease in the χT value to 0.5 cm^3 K mol^{-1} at very low temperatures is due to the ZFS and second order Zeeman effects.

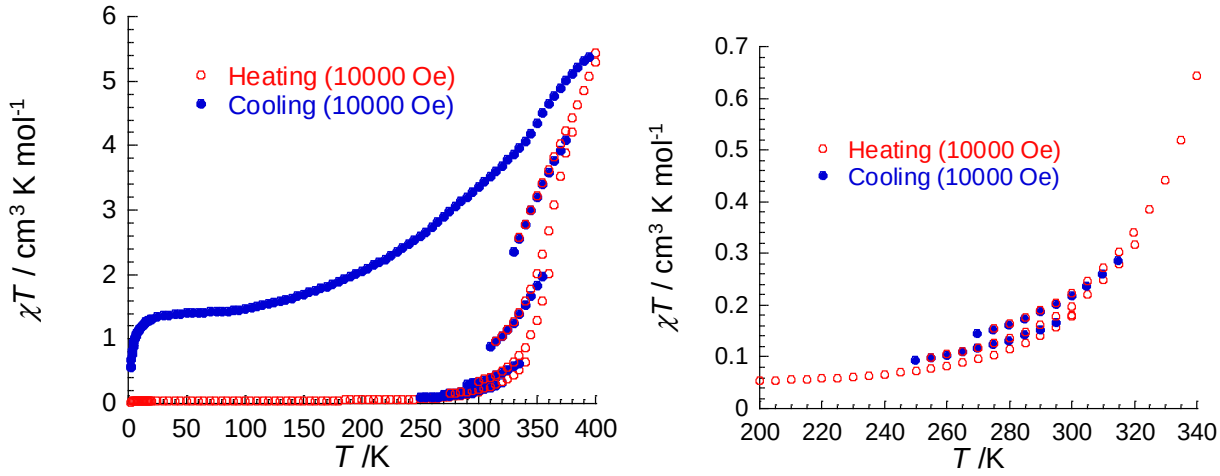

*Figure 2.4.2.i: (left) The χT vs. T plot for **2.13** between 1.85 and 400 K with an applied field of 10000 Oe with a scan rate of 0.4 K min^{-1}. Cooling cycles are shown in blue while the heating cycles are shown in red. (right) The χT vs. T plot for **2.13** between 200 and 340 K, indicating the reproducibility of the heating and cooling cycles between these two temperatures.*

2.4.3 $[Fe_4(L2.5)_4]$, 2.15

DC magnetic susceptibility measurements were carried out on a freshly filtered crystalline sample of **2.15**. The magnetic measurements were carried out using a SQUID magnetometer with applied fields of 1000 and 10000 Oe and a scan rate of 0.4 K min^{-1}. The χT *vs. T* plot reveals that the sample is indeed paramagnetic at 1.85 K (*Figure 2.4.3.i*). This is in agreement with the crystal structure which shows all Fe(II) centres exist in the HS state at 120 K. The χT *vs. T* plot at 10000 Oe shows a gradual increase in the χT value below 65 K with a maxima at 25 K. This behavior can be attributed to crystallite orientation in the presence of a strong magnetic field which is a known phenomenon for HS Fe(II) compounds (*Appendix Figure 2.8.6.i*). At an applied field of 1000 Oe, the complex follows the Curie law until 60 K after which there is a decrease in the χT value due to the effect of ZFS and second order Zeeman effects. The χT value at 270 K is 15.1 cm^3 K mol^{-1} (3.8 cm^3 K mol^{-1} per Fe(II) centre, g = 2.24). This is higher than the theoretical spin only magnetic susceptibility of 12 cm^3 K mol^{-1} for an S = 2 system (3.0 cm^3 K mol^{-1} per Fe(II) centre g = 2). This indicates a mild angular contribution to the magnetic susceptibility common for HS Fe(II).

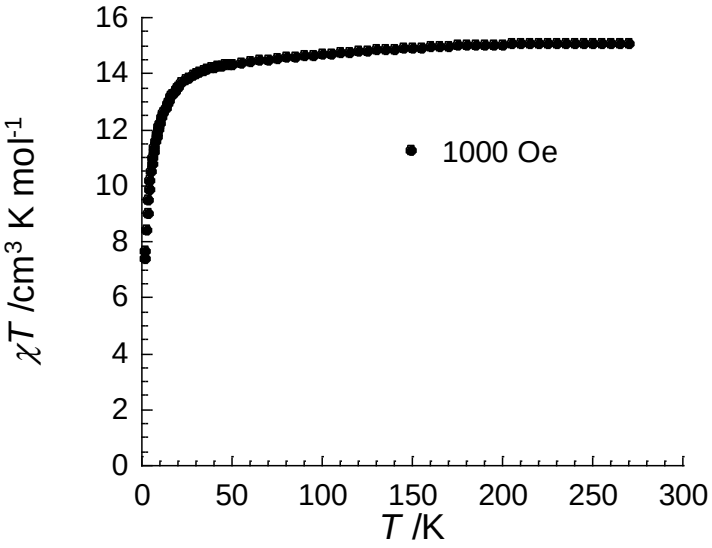

*Figure 2.4.3.i: The χT vs. T plot for **2.15** between 1.85 and 300 K with an applied field of 1000 Oe and a scan rate of 0.4 K min^{-1}.*

As **2.15** is paramagnetic at low temperature, the field dependence of the magnetization at 1.85, 3, 5 and 8 K was measured (*Figure 2.4.3.ii*). At all temperatures saturation of magnetization is not reached at 70000 Oe. The magnetization at 1.85 K is 13.7 μ_B, which is lower than anticipated for four S = 2 centres (19.6 μ_B) as saturation of magnetization is not reached.

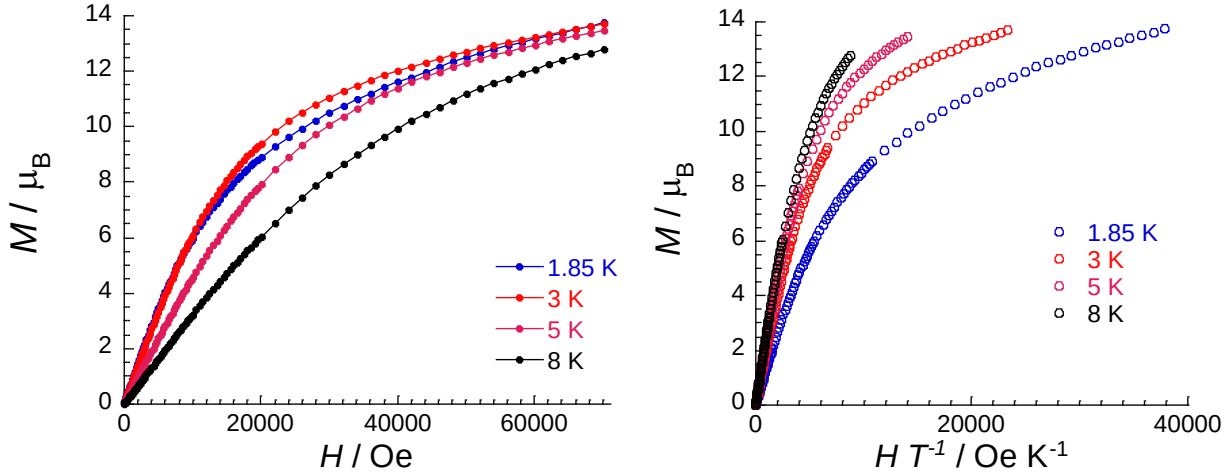

*Figure 2.4.3.ii: The M vs. H plot (right) and M vs. H T^{-1} (left) isotherms at 1.85 (blue), 3 (red), 5 (pink) and 8 K (black) for **2.15**.*

Unexpectedly the 1.85 K isotherm is more gradual than the 3 K isotherm which may be attributed to the crystallite orientation in the higher magnetic fields. The field dependence of the reduced

magnetization reveals the presence of significant anisotropy in the system. This causes the non-superposition of the curves at higher values of $H\,T^{-1}$, which is to be expected for HS Fe(II) centres.

2.4.4 $[Fe_4(L2.1)_4](PF_6)_4$, 2.16

DC magnetic susceptibility measurements were carried out on a freshly filtered crystalline sample of complex **2.16** using a SQUID magnetometer with an applied field of 10000 Oe and a scan rate of 0.4 K min^{-1} (*Figure 2.4.4.i*). As the sample is heated from 1.85 K, the χT value increases rapidly due to ZFS and second order Zeeman effects from 1.85 cm^3 K mol^{-1} until a plateau is reached at 25 K with a χT value of 2.39 cm^3 K mol^{-1}. This value of the χT is higher than the expected value of 1.50 cm^3 K mol^{-1} (g = 2) for four S = 1/2 Fe(III) centres. This is in agreement with the crystal structure which shows all the Fe(III) centres are in the LS state at 100 K. Assuming all four Fe(III) centres are in the LS state, g ≈ 2.5. The χT value is constant between 25 and 160 K however, as the sample is heated above 160 K it begins to gradually increase.

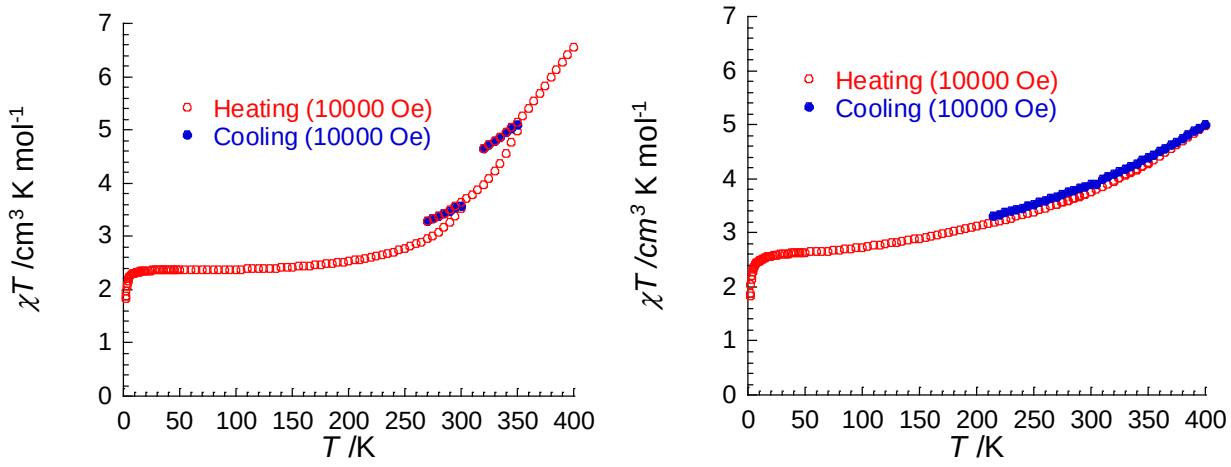

Figure 2.4.4.i: The χT vs. T plot for the solvated (left) and sample dried under vacuum (right) for ***2.17*** *with an applied field of 10000 Oe and a scan rate of 0.4 K min^{-1}. The heating cycles are shown in red and the cooling cycles are shown in blue.*

At 300 K the sample is cooled back to 270 K and then the heating of the sample is continued. While the χT value decreases upon cooling, it follows a different trace, indicative of at least partial de-solvation of the complex. At 350 K the sample is cooled to 320 K. Much like the previous cooling cycle, the χT value decreases upon cooling however it follows a different trace to the initial heating cycle, indicative of further de-solvation of the sample. At 400 K the χT value is 6.54 cm^3 K mol^{-1}, significantly lower than the expected 17.5 cm^3 K mol^{-1} for four S = 5/2 centres (g = 2).

Therefore, the SCO behavior exhibited by **2.17** is broad and intrinsically linked to the de-solvation of the sample. The sample **2.17** was then dried under vacuum at 50 °C and remeasured between 1.85 and 400 K with an applied field of 10000 Oe and a scan rate of 0.4 K min^{-1} (F*igure 2.4.4.i*). The χT value increased rapidly from 2.64 cm^3 K mol^{-1} at 1.85 K to 3.4 cm^3 K mol^{-1} at 40 K due to ZFS and second order Zeeman effects. This χT value is significantly higher than expected for four $S = 1/2$ centres ($g = 2$) and therefore $g \approx 2.6$. At 70 K, the χT value begins to increase very gradually until 400 K with a χT value of 5.05 cm^3 K mol^{-1}. This is significantly lower than the expected χT value of 17.5 cm^3 K mol^{-1} for four $S = 5/2$ centres ($g = 2$). Therefore, much like the solvated sample of **2.17**, the SCO is incomplete by 400 K. Upon cooling of the sample from 400 to 210 K, the χT value decreases following the same trace as the initial heating cycle, indicating this behavior is reversible.

2.5 Gas sorption measurements

The crystals of **2.19** were remarkably stable upon the removal of the solvent from the one-dimensional channels and retained crystallinity post-activation, as verified by PXRD. Therefore, the porosity of **2.19** was probed by gas sorption measurements. Attempts were made to accurately calculate the BET surface area by N_2 and H_2 isotherms at 77 K (*Appendix Figure 2.8.6.i*) but were hindered by slow diffusion kinetics. However, these measurements did provide preliminary confirmation of permanent porosity in **2.19**. Therefore, to assess the quality of sorption performance, single component gas sorption isotherms at 273 and 295 K were measured for the adsorbates CO_2, O_2, N_2, CH_4, C_2H_4 and C_2H_6 (*Figure 3.5.1*). As shown in *Table 2.5.1*, the uptake capacities at 295 K follows the trend $CO_2 > C_2H_4 > C_2H_6 > CH_4 > N_2 > O_2$, however, it should be noted, that the uptake of N_2 and O_2 within **2.19** was negligible. From the range of adsorbates tested, the performance of CO_2 and N_2 are the most striking (*Table 2.5.1*) and reveal significant uptake of CO_2 and very little of N_2. At 295 K and 1 bar, uptake capacities of CO_2 and N_2 are equal to 34.5 and 2.1 cm^3/g, respectively. The minimal uptake of N_2 may be a consequence of strong quadrupole interactions between N_2 molecules and the electrostatic field gradients of the pore window, thus blocking diffusion inside the one-dimensional channel. This behaviour is a highly desirable feature touted for materials used in CO_2 removal from flue gas streams and has been observed in other microporous physisorbent materials.[199, 425-427] Preliminary selectivity for CO_2 over N_2 (S_{CN}) was calculated from the uptakes of CO_2 at 0.15 bar and N_2 at 0.85 bar (resembling the partial pressures

of each gas in flue gas streams), at 295 K. Following this method, a S_{CN} of 48 was calculated for **2.19**, which is higher than those reported for a number of well-known MOFs, including CuBTC, SIFSIX-1-Cu and PCN-61.[428-429]

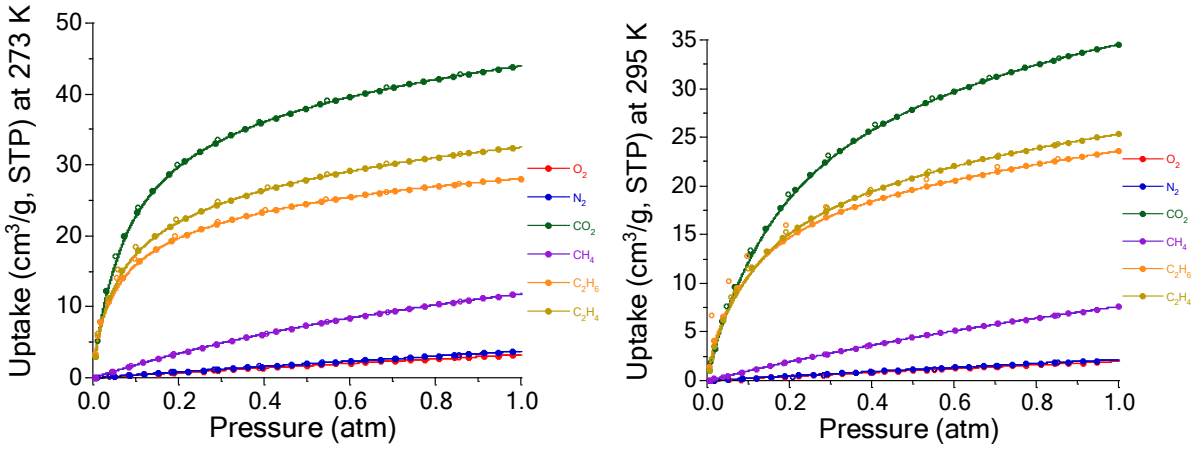

*Figure 2.5.1: Sorption isotherms for **2.19** at 273 K (left) and 295 K (right) for O_2, N_2, CO_2, CH_4, C_2H_6 and C_2H_4.*

To evaluate the strength of interactions between adsorbates and **2.19**, their isosteric heats of adsorption (Q_{st}) were calculated. For the six adsorbates, the magnitude of the Q_{st} values follow the same trend of the uptake capacities (*Table 2.5.1*). The fitting details and parameters for the calculation of the Q_{st} values are detailed in *Table 2.5.1* and *Figures 2.8.7.ii-xiii*.

Void space[a]	**N_2 uptake (cm^3 /g),[b] Q_{st} (-kJ/mol)[c]**	**CO_2 uptake (cm^3 /g),[b] Q_{st} (-kJ/mol)[c]**	**CH_4 uptake (cm^3 g/),[b] Q_{st} (-kJ/mol)[c]**	**C_2H_4 uptake (cm^3 g/),[b] Q_{st} (-kJ/mol)[c]**	**C_2H_6 uptake (cm^3 g/),[b] Q_{st} (-kJ/mol)[c]**	**O_2 uptake (cm^3 g/),[b] Q_{st} (-kJ/mol)[c]**	**CO_2/N_2 selectivity[d]**
26%	2.1 , 18.9	34.5, 36.0	7.5, 19.8	25.3, 35.5	23.6, 26.9	1.9, 17.7	48

Table 2.5.1: [a]The accessible void space and micropore volume were calculated with the program PLATON using a probe radius of 1.2 Å.[419] [b]Uptakes reported at 1 bar and 295 K (cm^3 / g). [c]Sorption data at 273 and 295 K was fitted to a virial function and the isosteric enthalpy of adsorption (Q_{st}, kJ/mol) was calculated using the Clausius–Clapeyron equation. [d]Preliminary selectivity values were calculated as a ratio of gas uptakes at a specified pressure and 295 K from single component N_2 and CO_2 data. Langmuir curves were fitted to the CO_2 isotherms and used to calculate uptake at pressure of 0.15 bar, a linear curve was fit to N_2 data and uptake calculated at 0.85 bar

Notably, for CO_2 the enthalpy at low loading is equal to 36 kJ mol^{-1}, and for N_2 19 kJ mol^{-1}. The stronger Q_{st} value for CO_2 over that for N_2 results from an enhanced interaction between the

polarisable CO_2 molecules and electronegative fluorine atoms of the tetrafluoroborate anions, which line the channel walls. A similar trend has been seen in related MOFs with similar pore chemistry, where accessibility of polarisable CO_2 guests to electronegative atoms of the sorbent promote stronger interactions.[174, 430-431] The strong quadrupole moment of the CO_2 interacts with the polar nature of the walls of the channel and resulting in F···C interactions occurring which stabilises CO_2 over N_2. It is also interesting to note that the Q_{st} for N_2 is higher than that of O_2 which is also observed in zeolites (*Figure 2.5.2*). The reverse is generally observed because O_2 has more electrons and therefore a stronger van der Waals interaction with the framework. However, the pores of **3.19** are lined with polar tetrafluoroborate anions and therefore the quadrupole moment of N_2 interacts with the electric field gradient inside the pore.

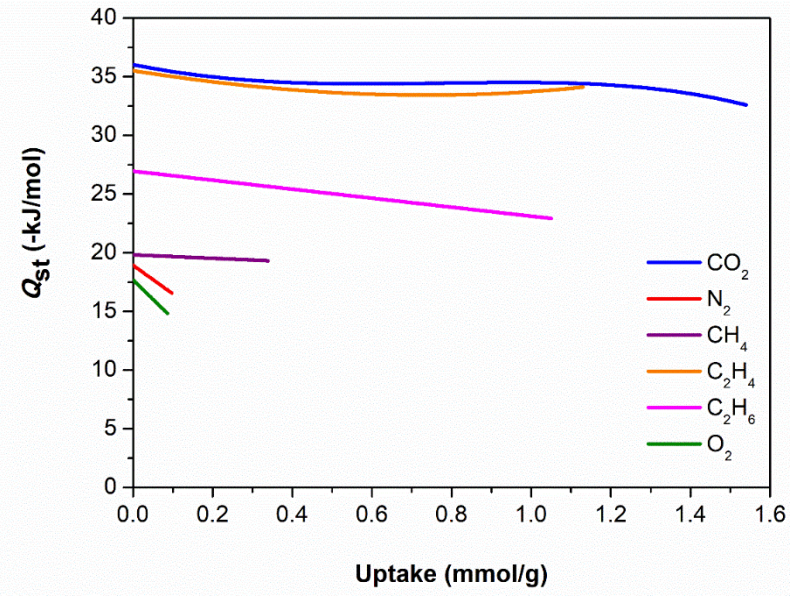

*Figure 2.5.2: The plot of Q_{st} vs. loading for sorbates within **2.19**.*

2.6 Summary and conclusions

Four rigid pyridylhydrazone ligands, three of which are novel have been shown to form tetranuclear grid complexes with Fe(II) and M(III) metal centres (M = Fe(III) and Co(III)) when coordinating in the tridentate anionic form. Despite difficulties associated with both the ligand and complex solubility and the air sensitive nature of the Fe(II) complexes, crystal structures containing the ligands **L2.1**, **L2.2**, **L2.3** and **L2.4** were obtained with Fe(II) to give complexes **2.12**, **2.13**, **2.14** and **2.15**. Complexes **2.12**, **2.14** and **2.15** all formed neutral tetranuclear grid type complexes with *syn* ligand conformations. However, while complex **2.13** also forms a neutral

tetranuclear complex, the conformation adopted by the ligands is different to the previous complexes. Two of the ligands adopt a *trans* conformation while the remaining two adopt the commonly observed *syn* conformation. This change in ligand conformation can be attributed to the occurrence of favorable halogen···halogen, halogen···π and non-conventional hydrogen bond interactions occurring in the crystal packing. Preliminary investigations into the solid-state SCO behavior of complexes **2.12**, **2.13** and **2.15** was carried out using a SQUID magnetometer. Complex **2.12** was diamagnetic across the entire temperature regime. Complex **3.13** exhibits a small degree of thermally induced SCO, however, at elevated temperature desolavtion occurs which strongly impacts the behaviour. Upon cooling back to room temperature, the χT trace follows a significantly different path with a larger proportion of the Fe(II) centres remaining in the HS state. Complex **2.15** was paramagnetic from 1.85 to 300 K and did not exhibit SCO. The Fe(III) analogue of **2.12**, complex **2.16**, was synthesised to investigate Fe(III) SCO. Complex **2.16** is a tetranuclear grid where all **L2.1** ligands adopt the *syn* conformation much like the previous complexes. Much like complex **2.13**, complex **2.16** displays a broad and incomplete SCO at higher temperatures complicated by desolavtion. The Co(III) analogue of **2.16**, complex **2.17** was synthesised by the spontaneous oxidation of Co(II) to Co(III) during the synthesis. This diamagnetic analogue allowed for NMR spectroscopy to be carried out which indicated that, on the NMR time scale, **2.17** is more symmetrical in solution than suggested by the solid-state single crystal structure. While a variety of complexes were synthesised with the pyridylhydrazone ligands coordinating in the tridentate anionic fashion, the insolubility of the complexes, low yield and the poor crystallinity hampered their structural and magnetic characterisations and therefore this work can be viewed as only preliminary due to the lack of corroborating analytical techniques. The high solvent content and typically strong ligand field imbued these complexes with very poor SCO behaviours and a significant alteration to the ligand would need to be made, should this work be continued.

A surprising coordination mode of this family of ligands was observed upon coordination to Fe(II) in the neutral imino-keto form. Instead of the expected tridentate coordination mode, the ligand coordinated in a bidentate mode. This resulted in the formation of a dinuclear triple mesocate, **2.18**. Substituting the pyridine ring for a pyrazine ring in complex **2.19** resulted in the formation of a similar dinuclear mesocate with hydrogen bonds between the hydrazide moieties and the pyrazine rings of neighbouring mesocates. This resulted in the crystal packing exhibiting one-

dimensional hexagonal channels. Due to the hydrogen bonding and π-π stacking interactions, the crystals were exceptionally stable upon the removal of the solvent molecules from the channels and therefore, gas sorption properties of **2.19** were investigated. The single component adsorption isotherms revealed a selectivity for CO_2 over N_2 which can be attributed to the fluorine atoms of the tetrafluoroborate anions lining the channels. Following this result, the effect of the modulation of the functionality at the 5-position of the central aromatic ring of the ligand was investigated. For this, the novel ligands H_2**L2.7**, H_2**L2.8**, H_2**L2.9** and H_2**L2.10** were synthesised featuring bromo, iodo, amino and methoxy substituents respectively. Complexes **2.20** and **2.21** featuring the bromo and iodo substituted ligands respectively crystallise in the same hexagonal space group as **2.19**. However, the packing is subtly different due to the occurrence of halogen bonding interactions, resulting in thinner hexagonal channels. Complex **2.22** containing the amino substituted ligand crystallised in an isomorphous manner to **2.19** and featured one dimensional hexagonal channels of a comparable size. Gas sorption measurements were not carried out for this complex due to difficulties in the isolation of a phase pure bulk sample as the poor solubility of the ligand is believed to hamper the crystallisation. Complex **2.23** exhibited significantly different crystal packing to the previously discussed mesocates due to the more sterically encumbered methoxy substituted ligand.

2.7 Experimental

2.7.1 General details

All reagents and solvents used were of reagent grade unless otherwise stated and did not require further purification and only distilled water was used. Chemicals were sourced from Sigma Aldrich and AK Scientific and were used as received. All reactions were carried out in air unless otherwise stated. Caution is advised when handling perchlorate salts as they are potentially explosive. Complexes **2.12** to **2.15** were particularly air sensitive in solution and therefore their synthesis and crystallization were carried out under an argon atmosphere in a Jacomex glove box at the Centre de Recherche Paul Pascal, CNRS, University of Bordeaux. Anhydrous solvents packed under argon purchased from Sigma Aldrich were used inside the glove box.

2.7.2 NMR spectroscopy

^{1}H and ^{13}C NMR measurements were carried out on an Agilent 400 MR spectrometer operating at 400 MHz for ^{1}H and 101 MHz for ^{13}C. Chemical shift values are given in parts per million (PPM).

2.7.3 Melting points

Melting points were carried out on an Electrothermal melting point apparatus and are uncorrected.

2.7.4 Infra-red spectroscopy

FT-IR spectra for organic compounds were recorded a Bruker ALPHA Platinum ATR FT-IR spectrometer measuring in the range 4000-450 cm^{-1}. The following abbreviations were used to describe the signals: s (strong), m (medium), w (weak), br (broad).

2.7.5 Mass-spectrometry

Mass spectrometry experiments were carried out on a Bruker maXis 4G time of flight spectrometer operating in ESMS+ mode by Dr Amelia Albrett, Dr Amanda Ingles and Dr Marie Squire. Values are given as MNa^{+} or MH^{+} (unless otherwise stated).

2.7.6 Thermal gravimetric analysis

TGA measurements were performed on an Alphatech SDT Q600 TGA/DSC under an inert nitrogen atmosphere. Samples were heated from 20 °C to 800 °C at a rate of 1.5 °C min^{-1}. TGA was not performed on perchlorate salts.

2.7.7 Elemental analysis

For C, H, N analysis samples were sent to Cambell Microanalytical Laboratories, Otago University, Dunedin. Samples were dried to constant weight before analysis.

2.7.8 Single crystal X-ray diffraction

Single crystal X-ray diffraction for complexes **2.12**, **2.14** and **2.15** was carried out at Centre de Recherche Paul Pascal on a Bruker APEX-II CCD using monochromatized Mo-Kα (λ = 0.71073 Å) as the radiation source. Single crystal X-ray diffraction for complex **2.13** was carried out at l'Institut des Sciences Moléculaires, University of Bordeaux on a Bruker APEX-II CCD using monochromatized Cu-Kα (λ = 1.54178 Å) as the radiation source. Single crystal X-ray diffraction

for complexes **2.16** to **2.18** was carried out at the Australian Synchrotron. Single crystal diffraction data for complexes **2.19** to **2.23** was carried out at the University of Canterbury on an Agilent Supernova diffractometer with an ATLAS CCD area detector using a graphite monochromatized Cu-Kα (λ = 1.54178 Å) radiation source. Structures were solved using intrinsic phasing with SHELXT[432] and refined in OLEX2[420] using all data (unless otherwise stated) by full matrix least-squares procedures with SHELXL-97.[433] Non-hydrogen atoms were refined with anisotropic displacement parameters unless otherwise stated. Hydrogen atoms were placed in calculated positions with isotropic displacement parameters 1.2 times the equivalent of their carrier atoms. The functions minimized were $\Sigma w(F^2_o-F^2_c)$ with $w = [\sigma^2(F^2_o) + aP_2+bP]^{-1}$ where $P = [\max(F_o)^2+2F^2_c]/3$. If the solvent was highly disordered and unable to be modelled atomically, the SQUEEZE[418] function of PLATON[419] was applied. All crystallographic information Files (CIF) are included as electronic supporting information.

2.7.9 Powder X-ray diffraction

PXRD for the freshly isolated and activated samples of **2.19** was carried out on an Agilent Supernova diffractometer with an ATLAS CCD area detector using graphite monochromatized Cu-Kα (λ = 1.54178 Å) as the radiation source, operating in the PXRD mode. Samples were prepared by grinding crystals of **3.19** and packing inside an open glass tube. A baseline correction was manually applied using the baseline feature within the CrysAlis^{Pro} analysis software.

2.7.10 Magnetic susceptibility measurements

Magnetic susceptibility measurements were carried out using a Quantum Design SQUID magnetometer MPMS-XL (CRPP) operating between 1.8 and 400 K for applied DC fields ranging from 0 to 7 T. Samples were entered into the SQUID magnetometer and centred at 100 K. Measurements in solid state were performed on microcrystalline samples that were filtered from the mother liquor and dried in air less than two minutes prior to its introduction at 200 K in the magnetometer. These solid samples were introduced in polypropylene bags (3 × 0.5 × 0.02 cm) for measurements. Magnetic measurements were carried out with applied fields of 1000 and 10000 Oe and a scan rate of 0.4 K min^{-1}.

2.7.11 Gas sorption measurements

Gas sorption isotherms for complex **2.19** were carried out on a Quantachrome Autosorb iQ2 instrument using ultrahigh-purity gases. After soaking in DCM for one week and regularly exchanging the solvent, **2.19** was then transferred to a pre-weighed analysis tube and activated by heating at 70 °C for 8 hours. Measurements were carried out at Massey University by Prof. Shane Telfer and Omid Qazvini.

2.7.12 Ligand synthesis

2.7.12.i Dimethyl isophthalate

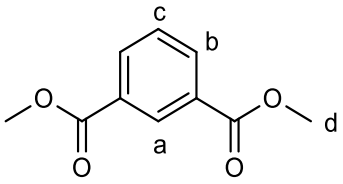

Dimethyl isophthalate was synthesised following a literature preparation.[434] Isophthalic acid (3.1 g, 27 mmol) was added to dry methanol (120 mL) and concentrated sulfuric acid (0.5 mL) and heated at reflux overnight. The solvent was removed under reduced pressure and the organic residue was extracted with DCM (200 mL) and washed with brine (100 mL) and a saturated $NaHCO_3$ solution (100 mL). The organic layer was dried over $MgSO_4$ and the solvent was removed under reduced pressure to give a white solid (3.1 g, 16 mmol, 59% yield).

M.pt. 63 °C Lit. 68 °C

^{1}H NMR: δ_H (400 MHz, $CDCl_3$) 3.94 (s, 6 H, H_D) 7.53 (t, J = 7.63 Hz, 1 H, H_c) 8.09 - 8.31 (m, 2 H, H_b) 8.68 (s,1 H, H_a)

2.7.12.ii Isophthaloyl hydrazide

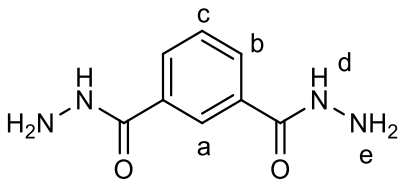

Isophthaloyl hydrazide was synthesised following a literature preparation.[434] Dimethyl isophthalate (1 g, 5 mmol) was dissolved in warm ethanol (5 mL). Hydrazine monohydrate (2 mL, 41 mmol) and the solution was heated at reflux for approximately 4 hours. A white precipitated formed which was separated by filtration once the solution was cooled to room temperature. The white solid was washed with water then cold ethanol and air dried (0.31 g, 1.6 mmol, 32% yield).

M.pt. 222 °C Lit. 224 °C

^{1}H NMR: δ_H (400 MHz, [D_6]-DMSO) 9.78 (br. s., 2 H, H_d), 8.23 (s, 1 H, H_a), 7.89 (d, J = 8.00 Hz, 2 H, H_b), 7.49 (t, J = 8.00 Hz, 1 H, H_c), 4.49 (s, 4 H, H_e)

*2.7.12.iii bis(1-(pyridin-2-yl)ethylidene)isophthalohydrazide, H_2**L2.1***

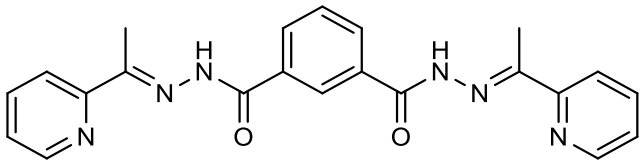

H_2**L2.1** was synthesised following a literature preparation.[402] Isophthaloyl hydrazide (0.5 g, 2.6 mmol) was suspended in ethanol (50 mL). 2-Acetylpyridine (0.67 mL, 6 mmol) was added and the suspension was heated at reflux overnight. The white suspension was then cooled to room temperature and the solid was separated by filtration and washed with ethanol (3x10 mL) then diethyl ether (10 mL) to give a white powder (0.81 g, 2.0 mmol, 77% yield).

M.pt. 225 °C Lit. not reported

The insolubility of the ligand prevented analysis via NMR spectroscopy

ESI-MS: meas. 401.1724 ($[M+H]^+$), $[C_{22}H_{21}N_6O]^+$ calc. 401.1721

IR: (ν_{max}/ cm^{-1}) 3207 (w, br.), 3033 (w, br.), 1678 (m), 1643 (m), 1617 (w), 1584 (w), 1563 (w), 1519 (s), 1467 (m), 1434 (s), 1368 (m), 1325 (m), 1304 (m), 1290 (m), 1254 (s), 1161 (m), 1120 (m), 1099 (w), 1081 (m), 1044 (m), 1028 (w), 1000 (w), 991 (w), 943 (w), 907 (w), 889 (w), 817 (w), 785 (s), 741 (m), 729 (w), 713 (s), 694 (w), 681 (m), 651 (m), 621 (w), 600 (s)

2.7.12.iv 5-Bromoisophthalic acid

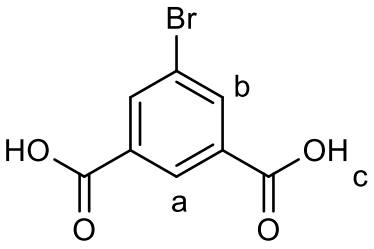

5-Bromoisophthalic acid was synthesised following a literature preparation.[435] N-Bromosuccinimide was recrystallized from water before use. Isophthalic acid (9 g, 54 mmol) was added to concentrated sulfuric acid (28 mL) and stirred at 60 °C to give an orange/yellow solution. N-bromosuccinimide (11.6 g, 65 mmol) was added portion wise over approximately one and a half hours. A further 10 mL of sulfuric acid was added and the resulting white suspension was stirred overnight at 60 °C. The suspension was then poured into ice water and filtered. The white solid was washed with water and dried in an oven at 60 °C for two days to give the crude product (13 g). The crude product was purified by recrystallization from ethyl acetate. (3.3 g, 13 mmol, 24% yield).

M.pt. 272 °C Lit. 274 °C

^{1}H NMR: δ_H (400 MHz, [D_6]-DMSO) 13.54 (br. s., 2 H, H_c), 8.39 (s, 1 H, H_a), 8.22 (s, 2 H, H_b)

2.7.12.v Dimethyl 5-bromoisophthalate

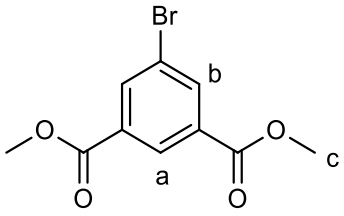

Dimethyl 5-bromoisophthalate was synthesised following a literature preparation.[435] 5-Bromo isophthalic acid (1.0 g, 4.1 mmol) was dissolved in hot methanol (15 mL) and followed by addition of concentrated sulfuric acid (0.75 mL) and the solution was heated at reflux for 12 hours. The solvent was then removed under reduced pressure and the resulting oil was basified with saturated sodium bicarbonate solution (100 mL). The organic layer was extracted with DCM (100 mL) and washed with brine (100 mL). The organic layer was dried over magnesium sulfate and the solvent was removed under reduced pressure to give a pale yellow solid (0.82 g, 3.0 mmol, 73% yield).

M.pt. 87 °C Lit. 88 °C

^{1}H NMR: δ_H (400 MHz, $CDCl_3$) 8.60 (s, 1 H, H_a), 8.35 (d, J = 1.17 Hz, 2 H, H_b), 3.95 (s, 6 H, H_c)

2.7.12.vi 5-Bromoisophthaloyl hydrazide

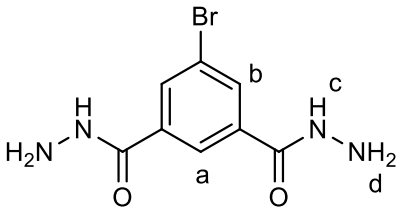

dimethyl 5-bromoisophthalate (0.8 g, 2.9 mmol) was dissolved in ethanol (3 mL) heated at reflux to give a yellow solution. Hydrazine monohydrate was added (0.70 mL, 15 mmol) and the resulting yellow solution which formed a white precipitate after several hours. A further 3 mL of ethanol was added and the white suspension heated at reflux overnight. The suspension was then cooled to room temperature and the white solid was separated by filtration and washed with ethanol (3 x 5 mL) then diethyl ether (2 x1 0 mL) to give a white powder (0.78 g, 2.9 mmol, 100% yield).

M.pt. 280 °C

^{1}H NMR: δ_H (400 MHz, [D_6]-DMSO) 9.93 (br. s., 2 H, H_c), 8.24 (d, J = 1.56 Hz, 2 H, H_a), 8.08 (d, J = 1.17 Hz, 2 H, H_b), 4.55 (br. s., 4 H, H_d)

^{13}C NMR: δ_H (400 MHz, [D_6]-DMSO) 122.02, 125.62, 132.25, 136.05, 164.24

ESI-MS: meas. 272.9983 ($[M+H]^+$), $[C_8H_{10}BrN_4O_2]^+$ calc. 272.9982

IR: (ν_{max}/ cm^{-1}) 3290 (s), 3176 (w), 3071 (w), 1638 (s), 1618 (s), 1571 (m), 1512 (s), 1430 (w), 1340 (m), 1313 (m), 1267(w), 1117 (m), 1005 (m), 914 (w), 888 (m), 788 (w), 769 (w), 741 (m), 731 (m), 675 (s), 624 (s)

*2.7.12.vii 5-bromo-N'1,N'3-bis(pyridin-2-ylmethylene)isophthaloyl hydrazide, H_2**L2.2***

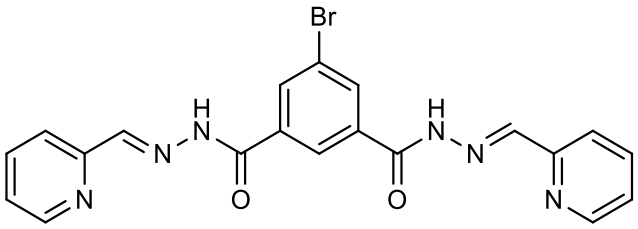

5-Bromoisophthaloyl hydrazide (0.703g, 2.57 mmol) was stirred in ethanol (50 mL) at room temperature. 2-Pyridine carboxaldehyde (564 µL, 5.92 mmol) was added followed by two drops of glacial acetic acid. The resulting white suspension was heated overnight at reflux. Upon cooling to room temperature, the white precipitate was filtered and washed with ethanol (2 x 10 mL) and then diethyl ether (2 x 10 mL) to give a white powder (0.85 g, 1.8 mmol, 74% yield).

M.pt. 256-258 °C

The insolubility of the ligand prevented analysis via NMR spectroscopy

ESI-MS: meas.451.0523 ($[M+H]^+$), $[C_{20}H_{16}BrN_6O_2]^+$ calc. 451.0513, meas. 227.0282 ($[M+2H]^{2+}$), $[C_{20}H_{17}BrN_6O_2]^{2+}$ calc. 227.0283

IR: (ν_{max}/ cm^{-1})3220 (w, br.), 3053 (w, br.), 1649 (s), 1587 (w), 1544 (s), 1470 (m), 1430 (m), 1368 (m), 1341 (w), 1295 (s), 1274 (s), 1249 (s), 1167 (m), 1148 (m), 1064 (m), 994 (m), 951 (m), 890 (m), 785 (s), 753 (w), 729 (s)

*2.7.12.viii bis(1-(pyrazin-2-yl)ethylidene)isophthalohydrazide, H_2**L2.5***

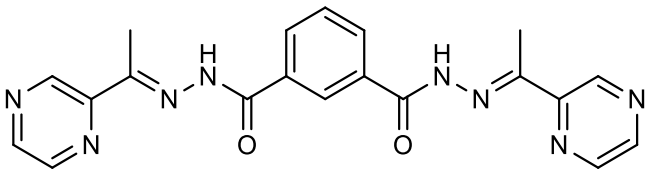

Isophthaloyl hydrazide (0.5 g, 2.6 mmol) was suspended in ethanol (50 mL). 2-Acetylpyrazine (0.67 g, 6 mmol) was added and the suspension was heated at reflux overnight. The white suspension was then cooled to room temperature and the white solid was separated by filtration and washed with ethanol (3 x 10 mL) then diethyl ether (10 mL) to give a white powder (0.85 g, 2.1 mmol 81% yield).

M.pt. 278-283 °C (decomposition)

The insolubility of the ligand prevented analysis via NMR spectroscopy

IR: (ν_{max}/ cm^{-1}) 3160 (w, br.), 2990 (w, br.), 1673 (m), 1652 (s), 1615 (w), 15334 (s), 1518 (m), 1471 (m), 1425 (m), 1407 (w), 1368 (w), 1322 (m), 1308 (s), 1257 (s), 1171 (m), 1154 (s), 1118 (s), 1089 (s), 1050 (w), 1024 (w), 1014 (s), 1001 (w), 983 (m), 934 (m), 889 (w), 861 (m), 852

(m), 819 (m), 799 (w), 773 (w), 761 (w), 744 (m), 719 (s), 690 (m), 662 (m), 651 (s), 622 (m), 602 (m)

ESI-MS: meas. 403.1634 ($[M+H]^+$), $[C_{20}H_{19}N_8O_2]^+$ calc. 403.1626

*2.7.12.ix 5-Bromobis(1-(pyrazin-2-yl)ethylidene) isophthalohydrazide, H_2**L2.6***

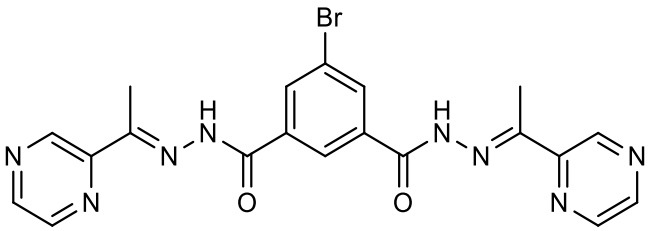

5-Bromoisophthaloyl hydrazide (0.6 g, 2.2 mmol) was stirred in ethanol (50 mL) at room temperature. 2-Acetylpyrazine (0.62 g, 5.1 mmol) was added followed by a catalytic amount of glacial acetic acid. The resulting white suspension was heated at reflux for two days. The suspension was filtered while warm and washed with ethanol (2 x 10 mL) the diethyl ether (10 mL) to give a white powder (1.0 g, 2.1 mmol, 95% yield).

M.pt. 298-300 °C (decomposition)

The insolubility of the ligand prevented analysis via NMR spectroscopy

ESI-MS: meas. 481.0738 ($[M+H]^+$), $[C_{20}H_{18}BrN_8O_2]^+$ calc. 481.0731

IR: (ν_{max}/ cm^{-1}) 3170 (br., w), 3020 (br., w), 1666 (m), 1646 (s), 1615 (w), 1539 (s), 1517 (m), 1470 (m), 1422 (m), 1368 (w), 1317 (m), 1307 (s), 1290 (m), 1268 (m), 1251 (s), 1172 (m), 1156 (m), 1128 (w), 1116 (w), 1075 (m), 1048 (w), 1024 (s), 1012 (w), 987 (w), 897 (m), 857 (m), 793 (m), 762 (w), 728 (s), 681 (m), 657 (br., m), 620 (w)

2.7.12.x Dimethyl 5-iodoisophthalate

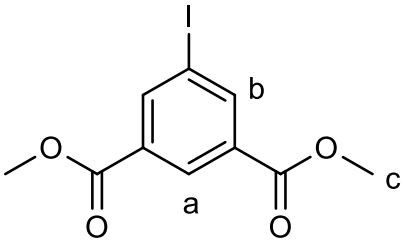

Dimethyl 5-iodoisophthalate was synthesised following a literature procedure.[436] Dimethyl 5-aminoisophthalate (2.4 g, 11 mmol) was added to a solution of hydrochloric acid (6M, 27 mL). An aqueous solution of sodium nitrite (820 mg, 12 mmol, 7 mL) was added dropwise to the suspension of dimethyl 5-amino isophthalate cooled in an ice bath. The suspension was stirred until all solid dissolves. To a cooled aqueous solution of potassium iodide (2.5 g, 15 mmol) was added the aqueous solution of dimethyl 5-diazonium isophthalate gradually. This resulted in an orange suspension which was stirred in an ice bath for 10 minutes and then poured into DCM (50 mL) followed by stirring overnight at room temperature to give a dark green solution. The organic layer was extracted and

washed with water (3x100 mL). The organic layer was dried over magnesium sulfate and the solvent removed under reduced pressure to give and oily brown residue that was purified by column chromatography (silica gel, ethyl acetate/PET ether 1:15) to give a orange powder (0.66 g, 2.1 mmol, 19% yield).

M.pt. 96-100 °C Lit. 103-104 °C

^{1}H NMR: δ_H (400 MHz, $CDCl_3$) 8.64 (1H, s, H_a), 8.55 (2H, s, H_b), 3.96 (s, 6H, H_c)

2.7.12.xi 5-Iodoisophthaloyl hydrazide

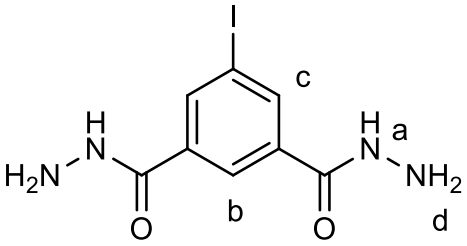

5-Iodoisophthaloyl hydrazide was synthesised following a literature procedure.[437] Dimethyl 5-iodoisophthalate (0.65 g, 2 mmol) was dissolved in ethanol (2 mL) at reflux. Hydrazine mono hydrate (0.5 mL, 10 mmol) was added and the orange solution was heated at reflux overnight. After cooling to room temperature, the precipitate was filtered and then washed with ethanol (3 x 5 mL) and diethyl ether (3 x 5 mL) to give an off-white powder (0.56 g, 1.8 mmol, 90% yield).

M.pt. 255-257 °C Lit. 261-262 °C

^{1}H NMR: δ_H (400 MHz, [D_6]-DMSO): 9.88 (1H, s, H_a), 8.22 (3H, s, H_b and H_c), 4.53 (s, 4H, H_d)

*2.7.12.xii 5-Iodo bis(1-(pyrazin-2-yl)ethylidene) isophthalohydrazide, H_2**L2.7***

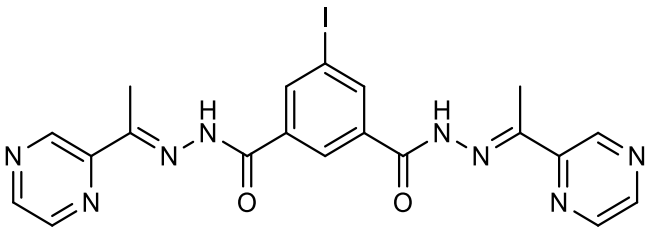

5-Iodoisophthaloyl hydrazide (400 mg, 1.2 mmol) was stirred in 25 mL ethanol at room temperature. 2-Acetylpyrazine (0.35 g, 2.9 mmol) was added followed by a catalytic amount of glacial acetic acid. The resulting white suspension was heated at reflux overnight. The suspension was filtered and washed with ethanol (2 x 5 mL) and diethyl ether (2 x 5 mL) to give an off-white powder (0.56 g, 1.1 mmol, 92% yield).

M.pt. >300 °C

The insolubility of the ligand prevented analysis via NMR spectroscopy

ESI-MS: inconclusive

IR: (ν_{max}/ cm^{-1}) 3171 (br., w), 3019 (br., w), 1665 (m), 1646 (s), 1615 (w), 1537 (s), 1468 (m), 1422 (m), 1369 (m), 1304 (w) 1252 (m), 1171 (s) 1155 (m) 1118 (s) 1073 (m), 1047 (m), 1012 (w), 986 (m), 928 (w), 866 (w), 855 (m), 821 (m), 789 (w), 761 (w), 728 (w), 713 (m), 682 (m), 652 (br., m), 564 (w), 459 (m)

2.7.12.xiii 5-Aminoisophthaloyl hydrazide

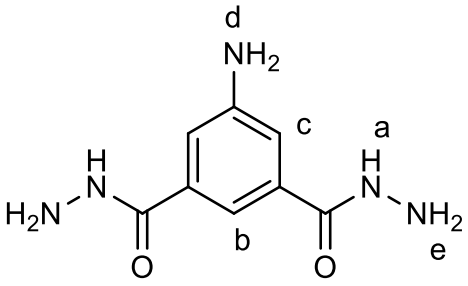

Dimethyl 5-aminoisophthalate (1 g, 4.8 mmol) was dissolved in ethanol (5 mL) at reflux. Hydrazine mono hydrate (1.9 mL, 38 mmol) was added and the resulting white suspension stirred at reflux overnight. After cooling to room temperature, the white precipitate was filtered and washed with ethanol (3 x 5 mL) and diethyl ether (10 mL) to give a white powder (0.97 g, 4.6 mmol, 96% yield).

M.pt. >300 °C

^{1}H NMR: δ_H (400 MHz, [D_6]-DMSO): 9.44 (2H, br., s, H_a), 7.29 (1H, s, H_b), 7.05 (2H, s, H_c), 5.39 (2H, s, H_d), 4.41 (4H, br., s, H_e)

^{13}C NMR: δ_C (101 MHz, [D_6]-DMSO): 167, 149, 135, 115, 113

ESI-MS: meas. 210.0988 ($[M+H]^+$), $[C_8H_{12}N_5O_2]^+$ calc. 210.0986

IR: (ν_{max}/ cm^{-1}) 3416(w), 3303 (br., m), 3219 (br., w), 1667 (m), 1589 (s), 1516 (s), 1309 (m), 1076 (w), 1001 (w), 946 (m), 869 (m), 818 (w), 750 (w), 729 (m), 679 (m), 598 (w), 443 (m)

*2.7.12.xiv 5-Bromo bis(1-(pyrazin-2-yl)ethylidene) isophthalohydrazide, H_2**L2.8***

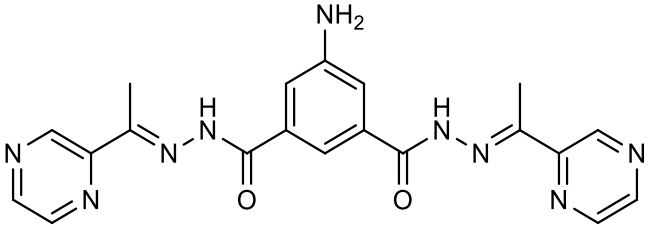

5-Aminoisophthaloyl hydrazide (0.6 g, 2.9 mmol) was stirred in ethanol (50 mL) at room temperature. 2-Acetylpyrazine was added followed by a catalytic amount of glacial acetic acid and the resulting white suspension stirred at reflux overnight. After cooling to room temperature, the precipitate was filtered and washed with ethanol (2 x 5 mL) and then diethyl ether (2 x 5 mL) to give a white powder (1.2 g, 2.9 mmol, 100% yield)

M.pt. >300 °C

The insolubility of the ligand prevented analysis via NMR spectroscopy

ESI-MS: meas. 418.1743 ($[M+H]^+$), $[C_{20}H_{20}N_9O_2]^+$ calc. 418.1735

IR: (ν_{max}/ cm^{-1}) 3396 (w), 3165 (br., w), 2961 (br. w), 1645 (s), 1615 (s), 1518 (s), 1471 (w), 1424 (m), 1346 (m), 1330 (m), 1258 (s), 1172 (m), 1156 (m), 1141 (m), 1118 (w), 1085 (m), 1052 (w), 1013 (m), 986 (w), 899 (w), 880 (w), 855 (s), 802 (w), 716 (w), 731 (w), 687 (m), 662 (br., m), 573 (w), 481 (w), 464 (w)

2.7.12.xv Dimethyl 5-methoxyisophthalate

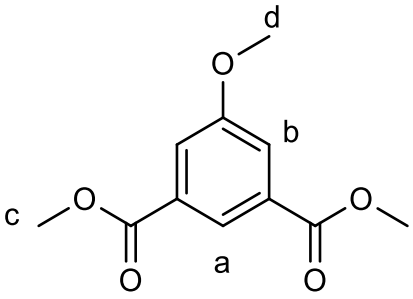

Dimethyl 5-methoxyisophthalate was synthesised following a literature procedure.[438] 5-Hydroxyisophthalic acid (3 g, 16 mmol) and potassium carbonate (6.8 g, 49 mmol) were degassed under an argon atmosphere. Acetone (80 mL) was added followed by dimethyl sulfate (8.6 mL, 91 mmol). The resulting yellow suspension was heated at reflux overnight. After cooling to room temperature, the suspension was poured into water (200 mL) and stirred for 10 minutes. The white precipitate was filtered and recrystallized from hot cyclohexane to give a white powder (2.16 g, 10 mmol, 63% yield).

M.pt. 105-107 °C Lit. 110-111 °C

^{1}H NMR: δ_H (400 MHz, CD_3OD) 8.18 (1H, s, H_a), 7.72 (2H, s, H_b), 3.92 (6H, s, H_c), 3.88 (3H, s, H_d)

2.7.12.xvi 5-Methoxyisophthaloyl hydrazide

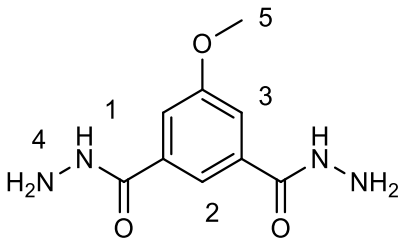

Dimethyl 5-methoxyisophthalate (1.5 g, 6.7 mmol) was dissolved in ethanol (10 mL) at reflux. Hydrazine mono hydrate (1.95 mL, 40 mmol) was added and the resulting yellow solution heated at reflux overnight. During this time a white suspension formed which was subsequently cooled to room temperature and then placed in the fridge for 15 minutes. The white precipitate was filtered and washed with ethanol (2 mL) and diethyl ether (10 mL) to give a white powder (1.4 g, 6.2 mmol, 91% yield).

M.pt. 230-233 °C

^{1}H NMR: δ_H (400 MHz, [D_6]-DMSO) 9.78 (2H, s, H_1), 7.84 (1H, s, H_2), 7.45 (2H, s, H_3), 4.49 (4H, br. s, H_4), 3.81 (3H, s, H_5)

^{13}C NMR: δ_C (101 MHz, [D_6]-DMSO): 166, 159, 135, 119, 115, 56

ESI-MS: meas. 225.0973 ($[M+H]^+$), $[C_9H_{13}N_4O_3]^+$ calc. 225.0983,

IR: (ν_{max}/ cm^{-1}) 3323 (br., w), 3301 (br., w), 1643 (m), 1622 (m), 1592 (s), 1535 (m), 1511 (s), 1468 (w), 1452 (w), 1358 (w), 1314 (s), 1285 (m), 1251 (w), 1164 (m), 1131 (w), 1059 (m), 1006 (m), 978 (m), 907 (m), 870 (m), 821 (w), 728 (w), 687 (s), 621 (m), 594 (s), 543 (s), 437 (w)

*2.7.12.xvii 5-methoxy bis(1-(pyrazin-2-yl)ethylidene) isophthalohydrazide, H_2**L2.9***

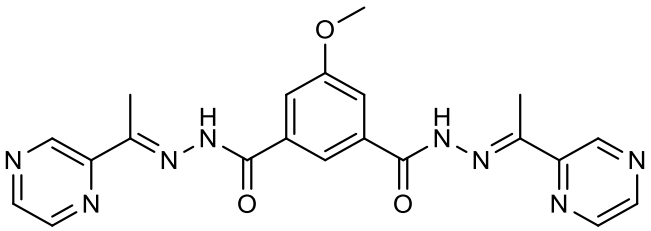

5-Methoxyisophthaloyl hydrazide (0.5 g, 2.2 mmol) was stirred in ethanol (40 mL) at room temperature. 2-Acetylpyrazine (0.63 g, 5.1 mmol) was added followed by a catalytic amount of glacial acetic acid. The resulting white suspension was stirred at reflux overnight. After cooling to room temperature, the precipitate was filtered and washed with ethanol (3 x 5 mL) and diethyl ether (10 mL) to give a white powder (0.88 g, 2.0 mmol, 91% yield).

M.pt. >300 °C

The insolubility of the ligand prevented analysis via NMR spectroscopy

ESI-MS: meas. 433.1738 ($[M+H]^+$), $[C_{21}H_{21}N_8O_3]^+$ calc. 433.1732

IR: (ν_{max}/ cm^{-1}) 3166 (br., w), 3014 (br., w), 2960 (br. w), 1664 (m), 1643 (s), 1596 (w), 1539 (s), 1516 (m), 1496 (m), 1426 (m) 1369 (w), 1338 (s), 1317 (s), 1291 (w), 1254 (s), 1171 (m), 1155 (m), 1141 (m), 1121 (m), 1081 (m), 1047 (m), 1012 (m), 988 w), 903 (w), 877 (w), 853 (m), 840 (s), 762 (w), 730 (w), 687 (m), 662 (br. m), 572 (w), 478 (w)

2.7.13 Complex Synthesis

*2.7.13.i $[Fe_4($**L2.1**$)_4]$, **2.12***

The following procedure was carried out in a glove box under an argon atmosphere. H_2**L2.1** (40 mg, 100 µmol) was added to methanol (3 mL) and stirred at room temperature. Triethylamine (60 µL) was added to give a very pale blue suspension. A solution of $Fe(ClO_4)_2 \cdot H_2O$ (27 mg, 100 µmol) in methanol (2 mL) was added to give a green suspension that was stirred at room temperature for 20 minutes. After standing at room temperature for approximately 10 minutes, the green solid was separated by filtration and allowed to dry on the filter paper to give a dark green powder (31 mg, 17 µmol, 68% yield). Crystals suitable for single crystal X-ray diffraction were obtained via slow evaporation of a DCM solution and vapor diffusion of methanol.

IR (ν_{max}/ cm^{-1}): 3174 (w), 3057 (w), 292 (w), 1667 (s), 1618 (w), 1579 (m), 1560 (m), 1482 (w), 1443 (m), 1414 (w), 1385 (s), 1326 (w), 1307 (m), 1288 (m), 1249 (w), 1200 (m), 1142 (m), 1093 (m), 1074 (w), 1035 (w), 996 (w), 986 (m), 957 (w), 899 (w), 860 (w), 772 (s), 733 (s), 675 (m), 617 (s), 578 (w), 558 (m)

*2.7.13.ii $[Fe_4(\mathbf{L2.2})_4]$, **2.13***

The following procedure was carried out in a glove box under an argon atmosphere. H_2**L32.2** (0.2 g, 0.44 mmol) was stirred in DCM (3 mL) and methanol (3 mL) to give a white suspension. Triethyl amine (18.6 μL, 1.33 mmol) was added and the suspension was stirred for one hour. $Fe(ClO_4)_2 \cdot H_2O$ (0.12 g, 0.44 mmol) dissolved in methanol (2 mL) was added to the ligand suspension resulting in the immediate formation of a green suspension that was stirred at room temperature for one hour. After standing at room temperature for half an hour, the suspension was filtered to give a green powder (78 mg, 0.4 mmol, 22% yield). Crystals suitable for single crystal X-ray diffraction were formed by layering a DMF solution of **2.13** with first a buffer layer of neat DMF then a layer of methanol.

IR: (ν_{max}/ cm^{-1}) 1656 (w, br.), 1596 (w), 1563 (w), 1483 (w), 1415 (m), 1329 (s), 1291 (m), 1241 (w), 1204 (w), 1175 (w), 1151 (w), 1106 (w), 1060 (m), 1016 (w), 917 (w), 888 (w), 742 (s), 665 (m), 579 (m)

Found: C, 44.31 H, 3.85 N, 15.39% $[Fe_4(C_{20}H_{13}BrN_6O_2)_4] \cdot C_3H_7NO \cdot 8.5H_2O \cdot CH_3OH$ requires: C, 44.28 H, 3.54 N, 15.37%

*2.7.13.iii $[Fe_4(\mathbf{L2.3})_4]$, **2.14***

The following procedure was carried out in a glove box under an argon atmosphere. Isophthalolyl hydrazide (39 mg, 0.2 mmol) was stirred in methanol (2 mL) and DCM (1 mL) at room temperature. A solution of 4-chloro-2-pyridinecarboxaldehyde (57 mg, 0.4 mmol) in DCM (3 mL) was added and the resulting yellow suspension was stirred at room temperature for one and a half hours. Triethyl amine (0.12 mL, 0.8 mmol) was added and the suspension was stirred at room temperature for one hour. A solution of $Fe(ClO_4)_2.H_2O$ (55 mg, 0.2 mmol) in methanol (1 mL) was added resulting in the formation of a green suspension that was stirred at room temperature for two hours. The suspension was allowed to stand at room temperature for half an hour and then filtered to give a green powder (60 mg, 30 μmol, 60%). Crystals suitable for single crystal X-ray diffraction were formed by vapor diffusion of water into a DMF solution of the complex.

*2.7.13.iv [Fe_4(**L2.4**)$_4$], **2.15***

The following procedure was carried out in a glove box under an argon atmosphere. Isophthalolyl hydrazide (39 mg, 0.2 mmol) was stirred in methanol (2 mL) and DCM (1 mL) at room temperature. A solution of 6-chloro-2-pyridinecarboxaldehyde (57 mg, 0.4 mmol) in DCM (1 mL) was added and the resulting yellow suspension was stirred at room temperature for one and a half hours. Triethyl amine (0.12 mL, 0.8 mmol) was added and the suspension was stirred at room temperature for one hour. A solution of $Fe(ClO_4)_2.H_2O$ (55 mg, 0.2 mmol) in methanol (1 mL) was added resulting in the formation of green suspension which was stirred at room temperature overnight. The suspension was allowed to stand at room temperature and then filtered resulting in a pale green solid and a green filtrate. The solid was washed with methanol (1 mL) and after several hours, green plate crystals suitable for single crystal X-ray diffraction formed in the filtrate.

*2.7.13.v [Fe_4(**L2.1**)$_4$](PF_6)$_4$, **2.16***

H_2**L2.1** (0.12g g, 0.3 mmol) was added to a solution of $Fe(NO_3)_3{\cdot}9H_2O$ (0.12 g, 0.3 mmol) in methanol (10 mL) and the resulting dark yellow/green solution was filtered. KPF_6 (0.6 g) was added resulting in a green precipitate. The green solid was separated by filtration and washed with water (4 mL) and dried in an oven at 60 °C to give the crude product as a green powder. This crude product was then slurried in 5 mL of water for one hour and filtered then washed with methanol (4 mL) and diethyl ether (4 mL). The product was air dried to give a green powder (0.11 g, 3.6 µmol, 48% yield). Crystals suitable for single crystal X-ray diffraction were obtained by vapor diffusion of diisopropyl ether into an acetonitrile solution of the complex.

Elemental: $[Fe_4(C_{22}H_{18}N_6O_2)_4](PF_6)_4{\cdot}C_6H_{14}O{\cdot}H_2O$ requires: C, 44.48 H, 3.38 N, 13.54 % found: C, 44.47 H, 3.81 N, 13.33 %

IR: (ν_{max}/ cm^{-1}) 1600 (m), 1566 (w), 1496 (w), 1438 (br., m), 1374 (m), 1348 (m), 1325 (m), 1272 (w), 1154 (m), 1102 (w), 1064 (w), 1048 (m), 1023 (w), 835 (s), 775 (m), 738 (m), 720 (m), 687 (w), 662 (w), 644 (w), 556 (s), 500 (w), 470 (w), 415 (w)

*2.7.13.vi [Co_4(**L2.1**)$_4$(PF_6)$_4$, **2.17***

H_2**L2.1** (0.11 g, 0.27 mol) was added to a solution of $Co(NO_3)_2{\cdot}6H_2O$ (83 mg, 0.27 mol) in methanol (8 mL). The resulting orange/brown solution was stirred overnight at room temperature. The solution was filtered and an aqueous solution of KPF_6 (0.3 g) in water (3 mL) was added resulting in a yellow precipitate which was isolated by centrifugation and removal of the

supernatant. The solid was then suspended in water (4 mL) and filtered. The solid was then washed with water (3 x 4 mL) and dried in an oven at 60 °C for half an hour (63 mg 26 μmol, 39% yield). Crystals suitable for single crystal X-ray diffraction were obtained by vapor diffusion of diisopropyl ether into an acetonitrile solution of the complex.

Elemental: $[Co_4(C_{22}H_{18}N_6O_2)_4](PF_6)_4 \cdot CH_3CN \cdot 0.75C_6H_{14}O$ requires: C, 44.92 H, 3.41 N, 13.86 % found: C, 44.96 H, 3.38 N, 13.88 %

IR: (ν_{max}/ cm^{-1}) 1605 (w), 1499 (w), 1440 (w), 1378 (m), 1355 (m), 1278 (w), 1158 (m), 1105 (w), 1068 (w), 1052 (w), 838 (s), 774 (m), 749 (m), 722 (m), 697 (w), 599 (w), 557 (s), 496 (w)

*2.7.13.vii $[Fe_2(H_2$**L2.1**$)_3](PF_6)_4$, **2.18***

H_2**L2.1** (0.12 g, 0.3 mmol) was added to a solution of $FeCl_2$ (38 mg, 0.3 mmol) in methanol (10 mL) and the resulting purple solution stirred at room temperature for one hour. The solution was filtered and KPF_6 (0.4 g) was added to give a red/purple precipitate. The solid was separated by filtration and washed with water (4 mL) then dried in an oven at 60 °C for one hour. Crystals suitable for single crystal X-ray diffraction were formed by vapor diffusion of toluene into a nitromethane solution of the complex.

Elemental: $[Fe_2(C_{22}H_{20}N_6O_2)_3](PF_6)_4 \cdot 2CH_3NO_2 \cdot 10H_2O$ requires: C, 37.21 % H, 3.95 % N, 12.76 % found: C, 37.15% H, 2.76 % N, 12.74 %

IR: (ν_{max}/ cm^{-1}) 1688 (m), 1604 (w), 1477 (m), 1438 (w), 1373 (w), 1336 (w), 1229 (m), 1170 (w), 1112 (w), 1063 (w), 836 (s), 794 (m), 774 (m), 749 (m), 725 (w), 661 (w), 646 (w) 611 (w), 590 (w), 556 (s), 505 (w), 478 (w)

*2.7.13.viii $[Fe_2(H_2$**L2.5**$)_3](BF_4)_4$, **2.19***

H_2**L2.5** (15 mg, 37 μmol) and $Fe(BF_4)_2 \cdot 6H_2O$ (8.4 mg, 25 μmol) were stirred in nitromethane (10 mL) overnight at ambient temperature. The resulting red solution was filtered and vapor diffusion of the filtrate with toluene resulted in red prism crystals suitable for single crystal X-ray diffraction. $[Fe_2(C_{20}H_{18}N_8O_2)_3](BF_4)_4 \cdot C_7H_8 \cdot 8H_2O$ Found: C, 41.99 H, 4.35 N, 17.52% requires: C, 42.30 H, 4.13 N, 17.67%.

IR: (ν_{max}/ cm^{-1}) 3591 (br., w), 3226 (br., w), 1677 (s), 1634 (w), 1602 (w), 1570 (m), 1527 (w), 1505 (s), 1462 (s), 1430 (m), 1408 (w), 1376 (m), 1344 (m), 1290 (w), 1237 (m), 1193 (m), 1150 (w), 1032 (br., s), 914 (w), 849 (m), 796 (w), 763 (m), 731 (m), 668 (w), 645 (m), 600 (w), 505 (m), 462 (m)

*2.7.13.ix $[Fe_2(H_2$**L2.6**$)_3](BF_4)_4$,* ***2.20***

H_2**L2.6** (18 mg, 37 μmol) and $Fe(BF_4)_2 \cdot 6H_2O$ (8.4 mg, 25 μmol) were stirred in acetonitrile (10 mL) for one hour to give a dark red-purple solution. The solvent was removed under reduced pressure to give a purple solid. The purple solid was dissolved in nitromethane and stirred at room temperature for one hour with a pinch of ascorbic acid. After standing at room temperature for one hour the solution was filtered and vapor diffusion of the filtrate with diisopropyl ether gave dark red prism crystals suitable for single crystal X-ray diffraction.

$[Fe_2(C_{20}H_{11}BrN_8O_2)_3](BF_4)_4 \cdot 1.5C_6H_{17}O \cdot 16H_2O$ Found: C, 35.99 H, 3.59 N, 14.05% requires: C, 35.35 H, 4.47 N, 14.34%.

IR: (ν_{max}/ cm^{-1}) 3623 (br., w), 3249 (br., w), 3077 (w), 2972 (w), 1677 (m), 1598 (w), 1573 (w), 1498 (m), 1474 (m), 1423 (w), 1375 (m), 1341 (w), 1296 (w), 1241 (s), 1193 (m), 1057 (br., s), 931 (w), 901 (m), 844 (w), 808 (m), 762 (m), 736 (w), 689 (m), 651 (w), 602 (w), 556 (m), 519 (m), 474 (m)

*2.7.13.x $[Fe_2(H_2$**L2.7**$)_3](BF_4)_4$,* ***2.21***

H_2**L2.7** (20 mg, 37 μmol) and $Fe(BF_4)_2 \cdot 6H_2O$ (8.4 mg, 25 μmol) were stirred in acetonitrile (10 mL) for one hour to give a dark red-purple solution. The solvent was removed under reduced pressure to give a purple solid. The purple solid was dissolved in nitromethane and stirred at room temperature for one hour with a pinch of ascorbic acid. After standing at room temperature for one hour the solution was filtered and vapor diffusion of the filtrate with diisopropyl ether gave dark red block crystals suitable for single crystal X-ray diffraction.

$[Fe_2(C_{20}H_{11}IN_8O_2)_3](BF_4)_4 \cdot 2.25C_6H_{14}O \cdot 18H_2O$ Found: C, 34.06 H, 2.89 N, 12.91% requires: C, 33.98 H, 4.60 N, 12.94%

IR: (ν_{max}/ cm^{-1}) 3171 (br., w), 3019 (br., w), 1665 (m), 1646 (s), 1615 (w), 1537 (s), 1516 (m), 1468 (m), 1422 (m), 1369 (w), 1304 (m), 1252 (m), 1171 (s), 1155 (m), 1118 (m), 1073 (m)1047 (m), 1012 (w), 986 (w), 928 (m), 896 (m), 855 (w), 821 (w), 789 (w), 761 (w), 728 (w), 713 (m), 682 (m), 652 (m), 564 (w), 459 (m)

*2.7.13.xi $[Fe_2(H_2$**L2.8**$)_3](BF_4)_4$,* ***2.22***

H_2**L2.8** (16 mg, 37 μmol) and $Fe(BF_4)_2 \cdot 6H_2O$ (8.4 mg, 25 μmol) were stirred in nitromethane (15 mL) overnight at ambient temperature. The resulting red solution was filtered and vapor diffusion of the filtrate with toluene resulted in red prism crystals suitable for single crystal X-ray diffraction.

$[Fe_2(C_{20}H_{19}N_9O_2)_3](BF_4)_4 \cdot 3C_7H_8 \cdot 29H_2O$ Found: C, 38.94 H, 3.70 N, 14.72% requires: C, 38.75 H, 5.58 N, 15.07%

IR: 3207 (br., w), 1673 (m), 1632 (m), 1598 (s), 1571 (w), 1515 (w), 1492 (s), 1469 (s), 1374 (m), 1343 (w), 1288 (m), 1230 (m), 1190 (m), 1154 (w), 1035 (br., s) 881 (w), 849 (w), 798 (m), 761 (m), 693 (w), 669 (w), 650 (m), 602 (w), 580 (w), 490 (m)

*2.7.13.xii $[Fe_2(H_2$**L2.9**$)_3](BF_4)_4$, **2.23***

H_2**L2.9** (16 mg, 37 μmol) and $Fe(BF_4)_2 \cdot 6H_2O$ (8.4 mg, 25 μmol) were stirred in acetonitrile (10 mL) for one hour to give a dark red-purple solution. The solvent was removed under reduced pressure to give a purple solid. The purple solid was dissolved in nitromethane and stirred at room temperature for one hour with a pinch of ascorbic acid. After standing at room temperature for 1 hour the solution was filtered and vapor diffusion of the filtrate with diisopropyl ether gave dark red block crystals suitable for single crystal X-ray diffraction.

$[Fe_2(C_{21}H_{20}N_8O_3)_3](BF_4)_4 \cdot 3C_6H_{14}O \cdot 25H_2O$ Found: C, 38.76 H, 3.86 N, 13.15 requires: C, 38.71 H, 6.10 N, 13.38%

IR: (ν_{max}/ cm^{-1}) 3432 (br., w), 3523 (br., w), 1791 (w), 1663 (s), 1593 (s), 1524 (w), 1499 (w), 1471 (m), 1409 (w), 1375 (m), 1344 (m), 1312 (w), 1284 (w), 1237 (br., m), 1194 (w), 1152 (w), 1054 (br., s), 890 (w), 847 (w), 794 (m), 761 (m), 746 (m), 693 (w), 675 (w), 650 (m), 602 (m), 520 (m), 469 (m)

2.8 Appendix

2.8.1 Mass spectra

*2.8.1.i [Fe_4(**L2.1**)$_4$](PF_6)$_4$, **2.17***

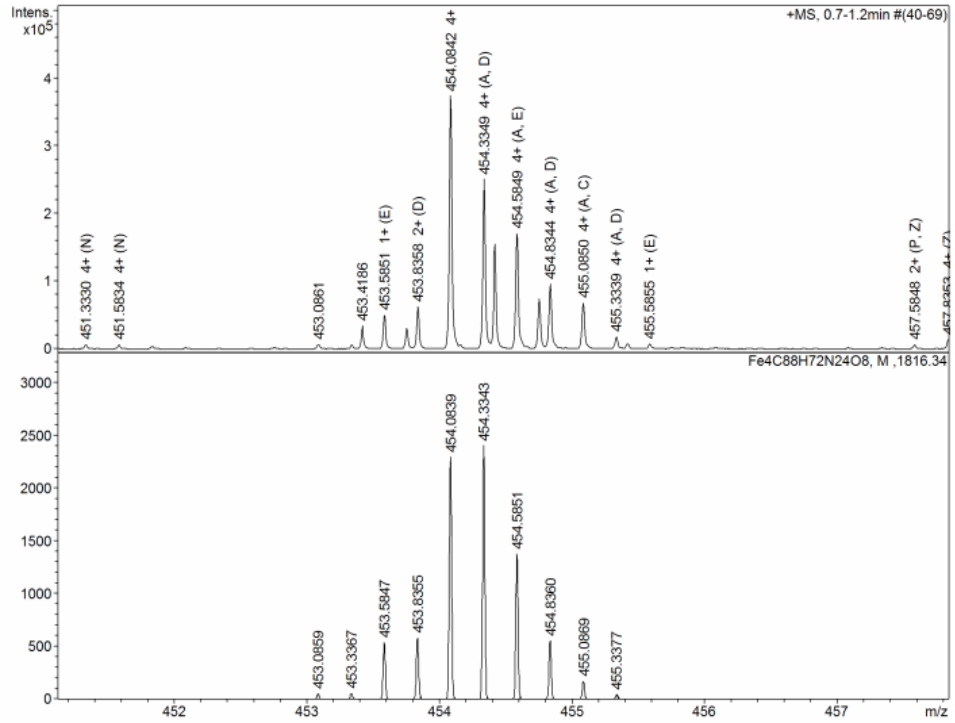

*Figure 2.8.1.i: The experimental (top) and calculated (bottom) isotopic splitting for [Co_4(**L2.1**)$_4$]$^{4+}$for **2.17**.*

Formula	Charge	Experimental	Calculated
$[C_{88}H_{72}Fe_4N_{24}O_8]^{4+}$	+4	454.3349	454.3344

*Table 2.8.1.i: Summary of major peak observed in mass spectrometry analysis for **2.17**.*

*2.8.2.ii Co_4(**L2.1**)$_4$]$(PF_6)_4$, **2.18***

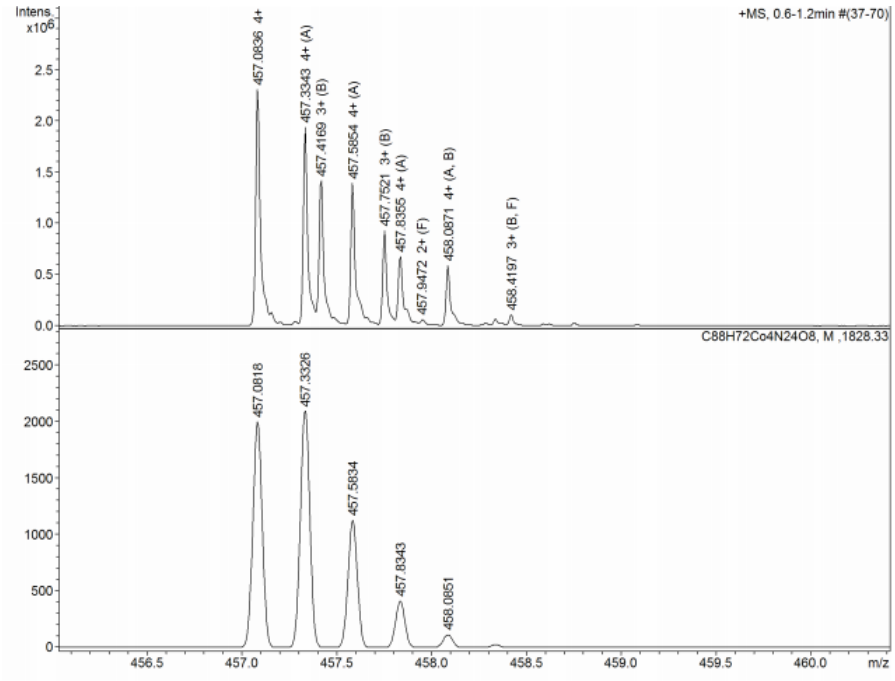

*Figure 2.8.1.ii: The experimental (top) and calculated (bottom) isotopic splitting for $[Co_4$(**L2.1**)$_4]^{4+}$ for **2.18**.*

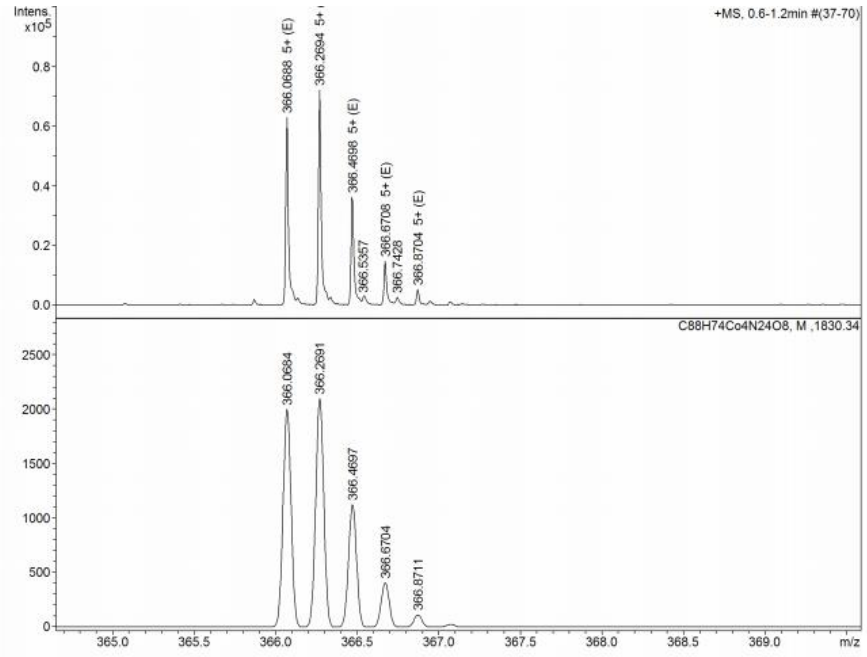

*Figure 2.8.1.iii: The experimental (top) and calculated (bottom) isotopic splitting for $[Co_4$(**L2.1**)$_4$+H]$^{5+}$ for **2.18**.*

Molecular formula	Charge	Experimental	Calculated
$[C_{88}H_{72}Co_4N_{24}O_8]^{4+}$	+4	457.0836	457.0818
$[C_{88}H_{74}Co_4N_{24}O_8]^{5+}$	+5	366.0688	366.0684

*Table 2.8.1.ii: Summary of major peaks observed in mass spectrometry analysis for **2.18**.*

2.8.2 NMR spectra

2.8.2.i $[Co_4(\mathbf{L2.1})_4](PF_6)_4$, ***2.18***

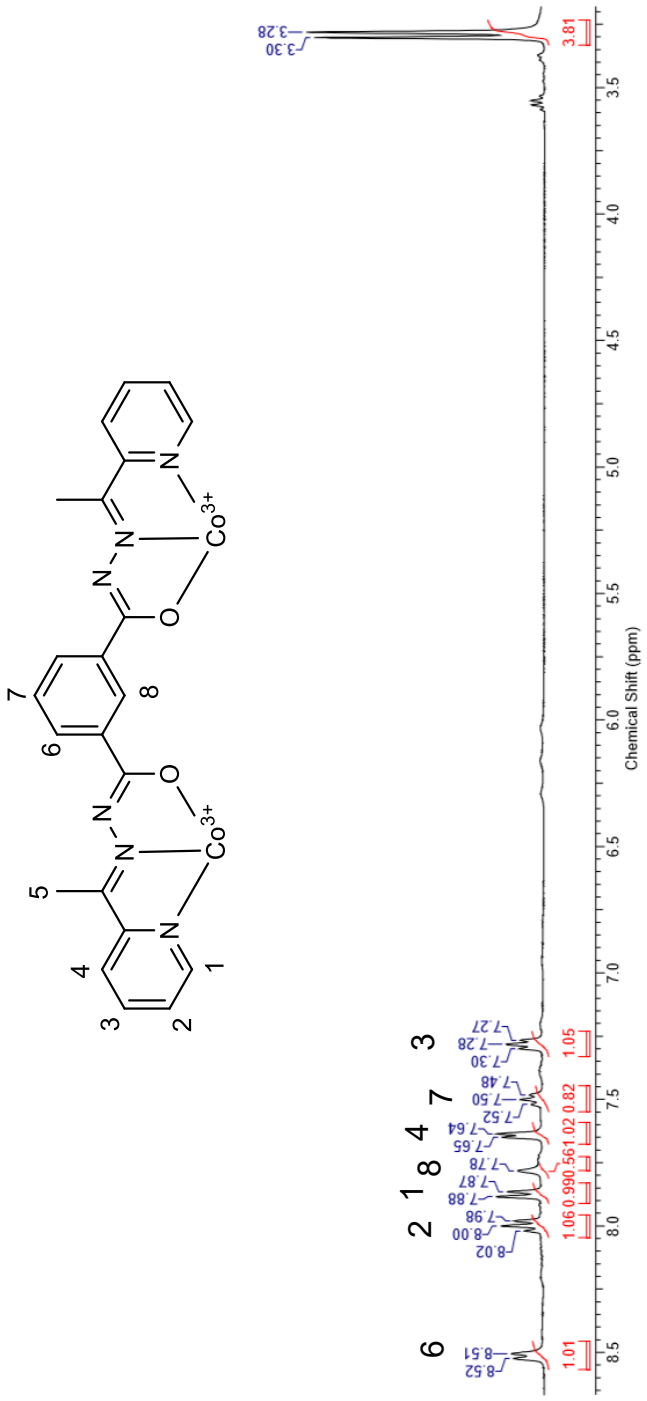

*Figure 2.8.2.i: ^1H NMR spectrum of **2.17** at 25 °C in CD_3CN.*

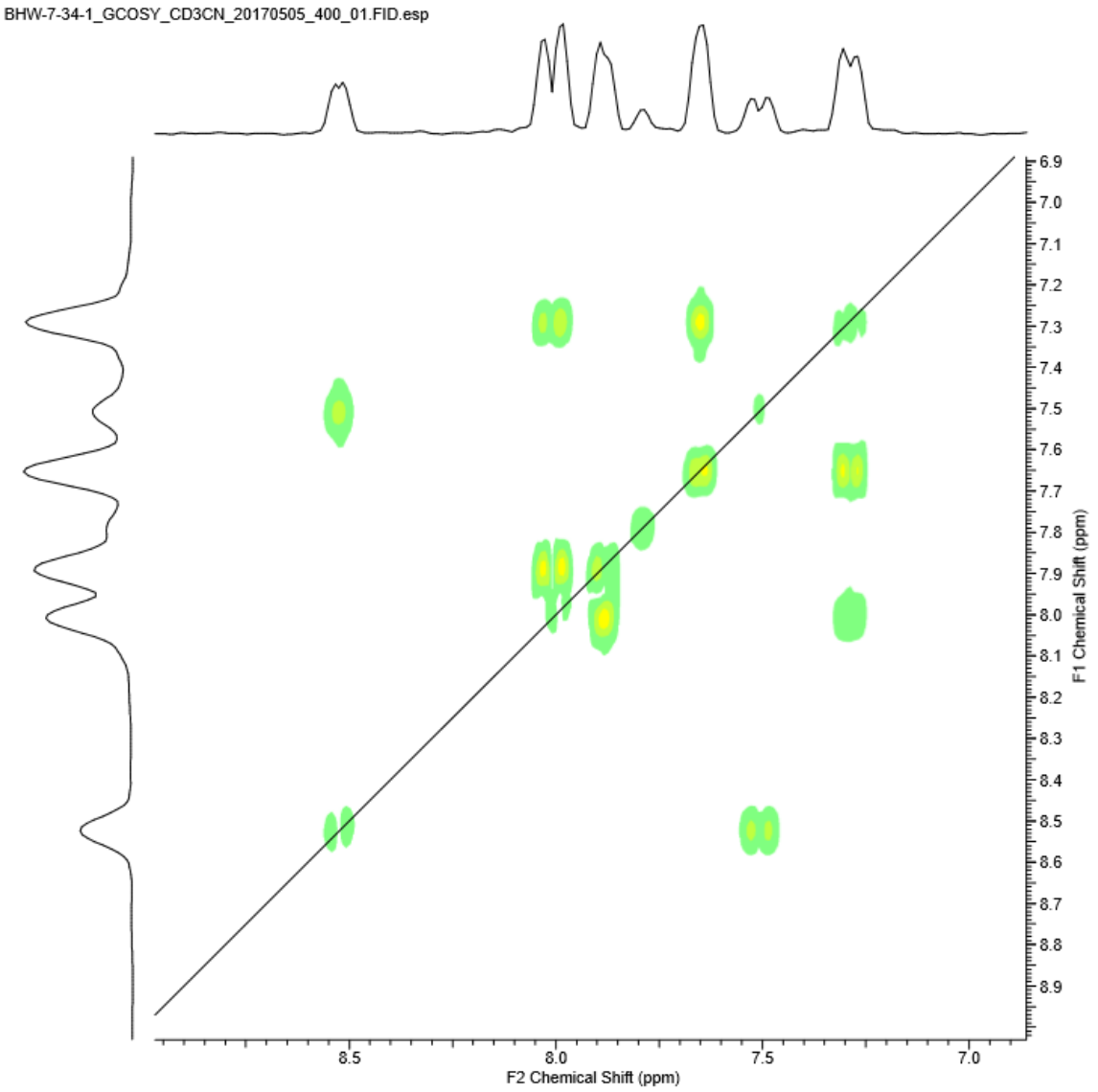

*Figure 2.8.2.ii: COSY NMR spectrum of **2.17** at 25 °C in CD_3CN.*

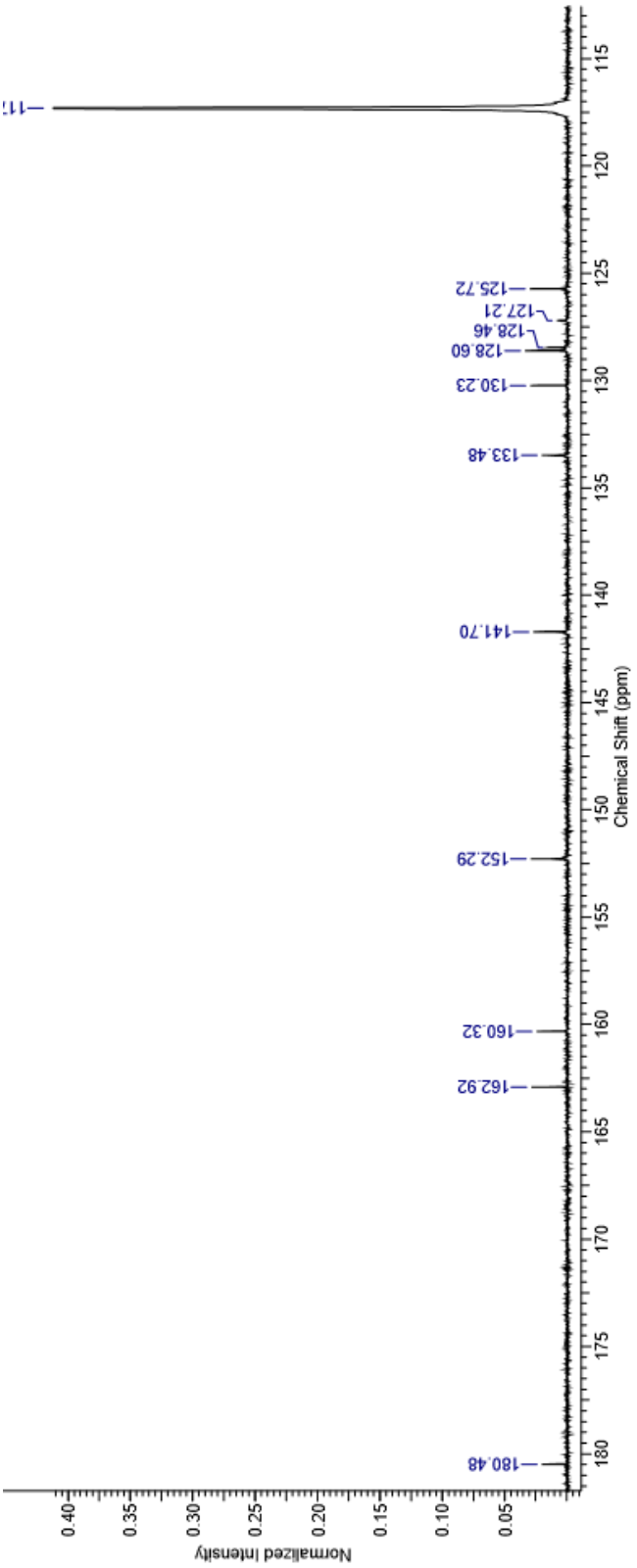

*Figure 2.8.2.iii: ^{13}C NMR spectrum of **2.17** at 25 °C in CD_3CN.*

*$[Fe_2(H_2$**L2.1**$)_3](PF_6)_4$,* ***2.18***

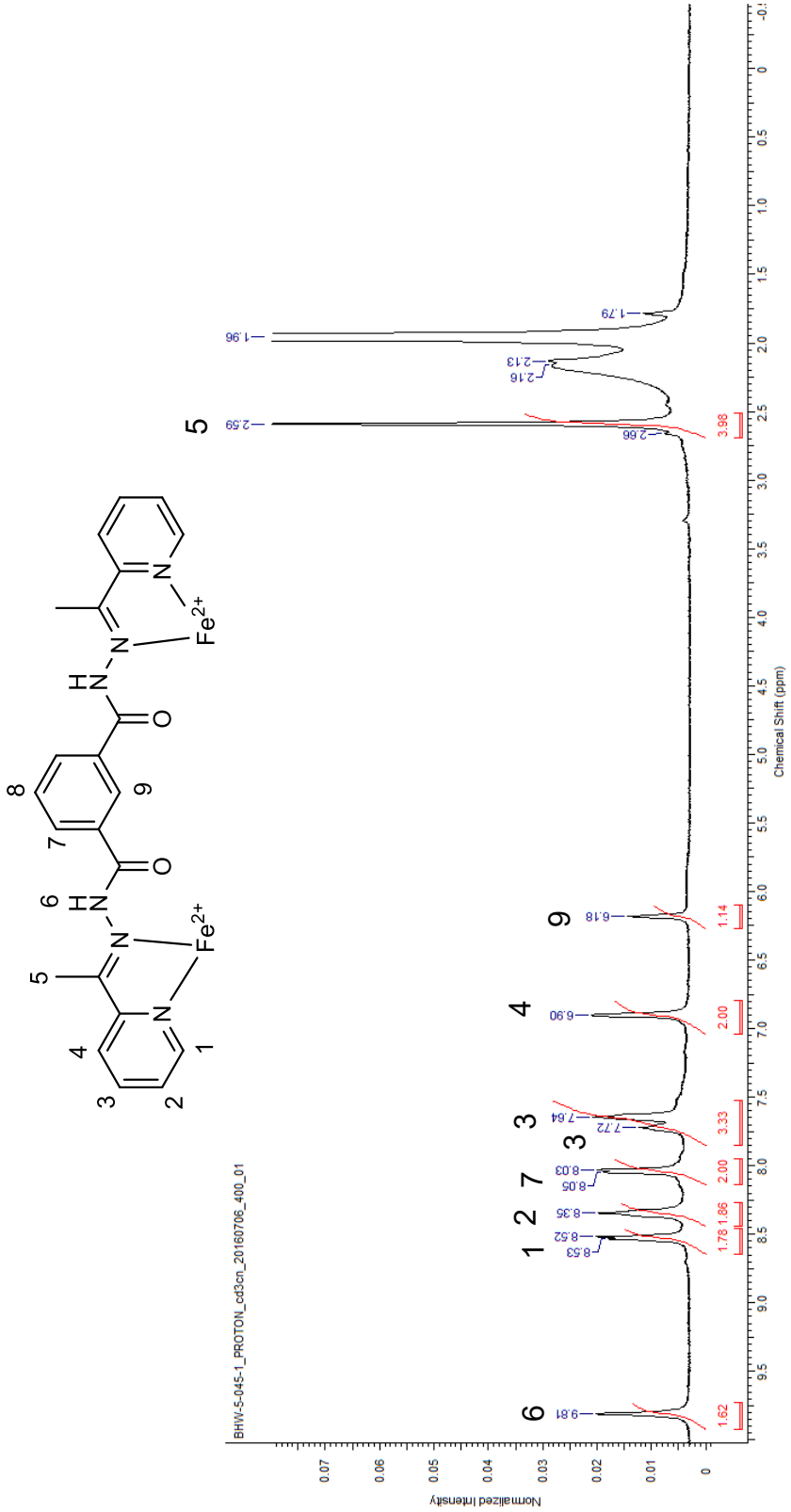

Figure 2.8.2.iv: ^{1}H NMR spectrum of ***2.18*** *at 25 °C in CD_3CN.*

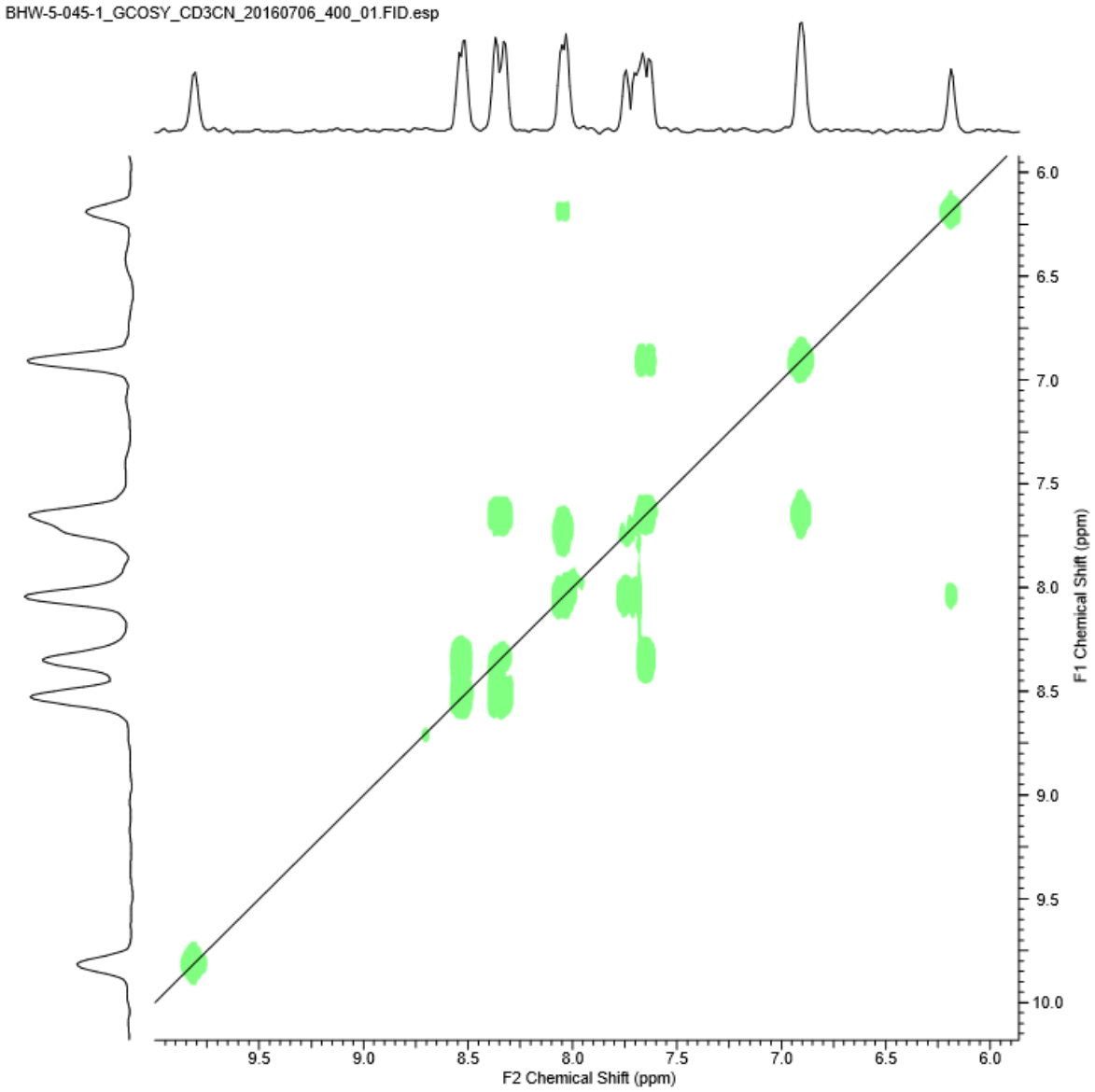

*Figure 2.8.2.v: COSY NMR spectrum of **2.18** at 25 °C in CD_3CN.*

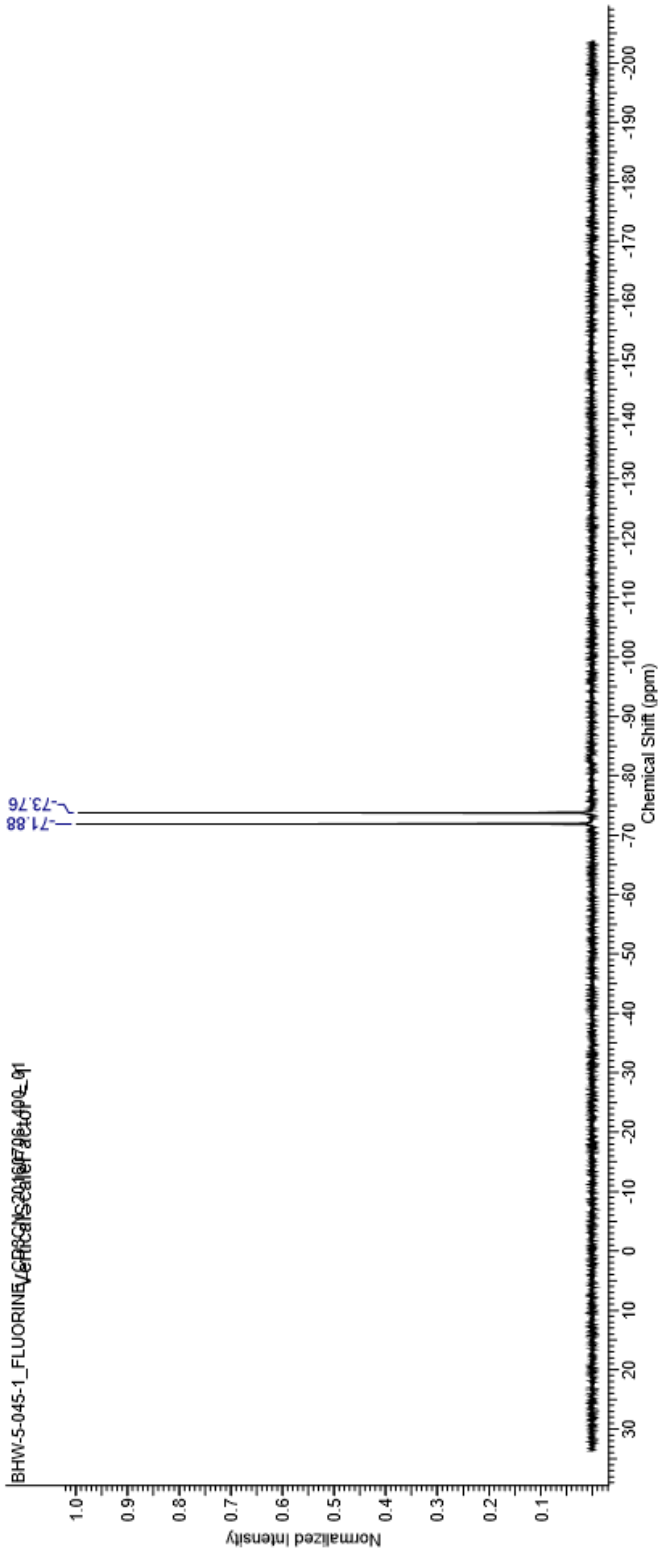

*Figure 2.8.2.vi: ^{19}F-NMR spectrum of **2.18** at 25 °C in CD_3CN.*

2.8.3 TGA

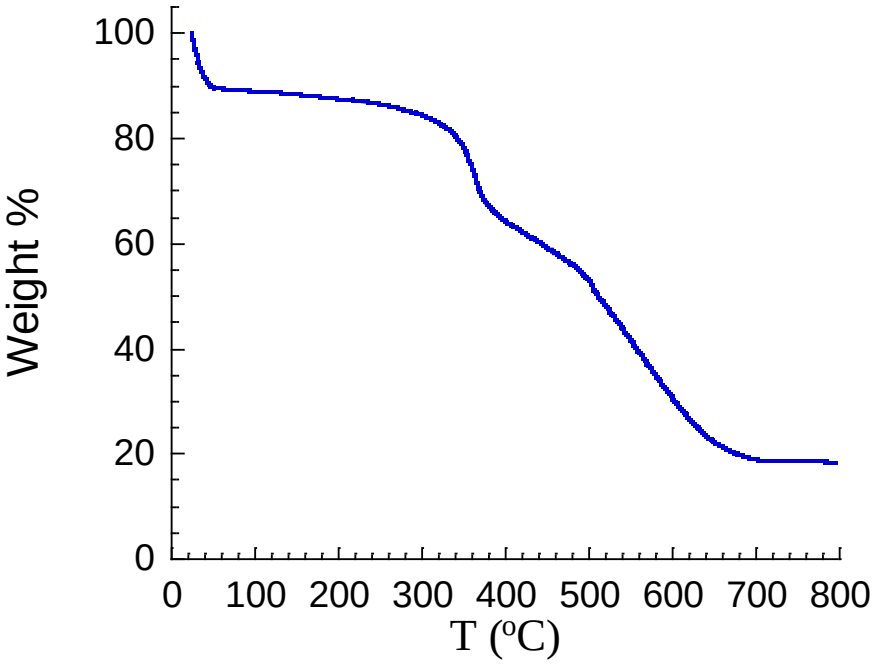

*Figure 2.8.3.i: TGA plot for complex **2.13**.*

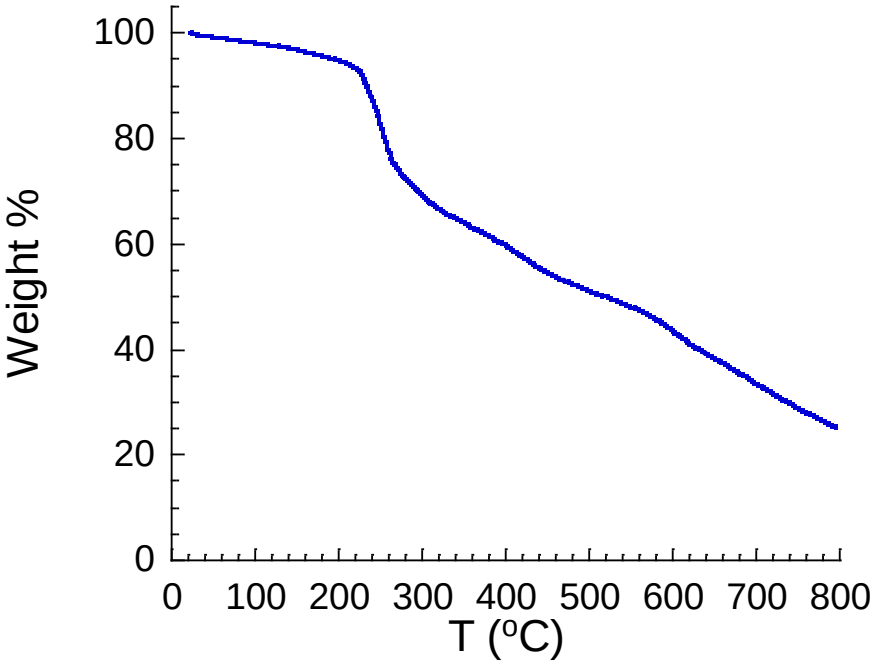

*Figure 2.8.3.ii: TGA plot for complex **2.18**.*

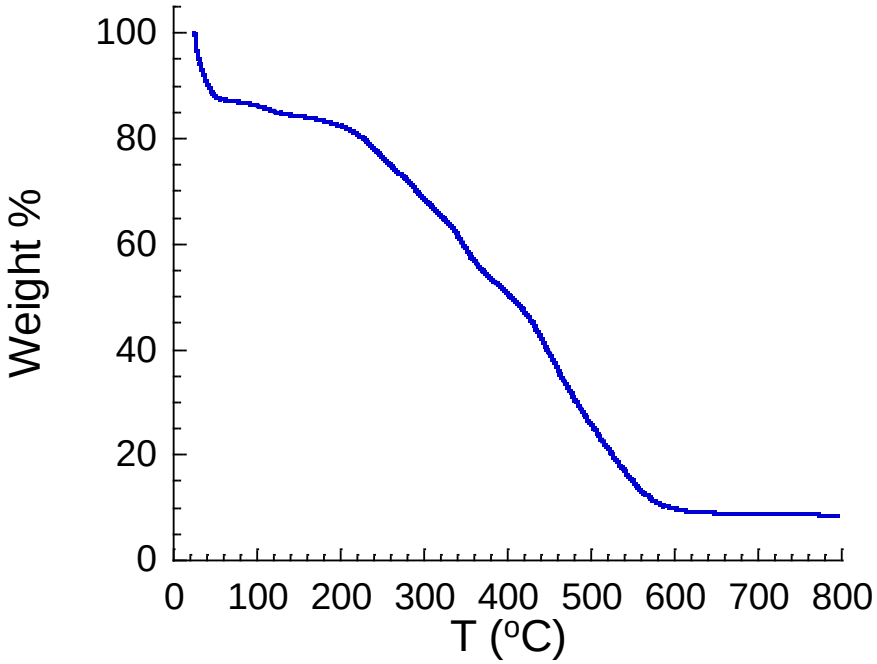

*Figure 2.8.3.iii: TGA plot for complex **2.19**.*

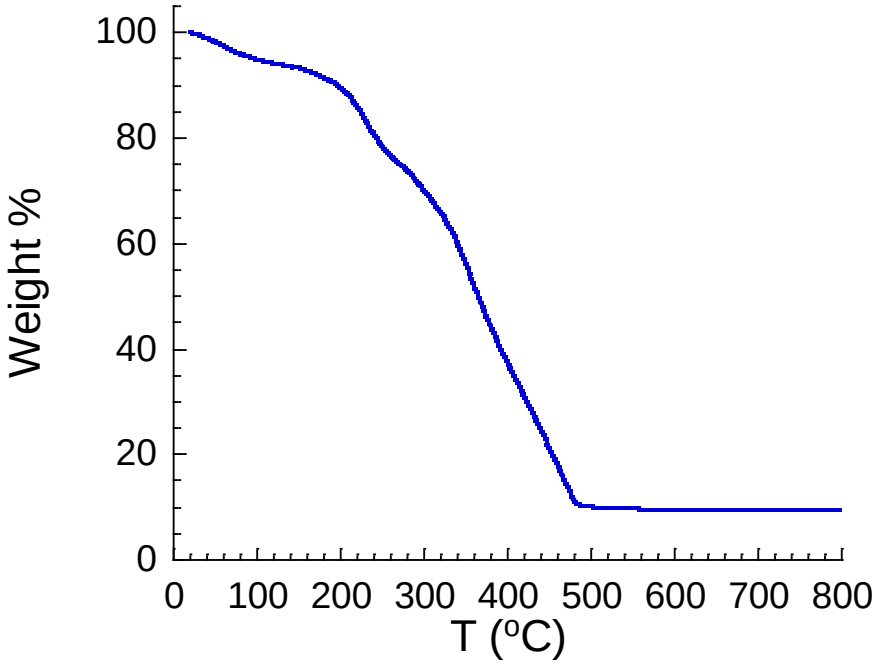

*Figure 2.8.3.iv: TGA plot for complex **2.20**.*

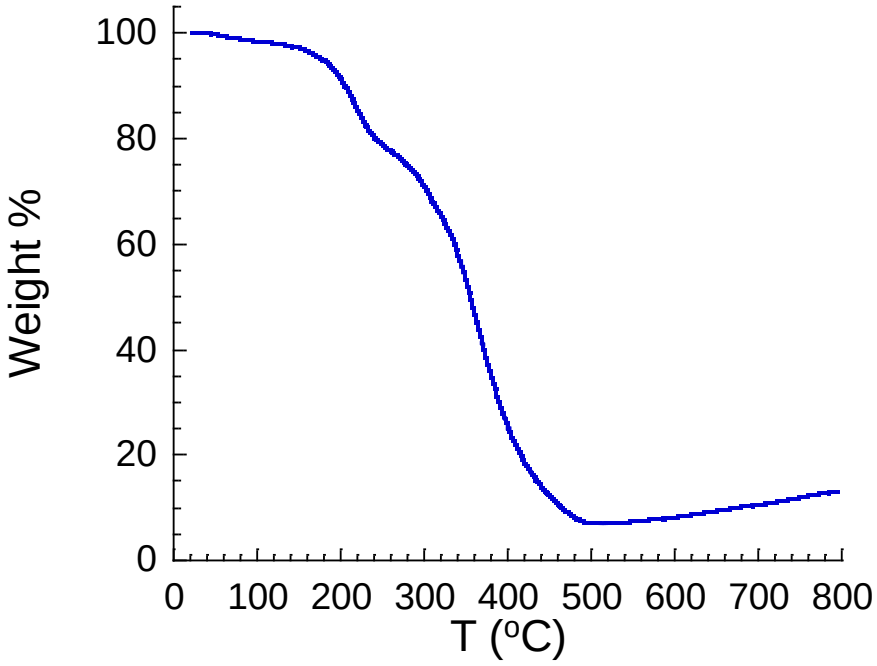

*Figure 2.8.3.v: TGA plot for complex **2.21**.*

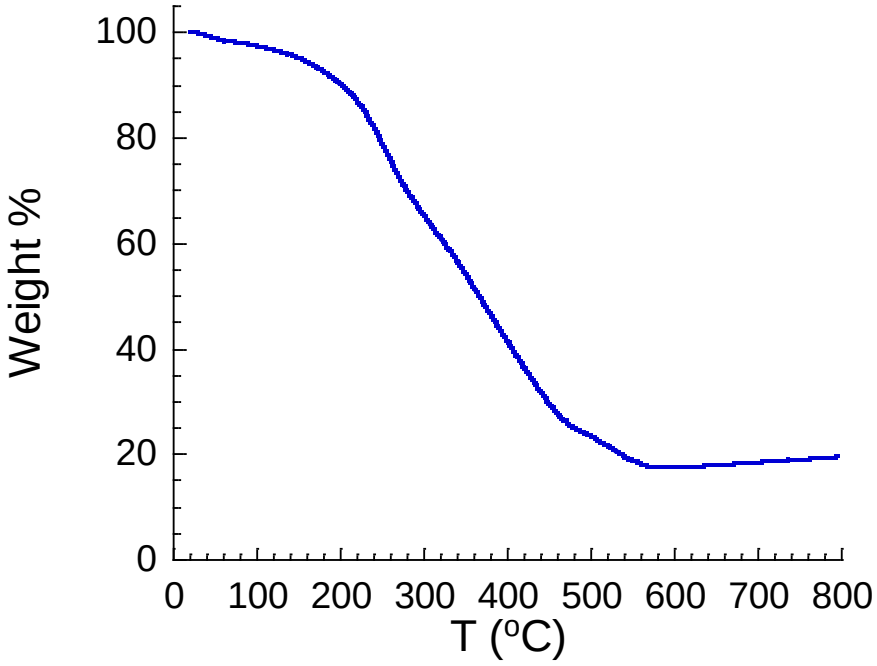

*Figure 2.8.3.vi: TGA plot for complex **2.22**.*

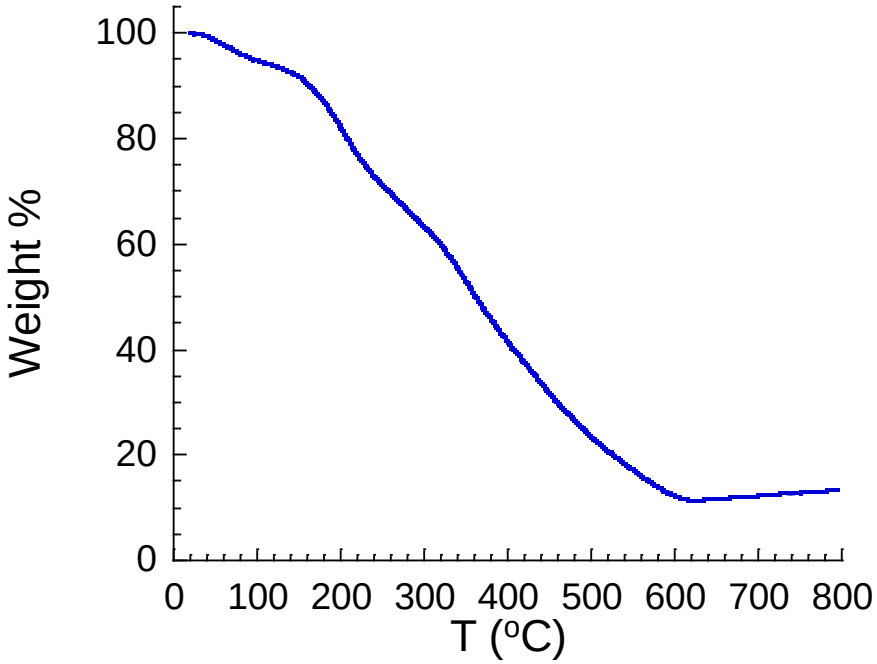

*Figure 2.8.3.vii: TGA plot for complex **2.23**.*

2.8.4 Crystallographic tables

	H_2**L2.2**	**2.12**	**2.13**	**2.14**
Empirical formula	$C_{20.5}H_{16}BrClN_6O_2$	$C_{92.5}H_{83.25}Fe_4N_{24.75}O_8$	$C_{83}H_{52}Br_4Fe_4N_{25}O_{8.88}$	$C_{96.9}H_{86}Cl_8Fe_4N_{29.8}O_{18.8}$
Formula weight	493.75	1892.98	2084.53	2475.76
Temperature/K	120.00(10)	120.02	296.15	120.15
Crystal system	triclinic	tetragonal	monoclinic	tetragonal
Space group	P-1	I4/m	C2/m	$I4_1/a$
a/Å	10.5439(4)	22.184(3)	51.9837(18)	18.0622(15)
b/Å	12.0465(6)	22.184(3)	22.3942(8)	18.0622(15)
c/Å	16.3854(3)	25.620(5)	19.2308(7)	37.904(4)
α/°	88.852(3)	90	90	90
β/°	86.802(2)	90	93.8800(10)	90
γ/°	83.424(4)	90	90	90
Volume/Å^3	2064.12(14)	12608(5)	22335.9(14)	12366(2)
Z	4	4	8	4
ρ_{calc}g/cm^3	1.589	0.997	1.240	1.330
μ/mm^{-1}	4.174	0.502	6.222	0.703
F(000)	996.0	3918.0	8320.0	5065.0
Crystal size/mm^3	0.121 × 0.043 × 0.023	0.4 × 0.2 × 0.01	0.15 × 0.1 × 0.01	0.194 × 0.165 × 0.041
Radiation	CuKα (λ = 1.54184)	MoKα (λ = 0.71073)	CuKα (λ = 1.54178)	MoKα (λ = 0.71073)
2Θ range for data collection/°	7.388 to 131.656	2.428 to 42.142	3.406 to 72.846	2.498 to 50.886
Index ranges	$-12 \le h \le 12$, $-14 \le k \le 14$, $-14 \le l \le 19$	$-22 \le h \le 22$, $-22 \le k \le 21$, $-25 \le l \le 25$	$-36 \le h \le 39$, $-17 \le k \le 17$, $14 \le l \le 14$	$-20 \le h \le 21$, $-21 \le k \le 21$, $-45 \le l \le 45$
Reflections collected	13535	171999	50408	88930
Independent reflections	7169 [R_{int} = 0.0389, R_{sigma} = 0.0557]	3478 [R_{int} = 0.1619, R_{sigma} = 0.0400]	5505 [R_{int} = 0.0502, R_{sigma} = 0.0318]	5723 [R_{int} = 0.1520, R_{sigma} = 0.0685]
Data/restraints/parameters	7169/0/550	3478/94/327	5505/1411/1219	5723/120/476
Goodness-of-fit on F^2	1.027	2.119	1.941	1.078
Final R indexes [I>=2σ (I)]	R_1 = 0.0408, wR_2 = 0.1043	R_1 = 0.1494, wR_2 = 0.4121	R_1 = 0.1277, wR_2 = 0.3769	R_1 = 0.0936, wR_2 = 0.2698
Final R indexes [all data]	R_1 = 0.0528, wR_2 = 0.1119	R_1 = 0.2363, wR_2 = 0.5276	R_1 = 0.1429, wR_2 = 0.3900	R_1 = 0.1495, wR_2 = 0.3189
Largest diff. peak/hole / e Å^{-3}	0.99/-0.89	1.58/-0.50	1.76/-0.55	1.70/-0.59

	2.15	**2.16**	**2.17**
Empirical formula	$C_{80}H_{48}Cl_8Fe_4N_{24}O_8$	$C_{88}H_{72}F_{24}Fe_4N_{24}O_8P_4$	$C_{88}H_{72}Co_4F_{24}N_{24}O_8P_4$
Formula weight	1980.42	2396.97	2409.29
Temperature/K	120.03	293(2)	100(2)
Crystal system	triclinic	orthorhombic	orthorhombic
Space group	P-1	Pmmn	Pmmn
a/Å	16.343(5)	22.362(4)	21.887(4)
b/Å	28.233(8)	34.240(7)	34.108(7)
c/Å	28.172(8)	9.1790(18)	9.1510(18)
α/°	115.409(8)	90	90
β/°	91.425(9)	90	90
γ/°	104.723(8)	90	90
Volume/Å^3	11221(6)	7028(2)	6831(2)
Z	4	2	2
ρ_{calc}g/cm^3	1.172	1.133	1.171
μ/mm^{-1}	0.751	0.530	0.606
F(000)	4000.0	2424.0	2432.0
Crystal size/mm^3	0.045 × 0.006 × 0.001	0.1 × 0.1 × 0.01	0.03 × 0.02 × 0.5
Radiation	MoKα (λ = 0.71073)	Synchrotron (λ = 0.710759)	Synchrotron (λ = 0.71073)
2Θ range for data collection/°	2.608 to 42.374	2.176 to 39.998	4.036 to 51.362
Index ranges	-16 ≤ h ≤ 16, -28 ≤ k ≤ 28, -28 ≤ l ≤ 27	-21 ≤ h ≤ 21, -32 ≤ k ≤ 32, -8 ≤ l ≤ 8	-26 ≤ h ≤ 26, -39 ≤ k ≤ 39, -11 ≤ l ≤ 11
Reflections collected	562518	21757	50434
Independent reflections	23895 [R_{int} = 0.1895, R_{sigma} = 0.0764]	3458 [R_{int} = 0.2431, R_{sigma} = 0.1261]	6511 [R_{int} = 0.0739, R_{sigma} = 0.0337]
Data/restraints/parameters	23895/2556/2221	3458/372/351	6511/21/374
Goodness-of-fit on F^2	2.343	1.142	1.103
Final R indexes [I>=2σ (I)]	R_1 = 0.2039, wR_2 = 0.5397	R_1 = 0.1222, wR_2 = 0.3168	R_1 = 0.0769, wR_2 = 0.2407
Final R indexes [all data]	R_1 = 0.2473, wR_2 = 0.5647	R_1 = 0.1664, wR_2 = 0.3680	R_1 = 0.0844, wR_2 = 0.2511
Largest diff. peak/hole / e Å^{-3}	3.53/-1.71	0.74/-0.51	1.01/-0.80

	2.18	**2.19**	**2.20**
Empirical formula	$C_{67}H_{60}F_{24}Fe_2N_{19}O_8P_4$	$C_{60}H_{54}B_4F_{16}Fe_2N_{24}O_6$	$C_{60}H_{51}B_4Br_3F_{16}Fe_2N_{24}O_6$
Formula weight	1950.92	1666.21	1902.89
Temperature/K	100(2)	120.00(10)	120.02(10)
Crystal system	hexagonal	hexagonal	hexagonal
Space group	$P6_3/m$	$P6_3/m$	$P6_3/m$
a/Å	10.3320(15)	14.3872(3)	12.928(3)
b/Å	10.3320(15)	14.3872(3)	12.928(3)
c/Å	41.188(8)	24.9442(4)	34.658(6)
α/°	90	90	90
β/°	90	90	90
γ/°	120	120	120
Volume/Å^3	3808(1)	4471.49(18)	5016(2)
Z	2	2	2
ρ_{calc}g/cm^3	1.702	1.238	1.260
μ/mm^{-1}	0.593	3.379	4.423
F(000)	1974.0	1692.0	1896.0
Crystal size/mm^3	0.02 × 0.1 × 0.1	0.288 × 0.106 × 0.083	0.125 × 0.064 × 0.033
Radiation	Synchrotron (λ = 0.71073)	CuKα (λ = 1.54184)	CuKα (λ = 1.54184)
2Θ range for data collection/°	4.658 to 54.2	7.088 to 140.12	7.896 to 133.198
Index ranges	$-13 \le h \le 13$, $-13 \le k \le 12$, $-52 \le l \le 52$	$-17 \le h \le 12$, $-17 \le k \le 16$, $-27 \le l \le 30$	$-11 \le h \le 16$, $-14 \le k \le 15$, $-42 \le l \le 43$
Reflections collected	29368	15316	3019
Independent reflections	2817 [R_{int} = 0.0552, R_{sigma} = 0.0243]	2906 [R_{int} = 0.0256, R_{sigma} = 0.0167]	3019 [R_{int} = 0.1293, R_{sigma} = 0.1759]
Data/restraints/parameters	2817/53/232	2906/69/224	3019/44/212
Goodness-of-fit on F^2	1.091	1.141	1.098
Final R indexes [I>=2σ (I)]	R_1 = 0.0587, wR_2 = 0.1468	R_1 = 0.0780, wR_2 = 0.2296	R_1 = 0.1324, wR_2 = 0.3620
Final R indexes [all data]	R_1 = 0.0594, wR_2 = 0.1471	R_1 = 0.0785, wR_2 = 0.2300	R_1 = 0.2059, wR_2 = 0.4145
Largest diff. peak/hole / e Å^{-3}	0.96/-1.10	1.18/-0.53	1.13/-0.67

	2.21	**2.22**	**2.23**
Empirical formula	$C_{60}H_{51}B_4F_{16}Fe_2I_3N_{24}O_6$	$C_{60}H_{57}B_4F_{16}Fe_2N_{27}O_6$	$C_{65.01}H_{64.55}B_4F_{16}Fe_2N_{26.01}O_{13.03}$
Formula weight	2034.33	1711.26	1877.86
Temperature/K	120.01(10)	120.01(10)	120.01(10)
Crystal system	hexagonal	hexagonal	triclinic
Space group	$P6_3/m$	$P6_3/m$	P-1
a/Å	13.0583(7)	14.3402(14)	16.8519(5)
b/Å	13.0583(7)	14.3402(14)	18.8040(5)
c/Å	34.5539(15)	24.8537(16)	19.7065(5)
α/°	90	90	64.586(3)
β/°	90	90	67.114(3)
γ/°	120	120	63.403(3)
Volume/Å^3	5102.7(6)	4426.2(9)	4891.5(3)
Z	2.00004	2	2
ρ_{calc}g/cm^3	1.324	1.284	1.275
μ/mm^{-1}	9.920	3.437	3.209
F(000)	1996.0	1740.0	1914.0
Crystal size/mm^3	0.283 × 0.031 × 0.028	0.09 × 0.059 × 0.037	0.364 × 0.124 × 0.056
Radiation	CuKα (λ = 1.54184)	CuKα (λ = 1.54184)	CuKα (λ = 1.54184)
2Θ range for data collection/°	7.818 to 140.072	7.114 to 140.066	6.676 to 134.172
Index ranges	$-15 \le h \le 15$, $-11 \le k \le 15$, $-42 \le l \le 19$	$-17 \le h \le 12$, $-16 \le k \le 14$, $-30 \le l \le 29$	$-20 \le h \le 20$, $-22 \le k \le 17$, $-23 \le l \le 19$
Reflections collected	15957	10665	38266
Independent reflections	3299 [R_{int} = 0.0580, R_{sigma} = 0.0416]	2887 [R_{int} = 0.1011, R_{sigma} = 0.0920]	17344 [R_{int} = 0.0307, R_{sigma} = 0.0404]
Data/restraints/parameters	3299/127/263	2887/71/239	17344/425/1474
Goodness-of-fit on F^2	1.200	0.981	1.070
Final R indexes [I>=2σ (I)]	R_1 = 0.0921, wR_2 = 0.2904	R_1 = 0.0707, wR_2 = 0.2041	R_1 = 0.0704, wR_2 = 0.2195
Final R indexes [all data]	R_1 = 0.1154, wR_2 = 0.3126	R_1 = 0.1103, wR_2 = 0.2355	R_1 = 0.0779, wR_2 = 0.2272
Largest diff. peak/hole / e Å^{-3}	1.58/-1.06	0.63/-0.42	1.10/-0.70

2.8.5 Selected crystallographic parameters

Bond	d(Fe-X) Å	Atoms	<(X-Fe-X) °	Atoms	<(X-Fe-X) °
N2-Fe1	2.01(1)	N2-Fe1-N3	81.5(5)	O4-Fe1-O7	88.8(4)
N3-Fe1	1.87(2)	N3-Fe1-O4	77.7(5)	O7-Fe1-N2	89.4(4)
O4-Fe1	1.99(1)	O4-Fe1-N6	102.3(4)	N3-Fe1-N5	100.3(5)
N5-Fe1	1.97(2)	N6-Fe1-N2	98.7(5)	N5-Fe1-N6	77.7(5)
N6-Fe1	1.89(1)	N2-Fe1-N5	98.0(5)	N6-Fe1-O7	79.7(4)
O7-Fe1	1.98(1)	N5-Fe1-O4	92.0(5)	O7-Fe1-N3	102.3(5)

*Table 2.8.5.i: Table of Fe-X bond lengths and X-Fe-X (X = O or N) bond angles for **2.12** from single crystal X-ray crystallographic data collected at 120 K.*

Fe1		***Fe2***		***Fe3***		***Fe4***	
Bond	**d(Fe-X) Å**	**Bond**	**d(Fe-X) Å**	**Bond**	**d(Fe-X) Å**	**Bond**	**d(Fe-X) Å**
Fe1-N5	1.97(2)	Fe2-N11	1.92(2)	Fe3-N19	1.98(2)	Fe4-N25	1.92(2)
Fe1-N6	1.76(2)	Fe2-N12	1.88(2)	Fe3-N20	1.92(2)	Fe4-N26	1.92(2)
Fe1-O7	1.87(1)	Fe2-O13	1.84(2)	Fe3-O21	1.92(2)	Fe4-O27	1.89(1)
Fe1-N8	2.01(2)	Fe2-N14	1.94(2)	Fe3-N22	1.95(1)	Fe4-N28	1.94(2)
Fe1-N9	1.88(2)	Fe2-N15	1.87(2)	Fe3-N23	1.96(2)	Fe4-N29	1.93(2)
Fe1-O10	1.91(2)	Fe2-O17	1.87(2)	Fe3-O24	1.88(2)	Fe4-O30	1.86(2)
Atoms	**<(X-Fe-X) °**	**Atoms**	**<(X-Fe-X) °**	**Atoms**	**<(X-Fe-X) °**	**Atoms**	**<(X-Fe-X) °**
N5-Fe1-N6	81.5(6)	N11-Fe2-N12	81.1(6)	N17-Fe3-N18	79.6(6)	N23-Fe4-N24	81.3(6)
N6-Fe1-O7	81.0(5)	N12-Fe2-O13	81.3(5)	N18-Fe3-O19	79.0(5)	N22-Fe4-O25	81.0(5)
O7-Fe1-N9	97.8(5)	O13-Fe2-N15	97.0(5)	O19-Fe3-N21	105.9(5)	O25-Fe4-N27	98.1(5)
N9-Fe1-N5	99.7(5)	N15-Fe2-N11	100.6(6)	N21-Fe3-N17	95.6(6)	N27-Fe4-N23	99.8(6)
N5-Fe1-N8	92.3(5)	N12-Fe2-N14	99.5(6)	N17-Fe3-N20	93.6(6)	N23-Fe4-N26	96.7(6)
N8-Fe1-O7	92.1(5)	N14-Fe2-N15	81.6(6)	N20-Fe3-O19	94.1(5)	N26-Fe4-O25	88.0(5)
O7-Fe1-O10	88.8(4)	N15-Fe2-O16	80.8(5)	O19-Fe3-O22	90.8(4)	O25-Fe4-O28	89.2(4)
O10-Fe1-N5	92.2(5)	O16-Fe2-N12	98.0(5)	O22-Fe3-N17	89.2(5)	O28-Fe4-N23	91.6(5)
N6-Fe1-N8	100.5(6)	N11-Fe2-N14	97.2(6)	N18-Fe3-N20	97.9(6)	N24-Fe4-N26	96.9(6)
N8-Fe1-N9	82.0(5)	N14-Fe2-O13	88.6(5)	N20-Fe3-N21	79.6(5)	N26-Fe4-N27	80.7(6)
N9-Fe1-O10	80.2(5)	O13-Fe2-O16	90.0(4)	N21-Fe3-O22	79.6(5)	N27-Fe4-O28	81.1(5)
O10-Fe1-N6	97.3(5)	O16-Fe2-N11	89.6(5)	O22-Fe3-N18	103.0(5)	O28-Fe4-N24	101.2(6)

*Table 2.8.5.ii: Table of Fe-X bond lengths and X-Fe-X (X = O or N) bond angles for **2.13** from single crystal X-ray crystallographic data collected at 120 K.*

Bond	d(Fe-X) Å	Atoms	<(X-Fe-X) °	Atoms	<(X-Fe-X) °
Fe1-N2	1.949(6)	N2-Fe1-N3	81.5(2)	O4-Fe1-O7	89.5(2)
Fe1-N3	1.856(6)	N3-Fe1-O4	80.4(2)	O7-Fe1-N2	89.5(2)
Fe1-O4	1.956(4)	O4-Fe1-N6	97.7(2)	N3-Fe1-N5	97.7(2)
Fe1-N5	1.964(6)	N6-Fe1-N2	100.5(2)	N5-Fe1-N6	81.0(2)
Fe1-N6	1.886(6)	N2-Fe1-N5	95.5(2)	N6-Fe1-O7	80.2(2)
Fe1-O7	1.970(4)	N5-Fe1-O4	91.4(2)	O7-Fe1-N3	100.9(2)

*Table 2.8.5.iii: Table of Fe-X bond lengths and X-Fe-X (X = O or N) bond angles for **2.14** from single crystal X-ray crystallographic data collected at 120 K.*

Fe1		***Fe2***		***Fe3***		***Fe4***	
Bond	**d(Fe-X) Å**	**Bond**	**d(Fe-X) Å**	**Bond**	**d(Fe-X) Å**	**Bond**	**d(Fe-X) Å**
Fe1-N9	2.28(2)	Fe2-N15	2.27(3)	Fe3-N21	2.26(2)	Fe4-N27	2.25(3)
Fe1-N10	2.05(2)	Fe2-N16	2.10(2)	Fe3-N22	2.09(2)	Fe4-N28	2.15(2)
Fe1-O11	2.09(2)	Fe2-O17	2.12(2)	Fe3-O23	2.08(2)	Fe4-O29	2.10(2)
Fe1-N12	2.28(2)	Fe2-N18	2.33(2)	Fe3-N24	2.22(3)	Fe4-N30	2.30(2)
Fe1-N13	2.13(2)	Fe2-N19	2.08(3)	Fe3-N25	2.11(2)	Fe4-N31	2.12(2)
Fe1-O14	2.07(1)	Fe2-O20	2.18(2)	Fe3-O26	2.09(2)	Fe4-O32	2.11(2)
Atoms	**<(X-Fe-X) °**	**Atoms**	**<(X-Fe-X) °**	**Atoms**	**<(X-Fe-X) °**	**Atoms**	**<(X-Fe-X) °**
N9-Fe1-N10	73.7(7)	N15-Fe2-N16	73.3(8)	Fe3-N21	2.26(2)	Fe4-N27	2.25(3)
N10-Fe1-O11	75.0(7)	N16-Fe2-O17	73.7(7)	Fe3-N22	2.09(2)	Fe4-N28	2.15(2)
O11-Fe1-N13	97.7(8)	O17-Fe2-N19	99.0(8)	Fe3-O23	2.08(2)	Fe4-O29	2.10(2)
N13-Fe1-N9	114.7(8)	N19-Fe2-N15	114.2(9)	Fe3-N24	2.22(3)	Fe4-N30	2.30(2)
N9-Fe1-N12	94.3(7)	N15-Fe2-N18	93.5(8)	Fe3-N25	2.11(2)	Fe4-N31	2.12(2)
N12-Fe1-O11	87.9(7)	N18-Fe2-O17	89.5(7)	Fe3-O26	2.09(2)	Fe4-O32	2.11(2)
O11-Fe1-O14	99.2(6)	O17-Fe2-O20	98.4(7)	N21-Fe3-N22	74.0(8)	N27-Fe4-N28	74.6(8)
O14-Fe1-N9	97.3(7)	O20-Fe2-N15	97.8(7)	N22-Fe3-O23	75.6(7)	N28-Fe4-O29	73.0(8)
N10-Fe1-N12	111.2(7)	N16-Fe2-N18	107.3(8)	O23-Fe3-N25	98.6(7)	O29-Fe4-N31	97.2(9)
N12-Fe1-N13	77.6(8)	N18-Fe2-N19	74.5(9)	N25-Fe3-N21	112.4(8)	N31-Fe4-N27	115.5(9)
N13-Fe1-O14	68.0(8)	N19-Fe2-O20	71.4(8)	N21-Fe3-N24	95.5(8)	N27-Fe4-N30	90.2(8)
O14-Fe1-N10	103.2(7)	O20-Fe2-N16	106.9(7)	N24-Fe3-O23	93.3(7)	N30-Fe4-O29	94.3(8)

*Table 2.8.5.iv: Table of Fe-X bond lengths and X-Fe-X (X = O or N) bond angles for **2.15** from single crystal X-ray crystallographic data collected at 120 K for Fe1 to Fe4.*

Fe5		*Fe6*		*Fe7*		*Fe8*	
Bond	**d(Fe-X) Å**	**Bond**	**d(Fe-X) Å**	**Bond**	**d(Fe-X) Å**	**Bond**	**d(Fe-X) Å**
Fe5-N33	2.24(2)	Fe6-N39	2.25(3)	Fe7-N45	2.25(3)	Fe8-N51	2.27(3)
Fe5-N34	2.05(2)	Fe6-N40	2.11(2)	Fe7-N46	2.05(2)	Fe8-N52	2.15(2)
Fe5-O35	2.08(2)	Fe6-O41	2.10(2)	Fe7-O47	2.09(2)	Fe8-O53	2.09(2)
Fe5-N35	2.32(2)	Fe6-N42	2.25(2)	Fe7-N48	2.24(3)	Fe8-N54	2.28(2)
Fe5-N37	2.07(2)	Fe6-N43	2.20(2)	Fe7-N49	2.12(2)	Fe8-N55	2.16(2)
Fe5-N33	2.24(2)	Fe6-O44	2.08(1)	Fe7-O50	2.09(2)	Fe8-O56	2.03(1)
Atoms	**<(X-Fe-X) °**	**Atoms**	**<(X-Fe-X) °**	**Atoms**	**<(X-Fe-X) °**	**Atoms**	**<(X-Fe-X) °**
N33-Fe5-N34	73.7(8)	N39-Fe6-N40	75.7(8)	N45-Fe7-N46	75.2(9)	N51-Fe8-N52	72.4(8)
N34-Fe5-O35	74.3(7)	N40-Fe6-O41	73.1(8)	N46-Fe7-O47	73.3(8)	N52-Fe8-O53	74.6(7)
O35-Fe5-N37	99.3(7)	O41-Fe6-N43	99.7(7)	O47-Fe7-N49	101.6(8)	O53-Fe8-N55	97.5(7)
N37-Fe5-N33	114.0(8)	N43-Fe6-N39	111.9(8)	N49-Fe7-N45	110.1(9)	N55-Fe8-N51	116.4(8)
N33-Fe5-N36	93.4(7)	N39-Fe6-N42	91.9(8)	N45-Fe7-N48	97(1)	N51-Fe8-N54	91.7(8)
N36-Fe5-O35	88.3(7)	N42-Fe6-O41	92.3(8)	N48-Fe7-O47	95.1(9)	N54-Fe8-O53	91.5(7)
O35-Fe5-O38	98.1(6)	O41-Fe6-O44	98.1(7)	O47-Fe7-O50	98.5(8)	O53-Fe8-O56	96.3(6)
O38-Fe5-N33	98.1(7)	O44-Fe6-N39	95.4(7)	O50-Fe7-N45	88.1(9)	O56-Fe8-N51	97.9(7)
N34-Fe5-N36	111.4(8)	N40-Fe6-N42	108.1(8)	N46-Fe7-N48	120(1)	N52-Fe8-N54	111.9(9)
N36-Fe5-N37	76.4(8)	N42-Fe6-N43	76.2(8)	N48-Fe7-N49	70.9(9)	N54-Fe8-N55	74.8(8)
N37-Fe5-O38	71.6(7)	N43-Fe6-O44	70.9(7)	N49-Fe7-O50	75.2(9)	N55-Fe8-O56	75.5(7)
O38-Fe5-N34	100.6(7)	O44-Fe6-N40	105.1(8)	O50-Fe7-N46	94.3(9)	O56-Fe8-N52	98.0(7)

*Table 2.8.5.v: Table of Fe-X bond lengths and X-Fe-X (X = O or N) angles for **2.15** from single crystal X-ray crystallographic data collected at 120 K for Fe5 to Fe8.*

	Σ (°)	**Fe(II) Centre**	**Σ (°)**
Fe1	155	Fe5	151
Fe2	155	Fe6	147
Fe3	146	Fe7	154
Fe4	146	Fe8	144

*Table 2.8.5.vi: Table of octahedral distortion parameters (Σ) for **2.15**.*

D-H···A	d(D-H) Å	d(D-H···A) Å	d(D···A) Å	<(D-H···A) °	Symmetry Code
C59-H59···O44	0.9500(3)	2.26(2)	3.20(2)	167.1(4)	x, y, z
					-1+x, y, -1+z
C107-H107···O56	0.9503(3)	2.29(1)	3.19(1)	158.3(3)	x, y, z
					x, y, z
C150-H150···N64	0.95(2)	2.62(2)	3.56(3)	170(1)	x, y, z
					-x, -y, -z
C155-H155···O20	0.9487(3)	2.39(2)	3.34(2)	172.9(4)	x, y, z
					x, y, z
C203-H203···O32	0.9506(3)	2.32(2)	3.27(2)	172.8(5)	x, y, z
					1+x, y, 1+z
C246-H246···N160	0.95(3)	2.72(2)	3.64(4)	164(2)	x, y, z
					1-x, -y, 1-z

*Table 2.8.5.vii: Table of C-H···O and C-H···N interactions for **2.15***

Bond	d(Fe-X) Å	Atoms	<(X-Fe-X) °	Atoms	<(X-Fe-X) °
Fe1-N2	1.94(1)	N2-Fe1-N3	80.5(4)	O4-Fe1-O7	95.4(3)
Fe1-N3	1.896(9)	N3-Fe1-O4	82.9(4)	O7-Fe1-N2	89.9(4)
Fe1-O4	1.907(7)	O4-Fe1-N6	95.0(4)	N5-Fe1-N6	80.0(5)
Fe1-N5	1.96(1)	N6-Fe1-N2	101.7(5)	N6-Fe1-O7	83.5(4)
Fe1-N6	1.901(1)	N2-Fe1-N5	91.2(5)	O7-Fe1-N3	95.9(4)
Fe1-O7	1.867(7)	N5-Fe1-O4	88.3(4)	N3-Fe1-N5	100.7(5)

*Table 2.8.5.viii: Table of Fe-X bond lengths and X-Fe-X (X = O or N) bond angles for **2.16** from single crystal X-ray crystallographic data collected at 100 K.*

Bond	d(Co-X) Å	Atoms	<(X-Co-X) °	Atoms	<(X-Co-X) °
Co1-N2	1.922(4)	N2-Co1-N3	82.8(1)	N2-Co1-N3	82.8(1)
Co1-N3	1.861(3)	N2-Co1-N5	95.2(2)	N3-Co1-O4	83.1(1)
Co1-O4	1.892(3)	N2-Co1-N6	100.7(2)	O4-Co1-N6	93.3(1)
Co1-N5	1.915(4)	N2-Co1-O7	88.5(1)	N6-Co1-N2	100.7(2)
Co1-N6	1.849(4)	N3-Co1-N5	98.8(2)	N2-Co1-N5	95.2(2)
Co1-O7	1.896(3)	N3-Co1-O4	83.1(1)	N5-Co1-O4	88.6(2)

*Table 2.8.5.ix: Table of Co-X bond lengths and X-Co-X (X = O or N) bond angles for **2.17** from single crystal X-ray crystallographic data collected at 100 K*

Fe1		*Fe2*	
Bond	**d(Fe-N) Å**	Bond	**d(Fe-N) Å**
Fe1-N3	1.956(7)	Fe2-N9	1.956(5)
Fe1-N4	1.948(7)	Fe2-N10	1.962(8)
Fe1-N5	1.953(8)	Fe2-N11	1.957(7)
Fe1-N6	1.954(8)	Fe2-N12	1.958(9)
Fe1-N7	1.946(8)	Fe2-N13	1.93(1)
Fe1-N8	1.971(7)	Fe2-N14	1.965(5)
Atoms	**<(N-Fe-N) °**	**Atoms**	**<(N-Fe-N) °**
N3-Fe1-N4	80.8(1)	N9-Fe2-N10	80.1(1)
N4-Fe1-N6	93.0(2)	N10-Fe2-N12	93.0(2)
N6-Fe1-N7	90.6(1)	N12-Fe2-N13	91.7(2)
N7-Fe1-N3	96.0(1)	N13-Fe2-N9	95.6(1)
N3-Fe1-N5	95.3(1)	N9-Fe2-N11	95.3(1)
N5-Fe1-N6	80.6(1)	N11-Fe2-N12	80.4(2)
N6-Fe1-N8	94.0(2)	N12-Fe2-N14	94.7(2)
N8-Fe1-N3	90.7(1)	N14-Fe2-N9	90.2(2)
N4-Fe1-N5	92.1(1)	N10-Fe2-N11	91.7(2)
N5-Fe1-N7	94.0(1)	N11-Fe2-N13	95.3(1)
N7-Fe1-N8	80.4(1)	N13-Fe2-N14	80.3(2)
N8-Fe1-N4	93.8(1)	N14-Fe2-N10	92.9(2)

*Table 2.8.5.x: Fe-N bond lengths and N-Fe-N cis bond angles for the two crystallographically unique Fe(II) centres of **2.23** at 120 K.*

Hydrazone torsion		*Carbonyl torsion*	
$C_{hydrazone}$-$N_{hydrazone}$-$N_{hydrazone}$-$C_{carbonyl}$	**<($C_{hydrazone}$-$N_{hydrazone}$-$N_{hydrazone}$-$C_{carbonyl}$) °**	**$O_{carbonyl}$-$C_{carbonyl}$-C_{phenyl}-C_{phenyl}**	**<($O_{carbonyl}$-$C_{carbonyl}$-C_{phenyl}-C_{phenyl}) °**
C20-N3-N22-C23	60.5(4)	O24-C23-C25-C26	22.5(6)
C27-N5-N49-C50	59.7(4)	O51-C50-C52-C53	22.8(4)
C76-N7-N78-C79	64.7(5)	O80-C79-C81-C82	22.3(5)
C36-N9-N35-C33	62.8(4)	O34-C33-C27-C26	22.5(7)
C64-N11-N63-C61	60.0(5)	O62-C61-C54-C53	23.1(4)
C92-N13-N91-C89	62.1(4)	O90-C89-C83-C82	19.3(5)

*Table 2.8.5.xi: Table of hydrazone and carbonyl torsion angles for **2.23** at 120 K.*

D-H···A	d(D-H) Å	d(D-H···A) Å	d(D···A) Å	<(D-H···A) °	Symmetry Code
N49-H49···O24	0.861(4)	2.408(4)	3.000(6)	126.4(2)	x, y, z
					x, y, z
N78-H78···O51	0.860(3)	2.439(3)	3.000(4)	123.4(3)	x, y, z
					x, y, z
N22-H22···O80	0.860(3)	2.285(3)	2.856(5)	124.0(2)	x, y, z
					x, y, z
N63-H63···O34	0.859(4)	2.339(3)	2.967(5)	130.2(2)	x, y, z
					x, y, z
N91-H91···O62	0.860(4)	2.582(3)	3.098(4)	119.5(2)	x, y, z
					x, y, z
N35-H35···O90	0.860(3)	2.423(4)	2.946(6)	119.9(3)	x, y, z
					x, y, z
N22-H22···O146	0.860(3)	2.470(5)	3.229(6)	147.4(2)	x, y, z
					x, y, z
N78-H78···F105	0.860(3)	2.129(4)	2.921(6)	152.9(3)	x, y, z
					x, y, z
N35-H35···F110	0.860(3)	2.275(5)	3.050(5)	149.8(4)	x, y, z
					x, y, z
C37-H37c···F101	0.961(5)	2.576(3)	3.274(5)	129.7(3)	x, y, z
					x, y, z
C59-H59a···F100	0.96(1)	2.293(3)	3.15(1)	148.3(7)	x, y, z
					x, y, z
N91-H91···F132	0.860(4)	2.152(5)	2.952(6)	154.6(2)	x, y, z
					x, y, z

*Table 2.8.5.xii: Table of conventional and non-conventional hydrogen bond interactions of the tetrafluoroborate anions about the Fe1 and Fe2 centres for **2.23** at 120 K.*

2.8.6 Magnetic susceptibility data

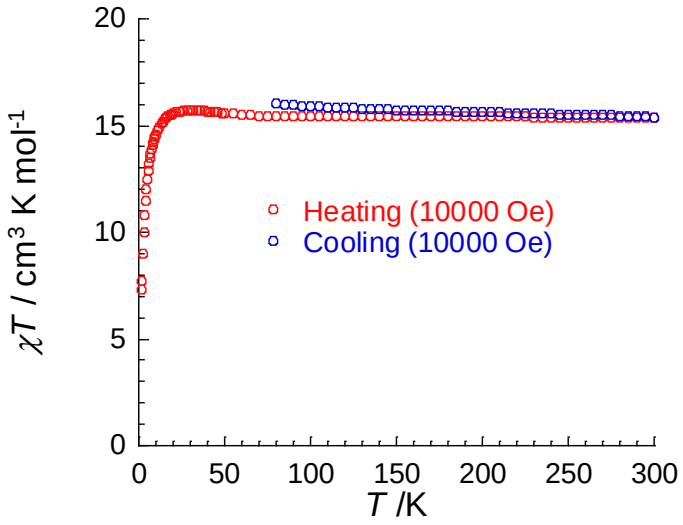

*Figure 2.8.6.i: χT vs. T plot for **2.14** with an applied field of 10000 Oe with a scan rate of 0.4 K min^{-1}. The heating cycle from 1.85 to 300 K is shown in red while the cooling cycle from 300 to 80 K is shown in blue.*

2.8.7 Gas sorption

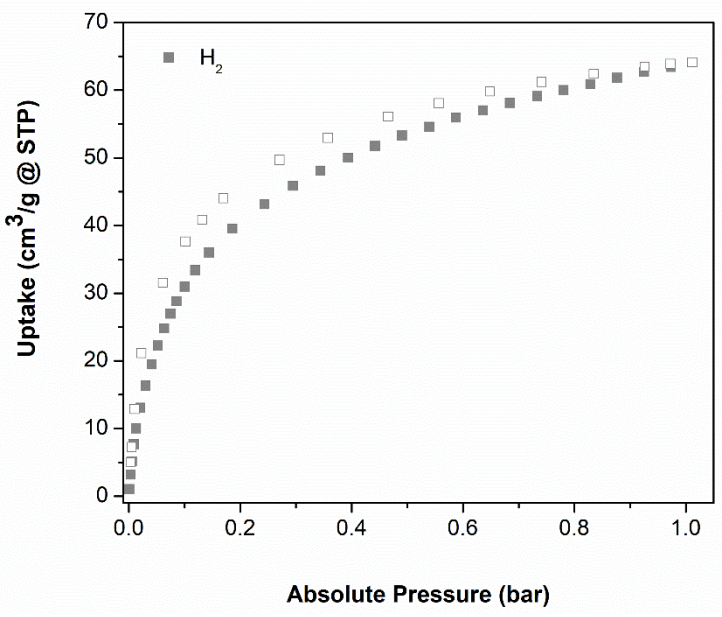

*Figure 2.8.7.i: H_2 sorption isotherm performed at 77 K for **2.19**.*

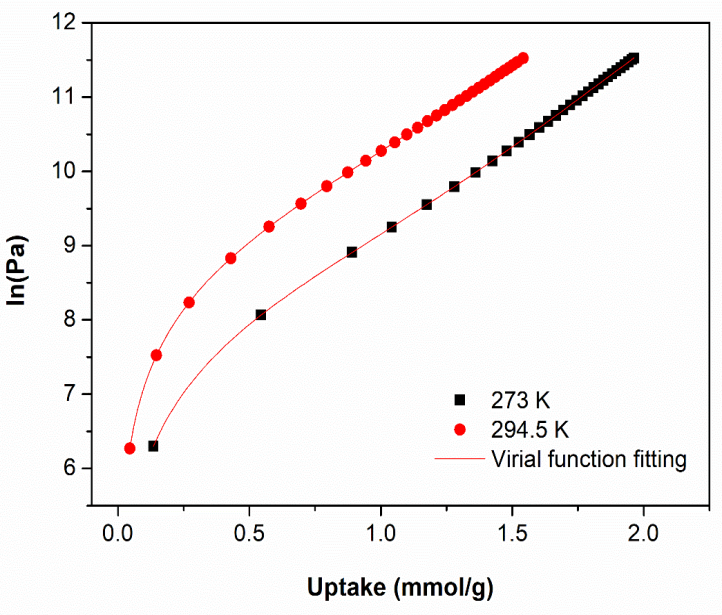

*Figure 2.8.7.ii: CO_2 adsorption isotherms of **2.19** at 273 and 294.5 K, fitted using the virial equation.*

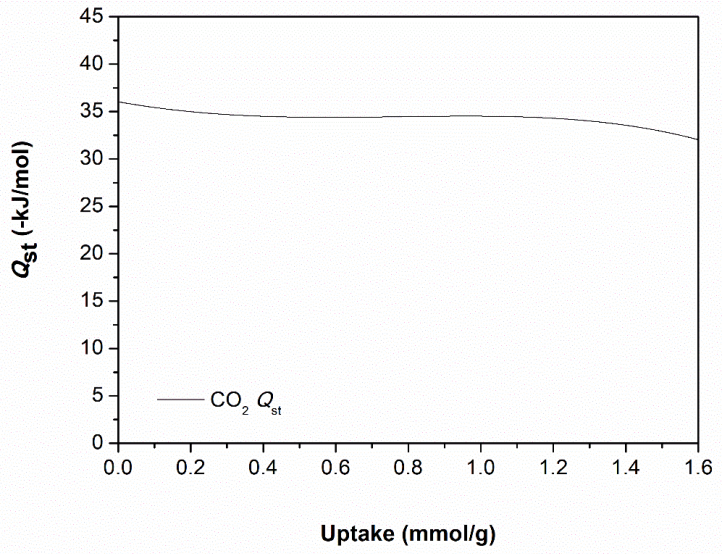

*Figure 2.8.7.iii: CO_2 isosteric heats of adsorption (Q_{st}) of **2.19** using the fitted data measured at 273 and 294.5 K.*

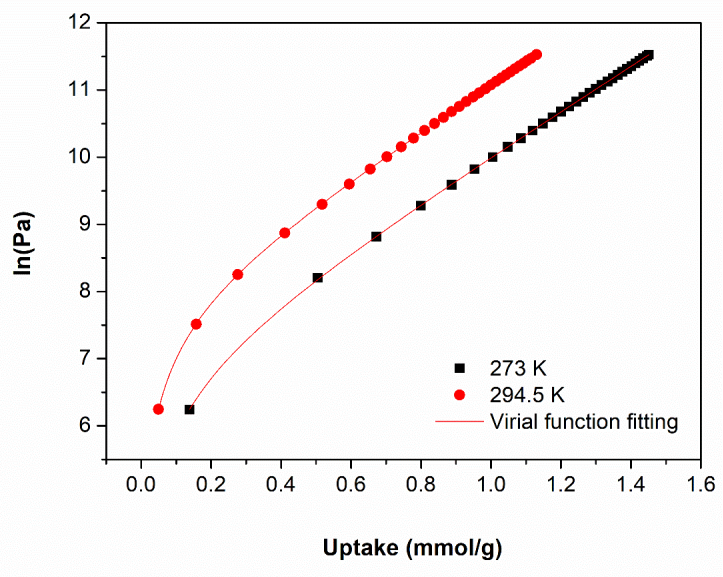

*Figure 2.8.7.iv: C_2H_4 adsorption isotherms of **2.19** at 273 and 294.5 K, fitted using the virial equation.*

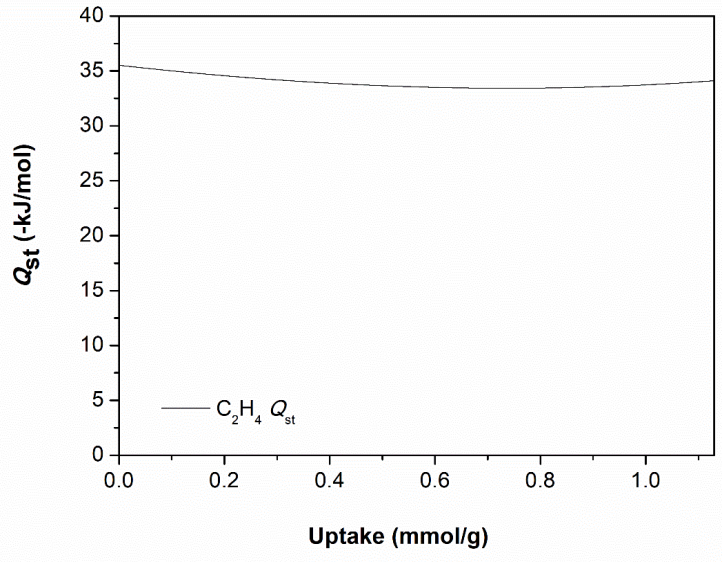

*Figure 2.8.7.v: C_2H_4 isosteric heats of adsorption (Q_{st}) of **2.19** using the fitted data measured at 273 and 294.5 K.*

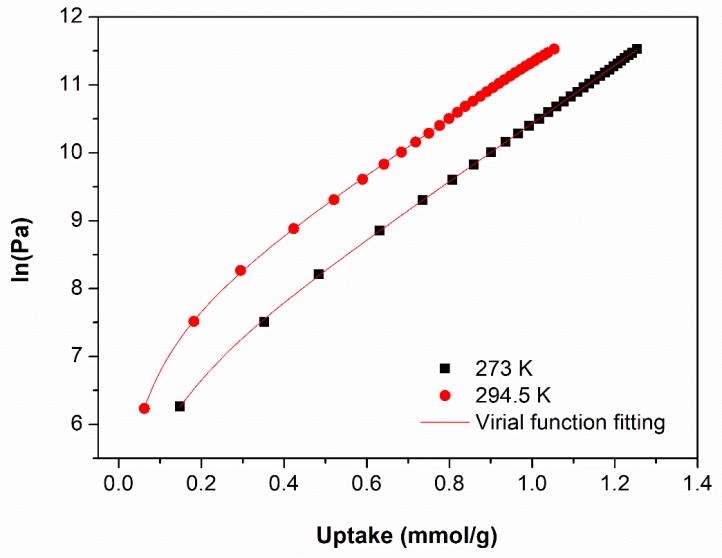

*Figure 2.8.7.vi: C_2H_6 adsorption isotherms of **2.19** at 273 and 294.5 K, fitted using the virial equation.*

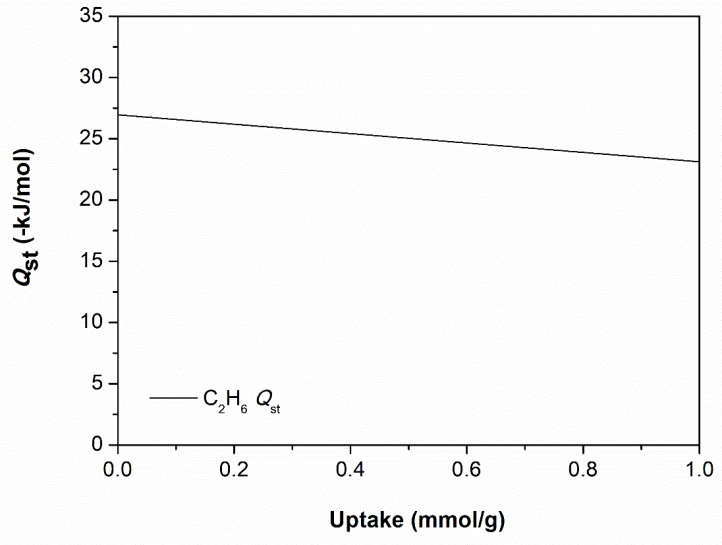

*Figure 2.8.7.vii: C_2H_6 isosteric heats of adsorption (Q_{st}) of **2.19** using the fitted data measured at 273 and 294.5 K.*

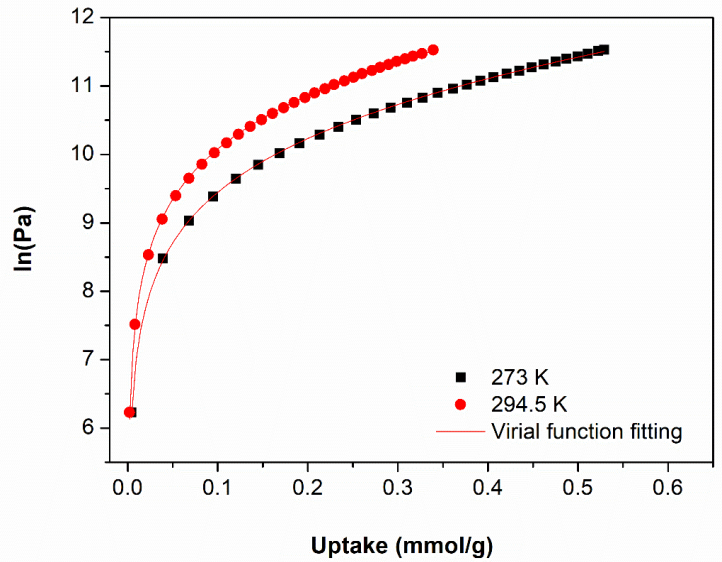

*Figure 2.8.7.viii: CH_4 adsorption isotherms of **2.19** at 273 and 294.5 K, fitted using the virial equation.*

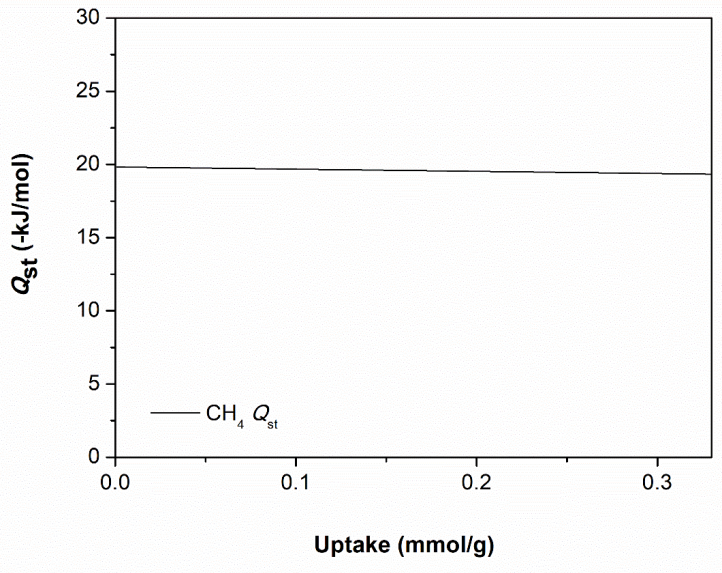

*Figure 2.8.7.ix: CH_4 isosteric heats of adsorption (Q_{st}) of **2.19** using the fitted data measured at 273 and 294.5 K.*

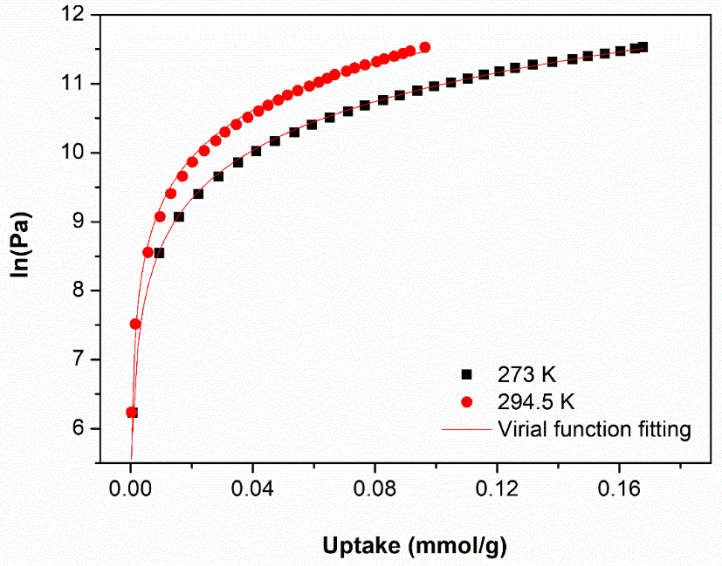

*Figure 2.8.7.x: N_2 adsorption isotherms of **2.19** at 273 and 294.5 K, fitted using the virial equation.*

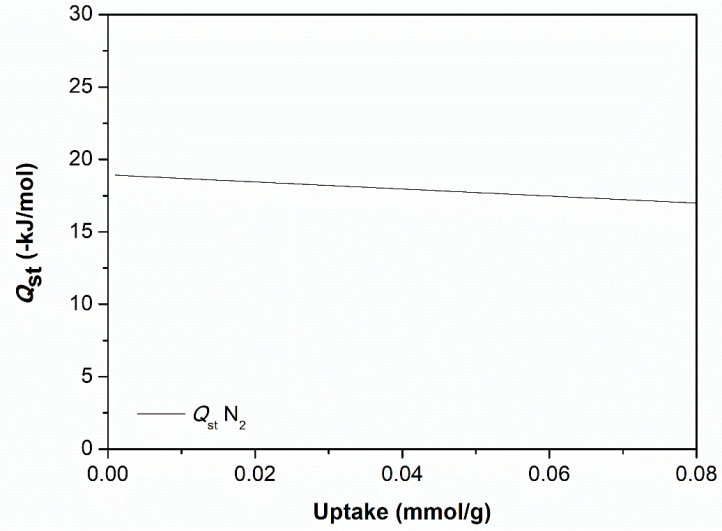

*Figure 2.8.7.xi: N_2 isosteric heats of adsorption (Q_{st}) of **2.19** using the fitted data measured at 273 and 294.5 K.*

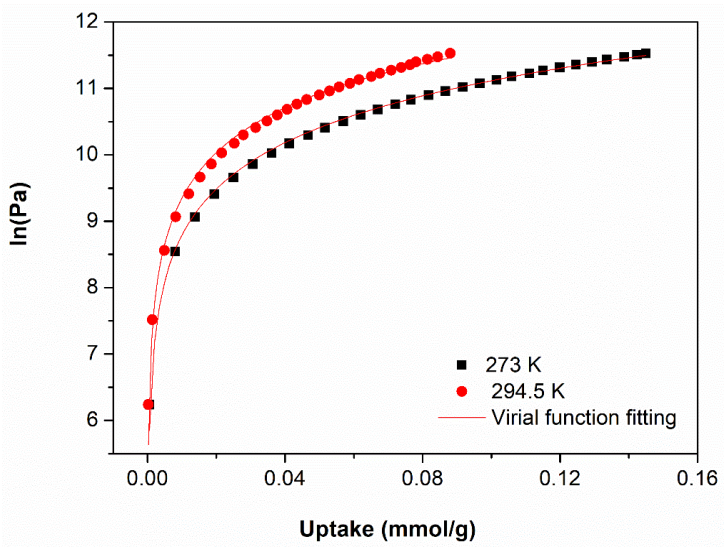

*Figure 2.8.7.xii: N_2 adsorption isotherms of **2.19** at 273 and 294.5 K, fitted using the virial equation.*

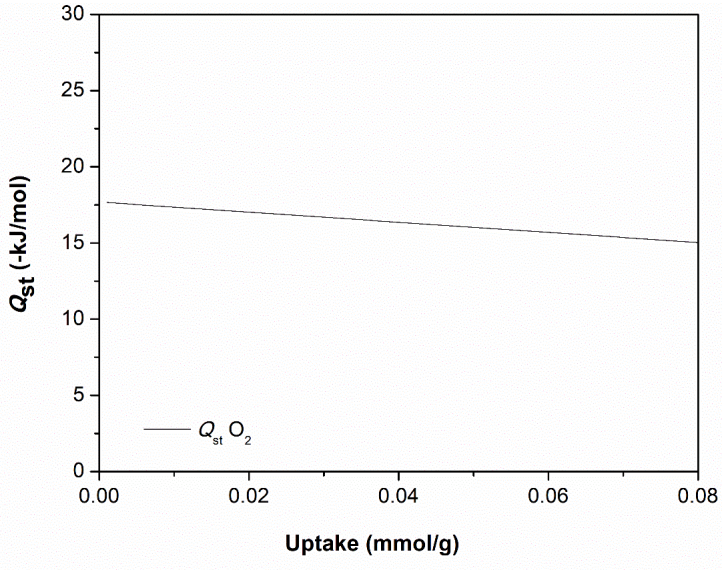

*Figure 2.8.7.xiii: O_2 isosteric heats of adsorption (Q_{st}) of **2.19** using the fitted data measured at 273 and 294.5 K.*

Chapter Three

Supramolecular Interactions of Co(II) Dinuclear Double Helicates

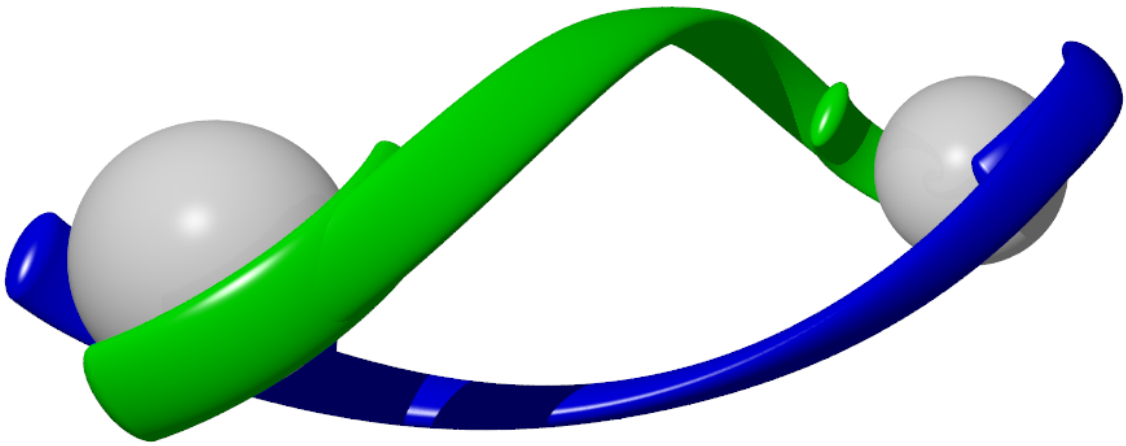

3.1 Introduction

3.1.1 Flexible ditopic pyridylhydrazone and related ligands

The pyridylhydrazone coordinating motif is commonly employed as a tridentate ligand to form bis-chelated complexes with first row transition metal ions in an octahedral coordination geometry. Ditopic pyridylhydrazone ligands and related pyridylacylimidrazone ligands are readily synthesised due to the facile ligand synthesis from simple carboxylate derivatives (*Figure 3.1.1.i*). ligands containing the succinate bridging moiety are commonly employed for the synthesis of metallo-helicates. A number of helicates featuring both the pyridylhydrazone and the structurally similar pyridyl-acylamidrazone coordinating motif, linked by the aforementioned sucinnate spacer, have been reported in the literature. Work by Gusev and co-workers illustrated how such ligands can form saturated dinuclear double helicates with Cu(II) and unsaturated dinuclear double helicates with Dy(III).[408-409]

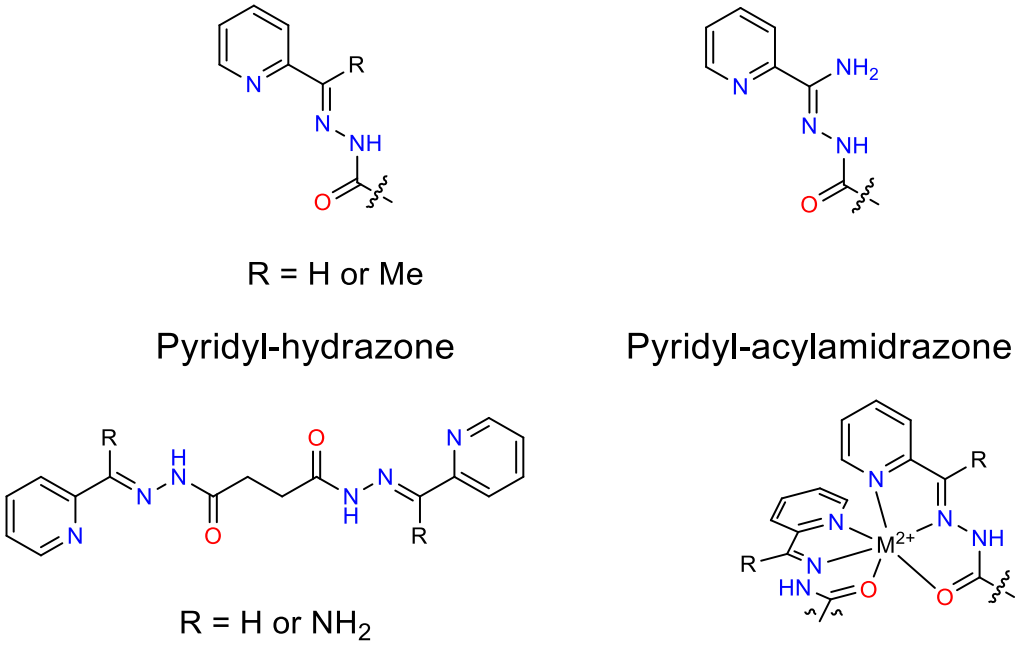

Figure 3.1.1.i: (top) comparison of the pyridylhydrazone and pyridylacylamidrazone coordinating moieties. (bottom left) The ditopic ligands reported in the work of Konar (R = H) and Lindert (R = NH_2). (bottom right): the bis-tridentate coordination mode of the pyridylhydrazone or pyridylacylamidrazone ligand in the neutral imino-keto form to a first-row transition metal (M^{2+}).

More recently Konar and co-workers synthesised a similar ligand containing the pyridylhydrazone motif. This ligand was employed to synthesise Co(II) and Cu(II) dinuclear double helicates.[407] Subsequent magnetic susceptibility measurements revealed that these Co(II) helicates displayed slow relaxation of the magnetic moment in the presence of an external magnetic field and therefore behaved as field induced SMMs. The application of this coordinating motif for the synthesis of Co(II) SMMs has been further explored by Powell and co-workers.[439] This work focused on the effect of the distortion of the coordination sphere from that of an idealised octahedron, on the dynamics of the magnetic relaxation. It has been previously observed that the number of degrees of freedom in the linker of ditopic ligands plays a key role upon whether a supramolecular helicate or mesocate is formed. The trend reported by Albrecht is that an even number of linker atoms results in a chiral helicate while an odd number of linker atoms results in an achiral mesocate.[113-114] The family of ligands outlined above represents an ideal system to test for this theory as there are a range of dicarboxylate precursors commercially available.

3.1.1 Importance of helicate supramolecular interactions

Metallo-helicates provide access to metallo-supramolecular structures exhibiting helical chirality which have potential applications in DNA binding[118-121, 440] and exhibiting magneto-chiral effects.[441] When an achiral ligand is employed, both enantiomers of the helicate are present and therefore a racemic mix is obtained. Recent work by Rissanen and co-workers utilised flexible ditopic pyridylhydrazone ligands in order to synthesise dinuclear double helicates. Chromatographic methods were used to separate the enantiomers which were subsequently used for asymmetric catalysis.[410] Work by Hillard and co-workers has demonstrated the applicability of chiral anions for the resolution of cationic metal complexes exhibiting helical chirality.[442] Therefore, an understanding of the effect of the anion on the crystal packing of the helicate is crucial. When the pyridylhydrazone functionality is coordinating in the neutral keto form, the N-H moiety is a potent hydrogen bond donor as briefly discussed in chapter two. Therefore, it is expected to interact strongly with anions acting as hydrogen bond acceptors.

3.1.2 Scope of research

The following work will first examine the effect of the peripheral ligand functionality and anion on the crystal packing. The ligands are based on the succinate linker which has shown promise in

previous studies outlined above. The selected anions consist of tetrahedral perchlorate and tetrafluoroborate anions and the less symmetrical triflate anion. Two coordinating moieties will be investigated: the pyridylhydrazone and the related quinolylhydrazone functionality. The latter is of interest as the larger aromatic π-system has a greater propensity for π-π stacking interactions which will have a significant effect on the crystal packing. Secondly, this work will then briefly investigate the effect of increasing the length of the flexible carbon linker of the ligand. The larger adipate spacer with four methylene units was employed for this purpose.

3.2 Ligand synthesis and characterisation

The ligands **L2.2**, **L2.3** and **L2.5** were all prepared via a two-step synthetic procedure from the appropriate diester (*Figure 3.2.1*). The dihydrazide intermediates were synthesised by reacting either diethyl succinate or diethyl adipate with an excess of hydrazine monohydrate in ethanol and were isolated in reasonable yields. While these dihydrazide intermediates **3.1** and **3.4** contained flexible alkyl moieties they were still relatively insoluble in organic solvents. Therefore, NMR spectroscopy was carried out in deuterated DMSO and mass-spectrometry from methanol solutions following the addition of a small amount of formic acid. The second step was carried out by reacting **3.1** or **3.4** with either 2-acetylpyridine or 2-quinolinecarboxaldehyde in ethanol at reflux (*Figure 3.2.1*). The ligands precipitated from the hot ethanol solutions as either white (pyridine) or yellow (quinoline) powders which were less soluble than the dihydrazide precursors. The yields ranged from 60% for **L3.3** and 54% for **L3.2** to 39% for **L3.5**. Tautomerism of the pyridylhydrazone moiety between the imino-keto and imino-enol forms can be observed if it is slower than the NMR time scale which is the case for **L3.2** and **L3.5** (*Figure 3.2.2*). However, **L3.3** is noticeably less soluble than **L3.2** and **L3.5** due to the presence of the quinoline moieties. Therefore, characterisation by NMR spectroscopy was challenging and carried out on a relatively dilute solution of **L3.3** in deuterated DMSO. Hence, the presence of the imino-enol tautomer may be masked by noise in the lower resolution ^{1}H NMR spectrum.

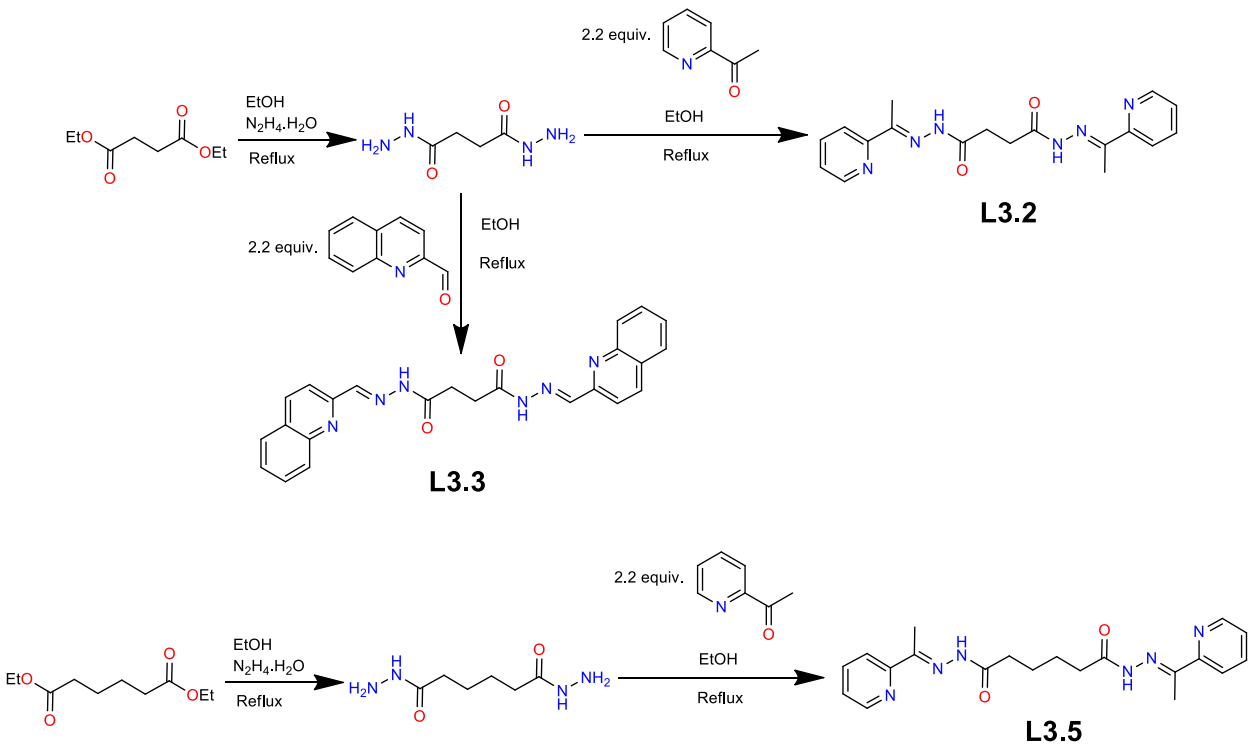

*Figure 3.2.1: Synthetic scheme used to synthesise ligands **L3.2** and **L3.3** from diethyl succinate and ligand **L3.5** from diethyl adipate. A 2.5-fold excess of hydrazine monohydrate was used to synthesise the dihydrazide intermediates in a reasonable yield. A 1.1-fold excess (per hydrazide) of 2-acetylpyridine or 2-quinolinecarbaldehyde was then used to synthesise the final ligands.*

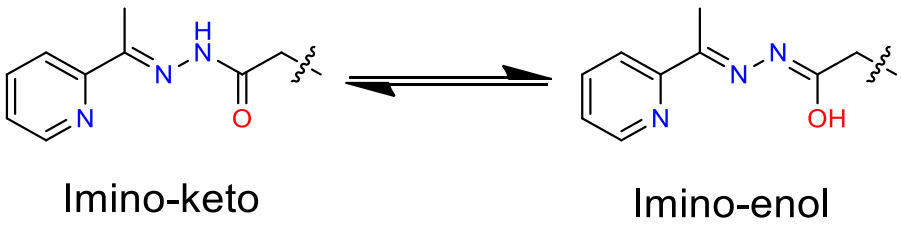

Figure 3.2.2: The tautomerism equilibrium between the imino-keto and imino-enol forms of the pyridylhydrazone moiety.

3.3 Complex synthesis and characterization

3.3.1 $[Co_2(L3.2)_2](ClO_4)_4$, 3.6

Stoichiometric amounts of Co(II) perchlorate and **L3.2** were stirred in acetonitrile to give a yellow solution. Vapor diffusion of benzene into the acetonitrile solution of the complex gave orange block crystals suitable for single crystal X-ray diffraction. The data were solved and refined in the monoclinic space group $P2_1/n$ (R = 4.64%). The asymmetric unit contained two **L3.2** ligands coordinated to two Co(II) ions resulting in a dinuclear double helicate. The two crystallographically distinct Co(II) centres exist in an N_4O_2 octahedral coordination environment made up of two tridentate meridional pyridylhydrazone binding sites of **L3.2** (*Figure 3.3.1.i*). The Co-N and Co-O bond lengths are indicative of HS Co(II), as anticipated with this weak field ligand (*Appendix Table 3.6.2.i*).

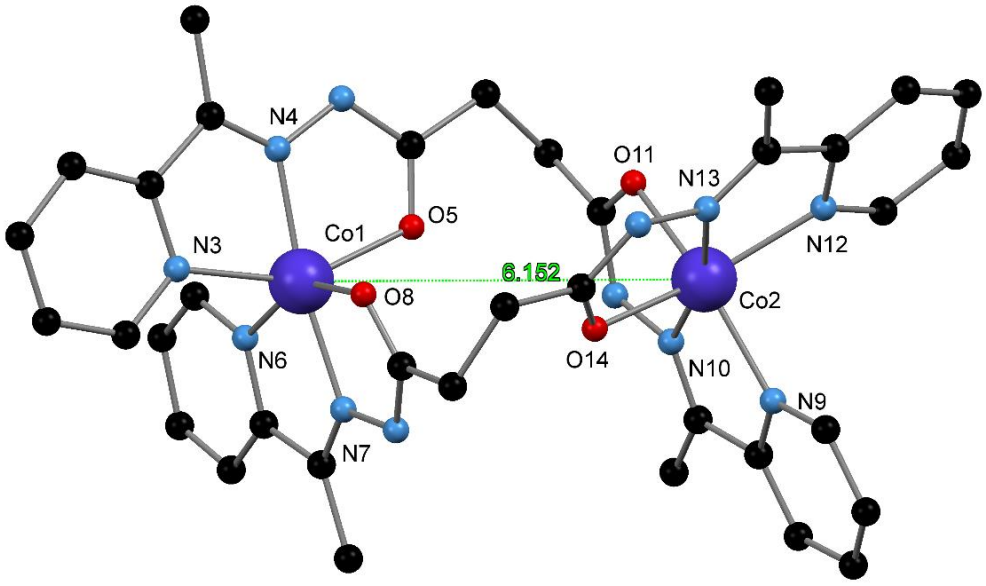

*Figure 3.3.1.i: The asymmetric unit of complex **3.6** with Co(II) centres and coordinating atoms labeled. The Co1···Co2 separation is shown in green. The hydrogen atoms, anions and solvent molecules have been omitted for clarity.*

The six coordinate Co(II) centres are significantly distorted from idealised octahedral symmetry with octahedral distortion parameters (Σ) of 129° and 134° for Co1 and Co2, respectively. The C-O bond lengths range from 1.239(3) to 1.243(3) Å and confirm that the ligand is coordinating in the neutral imino-keto form. There is a significant twist in the succinyl backbone of the ligand with two comparable torsion angles of 71.9(3)° and 72.4(3)°. The helicate in the asymmetric unit exhibits *M* helical chirality, while the *P* enantiomer is generated by the action of an inversion centre to give a racemic crystal. The Co1···Co2 separation for complex **3.6** measures 6.1524(5) Å (*Figure 3.3.1.i*). The charge of the $[Co_2(\mathbf{L3.2})_2]^{4+}$ helicate is balanced by four perchlorate anions, two of which were disordered and modelled as over two positions. Complex **3.6** crystallises with a number of solvent molecules. There is one water molecule hydrogen bond to the N-H moiety of the hydrazone functionality on one of the **L3.2** ligands. There are two complete occupancy benzene molecules, one of which is located on an inversion centre. A partial occupancy benzene molecule is disordered and modelled over two positions with occupancies of 10% and 75%, along with two partial occupancy water molecules both with occupancies of 15%. The three remaining N-H hydrazide moieties hydrogen bond to three of the perchlorate anions (*Figure 3.3.1.ii*). Two of these anions are located in the asymmetric unit while the third is generated by the action of a mirror plane. Two further hydrogen bond interactions occur between the two hydrogen atoms of the water molecule and two perchlorate anions. The hydrogen bond interactions are summarised in *Appendix Table 3.6.2.viii*. The perchlorate···water···hydrazide hydrogen bond interactions propagate as one-dimensional chains in the plane of the crystallographic *b*-axis. Neighbouring helicate units of complex **3.6** interact via off-set π-π stacking interactions between the coordinated pyridine rings with a π(centroid)···π(centroid) separation of 3.760(2) Å. These π-π interactions occur for one pyridine ring at either end of the helicate, such that the pyridine rings participating in the interaction are not located on the same ligand. These weak interactions form one-dimensional supramolecular chains that pack relatively 'loosely' together. The resultant cavity between these one-dimensional chains is occupied predominantly by perchlorate anions. One perchlorate anion forms a non-conventional C-H···O hydrogen bond interaction with a neighbouring helicate structure. This occurs with an H···O separation of 2.484(2) Å along with the aforementioned hydrogen bond interactions with the N-H moiety (*Figure 3.3.1.iii* and *Figure 3.3.1.iv*).

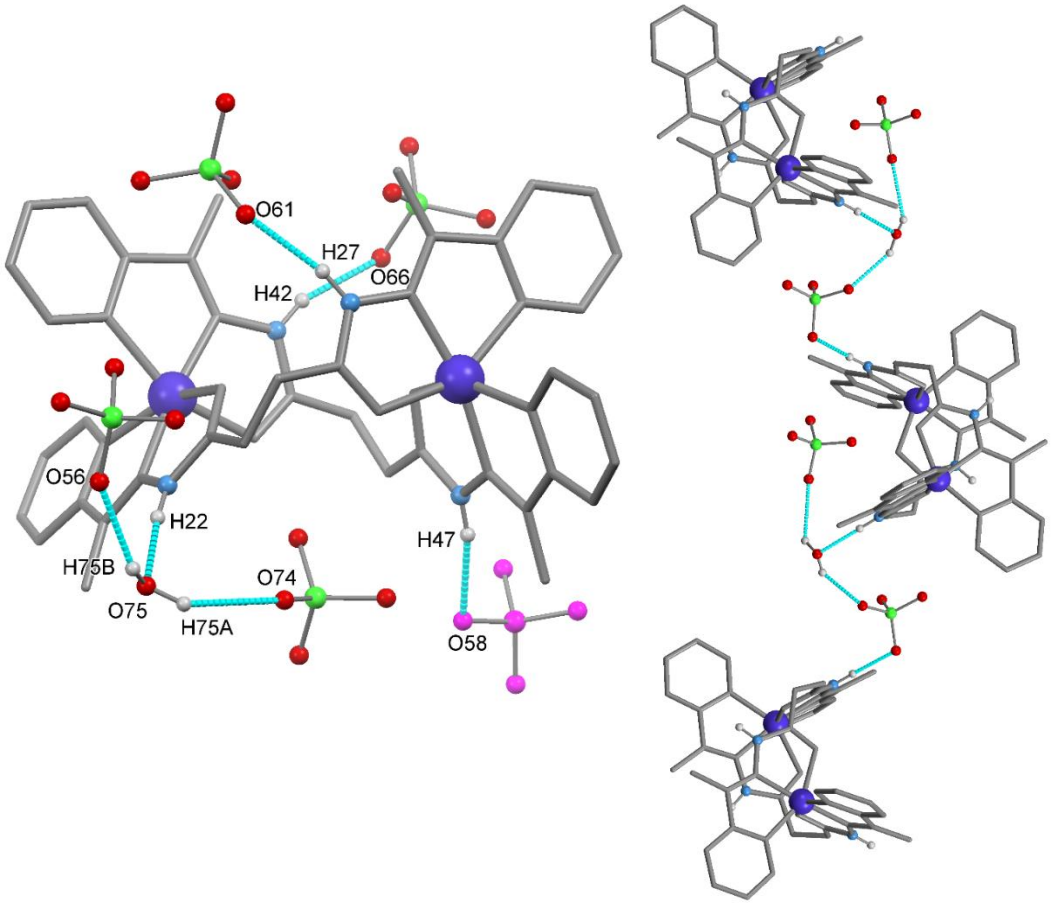

Figure 3.3.1.ii: (left) The hydrogen bond interactions of the N-H hydrazide moieties with the water molecule and the perchlorate anions. The symmetry generated perchlorate anion is shown in pink. (right) The one-dimensional hydrogen bond network formed between the helicate units via the perchlorate anions and the water molecule. Hydrogen bond interactions are shown in light blue. The atoms (aside from the Co(II) centres) not participating in hydrogen bond interactions are shown in grey with only the hydrazide hydrogen are shown for clarity.

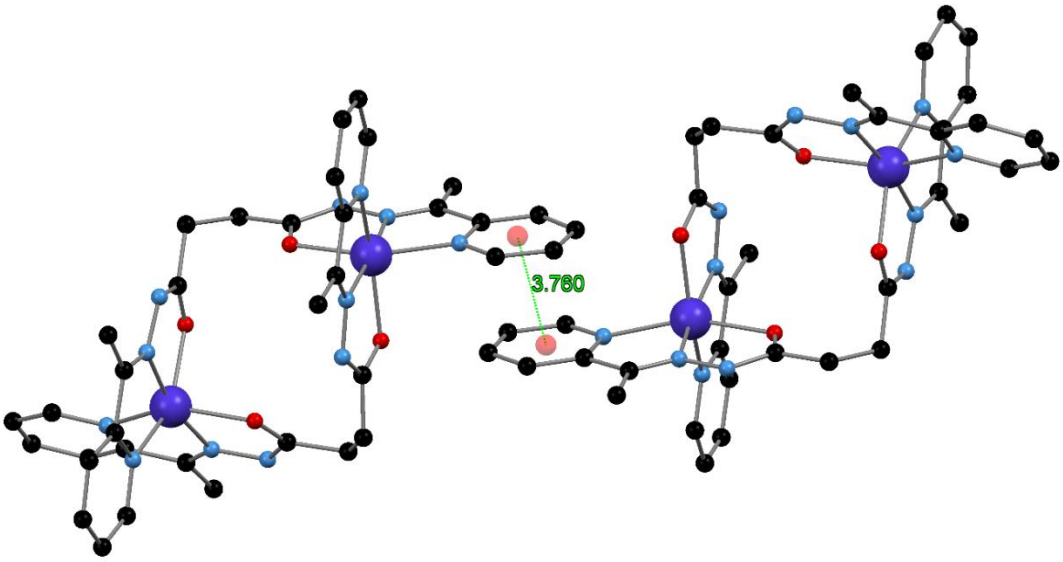

Figure 3.3.1.iii: The π-π stacking interactions of the coordinated pyridine rings with the π(centroid) represented by red spheres and π(centroid)···π(centroid) separations shown in green. Hydrogen atoms, anions and solvent molecules have been omitted for clarity.

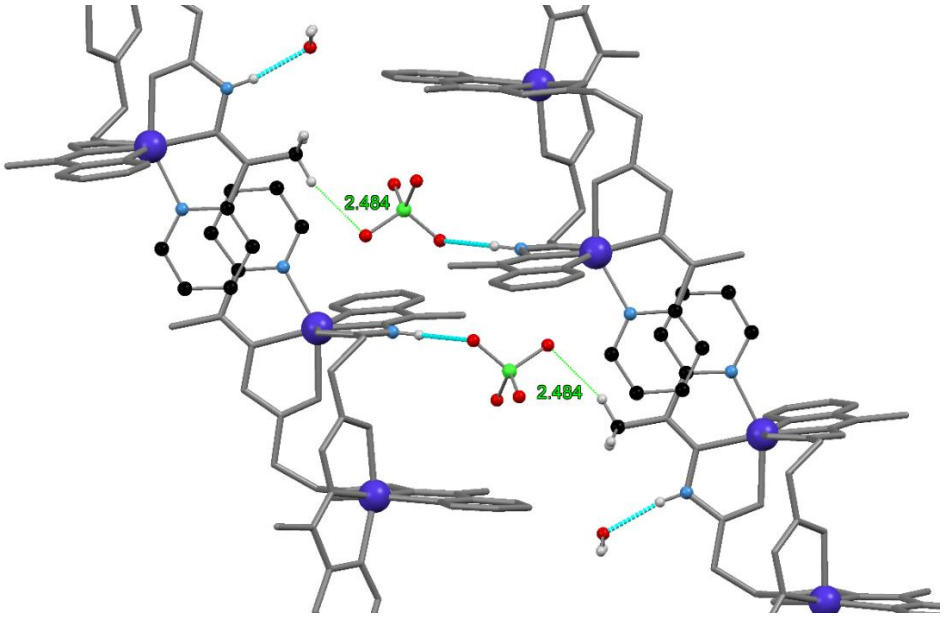

Figure 3.3.1.iv: The C-H···O non-conventional hydrogen bonds and N-H···O hydrogen bonds to the perchlorate anions which link the π-π stacked one-dimension chains. Hydrogen atoms and solvent molecules not participating in hydrogen bond interactions omitted for clarity. C-H···O interactions shown in green and N-H···O hydrogen bond interactions shown in light blue.

3.3.2 $[Co_2(L3.2)_2](OTf)_4$, 3.7

One equivalent of Co(II) chloride and two equivalents of Ag(I) triflate were stirred in acetonitrile resulting in the formation of a white precipitate corresponding to Ag(I) chloride. The resultant Co(II) triflate solution was filtered and ligand **L3.2** was added, generating a yellow solution. Vapor diffusion of benzene into the acetonitrile solution of **3.7** gave thin orange plate crystals suitable for single crystal X-ray diffraction with synchrotron radiation. The data were solved and refined in the non-centrosymmetric orthorhombic space group *Fdd*2 (R = 6.25%). The Flack parameter of 0.45(2) could not be refined to an unambiguous value and the structure was determined to be inversion twinned. The asymmetric unit contained one complete helicate complex made up of two **L3.2** ligands and two Co(II) ions and a further half helicate complex made up of one **L3.2** ligand and one Co(II) centre. The action of a 2-fold rotation axis generates the second part of the half helicate in the asymmetric unit (*Figure 3.3.2.i*).

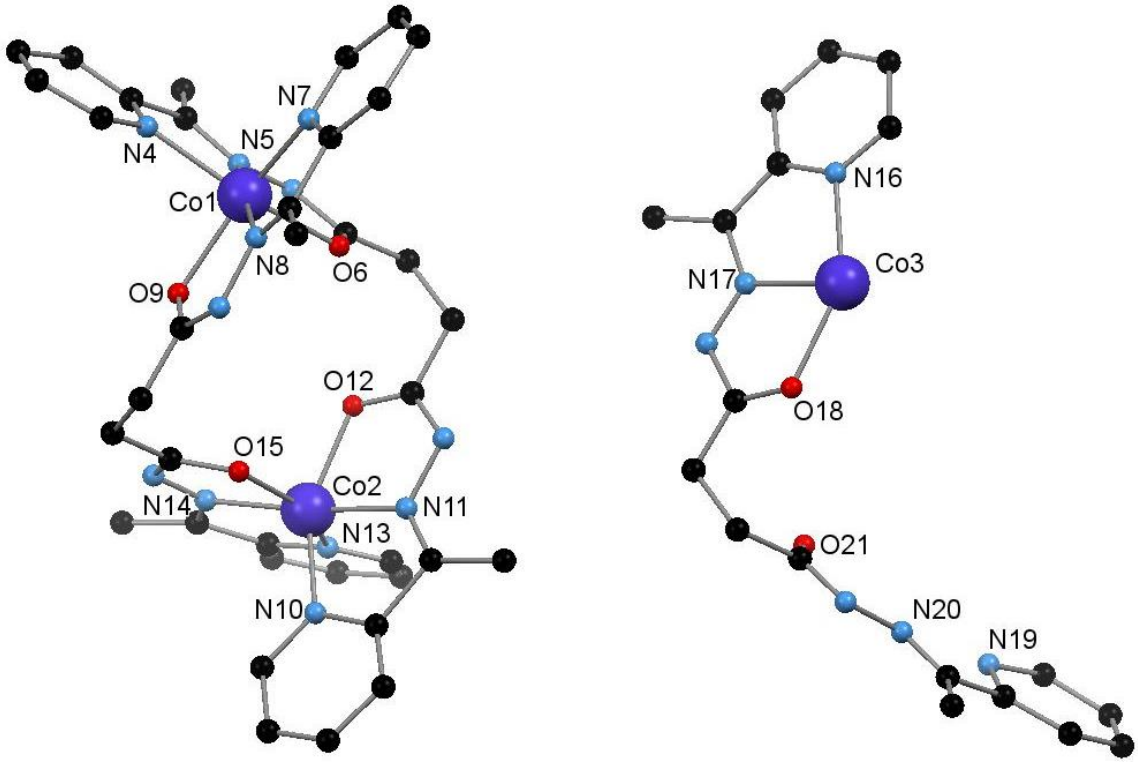

*Figure 3.3.2.i: The asymmetric unit of complex **3.7** composed of one complete helicate unit containing Co1 and Co2 and one half helicate containing Co3. Only the coordinating atoms and metal centres are labeled with the hydrogen atoms and anions are omitted for clarity.*

Therefore, there are three crystallographically unique Co(II) centres with the charge balanced by six triflate anions. The ligand coordinates to the Co(II) centres in the previously observed tridentate meridional manner and the Co(II) centres exist in a distorted octahedral N_4O_2 coordination sphere. The Co-N and Co-O bond lengths are indicative of HS Co(II), as anticipated with this weak field ligand much like the previous complexes (*Appendix Table 3.6.2.ii*). The Co(II) centres are significantly distorted from idealised octahedral symmetry with octahedral distortion parameters (Σ) for Co1, Co2 and Co3 of 128°, 126° and 135° respectively. The C-O bond lengths range from 1.18(2) to 1.31(2) Å and confirm that, like complex **3.6**, the ligand is coordinating in the neutral imino-keto form. There is a significant twist in the succinyl backbone of the ligand with three crystallographically unique torsion angles; 67(2)° and 70(2)° from the helicate containing Co1 and Co2 and 72(2)° from the helicate containing Co3. The complete helicate in the asymmetric unit exhibits *M* helical chirality, while the half helicate exhibits *P* helical chirality resulting in a non-centrosymmetric crystal.

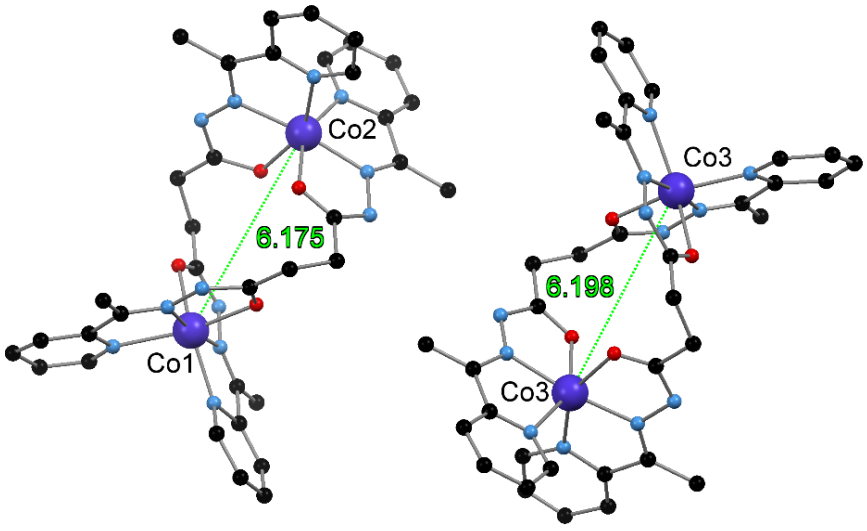

Figure 3.3.2.ii: The crystallographically unique helicate containing Co1 and Co2 and the helicate containing Co3 for which the complete helicate is generated by the action of a mirror plane. The Co1···Co2 and Co3···Co3' separations are shown in green (prime symbol ' denotes symmetry generated atom). Hydrogen atoms and anions are omitted for clarity.

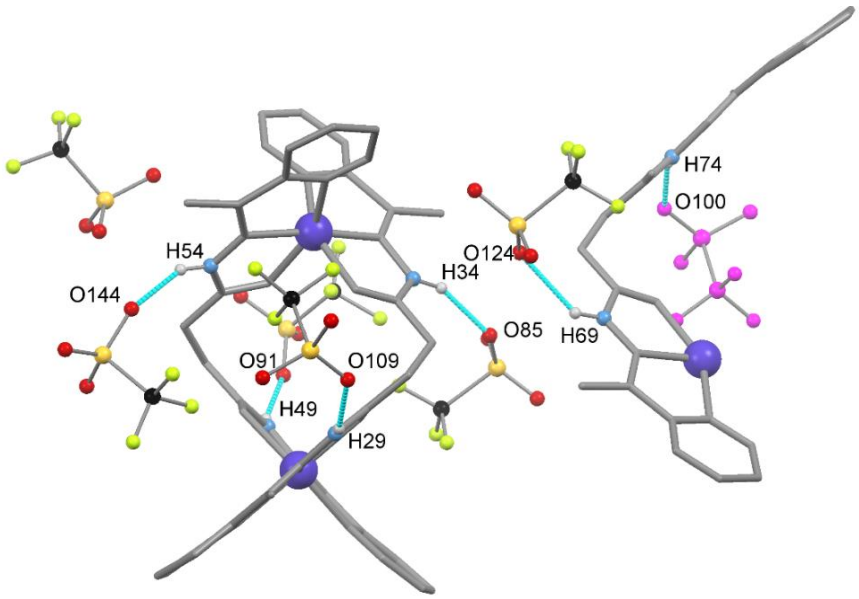

*Figure 3.3.2.iii: The contents of the asymmetric unit of **3.7** highlighting the hydrogen bond interactions between the N-H hydrazone moieties and the oxygen atoms of the triflate anions. The symmetry generated triflate anion is shown in purple and the hydrogen bond interactions are shown in light blue. Hydrogen atoms not participating in the illustrated interactions are omitted for clarity.*

The Co1···Co2 separation is 6.175(3) Å for the complete helicate while the Co3···Co3' (the prime symbol denotes symmetry generated atom) separation is 6.198(3) Å for the half helicate, both slightly more elongated than the previous example (*Figure 3.3.2.ii*). The complete helicate in the asymmetric unit features all N-H hydrazide moieties hydrogen bonding to the oxygen atoms of the surrounding triflate anions, as does the half helicate (*Figure 3.3.2.iii*). One triflate anion hydrogen bonding to the half helicate is generated by the action of a 2-fold rotation. These hydrogen bond interactions are summarised in *Appendix Table 3.6.2.ix*. Unlike complex **3.6**, there is no hydrogen bond network linking together neighbouring helicate units. In fact, the triflate anions promote a close packing of the helicate units and anions such that unlike the previous example **3.6**, no solvent molecules are present in the crystal structure.

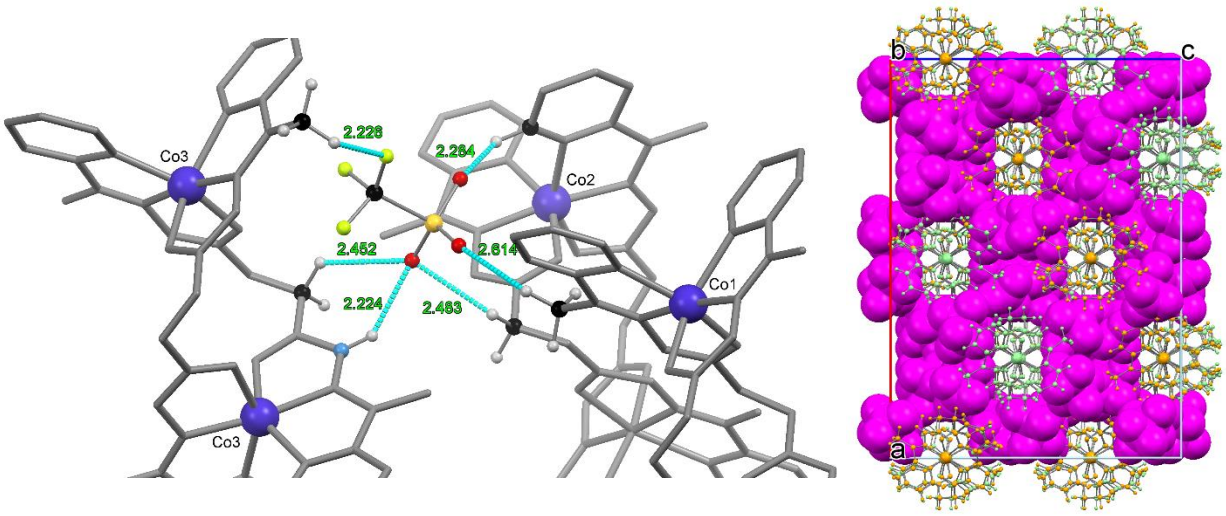

Figure 3.3.2.iv: (left) The non-conventional C-H···X (X = O or F) hydrogen bond interactions between the triflate anions and the hydrazone methyl group, the C-H moieties of the coordinating pyridine rings and the methyl groups of the spacer. C-H···X interactions are shown in light blue while hydrogen atoms not participating in the illustrated interactions omitted for clarity. (right) The packing of the helicates, shown in green (Co1 and Co2) and orange (Co3) with the triflate anions shown in space filling representation (purple) occupying the cavities between the helicates.

This close packing of the helicates and anions results in no observable π-π stacking interactions. The helicates pack such that the anions are enclosed in small 'pockets', stabilised by the formation of multiple weak C-H···O and C-H···F non-conventional hydrogen bonds. These interactions occur between the linker methylene groups, the methyl groups of the hydrazone moiety and C-H moieties of the coordinated pyridine rings. The H···O and H···F interactions range from 2.224(6) to 2.614(6) Å with the strongest interaction occurring between the fluorine atom of the triflate anions and the C-H moiety of a methyl group substituent of the hydrazone moiety (*Figure 3.3.2.iv*).The lack of solvent in the crystal structure resulted in a TGA with no mass loss until decomposition at 269 °C. The presence of impurities in the bulk phase is indicated by the elemental analysis. As there is no solvent modelled in the crystal structure, nor the presence of solvent indicated by TGA, the difference in the measured and calculated elemental analysis cannot be attributed to the occurrence of solvent molecules. Despite all attempts, a bulk phase pure sample of **3.7** could not be synthesised.

3.3.3 $[Co_2(L3.2)_2](BF_4)_4$, 3.8

Stoichiometric amounts of Co(II) tetrafluoroborate and **L3.2** were stirred in acetonitrile to give a yellow solution. Vapor diffusion of diisopropyl ether into the acetonitrile solution of **3.8** gave orange plate crystals suitable for single crystal X-ray diffraction. The data were solved and refined in the monoclinic space group *C*2/*c* (R = 8.89%). The asymmetric unit contained one **L3.2** ligand coordinated to one Co(II) ion with complete dinuclear double helicate structure formed by the action of a 2-fold rotation axis (*Figure 3.3.3.i*). Therefore, there is a single crystallographically unique Co(II) centre in an N_4O_2 octahedral coordination environment. The Co-N and Co-O bond lengths are indicative of HS Co(II), much like complexes **3.6** and **3.7** (*Appendix Table 3.6.2.iii*). The single crystallographically unique Co(II) centre is significantly distorted from idealised octahedral symmetry with an octahedral distortion parameter (Σ) of 130°. The C-O bond lengths range from 1.224(7) to 1.230(7) Å and confirm that, much like complexes **3.6** and **3.7**, the ligand is coordinating in the neutral imino-keto form. There is a significant twist in the succinyl backbone of the ligand with a torsion angle of 71.0(5)° comparable to the previous complexes. The helicate in the asymmetric unit exhibits *p* helical chirality, while the *m* enantiomer is generated by the action of an inversion centre to give a racemic crystal. The Co1···Co1' separation of **3.8** measures 6.206(2) Å (the prime symbol ' denotes a symmetry generated atom), slightly greater than that of complex **3.6** (*Figure 3.3.3.ii*).

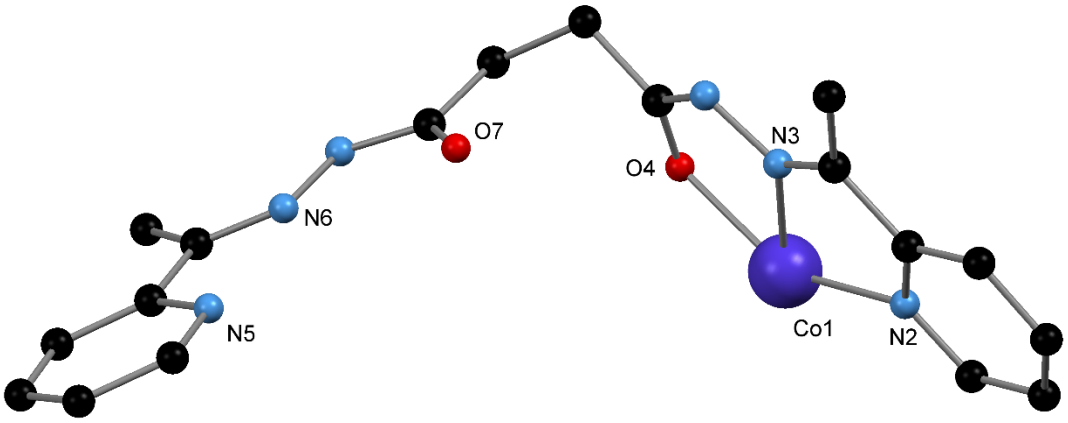

*Figure 3.3.3.i: (top) The asymmetric unit of **3.8** with coordinating atoms and the Co(II) centres labeled.*

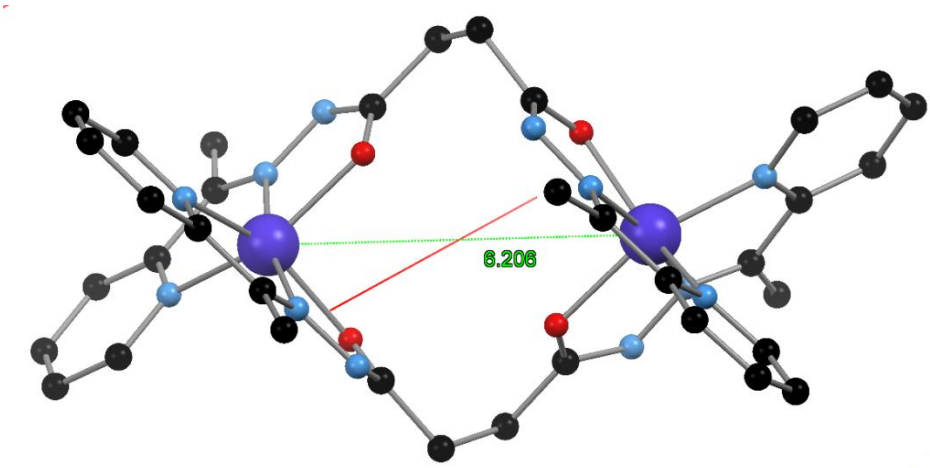

Figure 3.3.3.ii: The complete helicate structure as generated by the action of the 2-fold rotation axis shown in red. The Co1···Co1' separation is shown in green. Hydrogen atoms, anions and solvent molecules have been omitted for clarity.

The charge of the $[Co_2(\mathbf{L3.2})_2]^{4+}$ helicate is balanced by four tetrafluoroborate anions. As there is only one crystallographically unique Co(II) centre and consequently, there is one complete occupancy tetrafluoroborate anion and two partial occupancy tetrafluoroborate anions each modelled with 50% occupancy. One of the partial tetrafluoroborate anions and the full occupancy tetrafluoroborate anions both hydrogen bond to the hydrazide N-H moieties in the asymmetric unit. The partial occupancy anion is modelled as sharing the position with a half occupancy water molecule which participates in a similar hydrogen bond interaction (*Appendix Table 3.6.2.x*). Unlike **3.6**, there is no propagation of a hydrogen bond network between the anions and helicates (*Figure 3.3.3.iii*). A π-π stacking interaction occurs between the pyridine rings of neighbouring helicates with a π(centroid)···π(centroid) separation of 3.637(5) Å (*Figure 3.3.3.iv*). This occurs for the two crystallographically identical pyridine rings on each helicate, resulting in a one-dimensional chain in the *ab* crystallographic plane. This interaction is reinforced by a non-conventional C-H···O hydrogen bond interactions between a C-H moiety of the coordinated pyridine ring (participating in the π-π stacking interaction) and the coordinated oxygen on the hydrazone moiety. This interaction occurs with an H···O separation of 2.532(3) Å. As this water molecule also acts as a hydrogen bond acceptor to a hydrazide moiety, this results in the propagation of a non-conventional hydrogen bond network (*Figure 3.3.3.iii*).

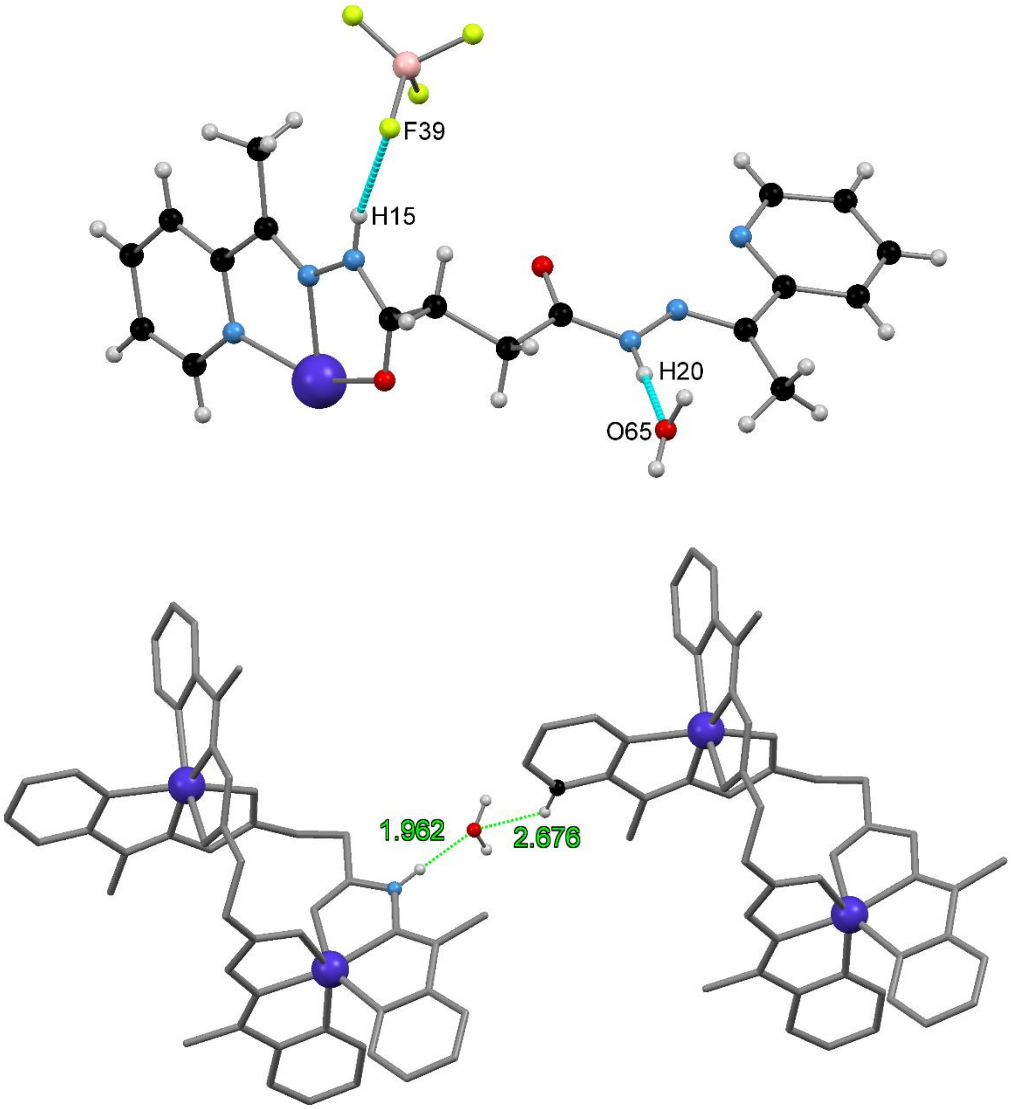

*Figure 3.3.3.iii: (top) The hydrogen bond interactions in the asymmetric unit of **3.8** between the N-H hydrazide moieties and the tetrafluoroborate anion and water molecule. The hydrogen bonds are shown in light blue. (bottom) The weak interaction between two neighbouring helicates via the N-H···O hydrogen bond interaction and a C-H···O non-conventional hydrogen bond are shown in green. Hydrogen atoms and anions not participating in interactions are omitted for clarity.*

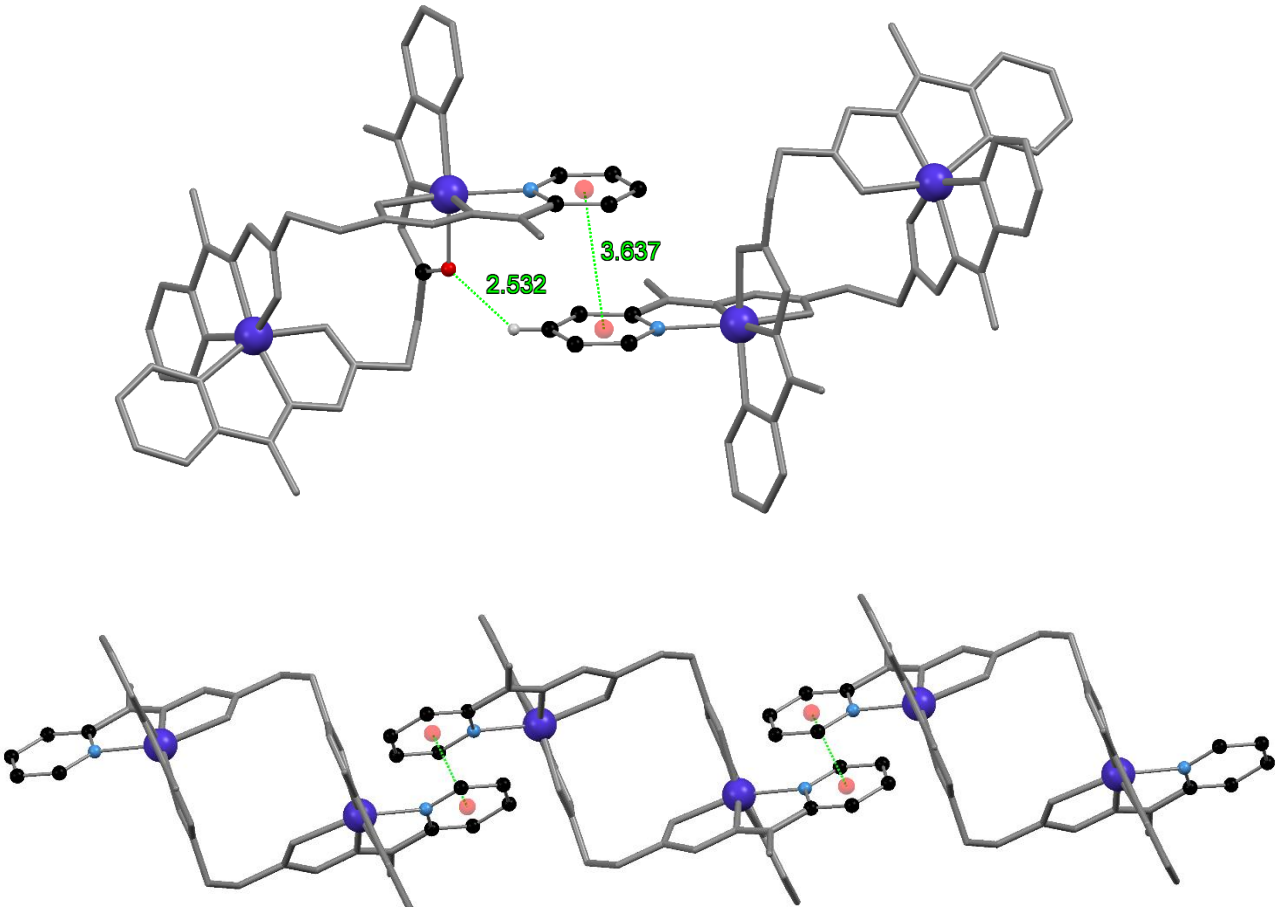

Figure 3.3.3.iv: (top) The π-π stacking interactions and the C-H···O interactions occurring between two coordinating pyridine rings and the hydrazone moieties on two neighbouring helicates. (bottom) The propagation of the π···π stacking interactions resulting in one dimensional supramolecular chains. The π(centroid) are represented as red spheres and the π(centroid)···π(centroid) separations are shown in green. Hydrogen atoms, anions and solvent molecules not participating in the illustrated interactions omitted for clarity.

There was a large amount of diffuse electron density due to the disordered nature of the solvent and therefore the SQUEEZE[418] function of PLATON[419] was employed (1.2 Å probe). The solvent accessible void was found to be 1281 $Å^3$ and calculated to contain approximately 366 electrons. This corresponds to 183 electrons per helicate and therefore the solvent content can be approximated as two diisopropyl ether and three acetonitrile solvent molecules (182 electrons). The crystals lost solvent extremely rapidly when removed from the mother liquor. TGA showed an immediate mass loss at room temperature until approximately 35 °C. Between 35 °C and 232

°C there is a further mass loss of 3.26% attributed to the loss of one acetonitrile molecule and half a water molecule (4.1%) from **3.8**·MeCN·0.5H_2O. There is one half occupancy acetonitrile and one-half occupancy water molecule modelled in the crystal structure and therefore one acetonitrile and one water molecule per helicate. The SQUEEZE results indicate that there is a further three acetonitrile molecules and two diisopropyl ether molecules of which two and three molecules, respectively, are lost upon removal of the crystals from the mother liquor. After 230 °C there is a rapid mass loss due to complex decomposition.

3.3.4 $[Co_2(L3.3)_2](ClO_4)_4$, 3.9

Stoichiometric amounts of Co(II) perchlorate and **L3.3** were stirred in acetonitrile to give a yellow/brown solution. Vapor diffusion of benzene into the acetonitrile solution of **3.9** gave orange block crystals suitable for single crystal X-ray diffraction. The data were solved and refined in the monoclinic space group $P2_1/n$ (R = 7.40%). The asymmetric unit contained two **L3.3** ligands coordinated to two Co(II) ions resulting in a dinuclear double helicate. The two crystallographically distinct Co(II) centres exist in an N_4O_2 octahedral coordination environment made up of two tridentate meridional pyridylhydrazone binding sites of **L3.3**. The Co-N and Co-O bond lengths are indicative of HS Co(II), as anticipated with this weak field ligand (*Appendix Table 3.6.2.iv*). The six coordinate Co(II) centres are significantly distorted from idealised octahedral symmetry with octahedral distortion parameters (Σ) of 153° and 143° for Co1 and Co2, respectively. These Σ values are noticeably higher than for complexes **3.6** to **3.8**. This can be attributed to the more sterically encumbered nature of the quinoline ring, promoting a more distorted coordination geometry. The C-O bond lengths range from 1.235(6) to 1.248(6) Å and confirm that the ligand is coordinating in the neutral imino-keto form. There is a significant twist in the succinyl backbone of the ligand with two comparable torsion angles of 72.7(4)° and 74.1(5)°. The helicate in the asymmetric unit exhibits *P* helical chirality, while the *M* enantiomer is generated by the action of an inversion centre to give a racemic crystal. The Co1···Co2 separation of **3.6** measures 6.460(1) Å, noticeably longer than the complexes with **L3.2** (*Figure 3.3.4.i*).

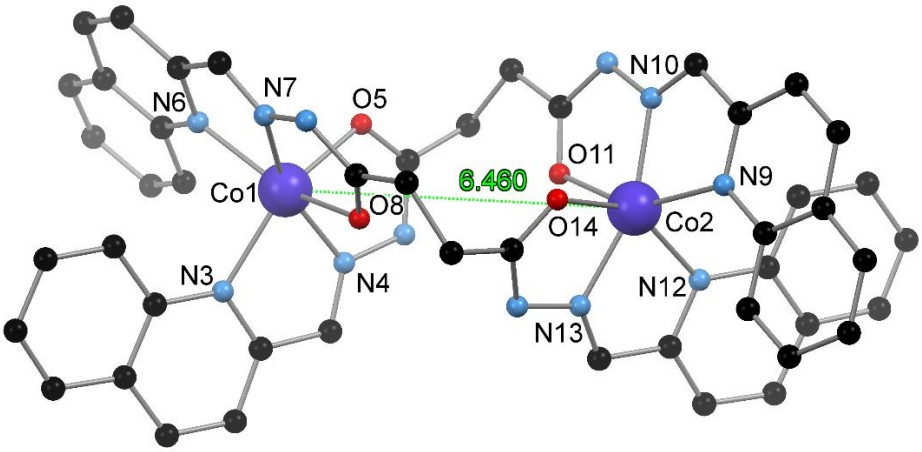

*Figure 3.3.4.i: The asymmetric unit of complex **3.9** with Co(II) centres and coordinating atoms labeled. The Co1···Co2 separation is shown in green. The hydrogen atoms, anions and solvent molecules have been omitted for clarity.*

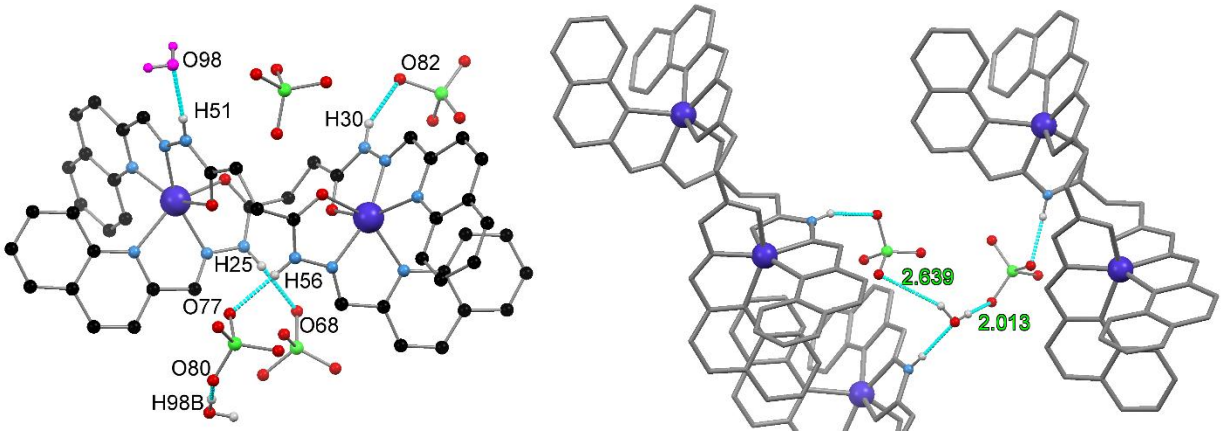

Figure 3.3.4.ii: (left) The hydrogen bond interactions of the N-H moieties with the water molecule and the oxygen atoms of the perchlorate anions. The symmetry generated water molecule is shown in purple. (right) The hydrogen bond network formed between three helicate units via the perchlorate anions and the water molecule. Hydrogen bond interactions are shown in light blue. Hydrogen atoms and anions not participating in the illustrated interactions omitted for clarity.

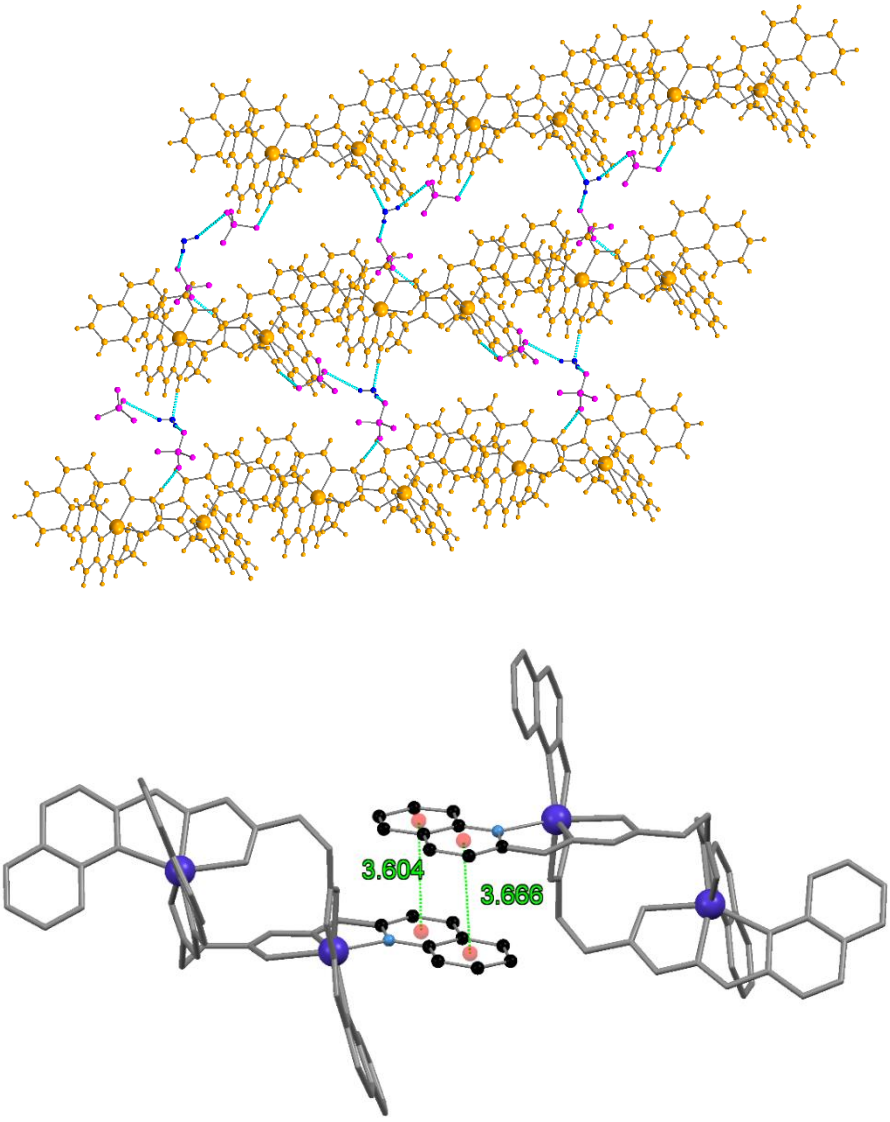

*Figure 3.3.4.iii: (top) The hydrogen bond network of **3.9** that results in the propagation of a two-dimensional supramolecular sheet. The dinuclear helicate units are shown in orange, the perchlorate anions in purple and the water molecules in dark blue. The hydrogen bond interactions are shown in light blue. (bottom) The π-π interactions for which the pyridine ring of one helicate overlaps with the benzene ring on a neighbouring helicate. The π(centroid) are represented by red spheres and the π(centroid)···π(centroid) separations are shown in green. Hydrogen atoms, solvent molecules and anions omitted for clarity.*

The charge of the $[Co_2(\mathbf{L3.3})_2]^{4+}$ helicate is balanced by four perchlorate anions, three of which are modelled as disordered over two positions. Complex **3.9** crystallises with a number of solvent

molecules. There is one full occupancy acetonitrile molecule and one full occupancy water molecule. Two partial occupancy acetonitrile molecules are modelled as disordered over the same position as a partial occupancy benzene molecule. There are two further partial occupancy benzene molecules, one of which is modelled as disordered over three positions and the other is located about an inversion centre.

Three of the four hydrazide N-H moieties participate in hydrogen bond interactions with the oxygen atoms of the perchlorate anions in the asymmetric unit *(Figure 3.3.4.ii*). The fourth hydrazide moiety hydrogen bonds to a symmetry generated water molecule. These hydrogen bond interactions are summarised in *Appendix Table 3.6.2.xi*. Two of the perchlorate anions hydrogen bonds to the water molecules. The hydrogen bond interaction of this water molecule with a neighbouring helicate and perchlorate anions generated by symmetry results in a hydrogen bond network that links three neighbouring helicates. The propagation of this network results in a supramolecular two-dimensional sheet in the *ab* crystallographic plane (*Figure 3.3.4.iii*). These hydrogen bond interactions are reinforced via the π-π stacking of the quinoline rings.

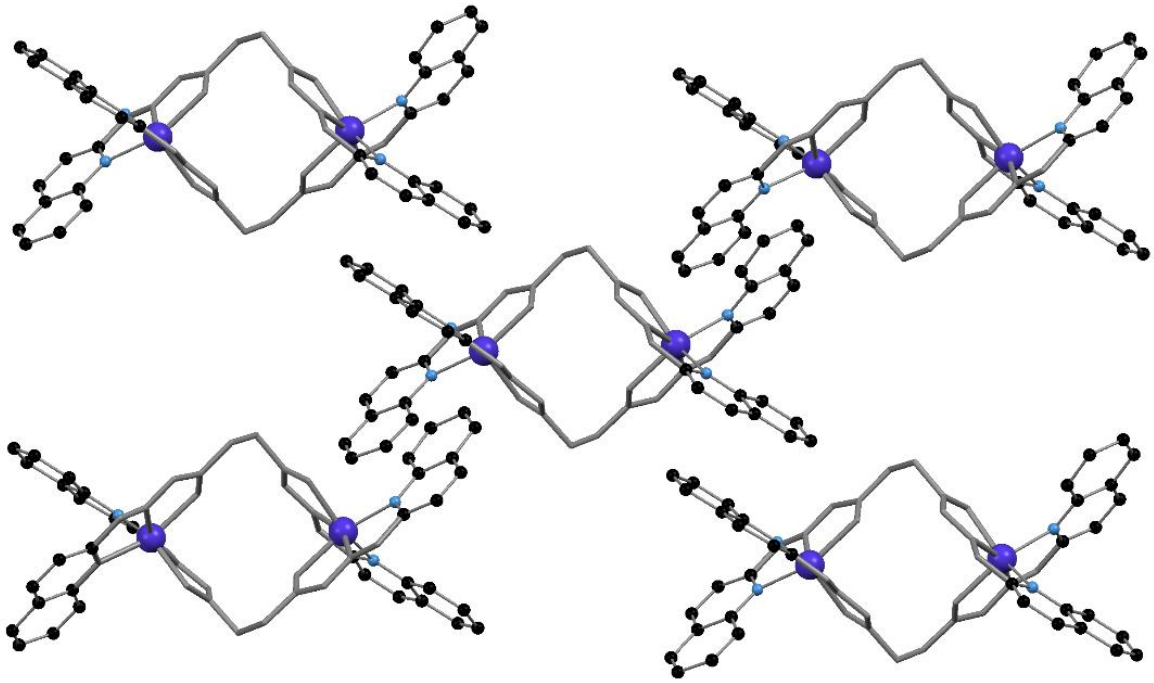

Fogure 3.3.4.iv: The two-dimensional supramolecular sheet generated by the two types of quinoline π-π stacking interactions. Hydrogen atoms, solvent molecules and anions omitted for clarity.

These π-π interactions between neighbouring helicates are measured via the π(centroid)···π(centroid) separation of the fused benzene and pyridine aromatic systems that form the quinoline functionality (*Figure 3.3.4.iv*). The π-π stacking interactions occur in two distinct forms. In one form the quinoline ring stack such that the benzene rings overlap with one another while the pyridine rings do not. The π(centroid)···π(centroid) separation of the two benzene rings is 3.509(4) Å. In the second form, the quinoline rings stack such that both the two benzene rings overlap, and the two pyridine rings overlap. The π(centroid)···π(centroid) separation of the two benzene rings is 3.666(4) Å while the pyridine rings are slightly closer at 3.604(4) Å (*Figure 3.3.4.iv*).

3.3.5 $[Co_2(L3.3)_2](OTf)_2$, 3.10

One equivalent of Co(II) chloride and two equivalents of Ag(I) triflate were stirred in acetonitrile resulting in the formation of a white precipitate corresponding to Ag(I) chloride. The resultant $Co(OTf)_2$ solution was filtered and ligand **L3.3** was added, generating a yellow/brown solution. Vapor diffusion of m-xylene into the acetonitrile solution of **3.10** gave orange block crystals suitable for single crystal X-ray diffraction. The data were solved and refined in the triclinic space group *P*-1 (R = 5.20%).

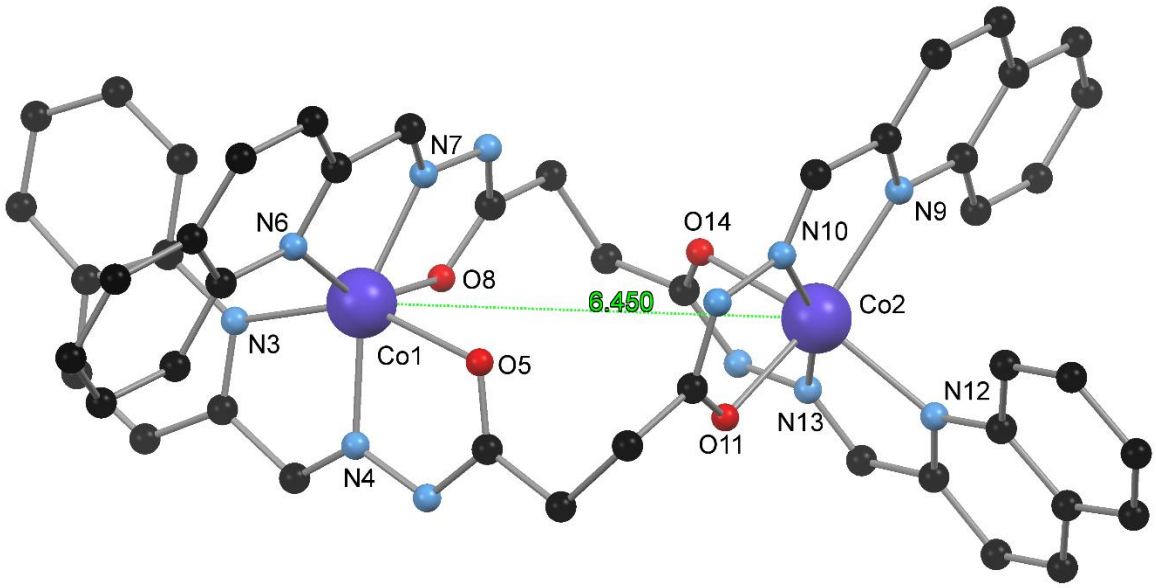

*Figure 3.3.5.i: The asymmetric unit of complex **3.10** with Co(II) centres and coordinating atoms labeled. The Co1···Co2 separation is shown in green. The hydrogen atoms, anions and solvent molecules have been omitted for clarity.*

The asymmetric unit contained two **L3.3** ligands coordinated to two Co(II) ions resulting in a dinuclear double helicate. The two crystallographically unique Co(II) centres exist in an N_4O_2 octahedral analogous to **3.9**. The Co-N and Co-O bond lengths are indicative of HS Co(II), as anticipated with this weak field ligand (*Appendix Table 3.6.2.v*). The octahedral Co(II) centres are significantly distorted from idealised octahedral symmetry with octahedral distortion parameters (Σ) of 140° and 132° for Co1 and Co2 respectively. The C-O bond lengths range from 1.239(4) to 1.244(3) Å and confirm that the ligand is coordinating in the neutral imino-keto form. There is a significant twist in the succinyl backbone of the ligand with two comparable torsion angles of 71.7(3)° and 71.0(3)°. The helicate in the asymmetric unit exhibits *M* helical chirality, while the *P* enantiomer is generated by the action of an inversion centre to give a racemic crystal. The the Co1···Co2 separation measures 6.4501(6) Å, similar to that of **3.9** (*Figure 3.3.5.i*). The charge of the $[Co_2(\mathbf{L3.3})_2]^{4+}$ helicate is balanced by four triflate anions, three of which are each modelled as disordered over two positions. Complex **3.10** crystallises with a number of solvent molecules. There are three acetonitrile solvent molecules, one of which is modelled as disordered over two positions with occupancies of 60% and 40%. There is a further full occupancy water molecule and two half occupancy water molecules in the structure also participating in hydrogen bond interactions. Three of the hydrazide N-H moieties participate in hydrogen bond interactions with the oxygen atoms of the triflate anions. The fourth N-H moiety participates in a hydrogen bond interaction with the oxygen atom of a water molecule (*Figure 3.3.5.ii*). The hydrogen bond interactions are summarised in *Appendix Table 3.6.2.xii*. The full occupancy water molecule, acting as a hydrogen bond acceptor to the hydrazide N-H moiety, also acts as a hydrogen bond donor to two neighbouring triflate anions. This results in a hydrogen bond network that links one helicate to two neighbouring helicates. This interaction occurs twice per helicate unit, once via a hydrogen bond to the water molecule and once via the hydrogen bond to the triflate anion. This results in the propagation of a hydrogen bond chain approximately parallel to the crystallographic *a*-axis (*Figure 3.3.5.iii*).

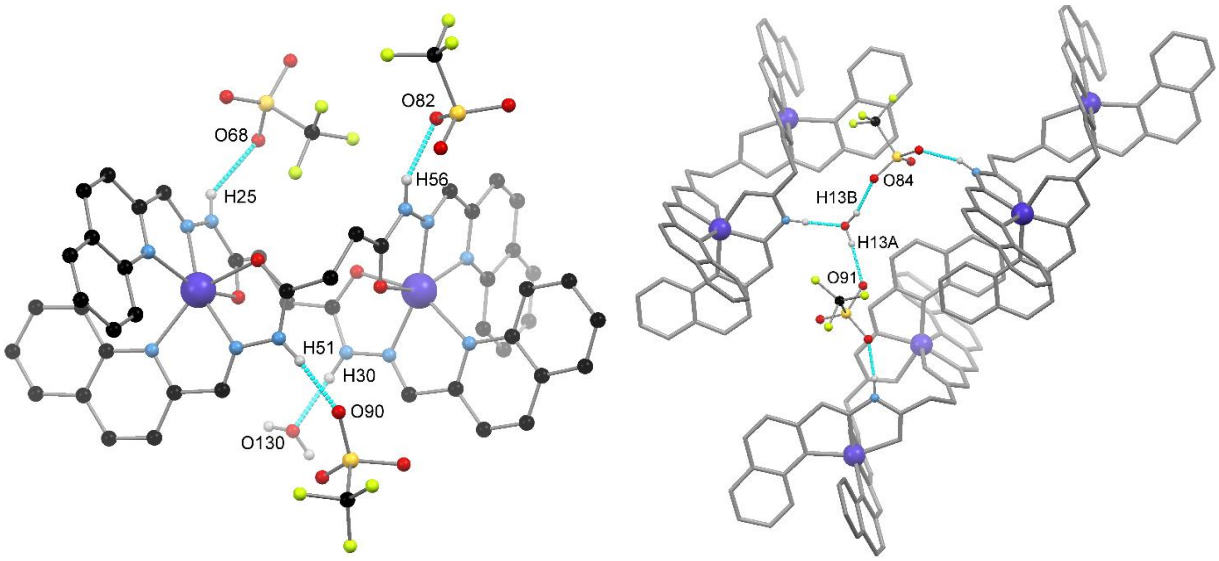

Figure 3.3.5.ii: (left) The hydrogen bond interactions of the N-H hydrazide moieties with the triflate anions and water molecule. (right) The hydrogen bond network linking three neighbouring helicates via a water molecule acting as both a hydrogen bond donor and acceptor and two triflate anions acting as two-fold hydrogen bond acceptors. Hydrogen bond interactions are shown in light blue. Hydrogen atoms, anions and solvent molecules not participating in the illustrated interactions omitted for clarity.

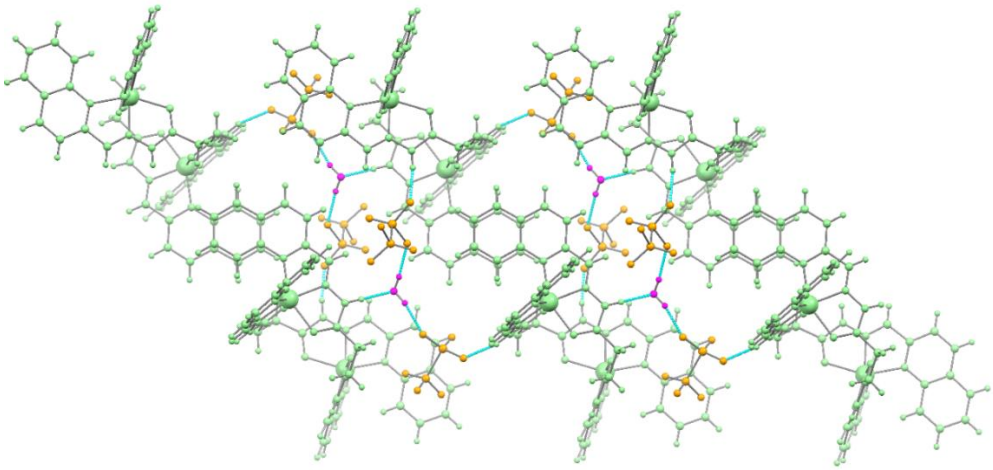

Figure 3.3.5.iii: The propagation of the hydrogen bond network. The helicates are shown in green while the triflate anions are shown in orange and the water molecules in purple. The hydrogen bond interactions are shown in light blue. Anions and solvent molecules not participating in the illustrated interactions omitted for clarity.

The benzene components of the quinoline rings overlap to form two types of π-π stacking interactions with π(centroid)···π(centroid) separations of 3.836(3) Å and 3.556(3) Å, referred to as type one and type two, respectively (*Figure 3.3.5.iv*). The first type of π-π stacking interaction occurs in conjunction with an edge-to-face C-H···π interaction with an H···π(centroid) separation of 2.740(1) Å. Alternating type one and type two interactions results in the formation of one-dimensional supramolecular chains running approximately parallel to the crystallographic [100] plane. These chains then interact with neighbouring chains via type two interactions to form a supramolecular two-dimensional sheet (*Figure 3.3.5.v*). The π-π interactions occurring in **3.10** are subtly different to those occurring in **3.9** due to the different relative orientations of the helicates due to the altered hydrogen bond network imposed by the triflate anions.

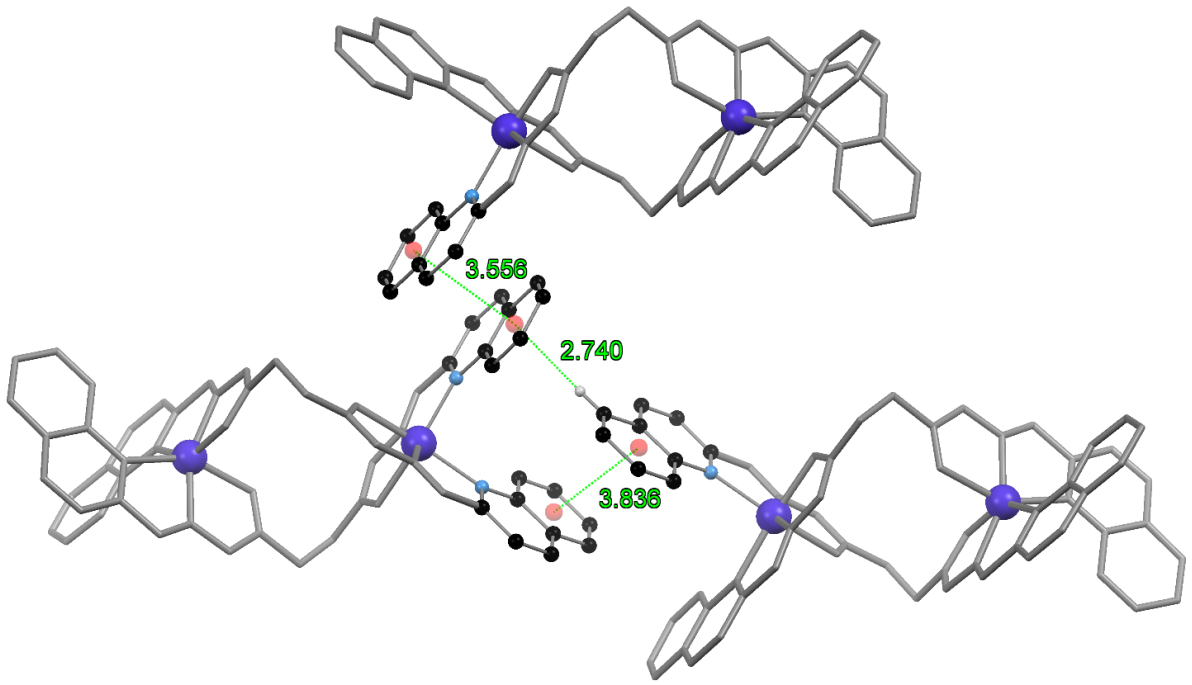

Figure 3.3.5.iv: The two types of π-π stacking interactions. Type one with a longer π···π separation occurs in conjunction with a C-H···π interaction. Type two occurs with a shorter π···π separation. The π(centroid) are represented by red spheres and π(centroid)···π(centroid) separations are shown in green. Hydrogen atoms not participating in the illustrated interactions, anions and solvent molecules omitted for clarity.

TGA analysis shows a gradual mass loss of 21.1% between 73 and 173 °C followed by a more rapid mass loss of 3.8% between 207 and 258 °C. Based on these results, it appears that upon the

removal of the crystals from the mother liquor, 1.5 acetonitrile molecules are lost to give **3.10**·1.5MeCN·2H_2O. The loss of two water molecules constitutes a mass loss of 2.1% to give **3.10**·1.5MeCN, followed by the loss of 1.5 acetonitrile molecules which constitutes a mass loss of 3.7% to give fully desolvated **3.10**. A rapid mass loss occurs after 360 °C due to complex decomposition

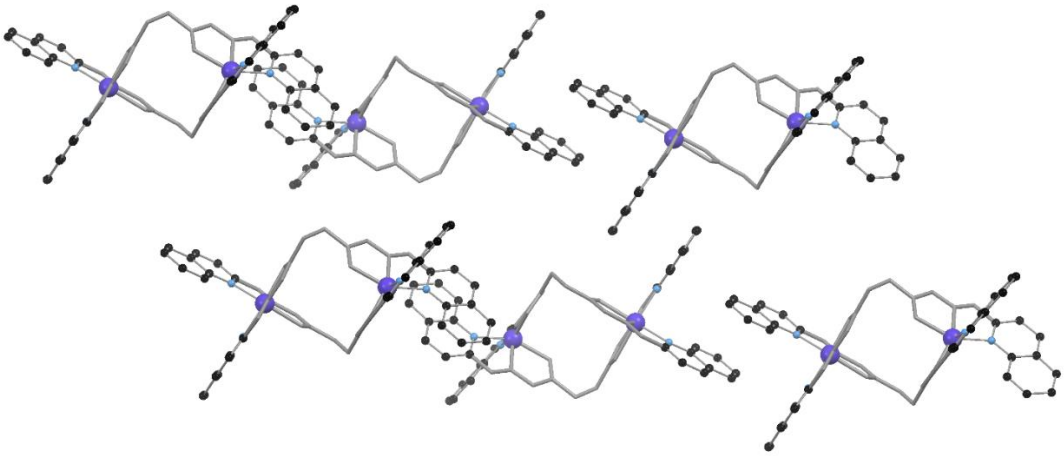

Figure 3.3.5.v: Alternating type one and type two π-π stacking interactions result in the formation of one-dimensional supramolecular chains which interact with neighbouring chains via type two π-π stacking interactions to give a two-dimensional supramolecular sheet. Hydrogen atoms, anions and solvent molecules omitted for clarity.

3.3.6 $[Co_2(L3.3)_2](BF_4)_4$, 3.11

Stoichiometric amounts of Co(II) tetrafluoroborate and **L3.3** were stirred in acetonitrile to give a yellow/brown solution. Vapor diffusion of diisopropyl ether into the acetonitrile solution of **3.11** gave orange block crystals suitable for single crystal X-ray diffraction. The data were solved and refined in the triclinic space group *P*-1 (R = 5.15%). The asymmetric unit contained two **L3.3** ligands coordinated to two Co(II) ions resulting in a dinuclear double helicate with a Co1···Co2 separation of 6.4341(5) Å (*Figure 3.3.6.i*). The two crystallographically unique Co(II) centres exist in an N_4O_2 coordination environment analogous to **3.9** and **3.10**. The Co-N and Co-O bond lengths are indicative of HS Co(II), as anticipated with this weak field ligand (*Appendix Table 3.6.2.vi*). The six coordinate Co(II) centres are significantly distorted from idealised octahedral symmetry with octahedral distortion parameters (Σ) of 140° and 136° for Co1 and Co2, respectively.

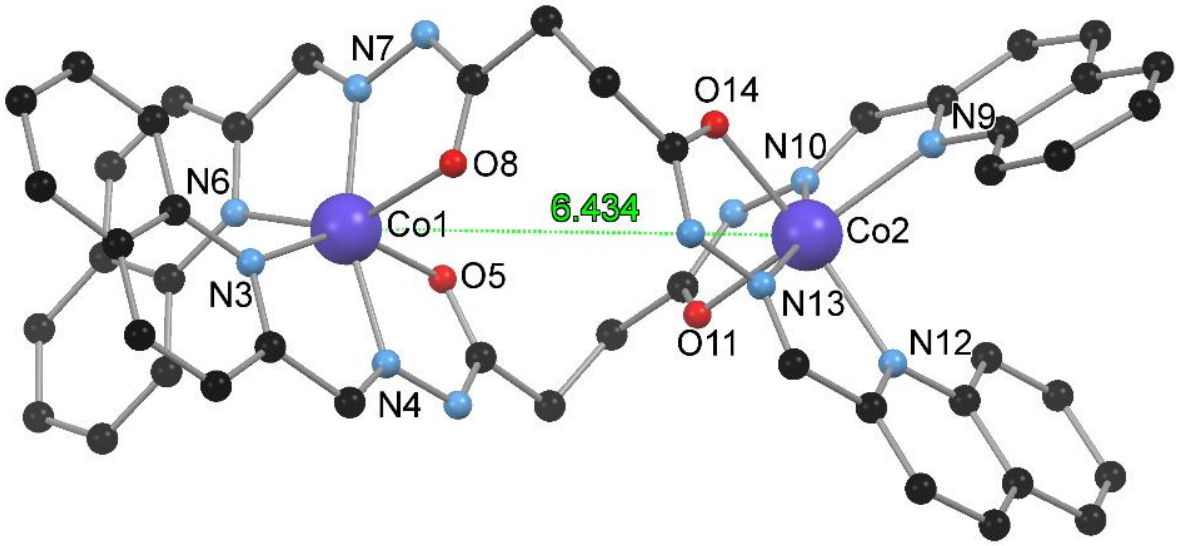

*Figure 3.3.6.i: The asymmetric unit of complex **3.11** with Co(II) centres and coordinating atoms labeled. The Co1···Co2 separation is shown in green. The hydrogen atoms, tetrafluoroborate anions and solvent molecules have been omitted for clarity.*

The C-O bond lengths range from 1.233(4) to 1.245(3) Å and confirm that the ligand is coordinating in the neutral imino-keto form. There is a significant twist in the succinyl backbone of the ligand with two comparable torsion angles of 70.6(3)° and 72.2(3)°. The helicate in the asymmetric unit exhibits *P* helical chirality, while the *M* enantiomer is generated by the action of an inversion centre to give a racemic crystal. The charge of the $[Co_2(\mathbf{L3.3})_2]^{4+}$ helicate is balanced by four tetrafluoroborate anions, two of which are modelled as disordered over two positions. Complex **3.11** crystallises with a number of solvent molecules. There are two disordered acetonitrile solvent molecules which are both modelled equally over two positions. A third partial occupancy acetonitrile molecule modelled over the same position as a partial occupancy water molecule with occupancies of 80% and 20% respectively.

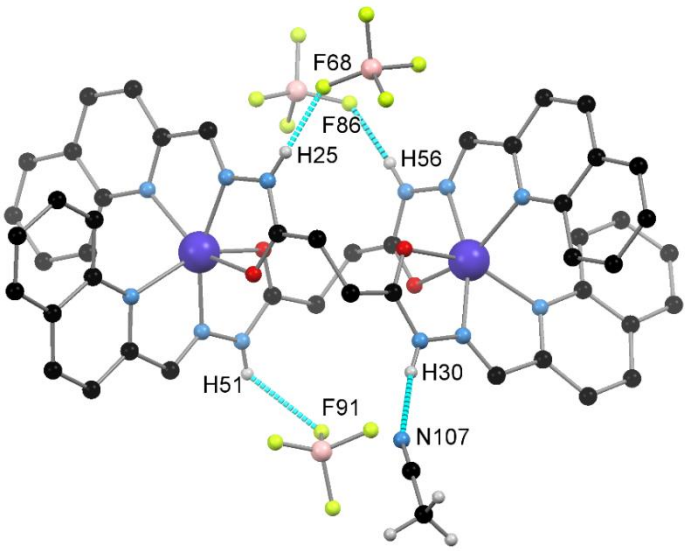

*Figure 3.3.6.ii: The hydrogen bond interactions in the asymmetric unit of **3.11** between the N-H hydrazide moieties and the tetrafluoroborate anion and acetonitrile molecule. Hydrogen bonds as shown in light blue. Hydrogen atoms, tetrafluoroborate anions and solvent molecules not participating in the illustrated interactions omitted for clarity.*

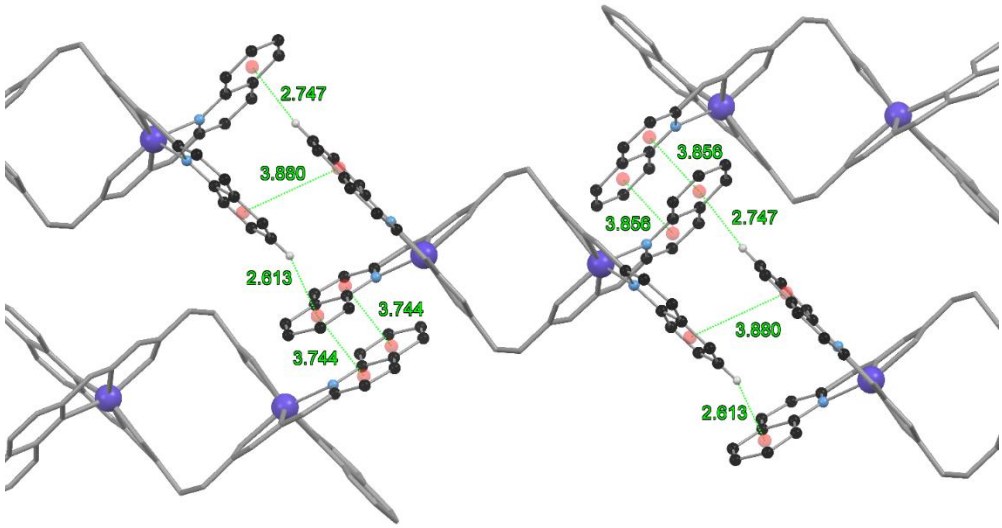

Figure 3.3.6.iii: The two types π-π stacking and C-H···π interactions occurring between neighbouring helicates. The π(centroid) are represented by red spheres and the C-H···π(centroid) and π(centroid)···π(centroid) separations are shown in green. Hydrogen atoms not participating in the illustrated interactions, solvent molecules and anions omitted for clarity.

Three of the hydrazide N-H moieties participate in hydrogen bond interactions with the tetrafluoroborate anions. The fourth N-H moiety participates in a hydrogen bond interaction with the nitrogen atom of an acetonitrile solvent molecule (*Figure 3.3.6.ii*). The hydrogen bond interactions are summarised in *Appendix Table 3.6.2.xiii*. The C-H moiety in the 6-position of the quinoline ring forms an edge-to-face C-H···π interaction with the benzene ring of a neighbouring quinoline moiety and vice versa, again resulting in a reciprocal interaction (*Figure 3.3.6.iii*). These two C-H···π interactions feature H···π(centroid) separations of 2.613(1) and 2.747(1) Å. A π-π stacking interaction occurs in a manner similar to that observed in **3.9** where the two pyridine and benzene rings of the quinoline moiety overlap to form a reciprocal interaction. Two crystallographically unique types of this interaction occur with π(centroid)···π(centroid) separations of 3.856(2) and 3.744(2) Å. These π-π and C-H···π interactions result in the formation of an undulating two-dimensional supramolecular sheet. These two-dimensional sheets then stack in an offset manner (*Figure 3.3.6.iv*).

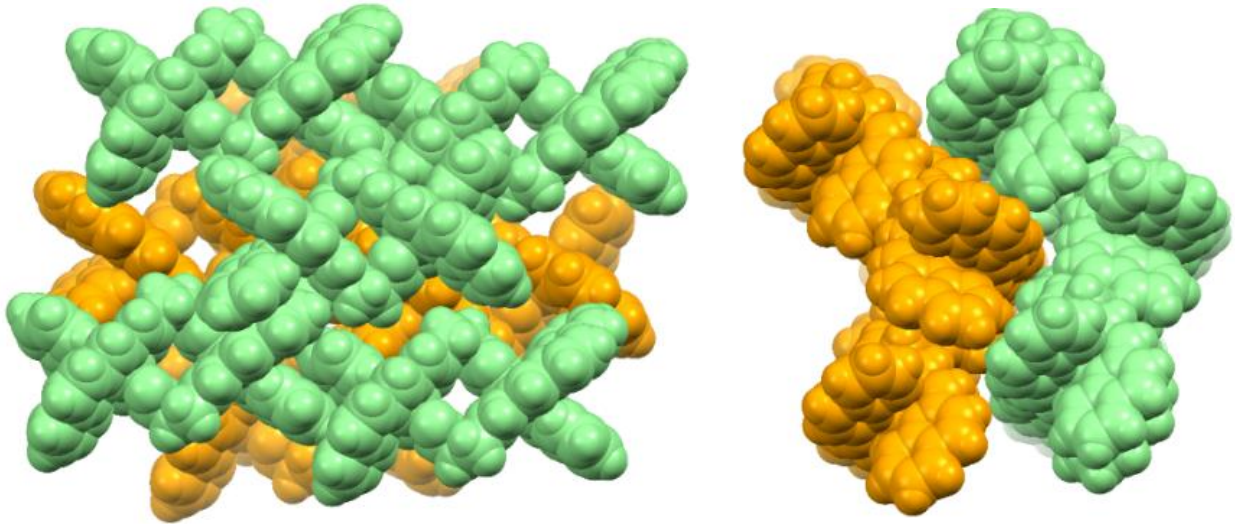

*Figure 3.3.6.iv: The packing of **3.11** is shown in space filling representation viewed down the crystallographic b- (left) and (right) c-axes. One undulating two-dimensional sheet is shown in green while the other is shown in orange. Solvent molecules and tetrafluoroborate anions omitted for clarity.*

3.3.7 $[Co_2(L3.5)_2](ClO_4)_4$, 3.12

Stoichiometric amounts of Co(II) perchlorate and **L3.5** were stirred in a 1:1 stoichiometric amount in acetonitrile to give a yellow solution. Vapor diffusion of benzene into the acetonitrile solution

of **3.12** gave orange block crystals suitable for single crystal X-ray diffraction. The data were solved and refined in the monoclinic space group $P2_1/c$ (R = 8.56%). The asymmetric unit contained two **L3.5** ligands coordinated to two Co(II) ions resulting in a dinuclear double helicate with a Co1···Co2 separation of 8.227(2) Å. The two crystallographically distinct Co(II) centres exist in an N_4O_2 octahedral coordination environment analogous to **3.6**-**3.8**. The Co-N and Co-O bond lengths are indicative of HS Co(II), as anticipated with this weak field ligand (*Appendix Table 3.6.2.vii*). The six coordinate Co(II) centres are significantly distorted from idealised octahedral symmetry with octahedral distortion parameters of 132° and 129° for Co1 and Co2 respectively. The C-O bond lengths range from 1.228(8) to 1.24(1) Å and confirm that the ligand is coordinating in the neutral imino-keto form. The adipate linker adopts a twisted 'L' type conformation (*Figure 3.3.7.i*).

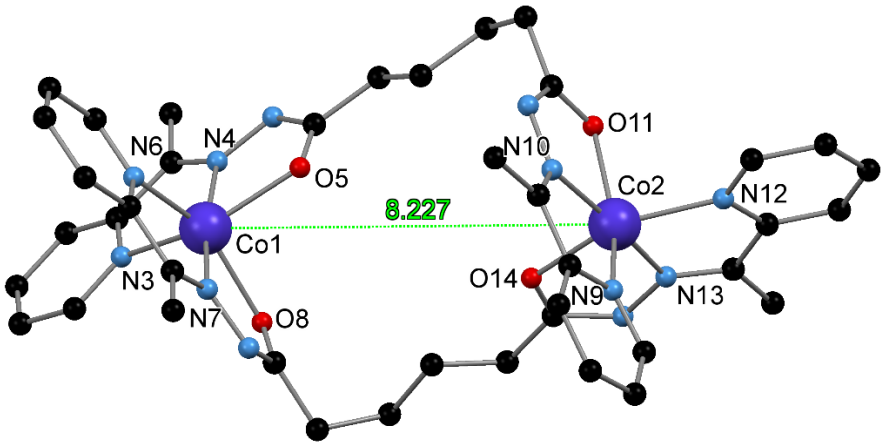

*Figure 3.3.7.i: The asymmetric unit of complex **3.12** with Co(II) centres and coordinating atoms labeled. The pitch of the helicate is shown in green. The hydrogen atoms, anions and solvent molecules have been omitted for clarity.*

Four of the carbon atoms exist in a *trans* straight chain alkane conformation. The last two carbon atoms are then twisted out of the plane by 85.3(4)° with torsion angles of the two strands of 61.5(8)° and 62.0(8)°. The helicate in the asymmetric unit exhibits *P* helical chirality, while the *M* enantiomer is generated by the action of an inversion centre to give a racemic crystal. The charge of the $[Co_2(\mathbf{L3.5})_2]^{4+}$ helicate is balanced by four perchlorate anions, three of which are disordered. One is modelled as disordered equally over two positions while the remaining two are modelled over over three positions with occupancies of 15, 25 and 60% and 25, 35 and 40%, respectively. Three of the N-H hydrazide moieties participate in hydrogen bond interactions with the perchlorate

anions (*Figure 3.3.7.ii*). The fourth N-H moiety participates in a hydrogen bond interaction with a water molecule which is, in turn, hydrogen bonding to a perchlorate anion. The hydrogen bond interactions are summarised in *Appendix Table 3.6.2.xiv*. These hydrogen bond interactions result in two types of hydrogen bond networks linking the neighbouring helicates. The first links two helicates together via the aforementioned perchlorate···water hydrogen bond bridge. This interaction is located about an inversion centre and therefore two crystallographically identical full occupancy water molecules and two full occupancy perchlorate anions make up an 8-membered hydrogen bond ring motif (*Figure 3.3.7.iii*). The two water molecules act as hydrogen bond donors in the ring and the perchlorate anions as hydrogen bond acceptors.

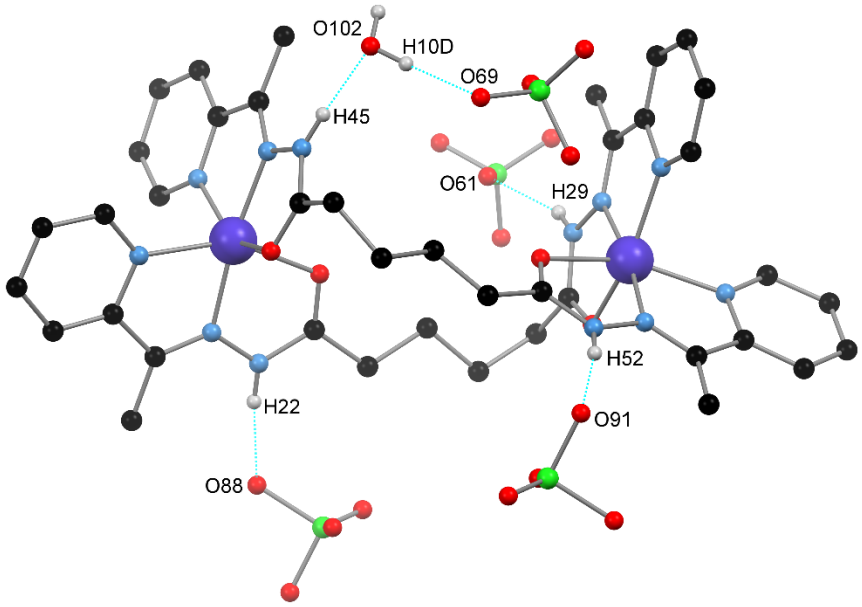

Figure 3.3.7.ii: The hydrogen bond interactions of the N-H hydrazide moieties occurring in ***3.12*** *with the water molecule and perchlorate anions. Hydrogen bonds are shown in light blue. Hydrogen atoms, anions and solvent molecules not participating in the illustrated interactions omitted for clarity.*

The water molecules also act as hydrogen bond acceptors, external to the aforementioned cyclic hydrogen bond motif. The second type of hydrogen bond network links three helicate units together in alternating directions. One perchlorate anion is disordered over two locations, one of which is about an inversion centre. Therefore, the partial occupancy perchlorate anion hydrogen bonds to two neighbouring helicates via crystallographcally identical N-H hydrazide moieties. A

second oxygen atom of the perchlorate anion then forms a hydrogen bond interaction to a third helicate unit via the N-H moiety. Due to the disorder of the anion about the inversion centre, this interaction is only partially present in the crystal structure.

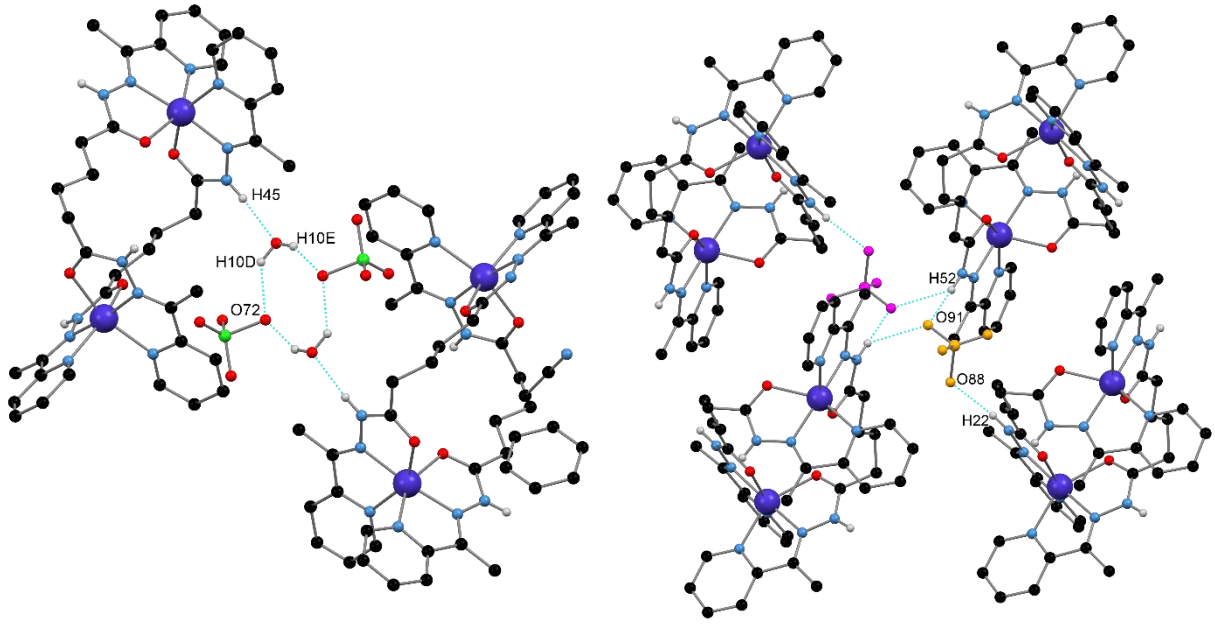

*Figure 3.3.7.iii: (left): The hydrogen bond network in **3.12** linking two neighbouring helicates via a cyclic hydrogen bond motif made up of two water molecules and two perchlorate anions. (right): The hydrogen bond network linking three neighbouring helicates in an alternating manner. The perchlorate anions are disordered about an inversion centre therefore the interaction alternates between the two positions of the perchlorate anion shown in purple and orange. Hydrogen bonds are shown in light blue. Hydrogen atoms, anions and solvent molecules not participating in the illustrated interactions omitted for clarity.*

There are a significant number of C-H···π interactions as the helicates interdigitate to form supramolecular dimers (*Figure 3.3.7.iv*). These interactions occur between the methyl C-H of the hydrazone functionality and the π-systems of the coordinated pyridine rings. There are three types of C-H···π interactions occurring, one of which is relatively weak with an H···π(centroid) separation of 3.781(3) Å. The other two are stronger with H···π(centroid) separations of 2.896(3) and 2.914(3) Å. Each interaction occurs twice per supramolecular dimer in a reciprocal fashion (*Figure 2.3.7.iv*).

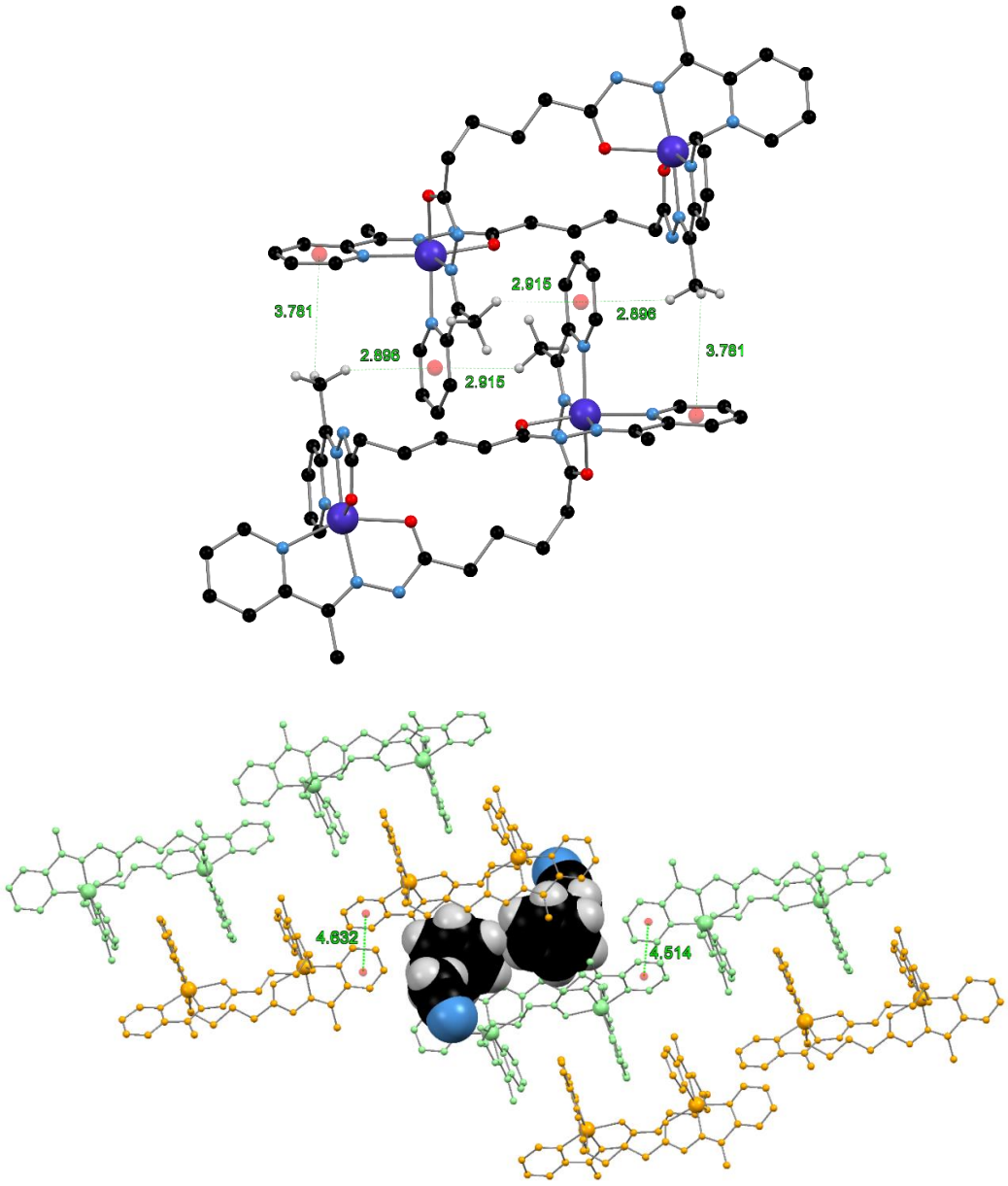

Figure 3.3.7.iv: (top) The C-H···π interactions resulting in the interdigitation of two neighbouring helicates. The π(centroid) are represented by red spheres and the C-H···π(centroid) and π(centroid)···π(centroid) separations shown in green. (bottom) The pairs of interdigitated helicates (orange and green) pack weakly together via π-π stacking interactions between the coordinated pyridine ring to form one-dimensional supramolecular chains. These chains pack together with the void between occupied by benzene and acetonitrile solvent molecules (space filling representation). Anions and hydrogen atoms not participating in the illustrated interactions omitted for clarity.

The helicate dimer units pack in one-dimensional chains via two crystallographically unique very weak π-π interactions with π(centroid)···π(centroid) separations of 4.632(5) and 4.514(5) Å. These one-dimensional chains pack weakly together resulting in a solvent accessible void that contains the benzene and acetonitrile solvent molecules (*Figure 3.3.7.iv*). Despite all attempts, not all of the the disorded solvent molecules were able to be atomically modelled and therefore the SQUEEZE[418] function of PLATON[419] was applied. This revealed a solvent accessible void of 286 $Å^3$ calculated to contain 107 electrons. This corresponds to 27 electrons per helicates which can be approximated as one acetonitrile molecule (22 electrons).

3.4 Summary and conclusions

The seven complexes are reported, complexes **3.6** to **3.12**, containing novel ligands. These complexes have demonstrated the propensity of the N-H moiety of the hydrazide functionality towards hydrogen bond interactions. As observed for **3.6**, **3.8**, **3.9**, **3.11** and **3.12**, which contain, perchlorate and tetrafluoroborate anions, three of these N-H moieties participate in hydrogen bond interactions with the anions, while the fourth forms an interaction with a water or acetonitrile molecule. Complexes **3.6** and **3.9** both contain perchlorate anions and feature a hydrogen bond interaction between a water molecule and an N-H hydrazide moiety that resulted in the formation of a hydrogen bond network. On the other hand, complexes **3.8** and **3.11** both had tetrafluoroborate anions and did not feature hydrogen bond networks between neighbouring helicate units. In the case of **3.7**, when the larger triflate anion is employed, the complexes crystallise with no solvent molecules. This resulted in all four of the hydrazide N-H moieties participating in hydrogen bond interactions with the triflate anions. The introduction of the quinoline ring into ligand **L3.3** has a profound effect on the crystal packing. The larger aromatic system, in comparison to the pyridine rings of ligands **L3.2** and **L3.5** favours the formation of π-π stacking interactions with neighbouring helicates. However, the crystallisation conditions (antisolvent) and the anion have a significant effect on the π-π interactions. For complex **3.9** each quinoline ring interacts with a quinoline ring on a neighbouring helicate via an offset π-π stacking interaction. However, for **3.10** and **3.11**, there are fewer π-π interactions and they occur in combination with C-H···π interactions. The extension of the flexible linker moiety from two carbon atoms in **L3.2** and **L3.3** to four carbon atoms in **L3.5** extended the pitch of the helicate but retained the helical chirality in complex **3.12**. It has been previously postulated in the literature that for ditopic ligands with a flexible linker, an

even number of carbons results in the formation of a helicate, while an odd number of carbons results in a mesocate. The limited findings presented in this chapter agree with this hypothesis.

3.5 Experimental

For details on general procedures: NMR, FT-IR, ESI-MS, melting points, elemental analysis and TGA see *section 2.7* of chapter two. Only details relevant to the work carried out in this chapter, not previous discussed will be given herein.

3.5.1 Single crystal X-ray diffraction

Diffraction data were collected at the University of Canterbury. For further details see *section 2.7* of chapter two.

3.5.2 Ligand synthesis

*3.5.2.i Succinic hydrazide, **3.1***

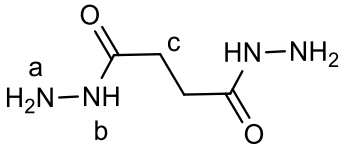

Succinic dihydrazide was synthesised following a literature preparation.[443] Diethyl succinate (2.8 mL, 17 mmol) and hydrazine monohydrate (4.2 mL, 85 mmol) were added sequentially to ethanol (10 mL) and the solution was heated at reflux for 12 hours during which time a white crystalline precipitate formed. After cooling to room temperature, the white precipitate was filtered and washed with ethanol (2 x 5 mL) then diethyl ether (2 x 5 mL) to give a white powder (1.25 g, 11 mmol, 65% yield).

M.pt. 160 °C Lit. 166 °C

^{1}H NMR: δ_H (400 MHz, [D_6]-DMSO): 8.95 (s, 1H, H_b), 4.12 (s, 2H, H_a), 2.23 (2H, s, H_c)

ESI-MS: meas. 147.0877 ($[M+H]^+$), $[C_4H_{11}N_4O_2]^+$ calc. 147.0877

*3.5.2.ii (N'1E,N'4E)-N'1,N'4-bis(1-(pyridin-2-yl)ethylidene)succinohydrazide, **L3.2***

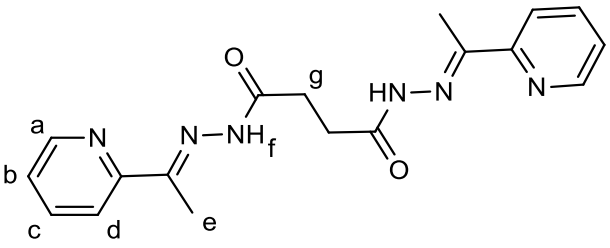

2-Acetylpyridine (1.1 mL, 10 mmol) was dissolved in ethanol (50 mL) at room temperature. Succinic dihydrazide (0.5 g, 4.4 mmol) was added and the resulting white suspension was then heated at reflux for 12

hours. The white suspension was then cooled to room temperature and filtered. The white precipitate was then washed with ethanol (2 x 5 mL) to give a white power (0.84 g, 2.4 mmol, 54% yield).

M.pt. 255 °C

^{1}H NMR: δ_H (400 MHz, [D$_6$]-DMSO) 10.63 and 10.55 (1 H, s,H$_f$), 8.57 (d, 1H,*J* = 4.3 Hz, H$_a$), 8.03 (d, *J* = 7, 1 H, H$_d$), 7.81 (q, *J* = 7.4, 1 H, H$_c$), 7.37 (t, *J* = 5.9, 1 H, H$_b$), 3.04 and 2.71 (s, 2 H, H$_g$), 2.35 and 2.32 (s, 3 H, H$_e$)

The poor solubility of **L3.2** precluded its analysis by ^{13}C NMR spectroscopy

ESI-MS: meas. 177.0894 ([M+2H]$^{2+}$), [C$_{18}$H$_{22}$N$_6$O$_2$]$^{2+}$ calc. 177.0897

IR: (ν_{max}/ cm^{-1}) 3181 (w), 3078 (w), 2999 (w), 1671 (m), 1624 (w), 1578 (m), 1562 (m), 1487 (m), 1458 (m), 1430 (m), 1383 (s), 1365 (s), 1313 (m), 1284 (m), 1247 (w), 1199 (s), 1150 (s), 1107 (w), 1083 (w), 1044 (w), 991 (m), 891 (w), 869 (m), 785 (s), 777 (s), 738 (m), 673 (m), 622 (s)

3.5.2.iii (N'1E,N'4E)-N'1,N'4-bis(quinolin-2-ylmethylene)succinohydrazide, ***L3.3***

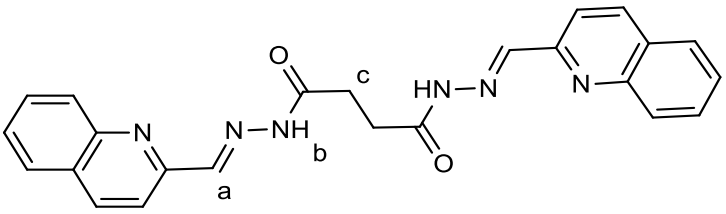

Quinoline-2-carbaldehyde (1.6 g, 10.1 mmol was dissolved in ethanol (50 mL) at reflux. Succinic dihydrazide (0.5 mg, 4.4 mmol) was added to give a brown suspension which was heated at reflux for 12 hours. The brown suspension was then cooled to room temperature and filtered. The pale brown solid was washed with boiling ethanol (2 x 5 mL) and oven dried for one hour to give a pale brown solid (1.1 g, 2.6 mmol, 60% yield).

M.pt. 260 °C (decomposition)

^{1}H NMR: δ_H (400 MHz, [D$_6$]-DMSO) 11.70 (s, 1 H, H$_b$), 8.36 (m, 2 H, H$_{quinoline}$), 8.18 (, s, 1H H$_a$), 8.02 (m, 2 H, H$_{quinoline}$), 7.77 (t, *J* = 7.6, 1 H, H$_{quinoline}$), 7.62 (m, 1 H, H$_{quinoline}$), 3.08 (s, 2H, H$_c$)

The poor solubility of **L3.3** precluded its analysis by ^{13}C NMR spectroscopy

ESI-MS: meas. 213.0896 ([M+2H]$^{2+}$), [C$_{24}$H$_{22}$N$_6$O$_2$]$^{2+}$ calc. 213.0897

IR: (ν_{max}/ cm^{-1}) 3062 (w), 2988 (w), 2950 (w), 2899 (w), 1669 (s) 1639 (w), 1588 (m), 1558 (w), 1519 (w), 1504 (m), 1458 (m), 1441 (m), 1429 (w), 1397 (s), 1349 (w), 1327 (w), 1311 (m), 1300

(m), 1237 (w), 1205 (m) 1153 (s), 1142 (s), 1113 (m), 1018 (w), 995 (w), 977 (m), 942 (s), 902 (m), 881 (w), 839 (s), 806 (s), 790 (m), 774 (m), 755 (s), 692 (w), 644 (w), 621 (m)

*3.5.2.iv Adipic hydrazide, **3.4***

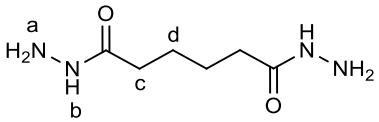

Adipic hydrazide was synthesised following an adapted literature procedure.[444] Diethyl adipate (3 mL, 15 mmol) was dissolved in ethanol (1 mL). Hydrazine monohydrate (1.8 mL, 37 mmol) was added and the resulting pale-yellow solution was heated at reflux for 12 hours. Upon cooling to room temperature, a white crystalline solid formed. The precipitate was separated by filtration and washed with cold ethanol (2 x 5 mL) and diethyl ether (2 x 5 mL) to give a white power (1.8 g, 11 mmol, 70% yield).

M.pt. 176-178 °C

^{1}H NMR: δ_H (400 MHz, [D_6]-DMSO) 8.90 (s, 2 H, H_b), 4.12 (s, 4 H, H_a), 1.96 (t, J = 6.00, 4 H, H_c), 1.41 (t, J = 4 H, H_d)

*3.5.2.v (N'1E,N'6E)-N'1,N'6-bis(1-(pyridin-2-yl)ethylidene)adipohydrazide, **L3.5***

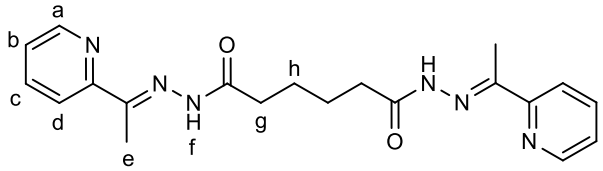

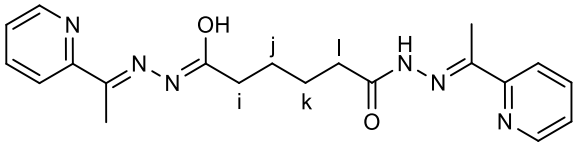

Adipic acid dihydrazide (0.5 g, 2.9 mmol) was suspended in ethanol (30 mL) and heated to reflux to give a white suspension. 2-Acetylpyridine (0.74 mL, 6.6 mmol) was added and the resulting off white suspension heated at reflux overnight to give a yellow solution. The yellow solution was reduced in volume and allowed to stand at room temperature during which time a white precipitate formed. The white precipitate was separated by filtration and washed with ethanol (2 x 5 mL) and then diethyl ether (2 x 5 mL) to give a white powder (0.43 g, 1.1 mmol, 39% yield)

M.pt. 178-180 °C

^{1}H NMR: δ_H (400 MHz, [D_6]-DMSO) 10.53 and 10.45 (s, 2 H, H_f), 8.55 (br., s., 2 H, H_a), 7.99 (t, J = 8.80, 2 H, H_d), 7.76 (m, 2 H, H_c), 7.35 (m, 2 H, H_b), 2.72 (s, 1.55 H, H_j), 2.38 (s, 1.55 H, H_l), 2.29 (m, 6 H, H_e), 1.96 (s, 0.45 H, H_g), 1.67 (m, 3.1 H, H_j and H_k), 1.42 (s, 0.45 H, H_h)

The poor solubility of **L3.5** precluded its analysis by ^{13}C NMR spectroscopy

IR: (ν_{max}/ cm^{-1}) 3199 (br., w) 3052 (br., w), 2891 (w), 1672 (s), 1626 (w), 1581 (m), 1461 (m), 1399 (br., s), 1297 (m), 1282 (m), 1250 (m), 1232 (m), 1197 (m), 1165 (m), 1138 (m), 1084 (m), 1043 (w), 993 (w), 962 (w), 856 (w), 811 (w), 781 (s), 743 (m), 726 (m), 701 (m), 627 (m), 606 (m), 591 (m), 567 (w), 486 (w)

ESI-MS: meas. 381.2042 ($[M+H]^+$), $[C_{20}H_{25}N_6O_2]^+$ calc. 381.2034

3.5.3 Complex synthesis

*3.5.3.i $[Co_2(\mathbf{L3.2})_2](ClO_4)_4$, **3.6***

$Co(ClO_4)_2.6H_2O$ (10.4 mg, 28.4 μmol) was dissolved in acetonitrile (15 mL). **L3.2** (10.0 mg, 28.4 μmol) was added to give a yellow/orange solution that was stirred at room temperature for 5 hours. The solution was then left to stand at room temperature for 3 hours and then filtered. Vapor diffusion of the filtrate with benzene gave orange prism crystals suitable for single crystal X-ray diffraction.

Found: C, 39.52 H, 3.93 N, 12.98% $[Co_2(C_{18}H_{20}N_6O_2)_2](ClO_4)_4 \cdot 1.25C_6H_6 \cdot 0.25CH_3CN$ requires: C, 39.19 H, 3.61 N, 12.73%

IR: (ν_{max}/ cm^{-1}) 3554 (w, br.), 1620 (m), 1529 (m), 14701 (m), 1443 (w), 1406 (w), 1379 (w), 1330 (w), 1244 (m), 1213 (w), 1176 (m), 1091 (s), 1046 (s), 1023 (s), 929 (m), 783 (s), 734 (m), 697 (w), 620 (s)

*3.5.3.ii $[Co_2(\mathbf{L3.2})_2](OTf)_4$, **3.7***

$CoCl_2.6H_2O$ (6.7 mg, 28 μmol) was dissolved in acetonitrile (5 mL). AgOTf (14.6 mg, 56.8 μmol) was added resulting in the immediate formation of a white precipitate. The solution was filtered into a suspension of **L3.2** (10.0 mg, 28.4 μmol) in acetonitrile (5 mL). The resulting white suspension was stirred at room temperature for 5 hours to give a yellow/orange solution. The solution was then left to stand at room temperature for 3 hours and then filtered. Vapor diffusion of the filtrate with m-xylene gave yellow plate crystals suitable for single crystal X-ray diffraction using synchrotron radiation.

Found: C, 35.47 H, 3.04 N, 12.44% $[Co_2(C_{18}H_{20}N_6O_2)_2](CF_3SO_3)_4$ requires: C, 33.86 H, 2.84 N, 11.85%

IR: (ν_{max}/ cm^{-1}) 3199 (br., w), 3136 (br., w), 2993 (br., w), 1631 (m), 1599 (w), 1534 (m), 1500 (w), 1469 (w), 1447 (w), 1407 (w), 1333 (w), 1285 (s), 1251 (s), 1225 (s), 1150 (s), 1104 (m), 1028 (s), 780 (m), 759 (w), 748 (w), 708 (w), 674 (w), 636 (s), 555 (s), 514 (m), 470 (m)

*3.5.3.iii $[Co_2(\mathbf{L3.2})_2](BF_4)_4$, **3.8***

$Co(BF_4)_2.6H_2O$ (8.6 mg, 28 μmol) was dissolved in acetonitrile (15 mL). **L3.2** (10.0 mg, 28.4 μmol) was added to give a yellow/orange solution that was stirred at room temperature for 5 hours. The solution was then left to stand at room temperature for 3 hours and then filtered. Vapor diffusion of the filtrate with diisopropyl ether gave orange prism crystals suitable for single crystal X-ray diffraction.

Found: C, 36.96 H, 3.34 N, 14.90% $[Co_2(C_{18}H_{20}N_6O_2)_2](BF_4)_4$ requires: C, 36.96 H, 3.45 N, 14.37%

IR: (ν_{max}/ cm^{-1}) 3607 (br., w), 3268 (br., w), 1619 (s), 1532 (s), 1496 (w), 1471 (m), 1451 (m), 1408 (w), 1382 (m), 1333 (m), 1297 (w), 1245 (m), 1213 (w), 1178 (m), 1054 (br., s), 1012 (s), 922 (m), 784 (m), 748 (w), 640 (w), 567 (m), 519 (w), 747 (w)

*3.5.3.iv $[Co_2(\mathbf{L3.3})_2](ClO_4)_4$, **3.9***

$Co(ClO_4)_2.6H_2O$ (8.6 mg, 24 μmol) was dissolved in acetonitrile (15 mL) and was stirred at room temperature. **L3.3** (10.0 mg, 23.6 μmol) was added to give a pale brown/yellow suspension and stirred for approximately five hours to give an orange/brown cloudy solution. The cloudy solution was allowed to stand at room temperature for two hours and then filtered to give a yellow/brown solution. Vapor diffusion of the filtrate with benzene gave orange block crystals suitable for single crystal X-ray diffraction.

Found: C, 40.53 H, 2.83, N, 11.52% $[Co_2(C_{24}H_{20}N_6O_2)_2](ClO_4)_4 \cdot 5H_2O \cdot 0.25CH_3CN \cdot 0.25C_6H_6$ requires: C, 40.46 H, 3.55 N, 11.56%

IR: (ν_{max}/ cm^{-1}) 3527 (w, br.) 290 (w, br.) 1617 (m) 1590 (w) 1554 (m) 1509 (m) 1435 (w) 1404 (w) 1381 (w) 1336 (M) 1299 (w) 1250 (w) 1213 (m) 1176 (m) 1062 (s, br.) 1000 (s) 931 (m) 871 (w) 832 (m) 786 (m) 755 (m) 621 (s)

*3.5.3.v [Co_2(**L3.3**)$_2$](OTf)$_4$, **3.10***

$CoCl_2.6H_2O$ (3.6 mg, 24 μmol) was dissolved in acetonitrile (5 mL). AgOTf (12.1 mg, 47.2 μmol) was added resulting in the immediate formation of a white precipitate. The solution was filtered into a suspension of **L3.3** (10.0 mg, 23.6 μmol) in acetonitrile (5 mL). The pale brown/yellow suspension and stirred for approximately 5 hours to give an orange/brown cloudy solution. The cloudy solution was allowed to stand at room temperature for 2 hours and then filtered to give a yellow/brown solution. Vapor diffusion of the filtrate with m-xylene gave orange block crystals suitable for single crystal X-ray diffraction.

Found: C, 38.24 H, 2.84, N, 10.39% $[Co_2(C_{24}H_{20}N_6O_2)_2](CF_3SO_3)_4 \cdot 3.75H_2O$ requires: C, 38.30 H, 2.94 N, 10.31%

IR: (ν_{max}/ cm^{-1}) 3491 (br., w), 3197 (br., w), 2939 (br.,w), 1619 (m), 1589 (w), 1544 (m), 1510 (m), 1436 (w), 1407 (w), 1382 (m), 1336 (w), 1244 (s), 1224 (s), 1166 (s), 1140 (s), 1025 (s), 999 (m), 937 (m), 918 (w), 871 (w), 829 (m), 786 (m), 753 (m), 698 (w), 634 (s), 573 (m), 514 (m), 483 (m)

*3.5.3.vi [Co_2(**L3.3**)$_2$](BF_4)$_4$, **3.11***

$Co(BF_4)_2.6H_2O$ (8.6 mg, 24 μmol) was dissolved in acetonitrile (15 mL) and was stirred at room temperature. **L3.3** (10.0 mg, 23.6 μmol) was added to give a pale brown/yellow suspension and stirred for approximately 5 hours to give an orange/brown cloudy solution. The cloudy solution was allowed to stand at room temperature for two hours and then filtered to give a yellow/brown solution. Vapor diffusion of the filtrate with diisopropyl ether gave orange block crystals suitable for single crystal X-ray diffraction.

Found: C, 42.37 H, 3.36, N, 12.05% $[Co_2(C_{20}H_{24}N_6O_2)_2](BF_4)_4 \cdot 2.7H_2O$ requires: C, 42.31 H, 3.36 N, 12.36%

IR: (ν_{max}/ cm^{-1}) 3579 (br., w), 3215 (br., w) 3048 (br., w), 1616 (m), 1592 (w), 1545 (m), 1509 (s), 1436 (w), 1405 (w), 1381 (m), 1337 (w), 1299 (w), 1250 (m), 1214 (w), 1177 (w), 1144 (m), 1128 (m), 1017 (s), 992 (s), 936 (m), 872 (w), 835 (m), 786 (m), 750 (m), 699 (w), 679 (w), 617 (w), 593 (w), 569 (w), 519 (m), 486 (m)

*3.5.3.vii $[Co_2(\mathbf{L3.5})_2](ClO_4)_4$, **3.12***

$Co(ClO_4)_2.6H_2O$ (10.4 mg, 28 µmol) was dissolved in acetonitrile (15 mL). **L3.5** (10.0 mg, 28.4 µmol) was added to give a yellow/orange solution that was stirred at room temperature for 5 hours. The solution was then left to stand at room temperature for three hours and then filtered. Vapor diffusion of the filtrate with benzene gave orange prism crystals suitable for single crystal X-ray diffraction.

Found: C, 35.11 H, 4.25, N, 12.08% $[Co_2(C_{20}H_{24}N_6O_2)_2](ClO_4)_4 \cdot 5H_2O$ requires: C, 35.15 H, 4.28 N, 12.30%

IR: (ν_{max}/ cm^{-1}) 3527 (br., w), 3253 (br., w), 2936 (w), 1613 (br., s), 1523 (br., m), 1470 (m), 1442 (w), 1376 (w), 1332 (w), 1275 (w), 1213 (m), 1051 (br., s), 928 (m), 849 (w), 778 (m), 745 (w), 693 (w), 621 (s), 569 (w), 534 (w), 459 (w)

3.6 Appendices

3.6.1 Crystallographic tables

	3.6	**3.7**	**3.8**
Empirical formula	$C_{50.1}H_{56.1}Cl_4Co_2N_{12}O_{21.3}$	$C_{40}H_{40}Co_2F_{12}N_{12}O_{16}S_4$	$C_{38}H_{45}B_4Co_2F_{16}N_{13}O_5$
Formula weight	1426.83	1418.94	1228.97
Temperature/K	120.0 (1)	100(2)	120.01(10)
Crystal system	monoclinic	orthorhombic	monoclinic
Space group	P21/n	Fdd2	C2/c
a/Å	16.2286(3)	33.393(7)	16.7126(9)
b/Å	22.7700(5)	40.011(8)	22.3604(9)
c/Å	16.8658(4)	24.344(5)	17.2344(12)
α/°	90	90	90
β/°	94.834(2)	90	97.816(6)
γ/°	90	90	90
Volume/Å^3	6210.2(2)	32526(11)	6380.7(6)
Z	4	24	4
ρ_{calc}g/cm^3	1.526	1.739	1.279
μ/mm^{-1}	6.496	0.886	4.899
F(000)	2932.0	17232.0	2488.0
Crystal size/mm^3	0.134 × 0.123 × 0.06	0.1 × 0.05 × 0.01	0.526 × 0.117 × 0.061
Radiation	CuKα (λ = 1.54184)	Synchrotron (λ = 0.71073)	CuKα (λ = 1.54184)
2Θ range for data collection/°	6.536 to 153.922	2.306 to 52.744	7.908 to 136.502
Index ranges	-20 ≤ h ≤ 17, -28 ≤ k ≤ 28, -21 ≤ l ≤ 16	-41 ≤ h ≤ 41, -50 ≤ k ≤ 50, -30 ≤ l ≤ 30	-20 ≤ h ≤ 14, -26 ≤ k ≤ 26, -20 ≤ l ≤ 20
Reflections collected	46051	65305	28005
Independent reflections	12905 [Rint = 0.0400, Rsigma = 0.0322]	16584 [R_{int} = 0.0956, R_{sigma} = 0.0812]	5838 [R_{int} = 0.0928, R_{sigma} = 0.0587]
Data/restraints/parameters	12905/42/920	16584/236/1240	5838/233/534
Goodness-of-fit on F^2	1.101	1.021	1.058
Final R indexes [I>=2σ (I)]	R1 = 0.0464, wR2 = 0.1324	R_1 = 0.0625, wR_2 = 0.1556	R_1 = 0.0889, wR_2 = 0.2552
Final R indexes [all data]	R1 = 0.0608, wR2 = 0.1487	R_1 = 0.1071, wR_2 = 0.1835	R_1 = 0.1169, wR_2 = 0.2897
Largest diff. peak/hole / e Å^{-3}	0.58/-0.68	0.80/-0.84	0.95/-0.42
Flack Parameter		0.45(2)	

	3.9	3.10	3.11	3.12
Empirical formula	$C_{59.25}H_{55.05}Cl_4Co_2N_{13.8}O_{21}$	$C_{58}H_{53}Co_2F_{12}N_{15}O_{18}S_4$	$C_{53.6}H_{48.8}B_4Co_2F_{16}N_{14.8}O_{4.2}$	$C_{45.5}H_{55}Cl_4Co_2N_{12.5}O_{21}$
Formula weight	1556.08	1722.25	1432.57	1372.68
Temperature/K	120.01(10)	120.00(10)	120.00(10)	120.00(10)
Crystal system	monoclinic	triclinic	triclinic	monoclinic
Space group	P21/n	P-1	P-1	$P2_1/c$
a/Å	13.1060(3)	13.4354(5)	13.9261(3)	18.1865(7)
b/Å	22.6085(5)	13.5374(5)	14.4689(4)	11.9225(7)
c/Å	22.8183(6)	21.5640(7)	16.3037(4)	28.7449(12)
α/°	90	102.920(3)	92.099(2)	90
β/°	93.273(2)	100.363(3)	95.198(2)	98.832(4)
γ/°	90	104.381(3)	107.162(2)	90
Volume/$Å^3$	6750.2(3)	3586.0(2)	3119.00(14)	6158.8(5)
Z	4	2	2	4
$\rho_{calc}g/cm^3$	1.531	1.595	1.525	1.480
μ/mm^{-1}	6.038	5.687	5.106	6.523
F(000)	3189.0	1752.0	1451.0	2822.0
Crystal size/mm^3	0.337 × 0.12 × 0.06	0.246 × 0.142 × 0.045	0.2 × 0.119 × 0.039	0.122 × 0.092 × 0.043
Radiation	CuKα (λ = 1.54184)	CuKα (λ = 1.54184)	CuKα (λ = 1.54184)	CuKα (λ = 1.54184)
2Θ range for data collection/°	7.598 to 148.994	7.014 to 140.148	7.748 to 140.15	7.318 to 140.13
Index ranges	$-13 \le h \le 16$, $-28 \le k \le 28$, $-28 \le l \le 24$	$-16 \le h \le 11$, $-16 \le k \le 16$, $-24 \le l \le 26$	$-14 \le h \le 16$, $-17 \le k \le 17$, $-19 \le l \le 19$	$-21 \le h \le 22$, $-14 \le k \le 10$, $-35 \le l \le 35$
Reflections collected	29954	39712	33954	40634
Independent reflections	13694 [Rint = 0.0601, Rsigma = 0.0823]	13621 [R_{int} = 0.0522, R_{sigma} = 0.0498]	11815 [R_{int} = 0.0467, R_{sigma} = 0.0443]	11685 [R_{int} = 0.0881, R_{sigma} = 0.0880]
Data/restraints/parameters	13694/179/1060	13621/100/1184	11815/166/1053	11685/327/987
Goodness-of-fit on F^2	1.064	1.033	1.034	1.024
Final R indexes [I>=2σ (I)]	R1 = 0.0740, wR2 = 0.2051	R_1 = 0.0520, wR_2 = 0.1415	R_1 = 0.0515, wR_2 = 0.1414	R_1 = 0.0858, wR_2 = 0.2412
Final R indexes [all data]	R1 = 0.1136, wR2 = 0.2254	R_1 = 0.0631, wR_2 = 0.1511	R_1 = 0.0572, wR_2 = 0.1475	R_1 = 0.1451, wR_2 = 0.2930
Largest diff. peak/hole / e $Å^{-3}$	1.17/-0.87	0.85/-0.64	1.17/-0.93	0.93/-0.99

3.6.2 Selected crystallographic parameters

Bond	**d(Co-X) Å**	**Bond**	**d(Co-X) Å**
Co1-N3	2.110(2)	Co2-N9	2.118(2)
Co1-N4	2.040(2)	Co2-N10	2.052(2)
Co1-O5	2.119(2)	Co2-O11	2.124(2)
Co1-N6	2.103(2)	Co2-N12	2.112(2)
Co1-N7	2.047(2)	Co2-N13	2.055(2)
Co1-O8	2.112(2)	Co2-O14	2.146(2)
Atoms	**<(X-Co-X) °**	**Atoms**	**<(X-Co-X) °**
N3-Co1-N4	75.54(8)	N9-Co2-N10	75.49(9)
N4-Co1-O5	76.16(8)	N10- Co2-O11	75.61(8)
O5-Co1-N7	97.54(8)	O11- Co2-N13	95.44(8)
N7-Co1-N3	110.88(9)	N13- Co2-N9	114.36(9)
N6-Co1-N7	75.62(9)	O14- Co2-N13	75.21(8)
N7-Co1-O8	75.89(8)	N13- Co2-N12	75.18(8)
O8-Co1-N4	99.50(8)	N12- Co2-N10	114.82(9)
N4-Co1-N6	109.68(9)	N10- Co2-O14	95.71(8)
N3-Co1-N6	91.84(9)	N9- Co2-N12	91.60(9)
N6-Co1-O5	95.29(8)	N12- Co2-O11	93.48(8)
O5-Co1-O8	95.96(7)	O11- Co2-O14	97.08(7)
O8-Co1-N3	91.12(8)	O14- Co2-N9	93.38(8)

*Table 3.6.2.i: Table of Co-X (X = O or N) bond lengths and cis-bond angles of the two crystallographically unique Co(II) centres in **3.6**.*

Bond	**d(Co-X) Å**	**Bond**	**d(Co-X) Å**	**Bond**	**d(Co-X) Å**
Co1-N4	2.16(1)	Co2-N10	2.06(1)	Co3-N16	2.18(1)
Co1-N5	2.06(1)	Co2-N11	2.04(1)	Co3-N17	2.05(1)
Co1-O6	2.12(1)	Co2-O12	2.095(9)	Co3-O18	2.16(1)
Co1-N7	2.07(1)	Co2-N13	2.18(1)	Co3-N19	2.07(1)
Co1-N8	2.03(1)	Co2-N14	2.07(1)	Co3-N20	2.02(1)
Co1-O9	2.137(9)	Co2-O15	2.11(1)	Co3-N21	2.139(9)
Atoms	**<(X-Co-X) °**	**Atoms**	**<(X-Co-X) °**	**Atoms**	**<(X-Co-X) °**
N4-Co1-N5	75.5(4)	N10-Co2-N11	75.6(5)	N16-Co3-N17	75.3(4)
N5-Co1-O6	76.8(4)	N11-Co2-O12	75.8(4)	N17-Co3-O18	75.3(4)
O6-Co1-N8	97.3(4)	O12-Co2-N14	100.3(4)	O18-Co3-N20	102.5(4)
N8-Co1-N4	110.4(4)	N14-Co2-N10	108.4(4)	N20-Co3-N16	107.4(5)
N5-Co1-N7	108.6(4)	N11-Co2-N13	109.0(5)	N17-Co3-N19	113.2(4)
N7-Co1-N8	74.7(4)	N13-Co2-N14	76.5(4)	N19-Co3-N20	74.4(5)
N8-Co1-O9	76.0(4)	N14-Co2-O15	76.0(4)	N20-Co3-O21	75.3(4)
O9-Co1-N5	100.9(4)	O15-Co2-N11	98.6(4)	O21-Co3-N17	97.1(4)
N4-Co1-N7	95.9(4)	N10-Co2-N13	96.3(5)	N16-Co3-N19	96.0(5)
N7-Co1-O6	91.9(4)	N13-Co2-O12	90.8(4)	N19-Co3-O21	90.4(4)
O6-Co1-O9	95.3(4)	O12-Co2-O15	95.4(4)	O18-Co3-O21	96.4(4)
O9-Co1-N4	90.9(4)	O15-Co2-N10	91.2(4)	O21-Co3-N16	92.7(4)

*Table 3.6.2.ii: Table of Co-X (X = O or N) bond lengths and cis-bond angles of the three crystallographically unique Co(II) centres in **3.7**.*

Bond	d(Co-X) Å
Co1-N2	2.120(5)
Co1-N3	2.046(4)
Co1-O4	2.112(4)
Co1-N5	2.018(5)
Co1-N6	2.034(4)
Co1-O7	2.131(3)
Atoms	**<(X-Co-X) °**
N2-Co1-N3	74.9(2)
N3-Co1-O4	75.8(1)
O4-Co1-N6	99.3(1)
N6-Co1-N2	111.5(2)
N2-Co1-N5	91.2(2)
N5-Co1-O4	92.2(2)
O4-Co1-O7	92.2(1)
O7-Co1-N2	96.5(2)
N3-Co1-N5	115.2(2)
N5-Co1-N6	75.6(2)
N6-Co1-O7	75.8(2)
O7-Co1-N3	93.6(1)

*Table 3.6.2.iii: Table of Co-X (X = O or N) bond lengths and cis-bond angles of the crystallographically unique Co(II) centre in **3.8**.*

Bond	d(Co-X) Å	Bond	d(Co-X) Å
Co1-N3	2.176(4)	Co2-N9	2.154(4)
Co1-N4	2.054(4)	Co2-N10	2.043(4)
Co1-O5	2.164(4)	Co2-O11	2.178(4)
Co1-N6	2.165(4)	Co2-N12	2.157(4)
Co1-N7	2.054(5)	Co2-N13	2.036(4)
Co1-O8	2.161(4)	Co2-O14	2.156(4)
Atoms	**<(X-Co-X) °**	**Atoms**	**<(X-Co-X) °**
N3-Co1-N4	75.3(2)	N9-Co2-N10	75.7(2)
N4-Co1-O5	74.2(2)	N10- Co2-O11	75.0(2)
O5-Co1-N7	98.0(2)	O11- Co2-N13	87.5(2)
N7-Co1-N3	115.9(2)	N13- Co2-N9	122.2(2)
N6-Co1-N7	75.9(2)	O14- Co2-N13	74.7(2)
N7-Co1-O8	74.6(2)	N13- Co2-N12	75.5(2)
O8-Co1-N4	85.7(2)	N12- Co2-N10	117.0(2)
N4-Co1-N6	123.5(2)	N10- Co2-O14	95.9(2)
N3-Co1-N6	96.6(2)	N9- Co2-N12	93.1(2)
N6-Co1-O5	87.9(2)	N12- Co2-O11	96.1(2)
O5-Co1-O8	97.2(1)	O11- Co2-O14	96.8(1)
O8-Co1-N3	95.2(2)	O14- Co2-N9	90.6(2)

*Table 3.6.2.iv: Table of Co-X (X = O or N) bond lengths and cis-bond angles of the two crystallographically unique Co(II) centres in **3.9**.*

Bond	d(Co-X) Å	Bond	d(Co-X) Å
Co1-N3	2.142(2)	Co2-N9	2.151(3)
Co1-N4	2.046(3)	Co2-N10	2.046(3)
Co1-O5	2.175(2)	Co2-O11	2.138(2)
Co1-N6	2.150(3)	Co2-N12	2.171(2)
Co1-N7	2.035(3)	Co2-N13	2.027(3)
Co1-O8	2.163(2)	Co2-O14	2.187(2)
Atoms	**<(X-Co-X) °**	**Atoms**	**<(X-Co-X) °**
N3-Co1-N4	75.8(1)	N9-Co2-N10	75.9(1)
N4-Co1-O5	75.11(9)	N10- Co2-O11	75.27(9)
O5-Co1-N7	87.12(9)	O11- Co2-N13	91.73(9)
N7-Co1-N3	122.2(1)	N13- Co2-N9	117.3(1)
N6-Co1-N7	76.2(1)	O14- Co2-N13	74.58(9)
N7-Co1-O8	74.64(9)	N13- Co2-N12	75.8(1)
O8-Co1-N4	91.97(9)	N12- Co2-N10	115.8(1)
N4-Co1-N6	119.1(1)	N10- Co2-O14	93.93(9)
N3-Co1-N6	96.0(1)	N9- Co2-N12	96.8(1)
N6-Co1-O5	94.00(9)	N12- Co2-O11	91.88(9)
O5-Co1-O8	95.24(8)	O11- Co2-O14	92.92(8)
O8-Co1-N3	90.40(9)	O14- Co2-N9	93.20(9)

*Table 3.6.2.v: Table of Co-X (X = O or N) bond lengths and cis-bond angles of the two crystallographically unique Co(II) centres in **3.10**.*

Bond	d(Co-X) Å	Bond	d(Co-X) Å
Co1-N3	2.158(2)	Co2-N9	2.158(2)
Co1-N4	2.047(2)	Co2-N10	2.043(3)
Co1-O5	2.143(2)	Co2-O11	2.145(2)
Co1-N6	2.173(2)	Co2-N12	2.173(2)
Co1-N7	2.051(2)	Co2-N13	2.044(2)
Co1-O8	2.174(2)	Co2-O14	2.150(2)
Atoms	**<(X-Co-X) °**	**Atoms**	**<(X-Co-X) °**
N3-Co1-N4	75.42(8)	N9-Co2-N10	75.70(8)
N4-Co1-O5	74.81(8)	N10- Co2-O11	74.85(8)
O5-Co1-N7	92.72(8)	O11- Co2-N13	91.30(8)
N7-Co1-N3	118.79(9)	N13- Co2-N9	119.49(8)
N6-Co1-N7	75.42(8)	O14- Co2-N13	74.87(8)
N7-Co1-O8	74.23(8)	N13- Co2-N12	75.71(9)
O8-Co1-N4	91.23(8)	N12- Co2-N10	116.99(9)
N4-Co1-N6	119.50(8)	N10- Co2-O14	93.62(8)
N3-Co1-N6	96.08(8)	N9- Co2-N12	92.49(8)
N6-Co1-O5	89.47(8)	N12- Co2-O11	92.52(8)
O5-Co1-O8	97.14(7)	O11- Co2-O14	96.42(7)
O8-Co1-N3	93.83(8)	O14- Co2-N9	94.64(8)

*Table 3.6.2.vi: Table of Co-X (X = O or N) bond lengths and cis-bond angles of the two crystallographically unique Co(II) centres in **3.11**.*

Bond	d(Co-X) Å	Bond	d(Co-X) Å
Co1-N3	2.104(5)	Co2-N9	2.107(7)
Co1-N4	2.046(6)	Co2-N10	2.050(6)
Co1-O5	2.158(5)	Co2-O11	2.120(6)
Co1-N6	2.117(6)	Co2-N12	2.118(7)
Co1-N7	2.050(6)	Co2-N13	2.037(6)
Co1-O8	2.130(5)	Co2-O14	2.148(5)
Atoms	**<(X-Co-X) °**	**Atoms**	**<(X-Co-X) °**
N3-Co1-N4	76.3(2)	N9-Co1-N10	76.1(2)
N4-Co1-O5	75.4(2)	N10- Co1-O11	75.3(2)
O5-Co1-N7	96.3(2)	O11- Co1-N13	100.3(2)
N7-Co1-N3	111.9(2)	N13- Co1-N9	108.8(2)
N6-Co1-N7	75.4(2)	O14- Co1-N13	75.7(2)
N7-Co1-O8	74.8(2)	N13- Co1-N12	75.6(3)
O8-Co1-N4	105.2(2)	N12- Co1-N10	110.8(3)
N4-Co1-N6	105.8(2)	N10- Co1-O14	97.8(2)
N3-Co1-N6	90.7(2)	N9- Co1-N12	92.6(2)
N6-Co1-O5	98.9(2)	N12- Co1-O11	92.7(2)
O5-Co1-O8	94.8(2)	O11- Co1-O14	92.6(2)
O8-Co1-N3	90.6(2)	O14- Co1-N9	96.4(2)

*Table 3.6.2.vii Table of Co-X (X = O or N) bond lengths and cis-bond angles of the two crystallographically unique Co(II) centres in **3.12***

D-H···A	d(D-H) Å	d(D-H···A) Å	d(D···A) Å	<(D-H···A) °	Symmetry Code
N22-H22···O75	0.860(2)	1.956(2)	2.809(3)	170.8(2)	x, y, z x, y, z
N27-H27···O61	0.860(2)	2.024(2)	2.863(3)	165.3(2)	x, y, z x, y, z
N42-H42···O66	0.860(2)	2.02(1)	2.85(1)	160.1(3)	x, y, z x, y, z
N47-H47···O58	0.860(2)	2.049(2)	2.885(3)	163.8(2)	x, y, z ½+x, ½-y, -1/2+z
O75-H75B···O56	0.850(2)	2.115(3)	2.863(4)	146.6(2)	x, y, z x, y, z

*Table 3.6.2.viii: Hydrogen bond parameters for **3.6**.*

D-H···A	d(D-H) Å	d(D-H···A) Å	d(D···A) Å	<(D-H···A) °	Symmetry Code
N29-H29···O109	0.88(2)	2.061(9)	2.86(1)	150.4(8)	x, y, z
					x, y, z
N34-H34···O85	0.88(1)	1.92(1)	2.74(2)	156.0(9)	x, y, z
					x, y, z
N49-H49···O91	0.88(1)	1.96(1)	2.76(2)	150.8(8)	x, y, z
					x, y, z
N54-H54···O144	0.88(1)	2.004(9)	2.81(2)	151.8(8)	x, y, z
					x, y, z
N69-H69···O124	0.88(1)	1.999(7)	2.79(1)	149.0(8)	x, y, z
					x, y, z
N74-H74···O100	0.88(1)	1.97(1)	2.77(2)	151.7(8)	x, y, z
					1-x, 1.5-y, -1/2+z

*Table 3.6.2.ix: Hydrogen bond parameters for **3.7**.*

D-H···A	d(D-H) Å	d(D-H···A) Å	d(D···A) Å	<(D-H···A) °	Symmetry Code
N15-H15···F39	0.860(4)	2.37(2)	3.16(2)	154.1(6)	x, y,z
					x, y, z
N20-H20···O65	0.859(4)	1.96(1)	2.80(1)	163.5(5)	x, y, z
					x, y, z

*Table 3.6.2.x: Hydrogen bond parameters for **3.8**.*

D-H···A	d(D-H) Å	d(D-H···A) Å	d(D···A) Å	<(D-H···A) °	Symmetry Code
N25-H25···O68	0.860(4)	2.15(1)	2.97(1)	159.1(4)	x, y, z
					x, y, z
N30-H30···O82	0.860(5)	1.97(2)	2.78(2)	157.7(5)	x, y, z
					x, y, z
N51-H51···O98	0.861(5)	1.921(5)	2.768(6)	167.8(3)	x, y, z
					1.5-x, ½+y, ½-z
N56-H56···O77	0.861(4)	1.905(6)	2.762(7)	173.2(3)	x, y, z
					x, y, z
O98-H98A···O89	0.778(5)	2.15(3)	2.93(3)	152.1(8)	x, y, z
					½-x, -1/2+y, ½-z
O98-H98B···O80	0.850(5)	2.013(7)	2.847(8)	166.8(4)	x, y, z
					x, y, z

*Table 3.6.2.xi: Hydrogen bond parameters for **3.9**.*

D-H···A	d(D-H) Å	d(D-H···A) Å	d(D···A) Å	<(D-H···A) °	Symmetry Code
N25-H25···O68	0.879(2)	2.126(3)	2.861(3)	140.7(2)	x, y, z
					x, y, z
N30-H30···O130	0.880(2)	1.802(2)	2.680(3)	175.2(2)	x, y, z
					x, y, z
N51-H51···O90	0.880(2)	1.79(2)	2.67(2)	171(1)	x, y, z
					x, y, z
N56-H56···O82	0.880(2)	1.918(2)	2.730(3)	152.7(2)	x, y, z
					x, y, z
O118-H11C···O104	0.850(9)	1.857(3)	2.698(9)	169.8(7)	-1+x, y, z
					-1+x, -1+y, z
O118-H11D···N119	0.850(8)	2.221(5)	3.03(1)	158.2(6)	x, y, z
					-1+x, y, z
O130-H13A···O91	0.850(3)	1.93(1)	2.78(1)	174.3(3)	x, y, z
					1-x, 1-y, 1-z
O130-H13B···O84	0.849(3)	1.895(3)	2.728(4)	166.8(2)	x, y, z
					1+x, y, z

*Table 3.6.2.xii: Hydrogen bond parameters for **3.10**.*

D-H···A	d(D-H) Å	d(D-H···A) Å	d(D···A) Å	<(D-H···A) °	Symmetry Code
N25-H25···F68	0.860(2)	1.79(1)	2.61(1)	158.9(5)	x, y, z
					x, y, z
N30-H30···N107	0.859(2)	2.037(5)	2.879(5)	166.3(2)	x, y, z
					1-x, -y, 1-z
N51-H51···F91	0.861(2)	2.277(5)	2.876(6)	126.7(2)	x, y, z
					x, y, z
N56-H56···F86	0.861(2)	1.871(2)	2.730(3)	175.6(2)	x, y, z
					x, y, z

*Table 3.6.2.xiii: Hydrogen bond parameters for **3.11**.*

D-H···A	d(D-H) Å	d(D-H···A) Å	d(D···A) Å	<(D-H···A) °	Symmetry Code
N22-H22···O88	0.860(6)	2.05(2)	2.90(2)	166.3(6)	x, y, z
					x, y, z
N29-H29···O61	0.860(6)	2.068(7)	2.872(9)	155.3(4)	x, y, z
					x, y, z
N45-H45···O102	0.859(6)	1.951(7)	2.798(9)	168.4(4)	x, y, z
					x, y, z
N52-H52···O91	0.860(6)	2.06(4)	2.91(4)	171(1)	x, y, z
					1-x, 1-y, 1-z
O102-H10D···O69	0.848(7)	2.16(2)	2.96(2)	156.8(7)	x, y, z
					x, y, z
O102-H10E···O72	0.850(7)	2.06(1)	2.686(1)	155.9(6)	x, y, z
					-x, 2-y, 1-z

*Table 3.6.2.xiv: Hydrogen bond parameters for **3.12**.*

3.6.3 TGA

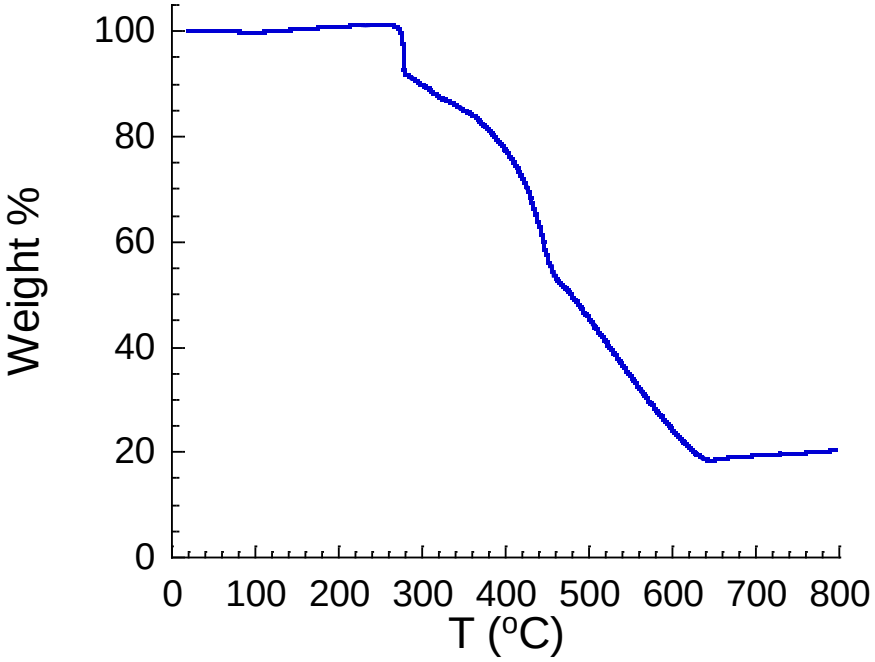

*Figure 3.6.3.i: TGA plot for complex **3.7**.*

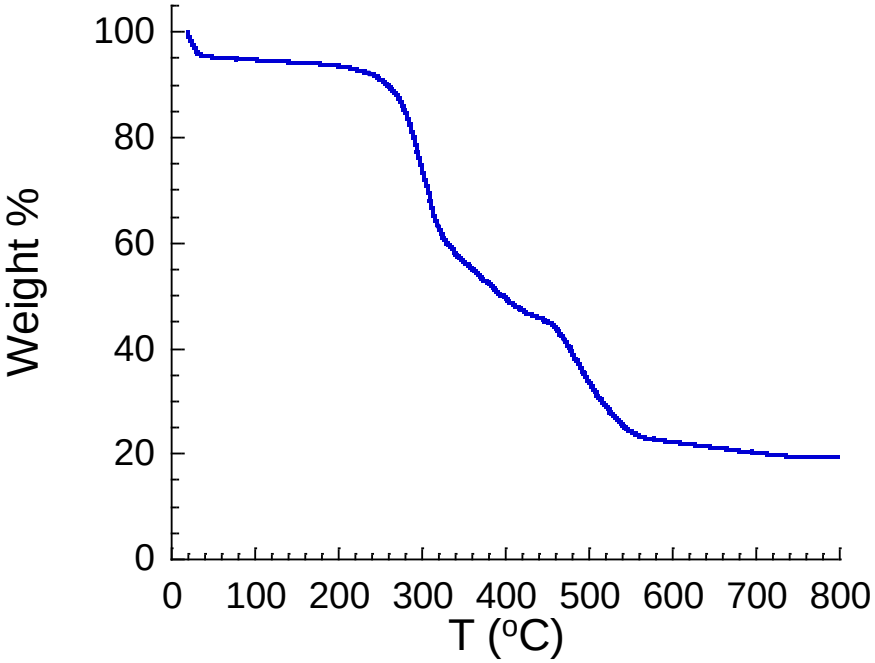

*Figure 3.6.3.ii: TGA plot for complex **3.8**.*

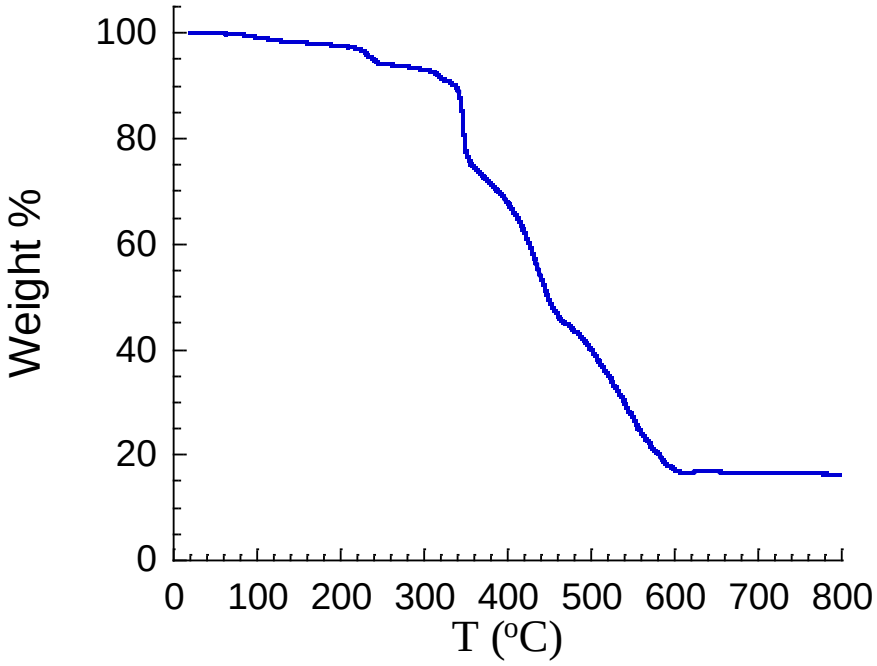

*Figure 3.6.3.iii: TGA plot for **3.10**.*

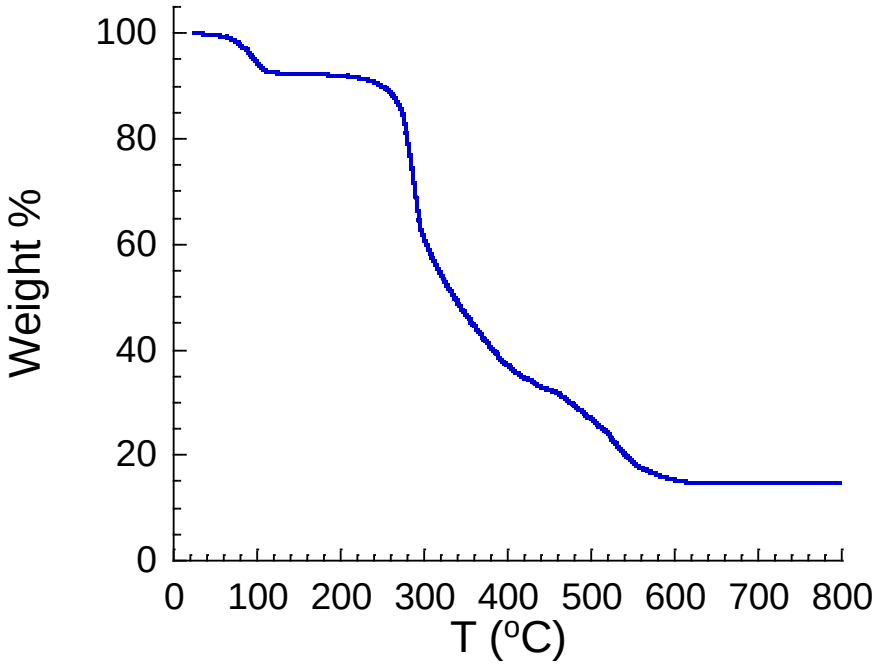

*Figure 3.6.3.iv: TGA plot for **3.11**.*

Chapter Four

SCO and Single molecule Magnet Behavior of Dinuclear Triple Helicates

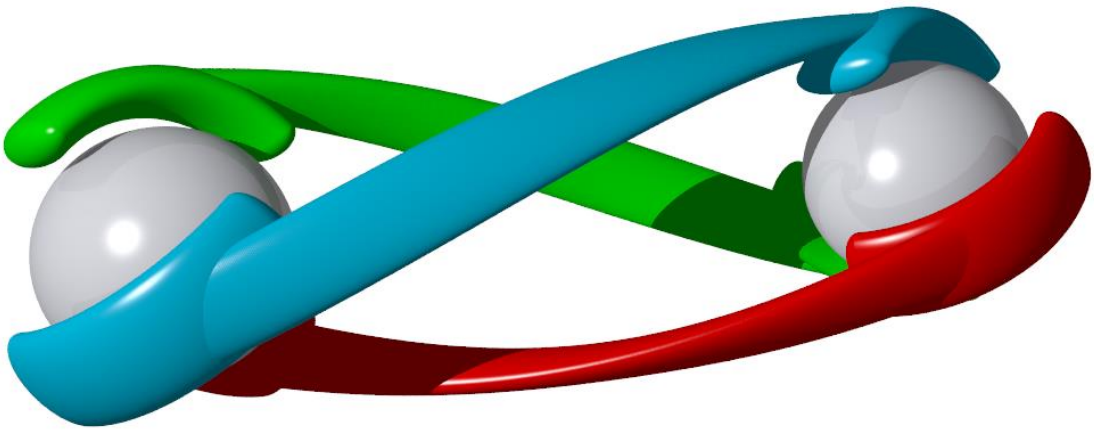

4.1 Introduction

4.1.1 Spin crossover helicates

One of the metallo-supramolecular architectures most commonly studied in the context of multinuclear SCO are metallo-helicates. They are an attractive species for the incorporation of SCO behavior as their polynuclear nature may introduce intramolecular cooperativity. In general, discrete multinuclear species are of interest, as incorporating more than one SCO centre into the molecule may result in multi-stepped SCO, as has been observed in previous compounds.[328, 445]

Helicate assemblies are often associated with ligands containing flexible linkers bridging the coordinating moieties.[311-312, 315-316, 318-319, 322] However, rigid linkers which are sufficiently angular in nature are also capable of forming helical assemblies. The latter is particularly important to SCO helicates, as a more rigid linker has a higher probability of introducing cooperativity into the system.[313-314, 317, 321, 446-447]

Interactions around the periphery of the metal ion coordination site can have a large impact on the SCO properties. The predominate interaction of interest in this chapter is the hydrogen bonding of anions or solvent molecules to the ligand. The effect of these interactions is two-fold: firstly, hydrogen bond interactions can influence the field strength of the ligand and, secondly; the formation of hydrogen bond networks can link SCO active centres together and introduce cooperativity to the system. The imidazolylimine motif is a particularly useful coordinating group to probe these effects due to the hydrogen bond donor present in the N-H moiety. Like many large metallo-supramolecular assemblies, helicates often crystallise with a significant number of solvent molecules and the degree of solvation of such complexes has been shown to have a profound impact on the SCO properties.[320]

4.1.2 Previous work

Recently, the Kruger group reported a small family of helicates featuring a relatively rigid linker based on 3,3′-1,1′-(hydrazine-1,2-diylidine)bis(ethan-1-yl-1ylidene)dianiline and containing an imidazolylimine coordinating motif. Helicates containing both the 2-imidazolylimine and 4-imidazolylimine moieties exhibited SCO. The latter exhibited a significant photomagnetic effect while the former displayed SCO in solution between 273 and 353 K.[321]

4.1.3 Scope of research

The following work looks to expand upon this family of helicates to gain a deeper insight into how the interactions of the solvent and anions influence the crystal packing and in turn the SCO behavior. Building on the work carried out in the group, the previously used 4-imidazolylimine moiety was selected for this study. The 4-imidazolylimine coordinating moiety has a weaker field strength than the 2-imidazolylimine moiety, resulting in SCO behavior that occurs in a temperature regime that is more amenable for analysis using SQUID magnetometers and absolute reflectivity instruments. The 5-methyl-4-imidazolylimine analogue was also investigated as the incorporation of the methyl group adjacent to the N-H hydrogen bond donor was expected to modify the hydrogen bond affinity. This is due to the more sterically encumbered nature of the site. All of the complexes reported herein were synthesised following the sub-component self-assembly approach using the precursor diamine and either 4-imidazolecarboxaldehyde or 4-methyl-5-imidazolecarboxaldehyde. A two anions of differing geometries and hydrogen bond acceptor atoms were also employed; triflate and tetrafluoroborate.

More recent work in the Kruger group has revealed that when Co(II) is used in the place of Fe(II) in coordinating environments like those described above, the complexes can display SMM properties.[448] A preliminary investigation of the use of Co(II) to synthesise SMM helicates was therefore also carried out.

4.2 Ligand synthesis and characterization

The diamine precursor **4.1** was synthesised via a di-imine condensation between one equivalent of hydrazine monohydrate and two equivalents of 3-aminoacetophenone. This was carried out in methanol at reflux with a catalytic amount of glacial acetic acid to give **4.1** as pale-yellow needle crystals in a 63% yield (*Figure 4.1.3.i*). This resulted in the formation of the hydrazone linked diamine pro-ligand which was used in subsequent sub-component self-assembly reaction with the appropriate imidazolecarboxaldehyde and M(II) salt. The poor solubility of the previously reported complete imidazolylimine ligands was the motivation for the sub-component self-assembly approach utilized in this chapter.

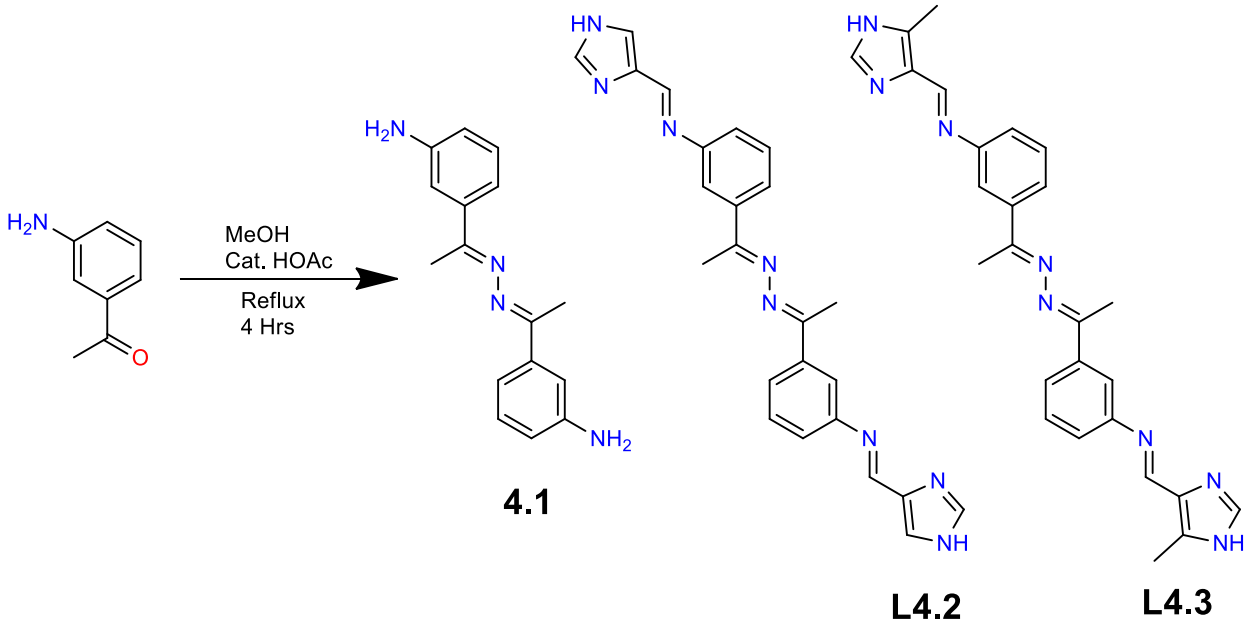

*Figure 4.1.3.i: The one step synthesis scheme employed to synthesise **4.1**. The ligands **L4.2** and **L4.3** were synthesised in situ following a sub-component self-assembly methodology from the diamine precursor **4.1** and 4-imidazolecarboxaldehyde (**L4.2**) or 4-methyl-5-imidazolecarboxaldehyde (**L4.3**).*

4.3 Complex synthesis and characterization

4.3.1 $[Fe_2(L4.2)_3](OTf)_4$, 4.4

Complex **4.4** was synthesised following a sub-component self-assembly methodology. Six equivalents of 4-imidazolecarboxaldehyde and two equivalents of Fe(II) triflate were dissolved in acetonitrile. Three equivalents of **4.1** were added and the resulting orange solution was stirred at 50 °C overnight. Vapor diffusion of diisopropyl ether into the acetonitrile solution gave orange block crystals suitable for single crystal X-ray diffraction. A crystal was mounted on the diffractometer directly at 120 K which resulted in an immediate colour change from orange to dark red. The subsequent diffraction data that were collected were solved and refined in the triclinic space group *P*-1 (R = 6.60%). The asymmetric unit contained two Fe(II) centres bridged by three **L4.2** ligands. The charge balance was provided by the presence of four triflate anions. The bidentate imidazolylimine moieties coordinate to the Fe(II) centres in a *fac* configuration. The Fe-N bond lengths indicate that both Fe1 and Fe2 exist in the LS state (*Appendix Table 4.10.2.i*) and

for both Fe(II) centres the Fe-N_{imine} bond lengths are slightly longer than the Fe-$N_{imidazole}$ bond lengths. The crystal was then warmed to 240 K at 5 K min^{-1}, however, the crystal exhibited no significant colour change. A second data collection was carried out at 240 K and data were solved and refined in the triclinic space group *P*-1 (R = 13.12%) (*Figure 4.3.1.i*). The unit cell dimensions are broadly similar to those obtained from the single crystal diffraction carried out at 120 K, however, the *a*-, *b*- and *c*-axes are all slightly expanded at 240 K (*Table 4.3.1.i*).

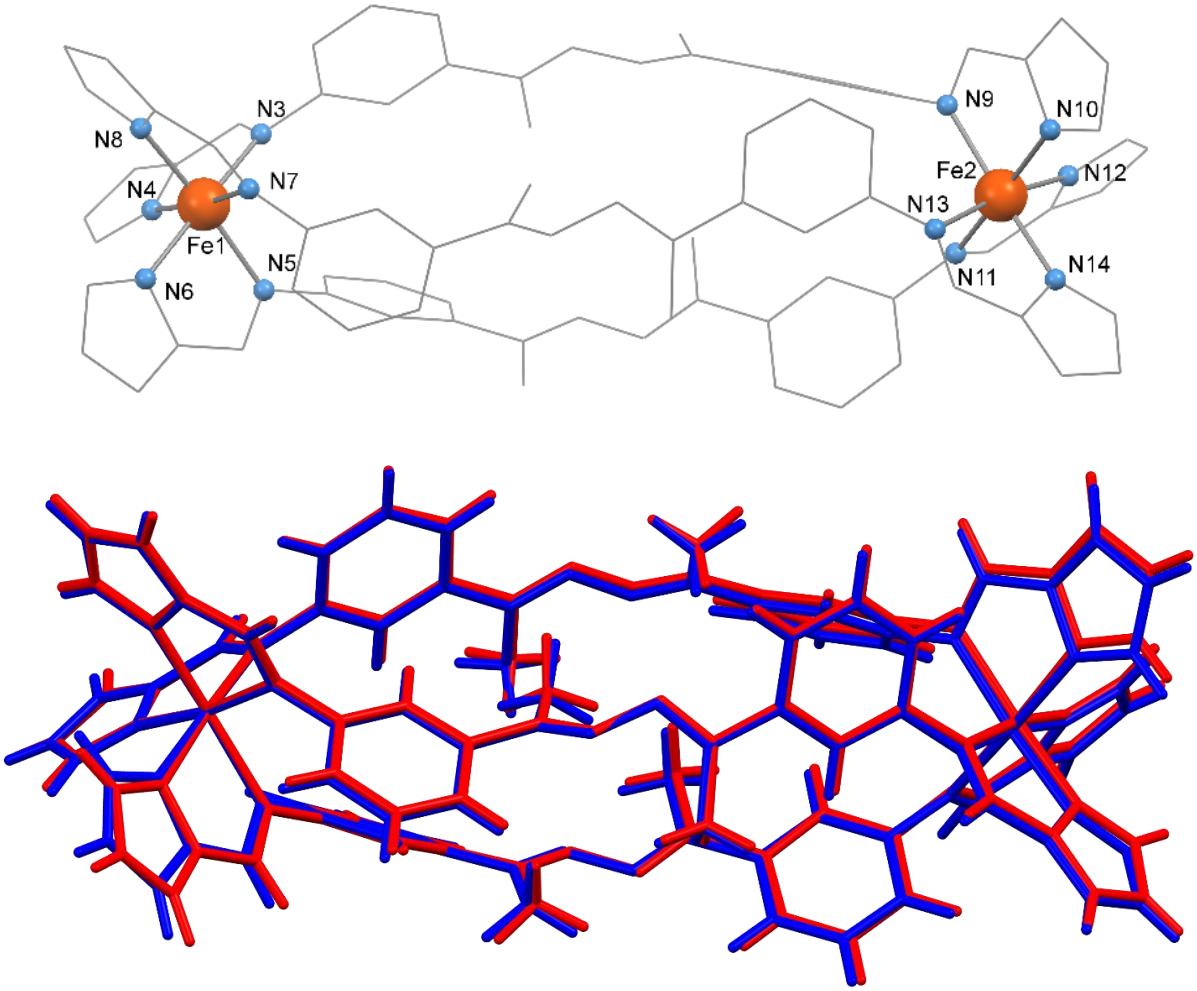

Figure 4.3.1.i : *(top) The asymmetric unit of **4.4** with the two crystallographically unique Fe(II) centres and coordinating nitrogen atoms labeled. Hydrogen atoms, solvent molecules and triflate anions omitted for clarity. (bottom) Overlaid structures of **4.4** at 120 K (blue) and 240 K (red). Solvent molecules and triflate anions are omitted for clarity.*

Analysis of the Fe-N bond lengths at 240 K indicates that Fe1 is HS as both the Fe-N_{imine} and the Fe-$N_{imidazole}$ bond lengths have increased (*Appendix Table 4.10.2.ii*). The Fe-N bond lengths for Fe2 have not shown any significant increase, indicating that it remains in the LS state. Much like the 120 K structure, the Fe-N_{imine} bond lengths are longer than the Fe-$N_{imidazole}$ bond lengths. The increase in the octahedral distortion parameter (Σ) for Fe1 is significantly greater than that of Fe2. This is commensurate with the increase in the Fe-N bond lengths for Fe1, implying some degree of SCO has occurred. The negligible increase in the Fe-N bond lengths for Fe2 indicate no SCO has occurred. Therefore, there is no significant increase in the distortion of the coordination sphere and only a small increase in Σ (*Table 4.3.1.ii*).

Dimension	**120 K**	**240 K**	**Percent increase**
a (Å)	15.2845(5)	15.4925(3)	1.36%
b (Å)	19.1761(6)	19.3481(5)	0.90%
c (Å)	20.5638(7)	20.6900(7)	0.61%
Volume ($Å^3$)	5287.96	5474.43	3.53%

*Table 4.3.1.i: The unit cell parameters for **4.4** obtained from the crystal structure at 120 K and 240 K.*

Σ (°)	**120 K**	**240 K**	**Percent increase**
Fe1	63	83	32%
Fe2	56	65	17%

*Table 4.3.1.ii: The octahedral distortion parameters (Σ) for **4.4** obtained from the crystal structure at 120 K and 240 K.*

The Fe1···Fe2 separation at 120 K measures 14.943(1) Å and slightly increases to 15.063(2) Å at 240 K. The phenyl rings are significantly twisted out of the plane of the coordinating imine (*Appendix Table 4.10.2.viii*). This allows for the phenyl rings to form C-H···π interactions with H···π(centroid) separations ranging from 2.841(1) to 3.047(1) Å at 120 K, which stabilizes the twisted nature of the three ligands. At 240 K, these C-H···π interactions increase slightly to 2.971(1) to 3.245(1) Å (*Appendix Table 4.10.2.xviii*). The central N-N bond of the ligand retains its single bond character with the bond lengths ranging from 1.388(3) to 1.402 (4) Å at 120 K and 1.38(1) to 1.42(2) Å at 240 K. However, there is a significant twist about the central hydrazone component with torsion angles ranging from 109.7(3)° to 157.2(2)° at 120 K. There is no significant change in the torsion angles upon warming to 240 K, with values ranging from 114.5(9) to 157.1(9) Å (*Appendix Table 4.10.2.xiii*). Therefore, the extent of the distortion is localized

around the two Fe(II) centres. Non-conventional hydrogen bonds occur between the imine hydrogen atoms and the nitrogen atoms of the central hydrazone linker on a neighbouring helicate. Two alternating crystallographically unique types of this interaction occur with H···N separations of 2.484(3) and 4.88(2) Å (*Figure 4.3.1.ii*). These interactions are reciprocal in nature with two crystallographically identical interactions between the pair of helicates. These interactions are reinforced by reciprocal C-H···π interactions occurring between the methyl groups of the hydrazone linker moiety and the aromatic rings on a neighbouring helicate. Two alternating crystallographically unique types of this interaction occur, with H···π(centroid) separations of 3.140(1) and 3.442(2) Å (*Figure 4.3.1.ii*). The combination of the non-conventional hydrogen bonds and the C-H···π interactions results in the stacking of the helicates in offset supramolecular chains. These run parallel to the crystallographic *b*-axis. Four of the N-H imidazole moieties participate in hydrogen bond interactions with the oxygen atoms of the triflate anions. One N-H moiety participates in a hydrogen bond interaction with a water molecule. The final N-H moiety participates in a hydrogen bond interaction with the nitrogen atom of an acetonitrile molecule (*Figure 4.3.1.iii).* The H···A (A = O or N) separations range from 1.90(1) to 2.12(2) Å. One hydrogen atom of the water molecule participates in a hydrogen bond interaction with the oxygen of a triflate anion with and H···O distance of 2.387(9) Å. The hydrogen bond interactions are summarized in (*Appendix Table 4.10.2.xxiii*). This triflate anion is also engaged in a hydrogen bond interaction with the N-H moiety on a neighbouring helicate via a different oxygen atom. The reverse interaction also occurs between the two helicates resulting in the occurrence of two reciprocal interactions per pair of helicates producing hydrogen bonded dimers linked end on end (*Figure 4.3.1.iii*).

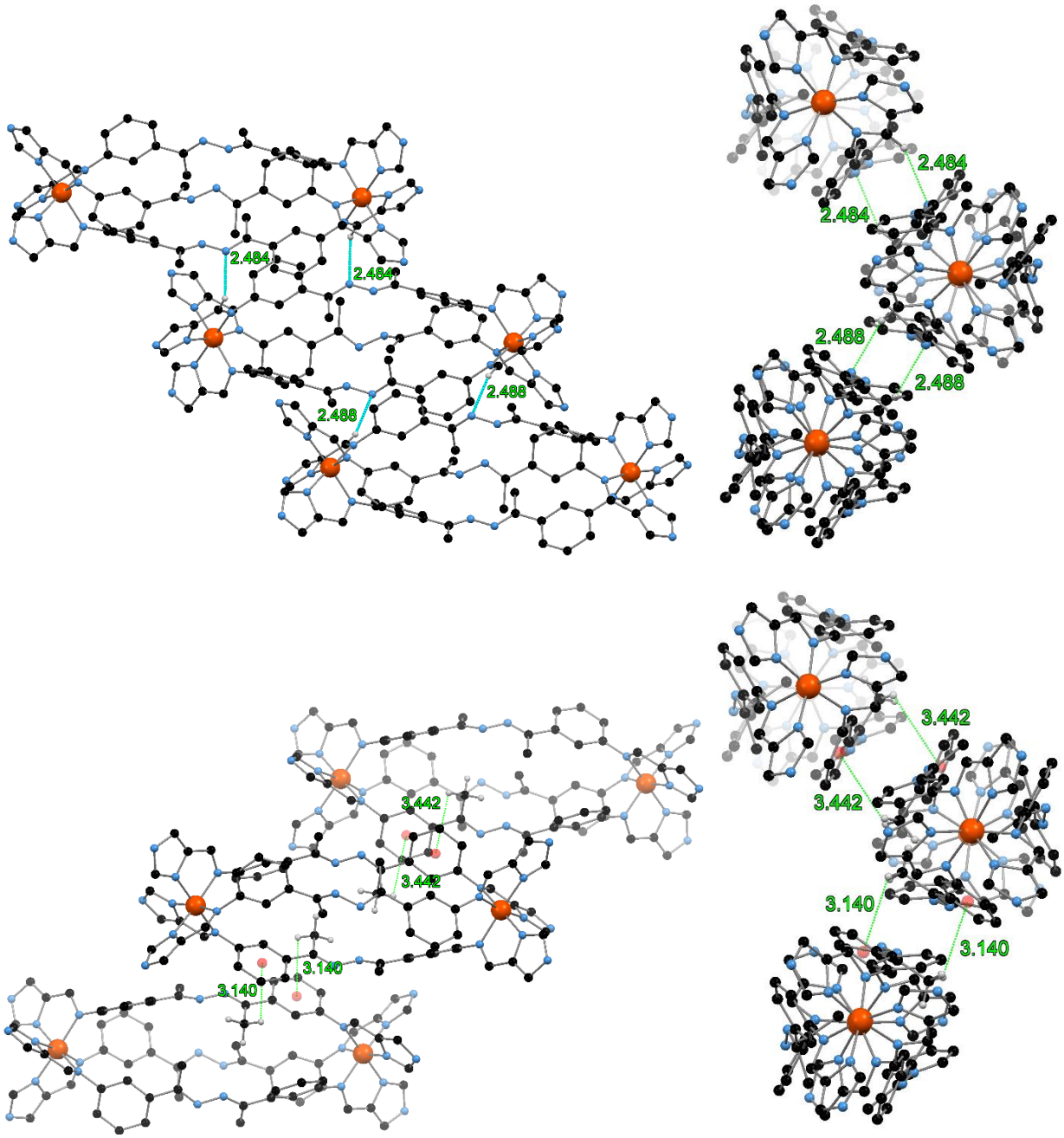

Figure 4.3.1.ii: (top) The reciprocal imine···hydrazone C-H···N non-conventional hydrogen bond interactions, shown in green, viewed down an arbitrary direction (left) highlighting the offset packing and the same interactions viewed down helical axis (right), highlighting the zig-zag packing of the helicates. (bottom) The reciprocal C-H···π interactions shown in green, viewed down an arbitrary direction (left) and the same interactions viewed down the helical axis (right). Hydrogen atoms not participating in the illustrated interactions, solvent molecules and triflate anions omitted for clarity.

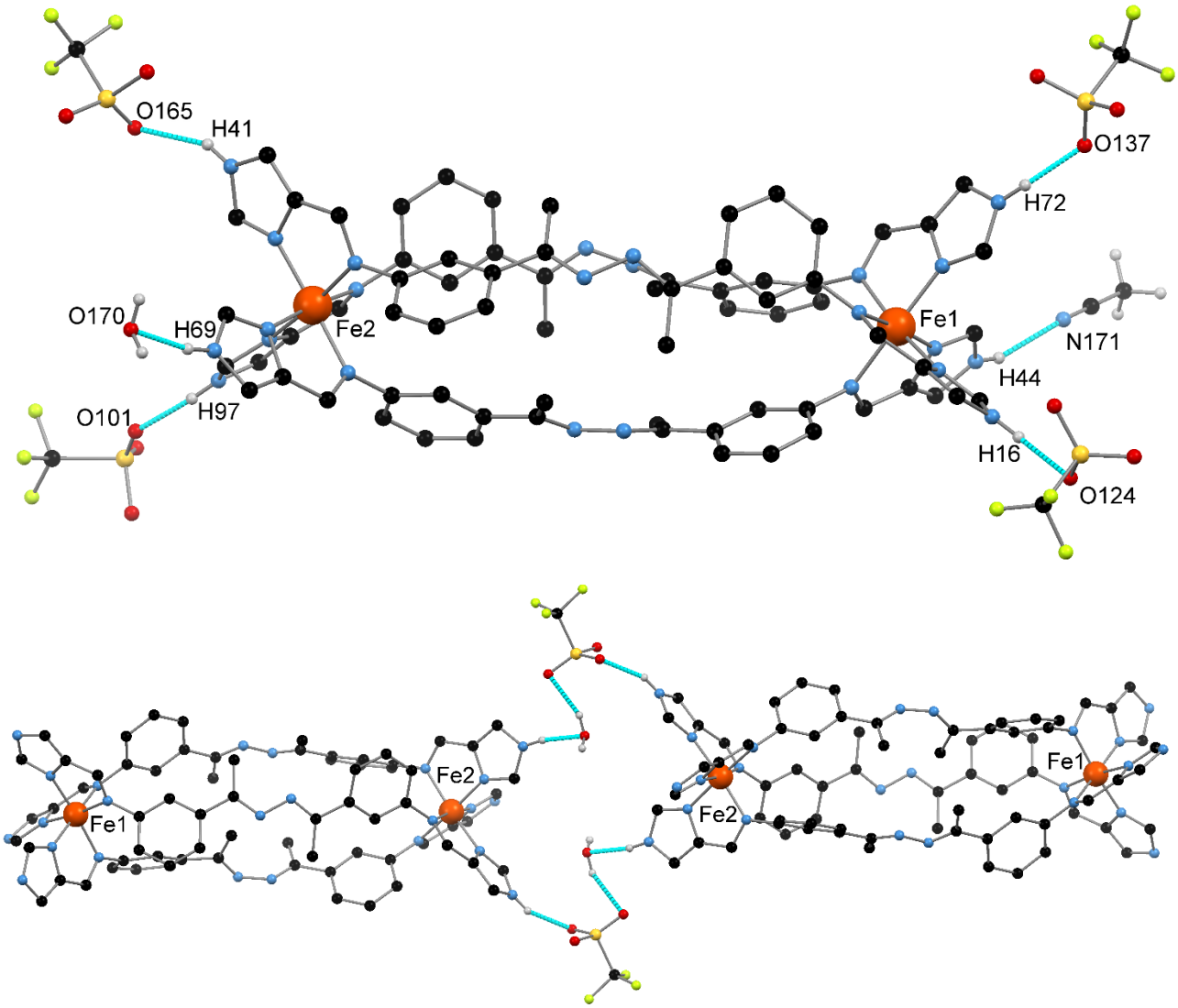

Figure 4.3.1.iii: (top) The hydrogen bond interactions occuring at each of the N-H moieties with the triflate anions and the water and acetonitrile solvent molecules. (bottom) The reciprocal hydrogen bonded bridge linking two neighbouring helicates end on end. Hydrogen atoms, solvent molecules and triflate anions not participating in the illustrated reactions omitted for clarity. Hydrogen bond interactions shown in light blue.

Complex **4.4** crystallises with a large amount of solvent. Despite attempts, not all the acetonitrile and diisopropyl ether molecules could be modeled satisfactorily and therefore the SQUEEZE[418] function of PLATON[419] was employed (1.2 Å probe). This revealed a solvent accessible void of 602 $Å^3$ calculated to contain 158 electrons, which equates to 79 electrons per helicate. This corresponds to one diisopropyl ether and one acetonitrile molecule (80 electrons) per helicate.

Therefore, along with the 2.9 molecules of acetonitrile modeled crystallographically, the solvent content of the single crystal can be approximated as 3.9 acetonitrile, one water and one diisopropyl ether molecule. TGA was carried out on a filtered sample of the crystals left to stand under a nitrogen flow for half an hour. Between 80 and 250 °C a mass loss of 2.1% occurs. This roughly corresponds to the loss of one acetonitrile solvent molecule from **4.4**·3.9MeCN·H_2O (1.9%). This number of acetonitrile and water molecules is the same to that approximated for the crystal structure. The loss of diisopropyl ether solvent molecules is not observed as they are highly volatile and are lost upon standing the filtered dry crystals at room temperature. This rapid loss of solvent is expected as the crystals rapidly lose crystallinity upon removal from the mother liquor, attributed to solvent loss. There is a more abrupt mass loss of 4.9% between 250 and 290 °C. This can be attributed to the further loss of 2.5 acetonitrile solvent molecules (4.9%). Above 290 °C decomposition of the complex occurs. For elemental analysis, the crystals were dried to constant weight under vacuum. This gave results corresponding to a molecular formula of **4.4**·0.5H_2O showing that much of the solvent is lost during the sample preparation.

4.3.2 $[Fe_2(L4.2)_3](OTf)_4$, 4.5

The same sub-component self-assembly synthesis procedure as **4.4** was carried out. However, vapor diffusion of chloroform was used instead of diisopropyl ether employed for **4.4**. This gave yellow needle crystals suitable for single crystal X-ray diffraction. A crystal was mounted directly on the diffractometer at 120 K, resulting in an immediate colour change to dark red/purple and a data collection was carried out. The data were solved and refined in the monoclinic space group *C*2/*c* (R = 6.70%). The asymmetric unit contained one Fe(II) centre coordinated to one complete ligand, one half ligand while the charge of the asymmetric unit is compensated by two triflate anions (*Figure 4.3.2.i*). The complete helicate structure is generated by the action of a 2-fold rotation perpendicular to the helical axis. The bidentate imidazolylimine moieties coordinate to the Fe(II) centres in a *fac* configuration. The Fe-N bond lengths indicate that Fe1 exists in the LS state and much like **4.4** the Fe-N_{imine} bond lengths are slightly longer than the Fe-$N_{imidazole}$ bond lengths (*Appendix Table 4.10.2.iii*). The octahedral distortion parameter (Σ) for the crystallographically unique Fe1 centre is 65°, indicative of LS Fe(II).

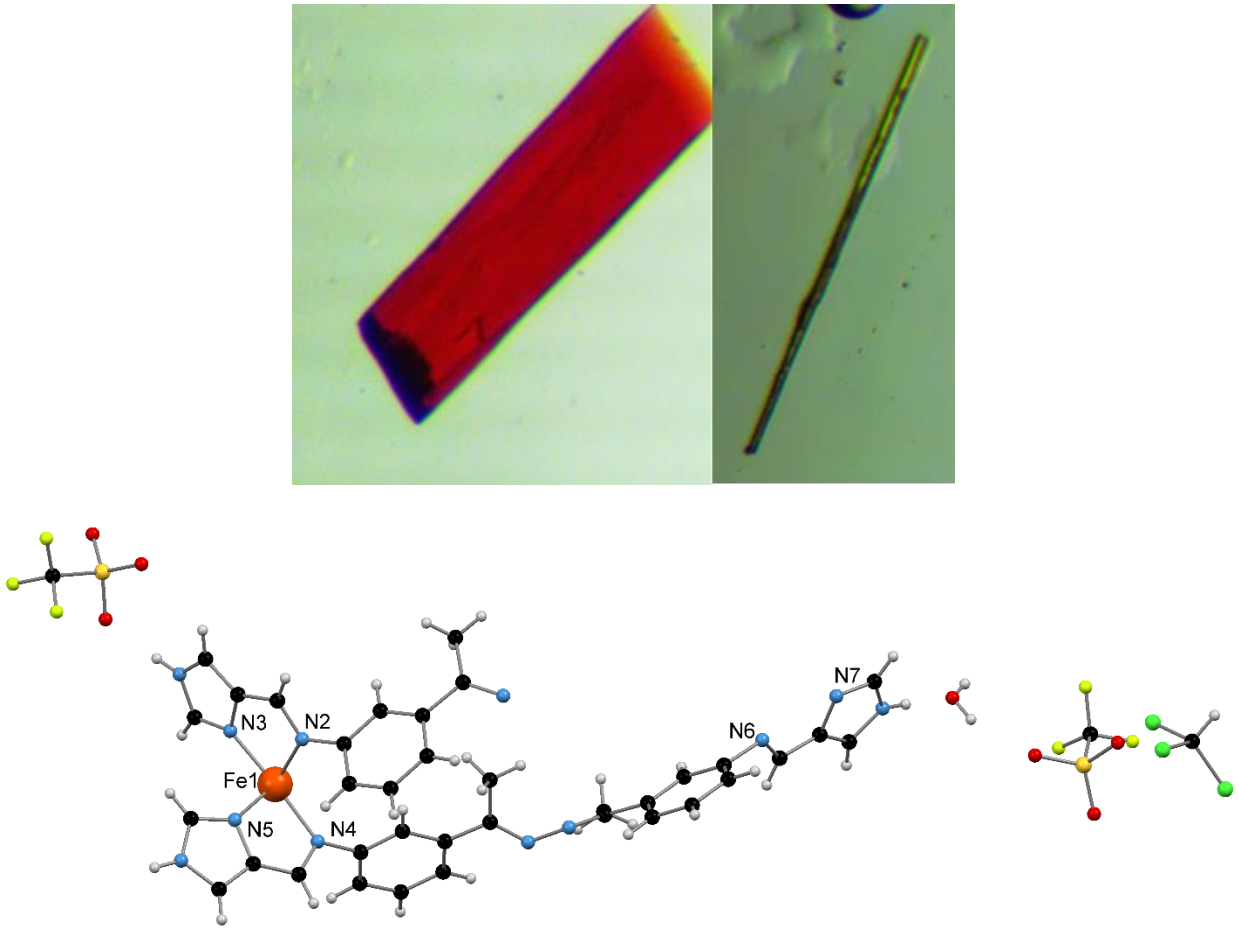

*Figure 4.3.2.i: (top) The orange block crystals of **4.4** from vapor diffusion of diisopropyl ether (left) and the yellow rod crystals of **4.5** from vapor diffusion of chloroform (right). (bottom)The asymmetric unit of **4.5** containing the one half of the dinuclear triple helicate with the Fe(II) centre and coordinating donor atoms labeled.*

The Fe1···Fe1' (prime symbol ' indicates a symmetry generated atom) separation is 14.970(2) Å at 120 K. The phenyl rings are significantly twisted out of the plane of the coordinating imine (*Appendix Table 4.10.2.ix*). This allows the phenyl rings to form C-H···π interactions with H···π(centroid) separations ranging from 2.841(1) to 3.047(1) Å at 120 K which stabilizes the twisted nature of the three ligands (*Appendix Table 4.10.2.xix*). The central N-N bond of the ligand retains its single bond character with the bond lengths of 1.387(6) and 1.409(7) Å at 120 K. However, there is a significant twist about the central hydrazone component with torsion angles ranging from 129.9(4)° to 166.33(5)° (*Appendix Table 4.10.2.xiv*).

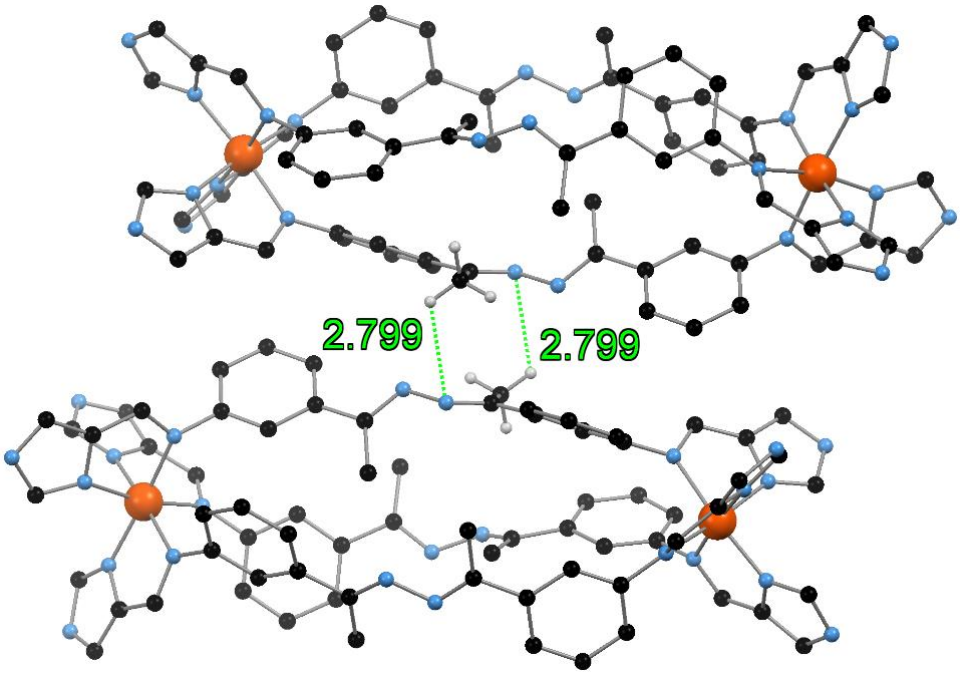

Figure 4.3.2.ii: The C-H···N non-conventional hydrogen bond interactions occurring between the methyl substituent of the central hydrazone spacer and the nitrogen atom of the hydrazone spacer on a neighbouring helicate are shown in green. Hydrogen atoms not participating in the illustrated interactions, triflate anions and solvent molecules omitted for clarity.

There is no apparent disorder of the central methyl groups unlike the previous helicate **4.4**. Two crystallographically identical C-H···N non-conventional hydrogen bonds occur with H···N separations of 2.799(5) Å. These occur between the central methyl groups of the ligand and the nitrogen atoms of the central hydrazone linker. This interaction is reciprocal in nature with two interactions occurring between two neighbouring helicates (*Figure 4.3.2.ii*). In the asymmetric unit two imidazole N-H moieties are participating in hydrogen bond interactions with the oxygen atoms of the triflate anions. The third N-H moiety is participating in an hydrogen bond interaction with a water molecule. These interactions are summarized in *Appendix Table 4.10.2.xxiv*. A hydrogen bond interaction occurs between the water molecule and a triflate anion resulting in a hydrogen bond bridge between two neighbouring helicates. This interaction, in conjunction with the aforementioned C-H···N non-conventional hydrogen bonds, results in the helicate units stacking upon one another with the triflate anions and water molecules acting as a hydrogen bond bridge at either end (*Figure 4.3.2.iii)*.

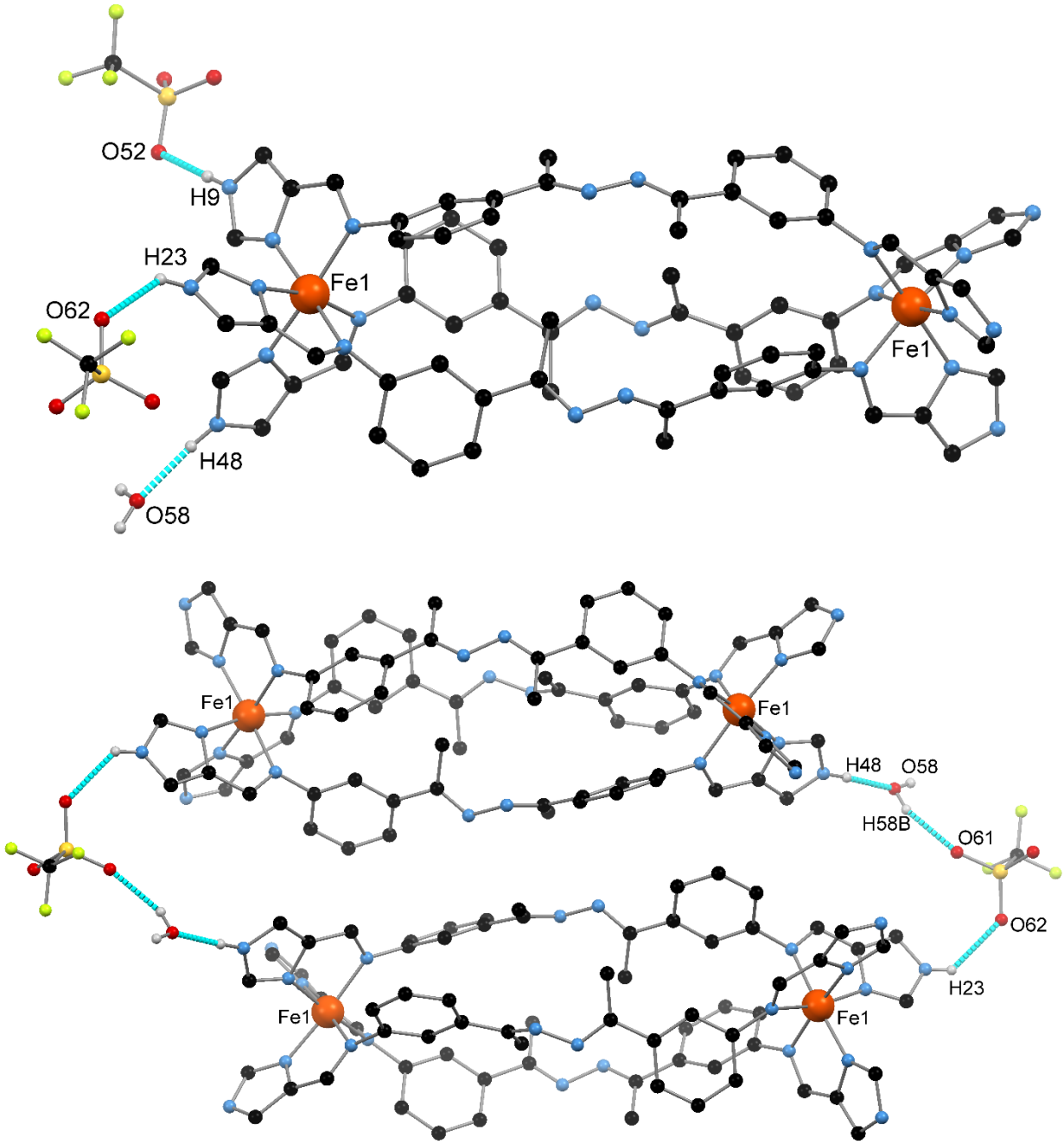

Figure 4.3.2.ii: (top) The crystallographically unique hydrogen bond interactions occur between the N-H moieties and the triflate anions and water molecule. (bottom) The reciprocal hydrogen bond bridge linking two neighbouring helicates in an off-set manner. The interaction is mediated via a water molecule triflate anion hydrogen bond. Hydrogen atoms, solvent molecules and triflate anions not participating in the illustrated interactions omitted for clarity. Hydrogen bond interactions shown in light blue.

This one-dimensional supramolecular chain runs parallel to the crystallographic *c*-axis. The helicates pack in a zig-zag manner such that the one-dimensional chains pack in an offset fashion when viewed down the crystallographic *c*-axis. The Fe···Fe separation between Fe(II) centres in neighbouring helicates is 9.284(1) Å. The second triflate anion in the asymmetric unit does not contribute to the propogation of a hydrogen bond network. There is a large amount of disordered solvent in the asymmetric unit. One water molecule and a chloroform molecule were modeled while the remaining electron density was removed by the SQUEEZE[418] function of PLATON (1.2 Å probe).[419] The solvent accessible void was revealed to be 1342 $Å^3$ calculated to contain 361 electrons, which equates to 90 electrons per helicate. Therefore, along with the two water and two chloroform molecules modelled, the solvent content can be approximated as three chloroform, two water and 2.5 acetonitrile solvent molecules per helicate. TGA showed initially there is a mass loss between room temperature and 130 °C, due to the loss of volatile solvent molecules. As the mass is not initially constant, the nature and number of the solvent molecules lost in this process cannot be quantified. Between 130 and 300 °C there is a plateau after which there is a rapid mass loss due to decomposition of the complex. For elemental analysis, the crystals were not dried to constant weight under vacuum and instead were analyzed as received (see details in experimental section). Therefore, a much larger proportion of the solvents of crystallization can be observed compared to other complexes and indicates a molecular formula of **4.5**·$4CHCl_3$·$9H_2O$·CH_3CN. The replacement of the solvent molecules with water molecules is commonly observed for multinuclear supramolecular complexes. Upon removal from the mother liquor, the crystals lose crystallinity due to desolvation.

4.3.3 $[Fe_2(L4.3)_3](BF_4)_4$, 4.6

Complex **4.6** was synthesised following a sub-component self-assembly methodology. Six equivalents of 4-methyl-5-imidazolecarboxaldehyde and two equivalents of Fe(II) tetrafluoroborate were dissolved in nitromethane. Three equivalents of **4.1** was added and the resulting orange solution was stirred at 50 °C overnight. Vapor diffusion of diethyl ether into the nitromethane solution of **4.6** gave orange block crystals suitable for single crystal X-ray diffraction. A crystal was mounted on the diffractometer directly at 120 K resulting in an immediate colour change from orange to dark red. The diffraction data were collected and solved and refined in the triclinic space group *P*-1 (R = 5.67%). The asymmetric unit contained two Fe(II)

centres bridged by three **L4.3** ligands *(Figure 4.3.3.i*). The charge balance was provided by four tetrafluoroborate anions.

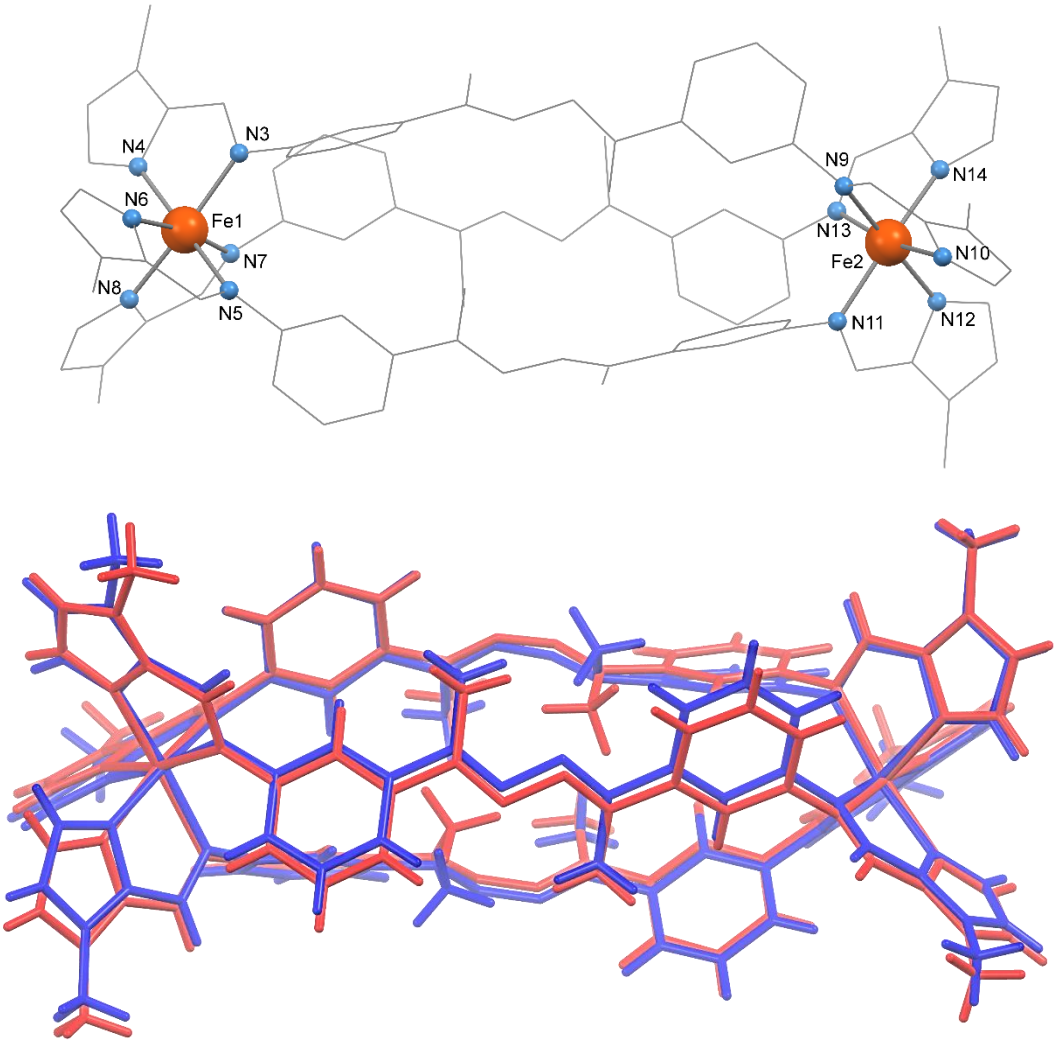

*Figure 4.3.3.i: (top) The asymmetric unit of **4.6** with the two crystallographically unique Fe(II) centres and coordinating nitrogen atoms labeled. Hydrogen atoms, solvent molecules and tetrafluoroborate anions omitted for clarity. (bottom) Overlaid structures of **4.6** at 120 K (blue) and 240 K (red). Solvent molecules and tetrafluoroborate anions omitted for clarity.*

The bidentate imidazolylimine moieties coordinate to the Fe(II) centres in a *fac* manner. The Fe-N bond lengths indicate that both Fe1 and Fe2 exist in the LS state (*Appendix Table 4.10.2.iv*). For both Fe1 and Fe2 the Fe-N_{imine} bond lengths are slightly longer than the Fe-$N_{imidazole}$ bond lengths. The crystal was then warmed to 240 K at 5 K min^{-1}, resulting in a colour change from red to orange, and a second data collection was carried out. The data were solved and refined in the triclinic space

group *P*-1 (R = 5.75%). The unit cell dimensions are broadly similar to those obtained from the single crystal diffraction carried out at 120 K, however, the *a*-, *b*- and *c*-axes were all slightly expanded at 240 K. This resulted in an increase in the unit cell volume from 5216.51 $Å^3$ (120 K) to 5474.18 $Å^3$ (240 K) which may indicate that SCO has occurred (*Table 4.3.3.i*).

Dimension	**120 K**	**240 K**	**Percent increase**
a (Å)	14.0309(3)	14.2166(2)	1.32 %
b (Å)	16.0603(4)	16.3976(4)	2.10 %
c (Å)	24.1203(6)	24.5707(6)	1.87 %
Volume ($Å^3$)	5216.51	5474.18	4.94 %

*Table 4.3.3.i: The unit cell parameters for **4.6** obtained from the crystal structure at 120 K and 240 K.*

Analysis of the Fe-N bond lengths at 240 K confirms the occurrence of SCO as both the Fe-N_{imine} and the Fe-$N_{imidazole}$ bond lengths increase (*Appendix Table 4.10.2.v*). As observed for the 120 K structure, the Fe-N_{imine} bond lengths are longer than the Fe-$N_{imidazole}$ bond lengths. Accompanying the increase in the Fe-N bond lengths is a concomitant increase in the distortion of the coordination sphere for both Fe1 and Fe2 represented by the octahedral distortion parameter (Σ) (*Table 4.3.3.ii*). There is a significant increase in Σ values for both Fe1 and Fe2 between 120 K and 240 K as the SCO results in a more distorted coordination sphere.

Σ (°)	**120 K**	**240 K**	**Percent increase**
Fe1	54	87	61%
Fe2	60	89	47%

*Table 4.3.3.ii: The octahedral distortion parameters (Σ) for **4.6** at 120 and 240 K.*

The Fe1···Fe2 separation is 14.9270(7) Å at 120 K and increases slightly to 15.1853(7) Å at 240 K. The phenyl rings are significantly twisted out of the plane of the coordinating imine (*Appendix Table 4.10.2.x*). This allows the phenyl rings to form C-H···π interactions with H···π(centroid) interactions ranging from 2.841(1) to 3.047(1) Å at 120 K. This stabilizes the twisted nature of the three ligands. At 240 K, these C-H···π interactions increase slightly to 2.971(1) to 3.245(1) Å (*Appendix Table 4.10.2.xx*). The central N-N bond of the ligand retains its single bond character. The bond lengths range from 1.392(3) to 1.397(3) Å at 120 K and 1.388(3) to 1.399(3) Å at 240 K. However, there is a significant twist about the central hydrazone component with angles ranging from 125.3(3) to 148.4(2)° at 120 K. There is no significant change in the torsion angles upon

warming to 240 K. Therefore, the extent of the distortion is localized around the two Fe(II) centres (*Appendix Table 4.10.2.xv*).

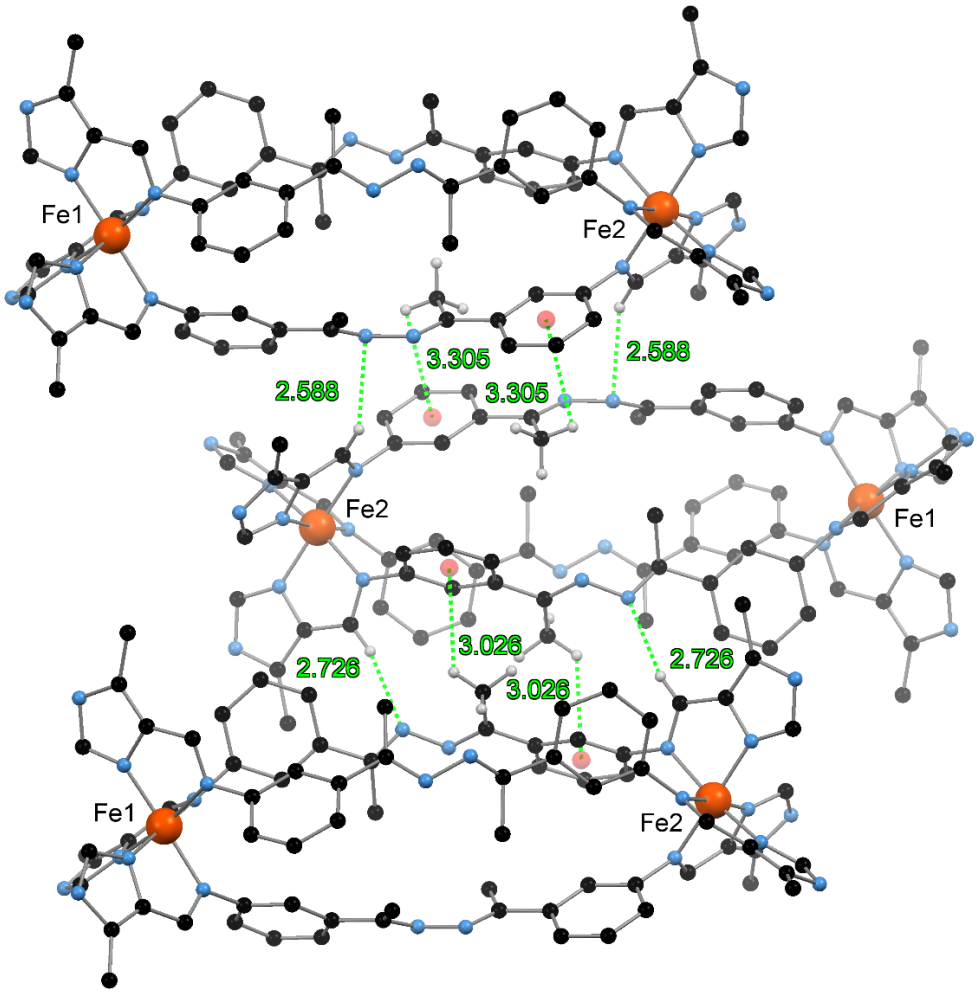

Figure 4.3.3.ii: The alternating reciprocal pairs of C-H···π and non conventional imine C-H hydrogen bond interactions between neighbouring helicates are shown in green while π(centroid) are represented by red spheres. Hydrogen atoms not participating in the illustrated interactions, tetrafluoroborate anions and solvent molecules omitted for clarity.

On one ligand, the central methyl groups are both orientated away from the intrahelical cavity. However, on the two remaining ligands one methyl group is orientated away and the other disordered over two positions: one toward the interhelical cavity and one away. The methyl groups orientated away from the intra helical cavity participate in two alternating C-H···π interactions with H···π(centroid) separations of 3.026(1) and 3.305(1) Å (*Figure 4.3.3.ii*). These interactions

are reciprocal with two crystallographically identical interactions occuring between two neighbouring helicates. This results in the formation of off-set one-dimensional chains running parallel to the crystallographic *b*-axis. A reciprocal pair of non-conventional hydrogen bonds occurs between the imine C-H moiety and the nitrogen atom of the hydrazone linker on a neighbouring helicate (*Figure 4.3.3.ii*). This interaction occurs with an H···N separation of 2.588(2) Å. All six of the N-H moieties of the imidazole ring participate in hydrogen bond interactions with the tetrafluoroborate anions. These interactions are summarized in *Appendix Table 4.10.2.xxv*.

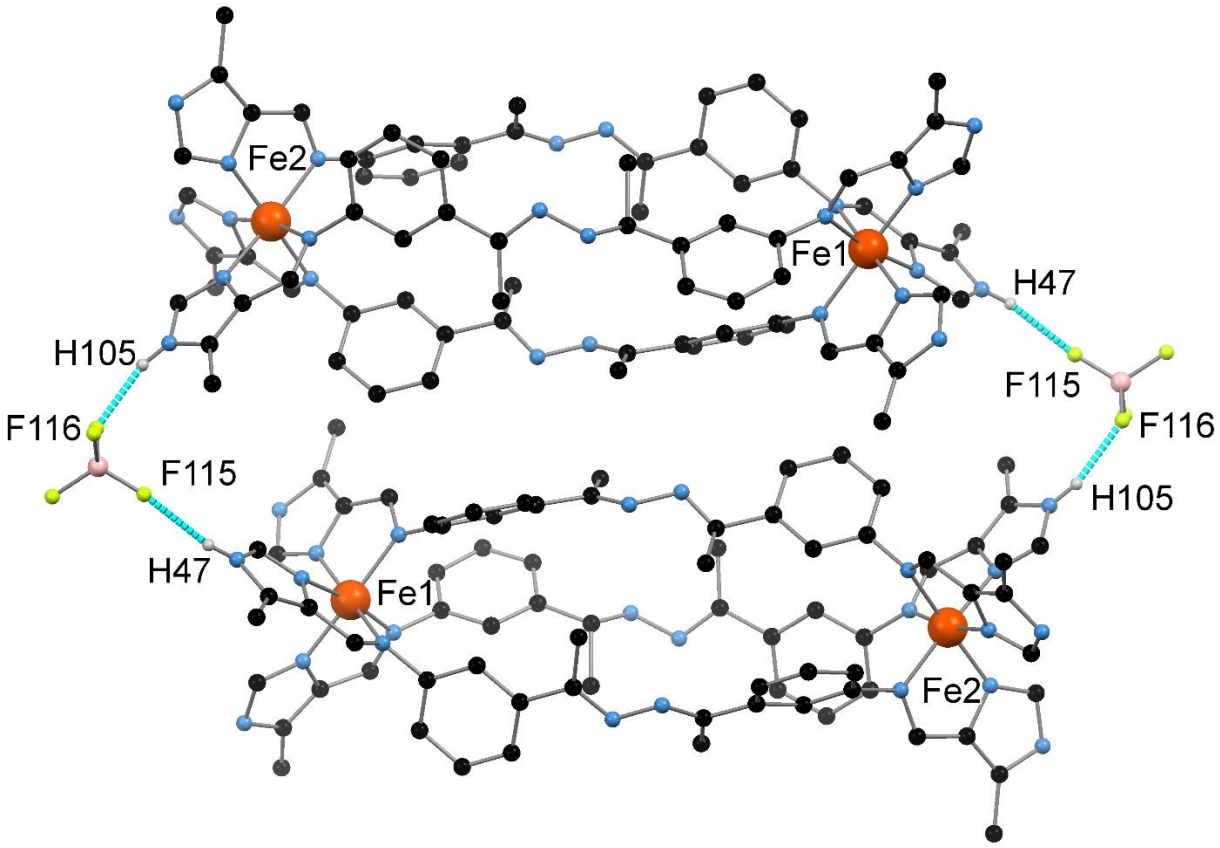

Figure 4.3.3.iii: The hydrogen bond interactions between the tetrafluoroborate anions and the N-H moieties of the imidazole rings. Two tetrafluoroborate anions bridge two helicates stacked upon one another at either end to form hydrogen bonded dimers. Hydrogen bonds are shown in light blue.

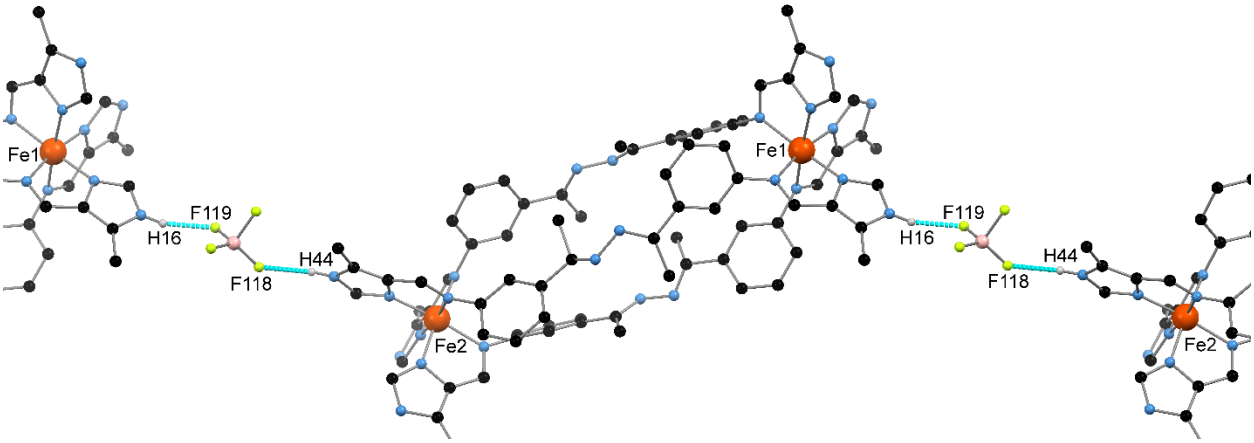

Figure 4.3.3.iv: The one-dimensional chains formed by bridging tetrafluoroborate anions. Hydrogen atoms not participating in the illustrated interaction, anions and solvent molecules omitted for clarity. Hydrogen bonds are shown in light blue.

Two crystallographically identical tetrafluoroborate anions form a hydrogen bond bridge between two neighbouring helicates at either end (*Figure 4.3.3.iii*). These alternate with non-classical hydrogen bonds between the methyl groups of the central hydrazone linker and the hydrazone moiety on a neighbouring helicate with an H···N separation of 2.831(2) Å. This results in the formation of hydrogen bond chains running parallel to the [110] crystallographic plane. Two other tetrafluoroborate anions act as a bridge at either end of the helicate to two other neighbouring helicates. This results in the formation of one-dimensional hydrogen bond chains propagating along the [101] crystallographic plane (*Figure 4.3.3.iv*). The two remaining tetrafluoroborate anions surrounding the helicate do not participate in the propagation of a hydrogen bond network. Complex **4.6** crystallises with a large amount of disordered solvent. Despite attempts, not all of the nitromethane and diethyl ether molecules could be modeled satisfactorily and therefore the SQUEEZE[418] function of PLATON[419] was employed (1.2 Å probe). This revealed a solvent accessible void of 852 $Å^3$ calculated to contain 246 electrons. This corresponds to 123 electrons per helicate and is approximated as one diethyl ether and 2.5 nitromethane molecules (122 electrons). This means that along with the 3.5 molecules of nitromethane modeled crystallographically, the solvent content of the crystal structure can be approximated as six nitromethane and one diethyl ether molecule. TGA was carried out on a filtered sample of the crystals that was allowed to stand under a nitrogen flow until a constant weight was achieved. The mass is constant between room temperature and 250 °C after which decomposition occurs. The

volatile nitromethane and diethyl ether molecules are lost during sample preparation and therefore their loss is not observed in the TGA experiment. For elemental analysis, the crystals were dried to constant weight under vacuum. This gave results corresponding to a molecular formula of **4.6**·4H_2O. The replacement of the solvent molecules with water in the complex is commonly observed for multinuclear supramolecular complexes susceptible to desolvation. The crystals rapidly lose crystallinity upon removal from the mother liquor which can be attributed to the loss of solvent.

4.3.4 $[Fe_2(L4.3)_3](OTf)_4$, 4.7

A similar synthesis procedure to **4.6** was carried out with Fe(II) triflate used in the place of Fe(II) tetrafluoroborate. Vapor diffusion of diisopropyl ether into the nitromethane solution of **4.7** gave orange block crystals suitable for single crystal X-ray diffraction. A crystal was mounted on the diffractometer directly at 120 K resulting in an immediate colour change from orange to dark red. The diffraction data were collected and solved and refined in the monoclinic space group $P2_1/c$ (R = 5.35%).

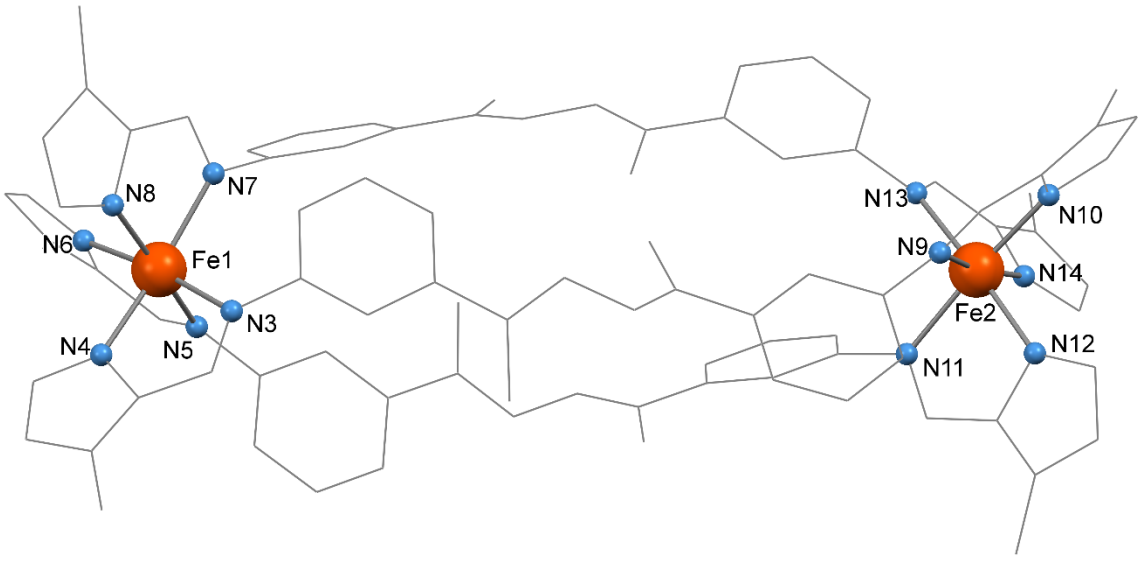

*Figure 4.3.4.i: The asymmetric unit of **4.7** with the two crystallographically unique Fe(II) centres and coordinating nitrogen atoms labeled. Hydrogen atoms, solvent molecules and triflate anions omitted for clarity.*

The asymmetric unit contained two Fe(II) centres bridged by three **L4.3** ligands (*Figure 4.3.4.i*) and the charge balance was provided by four triflate anions. The bidentate imidazolylimine

moieties coordinate to the Fe(II) centres in a *fac* manner. The Fe-N bond lengths indicate that both Fe1 and Fe2 exist in the LS state (*Appendix Table 4.10.2.vi*). For both Fe1 and Fe2 the Fe-N_{imine} bond lengths are slightly longer than the Fe-$N_{imidazole}$ bond lengths. The octahedral distortion parameters (Σ) for Fe1 and Fe2 are 58° and 64° respectively indicative of LS Fe(II) at 120 K. The Fe1···Fe2 separation is 14.8888(7) Å, similar to that of **4.6**. The phenyl rings are significantly twisted out of the plane of the coordinating imine (*Appendix Table 4.10.2.xi*). This allows them to form C-H···π interactions with H···π(centroid) separations ranging from 2.874(1) to 3.020(1) Å which stabilizes the twisted nature of the three ligands (*Appendix Table 4.10.2.xxi*). The central N-N bond of the ligand retains its single bond character with the bond lengths ranging from 1.386(3) to 1.405(3) Å at 120 K, slightly longer than **4.6**. However, there is a significant twist about the central hydrazone component with torsion angles ranging from 117.5(3)° to 159.0(2)°, similar to **4.6** (*Appendix Table 4.10.2.xvi*).

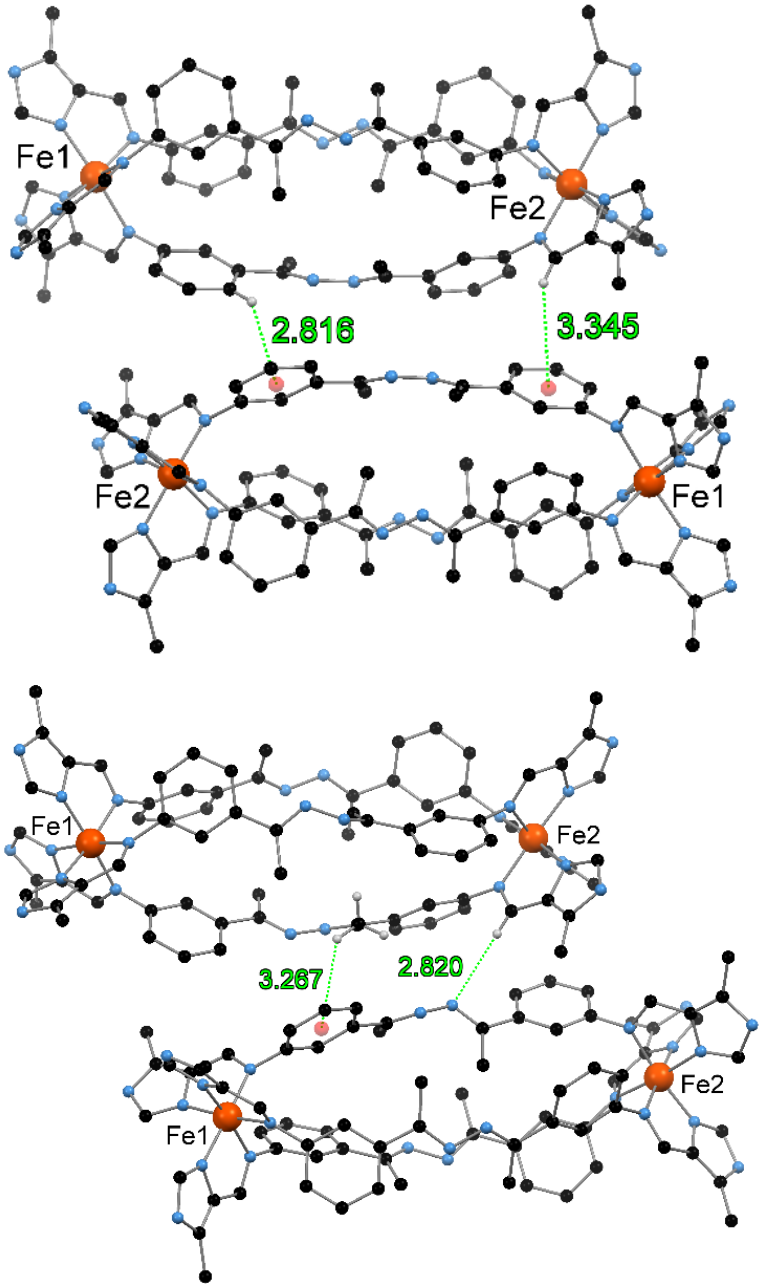

Figure 4.3.4.ii: (left) The reciprocal C-H···π interactions occurring between two neighbouring helicates. (right) The complementary non-conventional C-H···N hydrogen bond and C-H···π interaction formed to a different neighbouring helicate. Hydrogen atoms not participating in the illustrated interactions, triflate anions and solvent molecules omitted for clarity. The C-H···π and C-H···N interactions are shown in green while the π(centroid) are represented by red spheres.

Only one of the methyl groups on the central hydrazone spacer is orientated towards the intra helical cavity, However, unlike **4.6**, none of the methyl groups are modeled as disordered. The

methyl groups orientated away from the intrahelical cavity participate in C-H···π and C-H···N non-conventional hydrogen bonds (*Figure 4.3.4.ii*). The C-H···π interaction occurs between the methyl group and the phenyl ring on a neighbouring helicate with an H···π(centroid) separation of 3.627(1) Å. The C-H···N non-conventional hydrogen bond occurs between the methyl group and one of the nitrogen atoms of the hydrazone linker on a neighbouring helicate with an H···N separation of 2.877(2) Å. There are further C-H···π and non-conventional C-H···N hydrogen bond interactions formed to a different neighbouring helicate. These involve the C-H moieties of the phenyl ring and the C-H moiety of the imine respectively (*Figure 4.3.4.ii*). The C-H···π interaction occurs between the C-H moiety *ortho* to the hydrazone moiety on one aromatic ring and the phenyl ring π-system on the neighbouring helicate. A second C-H···π interaction occurs between an imine C-H moiety and the phenyl ring π-system on the neighbouring helicate with an H···π(centroid) separation of 3.345(1) Å. The non-conventional C-H···N hydrogen bond interaction occurs between another imine C-H moiety and a nitrogen atom of the central hydrazone linker on the neighbouring helicate with an H···π(centroid) separation of 2.820(2) Å.

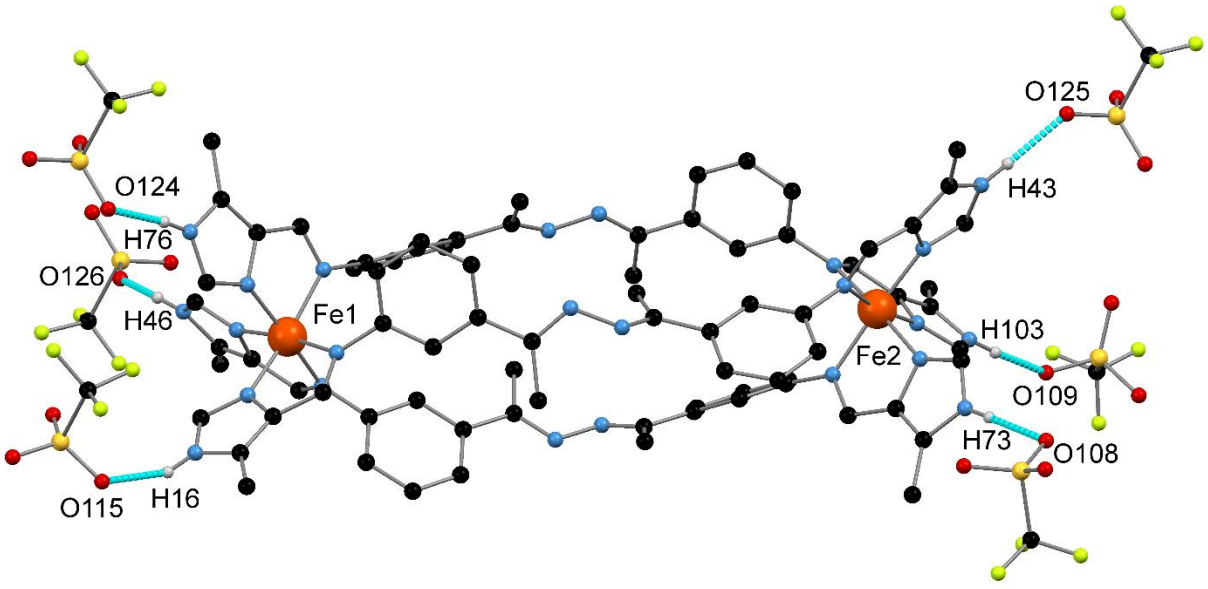

Figure 4.3.4.iii: (top) The crystallographically unique hydrogen bond interactions between the N-H moieties and the oxygen atoms of the triflate anions. Hydrogen bond interactions are shown in light blue.

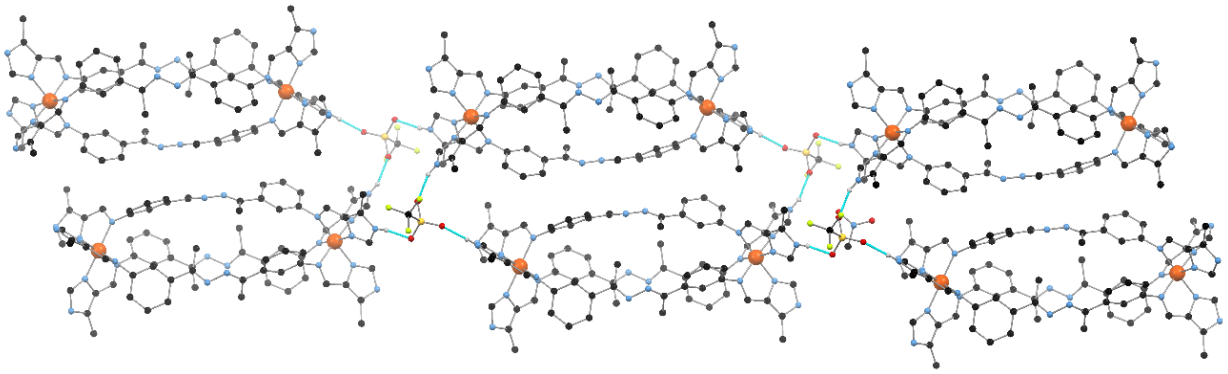

Figure 4.3.4.iv: The one-dimensional supramolecular chain formed via the triflate anion hydrogen bonds to three separate helicates. Two crystallographically identical interactions occur at either end of each helicate. Hydrogen atoms, triflate anions and solvent molecules not participating in the illustrated interactions omitted for clarity. Hydrogen bonds shown in light blue.

Each of the N-H moieties of the imidazole rings are participating in hydrogen bond interactions with the oxygen atoms of the trilflate anions. These hydrogen bonds range in length from 1.879(1) to 2.110(2) Å and are summarized *Appendix Table 4.10.2.xxvi*. One triflate anion forms hydrogen bond interactions to three imidazole N-H moieties on three neighbouring helicates via the three oxygen atoms (*Figure 4.3.4.iii*). This hydrogen bond interaction occurs twice per helicate resulting in two side by side helicates being linked head-to-tail to form a linear hydrogen bond chain (*Figure 4.3.4.iv*). These linear hydrogen bond chains run approximately perpendicular to the crystallographic *b*-axis. The second mode of triflate hydrogen bond links just two neighbouring helicates in an off-set side-by-side manner (*Figure 4.3.4.v*). The triflate anion hydrogen bonds to two different imidazole N-H moieties via two oxygen atoms. This results in a zig-zag packing of neighbouring helicates in one-dimensional hydrogen bond chains parallel to the crystallographic *c*-axis. The final mode of triflate hydrogen bonding occurs between one oxygen atom of the triflate anion and an imidazole N-H moiety, with no formation of any hydrogen bond network. Complex **4.7** crystallized with a number of solvent molecules. However, the degree of disorder was much lower than observed for the other complexes in this chapter and therefore all the solvent molecules were able to be modeled. Crystallographically, the solvent content of **4.7** is 2.75 nitromethane solvent molecules. TGA was carried out on a filtered sample of the crystals that was allowed to stand under a nitrogen flow until a constant weight was achieved.

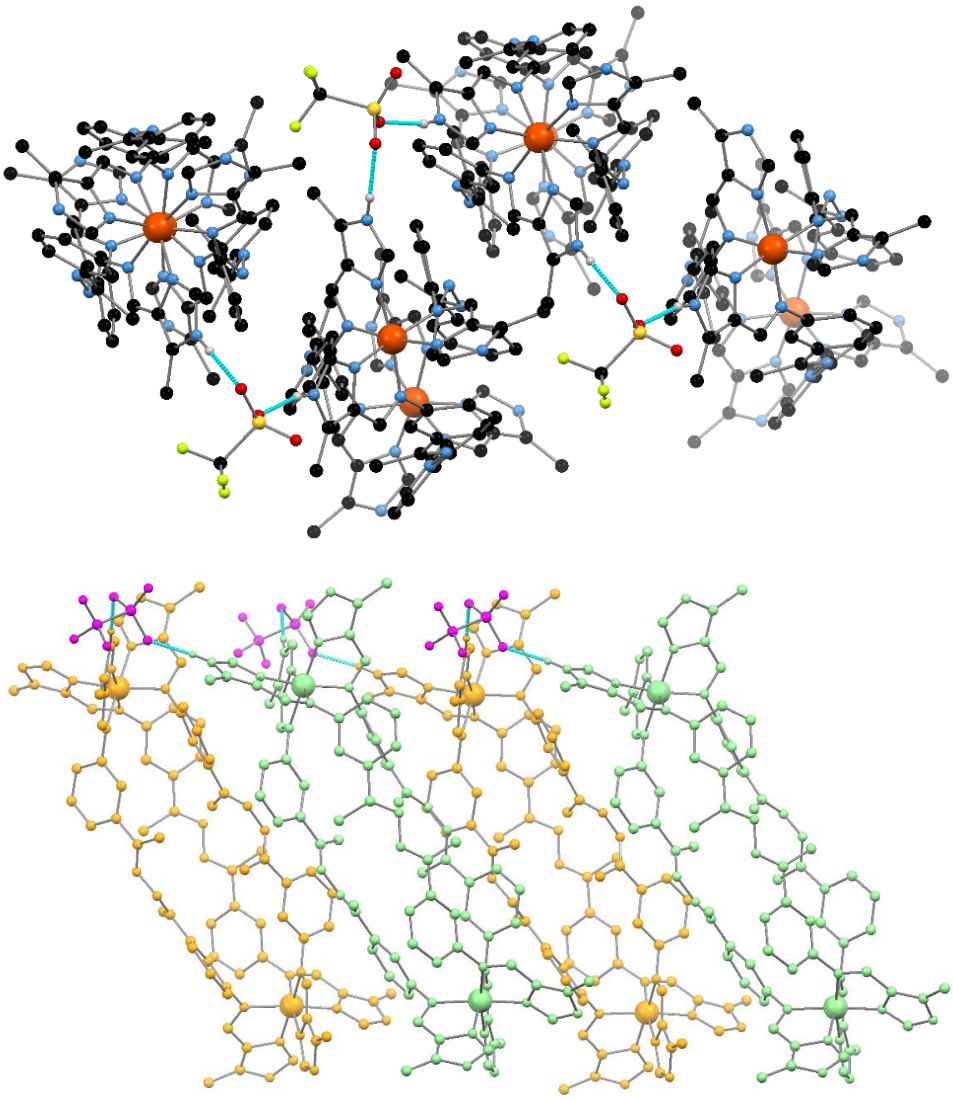

Figure 4.3.4.v: (top) The off-set packing induced by the second mode of triflate hydrogen bond as viewed down the crystallographic a-axis. (bottom) View down the crystallographic b-axis of the crystal packing. The triflate anions (purple) hydrogen bond to two helicates (green and orange). Hydrogen atoms and anions not participating in the illustrated interactions and solvent molecules omitted for clarity. The hydrogen bonds are shown in light blue.

Between 250 and 280 °C a mass loss of 4.14% occurs. This can be attributed to the loss of 1.5 nitromethane solvent molecules from **4.7**·1.5$MeNO_2$ (4.2%), therefore, 1.25 nitromethane molecules have already been lost. This was not unexpected as the crystals rapidly desolvate and lose crystallinity upon removal from the mother liquor. There is a rapid mass loss due to complex

decomposition above 280 °C. The elemental analysis shows the absence of nitromethane, further evidence to support the facile loss of nitromethane from the complex. The elemental analysis indicates that there is instead one water molecule, to give a formula **4.7**·H_2O. The replacement of the solvent molecules with water from the atmosphere is commonly observed for multinuclear supramolecular complexes.

4.3.5 $[Co_2(L4.3)_3](BF_4)_4$, 4.8

An analogous procedure to that of **4.6** was employed with Co(II) tetrafluoroborate used in the place of Fe(II) tetrafluoroborate. As with **4.6**, vapor diffusion of diethyl ether into the nitromethane solution of **4.8** gave yellow/orange block crystals suitable for single crystal X-ray diffraction. The diffraction data were collected at 120 K and solved and refined in the triclinic space group *P*-1 (R = 5.14%). The asymmetric unit contained two Co(II) centres bridged by three **L4.3** ligands (*Figure 4.3.5.i).* The charge balance was provided by four tetrafluoroborate anions. The unit cell parameters are near identical to **4.6** indicating the complex is isostructural (*Table 4.3.5.i*). The Co-N bond lengths indicate that both Co1 and Co2 are HS (*Appendix Table 4.10.2.vii*). For both Co1 and Co2 the Co-N_{imine} bond lengths are slightly longer than the Co-$N_{imidazole}$ bond lengths, the same trend observed for the Fe(II) analogue **4.6**.

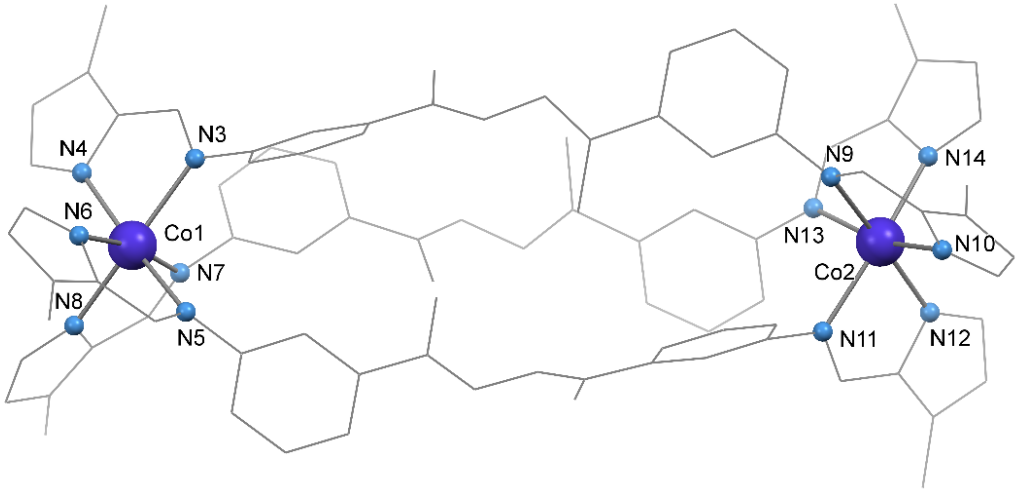

Figure 4.3.5.i: The asymmetric unit of ***4.7*** *with the two crystallographically unique Co(II) centres and coordinating nitrogen atoms labeled. Hydrogen atoms, solvent molecules and tetrafluoroborate anions omitted for clarity.*

The Co(II) centres exist in a distorted octahedral coordination environment with octahedral distortion parameters (Σ) of 86° and 84° for Co1 and Co2 respectively. The Co1···Co2 separation measures 15.1683(7) Å very similar to that of **4.6**. The phenyl rings are significantly twisted out of the plane of the coordinating imine (*Appendix Table 4.10.2.xii*) and this allows the phenyl rings to form C-H···π interactions with H···π(centroid) separations ranging from 2.923(1) to 3.178(1) Å. This stabilizes the twisted nature of the three ligands (*Appendix Table 4.10.2.xxii*). Much like **4.6**, the central N-N bond of the ligand retains its single bond character and there is a significant twist about the central hydrazone component (*Appendix Table 4.10.2.xvii*).

Unit cell parameter	**4.6**	**4.8**	**Percent difference**
a (Å)	14.0309(3)	13.9909(3)	-0.3%
b (Å)	16.0603(4)	16.2461(4)	+1.1%
c (Å)	24.1203(6)	24.2457(6)	+0.5%
cell volume (Å^3)	5216.51	5285.83	+1.3%

*Table 4.3.5.i: Comparison of unit cell dimensions for **4.6** and **4.8** indicating the isostructural nature of the two complexes.*

On one ligand, the central methyl groups are both orientated away from the intrahelical cavity. However, on the two remaining ligands one methyl group is orientated away and the other toward the intrahelical cavity, analogous to **4.6**. As **4.8** is isostructural with **4.6**, only a brief overview of the supramolecular interactions will be given. The methyl groups orientated away from the intra helical cavity participate in two alternating C-H···π interactions of 2.993(1) and 3.208(1) Å. Non-classical hydrogen bonds form between the imine hydrogen atoms and the nitrogen atoms of the hydrazone moiety with a separation H···N separation of 2.6342(2) Å. These alternate with non-classical hydrogen bonds between the methyl groups of the central component of the linker and the hydrazone moiety on a neighbouring helicate with a separation of 2.825(2) Å. This results in the formation of hydrogen bonded chains running parallel to the [110] crystallographic plane. The hydrogen bond interactions occurring between the imidazole N-H moties and the tetrafluoroborate anions are identical to those of **4.6** (*Figure 4.3.5.ii*) and a summarized in *Appendix Table 4.10.2.xxvii*. The complex crystallises with a large amount of disordered solvent. Despite attempts, not all of the nitromethane and diethyl ether molecules could be modeled satisfactorily and therefore the SQUEEZE[418] function of PLATON[419] was employed (1.2 Å probe).

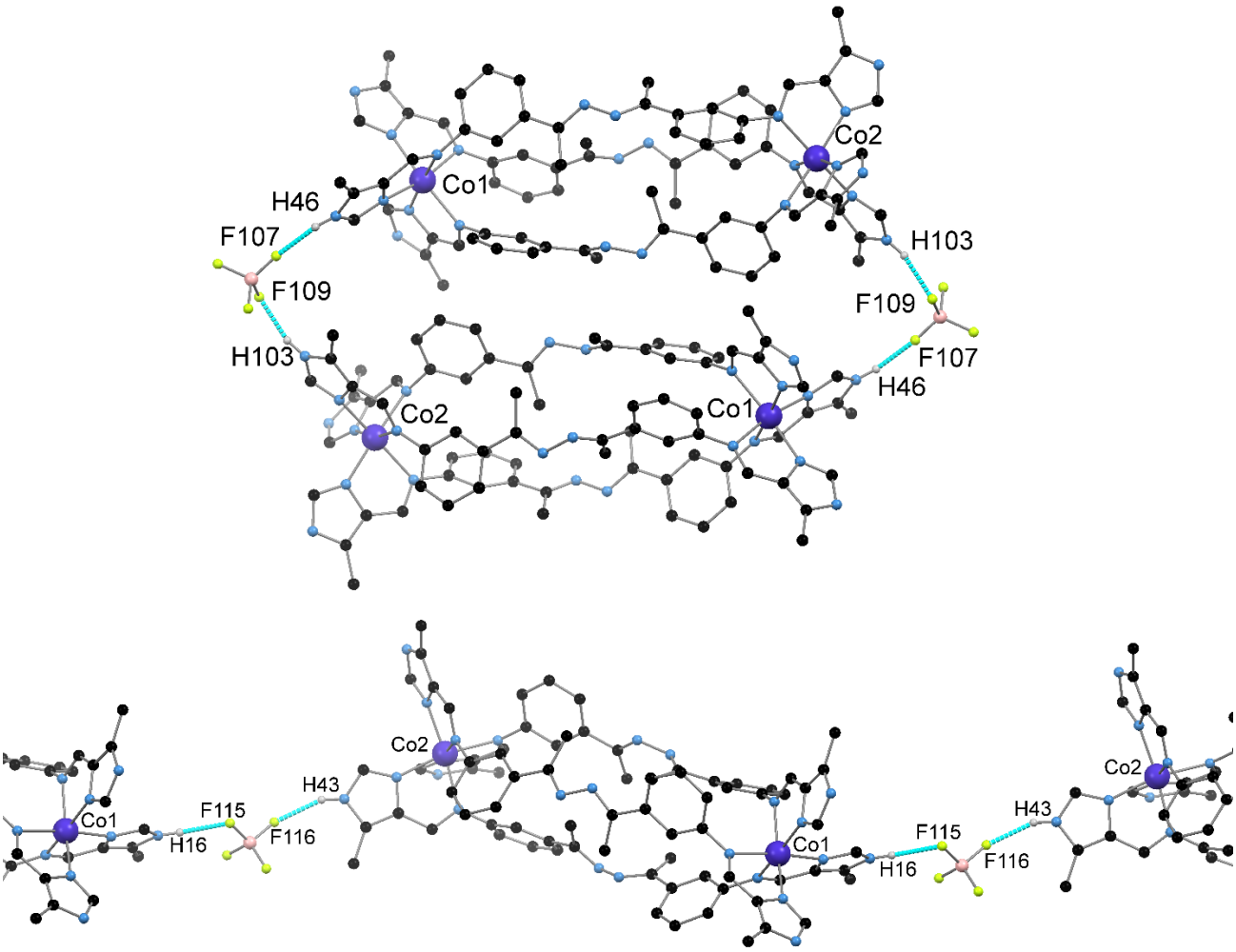

Figure 4.3.5.ii: The hydrogen bond interactions between the tetrafluoroborate anions and the N-H moieties of the imidazole rings with the crystallographically unique hydrogen bond donor and acceptor atoms labeled. (top) Two tetrafluoroborate anions bridge two helicates stacked upon one another at either end to form hydrogen bonded dimers. (bottom) The one-dimensional chains formed by bridging tetrafluoroborate anions. Hydrogen atoms not participating in the illustrated interaction, anions and solvent molecules omitted for clarity. The hydrogen bond interactions are shown in light blue.

This revealed a solvent accessible void of 487 $Å^3$ calculated to contain 119 electrons, corresponding to 60 electrons per helicate. This can be approximated as one diethyl ether and 0.5 nitromethane molecules (58 electrons). Therefore, along with the 5.5 molecules of nitromethane modeled crystallographically, the solvent content of the single crystal can be approximated as six nitromethane and one diethyl ether molecule. TGA was carried out on a filtered sample of the

crystals that was allowed to stand under a nitrogen flow for half an hour. Between 282 and 330 °C a mass loss of 18.3% occurs. This roughly corresponds to the loss of six nitromethane solvent molecules (16.8%) from **4.8**·6$MeNO_2$. This number of nitromethane solvent molecules is the same as approximated for the crystal structure. The loss of the diethyl ether solvent molecules is not observed as the highly volatile nature means they are lost upon standing the dry crystals at room temperature. It is not unexpected for the crystals to rapidly desolvate and lose crystallinity upon removal from the mother liquor. There is a rapid mass loss above 330 °C due to complex decomposition. For elemental analysis, the crystals were dried to constant weight under vacuum. This gave results corresponding to a molecular formula of **4.8**·4.8H_2O. The replacement of the solvent molecules with water molecules is commonly observed for multinuclear supramolecular complexes.

4.4 Magnetic susceptibility measurements

4.4.1 $[Fe_2(L4.2)_3](OTf)_4$, 4.4

As indicated by the SC-XRD experiments carried out on **4.4** at 120 and 240 K, it appears SCO at one Fe(II) centre occurs across this temperature range. Therefore, magnetic susceptibility measurements were carried out to investigate this further. Measurements were performed on a crystalline sample of **4.4** layered with a small amount of diisopropyl ether between 1.85 and 285 K with an applied field of 1000 Oe and a scan rate of 0.4 K min^{-1}. As the temperature is decreased from 285 K the χT value of 6.0 cm^3 K mol^{-1} begins to decrease immediately (*Figure 4.4.1.i*). A plateau is reached at 130 K with a χT value of 0.1 cm^3 K mol^{-1}, indicative of only 1% of the Fe(II) centres remaining in the HS state. This residual paramagnetism is most likely due to defects in the crystal resulting in HS Fe(II) centres or other paramagnetic impurities. The data were fitted to the ideal solution model, however, the HS χT value was fixed at 6.9 cm^3 K mol^{-1} (based on the results of the dried complex as discussed below) due to the incomplete nature of the SCO at high temperature. Fitting to the ideal solution model gave a $T_{1/2}$ of 232 K, an ΔS of 76 J K^{-1} mol^{-1} and an ΔH of 17.7 kJ mol^{-1}. The ΔS and ΔH values reported for the tetrafluoroborate analogue reported by Kruger and co-workers are 39 J K^{-1} mol^{-1} and 2.1 kJ mol^{-1} respectively, both of which are noticeably smaller. The $T_{1/2}$ for the previously reported complex however is almost 100 K lower at 148 K.

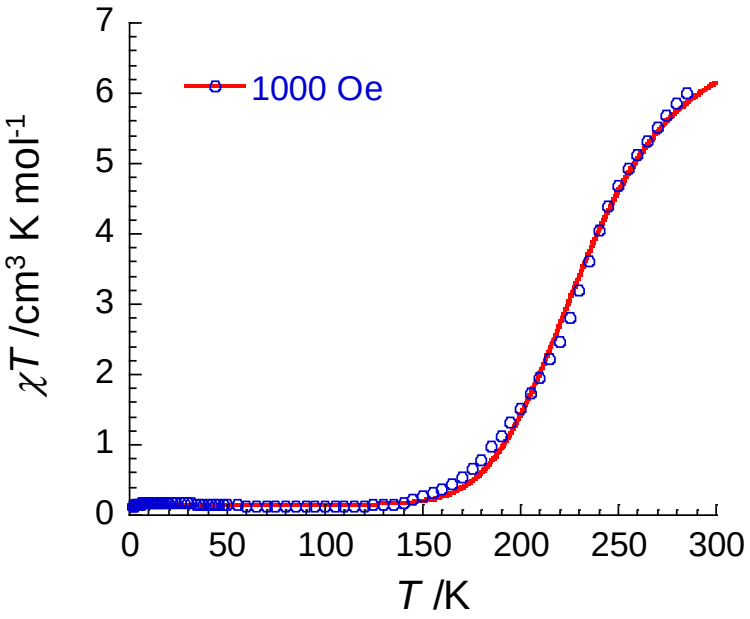

*Figure 4.4.1.i: The χT vs. T plot for **4.4** crystals layered with a small amount of mother liquor with an applied field of 1000 Oe and a scan rate of 0.4 K min^{-1}, measured between 1.85 and 285 K. The experimental data are shown in blue and the curve fit to the ideal solution is shown in red.*

The sample was then dried under vacuum at 50 °C in an attempt to remove all the volatile solvent molecules. The magnetic susceptibility of the complex was then remeasured while heating from 1.85 to 300 K (red) followed by cooling from 300 to 1.85 K (blue) (*Figure 4.4.1.ii*). Upon heating from 1.85 K the χT rapidly increases from 0.12 cm^3 K mol^{-1} to 0.36 cm^3 K mol^{-1} due to zero field splitting (ZFS) and second order Zeeman effects. The χT value is then constant until 90 K at which point it begins to gradually increase with a subtle point of inflection at 190 K, indicative of a multi-step process (*Figure 4.4.1.ii*). A clear maximum in the $d\chi T/dT$ *vs. T* plot occurs at 140 K, which is the $T_{1/2}$ for the first step of the SCO. The $T_{1/2}$ for the second step of the SCO cannot be elucidated from this plot as the SCO is incomplete at 300 K. The heating to 300 K appears to have resulted in further desolvation of the complex as the cooling cycle follows a different path. The first derivative of the cooling cycle clearly shows two maxima at 145 and 258 K, indicative of a more pronounced two-step SCO. The two aforementioned temperatures represent the $T_{1/2}$ values for the two parts of the multi-step process. The point of inflection for the cooling process occurs at 191 K

for which the χT value is 3.3 cm^3 K mol^{-1}, a reasonable value for half of the Fe(II) centres undergoing SCO to the LS state *(Figure 4.4.1.ii)*.

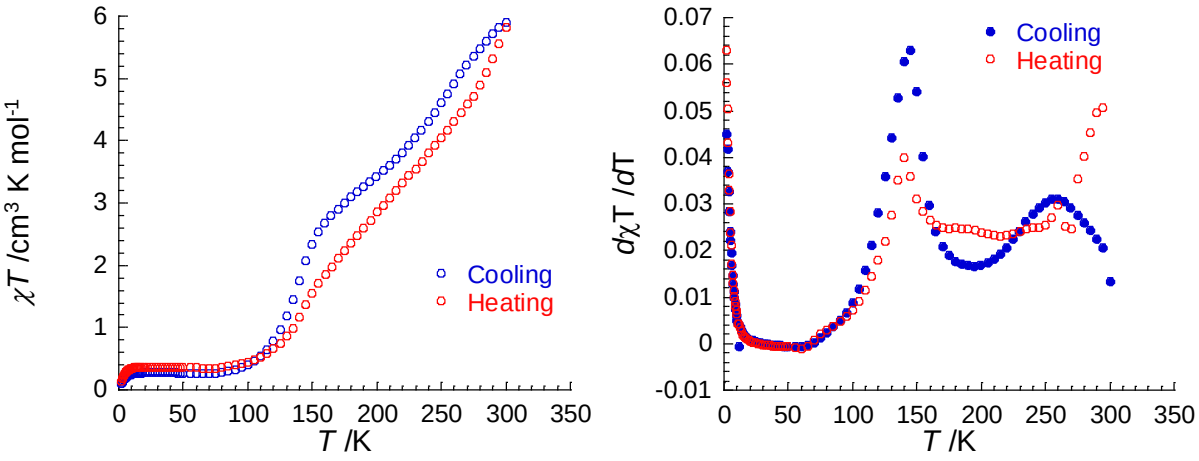

*Figure 4.4.1.ii: (left) The χT vs. T plot for **4.4** after heating the sample under vacuum at 50 °C. The sample is heated from 1.85 to 300 K (red open circles) followed by cooling from 300 K to 1.85 K (blue open circles). (right) The second derivative χT vs T plot for **4.4** between 1.85 and 300 K for the heating (red open circles) and cooling (blue filled circles) cycles. Measurements carried out with an applied field of 10000 Oe and a scan rate of 0.4 K min^{-1}.*

This two-stepped SCO is reversible, as while heating the sample to 400 K, the magnetic susceptibility followed the same path as the cooling from 300 K (*Figure 4.4.1.iii*). The χT value continues to increase as the temperature is increased above 300 K. A plateau is reached at 385 K with a χT value of 6.8 cm^3 K mol^{-1}, which is constant to 400 K and corresponds to two HS Fe(II) centres (g = 2.13). However, when cooling from 400 K, the magnetic susceptibility follows a significantly different path. The decrease in the χT value upon cooling from 400 K is initially a little more abrupt than the heating trace. However, at 226 K, when the χT value is 4.0 cm^3 K mol^{-1}, the decrease in the χT value becomes much more gradual. A plateau is reached at 68 K with a χT value of 2.5 cm^3 mol^{-1} that is approximately constant until 26 K. Below 26 K it rapidly drops to 0.86 cm^3 K mol^{-1} at 1.85 K due to ZFS and second order Zeeman effects. This significantly different trace may be due to two factors. Upon heating to 400 K in the low-pressure dry helium atmosphere of the SQUID the completely desolvated complex is formed. One possibility is that the completely desolvated complex adopts a structure such that only one centre is undergoing SCO while the other Fe(II) centre remains HS. However, the χT value of 2.5 cm^3 K mol^{-1} at low

temperatures is significantly lower than expected for half of the Fe(II) centres to be in the HS state (37% HS for g = 2.13). An alternative explanation is that the formation of the completely desolvated complex introduces a number of defects into the bulk sample of **4.4** resulting in 37% of the Fe(II) centres remaining in the HS state.

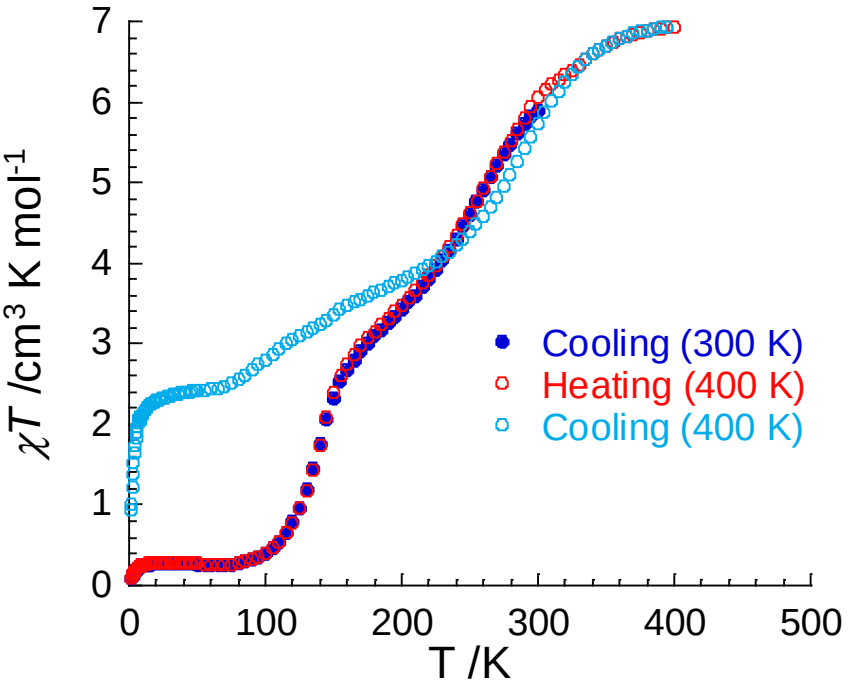

*Figure 4.4.1.iii: The χT vs. T plot for **4.4** between 1.85 and 400 K. The cooling cycle from 300 K (filled blue circles) is the same data shown in figure 4.4.1.ii. The sample is then heated from 1.85 to 400 K (red open circles) followed by cooling from 400 K back to 1.85 K (light blue open circles).*

4.4.2 $[Fe_2(L4.2)_3](OTf)_4$, 4.5

The change in crystallization conditions for **4.5** resulted in a different crystal morphology, space group and crystal packing compared to **4.4**. Therefore, it is likely that it will exhibit different SCO behavior. Magnetic susceptibility measurements were performed on a crystalline sample of **4.5** layered with a small amount of chloroform between 1.85 and 266 K with an applied field of 1000 Oe and a scan rate of 0.4 K min^{-1} (*Figure 4.4.2.i*). As the temperature is decreased from 265 K the χT value of 6.95 cm^3 K mol^{-1} is constant until 245 K after which it begins to decrease gradually. A plateau is reached at 77 K with a χT value of 1.5 cm^3 K mol^{-1}, indicative of approximately 20%

of the Fe(II) centres remaining in the HS state. At 26 K the χT value begins to rapidly decrease until it reaches a value of 0.5 cm^3 K mol^{-1} at 1.85 K due to ZFS and second order Zeeman effects. Fitting of the data to the ideal solution model was attempted however, the fit is relatively poor with the start of the SCO being more gradual and the end of the SCO being more abrupt than predicted by the model. The relatively rigid nature of the ligand may impose a degree of negative cooperativity which results in the SCO occurring more gradually than predicted by the ideal solution model. The effect of cooperativity can be quantified by the Γ parameter in the Slichter–Drickamer model,[225] with materials featuring negative cooperativity exhibiting $\Gamma < 0$.[449] In qualitative terms, this results in the SCO at the first Fe(II) centre from LS to HS stabalising the LS state for the second Fe(II) centre in a dinculear compound.[318, 450] The negative cooperativity observed for **4.5** is likely a consequence of the different crystal packing as this is not observed for complex **4.4** which contains an identical ligand. The values of the χT_{HS} and χT_{LS} need to be fixed to 1.57 and 7 cm^3 K mol^{-1} respectively, otherwise the fitting resulted in unrealistic values. This fitting gave a $T_{1/2}$ value of 161 K, an ΔS value of 60.1 J K^{-1} mol^{-1} and an ΔH value of 9.6 kJ mol^{-1}. The $T_{1/2}$ value returned by the data fitting is lower than that indicated by first derivative the χT *vs. T* plot which has a maximum at 179 K (*Figure 4.4.2.i*). The poor fit of the data to the model accounts for this discrepancy.

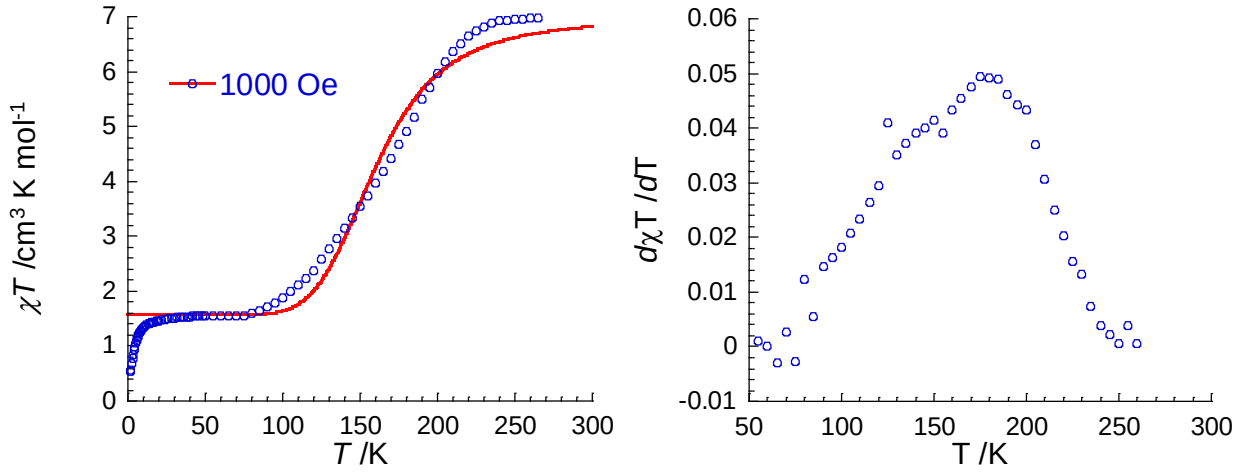

Figure 4.4.2.i: (left) The χT vs T plot for ***4.5*** *crystals layered with a small amount of chloroform between 1.85 and 266 K with an applied field of 1000 Oe and a scan rate of 0.4 K* min^{-1}*. The experimental data is shown in blue while the curve fit to the ideal solution model is shown in red.*

*(right) The first derivative (dχT/dT) vs T plot for **4.5** with a maximum at 179 K indicating the $T_{1/2}$ of the SCO.*

The sample of **4.5** was then dried under vacuum at 50 °C in an attempt to remove all the volatile solvent molecules. The magnetic susceptibility of the complex was then remeasured, between 1.85 to 400 K with an applied field of 10000 Oe and a scan rate of 0.4 K min^{-1} (*Figure 4.4.2.ii*). The initial χT value increases abruptly from 0.38 to 1.2 cm^3 K mol^{-1} at 30 K due to ZFS and second order Zeeman effects, after which a plateau is reached. At 75 K the χT value then begins to increase, at first very gradually, until it reaches a value of 6.95 cm^3 K mol^{-1} at 368 K after which it is constant. The sample was then cooled from 400 K back to 1.85 K. The plateau at high temperature is retained for longer with the decrease in the χT value starting at 350 K. This results in a SCO process which is slightly more gradual than for the initial heating cycle. A plateau at low temperature is reach at 72 K with a χT value of 1.55 cm^3 K mol^{-1}. The χT value is then constant until 23 K after which it begins to rapidly decrease due to ZFS and second order Zeeman effects at 1.85 K to a value of 1.4 cm^{-3} K mol^{-1}. The sample was then heated for a second time from 1.85 K to 400 K and the behavior mirrored that of the cooling cycle.

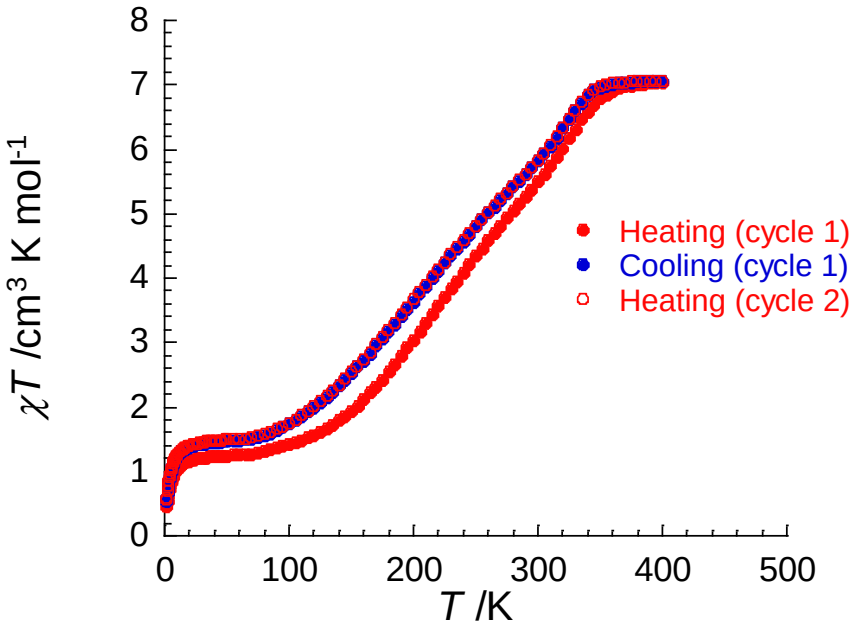

*Figure 4.4.2.ii: χT vs T plot for **4.5** after drying under vacuum at 50 °C. The sample was first heated from 1.85 to 400 K (filled red circles). It was then cooled back to 1.85 K (filled blue circles), following a different trace to the original heating cycle. The sample was heated for a*

second cycle to 400 K (open red circles) resulting in reproducible SCO behavior. Measurements were carried out with an applied field of 10000 Oe and a scan rate of 0.4 K min^{-1}.

The difference between the first heating cycle and the second is due to the loss of residual solvent at elevated temperature in the SQUID. The low-pressure dry helium atmosphere appears to be particularly effective at removing the residual solvent from the complex. The change is not as significant as observed for the previously discussed complex **4.4**.

4.4.3 $[Fe_2(L4.3)_3](BF_4)_4$, 4.6

The variable temperature SC-XRD experiments for **4.6** at 120 and 240 K were strongly indicative of SCO. Therefore, magnetic susceptibility measurements were undertaken to elucidate the full extent of the SCO. Measurements were performed on a crystalline sample of **4.6** layered with a small amount of diethyl ether between 1.85 and 255 K with an applied field of 1000 Oe and a scan rate of 0.4 K min^{-1}(*Figure 4.4.3.i*). The χT value at 255 K is 4.3 cm^3 K mol^{-1}, indicative of a significant proportion of Fe(II) centres existing in the HS state. The χT value immediately decreases in a gradual fashion, evidence that the SCO is incomplete by 255 K. As the crystals were highly susceptible to desolvation, higher temperatures were not accessible. A plateau is reached at 86 K with a χT value of 0.44 cm^3 K mol^{-1}.

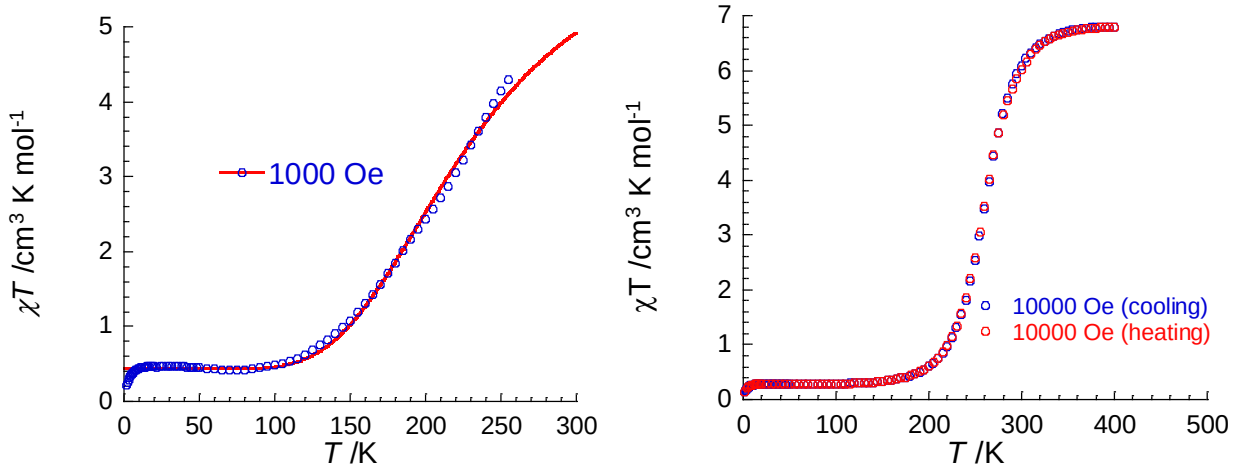

*Figure 4.4.3.i: (left) χT vs. T plot for **4.6** crystals layered with a small amount of diethyl ether between 1.85 and 255 K with an applied field of 1000 Oe and a scan rate of 0.4 K min^{-1}. The experimental data are shown in blue while the curve fit to the ideal solution model is shown in red. (right) The χT vs. T plot for **4.6** after drying at 50 °C under vacuum. The sample was cooled*

from 400 to 1.85 K (blue open circles) followed by heating back to 400 K (red open circles), revealing reproducible SCO behavior. Measurements were carried out with an applied field of 10000 Oe and a scan rate of 0.4 K min^{-1}.

This is representative of a small proportion of the Fe(II) centres remaining in the HS state due to defects in the crystal or paramagnetic impurities. The rapid decrease in the χT value at 12 K to 0.2 cm^3 K mol^{-1} is due to ZFS and second order Zeeman effects. Fitting of the data to the ideal solution model was attempted. As the SCO is incomplete at 255 K, χT_{HS} value was fixed at 6.9 cm K mol^{-1} (based on the results of the dried complex as discussed below) in order for the fitting to return reasonable values. The fitting gave a $T_{1/2}$ of 238 K, an ΔS of 32.8 J K^{-1} mol^{-1} and an ΔH of 7.8 kJ mol^{-1}. The fit begins to deviate from the data at higher temperatures. The sample of **4.6** was then dried under vacuum at 50 °C to remove the volatile solvent molecules. The magnetic susceptibility of the complex was then remeasured between 400 and 1.85 K with an applied field of 10000 Oe and a scan rate of 0.4 K min^{-1}. The χT value at 400 K is 6.81 cm^3 K mol^{-1}, which corresponds to two HS Fe(II) centres (g = 2.13). At 380 K the χT value gradually decreases until a plateau at 150 K with a χT value of 0.35 cm^3 K mol^{-1}. This is indicative of a small proportion of the Fe(II) centres (*ca*. 5%) remaining in the HS state at low temperatures due to defects in the sample of paramagnetic impurities. The χT value remains constant until 13 K at which point it then decreases to 0.12 cm^3 K mol^{-1} at 1.85 K due to ZFS and second order Zeeman effects. The behavior when the complex is warmed to 400 K from 1.85 K is identical to the cooling cycle, showing no hysteresis (*Figure 4.4.3.ii*).

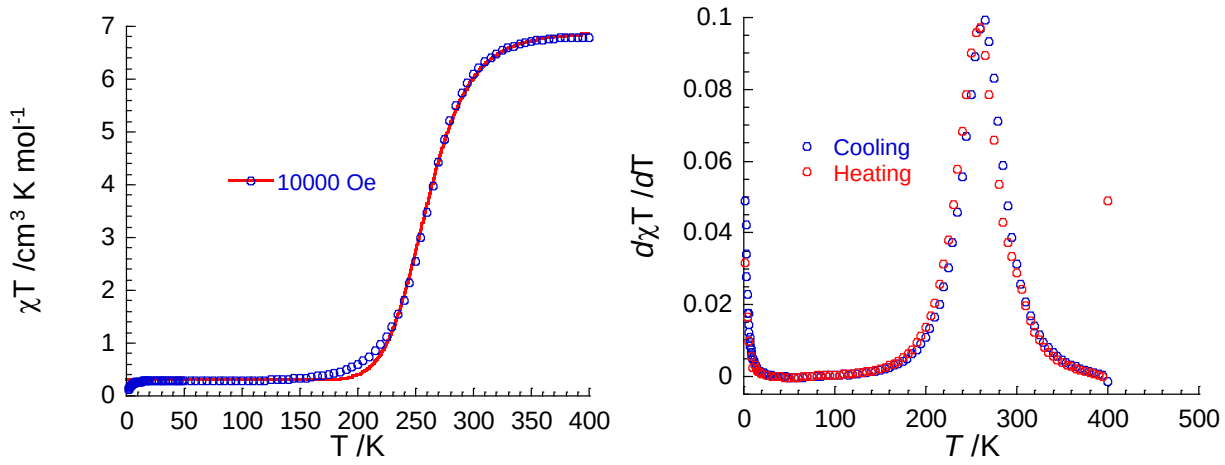

Figure 4.4.3.ii: (left) χT vs T plot for ***4.6*** *for the cooling of the dried sample from 400 to 1.85 K (blue open circles) fitted to the ideal solution model (red line). (right) the first derivative for the χT vs T plot for* ***4.6*** *for the cooling (blue open circles) and heating (red open circles) cycles.*

The first derivative of the heating and cooling cycles is further evidence for the lack of hysteresis as the maxima for the heating and cooling cycles occur at the same temperature (*Figure 4.4.3.ii*). The $T_{1/2}$ for the SCO, obtained from the maxima of the first derivative is 261 K. As the heating and cooling data were virtually identical, just the cooling data were fitted to the ideal solution model (*Figure 4.4.3.ii*). The fit is generally acceptable at most temperatures except between 150 and 230 K at the start of the SCO. This fitting gave a $T_{1/2}$ of 260 K, very similar to that obtained from the first derivative and an ΔS of 115.7 J K^{-1} mol^{-1} and an ΔH of 30.1 kJ mol^{-1}.

4.4.4 $[Fe_2(L4.3)_3](OTf)_4$, 4.7

The changes in the colour of the crystal of **4.7** upon cooling from room temperature to 120 K for the SC-XRD experiment demonstrates that, at least a partial, SCO process is occurring. Therefore, magnetic susceptibility measurements were performed on a crystalline sample of **4.7** layered with a small amount of diethyl ether between 1.85 and 280 K with an applied field of 1000 Oe (*Figure 4.4.4.i*).

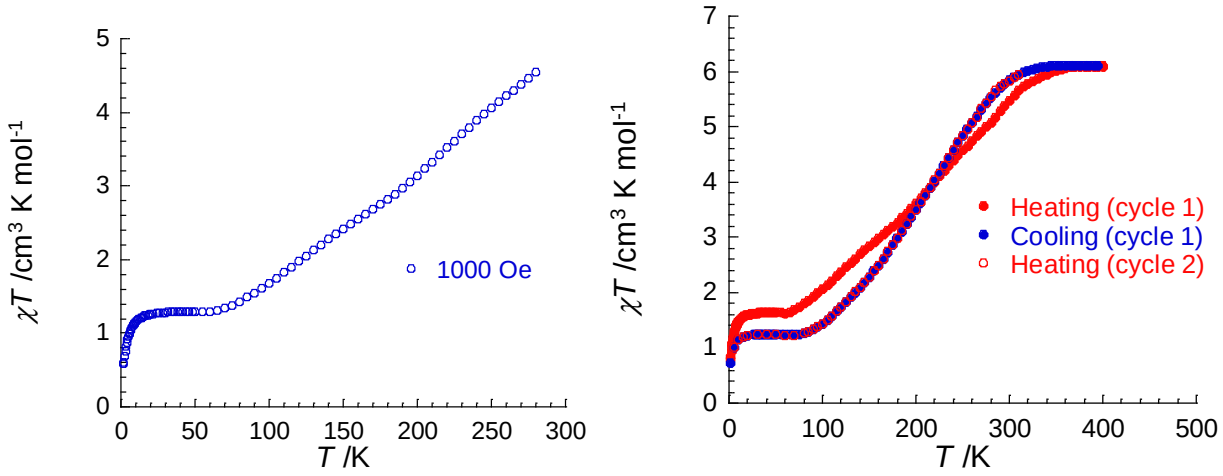

*Figure 4.4.4.i: (right) The χT vs. T plot for **4.7** crystals layered with a small amount of mother liquor measured between 1.85 and 200 K with an applied field of 1000 Oe and a scan rate of 0.4 K min^{-1}. (right) χT vs. T plot for **4.7** after drying at 50 °C under vacuum. The sample was first heated from 1.85 to 400 K (filled red circles) followed by cooling back to 1.85 K (filled blue circles) which follows a more abrupt path. The sample was then heated for a second cycle to 300 K to verify that the SCO behavior was now reproducible. Measurements were carried out with an applied field of 10000 Oe and a scan rate of 0.4 K min^{-1}.*

The χT value at 280 K is 4.5 cm^3 K mol^{-1} and immediately begins to decrease gradually as the temperature is decreased. A plateau is reached at 60 K with a χT value of 1.27 cm^3 K mol^{-1}. This is indicative of approximately 20% of the Fe(II) centres remaining in the HS state. As the temperature is decreased below 18 K, the χT value rapidly decreases to 0.56 cm^3 K mol^{-1} at 1.85 K due to ZFS and second order Zeeman effects. Fitting of the data to the ideal solution model was attempted, however, a sensible fit could not be obtained. The sample was then dried under vacuum at 50 °C in an attempt to remove all the volatile solvent molecules. The magnetic susceptibility of the complex was then remeasured between 400 and 1.85 K with an applied field of 10000 Oe. The sample was first heated from 1.85 K to 400 K (*Figure 4.4.4.i*). The χT value rapidly increased from 0.82 cm^3 K mol^{-1} at 1.85 K to 1.64 cm^3 K mol^{-1} due to ZFS and second order Zeeman effects. The χT value is then constant until 60 K at which point there is an abrupt change in the gradient of the χT *vs.* *T* curve. The abrupt change in the gradient is unusual for SCO as it is a thermal equilibrium process and therefore a smooth curve is expected. The abrupt change may be due to the conjunction of the SCO with some form of first order phase transition. The χT value gradually increases until

350 K at which a plateau at 6.02 cm^3 K mol^{-1} is reached and the χT value is constant until 400 K. The sample is then cooled from 400 K, resulting in the χT value decreasing at 330 K and following a different curve to the initial heating cycle. A plateau is reached at 80 K with a χT value of 1.24 cm^3 K mol^{-1}, lower than the plateau for the initial heating cycle. The rapid decrease in the χT value at 19 K to 0.73 at 1.85 K is due to ZFS and second order Zeeman effects. The sample was then heated from 1.85 in a second heating cycle. The χT value follows the same curve as the cooling cycle to 300 K. The difference between the heating and cooling curves of the first cycle is due to the loss of residual solvent from the complex. This is envisioned to alter the crystal packing and therefore the SCO behavior. In the case of **4.7**, the removal of residual solvent results in more abrupt SCO.

4.4.5 $[Co_2(L4.3)_3](BF_4)_4$, 4.8

Previous work by the Kruger group has shown that octahedral Co(II) centres coordinated to bidentate pyridylimine ligands can display SMM behaviour.[448] It has been reported in the literature that increasing the distortion about the coordination sphere can improve the SMM behaviour.[385-386, 393] The weaker field imidazolylimine ligands result in more distorted coordination spheres about Co(II) centres than pyridylimine ligands. Therefore, is was envisioned that the imidazolylimine ligands would result in Co(II) complexes with better SMM characteristics. Magnetic measurements were performed on a crystalline sample of **4.8** for both the sample layer with a small amount of diethyl ether and subsequently dried. Both sets of data were similar, so AC magnetic susceptibility experiments were performed on the dried sample only. The χT value at 250 K with an applied field of 10000 Oe indicates that there is an observable orbital contribution from the Co(II) centres to the magnetic moment. At 6.3 cm^3 K mol^{-1} it is significantly higher than that expected for two isolated Co(II) S = 3/2 centres; 3.8 cm^3 K mol^{-1} (*Figure 4.4.5.i*). The gradual decrease of the χT value suggests the presence of depopulation of low-lying excited states, which can be from ZFS or magnetic interactions between the Co(II) centres. The smallest Co⋯Co separation in the crystal structure is 9.8038(6) Å and therefore negligible magnetic coupling between the Co(II) centres is to be expected.

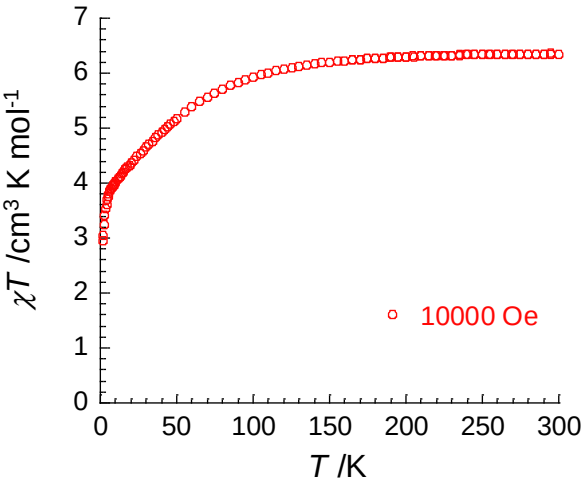

*Figure 4.4.5.i: The χT vs. T plot for the dried sample of **4.8** between 1.85 and 300 K with an applied filed of 10000 Oe and a scan rate of 0.4 K min^{-1}.*

The isothermal DC field (H) dependence of the magnetization (M) between 0 and 7 T at temperatures of 1.85, 3, 5 and 8 K was measured. At 1.85 and 3 K, saturation is reached at 7 T, with a measured magnetisation of 5.2 $N_A\mu_B$, significantly higher than the theoretical saturation of magnetisation for an S = 3/2 spin-only system (g = 2.0). This is indicative of the system possessing a high degree of anisotropy (*Figure 4.4.5.ii*). The non-superimposed *M vs. H T*$^{-1}$ curves are further evidence for the presence of anisotropy at low temperatures (*Figure 4.4.5.ii*).

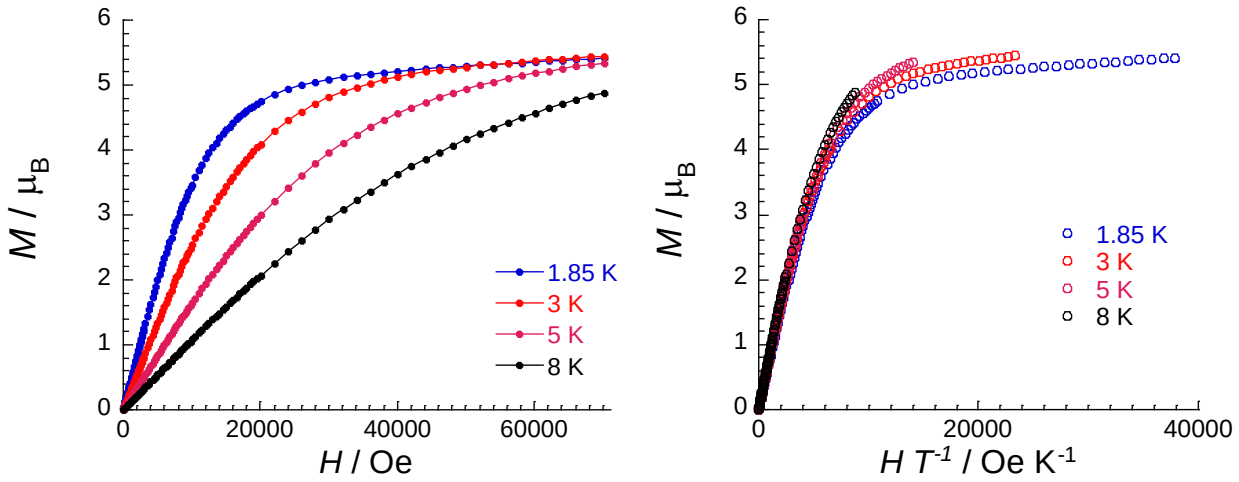

*Figure 4.4.5.ii: (left) The M vs. H plot and (right) M vs. H T^{-1} plot at 1.85 k (blue), 3 K (red), 5 K (purple) and 8 K (black) for **4.8**.*

4.5 AC Magnetic susceptibility measurements

4.5.1 $[Co_2(L4.3)_3](BF_4)_4$, 4.8

AC magnetic susceptibility measurements were performed on the dried sample to probe the magnetization dynamics and investigate the occurrence of any SMM behaviour for **4.8**. In the absence of an applied DC field at 2 K, the AC data exhibits a frequency independent in-phase magnetic susceptibility (χ') up to 10 kHz and exhibits no out-of-phase magnetic susceptibility (χ″). The application of a DC field results in the emergence of an out-of-phase component that displays both frequency and temperature dependence. Therefore, complex **4.8** displays slow relaxation of the magnetic moment and can be regarded as an SMM. The application of the external DC field is required to supress the otherwise rapid QTM mode of relaxation. The out-of-phase signal can first be detected at approximately 30 Hz under an applied field of 200 Oe at 2 K (*Figure 4.5.1.i*). The field dependence of the χ' and χ'' can be fitted to the generalised Debye model. As the applied field is increased from 0 Oe the frequency of relaxation decreases from 1380 Hz to a minima of 270 Hz at an applied field of 760 Oe. The frequency then rises as the applied field is increased to 70000 Oe. At low fields (1000 Oe), the α coefficient is relatively small ($\alpha \approx 0.1$) which indicates a small distribution of relaxation times, evidence that that the relaxation mode is dominated by a single process. However, the α coefficient at high fields becomes relatively large, indicative of a wide distribution of the relaxation times and therefore multiple relaxation processes occurring (*Figure 4.5.1.i*).

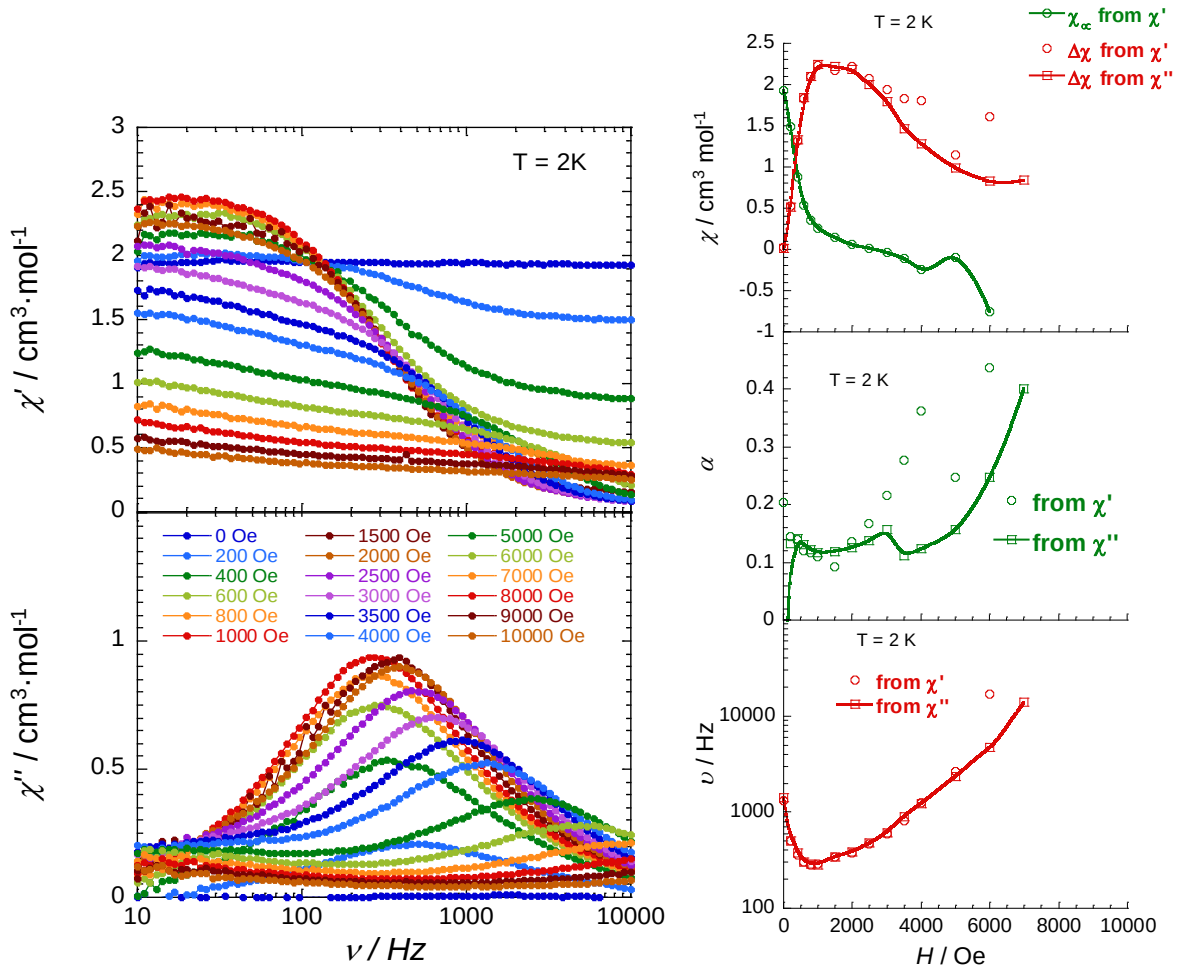

Figure 4.5.1.i: (left) The frequency dependence of the χ' (top) and the χ'' (bottom) components of the AC magnetic susceptibility at 2 K for applied DC fields between 0 and 10000 Oe for ***4.8****. The experimental data is represented by the circles while lines are to guide the eye. (right) The field dependence of the Δχ (top), α coefficient (middle) and ν (bottom). The Δχ is often referred to in the literature as χ_0-χ_∞ which represents the amplitude of the relaxation mode where χ_0 and χ_∞ are the AC susceptibilities at the zero and infinite AC limits, respectively. The α coefficient refers to the distribution of the relaxation times while ν refers to the characteristic AC frequency. Open circles and squares represent experimental data while lines are simply to guide the eye.*

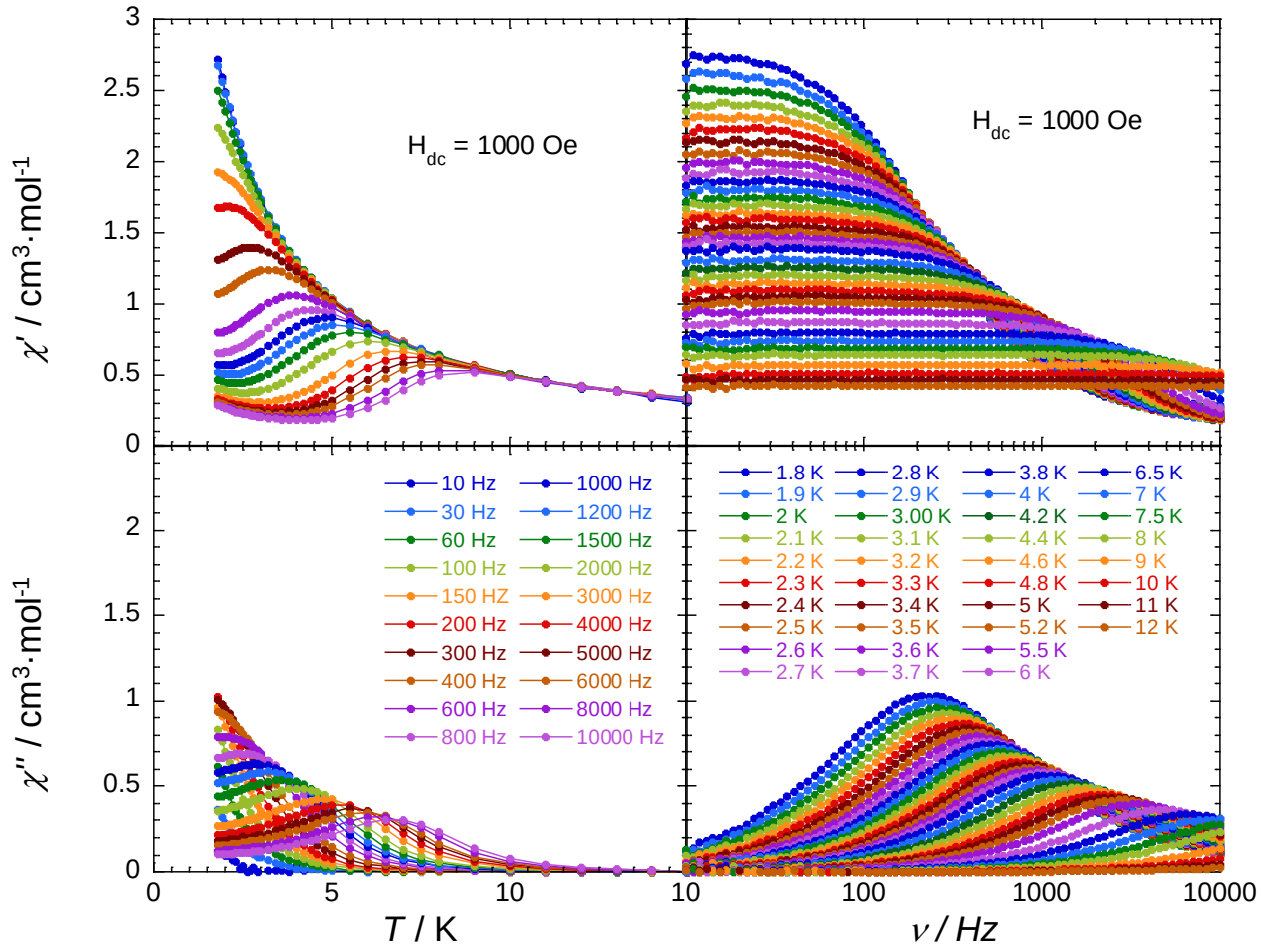

*Figure 4.5.1.ii: (left) The temperature dependence of the χ' (top) and χ'' (bottom) components of the AC susceptibility with an applied DC field of 1000 Oe measured between frequencies of 10 Hz and 10 kHz for **4.8**. The solid lines are guides for the eyes and do not represent fitting of the data. (right) The frequency dependence of the χ' (top) and χ'' (bottom) components of the AC susceptibility with an applied field of 1000 Oe measured at a range of temperatures between 1.8 and 12 K. Lines are to guide the eye.*

Due to this increase in the number of relaxation processes occurring at higher fields, the temperature and frequency dependence of the AC magnetic susceptibility were studied at 1000 Oe. The relaxation processes for both χ' and χ'' exhibit frequency and temperature dependence (*Figure 4.5.1.ii*). The frequency dependent χ'' reaches a local maximum of 6.51 cm^3 mol^{-1} at 6.5 K with the highest measured frequency of 10000 Hz. This maximum then shifts to higher values as both the temperature and frequency are decreased. The χ' below 20 Hz is 2.7 cm^3 mol^{-1} and upon

the increase of the frequency, χ' decays until a plateau is reached at 4000 Hz with a χ' of 0.2 cm^3 mol^{-1}. This is indicative of approximately only 7% of the Co(II) ions retaining their magnetisation and therefore there is no significant relaxation processes occurring at higher frequencies. By fitting the frequency dependant data of the χ' and χ'' to the generalised Debye model the relaxation time (τ) at each temperature was extracted and plotted as $ln(\tau)$ *vs.* T^{-1}.

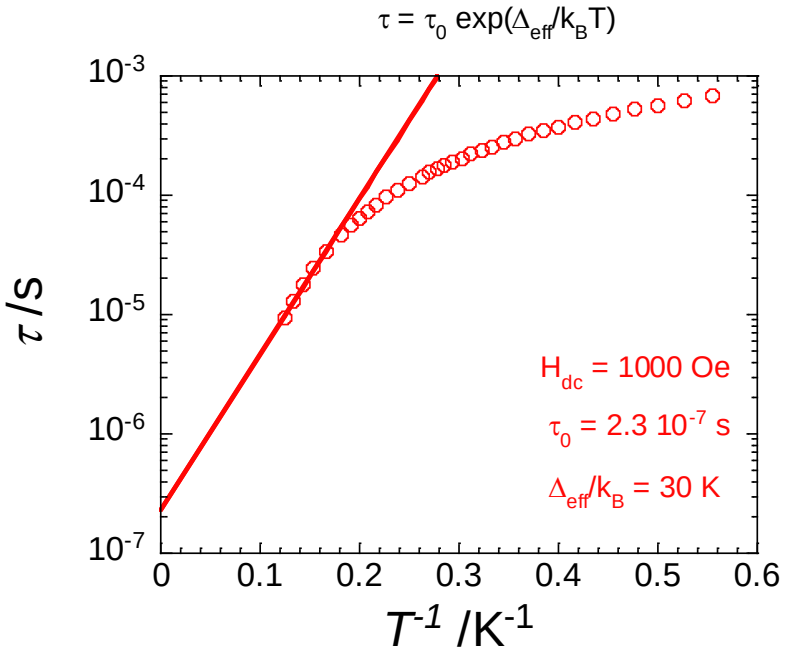

Figure 4.5.1.iii: The ln(τ) vs. T^{-1} plot with the experimental data represented by the red circles and the fitting of the high temperature data to the Arrhenius law represented by the red line. The low temperature data deviates from linearity and are therefore not included in the fitting to the Arrhenius law. Relaxation times are obtained from the fitting of the χ'' component of the AC susceptibility to the generalized Debye model.

The temperature dependence of the relaxation time at higher temperatures could be estimated from the Arrhenius plot for a thermally activated Orbach relaxation process with a pre-exponential factor of τ_0 of 2.3× 10^{-7} s and an energy gap (U_{eff}) of 30 K (*Figure 4.5.1.iii*). However, the plot of $ln(\tau)$ vs. T^{-1} deviates from Arrhenius type behaviour at lower temperatures. This is indicative of other relaxation processes occurring such as quantum tunnelling, direct and/or Raman processes. The temperature dependence of α, ν and χ_0-χ_∞, as deduced from the Debye model, are given in *Appendix Figure 4.10.5.i* and *Appendix Figure 4.10.5.ii*.

4.6 Absolute reflectivity measurements

4.6.1 $[Fe_2(L4.2)_3](OTf)_4$, 4.4

Reflectivity measurements were performed on a freshly isolated sample of **4.4**. The first measurement was carried out under weak white light irradiation of 0.08 mW cm^{-2} with a scan rate of 4 K min^{-1}. Upon cooling from 270 to 10 K, the reflectivity signal between 700 and 1000 nm increased, typical of Fe(II) SCO from HS to LS, with an isosbestic point at 705 nm (Figure *4.6.1.i*). The return heating mode exhibits the same behavior but in reverse (*Appendix Figure 4.10.6.i*). The greatest change in the reflectivity signal is observed between 270 and 200 K while no change is observed between 10 and 100 K. To better visualize the SCO, the reflectivity at 870 nm (AR_{870}) was plotted verses the temperature *(Figure 4.6.1.i*). At 10 K the AR_{870} value is 0.28 and is constant until 155 K after which it begins to decrease to a value of 0.14 at 270 K. The cooling trace shows the reverse behavior indicating that the SCO is reversible (*Appendix Figure 4.10.6.ii*). As no plateau is reached by 270 K, the SCO process is incomplete. The second measurement was carried out to investigate the possibility of light-induced SCO behavior. The sample was cooled to 10 K and then irradiated with white light for three hours (0.08 mW cm^{-2}).

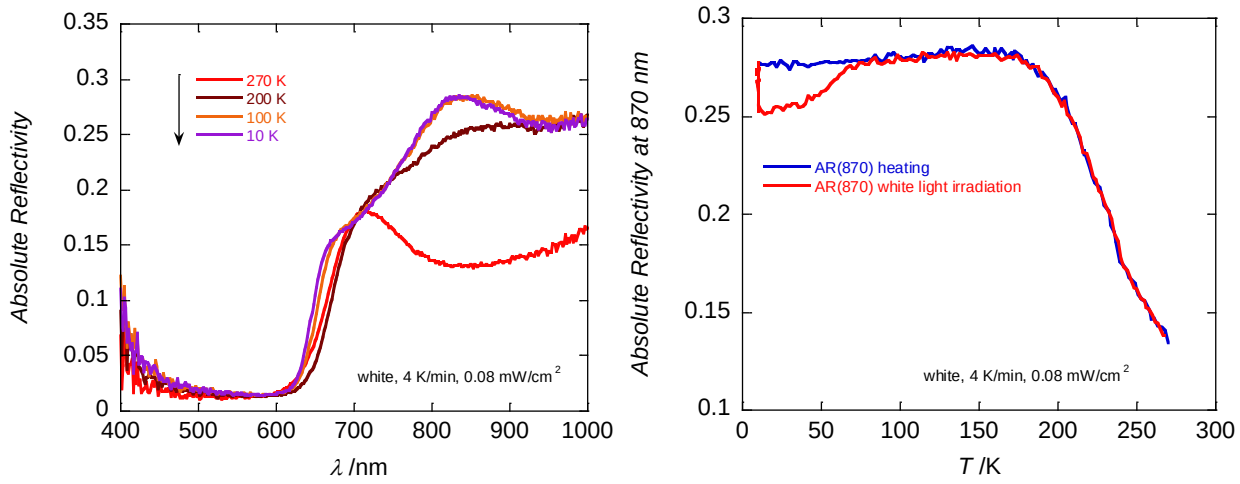

*Figure 4.6.1.i: (left) Selected surface reflectivity measurements of **4.4** collected with a white light spectroscopic source (0.08 mW cm^{-2}) as a function of the wavelength during cooling mode from 270 to 10 K. (right) The temperature dependence of the reflectivity signal at 870 nm for heating the sample (blue) and white light irradiation (0.08 mW cm^{-2}) at 10 K for three hours followed by heating (red).*

This white light irradiation resulted in a decrease in the AR_{870} from 0.28 to 0.25 (*Figure 4.6.1.i*). The sample was then heated to 270 K to probe the thermal relaxation of the HS state. At 25 K the AR_{870} begins to increase until 72 K at which point the initial AR_{870} value is recovered, indicating that complete thermal relaxation has occurred. As the sample is warmed above 155 K the AR_{870} begins to decrease due to thermally induced SCO following the same trace as the initial heating of the sample. The decrease in the AR_{870} value due to the light irradiation is significantly lower than when the sample is heated to 270 K. Therefore, the photo-induced SCO with white light is only a partial effect. In order to optimize the photo-excitation, 14 LED sources at wavelengths ranging from 365 to 1050 nm were trialed for increased efficiency at 10 K. This revealed the 625 nm LED proved to be the most efficient. Irradiation of the sample for 10 minutes at 10 K resulted in a decrease in the reflectivity between 700 and 1000 nm, such that the signal is similar in strength to that of the sample at 200 K (*Appendix Figure 4.10.6.iii*). The intensity of the light source has a significant effect on the proportion of the sample excited to the HS state with irradiation at 10 mW cm^{-2} showing significantly more excitation than 0.1 mW cm^{-2}. As with the white light irradiation experiments, heating of the sample resulted in thermal relaxation of the photo-induced HS state (*Figure 4.10.6.iv*). After irradiation with 625 nm light at 10 K, subsequent irradiation with 850 nm light resulted in partial photo de-excitation. This effect is completely reproducible over a number of cycles and demonstrates the sample shows both partial LIESST and partial reverse-LIESST effects. The magnitude of the de-excitation with 850 nm is significantly less than the initial photo-excitation with 625 nm light, meaning the reverse-LIESST effect is inefficient in comparison to the LIESST effect (*Appendix Figure 4.10.6.v*).

4.6.2 $[Fe_2(L4.2)_3](OTf)_4$, 4.5

Reflectivity measurements were performed on a freshly isolated sample of **4.5**. The first measurement was carried out under weak white light irradiation of 0.08 mW cm^{-2} with a scan rate of 4 K min^{-1}. Upon cooling from 270 to 10 K, the reflectivity signal between 700 and 1000 nm increases, typical of Fe(II) SCO from HS to LS, with an isosbestic point at 740 nm (*Figure 4.6.2.i*). The return heating mode exhibits the same behavior but in reverse (*Appendix Figure 4.10.6.vi*). The greatest change in the reflectivity signal is observed between 200 and 100 K while almost no change is observed between 10 and 100 K. To better visualize the SCO, the reflectivity at 870 nm (AR_{870}) was plotted verses the temperature (*Figure 4.6.2.i*). At 10 K the AR_{870} value is 0.46 and

is constant until 80 K after which it begins to decrease to a value of 0.29 at 230 K and thereafter remains constant. The cooling trace shows the reverse behavior indicating the SCO is reversible (*Appendix Figure 4.10.6.vii*). The plateau at high temperature indicates the SCO process is complete. The second measurement was carried out to investigate the possibility of light-induced SCO behavior. The sample was cooled to 10 K and then irradiated with white light for three hours (0.08 mW cm^{-2}). This white light irradiation resulted in a decrease in the AR_{870} from 0.46 to 0.35 (*Figure 4.6.2.i*). The sample was then heated to 270 K to probe the thermal relaxation of the HS state. At 36 K the AR_{870} begins to increase until 81 K at which point the initial AR_{870} value is recovered, indicating complete thermal relaxation has occurred. As the sample is warmed above 88 K the AR_{870} begins to decrease due to thermally induced SCO following the same trace as the initial heating of the sample. The decrease in the AR_{870} value due to white light irradiation is approximately half of that compared to heating the sample to 270 K. This indicates that that the photo-excitation with a weak white light source is relatively efficient compared to **4.4**.

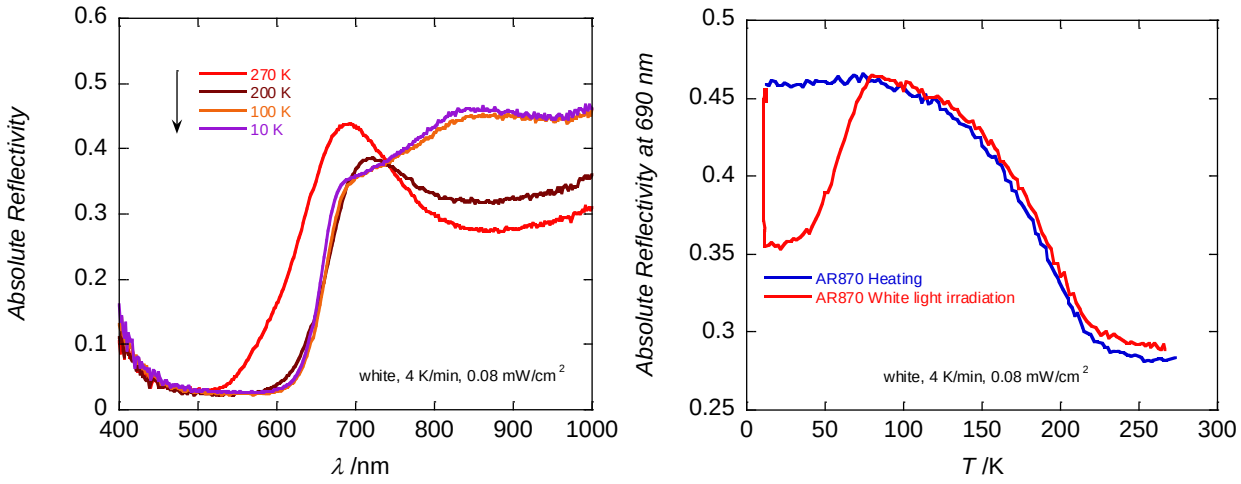

*Figure 4.6.2.i: Selected surface reflectivity measurements of **4.5** collected with a white light spectroscopic source (0.08 mW cm^{-2}) as a function of the wavelength during cooling mode from 270 to 10 K. (right) The temperature dependence of the reflectivity signal at 870 nm for heating the sample (blue) and white light irradiation (0.08 mW cm^{-2}) at 10 K for three hours followed by heating (red).*

In order to optimize the photo-excitation, 14 LED sources at wavelengths ranging from 365 to 1050 nm were trialed for increased efficiency at 10 K. This revealed the 625 nm LED proved to be the most efficient. Irradiation of the sample for 10 minutes at 10 K resulted in a decrease in the

reflectivity between 700 and 1000 nm such that the signal is slightly weaker in strength to that of the sample at 200 K (*Appendix Figure 4.10.6.viii*). The intensity of the light source has a significant effect on the proportion of the sample excited to the HS state with irradiation at 10 mW cm^{-2} showing significantly more excitation than 0.1 mW cm^{-2}. Heating of the sample resulted in thermal relaxation of the photo-induced HS state much like the white light irradiation experiments (*Appendix Figure 4.10.6.ix*). After irradiation with 625 nm light at 10 K, subsequent irradiation with 850 nm light resulted in partial photo de-excitation. This effect is completely reproducible over a number of cycles and demonstrates the sample shows both partial LIESST and partial reverse-LIESST effects. The magnitude of the de-excitation with 850 nm is significantly less than the initial photo-excitation with 625 nm light, meaning the reverse-LIESST effect is inefficient in comparison to the LIESST effect (*Appendix Figure 4.10.6.x*).

4.6.3 $[Fe_2(L4.3)_3](BF_4)_4$, 4.6

Reflectivity measurements were performed on a freshly isolated sample of **4.6**. The first measurement was carried out under weak white light irradiation of 0.08 mW cm^{-2} with a scan rate of 4 K min^{-1}. Upon cooling from 270 to 10 K, the reflectivity signal between 700 and 1000 nm increases, typical of Fe(II) SCO from HS to LS, with an isosbestic point at 737 nm (*Figure 4.6.3.i*).

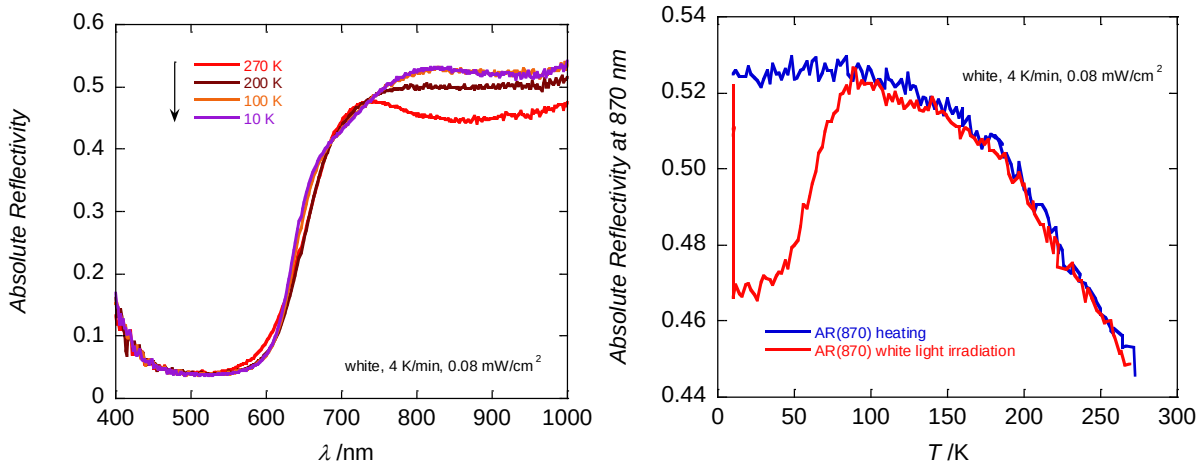

Figure 4.6.3.i: Selected surface reflectivity measurements of ***4.6*** *collected with a white light spectroscopic source (0.08 mW* cm^{-2}*) as a function of the wavelength during cooling from 270 to 10 K. (right) The temperature dependence of the reflectivity signal at 870 nm for heating the sample (blue) and white light irradiation (0.08 mW* cm^{-2}*) at 10 K for three hours followed by heating (red).*

The return heating mode exhibits the same behavior but in reverse (*Appendix Figure 4.10.6.xi*). The greatest change in the reflectivity signal is observed between 270 and 200 K while no change is observed between 10 and 100 K. To better visualize the SCO, the reflectivity at 870 nm (AR_{870}) was plotted verses the temperature (*Figure 4.6.3.i*). At 10 K the AR_{870} value is 0.52 and is constant until 98 K after which it begins to decrease to a value of 0.44 at 270 K. The cooling trace shows the reverse behavior indicating the SCO is reversible (*Appendix Figure 4.10.6.xii*). No plateau was observed by 270 K, indicating the SCO process is incomplete. The second measurement was carried out to investigate the possibility of light-induced SCO behavior. The sample was cooled to 10 K and the irradiated with white light for three hours. This white light irradiation resulted in a decrease in the AR_{870} from 0.52 to 0.47. The sample was then heated to 270 K to probe the thermal relaxation of the HS state. At 33 K the AR_{870} begins to increase until 91 K at which point the initial AR_{870} value is recovered, indicating complete thermal relaxation has occurred. As the sample is warmed above 100 K the AR_{870} begins to decrease due to thermally induced SCO following the same trace as the initial heating of the sample. In order to optimize the photo-excitation, 14 LEDs sources at wavelengths ranging from 365 to 1050 nm were trialed for increased efficiency at 10 K. This revealed the 625 nm LED proved to be the most efficient. Irradiation of the sample for 10 minutes at 10 K resulted in a decrease in the reflectivity between 700 and 1000 nm such that the signal is noticeably weaker in strength to that of the sample at 200 K, indicative of a significant photo-excitation (*Appendix Figure 4.10.6.xiii*). The intensity of the light source has a significant effect on the proportion of the sample excited to the HS state with irradiation at 10 mW cm^{-2} showing significantly more excitation than 0.1 mW cm^{-2}. As with the white light irradiation experiments, heating of the sample resulted in thermal relaxation of the photo-induced HS state (*Appendix Figure 4.10.6.xiv*). For all intensities there is a very rapid, near instantaneous decrease after the irradiation finishes, before the gradual relaxation. This type of behavior is often ascribed to surface only excitation. After irradiation with 625 nm light at 10 K, subsequent irradiation with 850 nm light resulted in partial photo de-excitation. This effect is completely reproducible over a number of cycles and demonstrates the sample shows both partial LIESST and partial reverse-LIESST effects. The magnitude of the de-excitation with 850 nm is significantly less than the initial photo-excitation with 625 nm light, meaning the reverse-LIESST effect is inefficient in comparison to the LIESST effect (*Appendix Figure 4.10.6.xv*).

4.6.4 $[Fe_2(L4.3)_3](OTf)_4$, 4.7

Reflectivity measurements were performed on a freshly isolated sample of **4.7**. The first measurement was carried out under weak white light irradiation of 0.08 mW cm^{-2} with a scan rate of 4 K min^{-1}. Upon cooling from 270 to 10 K, the reflectivity signal between 700 and 1000 nm increases, typical of Fe(II) SCO from HS to LS, with an isosbestic point at 718 nm (*Figure 4.6.4.i*). The return heating mode exhibits the same behavior but in reverse (*Appendix Figure 4.10.6.xvi*). The greatest change in the reflectivity signal is observed between 270 and 200 K while no change is observed between 10 and 100 K. To better visualize the SCO, the reflectivity at 870 nm (AR_{870}) was plotted verses the temperature (Figure *4.6.4.i*). At 10 K the AR_{870} value is 0.50 and is constant until 80 K after which it begins to decrease to a value of 0.43 at 270 K. The cooling trace shows the reverse behavior indicating the SCO is reversible (*Appendix Figure 4.10.6.xvii*). There is no plateau reached by 270 K, indicating the SCO process is incomplete. The second measurement was carried out to investigate the possibility of light-induced SCO behavior. The sample was cooled to 10 K and then irradiated with white light for three hours. This white light irradiation resulted in a decrease in the AR_{870} from 0.50 to 0.45. The sample was then heated to 270 K to probe the thermal relaxation of the HS state.

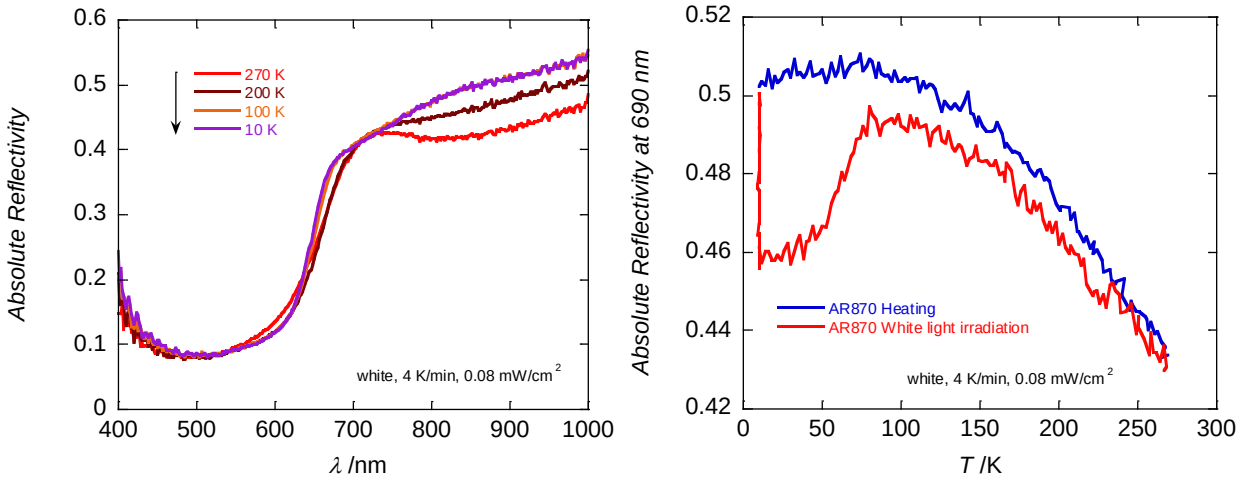

*Figure 4.6.4.i: Selected surface reflectivity measurements of **4.7** collected with a white light spectroscopic source (0.08 mW cm^{-2}) as a function of the wavelength during cooling mode between 270 – 10 K. (right) The temperature dependence of the reflectivity signal at 870 nm for heating the sample (blue) and white light irradiation (0.08 mW cm^{-2}) at 10 for three hours followed by heating (red).*

At 41 K the AR_{870} begins to increase until 80 K at which point the approximate initial AR_{870} value is recovered, indicating complete thermal relaxation has occurred. As the sample is warmed above 90 K the AR_{870} begins to decrease due to thermally induced SCO following the same trace as the initial heating of the sample. In order to optimize the photo-excitation, 14 LEDs sources at wavelengths ranging from 365 to 1050 nm were trialed for increased efficiency at 10 K. This revealed that the 625 nm LED proved to be the most efficient. Irradiation of the sample for 10 minutes at 10 K resulted in a decrease in the reflectivity between 700 and 1000 nm such that the signal is slightly weaker in strength to that of the sample at 200 K, indicative of a reasonable photo-excitation (*Appendix Figure 4.10.6.xviii*). The intensity of the light source has a significant effect on the proportion of the sample excited to the HS state with irradiation at 10 mW cm^{-2} showing significantly more excitation than 0.1 mW cm^{-2}. As with the white light irradiation experiments, heating of the sample resulted in thermal relaxation of the photo-induced HS state (*Appendix Figure 4.10.6.xix*). For all intensities there is a very rapid near instantaneous decrease after the irradiation finishes, before the gradual relaxation much like **4.6** and ascribed to surface only excitation. After irradiation with 625 nm light at 10 K, subsequent irradiation with 850 nm light resulted in partial photo de-excitation. This effect is completely reproducible over a number of cycles and demonstrates the sample shows both partial LIESST and partial reverse-LIESST effects. The magnitude of the de-excitation with 850 nm is significantly less than the initial photo-excitation with 625 nm light, meaning the reverse-LIESST effect is inefficient in comparison to the LIESST effect (*Appendix Figure 4.10.6.xx*).

4.7 Photomagnetic measurements

4.7.1 $[Fe_2(L4.2)_3](OTf)_4$, 4.4

The large photo-induced SCO effect observed for **4.4** made this complex a suitable candidate for further photo-magnetic measurements. Freshly isolated crystals of **4.4** were placed in a sealed plastic bag and entered into the SQUID magnetometer. Measurements were carried out at an applied field of 10000 Oe with a scan rate of 0.4 K min^{-1}. The sample was cooled from 295 to 1.85 K and a gradual SCO process occurs between 260 and 10 K (*Figure 4.7.1.i*). The initial χT value of 6.8 cm^3 K mol^{-1} decreases to 0.96 cm^3 K mol^{-1} at 80 K. The sample was then irradiated with 650 nm light for 330 minutes. Significant photo-excitation occured under these conditions, with a

conversion to the photo-excited HS state of approximately 90%. As the sample is heated at 0.4 K min^{-1}, thermal relaxation of the sample to the LS state occurs, which is complete by 73 K (*Figure 4.7.1.i*). The near complete switching of the sample indicates that this is not a surface only effect of the sample and adequate penetration of light through the sample occurs. While the sample is irradiated for 330 minutes, the photo induced SCO process is complete after only 150 minutes. This is significantly faster than the related helicate complexes previously reported by Kruger and co-workers.[321]

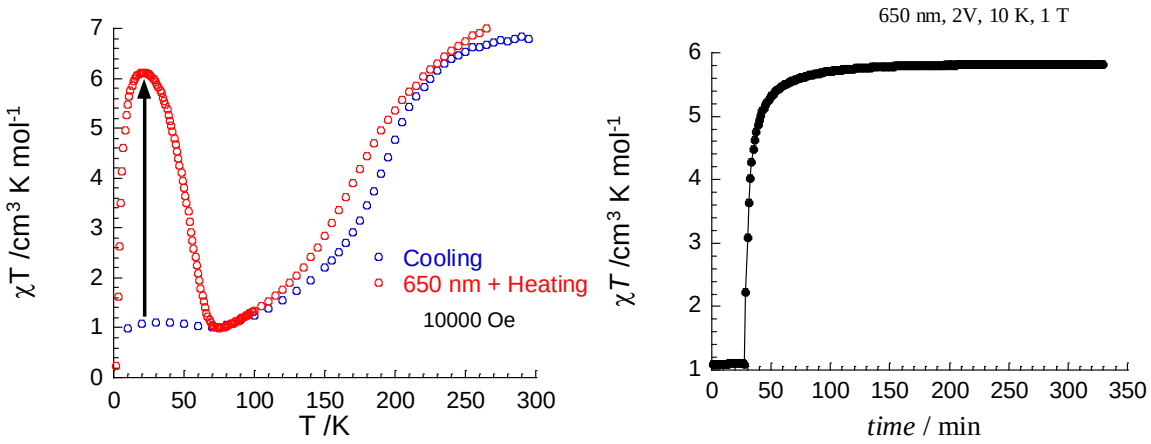

*Figure 4.7.1.i: (left) The χT vs. T plot for **4.4** between 260 and 10 K with an applied field of 1000 Oe and a scan rate of 0.4 K min^{-1}. The cooling of the sample is represented by the blue open circles while the irradiation with 650 nm followed by heating represented by the red open circles. (right) The χT vs. time plot for **4.4** at 10 K with 650 nm light and an applied field of 10000 Oe.*

4.8 Summary and conclusions

The above work has focused on the use of two ligands; **L4.2** and **L4.3** and two anions; tetrafluoroborate and triflate to form Fe(II) (**4.4** to **4.7**) or Co(II) (**4.8**) dinuclear triple helicates via sub-component self-assembly. Significant differences in the crystal packing occured by changing the peripheral functionality of the ligand in the form of a methyl group. Drastic changes were also induced by changing the crystallization conditions and anion. Complexes **4.4** and **4.5** both contain the same ligand (**L4.2**) and anion (triflate), however, the crystalisation conditions are different.

Complex **4.4** is crystallised using diisopropyl ether while **4.5** is crystallised using chloroform. The difference in the antisolvent resulted in the complexes crystalizing in triclinic and monoclinic space groups, respectively. This change in space group was due to the different crystal packing adopted by the complexes along with the symmetry of the helicates. The imidazole N-H moieties of both complexes participate in hydrogen bond interactions to the oxygen atoms of the triflate anions. The resultant hydrogen bond networks are significantly different by virtue of the different crystal packing. It is postulated that the incorporation of solvent molecules of different sizes and/or shapes during the crystallization prevents the complexes from packing in an identical manner. This results in the formation of hydrogen bond networks of different topologies that determine the final crystal packing. The difference in crystal packing has a dramatic effect on the SCO behavior of the two compounds which were investigated via magnetic susceptibility and reflectivity measurements. With regard to the SCO behavior of the solvated samples, magnetic susceptibility measurements revealed that **4.4** has a higher $T_{1/2}$ of 232 K than **4.5** ($T_{1/2}$ = 179 K). The SCO of **4.4** could be fitted to the ideal solution model, yielding ΔS and ΔH values noticeably greater than those reported previously for the tetrafluoroborate analogue.[321] This can be attributed to the different crystal packing imposed by the different anions. The SCO of **4.5** was broader and therefore the fit to the ideal solution model was poor. This broader SCO is thought to be the result of negative cooperativity induced by the different crystal packing. Reflectivity measurements revealed that at 10 K, both **4.4** and **4.5** exhibit a significant LIESST effect, particularly with excitation by 625 nm light. Therefore, both complexes are good candidates for further photomagnetic measurements and the effect of light on the magnetic susceptibility of **4.4** was investigated. Irradiation with 650 nm light resulted in 90% photo-excitation from LS to HS at 10 K. Near complete SCO occurs after only 150 minutes which is significantly faster than the previously reported tetrafluoroborate analogue.[321]

The ligand **L4.3** was selected as it is a comparison to **L4.2** as they both feature the 4-imidazole moiety. While **L4.3** features a methyl group in the 5-position, **L4.2** has a hydrogen atom. Therefore, the ability of anions to hydrogen bond to the neighbouring N-H moiety was expected to differ due to the more sterically encumbered nature of **L4.3**. Complex **4.7** contained ligand **L4.3** and the triflate anion and serves as a comparison to **4.4** and **4.5**. Unfortunately, crystals suitable for single crystal X-ray diffraction were unable to be generated from an acetonitrile solution. However, **4.7** could be crystallised from nitromethane allowing for structure elucidation. **4.7**

crystalises in the monoclinic space group $P2_1/c$ unlike **4.4** or **4.5**, with a significantly different crystal packing, as evidenced by noticeably different hydrogen bonding modes of the triflate anions. Magnetic susceptibility measurements illustrated how the alteration of the crystal packing is represented in the SCO behavior. The SCO of the solvated sample of **4.7** is broader in nature to that of **4.4** or **4.5**, with the SCO commencing at 60 K and incomplete by the end of the measurement at 280 K.

Complex **4.6** was synthesised as an **L4.3** analogue to the previously reported complex by Kruger and co-workers $[Fe_2(\mathbf{L4.2})_3](BF_4)_4$.[321] The hydrogen bond interactions of the tetrafluoroborate anions with the N-H moieties of the imidazole rings are subtlety different. However, the two complexes pack in broadly the same manner. These slight changes in the hydrogen bond interactions may be attributed to the presence of the adjacent methyl group in ligand **L4.3**. It is important to note that while the complex previously reported by Kruger and co-workers was crystallised from acetonitrile, **4.6** was crystallised from nitromethane. Interestingly, the $T_{1/2}$ for the solvated sample of **4.6** is 238 K, significantly higher than the complex previously reported by Kruger and co-workers ($T_{1/2}$ = 148 K). This demonstrates that the subtle change in ligand field by incorporating the methyl group on ligand **L4.3** and the concomitant change in the hydrogen bonding of the terafluoroborate anions has a significant effect.

Complex **4.8** was synthesised as the Co(II) analogue of **4.6** to investigate the occurrence of SMM. The high χT value at 300 K indicated a significant orbital contribution from the Co(II) centre while the non-superposition of the *M vs. H* T^{-1} isotherms indicated that the Co(II) centres possessed a degree of anisotropy. Therefore, AC magnetic susceptibility measurements were performed and revealed the occurrence of an out of phase magnetic susceptibility in the presence of an applied DC field. The AC susceptibility data were fitted to the generalized Debye model which allowed for the energy barrier (U_{eff}) to be extracted, after subsequent fitting of the data in an Arrhenius plot.

A common issue encountered for all the complexes in this chapter was the rapid loss of crystallinity upon removal from the mother liquor, due to solvent loss. This is a common problem with metallo-supramolecular complexes as they often contain large cavities in the structure filled with solvent molecules. Unless the solvent molecules are participating in hydrogen bond interactions with the complex, they are lost very easily. As the complexes lose crystallinity, the effect on the structure cannot be elucidated by crystallographic techniques so the exact effect of the solvent loss is

unknown. Therefore, the magnetic susceptibility measurements were performed on both the solvated and dried complexes which often exhibited very different behavior. Unfortunately, due to the setup of the reflectivity instrument, samples are unable to be measured in their mother liquor and therefore some degree of desolvation is unavoidable, particularly as these measurements are carried out over an extended period of time (several days typically).

The use of larger anions such as bis(trifluoromethanesulfonyl)imide may minimize the vacant space able to be occupied by solvents and therefore increase the stability of the crystals when removed from the mother liquor. Alternately, the use of strong hydrogen bond acceptors as anions such as carboxylates may result in hydrogen bonded frameworks which are capable of retaining their integrity upon partial or full solvent loss.

In conclusion, the family of Fe(II) helicates based on a rigid hydrazone core previously reported by Kruger and co-workers has been expanded to include different anions, new ligand functionality and Co(II) metal centres. The new ligand functionality and anions resulted in a family of SCO Fe(II) helicates with varied behavior in the solid state. The Co(II) complex illustrated how these imidazolylimine coordination motifs readily used for the synthesis of SCO helicates, can also be used to synthesise SMM materials.

4.9 Experimental

For details on general procedures, NMR, FT-IR, ESI-MS, melting points, elemental analysis and TGA see *section 2.7* of chapter two. Only details relevant to the work carried out in this chapter, not previously discussed will be given herein.

4.9.1 Elemental analysis

Elemental analysis for complex **4.5** was carried out at the CEISAM laboratory, UMR CNRS-6230, University of Nantes. The complex was analysed as received.

4.9.2 Single crystal X-ray diffraction

Diffraction data for **4.**4 to **4.**7 was collected at the University of Canterbury. Crystals were mounted on the diffractometer directly at 120 K. For **4.4** and **4.6**, the data collection was first carried out at

120 K. The crystals were then warmed at 5 K min^{-1} to 240 K and a second collection was carried out. For further details see *section 2.7* of chapter two.

4.9.3 Magnetic susceptibility measurements

Solvated samples were prepared as follows: a sample of crystals was placed in a plastic straw, sealed at one end and layered with a small amount of mother liquor. The sample was purged with an inert gas and sealed. Measurements for complexes layered with mother liquor were carried out at an applied field of 1000 Oe to minimize the orientation of the crystals in the magnetic field with a scan rate of 0.4 K min^{-1}. Dried samples were introduced in polypropylene bags (3 × 0.5 × 0.02 cm) for measurements at 10000 Oe with a scan rate of 0.4 K min^{-1}. For further details see *section 2.7* of chapter two.

4.9.4 Reflectivity measurements

Reflectivity experiments were carried out on a home-built apparatus at CRPP. The temperature range is from 10 to 300 K. The spectrometric range runs from 400–1000 nm. The light for spectrometry is a halogen-tungsten light source (Leica CLS 150 XD tungsten halogen source adjustable from 0.05 mW cm^{-2} to 1 W cm^{-2}). The measurements were calibrated by a NIST traceable standard for reflectance (sphereOptics, ref SG3054).

4.9.5 Photomagnetic measurements

The photomagnetic experiments were performed with different sources coupled through an optical fibre directed into the magnetometer cavity. Powdered samples of approximately 5 mg were packed in a plastic bag in a thermo-formed straw maintained at 3 cm to the optical fibre. For all experiments, the magnetic data were corrected for the sample holder and the diamagnetic contribution.

4.9.6 Ligand synthesis

*4.9.6.i 3,3′-1,1′-(Hydrazine-1,2-diylidine)bis(ethan-1-yl-1ylidene)dianiline, **4.1***

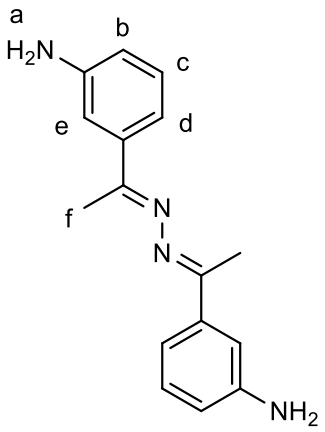

3,3′-1,1′-(Hydrazine-1,2-diylidine)bis(ethan-1-yl-1ylidene)dianiline was prepared following an adapted literature procedure.[321] *m*-Amino acetophenone (2 g, 14.8 mmol) was dissolved in methanol (20 mL) to give a yellow solution. Hydrazine monohydrate (0.4 mL, 8.2 mmol) was added, followed by several drops of glacial acetic acid. The yellow solution was heated at reflux for four hours. Upon cooling to room temperature, pale yellow needle crystals formed. The crystals were separated by filtration and washed with petroleum ether (2 x 5 mL) to give a pale yellow crystalline solid (1.24 g, 9.3 mmol, yield = 63%)

M.pt. 130-133 °C Lit. 130-132 °C

^{1}H-NMR: δ_H (400 MHz, [D_6]-DMSO) 7.13 (s, 1 H, H_e), 7.06 (t, J = 7.50, 1 H, H_c), 6.99 (d, J = 7.50, 1 H, H_d), 6.61 (d, J = 7.50, 1 H, H_b), 5.16 (s, 2 H, H_a), 2.15 (s, 3 H, H_f)

4.9.7 Complex synthesis

*4.9.7.i [Fe_2(**L4.2**)$_3$](OTf)$_4$, **4.4***

$Fe(CF_3SO_3)_2$ (17.7 mg, 0.05 mmol) and 4-imidazolecarboxaldehdye (14.4 mg, 0.15 mmol) were stirred in acetonitrile (10 mL) at room temperature for half an hour to give a yellow solution. **4.1** (20 mg, 0.075 mmol) was added and stirred at 50 °C overnight to give an orange solution. The solution was cooled to room temperature and filtered. Vapor diffusion of the filtrate with diisopropyl ether gave orange block crystals suitable for single crystal X-ray diffraction.

Found: C, 46.02 H, 3.85 N, 16.28% $[Fe_2(C_{24}H_{22}N_8)_3](CF_3SO_3)_4]\cdot 0.5H_2O$ requires: C, 46.00 H, 3.40 N, 16.94%

IR: (ν_{max}/cm^{-1}) 3141 (br., w), 2968 (w), 2882 (w), 1619 (s), 1596 (m), 1573 (m), 1517 (w), 1483 (w), 1424 (w), 1367 (w), 1278 (s), 1243 (s), 1223 (s), 1154 (s), 1090 (m), 1027 (s), 1007 (m), 934 (w), 887 (w), 848 (w), 825 (w), 796 (m), 758 (w), 695 (m), 635 (s), 616 (s), 573 (m), 538 (w), 515 (m), 417 (w)

*4.9.7.ii [Fe_2(**L4.2**)$_3$](OTf)$_4$, **4.5***

$Fe(CF_3SO_3)_2$ (17.7 mg, 0.05 mmol) and 4-imidazolecarboxaldehdye (14.4 mg, 0.144 mmol) were stirred in acetonitrile (10 mL) at room temperature for half an hour to give a yellow solution. **4.1** (20 mg, 0.075 mmol) was added and stirred at 50 °C overnight to give an orange solution. The solution was cooled to room temperature and filtered. Vapor diffusion of the filtrate with chloroform gave yellow rod crystals suitable for single crystal X-ray diffraction.

Found: C, 38.84 H, 3.06 N, 14.11% $[Fe_2(C_{24}H_{22}N_8)_3](CF_3SO_3)_4]\cdot 4CHCl_3\cdot 9H_2O\cdot CH_3CN$ requires: C, 38.96 H, 3.63 N, 13.85%

IR: (ν_{max}/cm^{-1}) 3510 (br., w), 3129 (br., w), 1618 (m), 1595 (m), 1571 (m), 1515 (w), 1482 (w), 1423 (m), 1367 (w), 1276 (s), 1245 (s), 1224 (s), 1154 (m), 1089 (m), 1027 (s), 1009 (m), 933 (w), 865 (w), 884 (w), 824 (w), 800 (m), 753 (m), 695 (m), 636 (s), 617 (s), 595 (w), 574 (m), 541 (w), 515 (m)

*4.9.7.iii[Fe_2(**L4.3**)$_3$](BF$_4$)$_4$, **4.6***

$Fe(BF_4)_2.6H_2O$ (16.9 mg, 0.05 mmol) and 4-methyl-5-imidazolecarboxaldehdye (16.4 mg, 0.15 mmol) were stirred in nitromethane (10 mL) at room temperature for half an hour to give a yellow solution. **4.1** (20 mg, 0.075 mmol) was added and stirred at 50 °C overnight to give an orange solution. The solution was cooled to room temperature and filtered. Vapor diffusion of the filtrate with diethyl ether gave orange block crystals suitable for single crystal X-ray diffraction.

Found: C, 49.77 H, 4.58 N, 17.83% $[Fe_2(C_{26}H_{26}N_8)_3](BF_4)_4]\cdot 4H_2O$ requires: C, 49.76 H, 4.60 N, 17.86%

IR: (ν_{max}/cm^{-1}) 3609 (br., w), 3307 (br., w), 1625 (s), 1572 (s), 1554 (s), 1521 (m), 1483 (w), 1438 (m), 1368 (m), 1336 (w), 1301 (m), 1253 (w), 1200 (w), 1050 (s), 1031 (s), 974 (s), 932 (m), 900 (w), 886 (w), 844 (m), 802 (m), 764 (w), 695 (s), 653 (m), 630 (m), 600 (m), 520 (m), 478 (w)

*4.9.7.iv [Fe_2(**L4.3**)$_3$](OTf)$_4$, **4.7***

$Fe(CF_3SO_3)_2$ (17.7 mg, 0.05 mmol) and 4-methyl-5-imidazolecarboxaldehdye (16.4 mg, 0.15 mmol) were stirred in nitromethane (10 mL) at room temperature for half an hour to give a yellow solution. **4.1** (20 mg, 0.075 mmol) was added and stirred at 50 °C overnight to give an orange

solution. The solution was cooled to room temperature and filtered. Vapor diffusion of the filtrate with diisopropyl ether gave orange block crystals suitable for single crystal X-ray diffraction.

Found: C, 47.97 H, 4.47 N, 15.70% $[Fe_2(C_{26}H_{26}N_8)_3](CF_3SO_3)_4 \cdot H_2O$ requires: C, 47.40 H, 3.88 N, 16.18%

IR: (ν_{max}/cm^{-1}) 3211 (br., w), 1624 (m), 1572 (m), 1553 (m), 1522 (w), 1484 (w), 1440 (w), 1368 (w), 1338 (w), 1278 (s), 1241 (s), 1224 (s), 1158 (s), 1106 (w), 1028 (s), 976 (w), 933 (w), 900 (w), 844 (w), 800 (m), 756 (w), 697 (m), 634 (s), 601 (w), 574 (m), 516 (m), 479 (w)

*4.9.7.v [Co$_2$(**L4.3**)$_3$](BF$_4$)$_4$, **4.8***

$Co(BF_4)_2.6H_2O$ (16.9 mg, 0.05 mmol) and 4-methyl-5-imidazolecarboxaldehdye (16.4 mg, 0.15 mmol) were stirred in nitromethane (10 mL) at room temperature for half an hour to give a yellow solution. **4.1** (20 mg, 0.075 mmol) was added and stirred at 50 °C overnight to give an orange solution. The solution was cooled to room temperature and filtered. Vapor diffusion of the filtrate with diethyl ether gave orange block crystals suitable for single crystal X-ray diffraction.

Found: C, 49.25 H, 3.90 N, 17.60% $[Co_2(C_{26}H_{26}N_8)_3](BF_4)_4] \cdot 4.8H_2O$ requires: C, 49.22 H, 4.64 N, 17.66%

IR: (ν_{max}/cm^{-1}) 3623 (br., w), 3300 (br., w), 3141 (w), 1625 (s), 1574 (s), 1523 (m), 1483 (w), 1441 (m), 1367 (m), 1338 (w), 1301 (m), 1254 (w), 1200 (w), 1031 (br., s), 974 (s), 932 (m), 902 (w), 887 (w), 843 (m), 801 (m), 763 (w), 695 (m), 654 (w), 631 (m), 599 (m), 541 (w), 519 (m), 444 (w)

4.10 Chapter Four Appendix

4.10.1 Crystallographic tables

Complex	**4.4** – 120 K	**4.4** – 240 K	**4.5**	**4.6** – 120 K
Empirical formula	$C_{83.8}H_{77.7}F_{12}Fe_2N_{27.9}O_{12.5}S_4$	$C_{76}H_{66}F_{12}Fe_2N_{24}O_{12}S_4$	$C_{78}H_{72}Cl_6F_{12}Fe_2N_{24}O_{14}S_4$	$C_{81.5}H_{88.5}B_4F_{16}Fe_2N_{27.5}O_7$
Formula weight	2143.57	1975.46	2250.23	2024.23
Temperature/K	120.00(10)	240.00(10)	120.01(10)	120.02(10)
Crystal system	triclinic	triclinic	monoclinic	triclinic
Space group	P-1	P-1	C2/c	P-1
a/Å	15.2845(5)	15.4923(5)	31.496(3)	14.0309(3)
b/Å	19.1761(6)	19.3481(5)	27.6229(10)	16.0603(4)
c/Å	20.5638(7)	20.6900(7)	14.1313(9)	24.1203(6)
α/°	105.462(3)	104.363(3)	90	95.292(2)
β/°	90.628(3)	91.010(3)	123.339(10)	100.811(2)
γ/°	113.323(3)	113.225(3)	90	99.851(2)
Volume/Å^3	5288.0(3)	5474.4(3)	10271.1(15)	5216.5(2)
Z	2	2	4	2
ρ_{calc}g/cm^3	1.346	1.198	1.455	1.289
μ/mm^{-1}	3.709	3.527	5.248	3.006
F(000)	2200.0	2020.0	4584.0	2084.0
Crystal size/mm^3	0.463 × 0.159 × 0.11	0.496 × 0.152 × 0.104	0.639 × 0.112 × 0.033	0.572 × 0.211 × 0.153
Radiation	CuKα (λ = 1.54184)	CuKα (λ = 1.54184)	CuKα (λ = 1.54184)	CuKα (λ = 1.54184)
2Θ range for data collection/°	7.286 to 140.138	7.196 to 127.38	6.718 to 136.498	6.536 to 140.14
Index ranges	$-18 \le h \le 18$, $-23 \le k \le 15$, $-24 \le l \le 25$	$-17 \le h \le 18$, $-22 \le k \le 20$, $-24 \le l \le 23$	$-37 \le h \le 36$, $-33 \le k \le 32$, $-13 \le l \le 17$	$-17 \le h \le 15$, $-19 \le k \le 19$, $-29 \le l \le 29$
Reflections collected	43704	37352	35337	48968
Independent reflections	20073 [R_{int} = 0.0244, R_{sigma} = 0.0316]	17639 [R_{int} = 0.0446, R_{sigma} = 0.0540]	9396 [R_{int} = 0.0763, R_{sigma} = 0.0629]	19806 [R_{int} = 0.0350, R_{sigma} = 0.0380]
Data/restraints/parameters	20073/333/1709	17639/480/1339	9396/3/664	19806/250/1432
Goodness-of-fit on F^2	1.033	1.634	1.032	1.048
Final R indexes [I>=2σ (I)]	R_1 = 0.0660, wR_2 = 0.1969	R_1 = 0.1312, wR_2 = 0.3794	R_1 = 0.0670, wR_2 = 0.1807	R_1 = 0.0567, wR_2 = 0.1637
Final R indexes [all data]	R_1 = 0.0743, wR_2 = 0.2049	R_1 = 0.1815, wR_2 = 0.4355	R_1 = 0.0978, wR_2 = 0.2025	R_1 = 0.0633, wR_2 = 0.1704
Largest diff. peak/hole / e Å^{-3}	1.04/-1.14	0.88/-2.10	0.70/-0.62	0.81/-0.59

Identification code	**4.6** – 240 K	**4.7**	**4.8**
Empirical formula	$C_{81}H_{87}B_4F_{16}Fe_2N_{27}O_6$	$C_{84.75}H_{86.25}F_{12}Fe_2N_{26.75}O_{17.5}S_4$	$C_{83.5}H_{94.5}B_4Co_2F_{16}N_{29.5}O_{11}$
Formula weight	1993.71	2227.49	2152.48
Temperature/K	240.00(10)	120.01(10)	120.00(10)
Crystal system	triclinic	monoclinic	triclinic
Space group	P-1	$P2_1/c$	P-1
a/Å	14.2166(2)	21.7960(3)	13.9909(3)
b/Å	16.3976(4)	31.2955(5)	16.2461(4)
c/Å	24.5707(6)	14.6253(2)	24.2457(6)
α/°	94.773(2)	90	95.317(2)
β/°	102.331(2)	91.5620(10)	101.387(2)
γ/°	99.655(2)	90	99.372(2)
Volume/Å^3	5474.2(2)	9972.5(3)	5285.8(2)
Z	2	4	2
ρ_{calc}g/cm^3	1.210	1.484	1.352
μ/mm^{-1}	2.849	3.990	3.290
F(000)	2052.0	4584.0	2216.0
Crystal size/mm^3	0.488 × 0.26 × 0.175	0.344 × 0.115 × 0.053	0.582 × 0.363 × 0.151
Radiation	CuKα (λ = 1.54184)	CuKα (λ = 1.54184)	CuKα (λ = 1.54184)
2Θ range for data collection/°	6.682 to 140.152	6.954 to 144.256	6.814 to 140.128
Index ranges	-17 ≤ h ≤ 12, -17 ≤ k ≤ 19, -29 ≤ l ≤ 29	-21 ≤ h ≤ 26, -37 ≤ k ≤ 38, -15 ≤ l ≤ 18	-11 ≤ h ≤ 17, -19 ≤ k ≤ 19, -29 ≤ l ≤ 29
Reflections collected	39240	89028	40357
Independent reflections	20760 [R_{int} = 0.0226, R_{sigma} = 0.0340]	19633 [R_{int} = 0.0486, R_{sigma} = 0.0363]	20039 [R_{int} = 0.0320, R_{sigma} = 0.0420]
Data/restraints/parameters	20760/372/1550	19633/238/1549	20039/91/1497
Goodness-of-fit on F^2	1.042	1.033	1.028
Final R indexes [I>=2σ (I)]	R_1 = 0.0575, wR_2 = 0.1795	R_1 = 0.0535, wR_2 = 0.1541	R_1 = 0.0514, wR_2 = 0.1441
Final R indexes [all data]	R_1 = 0.0690, wR_2 = 0.1932	R_1 = 0.0616, wR_2 = 0.1629	R_1 = 0.0592, wR_2 = 0.1522
Largest diff. peak/hole / e Å^{-3}	0.59/-0.46	1.37/-0.64	0.96/-0.61

4.10.2 Selected crystallographic parameters

Selected intermolecular bond lengths and angles

Bond	d(Fe-N) Å	Atoms	<(N-Fe-N) °	Atoms	<(N-Fe-N) °
Fe1-N3	1.998(2)	N3-Fe1-N4	80.6(1)	N9-Fe2-N10	81.1(1)
Fe1-N4	1.953(3)	N4-Fe1-N6	94.1	N10-Fe2-N14	93.1(1)
Fe1-N5	2.007(3)	N6-Fe1-N7	86.5(1)	N14-Fe2-N11	91.0(1)
Fe1-N6	1.966(3)	N7-Fe1-N3	99.1(1)	N11-Fe2-N9	95.0(1)
Fe1-N7	2.003(3)	N3-Fe1-N5	96.0(1)	N9-Fe2-N12	90.5(1)
Fe1-N8	1.965(4)	N5-Fe1-N6	81.0(1)	N12-Fe2-N14	92.7(1)
Fe2-N9	2.007(3)	N6-Fe1-N8	91.5(1)	N14-Fe2-N13	80.8(1)
Fe2-N10	1.966(3)	N8-Fe1-N3	91.9(1)	N13-Fe2-N9	96.4(1)
Fe2-N11	1.993(3)	N4-Fe1-N5	92.6(1)	N10-Fe2-N12	92.6(1)
Fe2-N12	1.955(3)	N5-Fe1-N7	94.3(1)	N12-Fe2-N11	80.7(1)
Fe2-N13	1.991(3)	N7-Fe1-N8	80.8(1)	N11-Fe2-N13	95.1(1)
Fe2-N14	1.975(3)	N8-Fe1-N4	92.4(1)	N13-Fe2-N10	92.0(1)

*Table 4.10.2.i: Fe-N bond lengths and N-Fe-N cis bond angles for complex **4.4** at 120 K.*

Bond	d(Fe-N) Å	Atoms	<(N-Fe-N) °	Atoms	<(N-Fe-N) °
Fe1-N3	2.106(8)	N3-Fe1-N4	78.2(4)	N9-Fe2-N10	79.1(3)
Fe1-N4	2.06(1)	N4-Fe1-N6	98.1(4)	N10-Fe2-N14	95.2(3)
Fe1-N5	2.162(9)	N6-Fe1-N7	86.1(3)	N14-Fe2-N11	90.8(3)
Fe1-N6	2.050(7)	N7-Fe1-N3	98.4(3)	N11-Fe2-N9	95.3(3)
Fe1-N7	2.156(8)	N3-Fe1-N5	96.1(3)	N9-Fe2-N12	90.5(3)
Fe1-N8	2.07(1)	N5-Fe1-N6	77.5(3)	N12-Fe2-N14	94.1(3)
Fe2-N9	2.080(8)	N6-Fe1-N8	94.4(4)	N14-Fe2-N13	79.3(3)
Fe2-N10	1.997(7)	N8-Fe1-N3	92.4(3)	N13-Fe2-N9	96.6(3)
Fe2-N11	2.042(7)	N4-Fe1-N5	93.9(4)	N10-Fe2-N12	93.7(3)
Fe2-N12	1.982(9)	N5-Fe1-N7	93.8(3)	N12-Fe2-N11	79.7(3)
Fe2-N13	2.026(8)	N7-Fe1-N8	77.6(3)	N11-Fe2-N13	94.4(3)
Fe2-N14	2.018(7)	N8-Fe1-N4	95.1(4)	N13-Fe2-N10	92.8(3)

*Table 4.10.2.ii: Fe-N bond lengths and N-Fe-N cis bond angles for complex **4.4** at 240 K.*

Bond	d(Fe-N) Å	Atoms	<(N-Fe-N) °	Atoms	<(N-Fe-N) °
Fe1-N2	2.064(4)	N2-Fe1-N3	80.1(2)	N7-Fe1-N6	79.8(2)
Fe1-N3	1.982(5)	N3-Fe1-N7	93.3(2)	N6-Fe1-N2	97.0(2)
Fe1-N4	2.040(5)	N7-Fe1-N4	88.0(2)	N3-Fe1-N5	94.2(2)
Fe1-N5	1.985(3)	N4-Fe1-N2	98.9(2)	N5-Fe1-N4	80.5(2)
Fe1-N6	2.051(3)	N2-Fe1-N5	94.4(2)	N4-Fe1-N6	92.3(2)
Fe1-N7	2.005(4)	N5-Fe1-N7	89.5(2)	N6-Fe1-N3	93.1(2)

*Table 4.10.2.iii: Fe-N bond lengths and N-Fe-N cis bond angles for complex **4.5** at 120 K.*

Bond	d(Fe-N) Å	Atoms	<(N-Fe-N) °	Atoms	<(N-Fe-N) °
Fe1-N3	2.017(2)	N3-Fe1-N4	80.26(9)	N9-Fe2-N10	80.73(9)
Fe1-N4	1.979(2)	N4-Fe1-N8	91.56(9)	N10-Fe2-N12	92.45(9)
Fe1-N5	2.025(2)	N8-Fe1-N5	90.53(9)	N12-Fe2-N13	93.61(9)
Fe1-N6	1.968(2)	N5-Fe1-N3	98.15(9)	N13-Fe2-N9	93.37(8)
Fe1-N7	2.025(2)	N3-Fe1-N6	95.54(9)	N9-Fe2-N11	98.09(8)
Fe1-N8	1.988(2)	N6-Fe1-N8	90.95(9)	N11-Fe2-N12	80.68(9)
Fe2-N9	2.013(2)	N8-Fe1-N7	90.10(9)	N12-Fe2-N14	93.34(9)
Fe2-N10	1.968(2)	N7-Fe1-N3	93.48(9)	N14-Fe2-N9	88.36(9)
Fe2-N11	2.009(2)	N4-Fe1-N6	94.42(9)	N10-Fe2-N11	93.92(9)
Fe2-N12	1.956(2)	N6-Fe1-N5	80.48(9)	N11-Fe2-N13	95.39(8)
Fe2-N13	2.017(2)	N5-Fe1-N7	98.38(9)	N13-Fe2-N14	80.60(9)
Fe2-N14	1.961(2)	N7-Fe1-N4	86.97(9)	N14-Fe2-N10	90.62(9)

*Table 4.10.2.iv: Fe-N bond lengths and N-Fe-N cis bond angles for complex **4.6** at 120 K.*

Bond	d(Fe-N) Å	Atoms	<(N-Fe-N) °	Atoms	<(N-Fe-N) °
Fe1-N3	2.212(2)	N3-Fe1-N4	76.79(9)	N9-Fe2-N10	76.94(9)
Fe1-N4	2.112(3)	N4-Fe1-N6	99.0(1)	N10-Fe2-N14	98.39(9)
Fe1-N5	2.207(2)	N6-Fe1-N7	87.52(9)	N14-Fe2-N11	86.71(9)
Fe1-N6	2.121(3)	N7-Fe1-N3	97.76(8)	N11-Fe2-N9	97.78(8)
Fe1-N7	2.222(2)	N3-Fe1-N5	94.03(8)	N9-Fe2-N12	91.69(9)
Fe1-N8	2.117(3)	N5-Fe1-N6	76.71(9)	N12-Fe2-N14	93.65(9)
Fe2-N9	2.213(2)	N6-Fe1-N8	93.6(1)	N14-Fe2-N13	76.71(8)
Fe2-N10	2.120(2)	N8-Fe1-N3	96.41(9)	N13-Fe2-N9	97.91(8)
Fe2-N11	2.215(2)	N4-Fe1-N5	96.13(9)	N10-Fe2-N12	93.48(9)
Fe2-N12	2.128(2)	N5-Fe1-N7	91.20(8)	N12-Fe2-N11	76.34(9)
Fe2-N13	2.195(2)	N7-Fe1-N8	76.69(9)	N11-Fe2-N13	91.25(8)
Fe2-N14	2.138(2)	N8-Fe1-N4	96.8(1)	N13-Fe2-N10	99.44(9)

*Table 4.10.2.v: Fe-N bond lengths and N-Fe-N cis bond angles for complex **4.6** at 240 K.*

Bond	d(Fe-N) Å	Atoms	<(N-Fe-N) °	Atoms	<(N-Fe-N) °
Fe1-N3	1.992(2)	N3-Fe1-N4	80.94(9)	N9-Fe2-N10	80.30(9)
Fe1-N4	1.958(2)	N4-Fe1-N6	93.41(9)	N10-Fe2-N14	91.1(1)
Fe1-N5	1.981(2)	N6-Fe1-N7	88.18(9)	N14-Fe2-N11	92.67(9)
Fe1-N6	1.967(2)	N7-Fe1-N3	97.92(9)	N11-Fe2-N9	95.88(9)
Fe1-N7	2.030(2)	N3-Fe1-N5	95.31(9)	N9-Fe2-N12	86.16(9)
Fe1-N8	1.947(2)	N5-Fe1-N6	81.19(9)	N12-Fe2-N14	93.9(1)
Fe2-N9	2.003(2)	N6-Fe1-N8	90.40(9)	N14-Fe2-N13	81.06(9)
Fe2-N10	1.959(2)	N8-Fe1-N3	93.28(9)	N13-Fe2-N9	99.52(9)
Fe2-N11	2.007(2)	N4-Fe1-N5	91.75(9)	N10-Fe2-N12	93.0(1)
Fe2-N12	1.984(4)	N5-Fe1-N7	96.40(9)	N12-Fe2-N11	80.79(9)
Fe2-N13	2.008(2)	N7-Fe1-N8	81.07(9)	N11-Fe2-N13	94.63(9)
Fe2-N14	1.948(2)	N8-Fe1-N4	90.90(9)	N13-Fe2-N10	91.89(9)

*Table 4.10.2.vi: Fe-N bond lengths and N-Fe-N cis bond angles for complex **4.7** at 120 K.*

Bond	d(Co-N) Å	Atoms	<(N-Co-N) °	Atoms	<(N-Co-N) °
Co1-N3	2.177(2)	N3-Co1-N4	77.54(8)	N9-Co2-N10	77.42(8)
Co1-N4	2.127(2)	N4-Co10N8	95.01(8)	N10-Co2-N12	95.86(8)
Co1-N5	2.198(2)	N8-Co1-N5	90.19(8)	N12-Co2-N13	96.24(8)
Co1-N6	2.086(2)	N5-Co1-N3	97.93(8)	N13-Co2-N9	91.13(7)
Co1-N7	2.187(2)	N3-Co1-N6	97.77(8)	N9-Co2-N11	97.84(7)
Co1-N8	2.114(2)	N6-Co1-N8	93.21(8)	N11-Co2-N12	77.51(8)
Co2-N9	2.215(2)	N8-Co1-N7	77.09(8)	N12-Co2-N14	98.81(8)
Co2-N10	2.101(2)	N7-Co1-N3	92.20(7)	N14-Co2-N9	86.98(8)
Co2-N11	2.191(2)	N4-Co1-N6	98.56(8)	N10-Co2-N11	96.71(8)
Co2-N12	2.089(2)	N6-Co1-N5	77.73(8)	N11-Co2-N13	92.98(7)
Co2-N13	2.199(2)	N5-Co1-N7	99.06(8)	N13-Co2-N14	77.56(8)
Co2-N14	2.103(2)	N7-Co1-N4	85.42(8)	N14-Co2-N10	93.42(8)

*Table 4.10.2.vii: Co-N bond lengths and N-Co-N cis bond angles for complex **4.8** at 120 K.*

Selected phenyl ring torsion angles

120 K		*240 K*	
C_{imine}-N_{imine}-C_{phenyl}-C_{phenyl}	<(C_{imine}-N_{imine}-C_{phenyl}-C_{phenyl}) °	C_{imine}-N_{imine}-C_{phenyl}-C_{phenyl}	<(C_{imine}-N_{imine}-C_{phenyl}-C_{phenyl}) °
C19-N3-C20-C21	64.5(4)	C19-N3-C20-C21	63(1)
C47-N5-C48-C49	59.3(4)	C47-N5-C48-C49	53(1)
C75-N7-C76-C77	103.8(4)	C75-N7-C76-C77	107(1)
C38-N9-C34-C33	72.0(4)	C38-N9-C34-C33	72.1(9)
C66-N11-C62-C61	78.4(4)	C66-N11-C62-C61	82(1)
C94-N13-C90-C89	63.2(4)	C94-N13-C90-C89	62.4(9)

*Table 4.10.2.viii: Phenyl ring torsion angles for **4.4** at 120 and 240 K*

120 K	
C_{imine}-N_{imine}-C_{phenyl}-C_{phenyl}	<(C_{imine}-N_{imine}-C_{phenyl}-C_{phenyl}) °
C12-N2-C13-C14	59.6(6)
C26-N4-C27-C28	111.5(5)
C45-N6-C41-C40	53.8(6)

*Table 4.10.2.ix: Phenyl ring torsion angles for **4.5** at 120 K*

120 K		*240 K*	
C_{imine}-N_{imine}-C_{phenyl}-C_{phenyl}	<(C_{imine}-N_{imine}-C_{phenyl}-C_{phenyl})	C_{imine}-N_{imine}-C_{phenyl}-C_{phenyl}	<(C_{imine}-N_{imine}-C_{phenyl}-C_{phenyl}) °
C20-N3-C21-C22	57.0(3)	C20-N3-C21-C22	57.6(3)
C51-N5-C52-C53	84.5(3)	C50-N5-C51-C52	57.9(3)
C81-N7-C82-C83	100.3(2)	C81-N7-C82-C83	104.8(3)
C40-N9-C36-C35	96.7(3)	C39-N9-C35-C36	91.3(3)
C70-N11-C66-C65	63.6(3)	C70-N11-C66-C65	104.3(3)
C101-N13-C97-C96	63.5(3)	C101-N13-C97-C96	52.4(3)

*Table 4.10.2.x: Phenyl ring torsion angles for **4.6** at 120 and 240 K*

120 K	
C_{imine}-N_{imine}-C_{phenyl}-C_{phenyl}	**<(C_{imine}-N_{imine}-C_{phenyl}-C_{phenyl}) °**
C20-N3-C21-C22	65.3(3)
C50-N5-C51-C52	77.8(3)
C80-N7-C81-C82	80.4(3)
C39-N9-C35-C34	106.5(3)
C69-N11-C65-C64	59.2(3)
C99-N13-C95-C94	66.7(3)

*Table 4.10.2.xi: Phenyl ring torsion angles for **4.7** at 120 K*

120 K	
C_{imine}-N_{imine}-C_{phenyl}-C_{phenyl}	**<(C_{imine}-N_{imine}-C_{phenyl}-C_{phenyl}) °**
C20-N3-C21-C22	52.2(2)
C50-N5-C51-C52	91.9(3)
C80-N7-C81-C82	105.1(2)
C39-N9-C35-C34	103.5(3)
C69-N11-C65-C64	57.3(2)
C99-N13-C95-C94	56.2(2)

*Table 4.10.2.xii: Phenyl ring torsion angles for **4.8** at 120 K*

	$C_{hydrazone}$-$N_{hydrazone}$-$N_{hydrazone}$-$C_{hydrazone}$	**<($C_{hydrazone}$-$N_{hydrazone}$-$N_{hydrazone}$-$C_{hydrazone}$) °**	**$N_{hydrazone}$-$N_{hydrazone}$**	**d($N_{hydrazone}$-$N_{hydrazone}$) Å**
120 K	C26-N28-N29-C30	157.2(3)	N28-N29	1.402(4)
	C54-N56-N57-C58	161.6(3)	N56-N57	1.399(4)
	C82-N84-N85-C86	109.7(3)	N84-N85	1.388(3)
240 K	C26-N28-N29-C30	155.0(7)	N28-N29	1.38(1)
	C54-N56-N57-C58	157.1(9)	N56-N57	1.38(1)
	C82-N84-N85-C86	114.5(9)	N84-N85	1.42(1)

*Table 4.10.2.xiii: Hydrazone torsion angles and bond lengths for **4.4** at 120 and 240 K*

$C_{hydrazone}$-$N_{hydrazone}$-$N_{hydrazone}$-$C_{hydrazone}$	**<($C_{hydrazone}$-$N_{hydrazone}$-$N_{hydrazone}$-$C_{hydrazone}$) °**	**$N_{hydrazone}$-$N_{hydrazone}$**	**d($N_{hydrazone}$-$N_{hydrazone}$) Å**
C33-N35-N36-C37	129.9(4)	N35-N36	1.387(6)
C19-N21-N21-C19	166.33(5)	N21-N21	1.409(7)

*Table 4.10.2.xiv: Hydrazone torsion angles and bond lengths for **4.5** at 120 K*

	$C_{hydrazone}$-$N_{hydrazone}$-$N_{hydrazone}$-$C_{hydrazone}$	<($C_{hydrazone}$-$N_{hydrazone}$-$N_{hydrazone}$-$C_{hydrazone}$) °	$N_{hydrazone}$-$N_{hydrazone}$	d($N_{hydrazone}$-$N_{hydrazone}$) Å
120 K	C88-N91-N92-C93	125.3(3)	N91-N92	1.392(3)
	C58-N60-N61-C62	148.4(2)	N60-N61	1.397(3)
	C27-N29-N30-C31	126.9(3)	N29-N30	1.392(3)
240 K	C27-N29-N30-C31	147.4(3)	N29-N30	1.399(3)
	C57-N59-N60-N61	125.5(3)	N59-N60	1.393(3)
	C88-N91-N92-C93	129.2(3)	N91-N92	1.388(3)

*Table 4.10.2.xv: Hydrazone torsion angles and bond lengths for **4.6** at 120 and 240 K*

$C_{hydrazone}$-$N_{hydrazone}$-$N_{hydrazone}$-$C_{hydrazone}$	<($C_{hydrazone}$-$N_{hydrazone}$-$N_{hydrazone}$-$C_{hydrazone}$) °	$N_{hydrazone}$-$N_{hydrazone}$	d($N_{hydrazone}$-$N_{hydrazone}$) Å
C27-C29-N30-C31	117.5(3)	N29-N30	1.386(3)
C57-N59-N60-C61	143.9(3)	N59-N60	1.397(4)
C87-N89-N90-C91	159.0(2)	N89-N90	1.405(3)

*Table 4.10.2.xvi: Hydrazone torsion angles and bond lengths for **4.7** at 120 K*

$C_{hydrazone}$-$N_{hydrazone}$-$N_{hydrazone}$-$C_{hydrazone}$	<($C_{hydrazone}$-$N_{hydrazone}$-$N_{hydrazone}$-$C_{hydrazone}$) °	$N_{hydrazone}$-$N_{hydrazone}$	d($N_{hydrazone}$-$N_{hydrazone}$) Å
C27-N29-N30-C31	127.2(2)	N29-N30	1.393(3)
C57-N59-N60-C61	147.5(2)	N59-N60	1.398(3)
C87-N89-N90-C91	122.2(3)	N89-N90	1.393(3)

*Table 4.10.2.xvii: Hydrazone torsion angle and bond lengths for **4.8** at 120 K*

Selected hydrogen bond and other weak supramolecular interactions

	C-H···π[centroid]	d(C-H···π[centroid]) Å	<(C-H···π[centroid]) °
120 K	C21-H21···[C48-C49-C50-C51-C52-C53]	3.007(1)	36.1(1)
	C49-H49···[C76-C77-C78-C79-C80-C81]	2.912(1)	30.4(2)
	C77-H77···[C20-C21-C22-C23-C24-C25]	2.743(1)	10.5(2)
	C33-H33···[C88-C89-C90-C91-C92-C93]	2.814(1)	27.5(1)
	C89-H89···[C60-C61-C62-C63-C64-C65]	2.853(1)	30.7(1)
	C61-H61···[C32-C33-C34-C35-C36-C37]	2.801(1)	21.6(2)
240 K	C21-H21···[C48-C49-C50-C51-C52-C53]	3.041(6)	38.5(3)
	C49-H49···[C76-C77-C78-C79-C80-C81]	3.111(4)	34.5(5)
	C77-H77···[C20-C21-C22-C23-C24-C25]	2.865(3)	8.9(5)
	C33-H33···[C88-C89-C90-C91-C92-C93]	2.940(3)	28.9(3)
	C89-H89···[C60-C61-C62-C63-C64-C65]	2.934(4)	31.6(4)
	C61-H61···[C32-C33-C34-C35-C36-C37]	2.902(3)	19.6(5)

*Table 4.10.2.xviii: C-H···π interactions for complex **4.4** at 120 and 240 K.*

	C-H···π[centroid]	d(C-H···π[centroid]) Å	<(C-H···π[centroid]) °
120 K	C14-H14···[C39-C40-C41-C42-C43-C44]	3.224(2)	45.4(2)
	C40-H40···[C27-C28-C29-C30-C31-C32]	2.994(2)	35.0(2)
	C28-H28···[C13-C14-C15-C16-C17-C18]	2.837(2)	7.8(2)

*Table 4.10.2.xix: C-H···π interactions for complex **4.5** at 120 K.*

	C-H···π[centroid]	d(C-H···π[centroid]) Å	<(C-H···π[centroid]) °
120 K	C22-H22···[C82-C83-C84-C85-C86-C87]	2.897(1)	135.1(2)
	C83-H83···[C52-C53-C54-C55-C56-C57]	2.959(1)	150.9(2)
	C53-H53···[C21-C22-C23-C24-C25-C26]	2.948(1)	33.3(2)
	C35-H35···[C64-C65-C66-C67-C68-C69]	2.841(1)	153.1(2)
	C65-H65···[C95-C96-C97-C98-C99-C100]	3.047(1)	41.1(2)
	C96-H96···[C34-C35-C36-C37-C38-C39]	2.864(1)	41.7(2)
240 K	C22-H22···[C51-C52-C53-C54-C55-C56]	3.245(1)	137.4(2)
	C52-H52···[C82-C83-C84-C85-C86-C87]	3.079(1)	134.4(2)
	C83-H83···[C21-C22-C23-C24-C25-C26]	2.971(1)	23.3(2)
	C34-H34···[C95-C96-C97-C98-C99-C100]	3.083(1)	150.5(2)
	C96-H96···[C64-C65-C66-C67-C68-C69]	2.988(1)	47.1(2)
	C65-H65···[C33-C34-C35-C36-C37-C38]	3.182(1)	27.7(2)

*Table 4.10.2.xx: C-H···π interactions for complex **4.6** at 120 and 240 K.*

	C-H···π[centroid]	d(C-H···π[centroid]) Å	<(C-H···π[centroid]) °
120 K	C22-H22···[C51-C52-C53-C54-C55-C56]	2.937(1)	32.5(1)
	C52-H52···[C81-C82-C83-C84-C85-C86]	2.945(1)	19.4(1)
	C82-H82···[C21-C22-C23-C24-C25-C26]	2.874(1)	25.9(1)
	C34-H34···[C93-C94-C95-C96-C97-C98]	2.867(1)	11.4(1)
	C94-H94···[C63-C64-C64-C66-C67-C68]	2.998(1)	34.6(1)
	C64-H64···[C33-C34-C35-C36-C37-C38]	3.020(1)	27.5(1)

*Table 4.10.2.xxi: C-H···π interactions for complex **4.7** at 120 K.*

	C-H···π[centroid]	d(C-H···π[centroid]) Å	<(C-H···π[centroid]) °
120 K	C22-H22···[C81 C82 C83 C84 C85 C86]	3.039(1)	133.1(2)
	C82-H82···[C51 C52 C53 C54 C55 C56]	3.166(1)	152.8(2)
	C52-H52···[C21 C22 C23 C24 C25 C26]	3.032(1)	30.2(2)
	C34-H34···[C63 C64 C65 C66 C67 C68]	2.923(1)	156.4(1)
	C64-H64···[C93 C94 C95 C96 C97 C98]	3.178(1)	42.5(2)
	C94-H94···[C33 C34 C35 C36 C37 C38]	3.028(1)	43.6(2)

*Table 4.10.2.xxii: C-H···π interactions for complex **4.8** at 120 K.*

D-H···A	d(D-H) Å	d(D-H···A) Å	d(D···A) Å	<(D-H···A) °	Symmetry Code
N16-H16···O124	0.881(3)	2.028(3)	2.871(4)	159.8(2)	x,y,z 1-x,2-y,1-z
N41-H41···O165	0.880(4)	2.074(5)	2.880(6)	151.9(3)	x,y,z x,y,1+z
N44-H44···N171	0.880(4)	2.12(2)	2.92(2)	151.6(4)	x,y,z -x,1-y,-z
N69-H69···O170	0.879(4)	1.925(7)	2.791(8)	168.3(4)	x,y,z 1-x,1-y,1-z
N72-H72···O137	0.881(4)	1.920(5)	2.799(6)	176.2(3)	x,y,z x,1+y,z
N97-H97···O101	0.880(4)	1.92(1)	2.78(2)	166.4(6)	x,y,z x,-1+y,z
O170-H17J···O165	0.852(7)	2.343(5)	3.07(1)	143.8(7)	x,y,z 1-x,1-y,1-z

*Table 4.10.2.xxiii: The hydrogen bond interactions for **4.4** at 120 K*

D-H···A	d(D-H) Å	d(D-H···A) Å	d(D···A) Å	<(D-H···A) °	Symmetry Code
N9-H9···O52	0.859(6)	2.066(8)	2.92(1)	176.0(3)	x,y,z
N23-H23···O62	0.860(5)	2.260(3)	2.938(5)	135.8(4)	x,y,z 1+x,1-y,1/2+z
N48-H48···O58	0.860(4)	1.907(5)	2.765(6)	174.7(4)	x,y,z
O58-H58B···O61	0.849(8)	2.078(7)	2.87(1)	154.9(3)	x,y,z

*Table 4.10.2.xxiv: The hydrogen bond interactions for **4.5** at 120 K*

D-H···A	d(D-H) Å	d(D-H···A) Å	d(D···A) Å	<(D-H···A) °	Symmetry Code
N16-H16···F119	0.860(3)	1.949(2)	2.781(3)	162.5(2)	x, y, z 2-x, 1-y, 2-z
N47-H47···F110	0.859(2)	2.044(8)	2.838(8)	141.8(3)	x, y, z 1+x, y, z
N77-H77···F127	0.859(3)	2.01(1)	2.88(1)	150.9(4)	x, y, z 2-x, 1-y, 2-z
N44-H44···F118	0.860(2)	2.110(3)	2.875(3)	147.9(2)	x, y, z 1-x, y, 1-z
N74-H74···F140	0.860(2)	1.924(7)	2.78(1)	165.3(3)	x, y, z -1+x, y, z
N105-H105···F116	0.860(3)	1.949(7)	2.74(1)	148.0(3)	x, y, z 1-x, 1-y, 1-z

*Table 4.10.2.xxv: The hydrogen bond interactions for **4.6** at 120 K.*

D-H···A	d(D-H) Å	d(D-H···A) Å	d(D···A) Å	<(D-H···A) °	Symmetry Code
N16-H16···O115	0.859(2)	2.060(2)	2.802(3)	144.1(2)	x,y,z x,1/2-y,-1/2+z
N43-H43···O125	0.861(3)	1.955(3)	2.815(4)	176.6(2)	x,y,z -1+x,y,z
N46-H46···O126	0.859(3)	2.075(3)	2.856(4)	151.0(2)	x,y,z 2-x,1-y,1-z
N73-H73···O108	0.861(3)	2.064(3)	2.925(4)	178.6(2)	x,y,z x,1/2-y,1/2+z
N76-H76···O124	0.860(3)	1.978(3)	2.829(4)	169.6(2)	x,y,z x,y,-1+z
N103-H103···O109	0.859(3)	1.985(2)	2.825(3)	165.4(2)	x,y,z x,y,1+z

*Table 4.10.2.xxvi: The hydrogen bond interactions for **4.7** at 120 K.*

D-H···A	d(D-H) Å	d(D-H···A) Å	d(D···A) Å	<(D-H···A) °	Symmetry Code
N16-H16···F115	0.881(2)	2.110(2)	2.870(3)	144.1(2)	x,y,z 2-x,2-y,2-z
N46-H46···F107	0.881(2)	2.064(5)	2.784(5)	138.3(2)	x,y,z 1+x,y,z
N76-H76···F121	0.880(2)	2.012(2)	2.835(3)	155.2(2)	x,y,z 2-x,2-y,2-z
N43-H43···F116	0.880(2)	2.049(2)	2.857(3)	152.1(2)	x,y,z 1-x,1-y,1-z
N73-H73···F127	0.880(2)	1.879(10)	2.76(1)	178.4(4)	x,y,z -1+x,y,z
N103-H103···F109	0.880(2)	1.964(3)	2.810(4)	160.5(2)	x,y,z 1-x,2-y,1-z

*Table 4.10.2.xxvii: The hydrogen bond interactions for **4.8** at 120 K.*

4.10.3 TGA

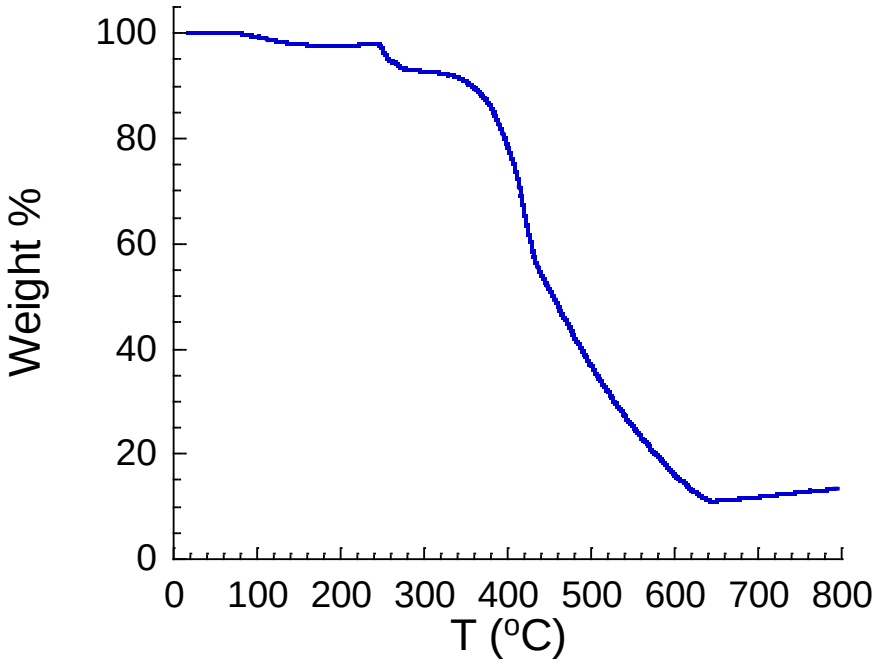

*Figure 4.10.3.i: TGA plot for complex **4.4**.*

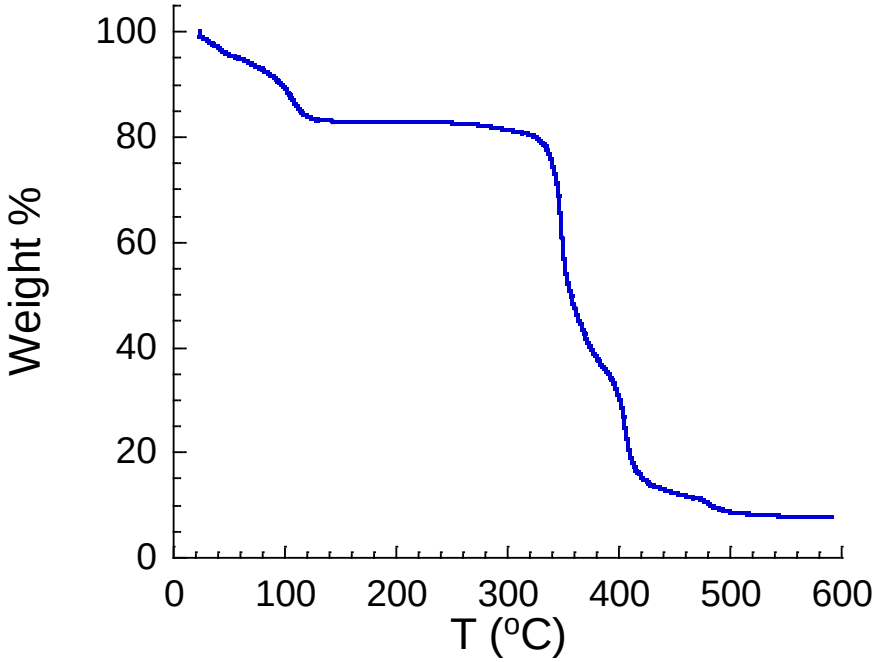

*Figure 4.10.3.ii: TGA plot for complex **4.5**.*

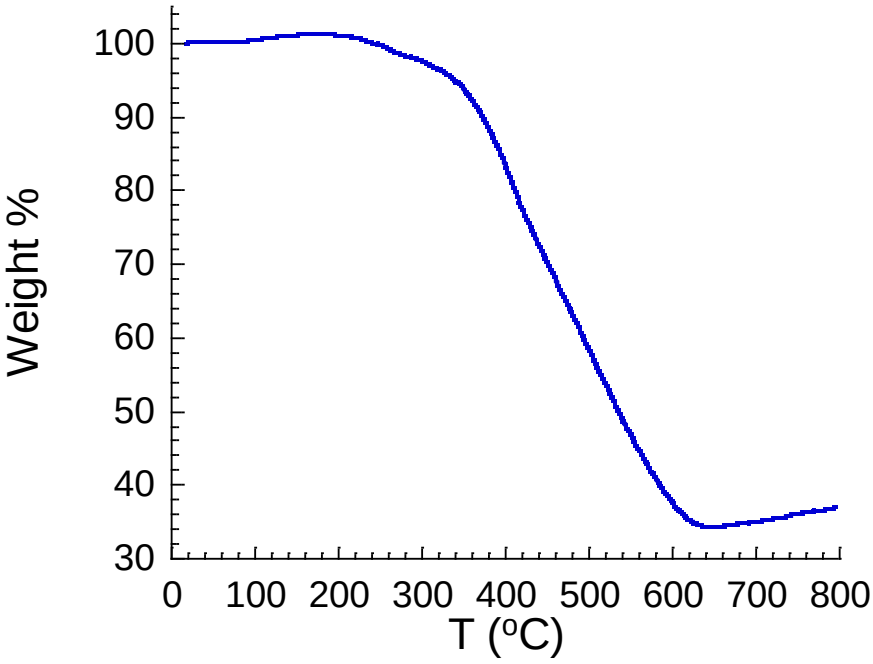

*Figure 4.10.3.iii: TGA plot for complex **4.6**.*

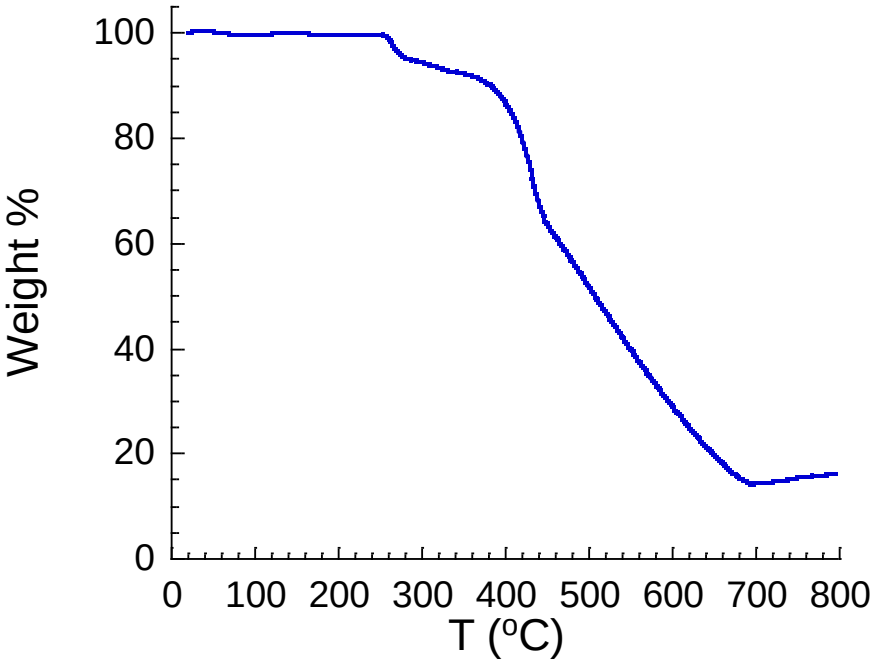

*Figure 4.10.3.iv: TGA plot for complex **4.7**.*

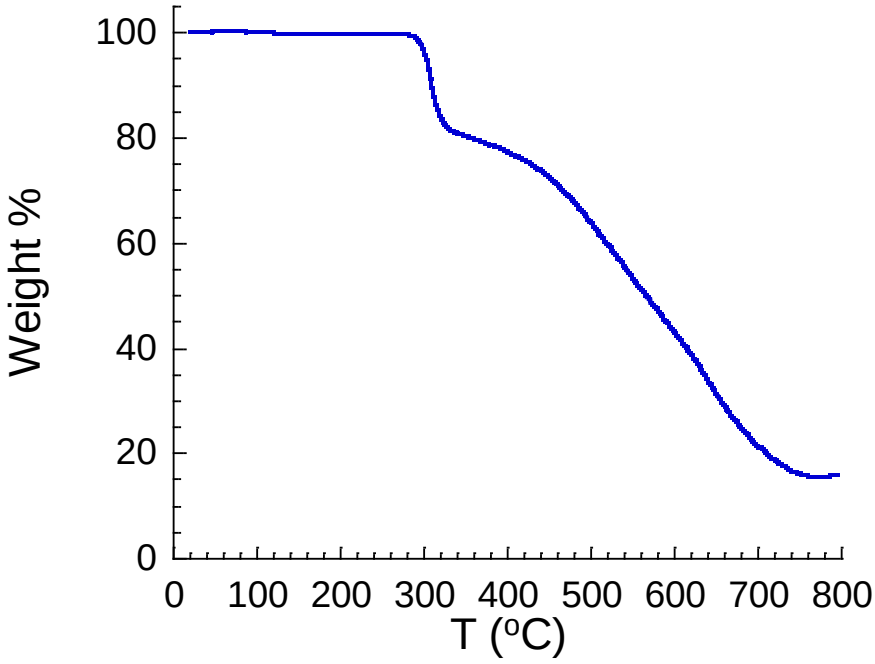

*Figure 4.10.3.v: TGA plot for complex **4.8**.*

4.10.4 Magnetic susceptibility data

4.10.4.i Ideal solution model

$$\chi T = \chi T_{LS} + \frac{\chi T_{HS} - \chi T_{LS}}{1 + exp\left(\frac{\Delta S}{R}\left(\frac{T_{1/2}}{T - 1}\right)\right)}$$

χT_{HS} is the χT value of the complex in the HS state, χT_{LS} is the χT value of the complex in the LS state, ΔS is the entropy of SCO, $T_{1/2}$ is the temperature at which there are even populations of the HS and LS states. $\Delta H = T_{1/2}\Delta S$, where ΔH is the enthalpy of the SCO.

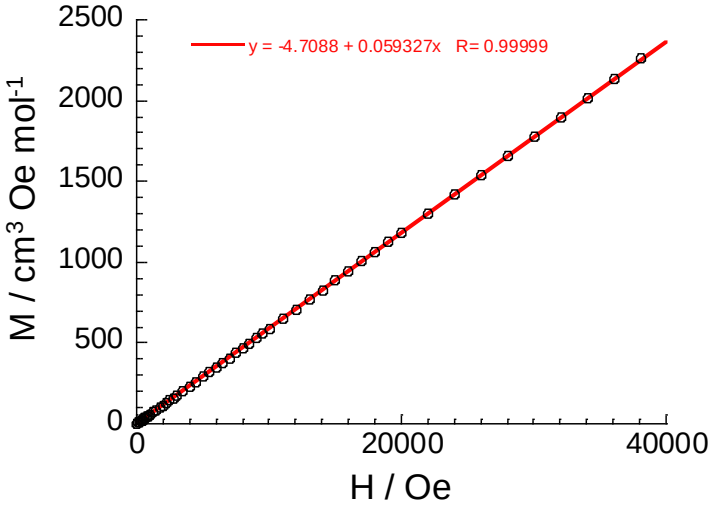

*Figure 4.10.4.i: The M vs. H plot for the dried sample of **4.15** at 100 K.*

4.10.5 AC magnetic susceptibility data

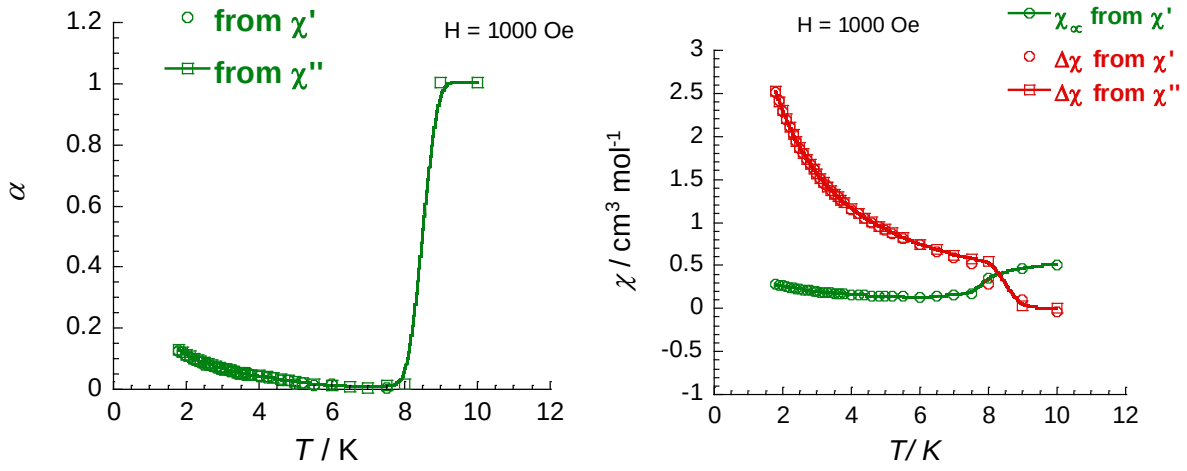

*Figure 4.10.5.i: The temperature dependence of the α factor (right) and of Δχ and $\chi_{\propto}$ for the dried sample of **4.15** with an applied field of 1000 Oe.*

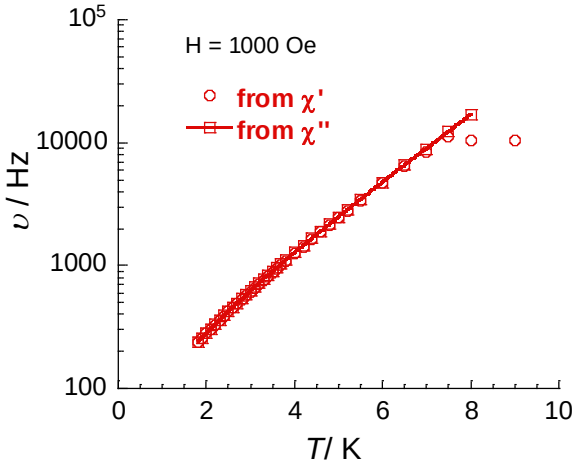

*Figure 4.10.5.ii: The temperature dependence of the α factor (right) and of Δχ and $\chi_{\propto}$ for the dried sample of **4.15** with an applied field of 1000 Oe.*

4.10.6 Absolute reflectivity

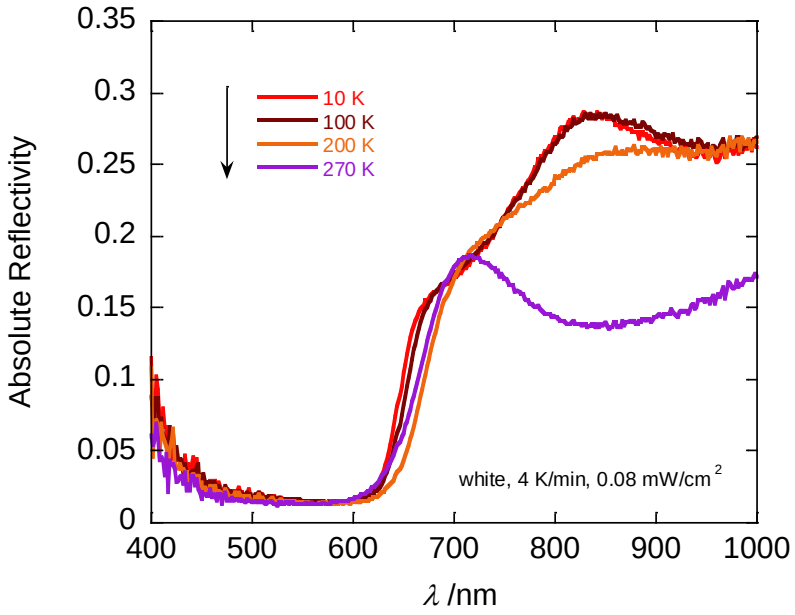

*Figure 4.10.6.i: Selected surface reflectivity measurements of **4.4** collected with a white light spectroscopic source (0.08 mW cm^{-2}) as a function of temperature during heating mode from 10 to 270 K.*

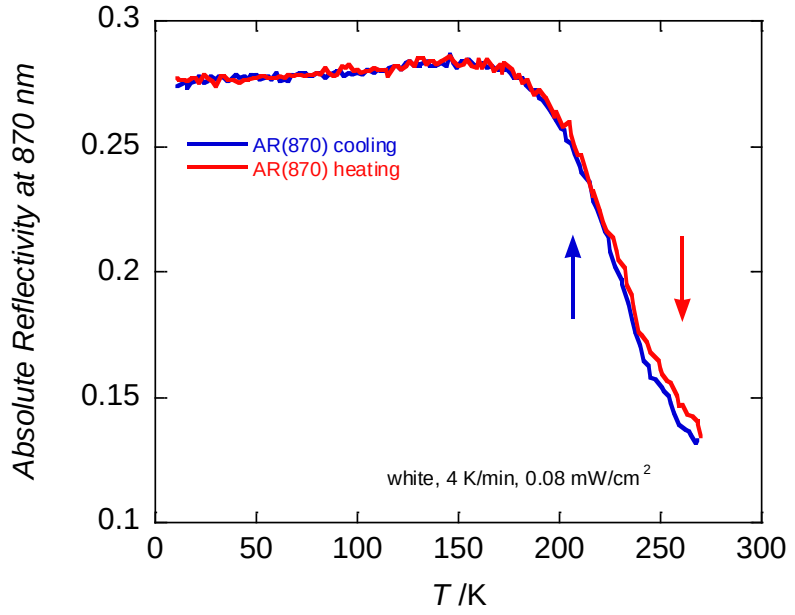

*Figure 4.10.6.ii: Thermal evolution of the reflectivity signal of **4.4** recorded at λ = 870 nm ± 5 nm during cooling mode, 270 to 10 K (blue trace) and heating mode 10 to 270 K (red trace).*

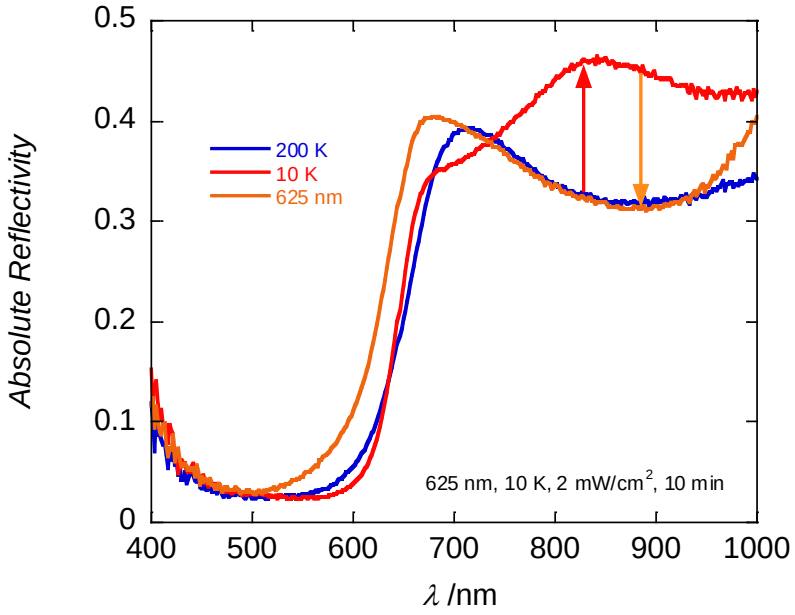

*Figure 4.10.6.iii: Surface reflectivity measurements of **4.4** collected with a white light spectroscopic source (0.08 mW cm^{-2}) at 200 K, 10 K and 10 K after irradiation with 625 nm light (2 mW cm^{-2}) at 10 K for 10 minutes.*

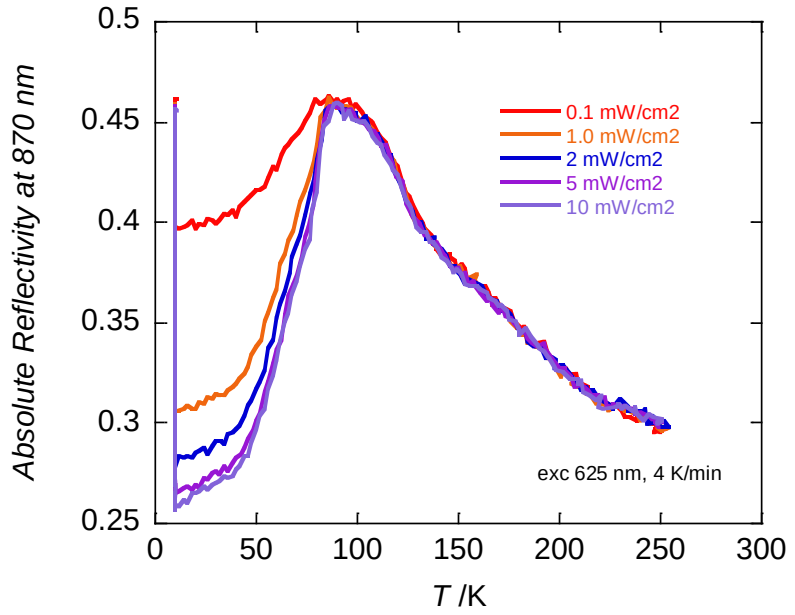

*Figure 4.10.6.iv: Thermal evolution of the reflectivity signal of **4.4** recorded at λ = 870 nm ± 5 nm during irradiation with 625 nm light at various intensities, followed by a heating cycle from 10 to 270 K.*

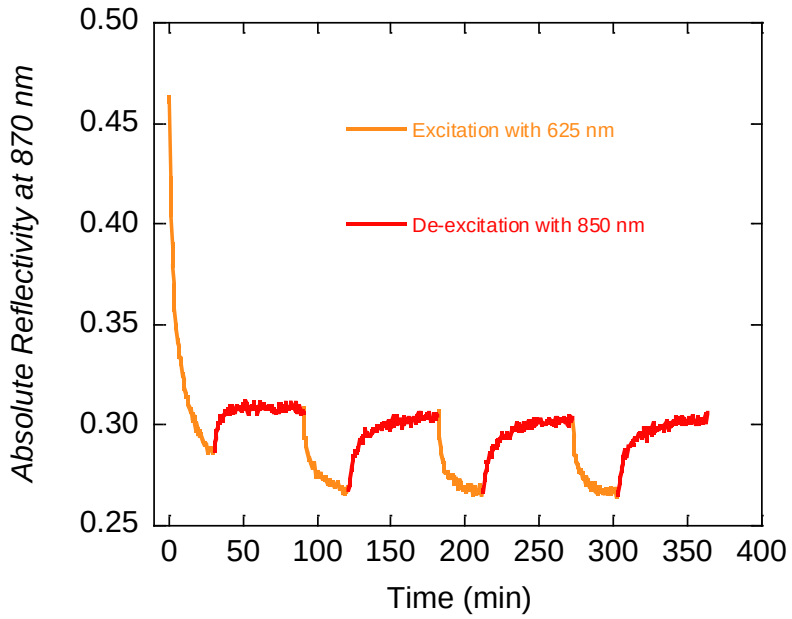

*Figure 4.10.6.v: Reflectivity signal of **4.4** recorded at λ = 870 ± 5 nm for four cycles of photo-excitation (625 nm) and photo de-excitation (850 nm) at 10 K.*

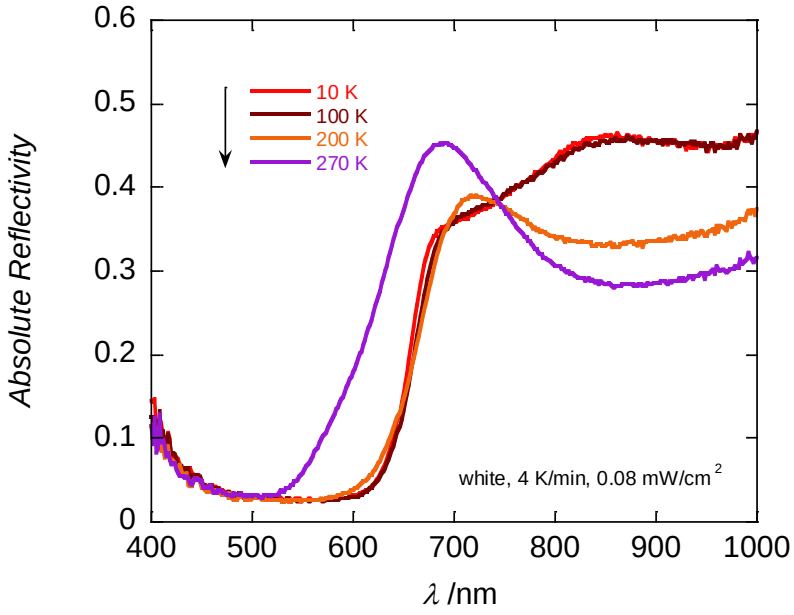

*Figure 4.10.6.vi: Selected surface reflectivity measurements of **4.5** collected with a white light spectroscopic source (0.08 mW cm^{-2}) as a function of temperature during heating mode between 10 to 270 K.*

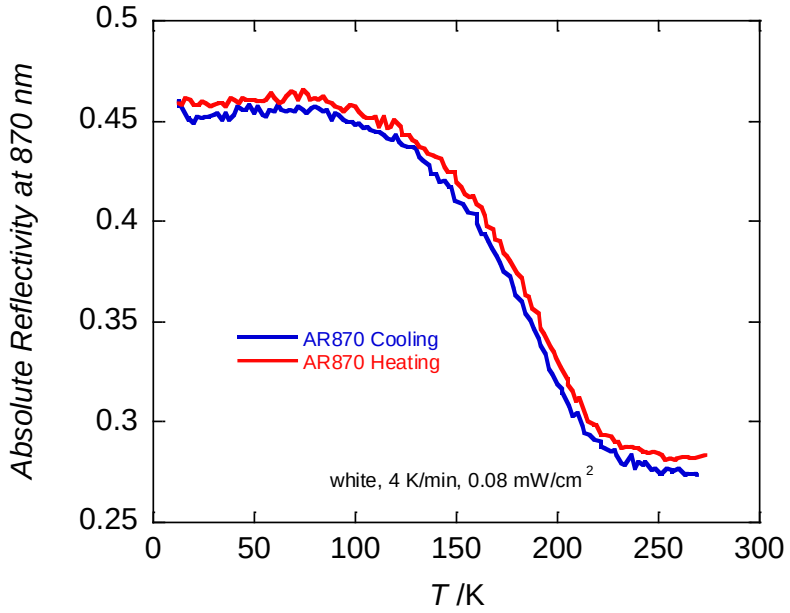

Figure 4.10.6.vii: Thermal evolution of the reflectivity signal of ***4.5*** *recorded at λ = 870 nm ± 5 nm during cooling mode, 270 to 10 K (blue trace) and heating mode 10 to 270 K (red trace).*

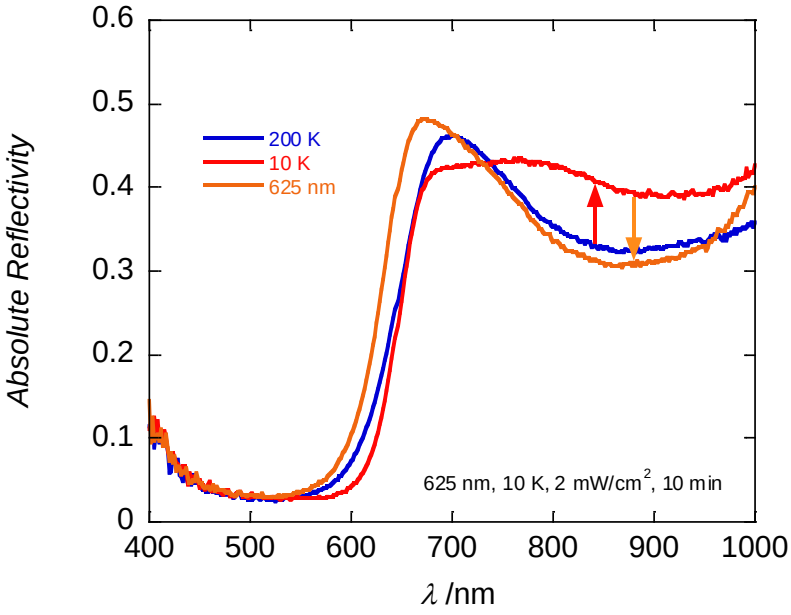

Figure 4.10.6.viii: Surface reflectivity measurements of ***4.5*** *collected with a white light spectroscopic source (0.08 mW cm^{-2}) at 200 K, 10 K and 10 K after irradiation with 625 nm light (2 mW cm^{-2}) at 10 K for 10 minutes.*

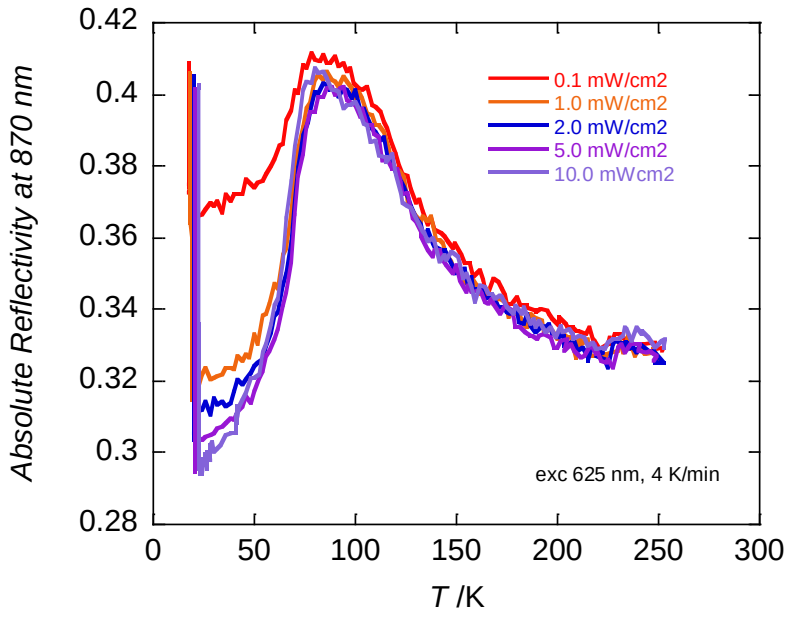

Figure 4.10.6.ix: Thermal evolution of the reflectivity signal of ***4.5*** *recorded at λ = 870 nm ± 5 nm during irradiation with 625 nm light at various intensities, followed by a heating cycle from 10 to 270 K.*

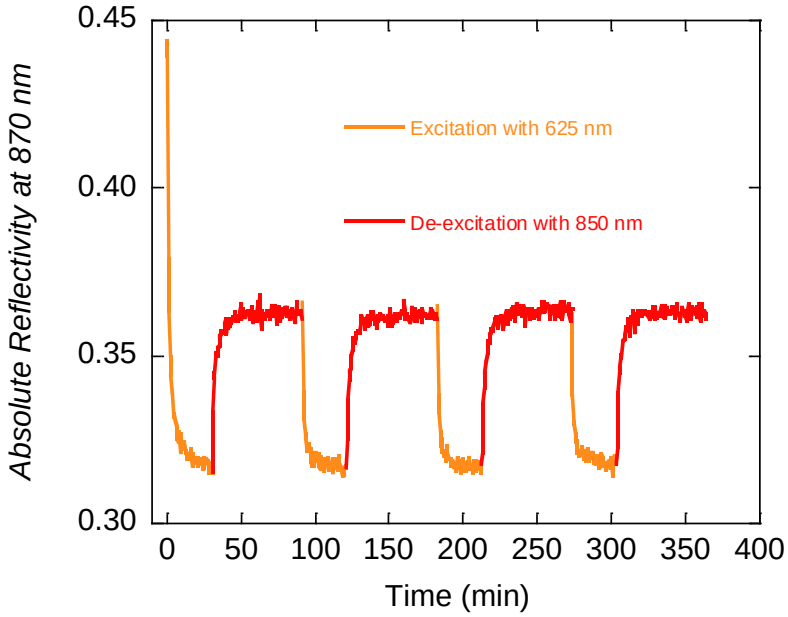

Figure 4.10.6.x: Reflectivity signal of ***4.5*** *recorded at λ = 870 ± 5 nm for four cycles of photo-excitation (625 nm) and photo de-excitation (850 nm) at 10 K.*

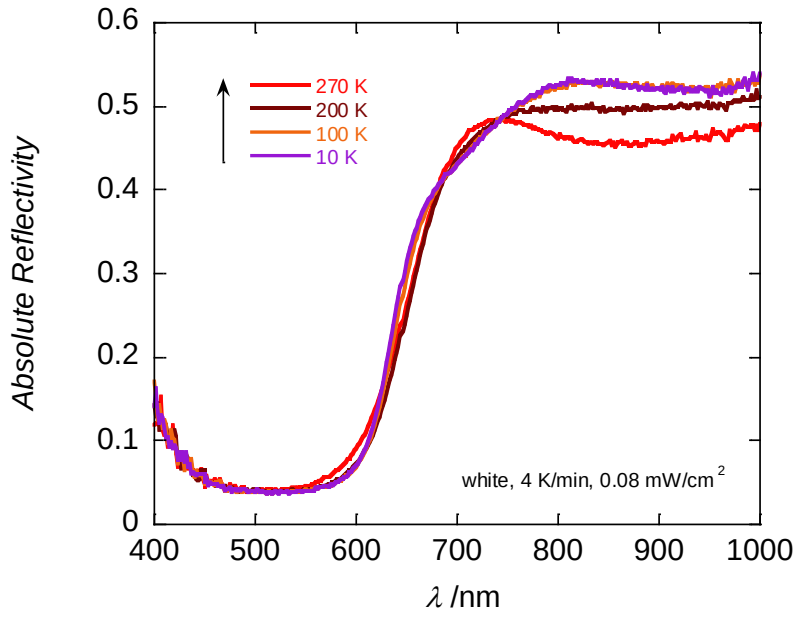

*Figure 4.10.6.xi: Selected surface reflectivity measurements of **4.6** collected with a white light spectroscopic source (0.08 mW cm^{-2}) as a function of temperature during heating mode between 10 to 270 K.*

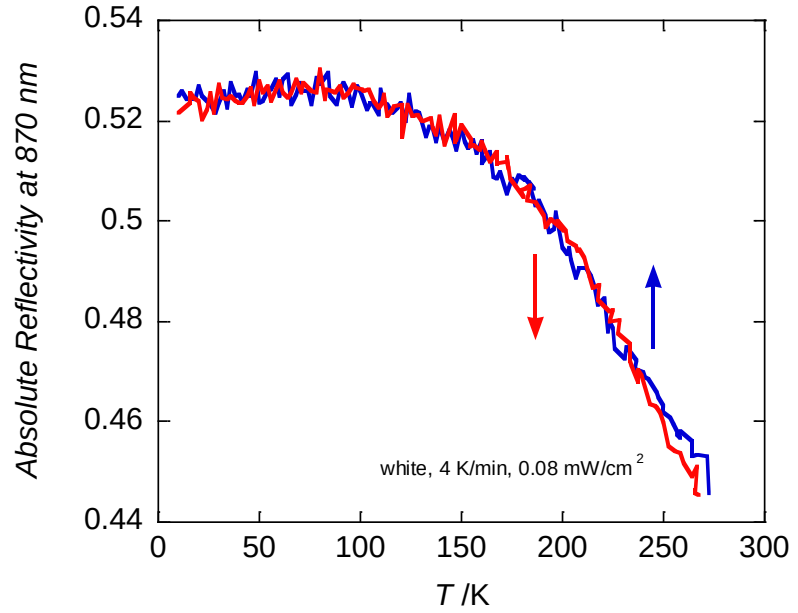

*Figure 4.10.6.xii: Thermal evolution of the reflectivity signal of **4.6** recorded at λ = 870 nm ± 5 nm during cooling mode, 270 to 10 K (blue trace) and heating mode 10 to 270 K (red trace).*

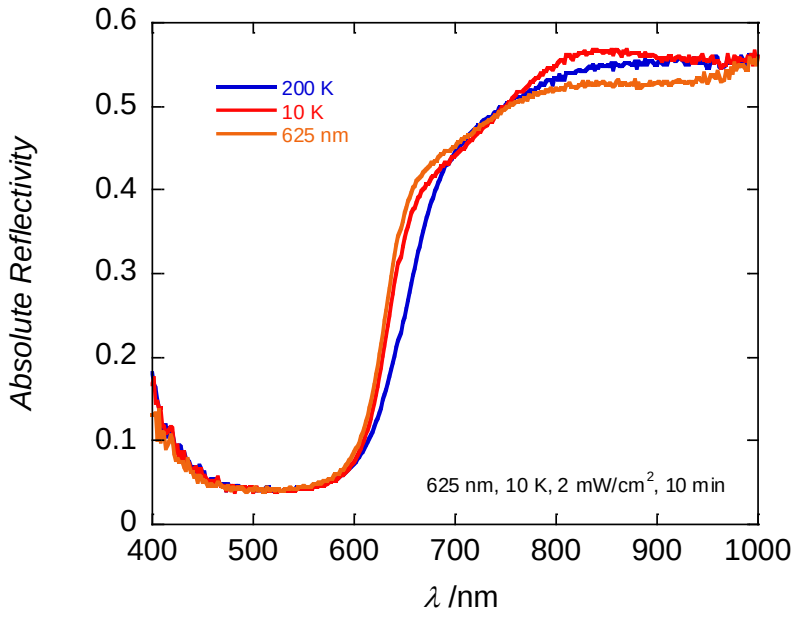

*Figure 4.10.6.xiii: Surface reflectivity measurements of **4.6** collected with a white light spectroscopic source (0.08 mW cm^{-2}) at 200 K, 10 K and 10 K after irradiation with 625 nm light (2 mW cm^{-2}) at 10 K for 10 minutes.*

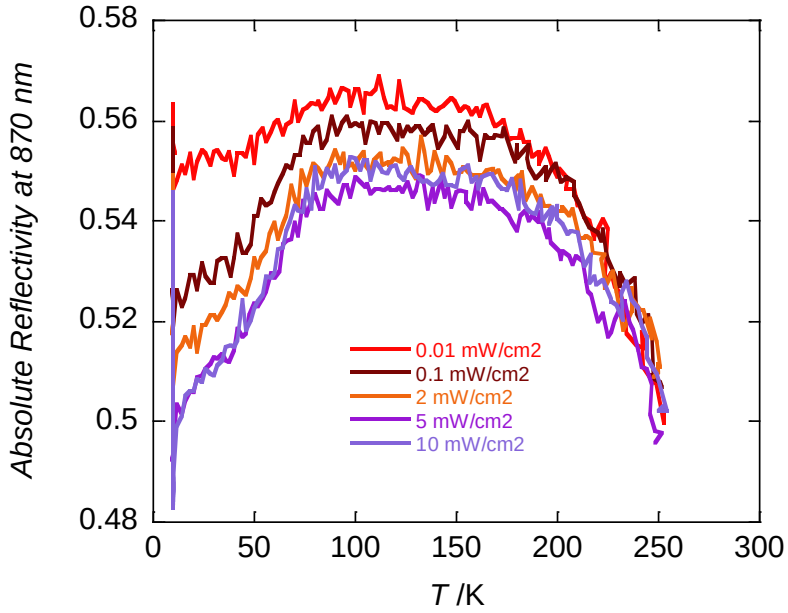

*Figure 4.10.6.xiv: Thermal evolution of the reflectivity signal of **4.6** recorded at λ = 870 nm ± 5 nm during irradiation with 625 nm light at various intensities, followed by a heating cycle from 10 to 270 K.*

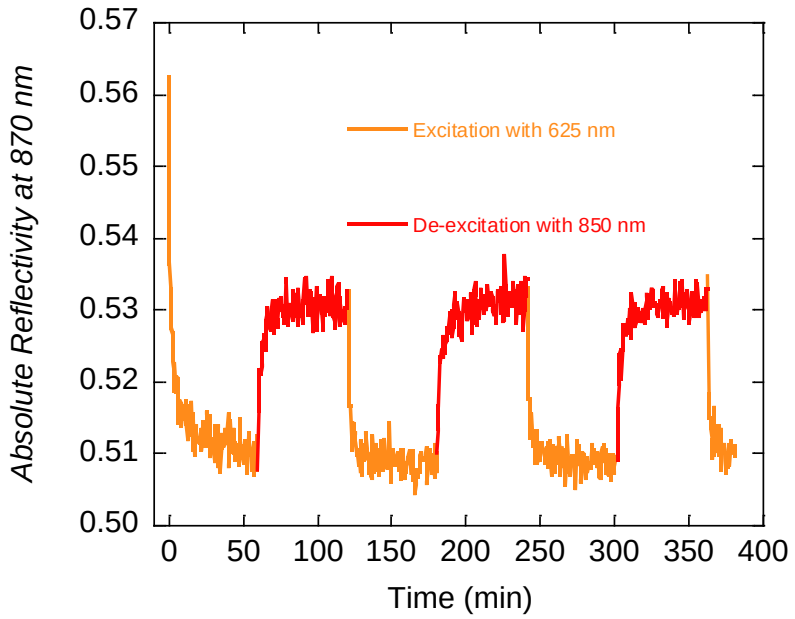

Figure 4.10.6.xv: Reflectivity signal of ***4.6*** *recorded at λ = 870 ± 5 nm for four cycles of photo-excitation (625 nm) and photo de-excitation (850 nm) at 10 K.*

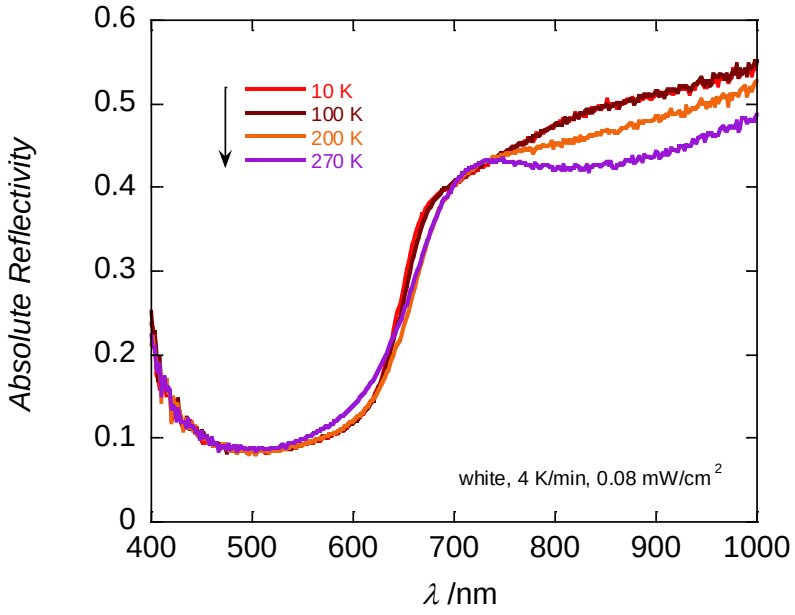

Figure 4.10.6.xvi: Selected surface reflectivity measurements of ***4.7*** *collected with a white light spectroscopic source (0.08 mW cm^{-2}) as a function of temperature during heating mode between 10 to 270 K.*

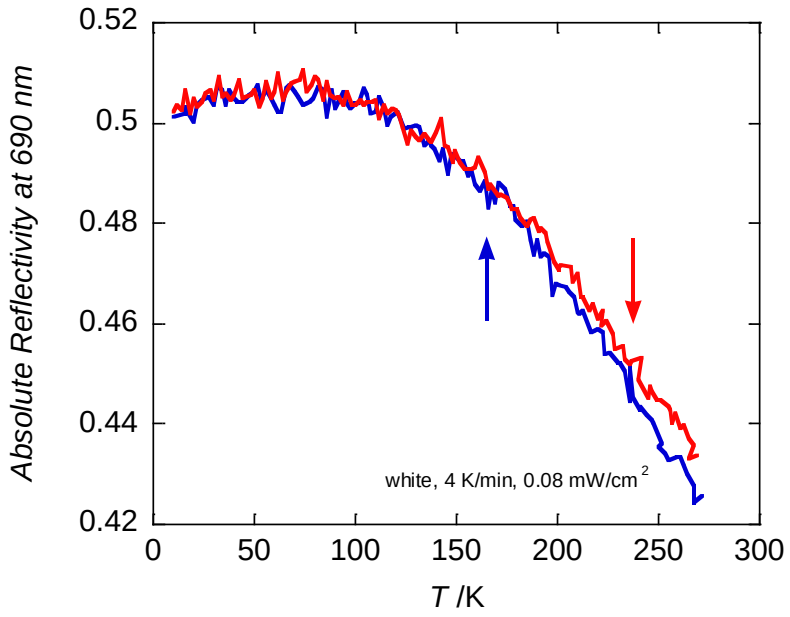

Figure 4.10.6.xvii: Thermal evolution of the reflectivity signal of ***4.7*** *recorded at λ = 870 nm ± 5 nm during cooling mode, 270 to 10 K (blue trace) and heating mode 10 to 270 K (red trace).*

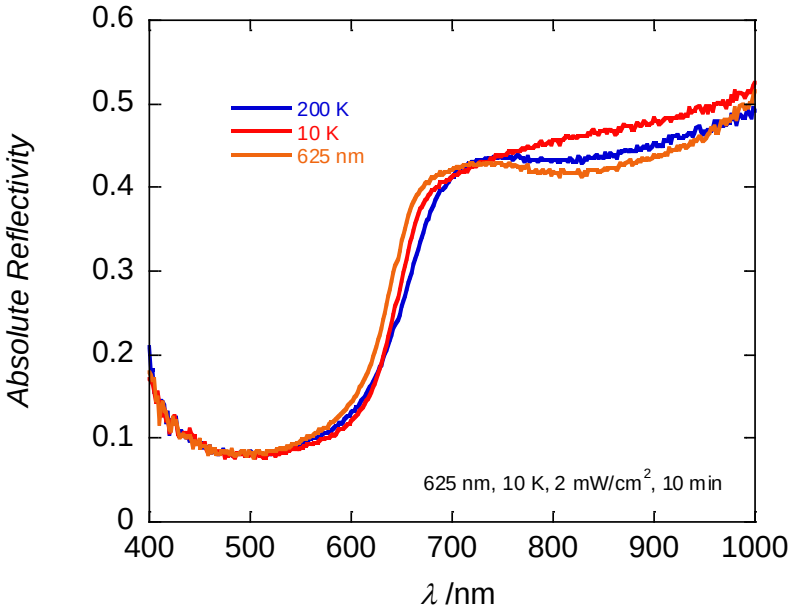

Figure 4.10.6.xviii: Surface reflectivity measurements of ***4.7*** *collected with a white light spectroscopic source (0.08 mW cm^{-2}) at 200 K, 10 K and 10 K after irradiation with 625 nm light (2 mW cm^{-2}) at 10 K for 10 minutes.*

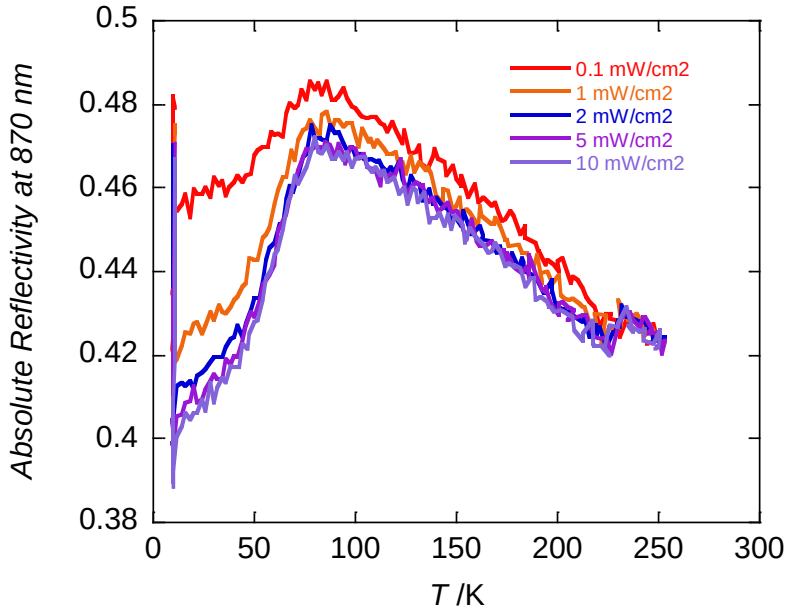

*Figure 4.10.6.xix: Thermal evolution of the reflectivity signal of **4.7** recorded at λ = 870 nm ± 5 nm during irradiation with 625 nm light at various intensities, followed by a heating cycle from 10 to 270 K.*

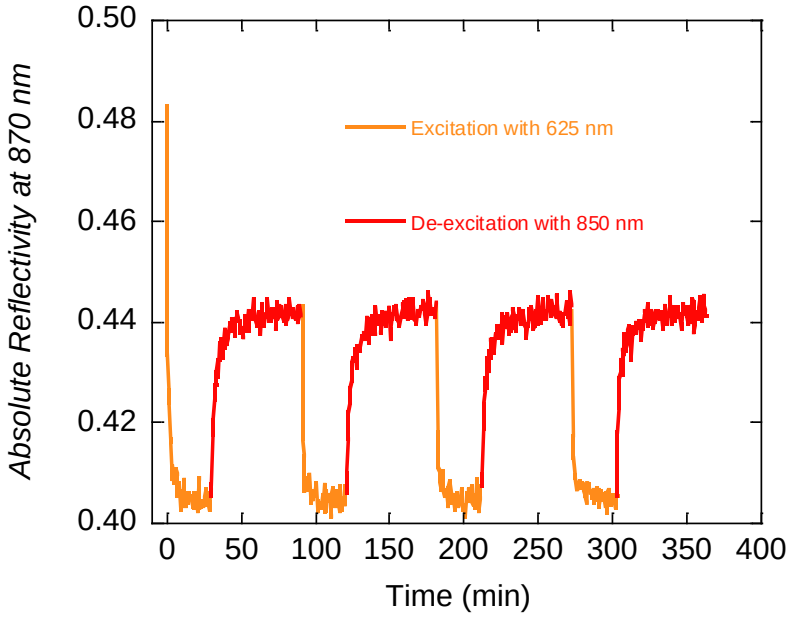

*Figure 4.10.6.xx: Reflectivity signal of **4.13** recorded at λ = 870 ± 5 nm for four cycles of photo-excitation (625 nm) and photo de-excitation (850 nm) at 10 K.*

Chapter Five

SCO of Dinuclear Triple Helicates Functionalized with Mesogenic Substituents

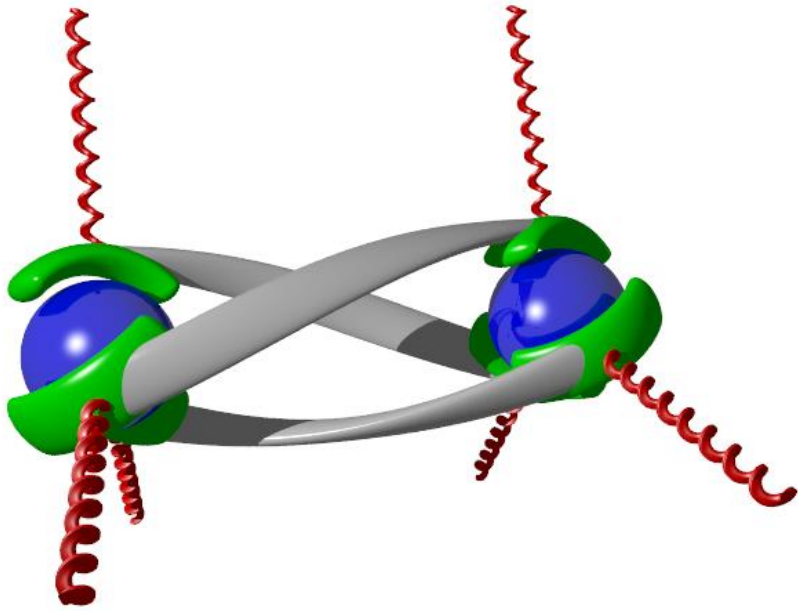

5.1 Introduction

5.1.1 Spin crossover helicates

A general introduction to SCO helicates has been provided in the preceding chapters. Consequently, only a discussion of specific examples directly relevant to the following work will be given. The most widely studied family of SCO helicates are formed from imidazolylimine based ligands, containing bis-aromatic imines bridged by either an oxo, methylene or sulfide linker (*Figure 5.1.1.i*). Previous work by the Kruger group has concerned the oxo bridged ligand synthesised from 4,4'-oxydianiline and N-methyl-2-imidazolecarboxaldehyde. Two different solvates of the perchlorate salt of the Fe(II) complex have been reported. One demonstrated complete SCO for both Fe(II) centres,[316] while the other exhibits partial SCO.[320] The groups of Hanon and Li have both reported helicates featuring a methylene linker and 4-imidazole moieties.[311, 319] The SCO behaviour of both complexes were broadly similar with only partial SCO occurring with a small hysteresis loop. Li and co-workers further expanded this family of helicates with oxo and sulfide bridged ligands.

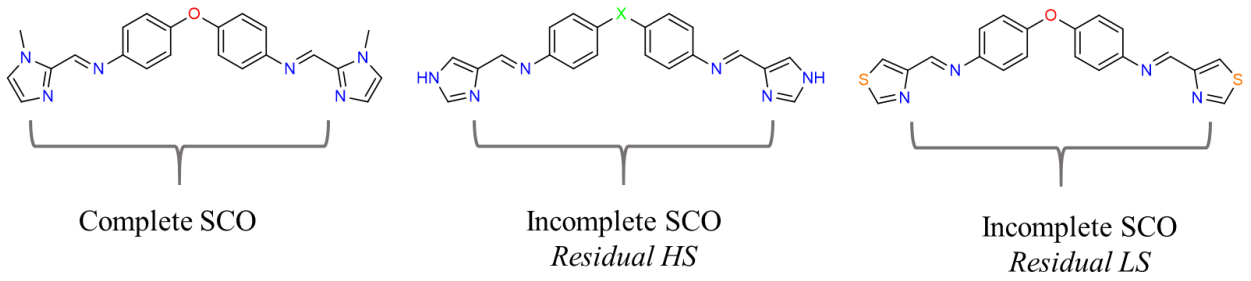

Figure 5.1.1.i: The family of bis-imiazolylimine based ligands of relevance to the work in this chapter. (left) The helicate complexes containing this ligand display either partial or complete SCO depending on the solvate. (middle) Helicate complexes containing this ligand type have been reported for x = O, CH_2 and S all of which exhibit partial SCO with a significant proportion of Fe(II) centres in the HS state at low temperature. (right) The Helicate complex containing this ligand exhibited partial SCO which is incomplete at 400 K.

Finally, Li and co-workers have reported a helicate based on the oxo bridged core and 4-thiazolylimine coordinating motif.[315] While strictly not an imidazolylimine based ligand, it possesses a strong similarity to the ligands and the resultant helicates. The replacement of the

nitrogen in the 1-position of the imidazole with a sulfur to give the thiazole analogue has a pronounced effect on the SCO behaviour. The ligand field strength is significantly stronger than that of the imidazole derivative, resulting in incomplete SCO occurring above room temperature.

5.1.2 Spin crossover mesogens

The functionalisation of Fe(II) complexes with mesogenic substituents is a rapidly growing area in SCO chemistry. These complexes may be neutral, featuring anionic ligands[300, 415] or charged, featuring neutral ligands.[352-353, 451-453] The former has been discussed briefly in chapter three, while the latter is the focus of this chapter. Complexes based on tripodal imiazolylimine and pyridylimine ligands have formed the basis for a number of studies of SCO mesogens.[352-353, 454] In these cases, the mesogens are long chain alkyl substituents attached via an alkoxy link to the pyridine ring or directly to the nitrogen of the imidazole ring. The synthesis of the 4-hydroxy-6-methyl pyridinecarboxaldehyde precursors requires a multistep synthesis while the imidazole precursors are commercially available and therefore, these ligands are more readily synthesised. When the alkyl-substituents are relatively short, *e.g.* butyl chains, the complexes form crystalline solids and can therefore be characterised by single crystal X-ray diffraction. In some cases, even complexes with long alkyl substituents such as decyl chains form crystalline solids.[415] In these cases, the SCO behaviour is intimately linked to the conformation of the chains, whether it be an order-disorder transition or the adoption of a new conformation by the alkyl chains. These alkyl chain reorganisations can result in unusual hysteretic behaviour associated with the SCO or so-called "reverse-SCO" reported by Hayami and co-workers.[455] In some cases, long alkyl substituents can result in the complex undergoing a phase change from a crystalline solid to a mesogenic phase upon heating of the complex.[456]

The orientation of the alkyl substituents has a strong influence on the liquid crystalline properties.[353] The 2-imidazolylimine based ligands coordinate to Fe(II) in a *fac* configuration due to their tripodal nature. This results in the alkyl chains being orientated outwards in the same plane in a triangular manner. This arrangement of star-shaped mesogens assembles into a one-dimensional column with the charged metal core and anions in the centre with the non-polar mesogenic tails radiating outwards (*Figure 5.1.2.i*). Depending of the position of the alkyl substituents on the pyridine ring, the tripodal pyridylimine based complexes can form two types of mesogenic phases.[352] When the alkoxy groups are in the 3-position, star-shaped mesogens much

like those described for the imidazolylimine based ligands are formed. Instead, if the alkoxy groups are in the 5-position of the pyridine rings, the alkyl chains are orientated in the same direction. This results in the formation of ionic lipid bilayers (*Figure 5.1.2.i*). Biphenyl terminated alkyl substituents are of interest as the biphenyl substituents promote more ordered liquid crystalline materials.[457-458]

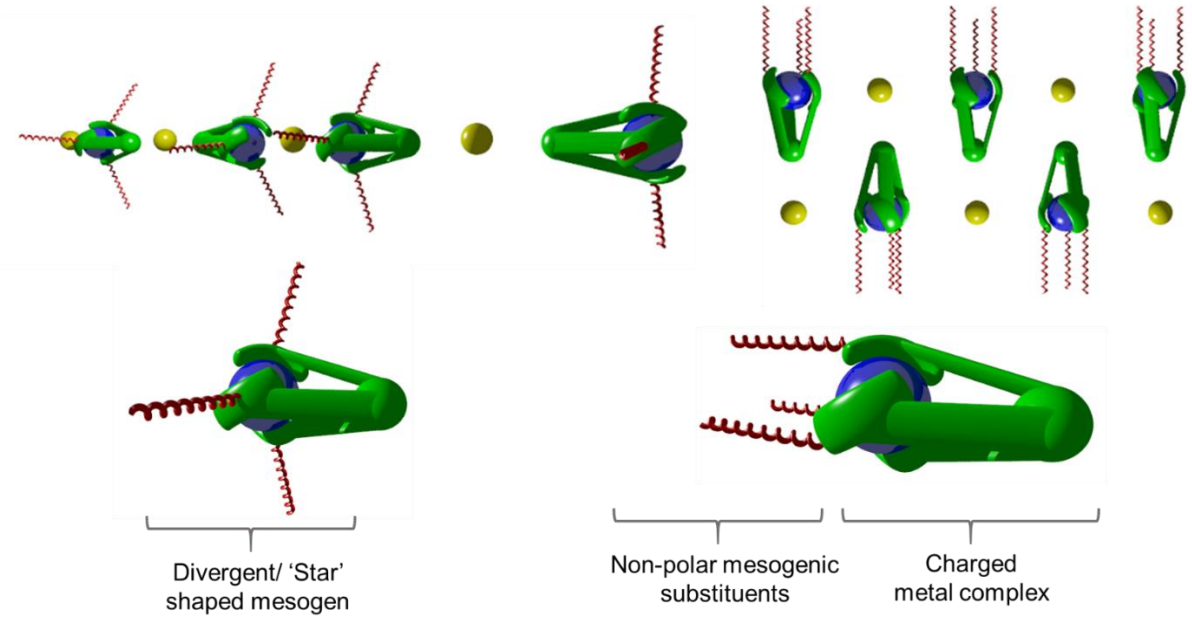

Figure 5.1.2.i: A schematic presentation of the two types of mesogenic phase proposed by Real and co-workers containing mononuclear Fe(II) imidazolylimine and pyridylimine complexes.[352-353] The phase on the left is formed with ligands containing functionalised 2-imidazole ligands or benzimidazole ligands for which the mesogenic substituents are divergent or 'star' shaped. The phase on the right is formed with alkoxy functionalised ligands for which the mesogenic substituents are all orientated in the same direction.

5.1.3 Scope of research

The following chapter details work carried out using N-alkyl-2-imidazole based ligands. These have been combined with diamine molecules to form bis-bidentate imidazolylimine ligands known to form dinuclear triple helicates which exhibit SCO. These ligands coordinate to Fe(II) in a *fac* manner and therefore the arrangement of the imidazolylimine moieties around the Fe(II) centres is analogous to that of the tripodal ligands. Therefore, when functionalised with mesogenic substituents, the helicates are anticipated to form the star-shaped mesogens. Two ligands are

utilised in this chapter, the first **L5.3** is derived from 4,4'-oxydianiline. The second, **L5.4**, is derived from 4,4'-diaminodiphenylmethane. The Fe(II) helicate complex based on the 4,4'-diaminodiphenylmethane core with the N-methyl-2-imidazolecarboxaldehyde moiety has not been reported in the literature and therefore the SCO behaviour is unknown.

5.2 Ligand synthesis

The N-alkyl-2-imidazolecarboxaldehyde precursor was synthesised via a two-step synthetic procedure (*Figure 5.2.1*). 4-Hydroxybiphenyl was reacted with an excess of 1,10-dibromodecane and potassium carbonate in methylethyl ketone. The product 4-((10-bromodecyl)oxy)biphenyl was purified via column chromatrography, eluting with DCM to give a white crystalline product in a 43% yield.

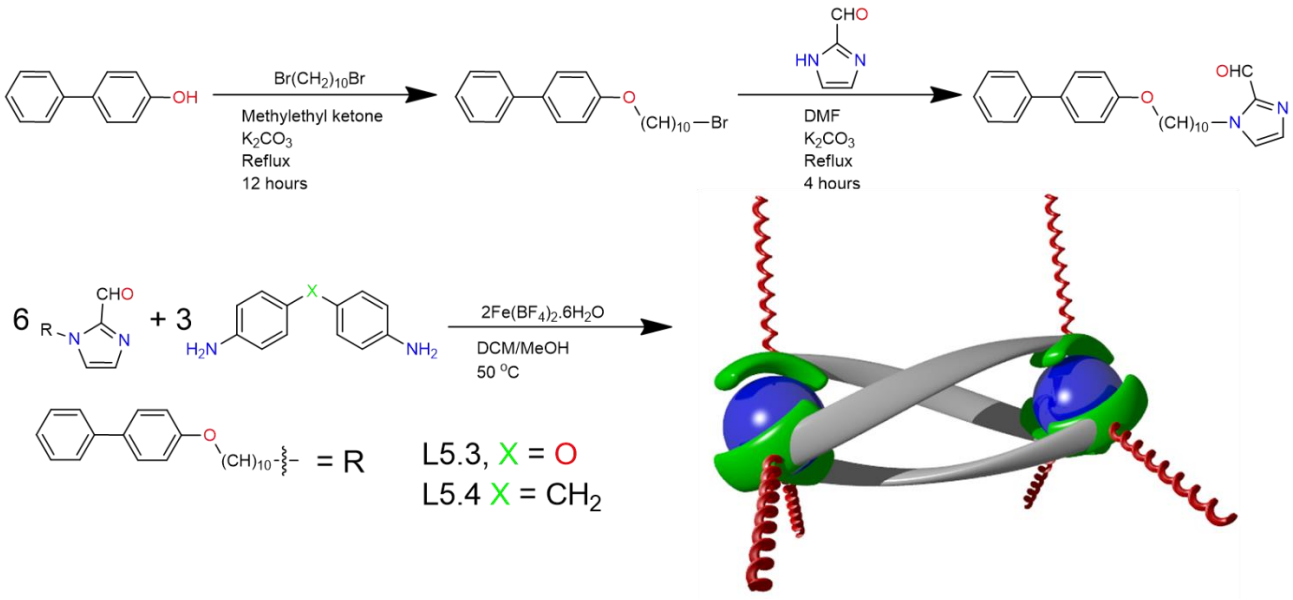

*Figure 5.2.1: (top) The two-step synthesis scheme employed to synthesise the N-functionalized 2-imidazolecarboxaldehyde precursor. (bottom) The sub-component self-assembly methodology used to synthesise complexes **5.5** and **5.6** forming the ligands **L5.3** and **L5.4** respectively in situ. Schematic of **5.5** and **5.6** shown on the right with Fe(II) centres (blue) coordinated to the imidaszolylimine moieties (green) bridged by the ligand core (grey) and the point of a attachment for the mesogenic substituents (red helicies).*

2-Imidazolecarboxaldehyde was reacted with 4-((10-bromodecyl)oxy)biphenyl and potassium carbonate in DMF at 100 °C to give N-(4-((10-decyl)oxy)biphenyl)-2-imidazolecarboxaldehyde as a white powder which was purified via recrystallisation from ethanol in a 78% yield. For the complex synthesis, ligands **L5.3** and **L5.4** were synthesised *in situ* via a sub component self-assembly methodology (*Figure 5.2.1*). Ligand **L5.3** was synthesised in its free form in order for the collection of an IR spectra to record the C=N imine stretch as reference for complexes **5.5** and **5.6**. Two equivalents of 2-imidazolecarboxaldehyde and 4,4'-oxydianiline were heated at reflux in DCM. The DCM was removed under reduced pressure to give ligand **L5.3** as a yellow oil in a 40% yield.

5.3 Complex synthesis and characterisation

Both complexes were synthesised via a subcomponent self-assembly methodology in which the coordinating imine functionalities were formed *in situ* from the amine and aldehyde starting components in the presence of Fe(II) tetrafluoroborate. Six equivalents of N-(4-((10-decyl)oxy)biphenyl)-2-imidazolecarboxaldehyde and three equivalents of either 4,4'-oxydianiline or 4,4'-diaminodiphenylmethane were stirred in DCM at reflux. A methanol solution of Fe(II) tetrafluoroborate (two equivalents) was added and the resulting dark red solution was stirred at reflux for several hours. The DCM was then removed under reduced pressure resulting in the separation of a dark red oil. The supernatant was decanted, and the oil was triturated in petroleum ether. This resulted in a red powder for complex **5.5** containing **L5.3** (oxo linker) and a dark red/purple powder for complex **5.6** containing **L5.4** (methylene linker). The IR spectra of **5.5** and **5.6** are near identical which is to be expected for complexes containing such similar ligands (*Figure 5.3.1*). The bands at 2930 and 2843 cm^{-1} can be attributed to alkane C-H stretches of the mesogenic substituents. The coordinated imine C=N stretch occurs at 1608 cm^{-1}, lower than the free ligand at 1620 cm^{-1} due to the weaker C=N bond. The peak at 1433 cm^{-1} may be attributed to alkane C-H bending, however, it is slightly lower than the expected value. The relatively strong peaks at 1239 and 1044 cm^{-1} can be attributed to the C-O stretches of the asymmetric ether of the mesogenic substituent. This moiety has two chemically distinct C-O stretches; C_{aryl}-O and C_{alkyl}-O.

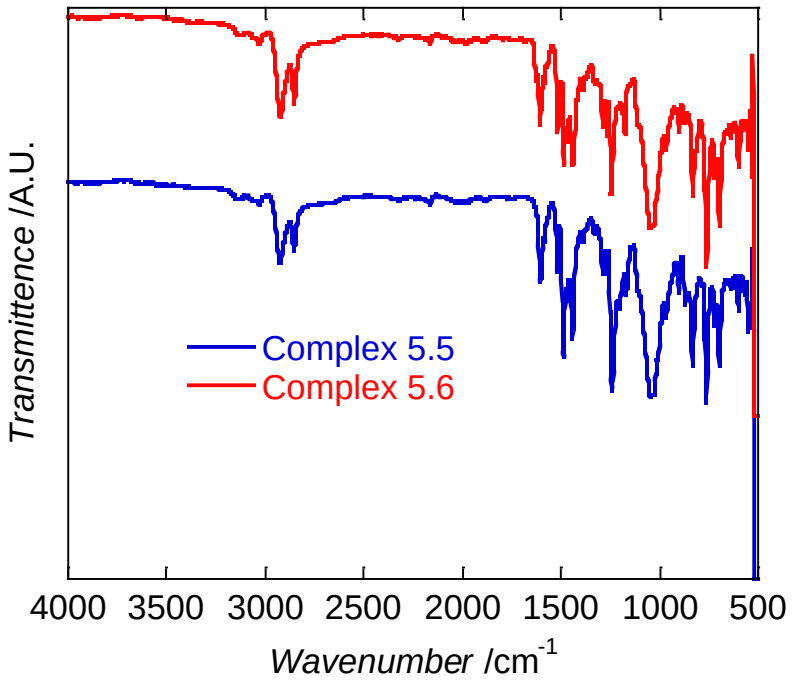

*Figure 5.3.1: The IR spectra for complex **5.5** in blue and complex **5.6** in red between 4000 to 500 cm^{-1}. The spectra have been off set on the y axis for clarity.*

5.4 Variable temperature Raman

The variable temperature Raman spectra of neat solid-state samples of **5.5** and **5.6** were examined. The low (~10-400 cm^{-1}) and mid (400-2000 cm^{-1}) frequency regions of these were measured simultaneously at 10 K intervals, from 103 K to 273 K using a 785 nm excitation laser (*Figure 5.4.1*). Three regions were examined, 0 to 400 cm^{-1} (a), 1100 to 1700 cm^{-1} (b) and 1550 to 1650 cm^{-1} (c). The intensities were normalized to the peak at ~1580 cm^{-1} to assist in comparing relative changes. In the low frequency region an undefined 'halo' (or boson peak) is observed. As the temperature is increased the intensity of this 'peak' increases suggesting an increase in disorder, expected with the presence of the flexible alkyl substituents. In the mid frequency region, significantly more variation is observed. In general complex **5.5** shows a red shifting of the peaks and decrease in intensity, with respect to the peak at 1580 cm^{-1}. The most significant variation is observed in peaks at 1208, 1286 and 1488 cm^{-1}, which undergo red shifts of 3-4 cm^{-1} and show a clear decrease in relative intensity. The peak at 1208 also exhibits broadening with the increase in temperature. Upon closer inspection of the peak at 1580 cm^{-1} (*Figure 5.4.1, c*) a decrease in

intensity at 1570 and 1610 cm^{-1} as temperature is increased is observed, resulting in a narrowing of the peak. At 1570 cm^{-1} there are roughly three groups of intensity changes. A rapid change in intensity occurs from 103 to 143 K before moving through a period of small and constant change. At approximately 253 K the change ceases, with the most noticeable drop in intensity at 1610 cm^{-1}. For **5.6**, less change is observed in the majority of the mid frequency region (*Figure 5.4.1, b*) with a decrease in intensity of the peak at 1290 cm^{-1} and red shift of the peak at 1210 cm^{-1} by 5 cm^{-1}. However, the 1590 cm^{-1} peak shows significant variations. At 1571 cm^{-1} a decrease in intensity is observed as the temperature increases, while at 1586 cm^{-1} an increase in intensity with temperature is seen, with a change in shape featuring an asymptote at 1580 cm^{-1}. Again, three groupings are observed; from 103 to 143 K. A rapid drop a in intensity at 1570 cm^{-1}occurs, before remaining relatively constant to 203 K. At 203 K a smaller step down in intensity occurs, then the intensity remains relatively constant again.

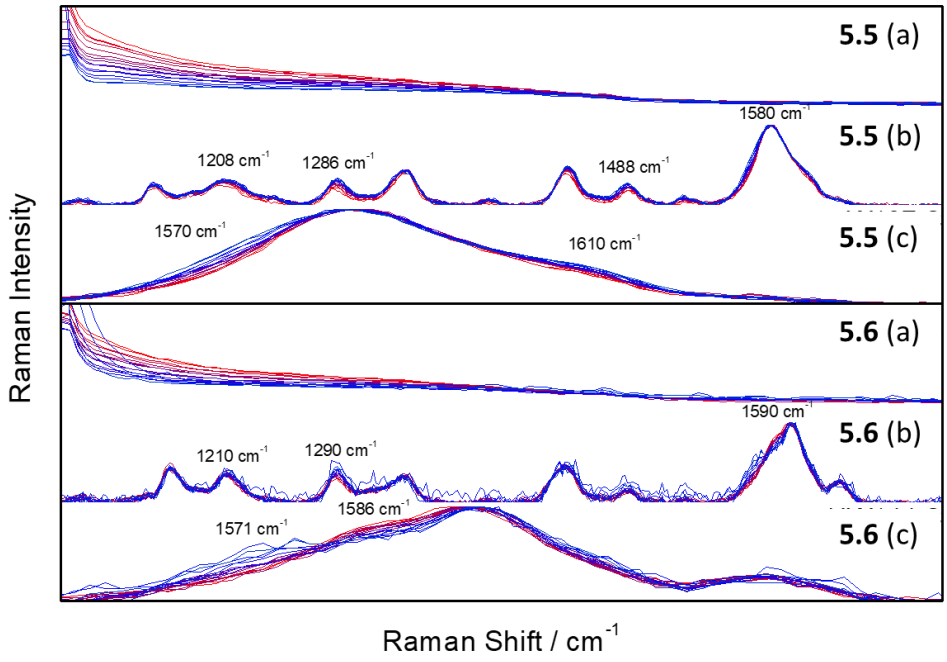

*Figure 5.4.1 Variable temperature Raman spectra for **5.5** and **5.6**, examining the low frequency region (0-200 cm^{-1}) (a), the mid frequency region (1100-1700 cm^{-1}) (b) and a key peak in detail (1550-1650 cm^{-1}) (c). Temperature sweep is from 103 K (blue) to 273 K (red) with measurements made at 10 K intervals.*

The change in intensity at 1586 cm^{-1} is much more consistent across the whole temperature range. This data suggests that the spin state is changing across the 143 to 253 K temperature range for **5.5** and from 143 K to 203 K for **5.6**. The data suggests for **5.5** the change is more gradual and occurs with small adjustments over the whole molecule, while for **5.6** there are more significant structural changes within a smaller region. The difference in the structural reorganization is unexpected due to the structural similarity of the ligands and therefore the resultant helicate complexes. However, the more crystalline nature of **5.6** observed via SAXS measurements in *section 5.7* may result the occurrence of a smaller structural reorganization. The two-dimensional correlation spectroscopy (2DCOS) plots of the non-normalized intensities (*Appendix Figure 5.12.4.i*) showed that for both **5.5** and **5.6**, the overall change in intensity of the peaks is in the same direction, as expected for such structurally similar complexes. When the normalized intensities are used to give a better indication of changes in relative band profile for complex **5.5**, all the changes in intensity are in the same direction relative to the 1580 cm^{-1} peak. The largest changes are seen for the peaks at 1286, 1446 and 1488 cm^{-1} and the shoulder at 1570 cm^{-1}. For complex **5.6**, it can clearly be seen that the intensity at 1586 cm^{-1} changes in the opposite direction to the rest of the peaks.

5.5Absolute reflectivity measurements

5.5.1 $[Fe_2(L5.3)_3](BF_4)_4$, 5.5

The first reflectively measurement performed on **5.5** was to investigate the occurrence of thermally induced SCO. A sample of **5.5** was cooled from 270 to 10 K at 4 K min^{-1} under the weak white light irradiation (0.08 mW cm^{-2}), followed by re-warming to 270 K at the same rate (*Figure 5.5.1.i*). Upon cooling, there is a noticeable increase in the visible region between 600 nm and 750 nm concurrent with a decrease in the near-IR region (>800 nm), resulting in a tight isosbestic point at 780 nm. There is no observable change between 100 and 10 K, indicating the SCO process is complete by 100 K. The heating mode simply shows the reverse of the cooling mode (*Appendix Figure 5.12.2.i*). In order to better visualise the changes in the visible region of the spectrum, the absorbance at 690 nm (AR_{690}) (*Figure 5.5.1.i*) and 870 nm (AR_{870}) (*Appendix Figure 5.12.2.iii*) were plotted verses the temperature. This highlights the gradual decrease in the reflectance of the visible region upon cooling from 270 K at 690 nm and the increase in reflectance above 700 nm that is typically associated with SCO for Fe(II). It also clearly shows that the change is completed

by 100 K and that both the cooling and heating cycle follow the same path and there is no evidence of hysteresis. The process is incomplete as there is no plateau before 270 K.

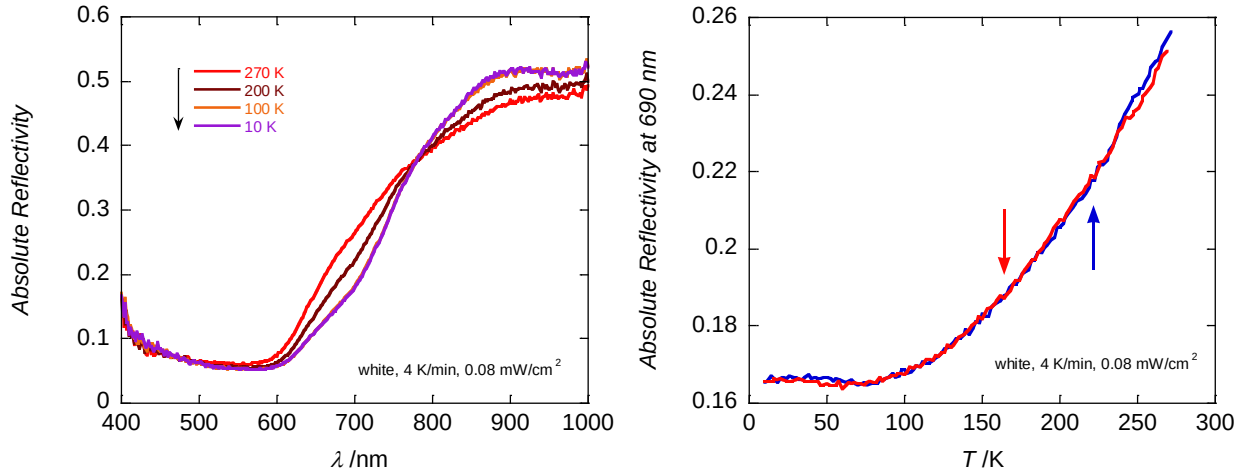

Figure 5.5.1.i: (left) Selected surface reflectivity measurements of ***5.5*** *collected with a white light spectroscopic source (0.08mW cm^{-2}) as a function of the wavelength during cooling mode from 270 to 10 K. (right) The temperature dependence of the reflectivity signal at 690 nm for heating the sample (red) and cooling the sample (blue).*

The second reflectivity measurement performed on **5.5** was to investigate the occurrence of photo-induced SCO. At 10 K, irradiation of the sample for three hours under white light resulted in mild excitation of the sample with an increase in the AR_{690} from 0.16 to 0.20 (*Appendix Figure 5.12.2.ii*). The sample was then heated at 4 K min^{-1} to 270 K and complete thermal relaxation to the LS state is achieved by 80 K. After 100 K, the AR_{690} increases due to thermally induced SCO. Similarly, irradiation of the sample for three hours at 10 K under white light results in a decrease in the AR_{870} from 0.50 to 0.48 (*Appendix Figure 5.12.2.iv*). Heating the sample results in gradual thermal relaxation that is complex by 80 K with the AR_{870} value gradually increasing. To optimise the photo-excitation, 14 different LED sources with wavelengths ranging from 365 to 1050 nm were trialled at 10 K. The 625 nm LED was found to be the most efficient for photo-excitation. After cooling from 200 to 10 K, the sample was irradiated with 625 nm light for 10 minutes resulting in partial photo-excitation to the HS state with a reflectivity value similar to the sample at 200 K. Irradiation with 625 nm light was carried out at various intensities to probe the effect on the proportion of the sample that is photo-excited. There is no significant difference between 0.1 and 10 mW cm^{-2} (*Appendix Figure 5.12.2.v*). The initial excitation at 10 mW cm^{-2} decays almost

instantaneously, followed by a more gradual thermal relaxation as the sample is warmed. This near instantaneous decrease in the reflectivity is typically associated with the photo-excitation being a surface only effect. Despite the near instantaneous decrease, the photo-excitation with 625 nm light is more efficient than white light (*Figure 0.i*). The AR_{690} value obtained after irradiation with 625 nm (0.1 mW cm^{-2}) is noticeably higher than that obtained with white light irradiation (0.08 mW cm^{-2}). As observed with white light irradiation, complete thermal relaxation is achieved by 80 K. After partial photo-excitation at 625 nm, irradiation at 850 nm results in partial de-excitation (*Appendix Figure 5.12.2.vi*). The degree of de-excitation with 850 nm light is significantly less than the initial photo-excitation with 625 nm light. This process is fully reversible at 10 K as evidenced by the four cycles of excitation and de-excitation. Therefore, **5.5** exhibits both partial LIESST and reverse-LIESST behaviour.

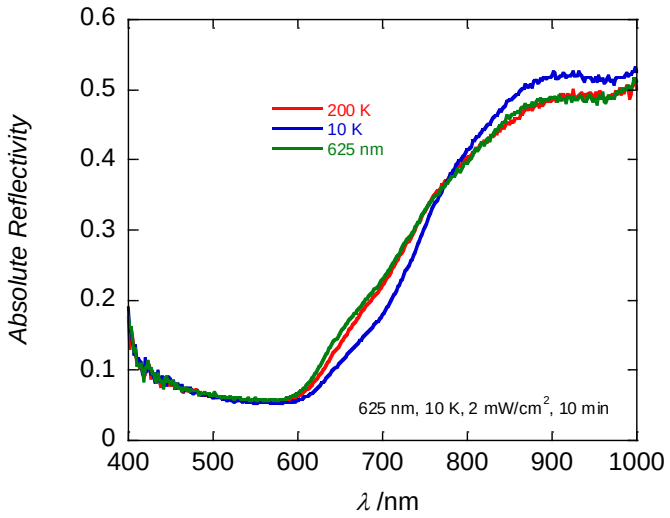

*Figure 0.i.ii: Surface reflectivity measurements of **5.5** collected with a white light spectroscopic source (0.08mW cm^{-2}) at 200 K, 10 K and 10 K after irradiation with 625 nm light (2 mW cm^{-2}) at 10 K for 10 minutes.*

5.5.2 $[Fe_2(L5.4)_3](BF_4)_4$, 5.6

The first reflectively measurement performed on **5.6** was to investigate the occurrence of thermally induced SCO. A sample of complex **5.6** was cooled from 270 K to 10 K at 4 K min^{-1} under the weak white light irradiation (0.08 mW cm^{-2}), followed by re-warming to 270 K at the same rate (*Figure 5.5.2.i*). Upon cooling, there is a noticeable increase in the visible region between 600 nm and 750 nm concurrent with a decrease in the near-IR region (>800 nm), resulting in a tight

isosbestic point at 780 nm (*Figure 5.5.2.i*). There is no observable change between 100 and 10 K indicating the SCO process is complete by 100 K. The heating mode simply shows the reverse of the cooling mode (*Appendix Figure 5.12.2.vii*). This behaviour is very similar to that observed for complex **5.5**.

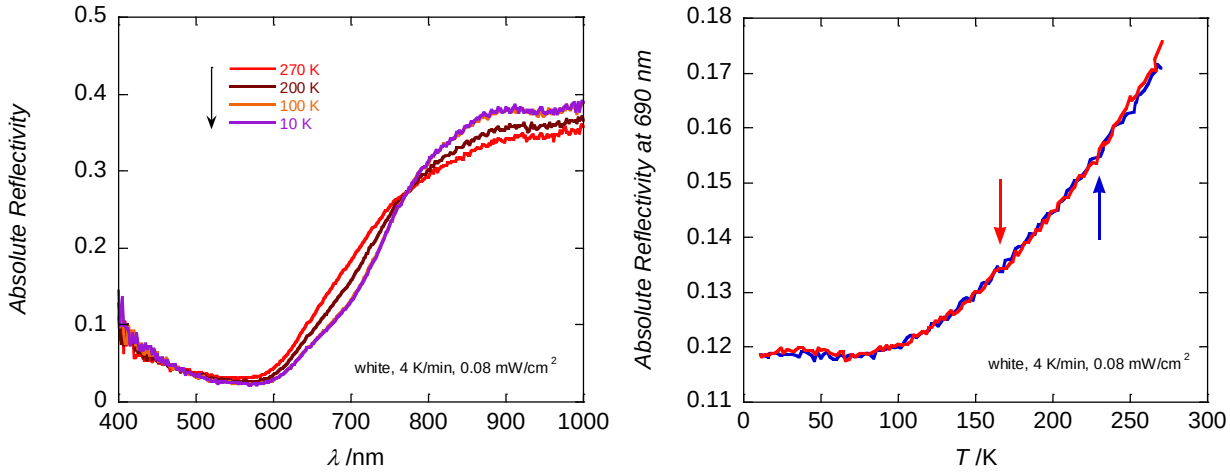

Figure 5.5.2.i: (left) Selected surface reflectivity measurements of ***5.6*** *collected with a white light spectroscopic source (0.08mW cm^{-2}) as a function of the wavelength during the cooling mode between 270 and 10 K. (right) The temperature dependence of the reflectivity signal at 690 nm for heating the sample (red) and cooling the sample (blue).*

In order to better visualise the changes in the visible region of the spectrum, the absorbance at 690 nm (AR_{690}) (*Figure 5.5.2.i*) and 870 nm (AR_{870}) (*Appendix Figure 5.12.2.ix*) were plotted verses temperature. This highlights the gradual decrease in the reflectance of the visible region upon cooling from 270 K at 690 nm and the increase in reflectance above 700 nm that is typically associated with SCO for Fe(II). It also clearly shows that the change is completed by 100 K and that both the cooling and heating cycle follow the same path and that there is no evidence of hysteresis. Much like **5.5** there is no plateau by 270 K indicating that the SCO is incomplete. The second reflectivity measurement performed on **5.6** was to investigate the occurrence of photo-induced SCO. At 10 K, irradiation of the sample for three hours under white light resulted in mild excitation of the sample with an increase in the AR_{690} from 0.12 to 0.14 (*Appendix Figure 5.12.2.viii*). The sample was then heated at 4 K min^{-1} to 270 K and by 75 K, the partial photoexcited HS state has thermally relaxed to the LS state. After 90 K, the AR_{690} increases due to thermally induced SCO. Similarly, irradiation of the sample for three hours under white light at 10 K resulted

in a decrease in the AR_{870} from 0.37 to 0.11 (*Appendix Figure 5.11.2.x*). Heating the sample results in gradual thermal relaxation that is complete by 75 K, with the AR_{870} value gradually increasing until 75 K. Above 75 K, the AR_{870} begins to decrease due to thermal relaxation of the HS state. To optimise the photo-excitation, 14 different LED sources with wavelengths ranging from 365 to 1050 nm were trialled at 10 K. The 625 nm LED was found to be the most efficient for photo-excitation. After cooling from 200 to 10 K, the sample was irradiated with 625 nm light for 10 minutes which resulted in partial photo-excitation to the HS state with a similar reflectivity value to the sample at 200 K (*Figure 5.6.2.ii*). Irradiation with 625 nm light was carried out at various intensities to probe the effect on the proportion of the sample that is photo-excited. This revealed no significant difference between 0.1 and 10 mW cm^{-2}. The initial excitation at 10 mW cm^{-2} decays almost instantaneously, followed by a more gradual thermal relaxation as the sample is warmed *(Appendix Figure 5.12.2.xi*). This instantaneous decrease is identical to that observed for **5.5** and can be ascribed to a surface photo-excitation.

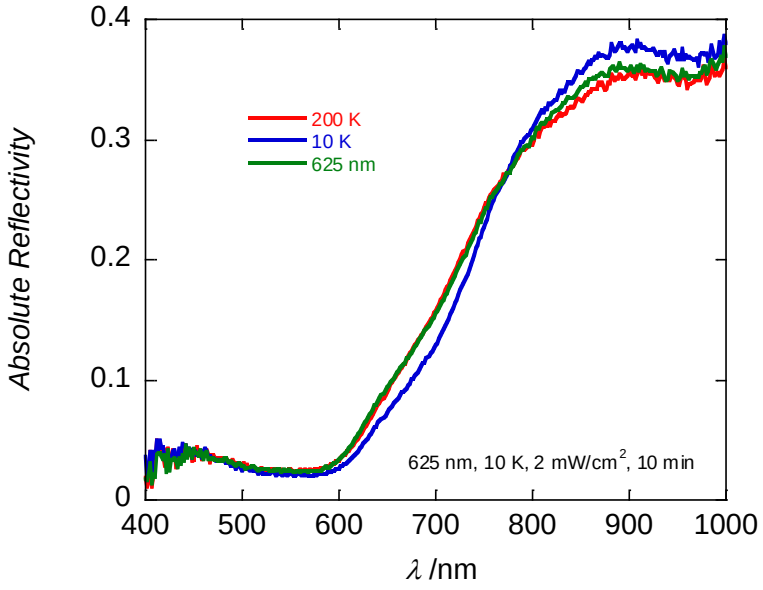

*Figure 0.i.ii: Surface reflectivity measurements of **5.6** collected with a white light spectroscopic source (0.08mW cm^{-2}) at 200 K, 10 K and 10 K after irradiation with 625 nm light (2 mW cm^{-2}) at 10 K for 10 minutes.*

Despite the near instantaneous decrease, the photo-excitation under 625 nm is more efficient than under white light. The AR_{690} value obtained after irradiation with 625 nm light (0.1 mW cm^{-2}) is noticeably higher than that obtained with white light irradiation (0.08 mW cm^{-2}). As observed with

white light irradiation, complete thermal relaxation is achieved by 80 K. After partial photo-excitation at 625 nm, irradiation at 850 nm results in partial de-excitation (*Appendix Figure 5.12.2.xii*). The degree of de-excitation with 850 nm light is significantly less than the initial photo-excitation with 625 nm light. This process is fully reversible at 10 K, as evidenced by the four cycles of photo-excitation and de-excitation. Therefore **5.6** displays both partial LIESST and reverse-LIESST behaviour.

5.6 Magnetic susceptibility data

Magnetic measurements were conducted on powder samples of **5.5** and **5.6** with an applied field of 10000 Oe and a scan rate of 0.4 K min^{-1}. For complex **5.5**, the magnetic susceptibility was measured between 1.85 and 310 K (*Figure 5.6.1*). Upon heating from 1.85 K the χT value rapidly increases from 1.64 to 4.0 cm^3 K mol^{-1} at 45 K due to ZFS and second order Zeeman effects. At this temperature, approximately 59% of the Fe(II) centres exist in the HS state (g = 2). However a plateau is not reached and the χT value continues to increase but in a more gradual manner. The χT values increases to 6.8 cm^3 K mol^{-1} at 310 K, where it is expected the vast majority of the Fe(II) centres exist in the HS state and this gradual increase is attributed to Fe(II) SCO. The *M vs. H* curve for complex **5.6** at 100 K featured a deviation from linearity at low fields (*Appendix Figure 5.12.3.i*). The elemental analysis for **5.6** is further evidence for the presence of an impurity as it does not fit well to the calculated C, H and N proportions like **5.5**. The magnetic susceptibility for complex **5.6** was measured between 1.85 and 400 K (*Figure 5.6.1*). Upon heating from 1.85 K the χT value rapidly increased from 1.0 cm^3 K mol^{-1} to 3.17 cm^3 K mol^{-1} at 90 K due to ZFS and second order Zeeman effects. At this temperature, approximately 51% of the Fe(II) centres exist in the HS state and much like complex **5.5**, no clear plateau is reached. The slope of the curve is then much more gradual as the χT value increased to 6.2 cm^3 K mol^{-1} at 400 K, where all the Fe(II) centres now exist in the HS state. The sample was then cooled back to 260 K to confirm the reproducibility of this behaviour at high temperature. The very broad and gradual SCO is in agreement with the results of the Raman measurements. However, the Raman data indicates that the SCO for **5.6** is complete by 203 K which is not the case as evidenced by the magnetic susceptibility and may be due the partial and broad SCO that is occurring.

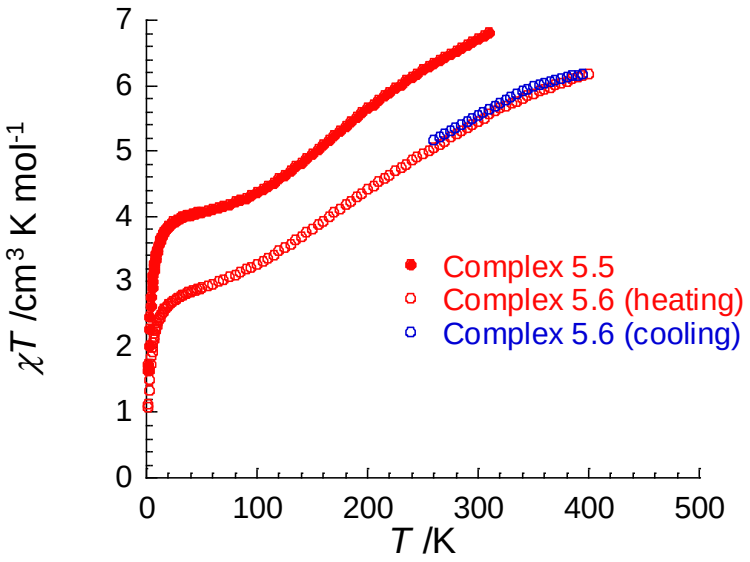

Figure 5.6.1: The χT vs. T plot for complex ***5.5*** *heated from 1.85 to 310 K (filled red circles) and χT vs. T plot for complex* ***5.6*** *heated from 1.85 to 400 K (open red circles) and cooled from 400 K to 260 K (open blue circles) for an applied magnetic field of 10000 Oe with a scan rate of 0.4 K min^{-1}.*

5.6Small angle X-ray scattering

5.7.1 $[Fe_2(L5.3)_3](BF_4)_4$, 5.5

Small angle X-ray scattering (SAXS) was used to investigate the crystallinity of the complexes and probe any phase changes that may occur. Complex **5.5** was initially measured at 298 K and was then heated to 473 K followed by cooling back to 298 K (*Figure 5.7.1.i*). For **5.5** there are three peaks of interest, a broad peak at 3° and a very small peak at 16°. Upon heating to 473 K there is a further reduction in the crystallinity as both peaks decrease in intensity. Upon cooling to 298 K the small peak at 16° no longer appears. There is a third very broad peak at 20° due to the alkyl substituents.[353] A second cycle of heating was then carried out for **5.5**. The sample was heated from 298 to 473 K, collecting spectra at 25 K intervals. No significant changes in the spectra are observed, in particular around the small broad peak at 3° (*Appendix Figure 5.12.5.i*).

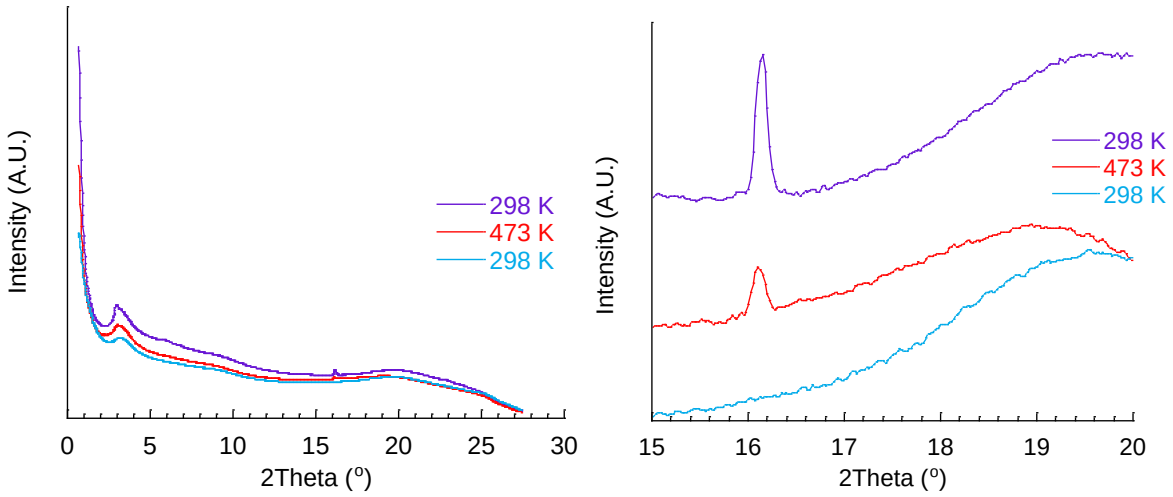

*Figure 5.7.1.i: (left) SAXS data for **5.5** between 0° and 27° at 298 K (purple), after heating to 473 K (red) followed by cooling back to 298 K (light blue). (right) SAXS data for **5.5** between 15° and 20° highlighting the peak at ca. 16° present initially at 298 K which decreases in intensity after heating to 473 K and is no longer present after the subsequent cooling back to 298 K.*

5.7.1 $[Fe_2(L5.4)_3](BF_4)_4$, 5.6

Complex **5.6** was measured in an analogous manner to **5.5**. Data were collected at 298 K and then the sample was heated to 473 K, followed by a second data collection. The sample was then cooled back to 298 K for a final data collection (*Figure 5.7.2.i*). The spectra are broadly similar to those obtained for complex **5.5**, however, **5.6** appears to exhibit higher crystallinity. The peak at 3° is significantly more pronounced than for **5.5**. On closer inspection, two small broad peaks at 5.7° and 6.7° are observed in the initial spectra collected at 298 K. There is also a very broad peak centred at 20° much like **5.5**. This broad peak at high angle can be attributed to the alkyl substituents.[353] Upon heating to 473 K, the peak at 3° decreases in intensity and remains this way when cooled back to 298 K. The two smaller peaks at 5° and 6.7° disappear during the heating process and are not recovered upon cooling back to 298 K. Much like **5.5**, no significant changes in the spectra are observed for the second heating cycle for which data were collected at 25 K intervals (*Appendix Figure 5.12.5.ii*).

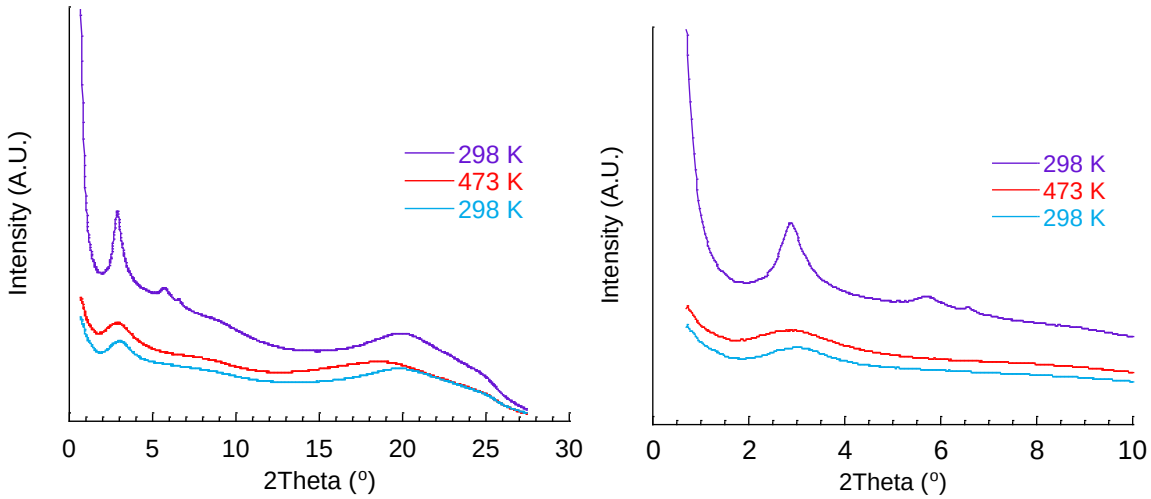

*Figure 5.7.2.i: (left) SAXS data for **5.6** between 0° and 27° at 298 K (purple), after heating to 473 K (red) followed by cooling back to 298 K (light blue). (right) SAXS data for **5.6** between 0 and 10° highlighting the peak at ca. 3° present initially at 298 K which decreases in intensity after heating to 473 K.*

5.8 Differential scanning calorimetry

DSC measurements were carried out for both complex **5.5** and **5.6** to investigate the possibly of the formation of a mesogenic phase. The first heating and cooling cycle between 180 and 470 K was performed with a scan rate of 5 K min^{-1}, while the second cycle was performed with a scan rate of 10 K min^{-1}. For both **5.5** and **5.6** broad peaks are observed in the first heating cycle however no peaks are observed in the reverse cooling cycle indicating that the change is irreversible (*Figure 5.8.1*). These peaks can be attributed to the loss of adsorbed water molecules. No peaks of any kind are observed in the second cycle for both **5.5** and **5.6**. This reveals that no melting process or phase change occurs at elevated temperature. Both complexes exhibit very poor crystallinity most likely due to the disordered of the flexible alkyl chains. Therefore, crystallographic phase changes due to the change in conformation of the alkyl substituents are likewise not observed.

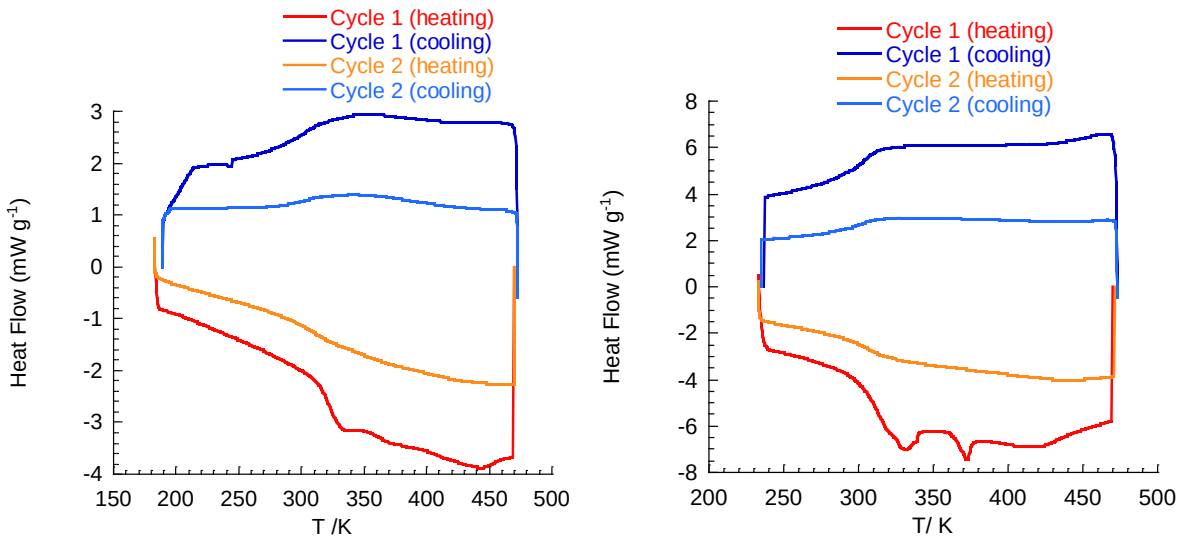

Figure 5.8.1: The heat flow (mW g^{-1}) vs. T (K) between 180 and 470 K for ***5.5*** *(left) and* ***5.6*** *(right). Cycle 1 is carried out with a scan rate of 5 K min^{-1} while cycle 2 is carried out with a scan rate of 10 K min^{-1}.*

5.9 Summary and conclusions

The synthesis of two novel metallo-helicate, featuring imidazolylimine moieties functionalised with 4-((10-decyl)oxy)biphenyl substituents is reported and carried out via a sub-component self-assembly methodology that has been outlined in earlier chapters of this thesis. The inclusion of mesogenic substituents resulted in complexes **5.5** and **5.6** exhibiting very poor crystallinity as shown via the SAXS measurements. Variable temperature SAXS and DSC measurements were used to investigate whether the formation of a mesogenic phase occurred at elevated temperatures. Unfortunately, the formation of such a phase was not observed. DSC measurements indicates the loss of solvent or water molecules adsorbed from the atmosphere or other phase. The lack of phase change was verified by SAXS measurements between 298 and 473 K. These measurements did however reveal that the heating of the complexes **5.5** and **5.6** resulted in the further loss of crystallinity upon at elevated temperature. The loss of crystallinity was less significant for **5.6** than **5.5**, as peaks were still observed in the SAXS spectrum at 298 K after heating to 473 K. Measurements above 473 K were not carried out as rapid decomposition of the complex occurs at *ca.* 550 K. The melting temperature appears to be higher than the temperature of decomposition which may be due to the +4 charge of the helicate. This high charge promotes a stronger cation-

anion interaction between the helicate and tetrafluoroborate anions which raises the melting point compared to the mononuclear analogues reported by Real and co-workers.[352-353] Furthermore, the divergent nature of the mesogenic substituents may not be the optimum arrangement for the formation of a liquid crystalline phase. A convergent type arrangement where the substituents at each Fe(II) centre are orientated in the same direction may be more suited to the formation of a liquid crystalline phase and facilitate the lowering of the melting temperature. The use of branched substituents may further lower the melting temperature and aid the formation of a liquid crystalline phase (*Figure 5.9.1*). Di- and tri-branched substituents have been shown to be highly effective for forming liquid crystalline arrays of metallo-supramolecular macrocycles.[459-460]

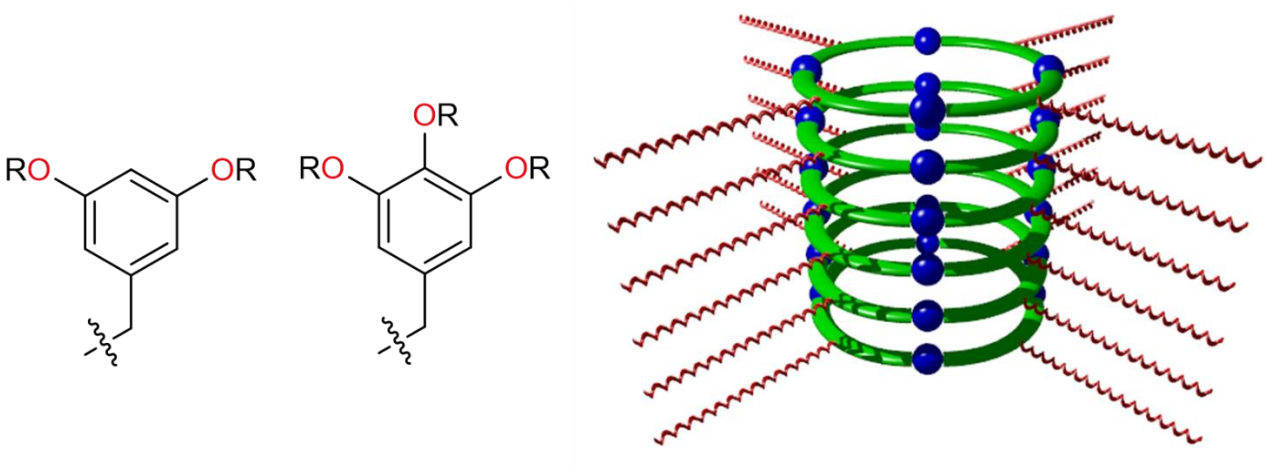

Figure 5.9.1: (left) Some examples of bi- and tri-branched branched mesogenic substituents where R = a alkyl chain. (right) A schematic representation of a family of macrocyles (metal ions, blue and ligands, green) functionalised with branched mesogenic substituents (red helices) which form columnar liquid crystals.

Both **5.5** and **5.6** display very gradual SCO as shown by variable temperature Raman, magnetic susceptibility and reflectively measurements. The latter also revealed that both complexes are weakly photo-active and exhibit minor LIESST and reverse-LIESST effects. The SCO is broader in comparison to the two previously reported analogues which feature methyl substituents in the two position of the imidazole ring. This can be attributed to the flexible alkyl chains reducing the cooperativity in the material. The flexible alkyl chains may ‘absorb’ the expansion of the complex due to the increase in the Fe-N bond lengths associated with SCO and thus stop it propagating to neighbouring complexes.

5.10 Experimental

For details on general procedures, NMR, FT-IR, ESI-MS, melting points, elemental analysis and TGA see *section 2.7* of chapter two. Details for reflectivity measurements are outlined in *section 4.9* of chapter four. Only details relevant to the work carried out in this chapter, not previously discussed will be given herein.

5.10.1 Infra-red spectroscopy

FT-IR spectra for complexes **5.5** and **5.6** were recorded on a Thermal Scientific NicoletTM 6700 ATR (attenuated total reflection) spectrometer equipped with a Smart iTR diamond window in the range 4000–500 cm^{-1}.

5.10.2 Variable temperature Raman measurements

The low frequency Raman data were collected using a setup previously recorded.[461-462] A 785 nm diode laser (SurelockTM LM Series, Ondax, USA) was used for excitation. Prior to irradiating the sample in 135° backscattering arrangement the excitation line was cleaned up using two ASE filters. The scattered light was collected, collimated and focused into a fiber optic. Three Volume Bragg gratings (BragGrateTM ,OptiGrate, USA) were used to block the Rayleigh scattering. The light from the fibre was dispersed using an Acton LS785 spectrometer (Princeton Instruments, USA) and measured using a PIXIS100 CCD (Princeton Instruments, USA), air cooled to -70°C. For variable temperature low frequency, a Specac Variable Temperature Cell (Specac, UK) was used. 2DCOS analysis was performed using 2Dshige (Shigeaki Morita, Kwansei-Gakuin University, Japan). Measurements were performed by Joshua Sutton and Prof. Keith Gordon, University of Otago, New Zealand.

5.10.3 Differential scanning calorimetry (DSC)

DSC measurements were performed with a Q2000 TA calorimeter using open aluminum pan. Thermograms were recorded at different scanning rates, at 5 and 10 K min^{-1} under nitrogen atmosphere.

5.10.4 Small angle X-ray scattering (SAXS)

SAXS experiments were collected on a laboratory-made experimental setup equipped with a Rigaku Nanoviewer (XRF microsource generator, MicroMax 007HF), with a 1200-W rotating anode coupled to a confocal Max-FluxH Osmic mirror (Applied Rigaku Technologies) and a MAR345 image plate detector (MARResearch). Measurements were performed by Dr Ahmed Bentaleb.

5.10.5 Magnetic susceptibility measurements

5.5 and **5.6** were dried overnight in a vacuum oven at 50 °C to remove any residual solvent as indicated in the DSC measurements. These solid samples were introduced in polypropylene bags (3 × 0.5 × 0.02 cm) for measurements. Measurements were performed as described in *section 2.7* of chapter two.

5.10.6 Ligand synthesis

*5.10.6.i 4-((10-bromodecyl)oxy)biphenyl, **5.1***

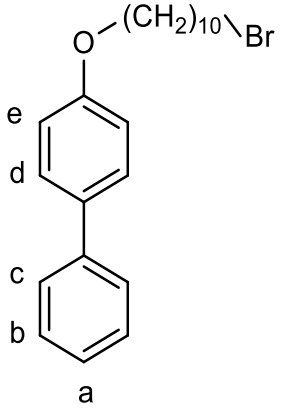

4-Hydroxybiphenyl (2 g, 11.8 mmol) and potassium carbonate (3.2 g, 23 mmol) were placed under an argon atmosphere via three evacuation and backfilling cycles. Butanone (50 mL) was added by syringe followed by 1,10-dibromodecane (13 mL, 59 mmol) and then the resulting suspension was heated at reflux for 24 hours. The reaction was filtered while hot and washed with 50 mL of hot DCM. The solvent was removed under reduced pressure and the resulting residue was purified by flash column chromatography on silica gel using pentane/dichloromethane (9:1) to give a white crystalline solid (2 g, 50 mmol, 43% yield).

M.pt. 84-85 °C Lit. 86-88 °C

^{1}H-NMR: δ_H (400 MHz, $CDCl_3$) 7.53 (m, 4 H, H_d and H_c), 7.41 (t, J = 7.83, 2 H, H_b), 7.30 (t, J = 7.20, 1 H, H_a), 6.97 (d, J = 8.61, 2 H, H_e), 3.99 (t, J = 6.65, 2 H, H_{alkyl}), 3.41 (t, J = 6.70, 2 H, H_{alkyl}), 1.9-1.75 (m, 4 H, H_{alkyl}), 1.52-1.27 (m, 12 H, H_{alkyl})

5.10.6.ii N-(4-((10-decyl)oxy)biphenyl)-2-imidazolecarboxaldehyde, ***5.2***

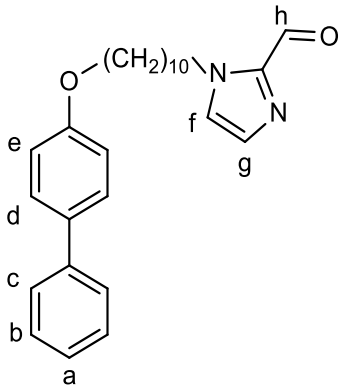

2-Imidazolecarboxaldehyde (0.35 g, 3.6 mmol), potassium carbonate (0.5 g, 3.6 mmol) and 4-((10-bromodecyl)oxy)biphenyl (1.4 g, 3.6 mmol) were placed under a nitrogen atmosphere via three evacuation and backfilling cycles. Dry DMF (15 mL) was added by syringe and the reaction was heated at 100 °C for 4 hours. After cooling to room temperature, the resulting suspension was poured into water (100 mL) resulting in a white precipitate. This solid was separated by filtration, recrystallized from hot ethanol and dried in a desiccator for 12 hours to give a white powder (1.14 g, 2.8 mmol, 78% yield).

M.pt. 73-75 °C

^{1}H-NMR: δ_H (400 MHz, $CDCl_3$) 9.89 (s, 1 H, H_h), 7.53 (m, 4 H, H_c and H_d), 7.41 (t, J = 7.63, 2 H, H_b), 7.29 (m, 2 H, H_a and H_g), 7.16 (s, 1 H, H_f), 6.96 (d, J = 8.61, 2 H, H_e), 4.39 (t, J = 7.43, 2 H, H_{alkyl}), 3.99 (t, J = 6.65, 2 H, H_{alkyl}), 1.79 (m, 4 H, H_{alkyl}), 1.45 (m, 2 H, H_{alkyl}), 1.13 (br. s, 10 H, H_{alkyl})

^{13}C-NMR: δ_C (101 MHz, $CDCl_3$) 159, 141, 134, 129, 128, 127, 126, 115, 110, 68, 48, 31, 29, 26

IR: (ν_{max}/cm^{-1}) 2916 (s), 2849 (s), 1680 (s), 1608 (m), 1586 (w), 1525 (m), 1489 (m), 1470 (m), 1436 (m), 1408 (w), 1369 (m), 1338 (m), 1306 (m), 1288 (m), 1272 (m), 1250 (s), 1198 (m), 1176 (m), 1150 (m), 1120 (w), 1065 (w), 1041 (w), 1025 (m), 1011 (m), 992 (w), 921 (w), 910 (w), 840 (m), 824 (w), 813 (w), 797 (w), 763 (s), 742 (m), 725 (m), 693 (m), 640 (w), 601 (m), 487 (m)

ESI-MS: meas. 405.2533 ([M+H]$^+$), [$C_{26}H_{33}N_2O_2$] calc. 405.2537

5.10.6.ii 4,4'-oxybis(1-(4-((10-decyl)oxy)biphenyl)-1H-imidazol-2-yl)methylene)aniline, ***L5.3***

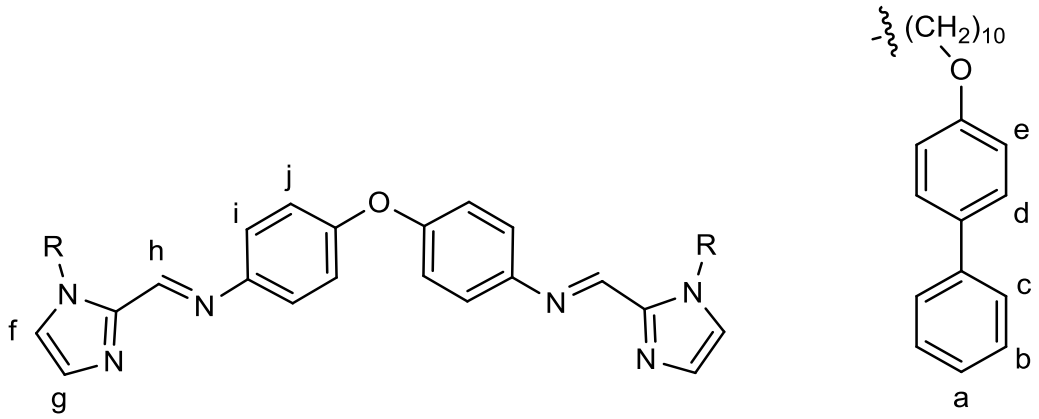

N-(4-((10-decyl)oxy)biphenyl)-2-imidazolecarboxaldehyde (0.6 mg, 1.5 mmol) was stirred in methanol (10 mL) at room temperature to give a white suspension. 4,4'-Oxydianiline (0.15 g, 0.74 mmol) was added and the suspension was heated at reflux for two hours until all solid had dissolved to give a yellow solution which was stirred at room temperature overnight. The solvent was then removed under reduced pressure to give a yellow oil (0.58 g, 0.6 mmol, 40% yield).

^{1}H-NMR: δ_H (400 MHz, $CDCl_3$) 8.56 (s, 1 H, H_h), 7.52 (m, 4 H, H_c and H_d), 7.40 (t, J = 7.63, 2 H, H_b), 7.29 (m, 1 H, H_a), 7.21 (m, 3 H, H_f and H_i), 7.06 (m, 3 H, H_g and H_j), 6.95 (d, J = 8.61, 2 H, H_e), 4.55 (t, J = 7.43, 2 H, H_{alkyl}), 3.97 (t, J = 6.80, 2 H, H_{alkyl}), 1.79 (m, 4 H, H_{alkyl}), 1.44 (m, 2 H, H_{alkyl}), 1.33 (m, 10 H, H_{alkyl})

^{13}C-NMR: δ_C (101 MHz, $CDCl_3$) 182, 159, 156, 150, 146, 143, 141, 133, 132, 129, 128, 127, 124, 124, 122, 121, 120, 118, 116, 115, 68, 48, 31, 29, 26

IR: (ν_{max}/cm^{-1}) 2919 (s), 2850 (s), 1620 (m), 1582 (w), 1517 (m), 1491 (s), 1468 (s), 1432 (m), 1391 (w), 1373 (w), 1288 (w), 1270 (m), 1235 (s), 1198 (s), 1176 (m), 1149 (m), 1107 (w), 1067 (w), 1045 (w), 1027 (w), 1012 (w), 1004 (w), 988 (w), 919 (w), 883 (w), 874 (w), 860 (m), 849 (m), 832 (s), 763 (s), 718 (m), 697 (s), 638 (w), 600 (m), 552 (m), 539 (m), 527 (m), 502 (m)

ESI-MS: meas. 973.5771 ($[M+H]^+$), $[C_{64}H_{73}N_6O_3]^+$ calc. 973.739,

5.10.7 Complex Synthesis

*5.10.7.i $[Fe_2(\mathbf{L5.3})_3](BF_4)_4$, **5.5***

N-(4-((10-decyl)oxy)biphenyl) imidazolecarboxaldehyde (0.39 g, 1.0 mmol) and 4,4'-oxydianiline (0.1 g, 0.5 mmol) were stirred at reflux in DCM (5 mL) for two hours. The resulting yellow solution was cooled to room temperature. A solution of $Fe(BF_4)_2.6H_2O$ (0.11 g, 0.33 mmol) in methanol (5 mL) was added to give a dark red solution that was stirred at room temperature for half an hour. The DCM was removed under reduced pressure to give a red oil. The remaining methanol was decanted the oil was triturated in petroleum ether (10 mL). The resulting red powder was filtered and washed with petroleum ether (5 x 10 mL) (0.37 mg, 0.11 mmol, yield = 67%)

Found: C, 66.72 H, 6.98 N, 7.22% $[Fe_2(C_{64}H_{72}N_6O_3)_3](BF_4)_4 \cdot 4.5H_2O$ requires: C, 66.65 H, 6.56 N, 7.29%

IR: (ν_{max}/cm^{-1}) 2923 (m), 2853 (m), 1605 (m), 1519 (m), 1488 (s), 1441 (s), 1331 (w), 1288 (w), 1270 (w), 1241 (s), 1203 (m), 1174 (w), 1048 (br., w), 966 (m), 901 (w), 867 (w), 832 (s), 762 (s), 719 (w), 697 (m), 637 (w), 600 (w), 570 (w), 518 (m) 456 (w)

*5.10.7.ii $[Fe_2(\mathbf{L5.4})_3](BF_4)_4$, **5.6***

N-(4-((10-decyl)oxy)biphenyl) imidazolecarboxaldehyde (0.43 g, 1.1 mmol) and 4,4'-diaminodiphenylmethane (0.11 g, 0.53 mmol) were stirred at reflux in DCM (5 mL) for two hours. The resulting yellow solution was cooled to room temperature. A solution of $Fe(BF_4)_2.6H_2O$ (0.12 g, 0.36 mmol) in methanol (5 mL) was added to give a dark red solution that was stirred at room temperature for half an hour. The DCM was removed under reduced pressure to give a red oil. The remaining methanol was decanted the oil was triturated in petroleum ether (10 mL). The resulting red/purple powder was filtered and washed with petroleum ether (5 x 10 mL) (0.44 g, 0.13 mmol, yield = 72%).

Found: C, 71.41 H, 8.36 N, 7.85% $[Fe_2(C_{65}H_{74}N_6O_2)_3](BF_4)_4$ requires: C, 69.43 H, 6.63 N, 7.46%

IR: (ν_{max}/cm^{-1}) 3130 (w), 3030 (w), 2923 (m), 2852 (m), 1607 (m), 1518 (m), 1485 (m), 1468 (m), 1439 (m), 1390 (m), 1288 (m), 1244 (s), 1175 (m), 1048 (br., s), 966 (m) , 899 (w), 875 (w), 832 (m), 761 (s), 718 (m), 696 (s), 638 (w), 599 (m), 549 (w), 518 (m), 506 (m)

5.11 Appendix

5.11.1 TGA

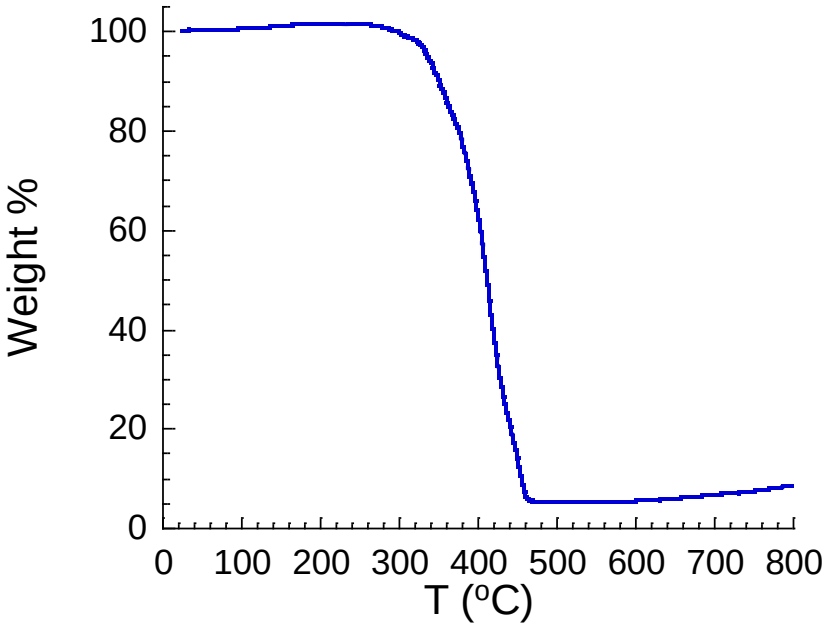

*Figure 5.11.1.i: TGA plot for **5.5**.*

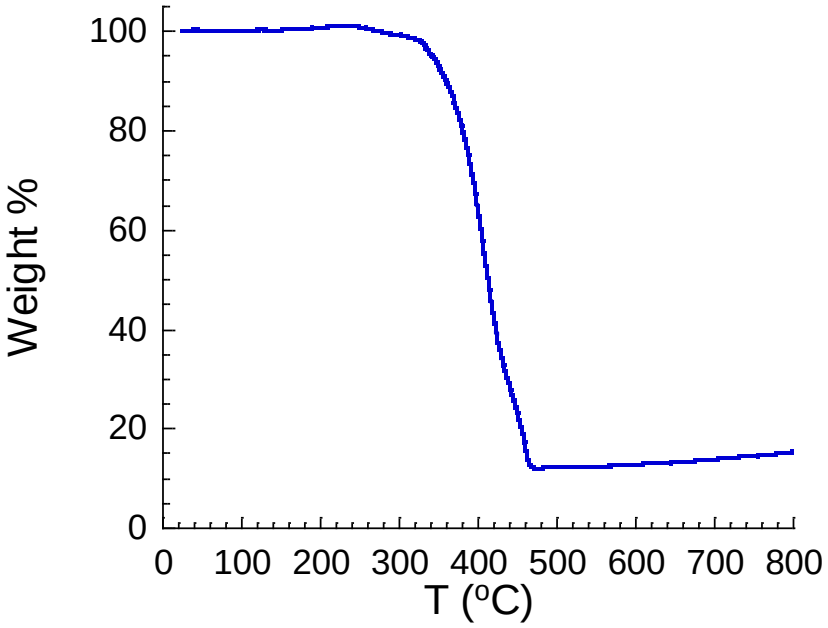

*Figure 5.11.1.i: TGA plot for **5.6**.*

5.11.2 Reflectivity measurements

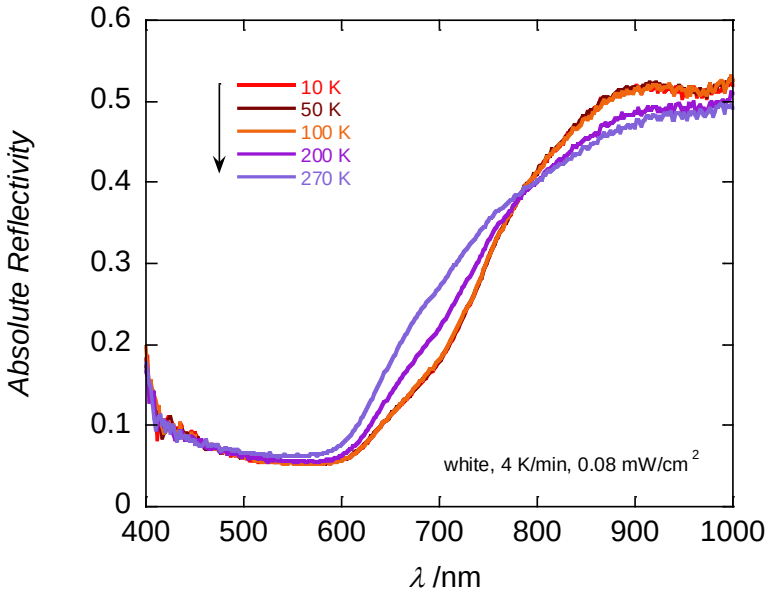

Figure 5.11.2.i: Selected surface reflectivity measurements of ***5.5*** *collected with a white light spectroscopic source (0.08 mW cm^{-2}) as a function of the wavelength during cooling mode between 10 to 270 K.*

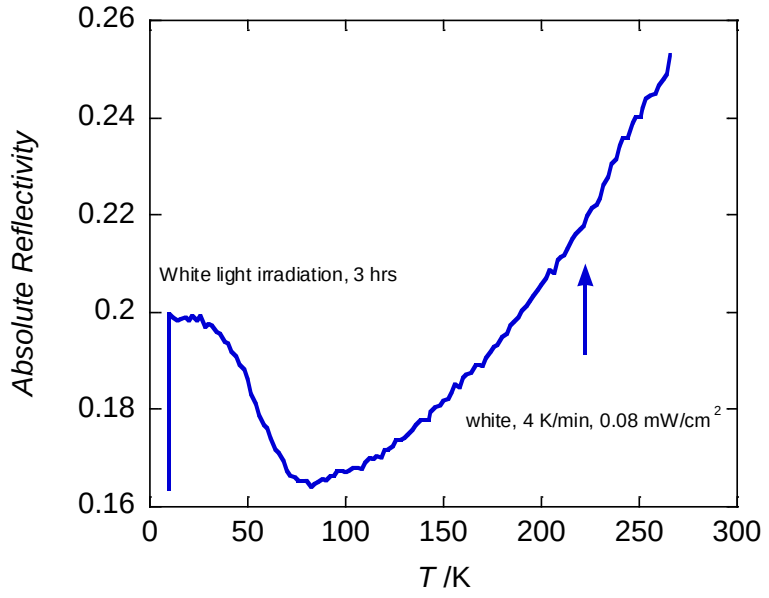

Figure 5.11.2.ii: Thermal evolution of the reflectivity signal of ***5.5*** *recorded at λ = 690 nm ± 5 nm following white light irradiation (0.08 mW cm^{-2}) for 3 hours at 10 K. The sample is heated from 10 to 270 K at 4 K min^{-1}.*

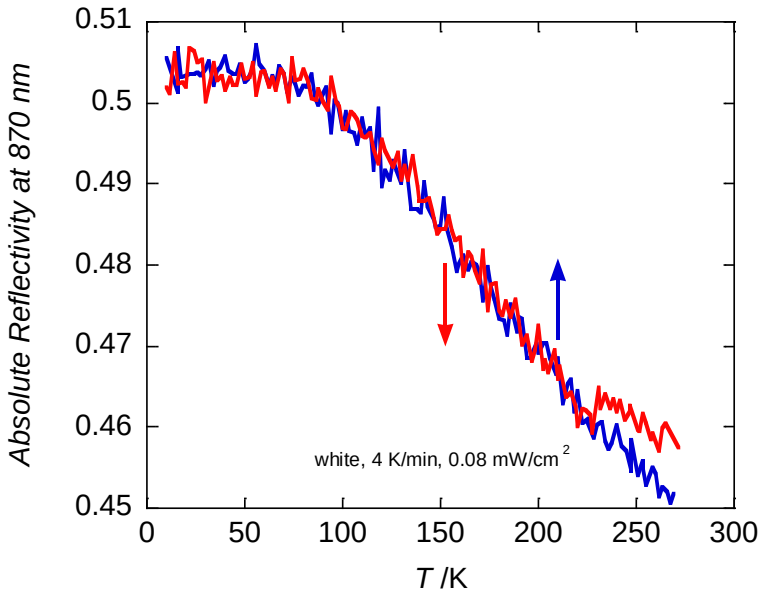

Figure 5.11.2.iii: Thermal evolution of the reflectivity signal of ***5.5*** *recorded at λ = 870 nm ± 5 nm during cooling mode, 270 to10 K (blue trace) and heating mode 10 to 270 K (red trace).*

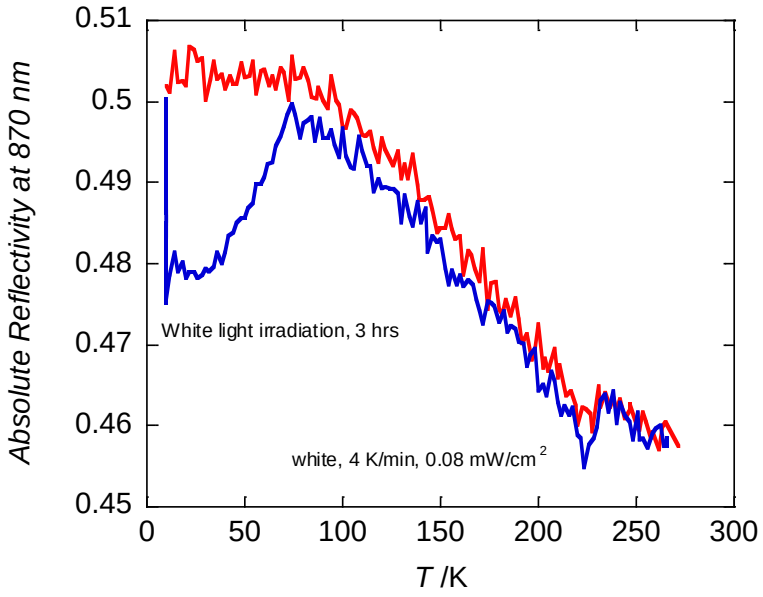

Figure 5.11.2.iv: Thermal evolution of the reflectivity signal of ***5.5*** *recorded at λ = 870 nm ± 5 nm following white light irradiation (0.08 mW cm^{-2}) for 3 hours at 10 K (blue trace) and heating mode 10 to 270 K (red trace).*

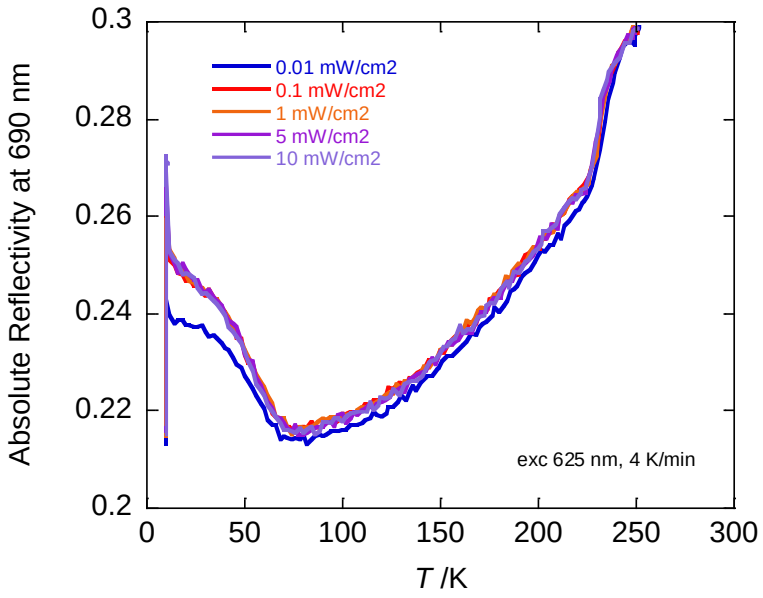

Figure 5.11.2.v: Thermal evolution of the reflectivity signal of ***5.5*** *recorded at λ = 690 nm ± 5 nm during irradiation with 625 nm light at various intensities, followed by a heating cycle from 10 K to 270 K.*

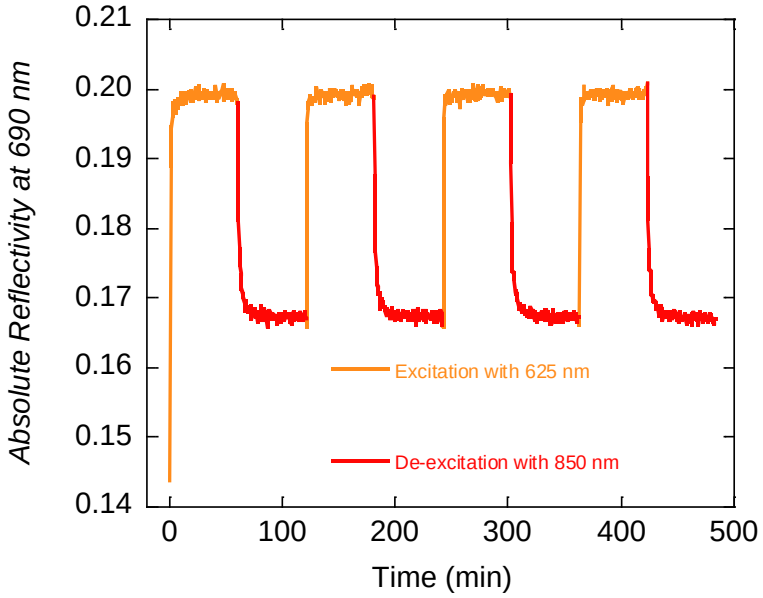

Figure 5.11.2.vi: Reflectivity signal of ***5.5*** *recorded at λ = 690 ± 5 nm for four cycles of photo-excitation (625 nm) and photo de-excitation (850 nm) at 10 K.*

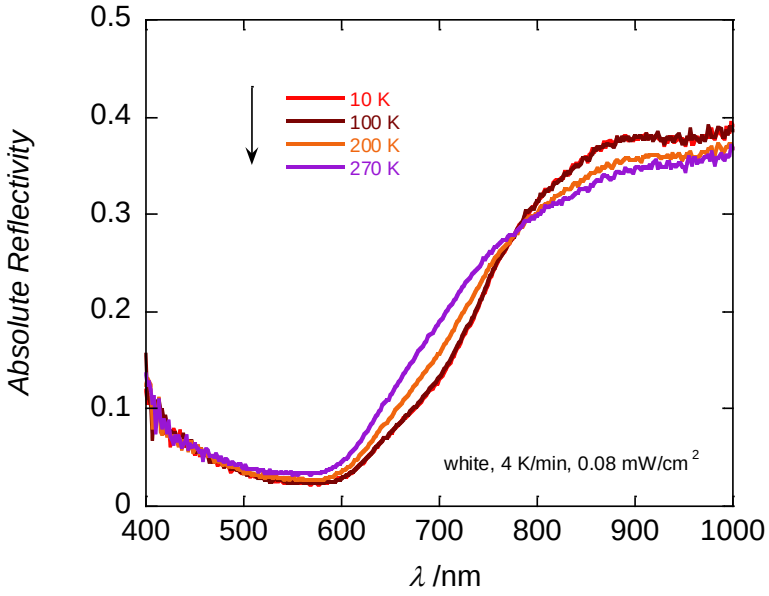

Figure 5.11.2.vii: Selected surface reflectivity measurements of ***5.6*** *collected with a white light spectroscopic source (0.08 mW cm^{-2}) as a function of the wavelength during cooling mode between 10 to 270 K.*

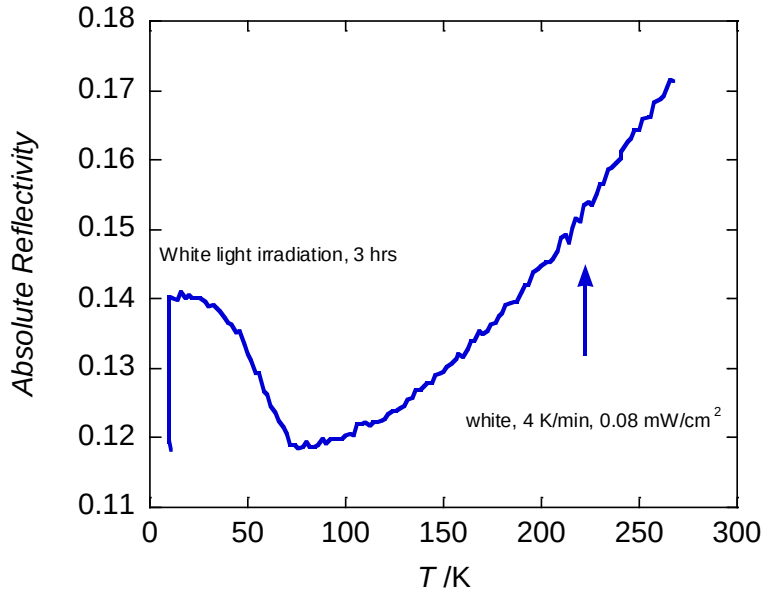

Figure 5.11.2.viii: Thermal evolution of the reflectivity signal of ***5.6*** *recorded at λ = 690 nm ± 5 nm following white light irradiation (0.08 mW cm^{-2}) for 3 hours at 10 K. The sample is heated from 10 to 270 K at 4 K min^{-1}.*

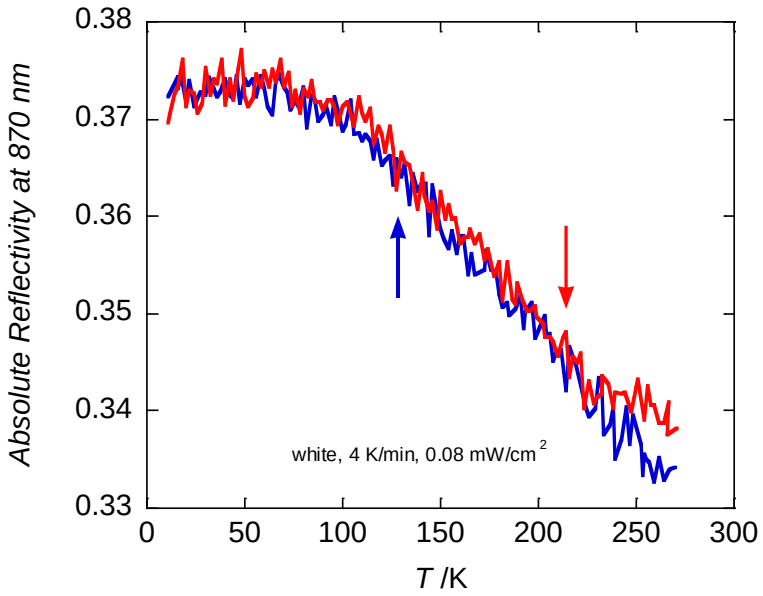

Figure 5.11.2.ix: Thermal evolution of the reflectivity signal of ***5.6*** *recorded at λ = 870 nm ± 5 nm during cooling mode, 270 to 10 K (blue trace) and heating mode 10 to 270 K (red trace).*

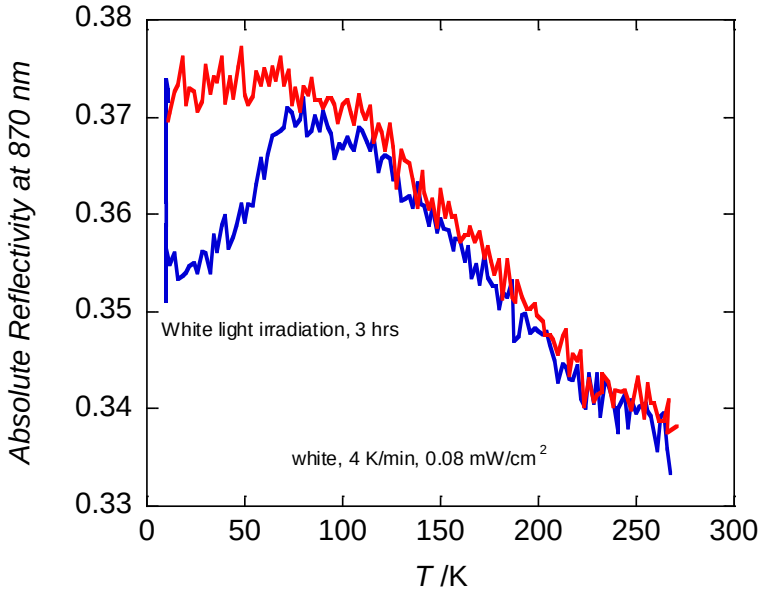

Figure 5.11.2.x: The temperature dependence of the reflectivity signal at 870 nm for heating the sample (blue trace) at 4 K min^{-1} and white light irradiation (0.08 mW cm^{-2}) at 10 K for 3 hours followed by heating (red trace) for ***5.6****.*

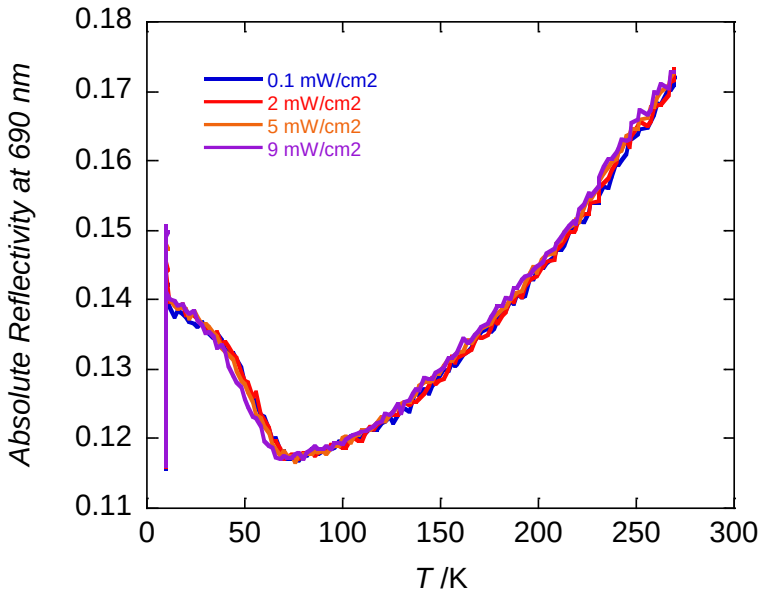

Figure 5.11.2.xi: Thermal evolution of the reflectivity signal of ***5.6*** *recorded at λ = 870 nm ± 5 nm during irradiation with 625 nm light at various intensities, followed by a heating cycle from 10 K to 270 K.*

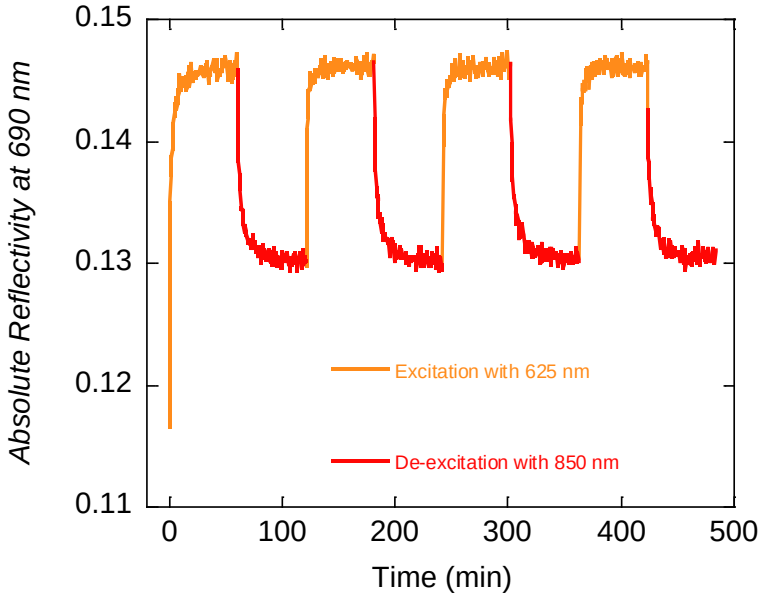

Figure 5.11.2.xii: Reflectivity signal of ***5.5*** *recorded at λ = 870 ± 5 nm for four cycles of photo-excitation (625 nm) and photo de-excitation (850 nm) at 10 K.*

5.11.3 Magnetic measurements

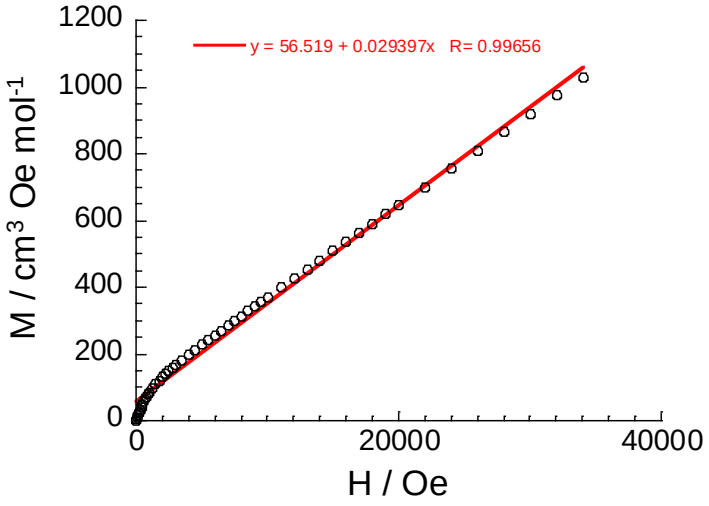

Figure 5.11.3.i: The M vs. H plot of 5.6 at 100 K. Experimental data is shown in black open circles and the data fit is shown by the red line.

5.11.4 Raman measurements

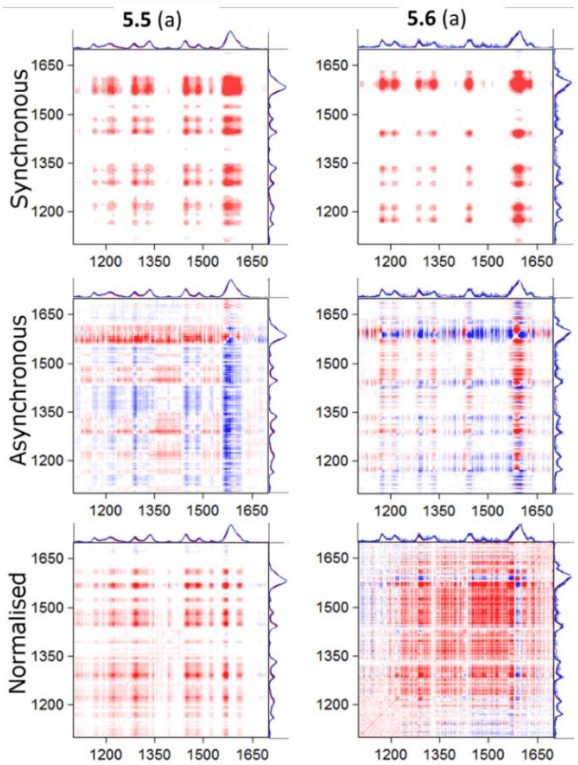

*Figure 5.11.4.i: 2DCOS plots of the non-normalized intensities for **5.5** and **5.6**.*

5.11.5 Small angle X-ray scattering measurements

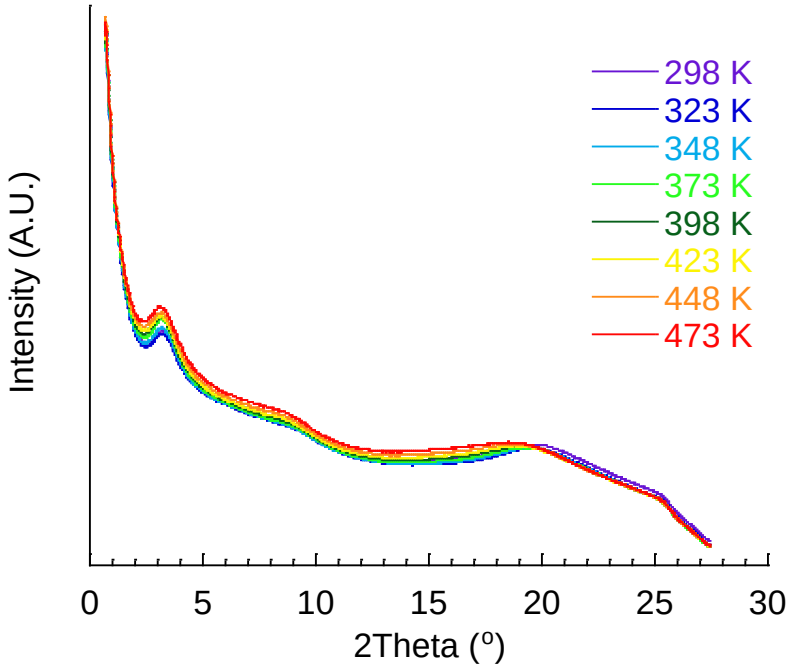

*Figure 5.11.5.i: SAXS recorded for **5.5** at 25 K intervals while heating from 258 K to 473 K.*

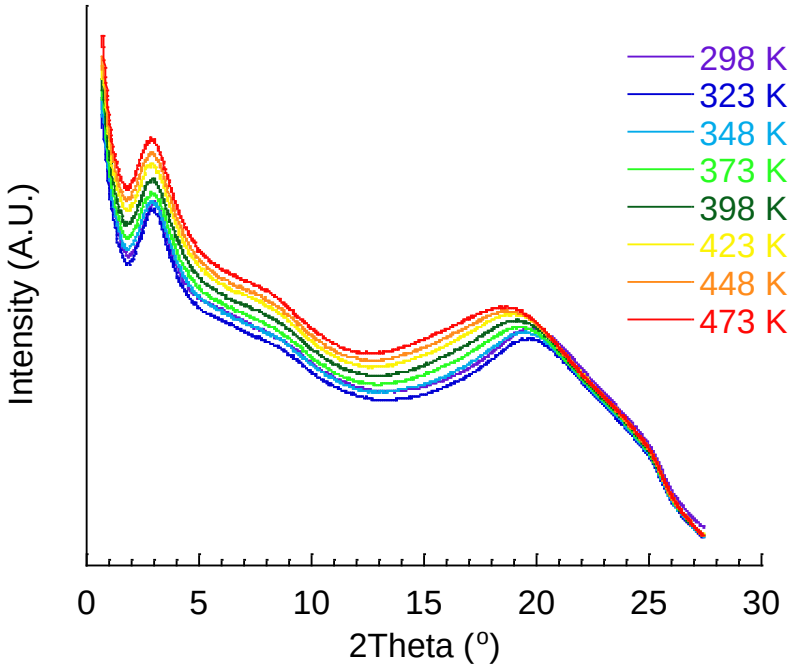

*Figure 5.11.5.ii: SAXS recorded for **5.6** at 25 K intervals while heating from 258 K to 473 K.*

Chapter Six

Conclusions and Future Work

6.1 Conclusions and final thoughts

The results discussed in the preceding chapters have illustrated how metallo-supramolecular assemblies can be used to synthesise functional materials incorporating properties such as porosity, SCO and SMM. Chapters two and three focused on complexes featuring ligands with pyridylhydrazone and related coordination motifs while chapters four and five focused on ligands featuring the imidazolylimine coordinating motif. The pyridylhydrazone moiety was of interest for two key reasons. Firstly, when the pyridylhydrazone moiety coordinates in the imino-keto form, the N-H moiety is a potent hydrogen bond donor which is of interest to crystal engineering. Secondly, when the pyridylhydrazone moiety coordinates to Fe(II) or Fe(III) in the deprotonated imino-enolate form, the complexes can exhibit SCO.

Chapter two featured ligands based on the rigid isophthalate core. Initially the coordination of the ligand in the anionic form was investigated with Fe(II), Fe(III) and Co(III). Tetranuclear grid complexes comprised of four ligands bridging four metal ions were formed, giving complexes **2.12** to **2.17**. In the case of the Fe(II), complexes **2.12** to **2.15**, the grid structures were neutral resulting in limited solubility which hindered the crystallisation and characterisation. The air sensitivity of the Fe(II) complexes required their synthesis and crystallisation to be carried out under an argon atmosphere. Complex **2.12** did not exhibit SCO and was diamagnetic between 1.85 and 400 K. However, complex **2.13**, featuring a peripheral bromo substituent, displayed partial SCO occurring in conjunction with desolvation of the crystal. When chloro substituents were included adjacent to the pyridylhydrazone binding site in complex **2.15**, the combined steric and electronic effects resulted in the Fe(II) centres remaining in the HS state. The Fe(III) analogue of **2.12**, complex **2.16**, displayed broad partial SCO between 160 and 400 K. The Co(III) analogue of **2.16**, complex **2.17** provided a diamagnetic system which facilitated analysis of the solution behaviour via NMR spectroscopy. During this study, an unusual bidentate coordination mode of the ligand in the neutral imino-keto form was serendipitously discovered. This resulted in the formation of an Fe(II) dinuclear triple mesocate **2.18**. The replacement of the pyridine with pyrazine moieties significantly altered the crystal packing for complex **2.19**, resulting in the occurrence of one-dimensional microporous channels in the structure. The hydrogen bond interactions between the pyrazine rings and the N-H hydrazide moieties resulted in the crystals of **2.19** exhibiting exceptional stability upon removal of the solvent of crystallisation under vacuum. Therefore, gas

sorption measurements were carried out which revealed a significant selectively for CO_2 over N_2 gas. Following this study, the functionality on the 5-position of the central isopthalate ring was modulated. The effect on the crystal packing was investigated to probe whether the nature of the pore functionality of the porous complex could be tuned. Bromo, iodo, amino and methoxy substituents were incorporated in complexes **2.20** to **2.23**, respectively. The halogen substituted complexes exhibited a similar packing to **2.19**. However, the one-dimensional channel was more compact due to the steric bulk of the halogen substituent and the formation of type II halogen bonds. The amino substituted complex was isostructural to **2.19**. The complex containing the methoxy substitutent did not exhibit the same hexagonal packing of the other mesocate complexes, which is believed to be due to the increased steric bulk of the methoxy substituent and is therefore non-porous.

Three novel ligands were synthesised in chapter three featuring either pyridylhydrazone (**L3.2** and **L3.5**) or the related quinolylhydrazone (**L3.3**) coordinating moieties bridged with succinic or adipate linker groups. Complexing the ligands to Co(II) resulted in a family of dinuclear helicates; **3.6** to **3.12**. The potency of the N-H hydrazide moiety as a hydrogen bond donor resulted in the formation of a hydrogen bond networks, the topology of which was anion specific. The quinolinyl group possessed a larger aromatic π-system and therefore the complexes containing ligand **L3.3** exhibited a greater propensity for the formation of π-π interactions.

Crystal packing is a significant feature of SCO and often polymorphic Fe(II) complexes will exhibit significantly different behaviour. The effect of crystal packing by solvent and anion modulation was investigated in chapter four. A family of helicates containing rigid imidazolylimine type ligands previously reported by the Kruger group was used as a basis for this study.[321] While all the complexes displayed thermally induced SCO, the abruptness of the spin state change and $T_{1/2}$ values were significantly different, reflecting the altered crystal packing. Of particular interest were complexes **4.4** and **4.5** which both contained the same ligand and triflate anion and differed only in the anti-solvent of crystallisation. However, the complexes exhibited different crystal packing and therefore different SCO behaviour. These complexes also displayed significant responses to light irradiation at low temperatures and therefore, further photomagnetic measurements were carried out to confirm the presence of a significant LIESST effect. Complexes **4.6** and **4.8** containing Fe(II) and Co(II) centres, respectively, featured the same ligand and counter

ion (tetrafluoroborate) and were isostructural. While **4.6** displayed complete SCO when dried, **4.8** behaved as an SMM in the presence of an applied DC field. This demonstrates the versatility of imidazolylimine type ligands for the synthesis of multinuclear structures displaying interesting magnetic behaviours

Finally, chapter five featured some preliminary work in the field of SCO mesogens. A family of SCO helicates previously reported by the Kruger group[316, 320] were functionalised with mesogenic substituents, with the aim of synthesising SCO liquid crystals. [316, 320 316, 320 316, 320 316, 320 316, 320 316, 320 316, 320] However, no phase change to a liquid crystalline state was detected via DSC or SAXS measurements. The two helicate complexes reported both exhibited partial SCO which was extremely gradual, characterised by absolute reflectivity, Raman and magnetic susceptibility measurements. Both of the complexes synthesised, **5.5** and **5.6**, exhibited very poor crystallinity. Therefore, no phase transition associated with the reorientation of the flexible alkyl chains upon heating or cooling was observed. It was postulated for a liquid crystalline state to be obtained, the mesogenic substituents of the ligand need to be orientated in different directions to those present in **5.5** and **5.6**, to facilitate the formation of a lamellar type phase. The use of branched alkyl substituents would further promote the liquid crystalline phase, as has been observed for other complexes in the literature.[459-460]

Several overarching conclusions can be drawn from the work conducted in the previous four chapters. First and foremost, large discrete metallo-supramolecular assemblies with low packing densities feature significant cavities that are occupied by solvent molecules when they crystallise. Unlike infinite assemblies such as MOFs, discrete assemblies such as those discussed in chapters two, three and four rapidly loose crystallinity due to solvent loss, upon removal from the mother liquor. Therefore, upon solvent loss the structure is unable to be elucidated and the exact cause of the change in the physical properties such SCO is somewhat speculative. One exception to this was complex **2.19** which retained crystallinity upon the removal of solvent due to a strong hydrogen bond network. The formation of similar hydrogen bond networks for the SCO species of this thesis would be desirable. However, the formation of molecular porous materials (MPMs) such as **2.19** is very system specific. For example, modification of the peripheral functionality in all but one example resulted in the loss of the hydrogen bond interaction responsible for the exceptional crystal stability.

In summary, the pyridylhydrazone motif is versatile for application in crystal engineering and Fe(II)/Fe(III) SCO. For the work reported in this thesis, the crystal engineering and synthesis of porous materials was more successful than the initial research into multinuclear SCO complexes. The imidazolylimine motif on the other hand reliably forms Fe(II) SCO and Co(II) SMM complexes and is readily applieds to the dinuclear triple helicates reported in this work. However, these helicate structures were not suitable for the synthesis of SCO mesogens.

6.2 Future work

6.2.1 Spin crossover liquid crystals

Based on the results obtained in chapter five, highly charged supramolecular complexes are not amenable to the formation of liquid crystalline phases. Neutral metallo-macrocycles functionalised with branched alky substituents have shown promise for the formation of liquid crystals.[459-460] The pyridylhydrazone motif coordinating in the anionic imino-enolate form results in neutral Fe(II) complexes, as investigated in chapter two.

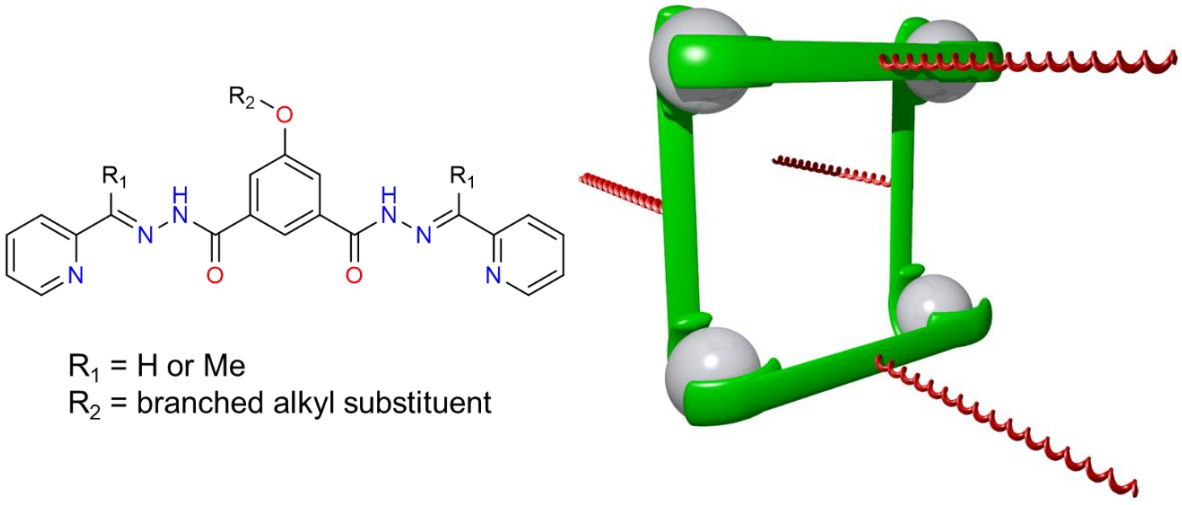

Figure 6.2.1.i: (left) The proposed ligand for the synthesis of SCO liquid crystals. The R_2 substituent attached at the oxygen atom in the 5'-position is a branched alkyl substituent. (right) A schematic representation of the tetranuclear grid complex functionalised with alkyl substituents represented by the red helicies.

Functionalisation of these complexes with branched alkyl substituents may allow for the formation of liquid crystalline phases upon heating. The relative orientation of the alkyl substituents can be controlled based on the point of attachment to the ligand (*Figure 6.2.1.i*). The ligand field for **2.12** was too strong resulting in a LS complex, while **2.13** was suitable for SCO. Mononuclear complexes, reported in the literature, containing pyridylhydrazone ligands displaying SCO typically feature hydroxy or alkoxy substituents on the aromatic ring conjugated to the hydrazone moiety. The electron rich ring may contribute to the weaker ligand field of these complexes and therefore SCO at more amenable temperatures. Hence, the proposed ligand would be the next logical step for improving the SCO behaviour of this family of tetranuclear Fe(II) complexes.

6.2.2 Chiral resolution of helicates

Many of the potential application of metallo-helicates arise from their intrinsic chirality. However, unless they are synthesised using a chiral ligand, the helicates are formed as a racemic mix. Methods for chiral resolution include separation of the enantiomers using column chromatography[410, 463] and more recently crystallisation with chiral anions.[442] Enantiomerically pure complexes are of interest as they crystallise in non-centrosymmetric space group and therefore exhibit non-linear optical (NLO) properties.[464-465] Of particular interest is the use of these chiral metal complexes for second harmonic generation as has been demonstrated by Rosa and co-workers with chiral $[Fe(phen)_3]^{2+}$ (phen = 1,10-phenanthroline) complexes.[466] There are a range of chiral anions suitable for enantiomeric separation such as tris(catechol)phosphate(V) (TRISCAT), tris(catechol)arsenate(V) (TRISCAS), tris(3,4,5,6-tetrachlorocatechol)phosphate(V) (TRISPHAT), antimonyl tartrate and arsenyl tatrate. The latter two are particularly amenable for chiral resolution via selective crystallization of one enantiomer because they are stable in solution and do not racemize.[442] Alternatively, the ligands featured in chapter three can be readily adapted to contain chiral functionality and therefore allow for the synthesis of enantiomerically pure helicate complexes. A related ligand to **L3.2** and **L3.3** can be synthesised from a tartaric acid derivative. Functionalization of the hydroxy groups of the tartaric acid based ligand with alkyl substituents would impart good solubilty of the ligand and resultant complex in organic solvents, aiding the synthesis and characterisation. Natural L-tartaric acid is commercially available and an analogue of ligand **L3.2** could be synthesised following a similar synthetic procedure used to synthesis the ligands in chapter two (*Figure 6.2.2.i*).

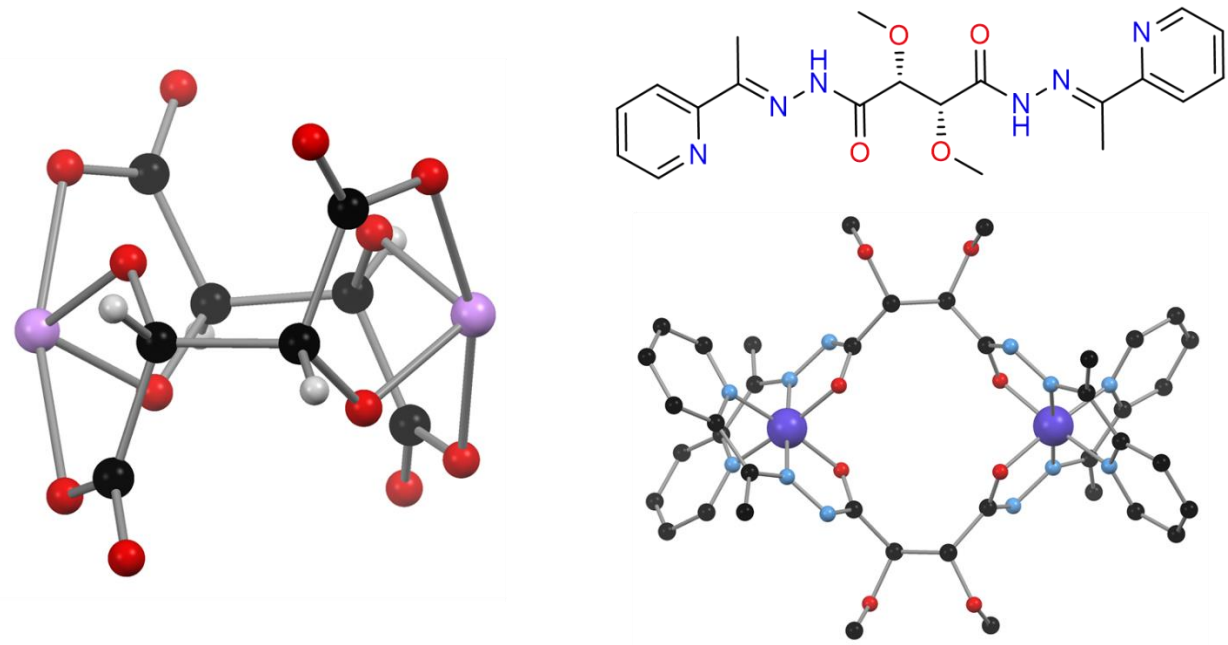

Figure 6.2.2.i: (left) Crystal structure of Λ-[As$_2$(L-tartrate)$_2$]$^{2-}$ from reference.[442] *(right) The proposed methoxy functionalised ligand derived from* ***L3.2****, synthesised from L-tartaric acid (top) and a molecular model of the resulting chiral Co(II) dinuclear double helicate analogous to those in chapter two (bottom).*

References

1. Cramer, F., Emil Fischer's Lock-and-Key Hypothesis after 100 years—Towards a Supracellular Chemistry. In *Perspectives in Supramolecular Chemistry*, Behr, J. P., Ed. Wiley: 2007.
2. Fischer, E., *Ber. Dtsch. Chem. Ges.* **1890,** *23*, 2611.
3. Fischer, E., *Ber. Dtsch. Chem. Ges.* **1894,** *27*, 2985.
4. Koshland, D. E., *Angew. Chem. Int. Ed.* **1995,** *33* (24), 2375.
5. Watson, J. D.; Crick, F. H. C., *Nature* **1953,** *171*, 737.
6. Lehn, J.-M., *Angew. Chem. Int. Ed.* **1988,** *27* (1), 89.
7. Lehn, J.-M., *J. Incl. Phenom.* **1988,** *6* (4), 351.
8. Lehn, J.-M., *Angew. Chem. Int. Ed.* **1990,** *29* (11), 1304.
9. Behr, J.-P.; Lehn, J.-M.; Dock, A.-C.; Moras, D., *Nature* **1982,** *295*, 526.
10. Lehn, J. M., *Acc. Chem. Res.* **1978,** *11* (2), 49.
11. Pedersen, C. J., *J. Am. Chem. Soc.* **1967,** *89* (10), 2495.
12. Cram, D. J.; Cram, J. M., *Science* **1974,** *183* (4127), 803.
13. Hoskins, B. F.; Robson, R., *J. Am. Chem. Soc.* **1989,** *111* (15), 5962.
14. Hoskins, B. F.; Robson, R., *J. Am. Chem. Soc.* **1990,** *112* (4), 1546.
15. Amabilino, D. B.; Stoddart, J. F., *Chem. Rev.* **1995,** *95* (8), 2725.
16. Balzani, V.; Credi, A.; Raymo, F. M.; Stoddart, J. F., *Angew. Chem. Int. Ed.* **2000,** *39* (19), 3348.
17. Balzani, V.; Gómez-López, M.; Stoddart, J. F., *Acc. Chem. Res.* **1998,** *31* (7), 405.
18. Bissell, R. A.; Córdova, E.; Kaifer, A. E.; Stoddart, J. F., *Nature* **1994,** *369*, 133.
19. Collier, C. P.; Mattersteig, G.; Wong, E. W.; Luo, Y.; Beverly, K.; Sampaio, J.; Raymo, F. M.; Stoddart, J. F.; Heath, J. R., *Science* **2000,** *289* (5482), 1172.
20. Browne, W. R.; Feringa, B. L., *Nat. Nanotech.* **2006,** *1*, 25.
21. Feringa, B. L., *Acc. Chem. Res.* **2001,** *34* (6), 504.
22. Feringa, B. L.; van Delden, R. A.; Koumura, N.; Geertsema, E. M., *Chem. Rev.* **2000,** *100* (5), 1789.
23. Koumura, N.; Zijlstra, R. W. J.; van Delden, R. A.; Harada, N.; Feringa, B. L., *Nature* **1999,** *401*, 152.
24. Lubbe, A. S.; Böhmer, C.; Tosi, F.; Szymanski, W.; Feringa, B. L., *J. Org. Chem.* **2018,** *83* (18), 11008.
25. Cesario, M.; Dietrich-Buchecker, C. O.; Guilhem, J.; Pascard, C.; Sauvage, J. P., *Chem. Commun.* **1985,** (5), 244.
26. Champin, B.; Mobian, P.; Sauvage, J.-P., *Chem. Soc. Rev.* **2007,** *36* (2), 358.
27. Collin, J.-P.; Dietrich-Buchecker, C.; Gaviña, P.; Jimenez-Molero, M. C.; Sauvage, J.-P., *Acc. Chem. Res.* **2001,** *34* (6), 477.
28. Dietrich-Buchecker, C.; Sauvage, J.-P., *Tetrahedron* **1990,** *46* (2), 503.
29. Dietrich-Buchecker, C. O.; Sauvage, J. P., *Chem. Rev.* **1987,** *87* (4), 795.
30. Dietrich-Buchecker, C. O.; Sauvage, J. P.; Kintzinger, J. P., *Tetrahedron Lett.* **1983,** *24* (46), 5095.
31. Ditrich-Buchecker, C. O.; Nierengarten, J. F.; Sauvage, J. P., *Tetrahedron Lett.* **1992,** *33* (25), 3625.

32. Jiménez, M. C.; Dietrich-Buchecker, C.; Sauvage, J.-P., *Angew. Chem. Int. Ed.* **2000,** *39* (18), 3284.
33. Sauvage, J.-P., *Acc. Chem. Res.* **1998,** *31* (10), 611.
34. Lewandowski, B.; De Bo, G.; Ward, J. W.; Papmeyer, M.; Kuschel, S.; Aldegunde, M. J.; Gramlich, P. M. E.; Heckmann, D.; Goldup, S. M.; D'Souza, D. M.; Fernandes, A. E.; Leigh, D. A., *Science* **2013,** *339* (6116), 189.
35. Milev, M., Nickel, O. M., Dominik, A. Povray model of a dna double helix. http://www.life-science-it.org/pages/research/projectPovrayHelix.html (accessed 29 August).
36. Sauvage, J. P., *Acc. Chem. Res.* **1990,** *23* (10), 319.
37. Bohne, C., *Chem. Soc. Rev.* **2014,** *43* (12), 4037.
38. Cook, T. R.; Zheng, Y.-R.; Stang, P. J., *Chem. Rev.* **2013,** *113* (1), 734.
39. Ludlow, R. F.; Otto, S., *Chem. Soc. Rev.* **2008,** *37* (1), 101.
40. Jeffrey, G., A., *An Introduction to Hydrogen Bonding*. Oxford University Press: Oxford, **1997**.
41. Steed, J. W.; Atwood, J., *Supramolecular chemistry*. John Wiley & Sons Ltd: Chichester, **2001**.
42. Hunter, C. A.; Sanders, J. K. M., *J. Am. Chem. Soc.* **1990,** *112* (14), 5525.
43. Martinez, C. R.; Iverson, B. L., *Chem. Sci.* **2012,** *3* (7), 2191.
44. Salonen, L. M.; Ellermann, M.; Diederich, F., *Angew. Chem. Int. Ed.* **2011,** *50* (21), 4808.
45. Cavallo, G.; Metrangolo, P.; Milani, R.; Pilati, T.; Priimagi, A.; Resnati, G.; Terraneo, G., *Chem. Rev.* **2016,** *116* (4), 2478.
46. Gilday, L. C.; Robinson, S. W.; Barendt, T. A.; Langton, M. J.; Mullaney, B. R.; Beer, P. D., *Chem. Rev.* **2015,** *115* (15), 7118.
47. Desiraju, G. R., *Nature* **2001,** *412*, 397.
48. Desiraju, G. R., *Angew. Chem. Int. Ed.* **1995,** *34* (21), 2311.
49. Corey, E. J., *Pure Appl. Chem.* **1967,** *14* (1), 19.
50. McNaugh, A. D.; Wilkinson, A., *IUPAC. Compendium of Chemical Terminology, 2nd ed. (the "Gold Book")*. Blackwell Scientific Publications: Oxford, **1997**.
51. Alkorta, I.; Rozas, I.; Elguero, J., *Chem. Soc. Rev.* **1998,** *27* (2), 163.
52. Calhorda, M. J., *Chem. Commun.* **2000,** (10), 801.
53. Steiner, T., *Chem. Commun.* **1997,** (8), 727.
54. Seto, C. T.; Whitesides, G. M., *J. Am. Chem. Soc.* **1990,** *112* (17), 6409.
55. Naseer, M. M.; Bauzá, A.; Alnasr, H.; Jurkschat, K.; Frontera, A., *CrystEngComm* **2018,** *20* (23), 3251.
56. Metrangolo, P.; Resnati, G., *IUCrJ* **2014,** *1* (1), 5.
57. Beale, T. M.; Chudzinski, M. G.; Sarwar, M. G.; Taylor, M. S., *Chem. Soc. Rev.* **2013,** *42* (4), 1667.
58. Ma, J. C.; Dougherty, D. A., *Chem. Rev.* **1997,** *97* (5), 1303.
59. Mahadevi, A. S.; Sastry, G. N., *Chem. Rev.* **2013,** *113* (3), 2100.
60. Schottel, B. L.; Chifotides, H. T.; Dunbar, K. R., *Chem. Soc. Rev.* **2008,** *37* (1), 68.
61. Wang, D.-X.; Wang, M.-X., *J. Am. Chem. Soc.* **2013,** *135* (2), 892.
62. McMorran, D. A.; Steel, P. J., *Supramol. Chem.* **2002,** *14* (1), 79.
63. O'Keefe, B. J.; Steel, P. J., *Inorg. Chem. Commun.* **2000,** *3* (9), 473.
64. Pyykkö, P., *Chem. Rev.* **1997,** *97* (3), 597.
65. Schmidbaur, H.; Schier, A., *Angew. Chem. Int. Ed.* **2014,** *54* (3), 746.
66. Schmidbaur, H.; Schier, A., *Chem. Soc. Rev.* **2012,** *41* (1), 370.

67. Schneider, J.; Lee, Y.-A.; Pérez, J.; Brennessel, W. W.; Flaschenriem, C.; Eisenberg, R., *Inorg. Chem.* **2008,** *47* (3), 957.
68. Constable, E. C., *Chem. Soc. Rev.* **2013,** *42* (4), 1637.
69. Constable, E. C.; Gale, P. A., *Chem. Soc. Rev.* **2013,** *42* (4), 1427.
70. Constable, E. C.; Housecroft, C. E., *Chem. Soc. Rev.* **2013,** *42* (4), 1429.
71. NobelPrize.org Alfred Werner – Biographical. https://www.nobelprize.org/prizes/chemistry/1913/werner/biographical/ (accessed 3 September).
72. George, P.; McClure, D. S.; Griffith, J. S.; Orgel, L. E., *J. Chem. Phys.* **1956,** *24* (6), 1269.
73. Griffith, J. S.; Orgel, L. E., *Chem. Soc. Rev.* **1957,** *11* (4), 381.
74. Smulders, M. M. J.; Riddell, I. A.; Browne, C.; Nitschke, J. R., *Chem. Soc. Rev.* **2013,** *42* (4), 1728.
75. Mathias, J. P.; Stoddart, J. F., *Chem. Soc. Rev.* **1992,** *21* (4), 215.
76. Guillerm, V.; Kim, D.; Eubank, J. F.; Luebke, R.; Liu, X.; Adil, K.; Lah, M. S.; Eddaoudi, M., *Chem. Soc. Rev.* **2014,** *43* (16), 6141.
77. Lu, W.; Wei, Z.; Gu, Z.-Y.; Liu, T.-F.; Park, J.; Park, J.; Tian, J.; Zhang, M.; Zhang, Q.; Gentle Iii, T.; Bosch, M.; Zhou, H.-C., *Chem. Soc. Rev.* **2014,** *43* (16), 5561.
78. O'Keeffe, M.; Yaghi, O. M., *Chem. Rev.* **2012,** *112* (2), 675.
79. Stock, N.; Biswas, S., *Chem. Rev.* **2012,** *112* (2), 933.
80. Chakrabarty, R.; Mukherjee, P. S.; Stang, P. J., *Chem. Rev.* **2011,** *111* (11), 6810.
81. Cook, T. R.; Stang, P. J., *Chem. Rev.* **2015,** *115* (15), 7001.
82. Fujita, M.; Oguro, D.; Miyazawa, M.; Oka, H.; Yamaguchi, K.; Ogura, K., *Nature* **1995,** *378*, 469.
83. Osuga, T.; Murase, T.; Ono, K.; Yamauchi, Y.; Fujita, M., *J. Am. Chem. Soc.* **2010,** *132* (44), 15553.
84. Yoshizawa, M.; Nakagawa, J.; Kumazawa, K.; Nagao, M.; Kawano, M.; Ozeki, T.; Fujita, M., *Angew. Chem. Int. Ed.* **2005,** *44* (12), 1810.
85. Wang, S.; Sawada, T.; Ohara, K.; Yamaguchi, K.; Fujita, M., *Angew. Chem. Int. Ed.* **2016,** *55* (6), 2063.
86. Browne, C.; Brenet, S.; Clegg, J. K.; Nitschke, J. R., *Angew. Chem. Int. Ed.* **2013,** *52* (7), 1944.
87. Mal, P.; Breiner, B.; Rissanen, K.; Nitschke, J. R., *Science* **2009,** *324* (5935), 1697.
88. Bilbeisi, R. A.; Clegg, J. K.; Elgrishi, N.; Hatten, X. d.; Devillard, M.; Breiner, B.; Mal, P.; Nitschke, J. R., *J. Am. Chem. Soc.* **2012,** *134* (11), 5110.
89. Hristova, Y. R.; Smulders, M. M. J.; Clegg, J. K.; Breiner, B.; Nitschke, J. R., *Chem. Sci.* **2011,** *2* (4), 638.
90. Meng, W.; Clegg, J. K.; Thoburn, J. D.; Nitschke, J. R., *J. Am. Chem. Soc.* **2011,** *133* (34), 13652.
91. Cullen, W.; Hunter, C. A.; Ward, M. D., *Inorg. Chem.* **2015,** *54* (6), 2626.
92. Paul, R. L.; Bell, Z. R.; Jeffery, J. C.; McCleverty, J. A.; Ward, M. D., *Proc. Natl. Acad. Sci.* **2002,** *99* (8), 4883.
93. Turega, S.; Whitehead, M.; Hall, B. R.; Meijer, A. J. H. M.; Hunter, C. A.; Ward, M. D., *Inorg. Chem.* **2013,** *52* (2), 1122.
94. Ward, M. D., *Chem. Commun.* **2009,** (30), 4487.
95. Ward, M. D.; Hunter, C. A.; Williams, N. H., *Acc. Chem. Res.* **2018,** *51* (9), 2073.
96. Beissel, T.; Powers, R. E.; Parac, T. N.; Raymond, K. N., *J. Am. Chem. Soc.* **1999,** *121* (17), 4200.

97. Caulder, D. L.; Powers, R. E.; Parac, T. N.; Raymond, K. N., *Angew. Chem. Int. Ed.* **2004,** *37* (14), 1840.
98. Caulder, D. L.; Raymond, K. N., *Acc. Chem. Res.* **1999,** *32* (11), 975.
99. Davis, A. V.; Fiedler, D.; Seeber, G.; Zahl, A.; van Eldik, R.; Raymond, K. N., *J. Am. Chem. Soc.* **2006,** *128* (4), 1324.
100. Ferguson, A.; Squire, M. A.; Siretanu, D.; Mitcov, D.; Mathoniere, C.; Clerac, R.; Kruger, P. E., *Chem. Commun.* **2013,** *49* (16), 1597.
101. Ferguson, A.; Staniland, R. W.; Fitchett, C. M.; Squire, M. A.; Williamson, B. E.; Kruger, P. E., *Dalton Trans.* **2014,** *43* (39), 14550.
102. Cullen, W.; Misuraca, M. C.; Hunter, C. A.; Williams, N. H.; Ward, M. D., *Nat. Chem.* **2016,** *8*, 231.
103. Turega, S.; Cullen, W.; Whitehead, M.; Hunter, C. A.; Ward, M. D., *J. Am. Chem. Soc.* **2014,** *136* (23), 8475.
104. Ward, M. D.; Hunter, C. A.; Williams, N. H., *Chem. Lett.* **2016,** *46* (1), 2.
105. Yang, L.; Jing, X.; He, C.; Chang, Z.; Duan, C., *Chem. Eur. J.* **2016,** *22* (50), 18107.
106. Smulders, M. M. J.; Jiménez, A.; Nitschke, J. R., *Angew. Chem. Int. Ed.* **2012,** *51* (27), 6681.
107. Ronson, T. K.; Zarra, S.; Black, S. P.; Nitschke, J. R., *Chem. Commun.* **2013,** *49* (25), 2476.
108. McConnell, A. J.; Aitchison, C. M.; Grommet, A. B.; Nitschke, J. R., *J. Am. Chem. Soc.* **2017,** *139* (18), 6294.
109. Mal, P.; Schultz, D.; Beyeh, K.; Rissanen, K.; Nitschke, J. R., *Angew. Chem. Int. Ed.* **2008,** *47* (43), 8297.
110. Piguet, C., *J. Incl. Phenom. Macrocycl. Chem.* **1999,** *34* (4), 361.
111. Piguet, C.; Bernardinelli, G.; Hopfgartner, G., *Chem. Rev.* **1997,** *97* (6), 2005.
112. Albrecht, M., *Chem. Rev.* **2001,** *101* (11), 3457.
113. Albrecht, M., *Chem. Eur. J.* **2000,** *6* (19), 3485.
114. Albrecht, M.; Kotila, S., *Angew. Chem. Int. Ed.* **1995,** *34* (19), 2134.
115. Lehn, J. M.; Rigault, A.; Siegel, J.; Harrowfield, J.; Chevrier, B.; Moras, D., *Proc. Natl. Acad. Sci.* **1987,** *84* (9), 2565.
116. Kramer, R.; Lehn, J. M.; Marquis-Rigault, A., *Proc. Natl. Acad. Sci.* **1993,** *90* (12), 5394.
117. Miyake, H.; Tsukube, H., *Chem. Soc. Rev.* **2012,** *41* (21), 6977.
118. Malina, J.; Hannon, M. J.; Brabec, V., *Sci. Rep.* **2016,** *6*, 29674.
119. Meistermann, I.; Moreno, V.; Prieto, M. J.; Moldrheim, E.; Sletten, E.; Khalid, S.; Rodger, P. M.; Peberdy, J. C.; Isaac, C. J.; Rodger, A.; Hannon, M. J., *Proc. Natl. Acad. Sci.* **2002,** *99* (8), 5069.
120. Pascu, G. I.; Hotze, A. C. G.; Sanchez-Cano, C.; Kariuki, B. M.; Hannon, M. J., *Angew. Chem. Int. Ed.* **2007,** *46* (23), 4374.
121. Uerpmann, C.; Malina, J.; Pascu, M.; Clarkson, G. J.; Moreno, V.; Rodger, A.; Grandas, A.; Hannon, M. J., *Chem. Eur. J.* **2005,** *11* (6), 1750.
122. Stevenson, K. A.; Melan, C. F. C.; Fleischel, O.; Wang, R.; Petitjean, A., *Cryst. Growth Des.* **2012,** *12* (11), 5169.
123. Hasenknopf, B.; Lehn, J.-M.; Boumediene, N.; Dupont-Gervais, A.; Van Dorsselaer, A.; Kneisel, B.; Fenske, D., *J. Am. Chem. Soc.* **1997,** *119* (45), 10956.
124. Hasenknopf, B.; Lehn, J.-M.; Kneisel, B. O.; Baum, G.; Fenske, D., *Angew. Chem. Int. Ed.* **1996,** *35* (16), 1838.
125. Hardy, J. G., *Chem. Soc. Rev.* **2013,** *42* (19), 7881.

126. Ruben, M.; Rojo, J.; Romero-Salguero, F. J.; Uppadine, L. H.; Lehn, J.-M., *Angew. Chem. Int. Ed.* **2004,** *43* (28), 3644.
127. Bassani, D. M.; Lehn, J.-M.; Fromm, K.; Fenske, D., *Angew. Chem. Int. Ed.* **1998,** *37* (17), 2364.
128. Breuning, E.; Ziener, U.; Lehn, J.-M.; Wegelius, E.; Rissanen, K., *Eur. J. Inorg. Chem.* **2001,** *2001* (6), 1515.
129. Hanan, G. S.; Volkmer, D.; Schubert, U. S.; Lehn, J.-M.; Baum, G.; Fenske, D., *Angew. Chem. Int. Ed.* **2003,** *36* (17), 1842.
130. Rojo, J.; Romero-Salguero, F. J.; Lehn, J.-M.; Baum, G.; Fenske, D., *Eur. J. Inorg. Chem.* **1999,** *1999* (9), 1421.
131. Ruben, M.; Lehn, J.-M.; Vaughan, G., *Chem. Commun.* **2003,** (12), 1338.
132. Hausmann, J.; Brooker, S., *Chem. Commun.* **2004,** (13), 1530.
133. Schäfer, B.; Greisch, J.-F.; Faus, I.; Bodenstein, T.; Šalitroš, I.; Fuhr, O.; Fink, K.; Schünemann, V.; Kappes, M. M.; Ruben, M., *Angew. Chem. Int. Ed.* **2016,** *55* (36), 10881.
134. Abedin, T. S. M.; Thompson, L. K.; Miller, D. O., *Chem. Commun.* **2005,** (44), 5512.
135. Baxter, P. N. W.; Lehn, J.-M.; Baum, G.; Fenske, D., *Chem. Eur. J.* **2000,** *6* (24), 4510.
136. Baxter, P. N. W.; Lehn, J.-M.; Kneisel, B. O.; Fenske, D., *Angew. Chem. Int. Ed.* **2003,** *36* (18), 1978.
137. Fujita, M., *Acc. Chem. Res.* **1999,** *32* (1), 53.
138. Fujita, M.; Ibukuro, F.; Hagihara, H.; Ogura, K., *Nature* **1994,** *367* (6465), 720.
139. Giri, C.; Topic, F.; Cametti, M.; Rissanen, K., *Chem. Sci.* **2015,** *6* (10), 5712.
140. Ayme, J.-F.; Beves, J. E.; Campbell, C. J.; Leigh, D. A., *Chem. Soc. Rev.* **2013,** *42* (4), 1700.
141. Forgan, R. S.; Sauvage, J.-P.; Stoddart, J. F., *Chem. Rev.* **2011,** *111* (9), 5434.
142. Ayme, J.-F.; Beves, J. E.; Leigh, D. A.; McBurney, R. T.; Rissanen, K.; Schultz, D., *Nat. Chem.* **2012,** *4* (1), 15.
143. dos Santos, C. M. G.; McCabe, T.; Watson, G. W.; Kruger, P. E.; Gunnlaugsson, T., *J. Org. Chem.* **2008,** *73* (23), 9235.
144. Pfeffer, F. M.; Gunnlaugsson, T.; Jensen, P.; Kruger, P. E., *Org. Lett.* **2005,** *7* (24), 5357.
145. Busschaert, N.; Caltagirone, C.; Van Rossom, W.; Gale, P. A., *Chem. Rev.* **2015,** *115* (15), 8038.
146. Custelcean, R.; Bonnesen, P. V.; Duncan, N. C.; Zhang, X.; Watson, L. A.; Van Berkel, G.; Parson, W. B.; Hay, B. P., *J. Am. Chem. Soc.* **2012,** *134* (20), 8525.
147. Yi, S.; Brega, V.; Captain, B.; Kaifer, A. E., *Chem. Commun.* **2012,** *48* (83), 10295.
148. Vardhan, H.; Verpoort, F., *Adv. Synth. Catal.* **2015,** *357* (7), 1351.
149. Yoshizawa, M.; Klosterman, J. K.; Fujita, M., *Angew. Chem. Int. Ed.* **2009,** *48* (19), 3418.
150. Yoshizawa, M.; Takeyama, Y.; Kusukawa, T.; Fujita, M., *Angew. Chem. Int. Ed.* **2002,** *41* (8), 1347.
151. Yoshizawa, M.; Tamura, M.; Fujita, M., *Science* **2006,** *312* (5771), 251.
152. Fiedler, D.; Bergman, R. G.; Raymond, K. N., *Angew. Chem. Int. Ed.* **2004,** *43* (48), 6748.
153. Fiedler, D.; van Halbeek, H.; Bergman, R. G.; Raymond, K. N., *J. Am. Chem. Soc.* **2006,** *128* (31), 10240.
154. Leung, D. H.; Bergman, R. G.; Raymond, K. N., *J. Am. Chem. Soc.* **2006,** *128* (30), 9781.
155. Leung, D. H.; Fiedler, D.; Bergman, R. G.; Raymond, K. N., *Angew. Chem. Int. Ed.* **2004,** *43* (8), 963.
156. Pluth, M. D.; Bergman, R. G.; Raymond, K. N., *Science* **2007,** *316* (5821), 85.

157. Brumaghim, J. L.; Michels, M.; Pagliero, D.; Raymond, K. N., *Eur. J. Org. Chem.* **2004,** *2004* (24), 5115.
158. Brumaghim, Julia L.; Michels, M.; Raymond, Kenneth N., *Eur. J. Org. Chem.* **2004,** *2004* (22), 4552.
159. Dong, V. M.; Fiedler, D.; Carl, B.; Bergman, R. G.; Raymond, K. N., *J. Am. Chem. Soc.* **2006,** *128* (45), 14464.
160. Langton, M. J.; Beer, P. D., *Acc. Chem. Res.* **2014,** *47* (7), 1935.
161. Lim, J. Y. C.; Marques, I.; Félix, V.; Beer, P. D., *J. Am. Chem. Soc.* **2017,** *139* (35), 12228.
162. Kassem, S.; Lee, A. T. L.; Leigh, D. A.; Markevicius, A.; Solà, J., *Nat. Chem.* **2015,** *8*, 138.
163. Pérez, E. M.; Dryden, D. T. F.; Leigh, D. A.; Teobaldi, G.; Zerbetto, F., *J. Am. Chem. Soc.* **2004,** *126* (39), 12210.
164. Zhang, L.; Marcos, V.; Leigh, D. A., *Proc. Natl. Acad. Sci.* **2018,** *115* (38), 9397.
165. Kay, E. R.; Leigh, D. A., *Angew. Chem. Int. Ed.* **2015,** *54* (35), 10080.
166. Bruns, C. J.; Stoddart, J. F., *Acc. Chem. Res.* **2014,** *47* (7), 2186.
167. Slater, A. G.; Cooper, A. I., *Science* **2015,** *348* (6238), 988.
168. Li, J.-R.; Kuppler, R. J.; Zhou, H.-C., *Chem. Soc. Rev.* **2009,** *38* (5), 1477.
169. Liao, P.-Q.; Chen, X.-W.; Liu, S.-Y.; Li, X.-Y.; Xu, Y.-T.; Tang, M.; Rui, Z.; Ji, H.; Zhang, J.-P.; Chen, X.-M., *Chem. Sci.* **2016,** *7* (10), 6528.
170. McDonald, T. M.; D'Alessandro, D. M.; Krishna, R.; Long, J. R., *Chem. Sci.* **2011,** *2* (10), 2022.
171. McDonald, T. M.; Mason, J. A.; Kong, X.; Bloch, E. D.; Gygi, D.; Dani, A.; Crocellà, V.; Giordanino, F.; Odoh, S. O.; Drisdell, W. S.; Vlaisavljevich, B.; Dzubak, A. L.; Poloni, R.; Schnell, S. K.; Planas, N.; Lee, K.; Pascal, T.; Wan, L. F.; Prendergast, D.; Neaton, J. B.; Smit, B.; Kortright, J. B.; Gagliardi, L.; Bordiga, S.; Reimer, J. A.; Long, J. R., *Nature* **2015,** *519*, 303.
172. Sumida, K.; Rogow, D. L.; Mason, J. A.; McDonald, T. M.; Bloch, E. D.; Herm, Z. R.; Bae, T.-H.; Long, J. R., *Chem. Rev.* **2012,** *112* (2), 724.
173. Burd, S. D.; Ma, S.; Perman, J. A.; Sikora, B. J.; Snurr, R. Q.; Thallapally, P. K.; Tian, J.; Wojtas, L.; Zaworotko, M. J., *J. Am. Chem. Soc.* **2012,** *134* (8), 3663.
174. Nugent, P.; Belmabkhout, Y.; Burd, S. D.; Cairns, A. J.; Luebke, R.; Forrest, K.; Pham, T.; Ma, S.; Space, B.; Wojtas, L.; Eddaoudi, M.; Zaworotko, M. J., *Nature* **2013,** *495*, 80.
175. Shekhah, O.; Belmabkhout, Y.; Chen, Z.; Guillerm, V.; Cairns, A.; Adil, K.; Eddaoudi, M., *Nat. Commun.* **2014,** *5*, 4228.
176. Skarmoutsos, I.; Belmabkhout, Y.; Adil, K.; Eddaoudi, M.; Maurin, G., *J. Phys. Chem. C* **2017,** *121* (49), 27462.
177. Ding, S.-Y.; Wang, W., *Chem. Soc. Rev.* **2013,** *42* (2), 548.
178. Han, Y.-F.; Yuan, Y.-X.; Wang, H.-B., *Molecules* **2017,** *22* (2), 266.
179. He, Y.; Xiang, S.; Chen, B., *J. Am. Chem. Soc.* **2011,** *133* (37), 14570.
180. Mastalerz, M.; Oppel, I. M., *Angew. Chem. Int. Ed.* **2012,** *51* (21), 5252.
181. Sozzani, P.; Bracco, S.; Comotti, A.; Ferretti, L.; Simonutti, R., *Angew. Chem. Int. Ed.* **2005,** *44* (12), 1816.
182. Hasell, T.; Miklitz, M.; Stephenson, A.; Little, M. A.; Chong, S. Y.; Clowes, R.; Chen, L.; Holden, D.; Tribello, G. A.; Jelfs, K. E.; Cooper, A. I., *J. Am. Chem. Soc.* **2016,** *138* (5), 1653.
183. Mitra, T.; Wu, X.; Clowes, R.; Jones, J. T. A.; Jelfs, K. E.; Adams, D. J.; Trewin, A.; Bacsa, J.; Steiner, A.; Cooper, A. I., *Chem. Eur. J.* **2011,** *17* (37), 10235.

184. Nugent, P. S.; Rhodus, V. L.; Pham, T.; Forrest, K.; Wojtas, L.; Space, B.; Zaworotko, M. J., *J. Am. Chem. Soc.* **2013,** *135* (30), 10950.
185. Pham, T.; Forrest, K. A.; Chen, K.-J.; Kumar, A.; Zaworotko, M. J.; Space, B., *Langmuir* **2016,** *32* (44), 11492.
186. Thomas-Gipson, J.; Beobide, G.; Castillo, O.; Fröba, M.; Hoffmann, F.; Luque, A.; Pérez-Yáñez, S.; Román, P., *Cryst. Growth Des.* **2014,** *14* (8), 4019.
187. Mouchaham, G.; Roques, N.; Brandès, S.; Duhayon, C.; Sutter, J.-P., *Cryst. Growth Des.* **2011,** *11* (12), 5424.
188. Roques, N.; Mouchaham, G.; Duhayon, C.; Brandès, S.; Tachon, A.; Weber, G.; Bellat Jean, P.; Sutter, J. P., *Chem. Eur. J.* **2014,** *20* (37), 11690.
189. Preston, D.; White, K. F.; Lewis, J. E. M.; Vasdev, R. A. S.; Abrahams, B. F.; Crowley, J. D., *Chem. Eur. J.* **2017,** *23* (44), 10559.
190. Wright, J. S.; Metherell, A. J.; Cullen, W. M.; Piper, J. R.; Dawson, R.; Ward, M. D., *Chem. Commun.* **2017,** *53* (31), 4398.
191. Duriska, M. B.; Neville, S. M.; Lu, J.; Iremonger, S. S.; Boas, J. F.; Kepert, C. J.; Batten, S. R., *Angew. Chem. Int. Ed.* **2009,** *48* (47), 8919.
192. Craig, G. A.; Larpent, P.; Kusaka, S.; Matsuda, R.; Kitagawa, S.; Furukawa, S., *Chem. Sci.* **2018,** *9*, 6463.
193. Li, J.-R.; Zhou, H.-C., *Nat. Chem.* **2010,** *2*, 893.
194. Teo, J. M.; Coghlan, C. J.; Evans, J. D.; Tsivion, E.; Head-Gordon, M.; Sumby, C. J.; Doonan, C. J., *Chem. Commun.* **2016,** *52* (2), 276.
195. Chen, Y.; Wang, Y.; Yang, C.; Wang, S.; Yang, J.; Li, J., *ACS Sustain. Chem. Eng.* **2017,** *5* (6), 5082.
196. Wang, S.; Belmabkhout, Y.; Cairns, A. J.; Li, G.; Huo, Q.; Liu, Y.; Eddaoudi, M., *ACS Appl. Mater. Interfaces* **2017,** *9* (39), 33521.
197. Wang, S.; Zhao, T.; Li, G.; Wojtas, L.; Huo, Q.; Eddaoudi, M.; Liu, Y., *J. Am. Chem. Soc.* **2010,** *132* (51), 18038.
198. Barbour, L. J., *Chem. Commun.* **2006,** (11), 1163.
199. Thomas-Gipson, J.; Beobide, G.; Castillo, O.; Cepeda, J.; Luque, A.; Perez-Yanez, S.; Aguayo, A. T.; Roman, P., *CrystEngComm* **2011,** *13* (10), 3301.
200. Bao, Z.; Xie, D.; Chang, G.; Wu, H.; Li, L.; Zhou, W.; Wang, H.; Zhang, Z.; Xing, H.; Yang, Q.; Zaworotko, M. J.; Ren, Q.; Chen, B., *J. Am. Chem. Soc.* **2018,** *140* (13), 4596.
201. Vitórica-Yrezábal, I. J.; Sava, D. F.; Timco, G. A.; Brown, M. S.; Savage, M.; Godfrey, H. G. W.; Moreau, F.; Schröder, M.; Siperstein, F.; Brammer, L.; Yang, S.; Attfield, M. P.; McDouall, J. J. W.; Winpenny, R. E. P., *Angew. Chem. Int. Ed.* **2017,** *56* (20), 5527.
202. *Spin Crossover in Transition Metal Compounds I*. Springer: **2004**.
203. *Spin Crossover in Transition Metal Compounds II*. Springer: **2004**.
204. *Spin Crossover in Transition Metal Compounds III*. Springer: **2004**.
205. Aguilà, D.; Prado, Y.; Koumousi, E. S.; Mathonière, C.; Clérac, R., *Chem. Soc. Rev.* **2016,** *45* (1), 203.
206. Koumousi, E. S.; Jeon, I.-R.; Gao, Q.; Dechambenoit, P.; Woodruff, D. N.; Merzeau, P.; Buisson, L.; Jia, X.; Li, D.; Volatron, F.; Mathonière, C.; Clérac, R., *J. Am. Chem. Soc.* **2014,** *136* (44), 15461.
207. Mathonière, C., *Eur. J. Inorg. Chem.* **2017,** *2018* (4), 248.
208. Adams, D. M.; Dei, A.; Rheingold, A. L.; Hendrickson, D. N., *Angew. Chem. Int. Ed.* **1993,** *32* (6), 880.

209. Gütlich, P.; Dei, A., *Angew. Chem. Int. Ed.* **2004,** *36* (24), 2734.
210. Gütlich, P.; Garcia, Y.; Goodwin, H. A., *Chem. Soc. Rev.* **2000,** *29* (6), 419.
211. Gütlich, P.; Hauser, A.; Spiering, H., *Angew. Chem. Int. Ed.* **1994,** *33* (20), 2024.
212. Halcrow, M. A., *Spin-Crossover Materials: Properties and Applications*. 1 ed.; Wiley: **2013**.
213. Real, J. A.; Gaspar, A. B.; Munoz, M. C., *Dalton Trans.* **2005,** (12), 2062.
214. Gutlich, P.; Garcia, Y.; Goodwin, H. A., *Chem. Soc. Rev.* **2000,** *29* (6), 419.
215. Gütlich, P.; Gaspar, A. B.; Garcia, Y., *Beilstein J. Org. Chem.* **2013,** *9*, 342.
216. Halcrow, A. M., *Crystals* **2016,** *6* (5).
217. Harding, D. J.; Harding, P.; Phonsri, W., *Coord. Chem. Rev.* **2016,** *313*, 38.
218. Krivokapic, I.; Zerara, M.; Daku, M. L.; Vargas, A.; Enachescu, C.; Ambrus, C.; Tregenna-Piggott, P.; Amstutz, N.; Krausz, E.; Hauser, A., *Coord. Chem. Rev.* **2007,** *251* (4), 364.
219. Klaeui, W.; Eberspach, W.; Guetlich, P., *Inorg. Chem.* **1987,** *26* (24), 3977.
220. Guionneau, P.; Marchivie, M.; Garcia, Y.; Howard, J. A. K.; Chasseau, D., *Phys. Rev. B* **2005,** *72* (21), 214408.
221. Sirirak, J.; Harding, D. J.; Harding, P.; Murray, K. S.; Moubaraki, B.; Liu, L.; Telfer, S. G., *Eur. J. Inorg. Chem.* **2015,** *2015* (15), 2534.
222. Cambi, L.; Szegö, L., *Ber. Dtsch. Chem. Ges.* **1931,** *64* (10), 2591.
223. Nihei, M.; Shiga, T.; Maeda, Y.; Oshio, H., *Coord. Chem. Rev.* **2007,** *251* (21), 2606.
224. Kahn, O., *Molecular Magnetism*. VCH Publishers: New York, **1993**.
225. Slichter, C. P.; Drickamer, H. G., *J. Chem. Phys.* **1972,** *56* (5), 2142.
226. Brooker, S., *Chem. Soc. Rev.* **2015,** *44* (10), 2880.
227. Dîrtu, M. M.; Naik, A. D.; Rotaru, A.; Spinu, L.; Poelman, D.; Garcia, Y., *Inorg. Chem.* **2016,** *55* (9), 4278.
228. Hayami, S.; Gu, Z.-z.; Yoshiki, H.; Fujishima, A.; Sato, O., *J. Am. Chem. Soc.* **2001,** *123* (47), 11644.
229. Lochenie, C.; Bauer, W.; Railliet, A. P.; Schlamp, S.; Garcia, Y.; Weber, B., *Inorg. Chem.* **2014,** *53* (21), 11563.
230. Phukkaphan, N.; Cruickshank, D. L.; Murray, K. S.; Phonsri, W.; Harding, P.; Harding, D. J., *Chem. Commun.* **2017,** *53* (70), 9801.
231. Bréfuel , N.; Watanabe, H.; Toupet, L.; Come, J.; Matsumoto, N.; Collet, E.; Tanaka, K.; Tuchagues, J.-P., *Angew. Chem.* **2009,** *121* (49), 9468.
232. Chernyshov, D.; Hostettler, M.; Törnroos, K. W.; Bürgi, H.-B., *Angew. Chem. Int. Ed.* **2003,** *42* (32), 3825.
233. Harding, D. J.; Phonsri, W.; Harding, P.; Murray, K. S.; Moubaraki, B.; Jameson, G. N. L., *Dalton Trans.* **2015,** *44* (34), 15079.
234. Ortega-Villar, N.; Muñoz, C. M.; Real, A. J., *Magnetochemistry* **2016,** *2* (1), 16.
235. Vieira, B. J. C.; Coutinho, J. T.; Santos, I. C.; Pereira, L. C. J.; Waerenborgh, J. C.; da Gama, V., *Inorg. Chem.* **2013,** *52* (7), 3845.
236. Vela, S.; Paulsen, H., *Inorg. Chem.* **2018,** *57* (15), 9478.
237. Clements, J. E.; Price, J. R.; Neville, S. M.; Kepert, C. J., *Angew. Chem. Int. Ed.* **2016,** *55* (48), 15105.
238. Murphy, M. J.; Zenere, K. A.; Ragon, F.; Southon, P. D.; Kepert, C. J.; Neville, S. M., *J. Am. Chem. Soc.* **2017,** *139* (3), 1330.

239. Trzop, E.; Zhang, D.; Piñeiro-Lopez, L.; Valverde-Muñoz, F. J.; Carmen Muñoz, M.; Palatinus, L.; Guerin, L.; Cailleau, H.; Real, J. A.; Collet, E., *Angew. Chem. Int. Ed.* **2016,** *55* (30), 8675.
240. McGravey, J. J.; Lawthers, I., *Chem. Commun.* **1982,** (16), 906.
241. Lawthers, I.; McGarvey, J. J., *J. Am. Chem. Soc.* **1984,** *106* (15), 4280.
242. Decurtins, S.; Gutlich, P.; Hasselbach, K. M.; Hauser, A.; Spiering, H., *Inorg. Chem.* **1985,** *24* (14), 2174.
243. Decurtins, S.; Gütlich, P.; Köhler, C. P.; Spiering, H.; Hauser, A., **1984,** *105* (1), 1.
244. Hauser, A., **1986,** *124* (6), 543.
245. Auböck, G.; Chergui, M., *Nat. Chem.* **2015,** *7*, 629.
246. Coronado, E.; Yamashita, M., *Dalton Trans.* **2016,** *45* (42), 16553.
247. Nelson, S. M.; McIlroy, P. D. A.; Stevenson, C. S.; König, E.; Ritter, G.; Waigel, J., *Dalton Trans.* **1986,** (5), 991.
248. Costa, J. S.; Balde, C.; Carbonera, C.; Denux, D.; Wattiaux, A.; Desplanches, C.; Ader, J.-P.; Gütlich, P.; Létard, J.-F., *Inorg. Chem.* **2007,** *46* (10), 4114.
249. Hayami, S.; Gu, Z.-z.; Einaga, Y.; Kobayasi, Y.; Ishikawa, Y.; Yamada, Y.; Fujishima, A.; Sato, O., *Inorg. Chem.* **2001,** *40* (13), 3240.
250. Wang, H.; Desplanches, C.; Dagault, P.; Létard, J.-F., *Dalton Trans.* **2014,** *43* (41), 15346.
251. Guionneau, P.; Le Gac, F.; Kaiba, A.; Costa, J. S.; Chasseau, D.; Létard, J.-F., *Chem. Commun.* **2007,** (36), 3723.
252. Aguilà, D.; Dechambenoit, P.; Rouzières, M.; Mathonière, C.; Clérac, R., *Chem. Commun.* **2017,** *53* (84), 11588.
253. Letard, J.-F., *J. Mater. Chem.* **2006,** *16* (26), 2550.
254. Létard, J.-F.; Capes, L.; Chastanet, G.; Moliner, N.; Létard, S.; Real, J.-A.; Kahn, O., *Chem. Phys. Lett.* **1999,** *313* (1–2), 115.
255. Boillot, M. L.; Pillet, S.; Tissot, A.; Rivière, E.; Claiser, N.; Lecomte, C., *Inorg. Chem.* **2009,** *48* (11), 4729.
256. Boillot, M.-L.; Roux, C.; Audière, J.-P.; Dausse, A.; Zarembowitch, J., *Inorg. Chem.* **1996,** *35* (13), 3975.
257. Venkataramani, S.; Jana, U.; Dommaschk, M.; Sönnichsen, F. D.; Tuczek, F.; Herges, R., *Science* **2011,** *331* (6016), 445.
258. Bannwarth, A.; Schmidt, S. O.; Peters, G.; Sönnichsen, F. D.; Thimm, W.; Herges, R.; Tuczek, F., *Eur. J. Inorg. Chem.* **2012,** *2012* (16), 2776.
259. Milek, M.; Heinemann, F. W.; Khusniyarov, M. M., *Inorg. Chem.* **2013,** *52* (19), 11585.
260. Herber, R. H., *Inorg. Chem.* **1987,** *26* (1), 173.
261. Koenig, E.; Madeja, K.; Watson, K. J., *J. Amer. Chem. Soc.* **1968,** *90* (5), 1146.
262. Kulshreshtha, S. K.; Iyer, R. M., *Chem. Phys. Lett.* **1984,** *108* (5), 501.
263. Baker, W. A.; Bobonich, H. M., *Inorg. Chem.* **1964,** *3* (8), 1184.
264. Decurtins, S.; Gutlich, P.; Kohler, C. P.; Spiering, H., *Chem. Commun.* **1985,** (7), 430.
265. Ganguli, P.; Gutlich, P.; Muller, E. W.; Irler, W., *Dalton Trans.* **1981,** (2), 441.
266. Koenig, E.; Madeja, K., *Inorg. Chem.* **1967,** *6* (1), 48.
267. Konig, E.; Madeja, K., *Chem. Commun.* **1966,** (3), 61.
268. Shklover, V.; Nesper, R.; Zakeeruddin, S. M.; Fraser, D. M.; Grätzel, M., *Inorg. Chim. Acta* **1996,** *247* (2), 237.
269. Onggo, D.; Hook, J. M.; Rae, A. D.; Goodwin, H. A., *Inorg. Chim. Acta* **1990,** *173* (1), 19.
270. Onggo, D.; Goodwin, H. A., *Aust. J. Chem.* **1991,** *44* (11), 1539.

271. Craig, D. C.; Goodwin, H. A.; Onggo, D., *Aust. J. Chem.* **1988,** *41* (8), 1157.
272. Sugiyarto, K. H.; Goodwin, H. A., *Aust. J. Chem.* **1988,** *41* (11), 1645.
273. Dosser, R. J.; Eilbeck, W. J.; Underhill, A. E.; Edwards, P. R.; Johnson, C. E., *J. Chem. Soc. A* **1969,** (0), 810.
274. Abushamleh, A. S.; Goodwin, H. A., *Aust. J. Chem.* **1979,** *32* (3), 513.
275. Burnett, M. G.; McKee, V.; Nelson, S. M., *Dalton Trans.* **1981,** (7), 1492.
276. Phan, H.; Hrudka, J. J.; Igimbayeva, D.; Lawson Daku, L. M.; Shatruk, M., *J. Am. Chem. Soc.* **2017,** *139* (18), 6437.
277. Schultz, D.; Nitschke, J. R., *Angew. Chem. Int. Ed.* **2006,** *45* (15), 2453.
278. Batschelet, W. H.; Rose, N. J., *Inorg. Chem.* **1983,** *22* (14), 2083.
279. Bowman, D. N.; Jakubikova, E., *Inorg. Chem.* **2012,** *51* (11), 6011.
280. Hong, K.; Cho, H.; Schoenlein, R. W.; Kim, T. K.; Huse, N., *Acc. Chem. Res.* **2015,** *48* (11), 2957.
281. Hagiwara, H.; Matsumoto, N.; Iijima, S.; Kojima, M., *Inorg. Chim. Acta* **2011,** *366* (1), 283.
282. Iijima, S.; Hagiwara, H.; Torigoe, H.; Matsumoto, N., *J. Nucl. Radiochem. Sci.* **2007,** *8* (2), 85.
283. Yamada, M.; Hagiwara, H.; Torigoe, H.; Matsumoto, N.; Kojima, M.; Dahan, F.; Tuchagues, J.-P.; Re, N.; Iijima, S., *Chem. Eur. J.* **2006,** *12* (17), 4536.
284. Yamada, M.; Fukumoto, E.; Ooidemizu, M.; Bréfuel, N.; Matsumoto, N.; Iijima, S.; Kojima, M.; Re, N.; Dahan, F.; Tuchagues, J.-P., *Inorg. Chem.* **2005,** *44* (20), 6967.
285. Brewer, C.; Brewer, G.; Patil, G.; Sun, Y.; Viragh, C.; Butcher, R. J., *Inorg. Chim. Acta* **2005,** *358* (12), 3441.
286. Yamada, M.; Ooidemizu, M.; Ikuta, Y.; Osa, S.; Matsumoto, N.; Iijima, S.; Kojima, M.; Dahan, F.; Tuchagues, J.-P., *Inorg. Chem.* **2003,** *42* (25), 8406.
287. Ikuta, Y.; Ooidemizu, M.; Yamahata, Y.; Yamada, M.; Osa, S.; Matsumoto, N.; Iijima, S.; Sunatsuki, Y.; Kojima, M.; Dahan, F.; Tuchagues, J.-P., *Inorg. Chem.* **2003,** *42* (22), 7001.
288. Brewer, G.; Butcher, R. J.; Viragh, C.; White, G., *Dalton Trans.* **2007,** (37), 4132.
289. Alvarado, L.; Brewer, C.; Brewer, G.; Butcher, R. J.; Straka, A.; Viragh, C., *CrystEngComm* **2009,** *11* (11), 2297.
290. Brewer, G.; Brewer, C.; Butcher, R. J.; Carpenter, E. E.; May, L.; White, G., *Inorg. Chim. Acta* **2007,** *360* (6), 2153.
291. Brewer, G.; Luckett, C.; May, L.; Beatty, A. M.; Scheidt, W. R., *Inorg. Chim. Acta* **2004,** *357* (8), 2390.
292. Brewer, C.; Brewer, G.; Butcher, R. J.; Carpenter, E. E.; Cuenca, L.; Noll, B. C.; Scheidt, W. R.; Viragh, C.; Zavalij, P. Y.; Zielaski, D., *Dalton Trans.* **2006,** (8), 1009.
293. Sunatsuki, Y.; Ohta, H.; Kojima, M.; Ikuta, Y.; Goto, Y.; Matsumoto, N.; Iijima, S.; Akashi, H.; Kaizaki, S.; Dahan, F.; Tuchagues, J.-P., *Inorg. Chem.* **2004,** *43* (14), 4154.
294. Sunatsuki, Y.; Ikuta, Y.; Matsumoto, N.; Ohta, H.; Kojima, M.; Iijima, S.; Hayami, S.; Maeda, Y.; Kaizaki, S.; Dahan, F.; Tuchagues, J.-P., *Angew. Chem. Int. Ed.* **2003,** *42* (14), 1614.
295. Ben Djamâa, A.; Clemente-León, M.; Coronado, E.; López-Jordà, M., *Polyhedron* **2013,** *64*, 142.
296. Thompson, J. R.; Archer, R. J.; Hawes, C. S.; Ferguson, A.; Wattiaux, A.; Mathoniere, C.; Clerac, R.; Kruger, P. E., *Dalton Trans.* **2012,** *41* (41), 12720.
297. Scott, H. S.; Staniland, R. W.; Kruger, P. E., *Coord. Chem. Rev.* **2018,** *362*, 24.

298. Phonsri, W.; Davies, C. G.; Jameson, G. N. L.; Moubaraki, B.; Ward, J. S.; Kruger, P. E.; Chastanet, G.; Murray, K. S., *Chem. Commun.* **2017,** *53* (8), 1374.
299. Phonsri, W.; Macedo, D. S.; Vignesh, K. R.; Rajaraman, G.; Davies, C. G.; Jameson, G. N. L.; Moubaraki, B.; Ward, J. S.; Kruger, P. E.; Chastanet, G.; Murray, K. S., *Chem. Eur. J.* **2017,** *23* (29), 7052.
300. Romero-Morcillo, T.; Seredyuk, M.; Muñoz, M. C.; Real, J. A., *Angew. Chem. Int. Ed.* **2015,** *54* (49), 14777.
301. Schönfeld, S.; Lochenie, C.; Thoma, P.; Weber, B., *CrystEngComm* **2015,** *17* (29), 5389.
302. Shongwe, M. S.; Al-Rahbi, S. H.; Al-Azani, M. A.; Al-Muharbi, A. A.; Al-Mjeni, F.; Matoga, D.; Gismelseed, A.; Al-Omari, I. A.; Yousif, A.; Adams, H.; Morris, M. J.; Mikuriya, M., *Dalton Trans.* **2012,** *41* (8), 2500.
303. Weber, B., *Novel Mononuclear Spin-Crossover Complexes*. Wiley: **2013**.
304. Zhang, L.; Xu, G.-C.; Wang, Z.-M.; Gao, S., *Eur. J. Inorg. Chem.* **2013,** *2013* (6), 1043.
305. Zhang, L.; Xu, G.-C.; Xu, H.-B.; Mereacre, V.; Wang, Z.-M.; Powell, A. K.; Gao, S., *Dalton Trans.* **2010,** *39* (20), 4856.
306. Zhang, L.; Xu, G.-C.; Xu, H.-B.; Zhang, T.; Wang, Z.-M.; Yuan, M.; Gao, S., *Chem. Commun.* **2010,** *46* (15), 2554.
307. Weber, B.; Bauer, W.; Obel, J., *Angew. Chem. Int. Ed.* **2008,** *47* (52), 10098.
308. Weber, B.; Carbonera, C.; Desplances, C.; Létard, J.-F., *Eur. J. Inorg. Chem.* **2008,** *2008* (10), 1589.
309. Weber, B.; Kaps, E.; Weigand, J.; Carbonera, C.; Letard, J.-F.; Achterhold, K.; Parak, F. G., *Inorg. Chem.* **2008,** *47* (2), 487.
310. McConnell, A. J., *Supramol. Chem.* **2017**, 1.
311. Craze, R. A.; Sciortino, F. N.; Badbhade, M. M.; Kepert, J. C.; Marjo, E. C.; Li, F., *Inorganics* **2017,** *5* (4), 62.
312. Darawsheh, M.; Barrios, L. A.; Roubeau, O.; Teat, S. J.; Aromí, G., *Chem. Eur. J.* **2016,** *22* (25), 8635.
313. Estrader, M.; Salinas Uber, J.; Barrios, L. A.; Garcia, J.; Lloyd-Williams, P.; Roubeau, O.; Teat, S. J.; Aromí, G., *Angew. Chem. Int. Ed.* **2017,** *56* (49), 15622.
314. Fujita, K.; Kawamoto, R.; Tsubouchi, R.; Sunatsuki, Y.; Kojima, M.; Iijima, S.; Matsumoto, N., *Chem. Lett.* **2007,** *36* (10), 1284.
315. Li, L.; Craze, A. R.; Akiyoshi, R.; Tsukiashi, A.; Hayami, S.; Mustonen, O.; Bhadbhade, M. M.; Bhattacharyya, S.; Marjo, C. E.; Wang, Y.; Lindoy, L. F.; Aldrich-Wright, J. R.; Li, F., *Dalton Trans.* **2018,** *47*, 2543.
316. Pelleteret, D.; Clerac, R.; Mathoniere, C.; Harte, E.; Schmitt, W.; Kruger, P. E., *Chem. Commun.* **2009,** (2), 221.
317. Sunatsuki, Y.; Kawamoto, R.; Fujita, K.; Maruyama, H.; Suzuki, T.; Ishida, H.; Kojima, M.; Iijima, S.; Matsumoto, N., *Inorg. Chem.* **2009,** *48* (18), 8784.
318. Telfer, S. G.; Bocquet, B.; Williams, A. F., *Inorg. Chem.* **2001,** *40* (19), 4818.
319. Tuna, F.; Lees, M. R.; Clarkson, G. J.; Hannon, M. J., *Chem. Eur. J.* **2004,** *10* (22), 5737.
320. Archer, R. J.; Hawes, C. S.; Jameson, G. N. L.; McKee, V.; Moubaraki, B.; Chilton, N. F.; Murray, K. S.; Schmitt, W.; Kruger, P. E., *Dalton Trans.* **2011,** *40* (45), 12368.
321. Archer, R. J.; Scott, H. S.; Polson, M. I. J.; Williamson, B. E.; Mathonière, C.; Rouzières, M.; Clérac, R.; Kruger, P. E., *Dalton Trans.* **2018,** *47* (24), 7965.
322. Hagiwara, H.; Tanaka, T.; Hora, S., *Dalton Trans.* **2016,** *45* (43), 17132.

323. Bilbeisi, R. A.; Zarra, S.; Feltham, H. L. C.; Jameson, G. N. L.; Clegg, J. K.; Brooker, S.; Nitschke, J. R., *Chem. Eur. J.* **2013,** *19* (25), 8058.
324. Li, L.; Saigo, N.; Zhang, Y.; Fanna, D. J.; Shepherd, N. D.; Clegg, J. K.; Zheng, R.; Hayami, S.; Lindoy, L. F.; Aldrich-Wright, J. R.; Li, C.-G.; Reynolds, J. K.; Harman, D. G.; Li, F., *J. Mater. Chem. C* **2015,** *3* (30), 7878.
325. Ren, D.-H.; Qiu, D.; Pang, C.-Y.; Li, Z.; Gu, Z.-G., *Chem. Commun.* **2015,** *51* (4), 788.
326. Zhang, F.-L.; Chen, J.-Q.; Qin, L.-F.; Tian, L.; Li, Z.; Ren, X.; Gu, Z.-G., *Chem. Commun.* **2016,** *52* (26), 4796.
327. Breuning, E.; Ruben, M.; Lehn, J.-M.; Renz, F.; Garcia, Y.; Ksenofontov, V.; Gütlich, P.; Wegelius, E.; Rissanen, K., *Angew. Chem. Int. Ed.* **2000,** *39* (14), 2504.
328. Matsumoto, T.; Newton, G. N.; Shiga, T.; Hayami, S.; Matsui, Y.; Okamoto, H.; Kumai, R.; Murakami, Y.; Oshio, H., *Nat. Commun.* **2014,** *5*.
329. Steinert, M.; Schneider, B.; Dechert, S.; Demeshko, S.; Meyer, F., *Inorg. Chem.* **2016,** *55* (5), 2363.
330. Dhers, S.; Mondal, A.; Aguilà, D.; Ramírez, J.; Vela, S.; Dechambenoit, P.; Rouzières, M.; Nitschke, J. R.; Clérac, R.; Lehn, J.-M., *J. Am. Chem. Soc.* **2018,** *140* (26), 8218.
331. Ruben, M.; Breuning, E.; Lehn, J.-M.; Ksenofontov, V.; Renz, F.; Gütlich, P.; Vaughan, G. B. M., *Chem. Eur. J.* **2003,** *9* (18), 4422.
332. Duriska, M. B.; Neville, S. M.; Moubaraki, B.; Cashion, J. D.; Halder, G. J.; Chapman, K. W.; Balde, C.; Létard, J.-F.; Murray, K. S.; Kepert, C. J.; Batten, S. R., *Angew. Chem. Int. Ed.* **2009,** *48* (14), 2549.
333. Duriska, M. B.; Neville, S. M.; Moubaraki, B.; Murray, K. S.; Balde, C.; Létard, J.-F.; Kepert, C. J.; Batten, S. R., *ChemPlusChem* **2012,** *77* (8), 616.
334. Struch, N.; Bannwarth, C.; Ronson Tanya, K.; Lorenz, Y.; Mienert, B.; Wagner, N.; Engeser, M.; Bill, E.; Puttreddy, R.; Rissanen, K.; Beck, J.; Grimme, S.; Nitschke Jonathan, R.; Lützen, A., *Angew. Chem. Int. Ed.* **2017,** *56* (18), 4930.
335. Kahn, O.; Martinez, C. J., *Science* **1998,** *279* (5347), 44.
336. Camarero, J.; Coronado, E., *J. Mater. Chem.* **2009,** *19* (12), 1678.
337. Shin, J. W.; Jeong, A. R.; Jeoung, S.; Moon, H. R.; Komatsumaru, Y.; Hayami, S.; Moon, D.; Min, K. S., *Chem. Commun.* **2018,** *54* (34), 4262.
338. Rotaru, A.; Gural'skiy, I. y. A.; Molnár, G.; Salmon, L.; Demont, P.; Bousseksou, A., *Chem. Commun.* **2012,** *48* (35), 4163.
339. Wang, J.-L.; Liu, Q.; Meng, Y.-S.; Liu, X.; Zheng, H.; Shi, Q.; Duan, C.-Y.; Liu, T., *Chem. Sci.* **2018,** *9* (11), 2892.
340. Han, W.-K.; Qin, L.-F.; Pang, C.-Y.; Cheng, C.-K.; Zhu, W.; Li, Z.-H.; Li, Z.; Ren, X.; Gu, Z.-G., *Dalton Trans.* **2017,** *46* (25), 8004.
341. Jornet-Mollá, V.; Duan, Y.; Giménez-Saiz, C.; Tang, Y.-Y.; Li, P.-F.; Romero, F. M.; Xiong, R.-G., *Angew. Chem. Int. Ed.* **2017,** *56* (45), 14052.
342. Dugay, J.; Aarts, M.; Giménez-Marqués, M.; Kozlova, T.; Zandbergen, H. W.; Coronado, E.; van der Zant, H. S. J., *Nano Lett.* **2017,** *17* (1), 186.
343. Dugay, J.; Giménez-Marqués, M.; Kozlova, T.; Zandbergen, H. W.; Coronado, E.; van der Zant, H. S. J., *Adv. Mater.* **2015,** *27* (7), 1288.
344. Lehmann, J.; Gaita-Arino, A.; Coronado, E.; Loss, D., *J. Mater. Chem.* **2009,** *19* (12), 1672.
345. Urdampilleta, M.; Ayela, C.; Ducrot, P.-H.; Rosario-Amorin, D.; Mondal, A.; Rouzières, M.; Dechambenoit, P.; Mathonière, C.; Mathieu, F.; Dufour, I.; Clérac, R., *Sci. Rep.* **2018,** *8* (1), 8016.

346. Reed, D. A.; Xiao, D. J.; Gonzalez, M. I.; Darago, L. E.; Herm, Z. R.; Grandjean, F.; Long, J. R., *J. Am. Chem. Soc.* **2016,** *138* (17), 5594.
347. Soyer, H.; Dupart, E.; Mingotaud, C.; Gomez-Garcia, C. J.; Delhaès, P., *Colloids Surf. A* **2000,** *171* (1), 275.
348. Soyer, H.; Mingotaud, C.; Boillot, M. L.; Delhaes, P., *Langmuir* **1998,** *14* (20), 5890.
349. Göbel, C.; Palamarciuc, T.; Lochenie, C.; Weber, B., *Chem. Asian J.* **2014,** *9* (8), 2232.
350. Otsubo, K.; Haraguchi, T.; Sakata, O.; Fujiwara, A.; Kitagawa, H., *J. Am. Chem. Soc.* **2012,** *134* (23), 9605.
351. Gonzalez-Prieto, R.; Fleury, B.; Schramm, F.; Zoppellaro, G.; Chandrasekar, R.; Fuhr, O.; Lebedkin, S.; Kappes, M.; Ruben, M., *Dalton Trans.* **2011,** *40* (29), 7564.
352. Seredyuk, M.; Gaspar, A. B.; Ksenofontov, V.; Galyametdinov, Y.; Kusz, J.; Gütlich, P., *J. Am. Chem. Soc.* **2008,** *130* (4), 1431.
353. Seredyuk, M.; Muñoz, M. C.; Ksenofontov, V.; Gütlich, P.; Galyametdinov, Y.; Real, J. A., *Inorg. Chem.* **2014,** *53* (16), 8442.
354. Grondin, P.; Roubeau, O.; Castro, M.; Saadaoui, H.; Colin, A.; Clérac, R., *Langmuir* **2010,** *26* (7), 5184.
355. Roubeau, O., *Chem. Eur. J.* **2012,** *18* (48), 15230.
356. Roubeau, O.; Colin, A.; Schmitt, V.; Clérac, R., *Angew. Chem. Int. Ed.* **2004,** *43* (25), 3283.
357. Kahn, O.; Martinez, C. J., *Science* **1998,** *279* (5347), 44.
358. Marchivie, M.; Guionneau, P.; Letard, J.-F.; Chasseau, D., *Acta Crystallogr. B* **2003,** *59* (4), 479.
359. Piguet, C., *J. Chem. Educ.* **1997,** *74* (7), 815.
360. Gatteschi, D.; Sessoli, R.; Villain, J., *Molecular Nanomagnets*. OUP Oxford: Oxford, England, **2006**.
361. Christou, G.; Gatteschi, D.; Hendrickson, D. N.; Sessoli, R., *MRS Bull.* **2011,** *25* (11), 66.
362. Meng, Y.-S.; Jiang, S.-D.; Wang, B.-W.; Gao, S., *Acc. Chem. Res.* **2016,** *49* (11), 2381.
363. Lis, T., *Acta Crystallogr. B* **1980,** *36* (9), 2042.
364. Sessoli, R.; Gatteschi, D.; Caneschi, A.; Novak, M. A., *Nature* **1993,** *365*, 141.
365. Neese, F.; Pantazis, D. A., *Faraday Discuss.* **2011,** *148*, 229.
366. Thomas, L.; Lionti, F.; Ballou, R.; Gatteschi, D.; Sessoli, R.; Barbara, B., *Nature* **1996,** *383*, 145.
367. Aromí, G.; Brechin, E. K., Synthesis of 3d Metallic Single-Molecule Magnets. In *Single-Molecule Magnets and Related Phenomena*, Winpenny, R., Ed. Springer Berlin Heidelberg: Berlin, Heidelberg, 2006; pp 1.
368. Milios, C. J.; Winpenny, R. E. P., Cluster-Based Single-Molecule Magnets. In *Molecular Nanomagnets and Related Phenomena*, Gao, S., Ed. Springer Berlin Heidelberg: Berlin, Heidelberg, 2015; pp 1.
369. Ako, A. M.; Hewitt, I. J.; Mereacre, V.; Clérac, R.; Wernsdorfer, W.; Anson, C. E.; Powell, A. K., *Angew. Chem. Int. Ed.* **2006,** *45* (30), 4926.
370. Goodwin, C. A. P.; Ortu, F.; Reta, D.; Chilton, N. F.; Mills, D. P., *Nature* **2017,** *548*, 439.
371. Guo, F.-S.; Day, B. M.; Chen, Y.-C.; Tong, M.-L.; Mansikkamäki, A.; Layfield, R. A., *Angew. Chem. Int. Ed.* **2017,** *56* (38), 11445.
372. Layfield, R. A., *Organometallics* **2014,** *33* (5), 1084.
373. Sessoli, R.; Powell, A. K., *Coord. Chem. Rev.* **2009,** *253* (19–20), 2328.
374. Woodruff, D. N.; Winpenny, R. E. P.; Layfield, R. A., *Chem. Rev.* **2013,** *113* (7), 5110.
375. Craig, G. A.; Murrie, M., *Chem. Soc. Rev.* **2015,** *44* (8), 2135.

376. Frost, J. M.; Harriman, K. L. M.; Murugesu, M., *Chem. Sci.* **2016,** *7* (4), 2470.
377. Murrie, M., *Chem. Soc. Rev.* **2010,** *39* (6), 1986.
378. Freedman, D. E.; Harman, W. H.; Harris, T. D.; Long, G. J.; Chang, C. J.; Long, J. R., *J. Am. Chem. Soc.* **2010,** *132* (4), 1224.
379. Mathonière, C.; Lin, H.-J.; Siretanu, D.; Clérac, R.; Smith, J. M., *J. Am. Chem. Soc.* **2013,** *135* (51), 19083.
380. Zadrozny, J. M.; Xiao, D. J.; Atanasov, M.; Long, G. J.; Grandjean, F.; Neese, F.; Long, J. R., *Nat. Chem.* **2013,** *5* (7), 577.
381. Feng, X.; Mathonière, C.; Jeon, I.-R.; Rouzières, M.; Ozarowski, A.; Aubrey, M. L.; Gonzalez, M. I.; Clérac, R.; Long, J. R., *J. Am. Chem. Soc.* **2013,** *135* (42), 15880.
382. Jin, X.-X.; Chen, X.-X.; Xiang, J.; Chen, Y.-Z.; Jia, L.-H.; Wang, B.-W.; Cheng, S.-C.; Zhou, X.; Leung, C.-F.; Gao, S., *Inorg. Chem.* **2018,** *57* (7), 3761.
383. Gatteschi, D.; Sessoli, R., *Angew. Chem. Int. Ed.* **2003,** *42* (3), 268.
384. Gómez-Coca, S.; Urtizberea, A.; Cremades, E.; Alonso, P. J.; Camón, A.; Ruiz, E.; Luis, F., *Nat. Commun.* **2014,** *5*, 4300.
385. Chen, L.; Zhou, J.; Cui, H.-H.; Yuan, A.-H.; Wang, Z.; Zhang, Y.-Q.; Ouyang, Z.-W.; Song, Y., *Dalton Trans.* **2018,** *47* (8), 2506.
386. Nemec, I.; Herchel, R.; Trávníček, Z., *Dalton Trans.* **2018,** *47* (5), 1614.
387. Varzatskii, O. A.; Penkova, L. V.; Kats, S. V.; Dolganov, A. V.; Vologzhanina, A. V.; Pavlov, A. A.; Novikov, V. V.; Bogomyakov, A. S.; Nemykin, V. N.; Voloshin, Y. Z., *Inorg. Chem.* **2014,** *53* (6), 3062.
388. Zhang, J.; Li, J.; Yang, L.; Yuan, C.; Zhang, Y.-Q.; Song, Y., *Inorg. Chem.* **2018,** *57* (7), 3903.
389. Villa-Pérez, C.; Oyarzabal, I.; Echeverría, G. A.; Valencia-Uribe, G. C.; Seco, J.; Soria, D. B., *Eur. J. Inorg. Chem.* **2016,** *2016* (29), 4835.
390. Novikov, V. V.; Pavlov, A. A.; Nelyubina, Y. V.; Boulon, M.-E.; Varzatskii, O. A.; Voloshin, Y. Z.; Winpenny, R. E. P., *J. Am. Chem. Soc.* **2015,** *137* (31), 9792.
391. Zadrozny, J. M.; Long, J. R., *J. Am. Chem. Soc.* **2011,** *133* (51), 20732.
392. Sottini, S.; Poneti, G.; Ciattini, S.; Levesanos, N.; Ferentinos, E.; Krzystek, J.; Sorace, L.; Kyritsis, P., *Inorg. Chem.* **2016,** *55* (19), 9537.
393. Boča, R.; Miklovič, J.; Titiš, J., *Inorg. Chem.* **2014,** *53* (5), 2367.
394. Buchholz, A.; Eseola, A. O.; Plass, W., *Comptes Rendus Chimie* **2012,** *15* (10), 929.
395. Ziegenbalg, S.; Hornig, D.; Görls, H.; Plass, W., *Inorg. Chem.* **2016,** *55* (8), 4047.
396. Mondal, A. K.; Parmar, V. S.; Biswas, S.; Konar, S., *Dalton Trans.* **2016,** *45* (11), 4548.
397. Gomez-Coca, S.; Cremades, E.; Aliaga-Alcalde, N.; Ruiz, E., *J. Am. Chem. Soc.* **2013,** *135* (18), 7010.
398. Cornia, A.; Rigamonti, L.; Boccedi, S.; Clérac, R.; Rouzières, M.; Sorace, L., *Chem. Commun.* **2014,** *50* (96), 15191.
399. Cole, K. S.; Cole, R. H., *J. Chem. Phys.* **1941,** *9* (4), 341.
400. Arts, F. M.; de Wijn, H. W.; van Duyneveldt, A. J.; Mydosh, J. A., *Phys. Rev. B* **1989,** *40*, 11243.
401. Liddle, S. T.; van Slageren, J., *Chem. Soc. Rev.* **2015,** *44* (19), 6655.
402. He, Z.; He, C.; Wang, Z.-M.; Gao, E.-Q.; Liu, Y.; Yan, C.-H., *Dalton Trans.* **2004,** (4), 502.
403. He, C.; Wu, X.; Kong, J.; liu, T.; Zhang, X.; Duan, C., *Chem. Commun.* **2012,** *48* (74), 9290.

404. He, C.; Lin, Z.; He, Z.; Duan, C.; Xu, C.; Wang, Z.; Yan, C., *Angew. Chem. Int. Ed.* **2008,** *47* (5), 877.
405. Wu, X.; Lin, Z.; He, C.; Duan, C., *New J. Chem.* **2012,** *36* (1), 161.
406. Sahoo, J.; Arunachalam, R.; Subramanian, P. S.; Suresh, E.; Valkonen, A.; Rissanen, K.; Albrecht, M., *Angew. Chem. Int. Ed.* **2016,** *55* (33), 9625.
407. Golla, U.; Adhikary, A.; Mondal, A. K.; Tomar, R. S.; Konar, S., *Dalton Trans.* **2016,** *45* (29), 11849.
408. Gusev, A. N.; Shul´gin, V. F.; Efimov, N. N.; Minin, V. V.; Aleksandrov, G. G.; Eremenko, I. L., *Russ. Chem. Bull.* **2015,** *64* (8), 1891.
409. Gusev, A. N.; Shul'gin, V. F.; Zamnius, E. A.; Ricci, M.; Minin, V. V.; Aleksandrov, G. G.; Eremenko, I. L.; Linert, W., *Inorg. Chim. Acta* **2015,** *430*, 120.
410. Arunachalam, R.; Chinnaraja, E.; Valkonen, A.; Rissanen, K.; Sen, S. K.; Natarajan, R.; Subramanian, P. S., *Inorg. Chem.* **2018**.
411. Wang, J.; Wu, H.; He, C.; Zhao, L.; Duan, C., *Chem. Asian J.* **2011,** *6* (5), 1225.
412. Wu, H.; He, C.; Lin, Z.; Liu, Y.; Duan, C., *Inorg. Chem.* **2009,** *48* (2), 408.
413. Zhao, L.; Wei, J.; Lu, J.; He, C.; Duan, C., *Angew. Chem. Int. Ed.* **2017,** *56* (30), 8692.
414. Zhao, L.; Niel, V.; Thompson, L. K.; Xu, Z.; Milway, V. A.; Harvey, R. G.; Miller, D. O.; Wilson, C.; Leech, M.; Howard, J. A. K.; Heath, S. L., *Dalton Trans.* **2004,** (9), 1446.
415. Rosario-Amorin, D.; Dechambenoit, P.; Bentaleb, A.; Rouzières, M.; Mathonière, C.; Clérac, R., *J. Am. Chem. Soc.* **2018,** *140* (1), 98.
416. Bernstein, J.; Davis, R. E.; Shimoni, L.; Chang, N.-L., *Angew. Chem. Int. Ed.* **1995,** *34* (15), 1555.
417. Etter, M. C., *Acc. Chem. Res.* **1990,** *23* (4), 120.
418. Van der Sluis, P.; Spek, A. L., *Acta Crystallogr. A* **1990,** *A46* (3), 194.
419. Spek, A. L. *PLATON, A Multipurpose Crystallographic Tool*, Utrecht University: Utrecht, The Netherlands, 2008.
420. Dolomanov, O. V.; Bourhis, L. J.; Gildea, R. J.; Howard, J. A. K.; Puschmann, H., *J. Appl. Crystallogr.* **2009,** *42* (2), 339.
421. Egli, M.; Sarkhel, S., *Acc. Chem. Res.* **2007,** *40* (3), 197.
422. Vantomme, G.; Jiang, S.; Lehn, J.-M., *J. Am. Chem. Soc.* **2014,** *136* (26), 9509.
423. Niel, V.; Milway, V. A.; Dawe, L. N.; Grove, H.; Tandon, S. S.; Abedin, T. S. M.; Kelly, T. L.; Spencer, E. C.; Howard, J. A. K.; Collins, J. L.; Miller, D. O.; Thompson, L. K., *Inorg. Chem.* **2008,** *47* (1), 176.
424. Wilson, B. H.; Scott, H. S.; Qazvini, O. T.; Telfer, S. G.; Mathonière, C.; Clérac, R.; Kruger, P. E., *Chem. Commun.* **2018,** *54* (95), 13391.
425. Aaron, D.; Tsouris, C., *Sep. Sci. Technol.* **2005,** *40* (1-3), 321.
426. Maji, T. K.; Matsuda, R.; Kitagawa, S., *Nat. Mater.* **2007,** *6*, 142.
427. Ok, K. M.; Sung, J.; Hu, G.; Jacobs, R. M. J.; O'Hare, D., *J. Am. Chem. Soc.* **2008,** *130* (12), 3762.
428. Zhang, Z.; Zhao, Y.; Gong, Q.; Li, Z.; Li, J., *Chem. Commun.* **2013,** *49* (7), 653.
429. Zheng, B.; Bai, J.; Duan, J.; Wojtas, L.; Zaworotko, M. J., *J. Am. Chem. Soc.* **2011,** *133* (4), 748.
430. Scott, H. S.; Ogiwara, N.; Chen, K.-J.; Madden, D. G.; Pham, T.; Forrest, K.; Space, B.; Horike, S.; Perry Iv, J. J.; Kitagawa, S.; Zaworotko, M. J., *Chem. Sci.* **2016,** *7* (8), 5470.

431. Chen, K.-J.; Scott, Hayley S.; Madden, David G.; Pham, T.; Kumar, A.; Bajpai, A.; Lusi, M.; Forrest, Katherine A.; Space, B.; Perry, John J.; Zaworotko, Michael J., *Chem* **2016,** *1* (5), 753.
432. Sheldrick, G., *Acta Crystallogr. A* **2015,** *71* (1), 3.
433. Sheldrick, G. M. *SHELXL-97, Programs for X-ray Crystal Structure Refinement*, University of Gottingen, 1997.
434. Sharma, S.; Hundal, M. S.; Walia, A.; Vanita, V.; Hundal, G., *Org. Biomol. Chem.* **2014,** *12* (25), 4445.
435. Song, C.; Ling, Y.; Feng, Y.; Zhou, W.; Yildirim, T.; He, Y., *Chem. Commun.* **2015,** *51* (40), 8508.
436. Lifshits, L. M.; Zeller, M.; Campana, C. F.; Klosterman, J. K., *Cryst. Growth Des.* **2017,** *17* (10), 5449.
437. Kraft, A., *J. Chem. Soc., Perkin Trans. 1* **1999,** (6), 705.
438. McCormick, L. J.; Morris, S. A.; Teat, S. J.; McPherson, M. J.; Slawin, A. M. Z.; Morris, R. E., *Dalton Trans.* **2015,** *44* (40), 17686.
439. Peng, Y.; Mereacre, V.; Anson, C. E.; Zhang, Y.; Bodenstein, T.; Fink, K.; Powell, A. K., *Inorg. Chem.* **2017,** *56* (11), 6056.
440. Malina, J.; Hannon, M. J.; Brabec, V., *Nucleic Acids Res.* **2008,** *36* (11), 3630.
441. Sessoli, R.; Boulon, M.-E.; Caneschi, A.; Mannini, M.; Poggini, L.; Wilhelm, F.; Rogalev, A., *Nat. Phys.* **2014,** *11*, 69.
442. Srinivasan, A.; Cortijo, M.; Bulicanu, V.; Naim, A.; Clérac, R.; Sainctavit, P.; Rogalev, A.; Wilhelm, F.; Rosa, P.; Hillard, E. A., *Chem. Sci.* **2018,** *9* (5), 1136.
443. Kurbah, S. D.; Kumar, A.; Sanentiba Ozukum, O.; Syiemlieh, I.; Lal, R. A., *J. Coord. Chem.* **2017,** *70* (17), 2969.
444. Basumatary, D.; Lal, R. A.; Kumar, A., *J. Mol. Struct.* **2015,** *1092*, 122.
445. Gaspar, A. B.; Muñoz, M. C.; Real, J. A., *J. Mater. Chem.* **2006,** *16* (26), 2522.
446. Gusev, A. N.; Shul'gin, V. F.; Riush, I. O.; Lyssenko, K. A.; Eremenko, I. L.; Linert, W., *Inorg. Chim. Acta* **2017,** *456*, 136.
447. Yan, Z.; Liu, W.; Peng, Y.-Y.; Chen, Y.-C.; Li, Q.-W.; Ni, Z.-P.; Tong, M.-L., *Inorg. Chem.* **2016,** *55* (10), 4891.
448. Staniland, R. W. *The Synthesis and Magnetic Properties of Metallosupramolecular Tetrahedral Cages and Cubes*. University of Canterbury, **2017**.
449. Sinitskiy, A. V.; Tchougréeff, A. L.; Dronskowski, R., *PCCP* **2011,** *13* (29), 13238.
450. Scott, H. S.; Ross, T. M.; Chilton, N. F.; Gass, I. A.; Moubaraki, B.; Chastanet, G.; Paradis, N.; Lètard, J.-F.; Vignesh, K. R.; Rajaraman, G.; Batten, S. R.; Murray, K. S., *Dalton Trans.* **2013,** *42* (47), 16494.
451. Fitzpatrick, A. J.; Martinho, P. N.; Gildea, B. J.; Holbrey, J. D.; Morgan, G. G., *Eur. J. Inorg. Chem.* **2015,** *2016* (13-14), 2025.
452. Hayami, S.; Moriyama, R.; Shigeyoshi, Y.; Kawajiri, R.; Mitani, T.; Akita, M.; Inoue, K.; Maeda, Y., *Inorg. Chem.* **2005,** *44* (21), 7295.
453. Hayami, S.; Moriyama, R.; Shuto, A.; Maeda, Y.; Ohta, K.; Inoue, K., *Inorg. Chem.* **2007,** *46* (19), 7692.
454. Delgado, T.; Tissot, A.; Guénée, L.; Hauser, A.; Valverde-Muñoz, F. J.; Seredyuk, M.; Real, J. A.; Pillet, S.; Bendeif, E.-E.; Besnard, C., *J. Am. Chem. Soc.* **2018,** *140* (40), 12870.
455. Hayami, S.; Shigeyoshi, Y.; Akita, M.; Inoue, K.; Kato, K.; Osaka, K.; Takata, M.; Kawajiri, R.; Mitani, T.; Maeda, Y., *Angew. Chem. Int. Ed.* **2005,** *44* (31), 4899.

456. Gaspar, A. B.; Seredyuk, M., *Coord. Chem. Rev.* **2014,** *268*, 41.
457. Gray, G. W., *Philos. Trans. Royal Soc. A* **1983,** *309* (1507), 77.
458. Taugerbeck, A.; Booth, C. J., *Design and Synthesis of Chiral Nematic Liquid Crystals*. Wiley: **2014**.
459. Kawano, S.-i.; Kato, M.; Soumiya, S.; Nakaya, M.; Onoe, J.; Tanaka, K., *Angew. Chem. Int. Ed.* **2017,** *57* (1), 167.
460. Kawano, S.-i.; Murai, T.; Harada, T.; Tanaka, K., *Inorg. Chem.* **2018,** *57* (7), 3913.
461. Lipiäinen, T.; Fraser-Miller, S. J.; Gordon, K. C.; Strachan, C. J., *J. Pharm. Biomed. Anal.* **2018,** *149*, 343.
462. Mah, P. T.; Fraser, S. J.; Reish, M. E.; Rades, T.; Gordon, K. C.; Strachan, C. J., *Vib. Spectrosc* **2015,** *77*, 10.
463. Kerckhoffs, J. M. C. A.; Peberdy, J. C.; Meistermann, I.; Childs, L. J.; Isaac, C. J.; Pearmund, C. R.; Reudegger, V.; Khalid, S.; Alcock, N. W.; Hannon, M. J.; Rodger, A., *Dalton Trans.* **2007,** (7), 734.
464. Hooper, D. C.; Mark, A. G.; Kuppe, C.; Collins, J. T.; Fischer, P.; Valev, V. K., *Adv. Mater.* **2017,** *29* (13), 1605110.
465. Iazzolino, A.; Ould Hamouda, A.; Naïm, A.; Stefánczyk, O.; Rosa, P.; Freysz, E., *Appl. Phys. Lett.* **2017,** *110* (16), 161908.
466. Naim, A.; Bouhadja, Y.; Cortijo, M.; Duverger-Nédellec, E.; Flack, H. D.; Freysz, E.; Guionneau, P.; Iazzolino, A.; Ould Hamouda, A.; Rosa, P.; Stefańczyk, O.; Valentín-Pérez, Á.; Zeggar, M., *Inorg. Chem.* **2018,** *57* (23), 14501.